

NASA/CP—1999—208598



## **20th Space Simulation Conference The Changing Testing Paradigm**

*Compiled by  
Joseph L. Stecher III*

*Proceedings of a conference held at  
the Holiday Inn Annapolis  
Annapolis, Maryland  
October 27–29, 1998*

National Aeronautics and  
Space Administration

**Goddard Space Flight Center**  
Greenbelt, Maryland 20771

---

February 1999

## The NASA STI Program Office ... in Profile

Since its founding, NASA has been dedicated to the advancement of aeronautics and space science. The NASA Scientific and Technical Information (STI) Program Office plays a key part in helping NASA maintain this important role.

The NASA STI Program Office is operated by Langley Research Center, the lead center for NASA's scientific and technical information. The NASA STI Program Office provides access to the NASA STI Database, the largest collection of aeronautical and space science STI in the world. The Program Office is also NASA's institutional mechanism for disseminating the results of its research and development activities. These results are published by NASA in the NASA STI Report Series, which includes the following report types:

- **TECHNICAL PUBLICATION.** Reports of completed research or a major significant phase of research that present the results of NASA programs and include extensive data or theoretical analysis. Includes compilations of significant scientific and technical data and information deemed to be of continuing reference value. NASA's counterpart of peer-reviewed formal professional papers but has less stringent limitations on manuscript length and extent of graphic presentations.
- **TECHNICAL MEMORANDUM.** Scientific and technical findings that are preliminary or of specialized interest, e.g., quick release reports, working papers, and bibliographies that contain minimal annotation. Does not contain extensive analysis.
- **CONTRACTOR REPORT.** Scientific and technical findings by NASA-sponsored contractors and grantees.
- **CONFERENCE PUBLICATION.** Collected papers from scientific and technical conferences, symposia, seminars, or other meetings sponsored or cosponsored by NASA.
- **SPECIAL PUBLICATION.** Scientific, technical, or historical information from NASA programs, projects, and mission, often concerned with subjects having substantial public interest.
- **TECHNICAL TRANSLATION.** English-language translations of foreign scientific and technical material pertinent to NASA's mission.

Specialized services that complement the STI Program Office's diverse offerings include creating custom thesauri, building customized databases, organizing and publishing research results . . . even providing videos.

For more information about the NASA STI Program Office, see the following:

- Access the NASA STI Program Home Page at <http://www.sti.nasa.gov/STI-homepage.html>
- E-mail your question via the Internet to [help@sti.nasa.gov](mailto:help@sti.nasa.gov)
- Fax your question to the NASA Access Help Desk at (301) 621-0134
- Telephone the NASA Access Help Desk at (301) 621-0390
- Write to:  
NASA Access Help Desk  
NASA Center for AeroSpace Information  
7121 Standard Drive  
Hanover, MD 21076-1320

NASA/CP—1999–208598



## **20th Space Simulation Conference The Changing Testing Paradigm**

*Compiled by  
Joseph L. Stecher III  
NASA Goddard Space Flight Center, Greenbelt, Maryland*

Sponsored by:  
National Aeronautics and Space Administration  
Institute of Environmental Sciences and Technology  
American Institute for Aeronautics and Astronautics  
American Society for Testing and Materials  
Canadian Space Agency

National Aeronautics and  
Space Administration  
  
**Goddard Space Flight Center**  
Greenbelt, Maryland 20771

---

February 1999

Available from:

NASA Center for AeroSpace Information  
7121 Standard Drive  
Hanover, MD 21076-1320  
Price Code: A17

National Technical Information Service  
5285 Port Royal Road  
Springfield, VA 22161  
Price Code: A10

# COMMITTEES FOR 20TH SPACE SIMULATION CONFERENCE

## MEETING MANAGEMENT COMMITTEE

|                          |   |
|--------------------------|---|
| General Chairman:        | Alda Simpson, NASA's Goddard Space Flight Center                          |
| Technical Program:       | John D. Hazen, Boeing Information Space and Defense Systems Group         |
| IES Meeting Chair:       | John D. Campbell, Consultant  |
| Publication Chairman:    | Joseph L. Stecher III, NASA's Goddard Space Flight Center                 |
| IEST Executive Director: | Julie Kendrick, Institute of Environmental Sciences and Technology        |
| Facilities Chairman:     | Russell T. Hollingsworth, Consultant                                      |
| Tutorial Co-Chair:       | John Packard, Mantech/NSI   |
| Tutorial Co-Chair:       | William O. Wilkinson, Johns Hopkins University Applied Physics Laboratory |
| Publicity Chairman:      | Harold G. Fox, Johns Hopkins University Applied Physics Laboratory        |

## TECHNICAL PROGRAM COMMITTEE

Dr. Raj K. Singhal, Canadian Space Agency  
Peter W. Brinkman, ESA/ESTEC  
Robert L. Tomkiewicz, Johns Hopkins University, Applied Physics Laboratory  
Terry C. Fisher, Jet Propulsion Laboratory  
Gregory F. Proulx, Hughes Space and Communications  
Robert G. Moss, Space Systems/Loral  
Patrick F. Neary, TRW  
William N. Breeden III, Lockheed Martin Astronautics

## JOINT POLICY COMMITTEE

### IES

John D. Campbell, Consultant  
Joseph L. Stecher III, NASA's Goddard Space Flight Center

### ASTM

Robert G. Moss, Space Systems/Loral  
Eugene N. Borson, Consultant

### AIAA

Terry Fisher, Jet Propulsion Laboratory



# TABLE OF CONTENTS

---

## SESSION 1A: MATERIALS /CONTAMINATION

---

|   |    |
|---|----|
| Innovative Contamination Certification of Multi-Mission Flight Hardware .....                     | 1  |
| <i>P.A. Hansen, D.W. Hughes, K.M. Montt, and J.J. Triolo</i>                                      |    |
| †Water Outgassing from Multi-Layer Insulation Blankets as a Diffusion<br>Controlled Process ..... | 15 |
| <i>D.M. Silver</i>  |    |
| Contamination Control for Environmental Tests on Optical Instruments .....                        | 17 |
| <i>F. Resch and C. Wuersching</i>   |    |

---

## SESSION 1B: MATERIALS /CONTAMINATION (continued)

---

|  |    |
|--|----|
| Moisture Content and Desorption Rate of a GR/EP Honeycomb Panel .....                                | 25 |
| <i>A.L. Lee</i>  |    |
| Statistical Evaluation of Molecular Contamination During Spacecraft Thermal<br>Vacuum Test .....     | 35 |
| <i>P. Chen, R. Hedgeland, A. Montoya, J. Roman-Velazquez, J. Dunn,<br/>J. Colony, and J. Petitto</i> |    |

---

## SESSION 2: DYNAMIC TESTING

---

|  |    |
|--|----|
| Challenging Pneumatic Requirements for Acoustic Testing of the Second Stage<br>for the New Delta III Rocket .....                    | 47 |
| <i>A. Webb</i>   |    |
| Potential and Limitations of the Modal Characterization of a Spacecraft Bus Structure<br>by Means of Active Structure Elements ..... | 59 |
| <i>A.M. Grillenbeck, S.A. Dillinger, and K.B. Elliott</i>  |    |
| Mechanical Flight Qualification Testing of the Advanced Composition Explorer<br>Observatory .....                                    | 71 |
| <i>T.M. Betenbaugh</i>   |    |

---

## SESSION 3: PROGRAM/SYSTEM TESTING REQUIREMENTS

---

|   |     |
|---|-----|
| Structural Weld Leak Testing in Support of the International Space Station Node 1,<br>Airlock, and Laboratory Flight Elements ..... | 105 |
| <i>S.D. Underwood and A. Holt</i>   |     |

† Abstract only

|  |     |
|--|-----|
| A New Thermal Vacuum Facility for Hughes Space and Communications<br>at El Segundo, California . . . . . | 113 |
| <i>R.N. Watson, and G.F. Proulx</i>  |     |
| Leak Rate Testing of the International Space Station Hatch in a Thermal Vacuum<br>Environment . . . . .  | 131 |
| <i>A. Holt and S.D. Underwood</i>  |     |
| International Space Station Node 1 Helium Accumulation Leak Rate Test . . . . .                          | 141 |
| <i>S.D. Underwood and A. Holt</i>  |     |
| Cable Bundle Wire Derating . . . . .   | 149 |
| <i>R.A. Lundquist and H. Leidecker</i>   |     |

---

**SESSION 4: THERMAL VACUUM TESTING**

---

|   |     |
|---|-----|
| Environmental Testing at Different Levels of the Sevirii Payload of the ESA<br>“Meteosat Second Generation” Program . . . . . | 159 |
| <i>R.A. Blanco, M. Montz, and M. Gill</i>   |     |
| Thermal Vacuum Testing of the Mars Surveyor Program and Stardust Spacecraft . . . . .   | 173 |
| <i>W.N. Breeden III</i>   |     |
| A New Method for Thermal Vacuum Tests Telecommunication Spacecraft—<br>The Simulation of Thermal Sink . . . . .               | 189 |
| <i>J.-L. Marcé, J. Merlet, Y. Charles, B. Poulain, and J. Gayraud</i>   |     |

---

**SESSION 5A: MATERIAL DEGRADATION IN ORBIT**

---

|  |     |
|--|-----|
| Atomic Oxygen Effects on Seal Leakage . . . . .  | 195 |
| <i>J.R. Christensen, S.D. Underwood, R. R. Kamenetzky, and J.A. Vaughn</i>   |     |
| Radiation Induced Degradation of White Thermal Control Paint . . . . .   | 207 |
| <i>D.L. Edwards, J.M. Zwiener, G.E. Wertz, J.A. Vaughn, R.R. Kamenetzky,<br/>M.M. Finckenor, and M.J. Meshishnek</i> |     |
| On-Orbit Teflon® FEP Degradation . . . . .   | 219 |
| <i>J.A. Townsend, P.A. Hansen, and J.A. Dever</i>  |     |
| Ground Simulation of Space Radiation Effects of Materials: Status of the<br>Proposed ISO Standard . . . . .          | 233 |
| <i>B.A. Briskman and E.N. Borson</i>   |     |

---

**SESSION 5B: MATERIAL DEGRADATION IN ORBIT (continued)**

---

Degradation of Teflon® FEP Following Charged Particle Radiation and Rapid Thermal Cycling ..... 247  
*J.A. Townsend, C. Powers, M. Viens, M. Ayers-Treusdell, and B. Munoz*

Effect of X-rays on the Mechanical Properties of Aluminized FEP Teflon® ..... 257  
*J.R. Gaier, M.R. Brinkmeier, and E.M. Gaier*

---

**SESSION 6: NEW APPROACHES AND FACILITIES**

---

The New Quality Assurance System of the ESA/ESTEC Environmental Test Center ..... 269  
*P.W. Brinkman and M. Panicucci*

A High Altitude Space Simulation Facility to Study Exhaust Plume Interactions and Contamination ..... 285  
*A.D. Ketsdever, F. Lufy, S.E. Vargo, and E.P. Muntz*

Portable Microvibration Test Facility for Spacecrafts ..... 303  
*G. Martín*

The U.S. Air Force Research Laboratory's Newly Upgraded SCEPTRE Facility ..... 311  
*C.A. Cerbus*

Refurbishment and Automation of the Thermal/Vacuum Facilities at the Goddard Space Flight Center ..... 319  
*J.T. Donohue, C. Johnson, R. Ogden, and J. Suson*

---

**SESSION 7: SPECIAL TOPICS**

---

Simulated Space Debris Impact Experiments on Toughened Laminated Thin Solar Cell Cover Glass ..... 323  
*R. Roybal, P. Tlomak, C. Stein, and P.H. Stokes*

Small-Scale Digital Photogrammetry in a Cryogenic Vacuum Environment ..... 333  
*R.E. Pazar*

Hypervelocity Meteorite Impact Simulation ..... 341  
*S. Ben-Shumel and S. Goldstein*

The MISTRAL Antenna Measurement Compact Range at INTESPACE ..... 355  
*R. Bergé, J.-L. Marcé, and P. Meisse*



# **INNOVATIVE CONTAMINATION CERTIFICATION OF MULTI-MISSION FLIGHT HARDWARE**

**Patricia A. Hansen**  
NASA, Goddard Space Flight Center

**David W. Hughes, Kristina M. Montt, and Jack J. Triolo**  
Swales Aerospace

## **ABSTRACT**

Maintaining contamination certification of multi-mission flight hardware is an innovative approach to controlling mission costs. Methods for assessing ground induced degradation between missions have been employed by the Hubble Space Telescope (HST) Project for the multi-mission (servicing) hardware. By maintaining the cleanliness of the hardware between missions, and by controlling the materials added to the hardware during modification and refurbishment both project funding for contamination recertification and schedule have been significantly reduced. These methods will be discussed and HST hardware data will be presented.

## **INTRODUCTION**

The Hubble Space Telescope (HST) was designed to be periodically serviced on-orbit during its 15 year mission. The Space Transportation System (STS) serves as the platform from which the HST is serviced and servicing carriers provide an interface from the Orbiter to the scientific instruments and orbital replacement units. While the servicing carriers are configured for each mission to accommodate mission unique orbital replacement units, the basic carrier (structure and support airborne flight equipment) remains unchanged. The HST servicing carriers were flown during the HST Servicing Mission 1 (SM1), STS-61 (December 1993) and the HST SM2, STS-82 (February 1997). Currently, the servicing carriers are being reconfigured for the HST SM3 (May 2000).

Due to the extreme sensitivity of the HST, scientific instrument, orbital replacement unit optics to molecular and particulate contamination, all aspects of a servicing mission are assessed for subsequent contamination effects to these optical elements. The assessment begins with the basic requirements for the telescope and extends to each mission component. Because of the large surface area of the servicing carriers, both outgassing levels and surface cleanliness levels are controlled during all aspects of integration, test, launch activities, and on-orbit operations.

By maintaining the cleanliness of the hardware between missions, and by controlling the materials added to the hardware during modification and refurbishment both project funding for contamination recertification and schedule have been significantly reduced. These methods will be discussed and HST hardware data will be presented.

## SERVICING CARRIER DESCRIPTION

The HST servicing carriers include: the Solar Array Carrier (SAC), the Orbital Replacement Unit Carrier (ORUC), the Flight Support System (FSS), the Rigid Array Carrier (RAC), the Second Axial Carrier (SAC), and the Multi-Use Lightweight Experiment (MULE). The carriers are shown in Figures 1-6 and the servicing mission manifest is illustrated in Table 1. The 15' long x 15' wide x 15' high Solar Array Carrier functioned as a load isolation system for the Solar Array 2 during the First Servicing Mission. For the Second Servicing Mission, the Solar Array Carrier was reconfigured, renamed the Second Axial Carrier, and provided a load isolation system for the Axial Scientific Instrument Protective Enclosure which in turn provided a contamination and thermally controlled environment for the Near Infrared Cosmic Origins Spectrograph (NICMOS).

Table 1. Carrier Mission Manifest

| Carrier                          | SM1 | SM2 | SM3 | SM4 |
|----------------------------------|-----|-----|-----|-----|
| Flight Support System            | ✓   | ✓   | ✓   | ✓   |
| Multi-Use Lightweight Explorer   |     |     | ✓   |     |
| Orbital Replacement Unit Carrier | ✓   | ✓   | ✓   | ✓   |
| Rigid Array Carrier              |     |     | ✓   |     |
| Second Axial Carrier             |     | ✓   |     |     |
| Solar Array Carrier              | ✓   |     |     |     |
| Unidentified Carrier(s)          |     |     |     | ✓   |

For the Third Servicing Mission, the Rigid Array Carrier, Orbital Replacement Unit Carrier, Flight Support System, and Multi-Use Lightweight Explorer have been manifested and are shown in the flight configuration in Figure 7. The Rigid Array Carrier and Orbital Replacement Unit Carrier are Spacehab pallets that have been modified to provide scientific instrument and orbital replacement unit stowage for the servicing mission. The 12' long x 15' wide x 15' high Rigid Array carrier functions as a load isolation system for the Solar Array 3 and will be used to stow the replaced Solar Array 2 during two extravehicular activity (EVA) days. The most contamination sensitive carrier is the 12' long x 15' wide x 15' high ORUC. The Orbital

Replacement Unit Carrier provides a load isolation system for an Axial Scientific Instrument Protective Enclosure (SIPE) and the Fine Guidance Sensor SIPE. These SIPEs, collectively known as the BISIPE, provide a contamination and thermally controlled environment for a stowed scientific instrument and Fine Guidance Sensor. Because of the optical sensitivity of the NICMOS, scientific instruments, and Fine Guidance Sensors, the Second Axial Carrier and the Orbital Replacement Unit Carrier are the most contamination sensitive carriers. The 5' long x 15' wide x 15' high Flight Support System is used as the maintenance platform to berth the HST to the Orbiter during the EVAs. The 5' long x 15' wide x 15' high Multi-Use Lightweight Explorer provides stowage for orbital replacement units and is shown with the Aft Shroud Cooling System radiators mounted.

The SIPEs provide a thermal environment equivalent to that inside the HST. The warm thermal environment not only ensures that the scientific instruments and Fine Guidance Sensors will remain within their temperature limits during the EVA. This also ensures that any outgassing inside the SIPEs, which would otherwise affect the optical performance, will not condense on the scientific instruments or Fine Guidance Sensors. The SIPEs also provide a purge interface, which allows the scientific instruments and Fine Guidance Sensors to be purged until launch (T-0). Vent restrictor plates (37  $\mu\text{m}$  mesh) inhibit particulate contamination of the scientific instruments or Fine Guidance Sensors during all ground and launch activities.

Due to the diversity of the orbital replacement units and scientific instruments manifested for each flight, the carriers provide the most flexible stowage capability for the servicing mission hardware. Because of this flexibility, two carriers will be flown for all planned servicing missions – the Orbital Replacement Unit Carrier and the Flight Support System. Because of the planned multiple missions of the Orbital Replacement Unit Carrier and Flight Support System over a decade, the HST contamination control program looked at the “big picture” to determine the most cost effective contamination control approach that both provides the needed contamination controlled environment for the scientific instruments and Fine Guidance Sensors while controlling cost. Because of the excessive cost and schedule required to recertify the molecular outgassing levels of the individual carriers for each servicing mission, the HST contamination control program looked at innovative methods to alleviate the recertification of the carriers for each mission. Controlling the material added to the carriers and individually certifying new hardware prior to integration onto the carrier accomplished this. The storage, integration and test environment is also controlled, with the carriers spending the majority of these activities in a Class 10,000 (M 5.5) cleanroom. When not in the cleanroom, the carriers are double bagged. During storage, the carriers are cleaned periodically to maintain the surface cleanliness levels.

## **SERVICING MISSION CONTAMINATION PROGRAM**

The servicing missions are complex and require that the telescope be exposed to the Orbiter (including carriers) environment during the installation of the scientific instruments and Fine Guidance Sensors into the HST Aft Shroud. This exposure is typically from one to seven hours. During the scientific instrument installation, one EVA crewmember (i.e., an astronaut) enters the Aft Shroud to guide both the old instrument out of the telescope and the new instrument into the telescope. Because of this exposure and to maintain the Ultraviolet (UV) capabilities of the

telescope, the contamination requirements placed on both the Orbiter and carriers are quite stringent. While one might argue that the scientific instrument is the most contamination sensitive element, in reality, maintaining the low contamination flux in the telescope's optical path is the primary contamination requirement.

Neither the Orbiter nor the extravehicular mobility unit (space suit) contamination levels can be verified by methods other than by visual examination. Outgassing levels are not measured, and by the nature of Orbiter, many materials generally not used around sensitive hardware are used for performance. Where possible, materials which are verified to be high outgassing, which would not impact the Orbiter performance have been removed for the HST servicing missions. In addition, a best effort is made to control contamination during Orbiter processing activities.

Ground processing activities, Orbiter integration and the overall mission activities are assessed for subsequent contamination effects to the HST and the scientific instruments and Fine Guidance Sensors for each servicing mission. This assessment begins with the basic requirements for the HST and extended to each mission component. An overall contamination budget is developed which allocates acceptable degradation among mission phases. The servicing mission cleanliness requirements and budgets are set with respect to hardware line-of-sight views of sensitive surfaces, purging of the scientific instruments for sustaining critical element functional lifetime, Orbiter and EVA effects, Orbiter cleanliness, cleanroom protocol, and Kennedy Space Center integration activities.

Prior to each servicing mission, the HST contamination control philosophy is reviewed to determine its applicability to reflown carrier hardware, new scientific instruments, new orbital replacement units, and HST optical performance. The current contamination control program evolved from both the SM1 and SM2 program and has been updated for SM3 based on post-mission results (1, 2). The servicing carriers met stringent outgassing requirements prior to SM1, and the integrity of the outgassing certification of the carriers have been maintained for both SM2 and SM3. Only new carriers, and significantly reworked contamination sensitive hardware, such as the SIPLEs, are certified to the required outgassing rate prior to a servicing mission.

## **Telescope and Scientific Instrument Requirements**

To maintain the UV performance of the telescope and therefore, the scientific instruments, the telescope contamination requirements address both the surface level cleanliness of the Primary and Secondary mirror and the allowable outgassing flux rate for the telescope's optical path (known as the hub area). The scientific instrument requirements are based on the optical sensitivity of the scientific instrument.

### **Primary and Secondary Mirrors**

The particulate contamination requirements are less than a 5 percent maximum area coverage for the summation of the Primary and Secondary Mirrors. This was determined pre-launch by measuring the obscuration ratio of optical witness mirrors. To date, no scientific instrument data has indicated that this requirement has been violated.

The molecular contamination requirement is less than a 10 percent decrease in reflectance at Lyman-Alpha (1216 Angstrom) wavelengths on the Primary and Secondary Mirrors after 5 years on-orbit. This was determined pre-launch by measuring optical witness mirrors. Neither integrated nor periodic measurements indicated that this requirement had been violated. The initial outgassing criteria was  $4.33 \times 10^{-13}$  g/cm<sup>2</sup>-s flux as measured with the mirrors at nominal operating temperatures and the collector at -20°C. The optical witness mirror reflectance degradation also needed to be less than 3 percent at Lyman-Alpha wavelengths.

#### Hub Area

The light path of the telescope is referred to as the hub area. The four axial and one radial scientific instrument apertures, the three Fine Guidance Sensor apertures and the back of the primary mirror define this area. To control the amount of contamination entering this area and to prevent cross contamination, contamination requirements are flowed down to the scientific instruments and Fine Guidance Sensors. The outgassing rate from an instrument aperture or a Fine Guidance Sensor aperture into the hub area cannot exceed  $1.32 \times 10^{-9}$  g/sec. The Fine Guidance Sensor's outgassing rate is measured with the instrument at worse case hot operational temperatures (approximately 25°C) and the collector at -65°C. Similarly, the surface level contamination requirements for any item entering the telescope are Level 400B per MIL-STD 1246.

#### Aft Shroud

Four axial scientific instruments are installed in the Aft Shroud. To control the amount of contamination entering this area and to prevent cross contamination, the scientific instruments must meet minimum surface level cleanliness and outgassing requirements. The scientific instrument exterior surface cleanliness level shall not exceed 400B per MIL-STD 1246. The outgassing requirement measured at the scientific instruments aft vent cannot exceed an equivalent rate of  $1.56 \times 10^{-9}$  g/hr-cm<sup>2</sup> based on the exterior surface area of the instrument. This outgassing rate is measured with the scientific instrument ten degrees above the worse case hot operational temperatures and the collector at -20°C. While the largest percentage of the outgassed products is vented through the telescope's aft vents, there is a small probability that an instrument could increase the flux in the hub area, affecting the telescope's performance.

#### Scientific Instruments and Fine Guidance Sensors

The scientific instruments and Fine Guidance Sensors have individual contamination requirements based on their optical sensitivity. For example, scientific instruments viewing in the UV wavelength regions would have the most sensitivity to molecular contamination. While those scientific instruments viewing in the infrared wavelength regions would have the greatest sensitivity to particulate contamination. The scientific instruments and Fine Guidance Sensors are delivered to NASA with verification of internal contamination levels. These levels are maintained throughout the integration, test and launch activities through contamination controls such as a gaseous Nitrogen purge.

## **Orbiter and EVA Effects**

In addition to many hardware cleanliness requirements, numerous analyses were performed for the Orbiter environment and EVA contamination impacts. These analyses provided critical assessments for controlling on-orbit contamination generating activities and provided the necessary quantitative details for imposing ground processing requirements for the Orbiter. The major analyses include plume impingement, waste/water dumps, SIPE, extravehicular mobility unit (EMU), Orbiter reboost, and HST configuration changes including deployed solar arrays. These analyses represent the core of the cleanliness concerns associated with the shuttle and EVAs. In addition to the analysis for the Orbiter, cleaning requirements were assessed and levied on the Orbiter payload bay. To quantify the effects of the crew compartment on subsequent EVAs relative to the particulate environment, two witness plates were flown on STS-51. These results were used to determine crew cabin and EMU (space suit) cleanliness requirements (4).

The analysis of the Orbiter plume impingement assessed the degradation of the HST surfaces due to gaseous and liquid droplet impingement from thruster firings during maneuvers and station keeping operations. Byproducts from the incomplete combustion, such as monomethyl hydrazine (MMH)-nitrate, can have detrimental effects on contamination sensitive and thermal control surfaces. The station keeping and attitude adjustments considered were low-Z and norm-Z modes. Because the byproduct mass flux in the Norm-Z thruster firing case was significant, limitations were imposed for Orbiter operations.

Significant droplets are formed during Orbiter waste/water exhaust. These droplets may pose a potential threat to the HST during EVA operations when the telescope's Aft Shroud doors are open. The estimation of the maximum effluent released during these dumps is approximately 320-lbm for each dump. Since this represents a significant amount of released material during the HST servicing operations, restrictions were set in both the First Servicing Mission and Second Servicing Mission flight rules. All dumps were constrained 120 minutes prior to and during EVA to preclude potential impingement on critical area of the HST.

Because the SIPEs provided cleanliness protection during launch, ascent, and on-orbit operations for the scientific instruments, a separate analysis was performed to assess contamination impacts. The primary objective was to examine impacts due to the particle control redistribution within the SIPEs, molecular flow, and moisture control within the SIPEs. All of the elements of this analysis accounted for any degradation to the scientific instruments during these phases.

During an EVA, the amount and type of contamination emitted by the astronaut was considered a threat to optical surfaces on the HST. In addition, the astronaut was in close proximity (e.g., line of sight) to the scientific instruments and Aft Shroud. The main concern was contamination contributions from the EMU (i.e., space suit). The EMU exhaust was analyzed and assessed for molecular and particulate contributions. The main byproduct of the EMU exhaust was estimated to be 1 to 1.5 lb/hr of water vapor/ice. Because the sensitive HST surface temperatures were above the water condensation temperature for a low pressure environment, no contaminant depositions from the EMUs were expected.

## Orbiter Payload Bay Cleanliness Requirements

The Orbiter payload bay liner and thermal control blankets (forward and aft bulkheads, Bays 12 and 13) provides thermal control to the payload and may be flown on many mission. A reflown liner section or thermal control blankets may provide a large outgassing source to a payload if contaminated by a previous payload on another mission. As this potential outgassing source could not be quantified or outgassing specified identified, a new, unflown payload bay liner was requested for the entire payload bay. The thermal blankets could not be replaced due to excessive cost; however, they were cleaned with an isopropyl alcohol (IPA)/deionized (DI) water mixture and verified to have no significant fluorescing molecular contamination. Small amounts of molecular contamination could be tolerated, but were evaluated on a case-by-case basis and were dependent on location within the payload bay.

Based on the hardware cleanliness requirements, for both the First and Second Servicing Mission a new payload bay liner was cleaned to visibly clean highly sensitive (VCHS), per Johnson Space Center Document Number SNC-0005C, with an IPA/DI water mixture. During the Orbiter servicing in the Orbiter Processing Facility (OPF), the payload bay liner and thermal blankets including bilge area and wire trays were vacuumed every three days. Both the Goddard Space Flight Center and Kennedy Space Center contamination teams were success orientated, and as such, cleaned the payload bay to VCHS at the Pad Payload Changeout Room (PCR). Vertical cleaning at the Pad provided both the best access to all levels, but also provided a top down cleaning approach so that any particles cleaned from the level above, but not captured, would fall to a level which would be subsequently cleaned. Again, the thermal blankets were verified to have no significant fluorescing molecular contamination.

## Cleanroom Protocol

The biggest contamination threat to the servicing carriers is the personnel working on or around them. To control this threat, the servicing carriers spend the majority of their time in a Class 10,000 (M 5.5) cleanroom. The cleanroom protocol, detailed in Reference 1, was derived from the hardware requirements, contamination control practices, and data from previous missions. Personnel constraints, cleanroom operating procedures, and site management issues are addressed for each facility in which the servicing mission hardware is assembled, integrated or tested. Activities, which have the potential to contaminate the hardware, were identified and controlled by procedure. These activities include crew familiarizations, alignment and envelopment measurements with the High Fidelity Mechanical Simulator and scientific instrument to SIPE fit checks and integration.

Launch site integration activities are also a challenge to maintaining the servicing carriers contamination levels. Because of their size, the servicing carriers must be integrated in Class 100,000 (M 6.5) facilities. However, the Class 10,000 (M 5.5) cleanroom protocols are used which typically results in a significantly lower operating level – Class 10,000 to Class 20,000 during typical integration activities. During the scientific instrument insertion into the SIPE, the cleanroom is run as a Class 10,000 (M 5.5) cleanroom with strict personnel limits (5). For both the First and Second Servicing Missions, these cleanroom protocols have resulted in hardware contamination levels significantly below the required limit.

## POST-MISSION RESULTS

The post-mission surface cleanliness results are similar for both SM1 and SM2. These levels were measured while the carriers were in the payload bay at the Orbiter Processing Facility within hours of the payload bay door opening. For both SM1 and SM2, the particle levels ranged from Level 200 to Level 2000, per MIL-STD 1246. Those samples, which measured Level 2000, typically included clothing fibers. Two swab samples were taken from each carrier, one along the centerline and one from either the starboard or port sides of the carrier depending on personnel access. These samples measured less than  $1.0 \text{ mg/m}^2$ . As the carriers were nominally  $2.0 \text{ mg/m}^2$  just prior to launch and no suspicious species were identified, it was concluded that neither the telescope nor the Orbiter had contaminated the carriers.

It should be noted that after the Second Servicing Mission, prior to the payload bay door opening, work was performed on the Orbiter Thermal Protection System located on the payload bay doors. When the carriers were inspected, debris was found on the carriers along the centerline of the Orbiter. The debris was later identified through chemical analyses to be RTV 560, the adhesive used to bond the Thermal Protection System to the Orbiter. The payload bay doors do not form a tight seal and the RTV fell into the payload bay and onto the carriers while the Thermal Protection System work was performed. The cleanliness levels above do not include this debris in the particle level results.

## CONCLUSION

A contamination control program has been developed for multi-mission flight hardware, which must meet stringent contamination requirements. The HST servicing carriers are integral to the HST servicing missions, but cannot be a potential contamination source to the telescope during EVA activities. Post-mission results from two servicing missions indicate that the servicing carriers do not contaminate the telescope and conversely, the HST and the Orbiter do not contaminate the servicing carriers. The main points of the HST servicing carrier contamination control program that are applicable to any multi-mission hardware are listed below.

1. Store, integrate, and test multi-mission hardware in stringently controlled environments, preferably a cleanroom. When not in a cleanroom, double bag hardware with approved bagging material.
2. Control the type and amount of all added materials to the multi-mission hardware so that outgassing limits are not violated. Verify, by test, that the batch of material used will not be a significant contamination source.
3. Certify outgassing levels of added (new) hardware at the sub-assembly level prior to integration onto the multi-mission hardware.
4. Maintain surface cleanliness levels during storage or low work periods. Periodic cleaning is required for multi-mission hardware that is not bagged.

## ACKNOWLEDGEMENTS

The authors would like to thank the many people whose collaborative effort ensures the HST Servicing Mission successes. The NSI Contamination Control Group who maintains the hardware cleanliness levels: Wayne Geer, John Di Bartolo, Leon Bailey, Jeff Mobley, Joe Hammerbacher, Scott Lange, Joe Colony, and Barry Greenberg. The NASA team who verifies all our surface levels: Alex Montoya, Mary Ayers-Treusdell, Doris Jallice, Neil Walter (Unisys), John Scialdone, Ben Reed (Unisys), and Fred Gross (Unisys). The modeling team who determines our cleanliness requirements: Shaun Thomson (NASA), Glenn Rosecrans (SA), Aleck Lee (LMMS), Mike Fong (LMMS), and Cliff Gee (LMMS). The Orbiter contamination team: Sally Hill (USA), Chris Webber (USA), Dave Baska (Boeing), Wayne Batungbacal (USA), Chuck Calin (USA), Jean Abernathy (NASA), Martin Mc Clellan (USA), Carol Nguyen (Boeing), and Gene Borson (SA). The purge team who provided a continuous purge to the carriers for five launch site facilities: Craig Chivatero (LMMS), Schonda Rodriguez (NASA), Max Swanko (NSI), and Larry Dell (LMTO).

## REFERENCES

1. R.J. Hedgeland, P.A. Hansen, and D.W. Hughes, "An Integrated Approach for Contamination Control and Verification for the Hubble Space Telescope First Servicing Mission", SPIE 2216: 10-21, July 1994.
2. P.A. Hansen, et. al., "Hubble Space Telescope Second Servicing Mission Contamination Control Program", SPIE 2864: 27-35, August 1996.
3. P.A. Hansen and C.R. Maag, "Contamination Control Program for the Hubble Space Telescope Second Servicing Mission", Proceedings of the 7<sup>th</sup> International Symposium on 'Materials in Space Environment', SP-399: 135-142, June 1997.
4. P.A. Hansen, R.J. Hedgeland, C.R. Maag, and C.H. Seaman, "Results of STS-51 Orbiter Crew Compartment Contamination Generation and EVA Payload Bay Transfer Experiment", SPIE 2261: 2-9, July 1994.
5. D.W. Hughes, R.J. Hedgeland, W.C. Geer, and B.N. Greenberg, "Maintaining a Class M 5.5 Environment in a Class M 6.5 Cleanroom", SPIE 2261: 46-57, July 1994.

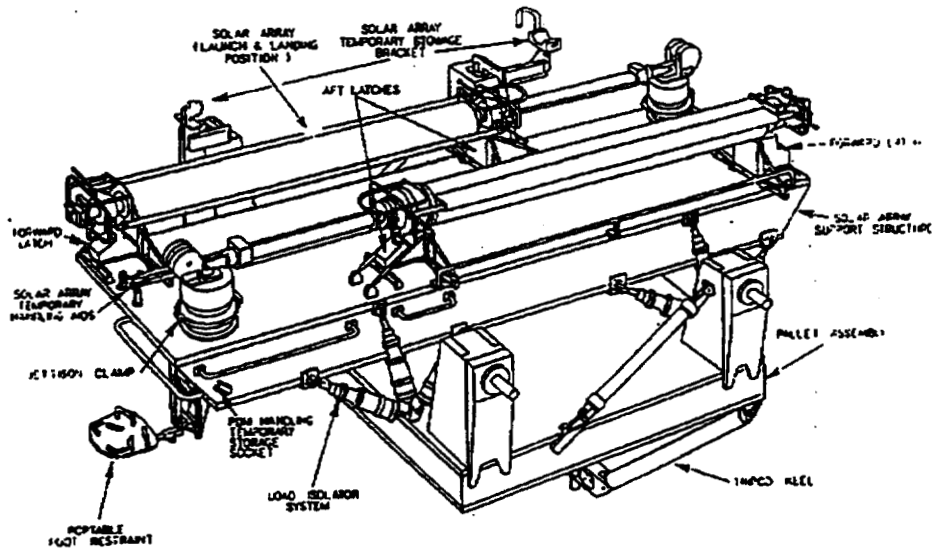


Figure 1. Solar Array Carrier

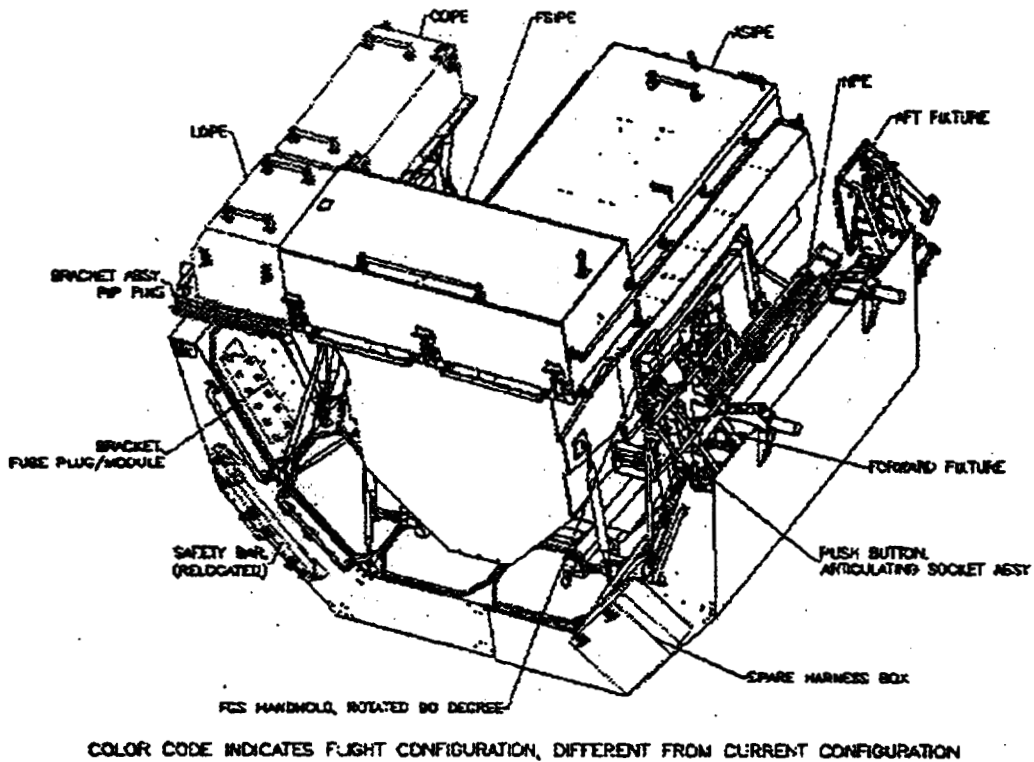


Figure 2. Orbital Replacement Unit Carrier

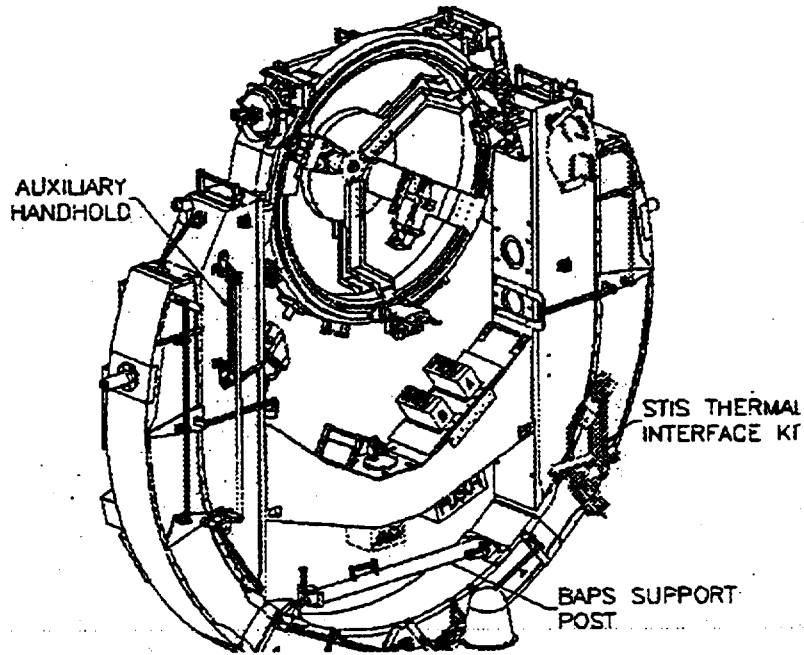


Figure 3. Flight Support System

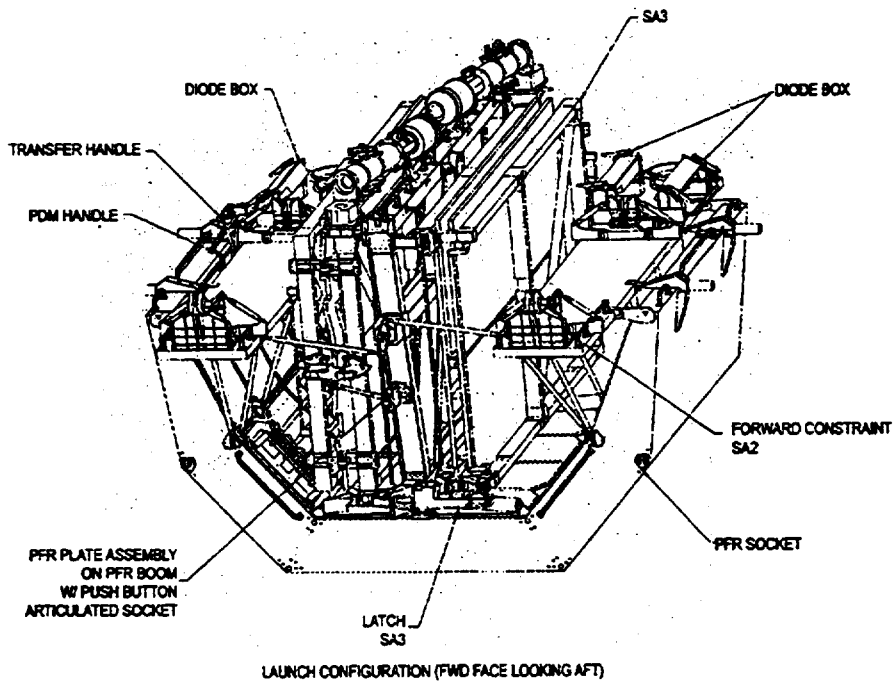


Figure 4. Rigid Array Carrier



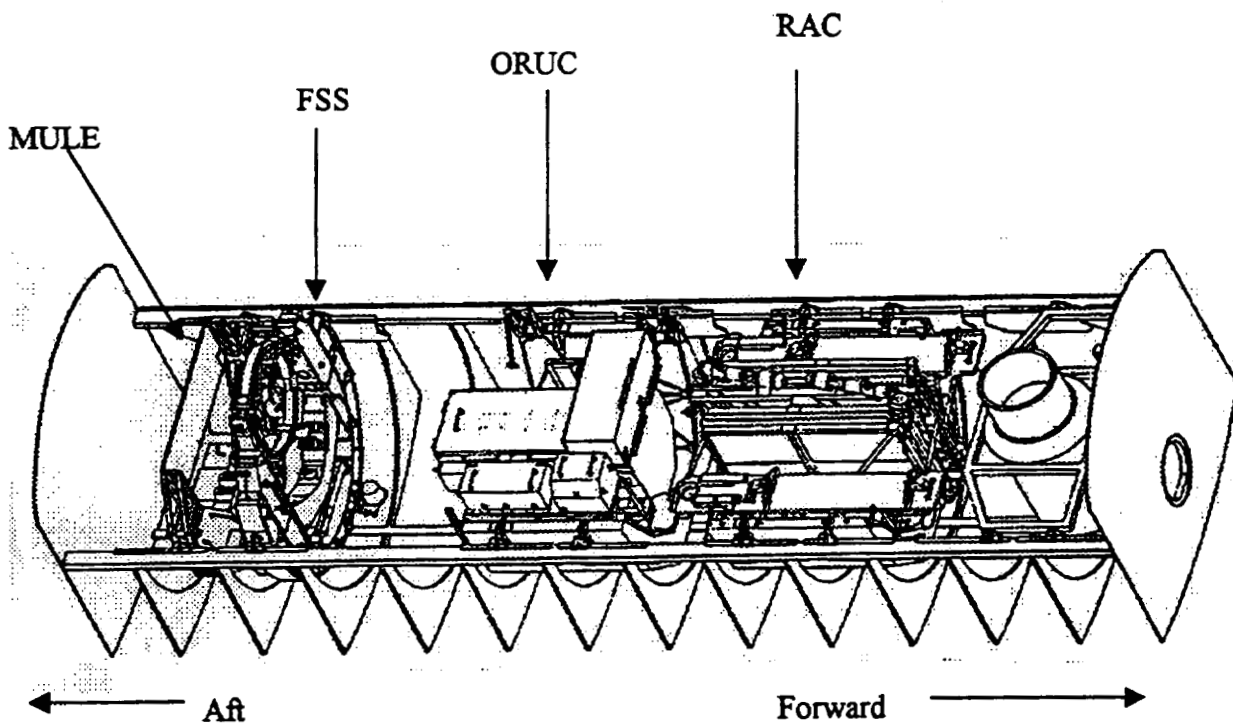


Figure 7. The HST SM3 Carrier Configuration

The servicing carriers are shown integrated with the Orbiter. From the Aft (tail) forward are the MULE, FSS, ORUC and RAC. The Orbiter external airlock is shown forward of the RAC.



# **WATER OUTGASSING FROM MULTI-LAYER INSULATION BLANKETS AS A DIFFUSION CONTROLLED PROCESS**

**David M. Silver**  
The Johns Hopkins University  
Applied Physics Laboratory  
Laurel, Maryland 20723

## **ABSTRACT**

Water is a pervasive molecular species that is inherent as a constituent in spacecraft materials, especially Multi-Layer Insulation (MLI) blankets. On orbit the outgassing of water occurs at rates that make a potential deleterious contaminant for cryogenic optical surfaces, either from direct, ricochet or collisional return flux. The outgassing process persists over time and is temperature dependent.

Laboratory measurements are available on the outgassing of water from MLI blanket materials, which include single-sided and double-sided metalized plastic films and synthetic netting. The results span a range of outgassing temperatures (-50C to +20C) over a time span of ~100 hours. Empirical fits of these data have been assembled for each layer of a twenty layer, double aluminized mylar (DAM) and Dacron netting (DN), MLI blanket (each layer at a specified temperature) to form an MLI blanket model. The MLI blanket model has been used to make predictions of the water outgassing environment for the Midcourse Space Experiment (MSX) spacecraft, launched in April 1996. Comparisons of the model with MSX on-orbit measurements, from a neutral mass spectrometer, total pressure sensor, krypton flash lamp and radiometer, showed excellent agreement for the first several hundred hours of spaceflight. However, the laboratory data forming the basis of the empirical model had been collected for only 100 hours and the consequences of extrapolating an empirical fitting to longer times became apparent from comparisons of on-orbit measurements taken about after 1000 hours of spaceflight.

The fundamental physical processes in outgassing of water from MLI materials are diffusion through the interstitial spaces and evaporation from the bounding surfaces. Since diffusion is the controlling mechanism, the approach described here is to use the solutions of the diffusion equations fitted to the boundary conditions and results of the laboratory experiments to construct a time and temperature dependent outgassing model. Then it is the time dependence of the physics-based governing differential equations that predict the behavior at long times. Such a model has been constructed for DAM-DN and incorporated into an MLI blanket model. Predictions from this model will be compared with on-orbit measurements collected by the MSX flight instruments over the past year.



# CONTAMINATION CONTROL FOR ENVIRONMENTAL TESTS ON OPTICAL INSTRUMENTS

F. Resch, C. Wuersching  
IABG mbH, Ottobrunn, Germany

## ABSTRACT

IABG is operating one of the ESA co-ordinated test centres within Europe with test facilities for space simulation/ thermal vacuum testing, vibration, acoustic noise, physical properties, EMC and magnetic field simulation. In this connection environmental tests on optical systems of satellites are performed under specific cleanliness requirements for the test facility and its surrounding equipment. Due to the contamination sensitivity of the optical systems the required cleanliness levels for the integration area but also for the test facility are significantly higher than for 'usual' spacecraft tests.

To perform the test programme on the ENVISAT instrument MIPAS (Michelson Interferometer for Passive Atmospheric Sounding) one of IABG's thermal vacuum facilities was upgraded according to the specific test requirements and was integrated in a clean class 100 environment. special precautions were taken for the design of the test facility to meet the cleanliness requirements inside the chamber (class 100 according to Fed. Std. 209). All materials used inside the facility and the integration area were selected with regard to their potential contamination risk for the test article.

During previous projects it was experienced that above all the integration and the setting to work phase of a facility is a contamination critical process. Therefore dedicated integration and cleanliness procedures were developed. To monitor the contamination level and the change of contamination versus time contamination measurements (PFO, IR-analyses, etc.) were performed during these phases. Prior to the first tests on flight hardware extensive acceptance and qualification programmes were carried out.

The paper will describe the specific measures taken for a reliable contamination control and the related experience gained during the test programme. Further it will discuss the results and problems associated with testing under severe cleanliness requirements.

Keywords: contamination control, cleanliness, environmental testing

## INTRODUCTION

For the qualification and verification of the thermal design of optical systems for space application environmental tests have to be performed under severe cleanliness conditions. Specific measures become necessary to avoid contamination during testing and to ensure reproducible measurement results.

A medium sized thermal vacuum facility of IABG is used for the alignment and the thermal vacuum testing performed on the ENVISAT MIPAS Instrument (EQM and FM). Due to the fact that both, particulate and organic (molecular) contamination degrade the performance of the optical instrument contamination control is mandatory in this test environment.

## CONTAMINATION CONTROL

### Particle Contamination

Particle contamination on optical surfaces lead to a degradation of the performance by generating straylight. For this reason a maximum permissible Bidirectional Reflectance Distribution Function (BRDF) value is correlated with a corresponding obscuration factor [1].

For the determination of particle contamination airborne particles and settled particles are measured. However, the real time measurement of airborne particles by laser particle counters is only useful for monitoring the potential contamination risk. Particles measured with this method are not yet fallen on the critical surface and especially smaller particles (<0.5 µm) can remain airborne for a long time.

With the second method only particles which have settled on a surface are measured by means of a so-called PFO-photometer. This offline method uses witness plates which are placed close to critical areas. In fixed intervals (> 1 day) the obscuration values are manually read by putting the plates in the PFO photometer. In contrast to the measurement of airborne particles the PFO method can also be used during thermal vacuum testing. Other methods, like tape lift or counting particles under the microscope are used on a case by case basis.

### Organic Contamination

Organic (molecular) contamination degrades the performance of optics by causing transmission loss, change in spectral transmittance and change of thermal behavior. Molecular contamination is mainly produced by outgassing of material from flight and test hardware, by personnel and by organic residuals in clean room air.

During thermal vacuum testing the potential risk for molecular contamination increases because the outgassing process from material is accelerated and contaminants are released from warm surfaces by evaporation and are collected from cold surfaces by condensation. Therefore it is mandatory to keep the most sensitive parts of the test article always at higher temperature than the other parts of the test set-up.

## SPECIFIC REQUIREMENTS FOR FACILITY CLEANLINESS

The standard requirements for molecular cleanliness of a thermal vacuum test facility and for integration areas are defined by ESA [2] as

- thermal vacuum facility       $1 \cdot 10^{-7}$  g/cm<sup>2</sup> for an empty chamber run of 24 hrs
- integration areas               $2 \cdot 10^{-7}$  g/cm<sup>2</sup> for period of 7 days

The molecular contamination is analyzed by means of IR-spectroscopy determining the amount of hydrocarbons, ester and silicones. For particulate contamination the Fed.Std. 209 is applied and usually clean class 100.000 is sufficient for most of the space programs. Beside this requirements for airborne particles ESA has defined limits for particle fall-out in relation to clean room classes [3].

For the MIPAS test program performed at IABG specific cleanliness requirements were defined. The following contamination limits for one vacuum cycle of the thermal vacuum chamber were specified:

- Molecular contamination <  $1.5 \cdot 10^{-8}$  g/cm<sup>2</sup>
- Particulate contamination < 33 ppm (measured by means of a PFO Photometer)

For the integration area in front of the facility that is used for the test preparation of the unprotected instrument the following limits were defined:

- Molecular contamination <  $2 \cdot 10^{-7}$  g/cm<sup>2</sup> per 7 days
- Clean room class 100 according to Fed. Std. 209
- Particulate contamination < 10 ppm per day (measured by means of a PFO Photometer)

To meet this requirements potential contamination sources already had to be identified during the design phase and installations and equipment foreseen to be used had to be checked for their cleanliness. Suitable cleaning methods and procedures had to be defined for the setting in operation phase and the final operation phases.

## DESCRIPTION OF THE TEST FACILITY

### Vacuum Chamber and Thermal System

The thermal vacuum test facility consists of a horizontal stainless steel vessel (length = 2.2 m, diameter = 2.1 m) mounted on a rigid steel frame. The chamber door is opened into a clean class 100 integration area.

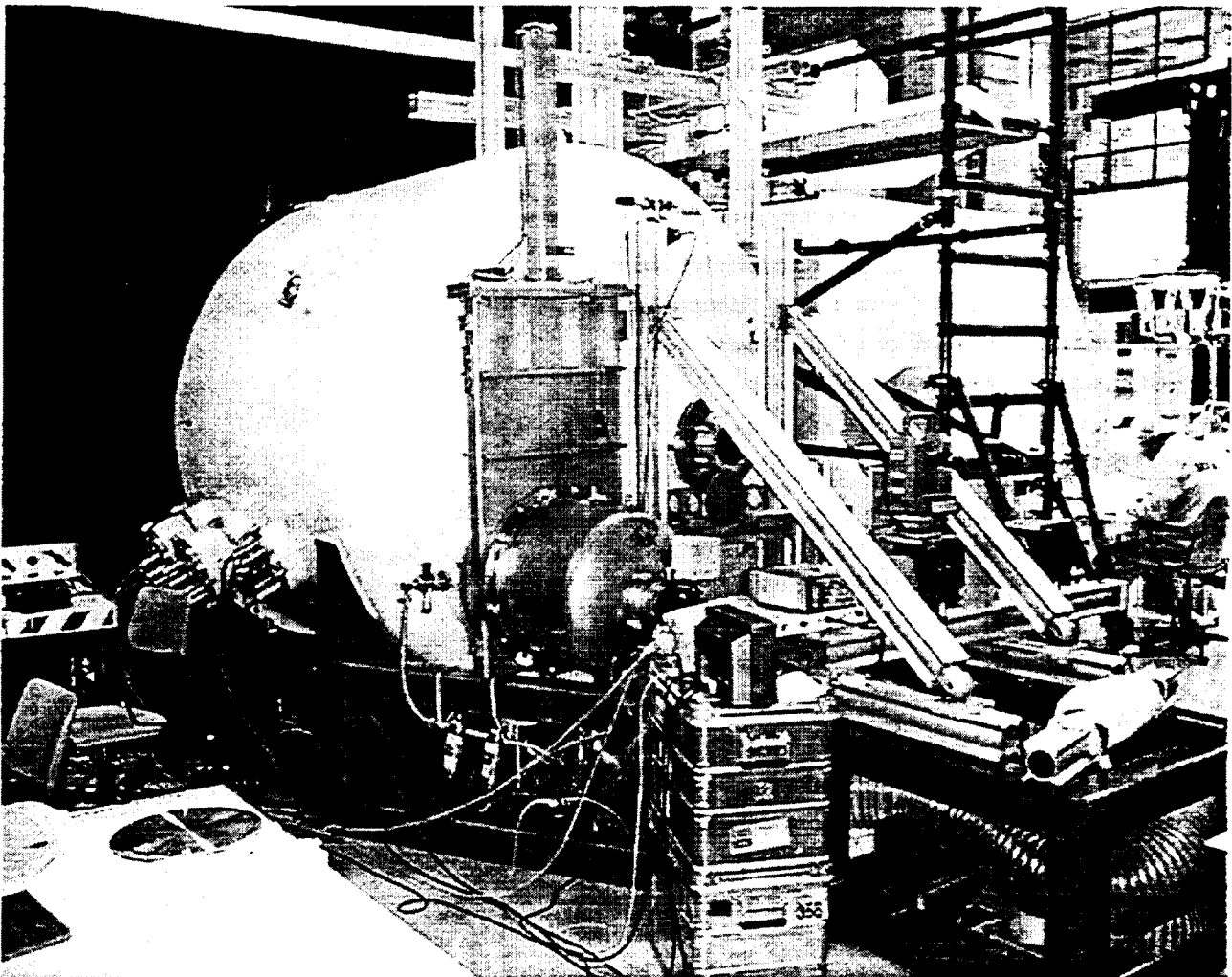


Fig. 1: Rear view of the 2-meter TV-facility

For the pumping system entirely oil free components were selected. For the range from atmospheric pressure to 10 Pa two scroll pumps in parallel configuration with a nominal pumping speed of 60 m<sup>3</sup>/h are installed combined with a hydro-kinetic drive Roots Pump with a nominal pumping speed of 500 m<sup>3</sup>/h. For the range from 10 Pa to high vacuum (<10<sup>-3</sup> Pa) a Helium refrigerator cryo-pump with a nominal pumping speed for N<sub>2</sub> of 1·10<sup>4</sup> l/s is installed. In order to avoid the introduction of vibrations into the test set-up which may disturb the alignment measurements during the test

the roughing pump system is mechanically de-coupled from the facility by flexible tubes. The cryo-pump which is connected directly to the vacuum chamber is equipped with vibration absorbers at its cold head.

The thermal shroud consists of a cylinder build from flat aluminum shields with aluminum tubes welded to the rear side of the shields. The temperature of the shroud is controlled with a combination of flow controlled LN<sub>2</sub> supply and electrical surface heaters attached to the rear side of the shroud. The flat side of the shroud that is facing into the test volume is painted with Electrodag 501 whereas the outer surface is unpainted. The thermal capabilities of the shroud system are:

- Temperature range                    -185 °C to +130 °C
- Max. temperature change rate    2 °C / min
- Normal emittance                     $\epsilon_n \geq 0.83$
- Solar absorptance                     $\alpha_s = 0.96$

To enable semi-automatic operation of the facility and to achieve a high degree of flexibility for future applications, both the vacuum system as well as the thermal control systems are operated by means of a PLC system.

#### **Data Acquisition System**

The data acquisition system is a mobile unit with and has a capacity of 400 measurement. With this equipment the facility data as well as the test article data are recorded. The system provides the following features:

- Graphical on-line monitoring, on-line printing of data and on-line data evaluation and plotting
- Acquisition of different of signal types (e.g. voltage, current, resistance, 4-wire measurements, etc.)
- min. scan intervals of 10 s for 400 channels
- Multitasking / multi-user system (UNIX OS)

#### **Clean Area**

To meet the specific cleanliness requirements a clean room class 100 is installed in front of the chamber. The complete installation is located within a clean room class 100,000. Due to the use of the pre-filtered class 100,000 air the life time of the class 100 particle filters is extended considerably. The technical data of the clean area are:

- Cleanliness Class                    100 (FED. STD. 209 D)
- Surface area (incl. airlock)        app. 30 m<sup>2</sup>
- Flow direction                        vertical
- Air speed                                0.3 - 0.5 m/s adjustable
- Material airlock                        2.3 m x 2 m
- Personal airlock equipped with an air shower
- Monitoring of airspeed and low pressure of pre-filter
- Shutter for darkening the area for dust control by UV-light

Figure 2 shows the situation of the facility integrated in the clean class 100 area. The chamber door and its flange is facing into the class 100 environment while the rest of the facility is exposed to a class 100,000 area.

The door flange of the vacuum chamber is integrated in the class 100 clean area to ensure that in the test volume and also in the integration area the required cleanliness condition are available and that the integration of the test article in the chamber can be done without leaving the clean environment.

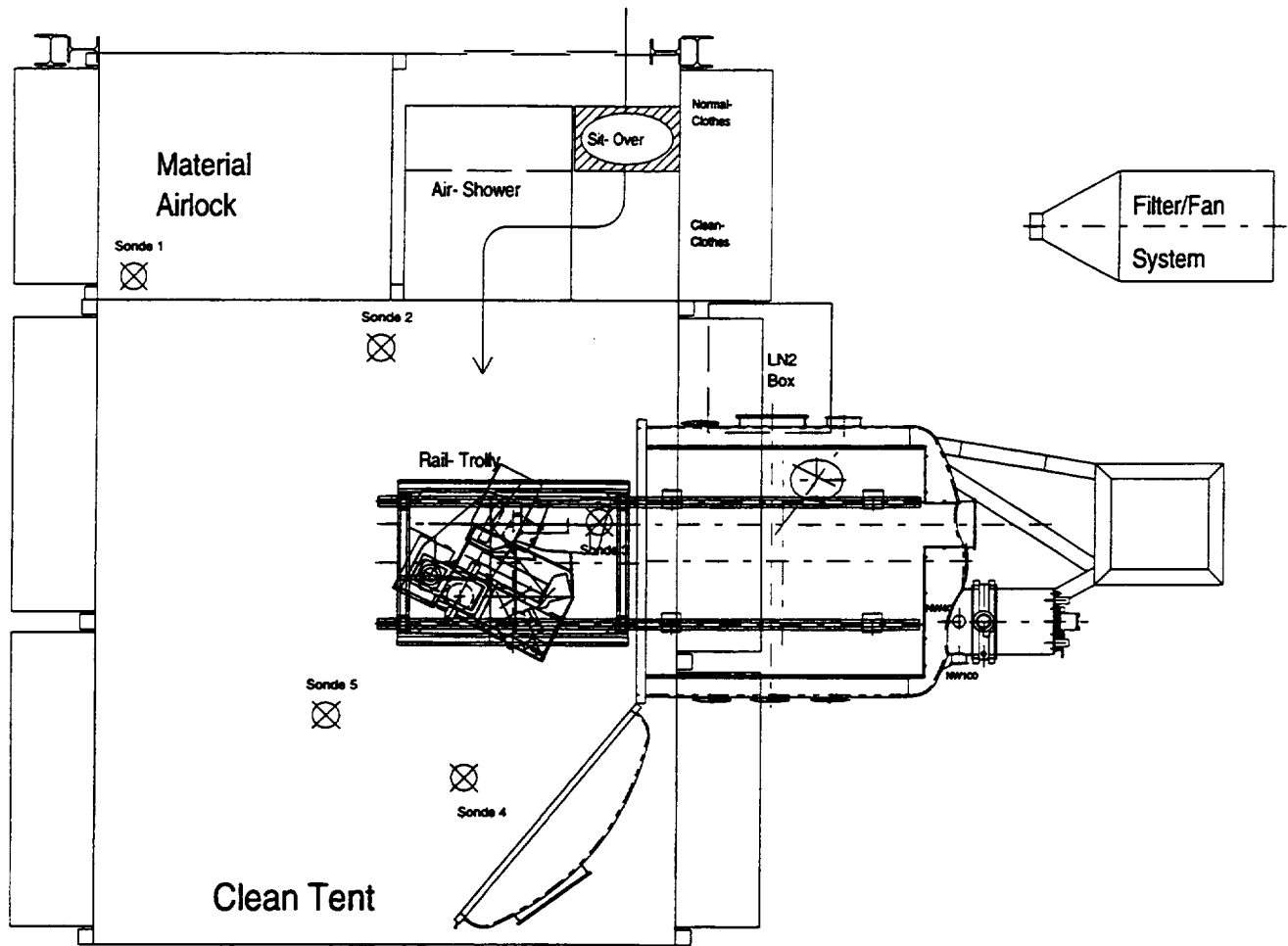


Figure 2: Schematic of Test Facility and Clean Area - Top View

Due to the situation of the building a vertical flow system had to be chosen. One advantage of the vertical flow is that the same level of cleanliness is available over the entire surface area of the clean tent. The drawback is that the quality of the cleanliness decreases from top to bottom. Therefore bending above critical areas must be avoided because the laminar flow is disturbed underneath.

### SPECIFIC MEASURES AND INSTALLATIONS FOR THE CONTAMINATION CONTROL

Already during the design phase a specific contamination control plan [4] was issued describing the measures to be taken to avoid contamination right from the beginning of the manufacturing phase. The major part of the pre-installations on subsystem level like assembly and instrumentation of the thermal shroud took place in a clean class 100,000 environment. All critical steps (e.g. integration of the thermal shroud in the chamber) and activities where a later cleaning was not feasible took place under clean class 100 conditions.

Prior to the installation of the thermal shroud into the chamber the Electrodag painting was outgassed at 150 °C under ambient conditions for a duration of 7 days. Furthermore a number of bake-out runs at temperatures up to +130 °C and at different vacuum levels were performed with the integrated facility. In the course of the bake-out runs the facility was purged up 8000 Pa with gaseous nitrogen several times. During this bake-out phase the decrease of the molecular contamination was monitored by taking wipe samples regularly. The decrease of the molecular contamination is shown in Fig. 3.

**Bake-Out 2m-TVK  
Molecular Contamination Analysis**

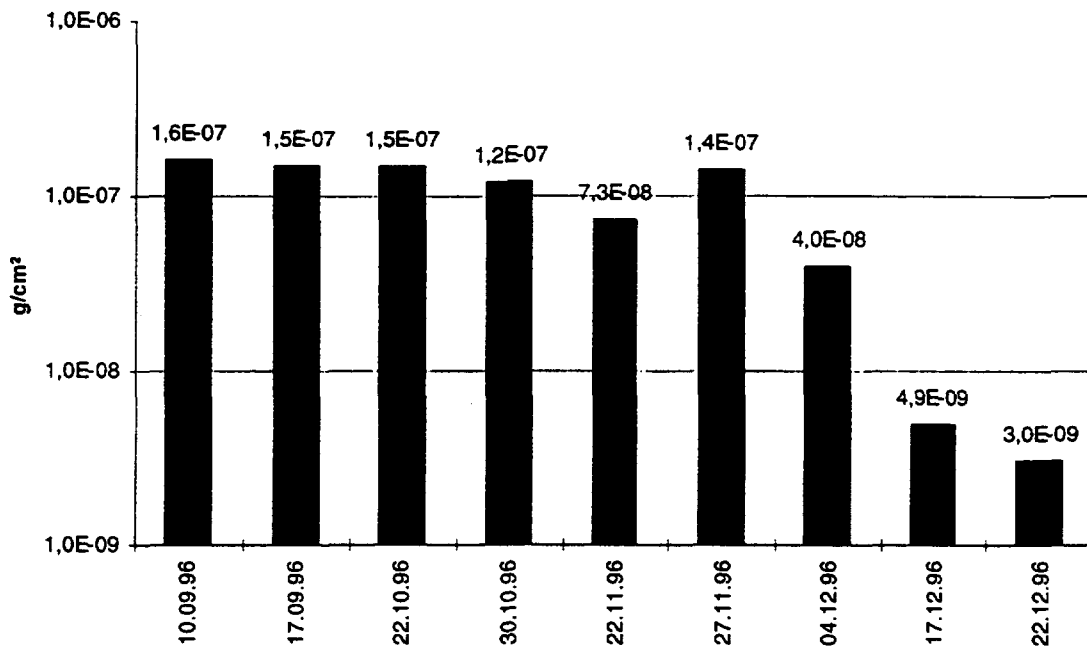


Fig. 3: Decrease of the molecular contamination due to bake-out of the test facility

For the operation of facility and integration area a specific cleanliness control procedure was issued describing the applicable measures to control and maintain the cleanliness. Special attention was paid to the venting process of the chamber to reduce turbulence at the inlet. The gas flow is extremely limited which leads to a venting time of about 6-8 hours. The venting is performed with gaseous nitrogen up to atmospheric pressure via a set of micro and charcoal filters. After the venting process entering of the chamber area is only allowed with a portable O<sub>2</sub>-concentration detector.

Because of the fact that the chamber door is integrated into the clean room only and the rest of the facility is exposed to the class 100,000 environment an external flow box providing clean class 100 air is connected to the rear side of the chamber. This flow box is switched on in case that chamber flanges or the chamber door must be opened. The airflow generates a slight overpressure in the chamber preventing particles from entering the chamber through the openings.

The monitoring of the cleanliness conditions in the integration area is performed by means of particle counters measuring the concentration of airborne particles at 6 different locations. Further PFO sensors and molecular contamination witness plates are exposed. On a regular basis those are measured or analyzed, respectively. The cleanliness conditions inside the chamber are monitored quantitatively by PFO sensors and molecular contamination witness plate. A qualitative inspection of the inner surfaces of the TV-chamber by means of UV-light is performed at least before and after each test run.

GORETEX jumpsuits, cover boots and hoods were selected as clean clothes. Investigations have shown that under similar conditions those release less particles than polyester garments and that GORETEX is more convenient for the personnel wearing this clothes frequently. It was experienced that for an acceptable live time and performance of the GORETEX garments the selection of a suitable cleaning company treating the garment according to the manufacturer's specification is mandatory.

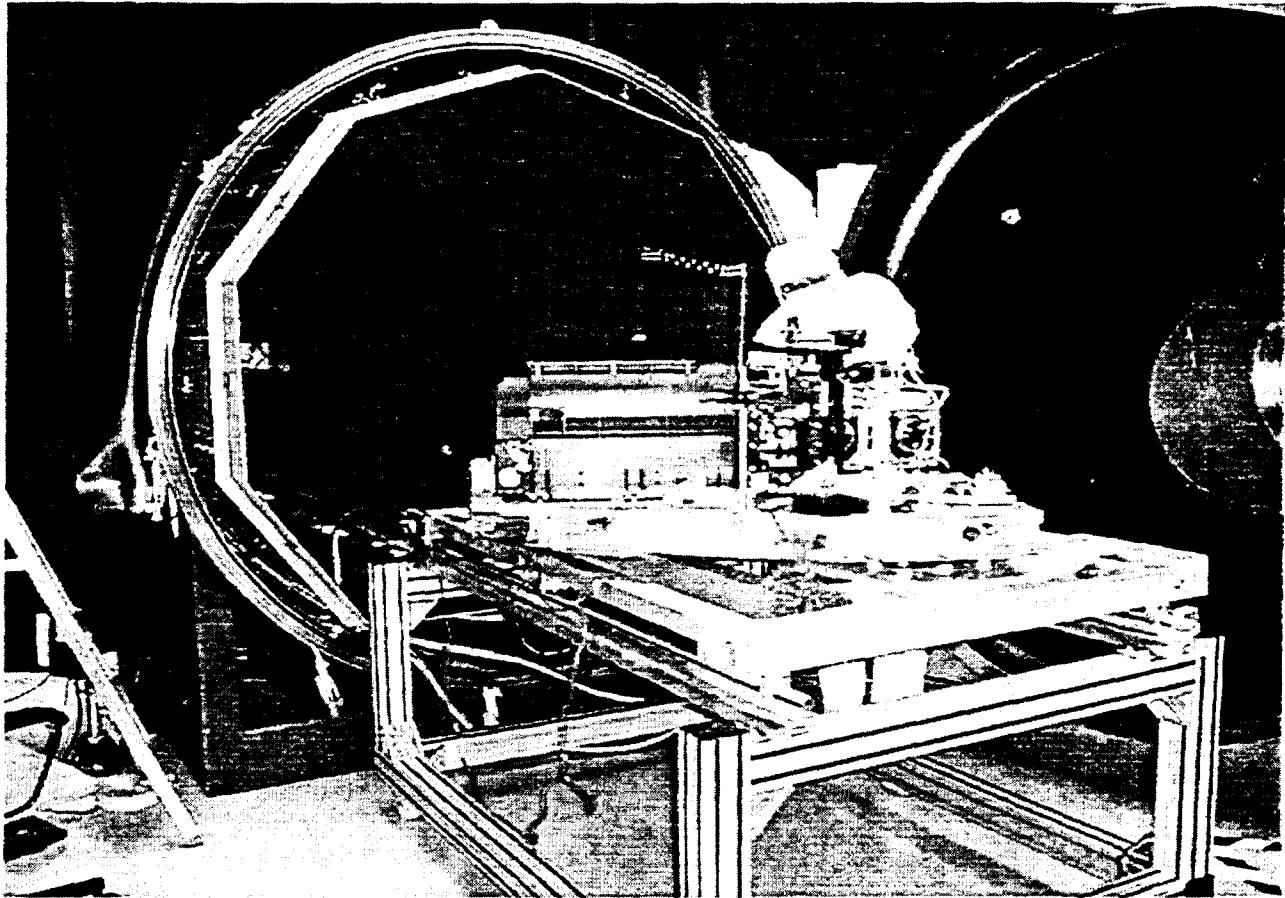


Fig. 4: MIPAS Instrument (EQM) in front of the open TV-chamber

## CONCLUSION

The meanwhile performed tests on the MIPAS EQM and FM instruments have proven the efficiency of the applied contamination control procedures. In general the required limits for particle and molecular contamination were kept during the past two years. The discipline and behavior of personnel in the clean room has a major influence on the quality of the cleanliness. Therefore it is obvious that people working in this areas need sufficient training.

The effort put into the cleanliness aspects during the design phase have prevented from major problems in the operational phase. If the material and equipment to be used is selected under consideration of their cleanliness and the design is such that all critical parts are accessible for cleaning the contamination risk for the test article can be reduced.

One of the findings during the test program is that the reproducibility and reliability of PFO measurements in clean rooms with laminar airflow is significantly better than in turbulent clean rooms. A reliable correlation between airborne particles and PFO measurements seem to be feasible.

## REFERENCES

1. *MIPAS Contamination Control Plan and Instrument Cleanliness Handling and Operational Constraints*, PO-PL-DAS-MP-0015, Deutsche Aerospace AG, 21.07.1994
2. *The Detection of Organic Contamination of Surfaces by Infrared Spectroscopy*, ESA-PSS-01-705, October 1982
3. *Particulate Contamination Control in Clean Rooms by Particle Fallout (PFO) Measurements*, ESA-PSS-01-204, September 1984
4. *Project MIPAS - Cleanliness Procedure*, IABG, May 1996



## MOISTURE CONTENT AND DESORPTION RATE OF A GR/EP HONEYCOMB PANEL

Aleck L. Lee  
Lockheed Martin Missiles & Space  
Sunnyvale, CA

### ABSTRACT

A diffusion outgassing model has been developed to predict the moisture content, concentration distribution and the surface desorption rate of a graphite epoxy panel as a function of temperature and time. The model was applied to a honeycomb panel with aluminum core and graphite epoxy face sheets. The analytical results have been used to predict the internal pressure of a spacecraft during a thermal vacuum test and to determine the temperature and the duration of the thermal vacuum bakeout. An example of the latter application related to the attitude reference platform of a scientific satellite is discussed. The results show that, with an initial moisture content of 0.002 by weight, the average moisture concentration in a 64-mil graphite epoxy panel is reduced to 1/10 of its initial value after 49 days at 240K. For a hot case at 250K, it requires 43 days to reduce the moisture content to the same level. The model was also applied to find the temperature of the face sheet so that the moisture content is reduced to 10% or 5% of its initial value in 30 days. The answers are 21.2°F (267K) and 54.5°F (285.5K), respectively, for the two-sided model.

### INTRODUCTION

Honeycomb panel with aluminum core and graphite epoxy (Gr/Ep) face sheets has found many applications on a spacecraft because of its light weight and high stiffness properties. Gr/Ep face sheet absorbs water moisture when it is exposed to ambient environments. The absorbed moisture is released in vacuum when the spacecraft is on-orbit. The loss of moisture has detrimental effects on satellite operations. Loss of moisture causes dimension instability of the Gr/Ep panel as it shrinks. The outgassed molecules also contribute to the ambient pressure. If the outgassed flux is vented into the enclosure of a satellite where high frequency equipment are located, the ambient pressure may be conducive to corona discharges and operation anomalies. The venting problem with the Gr/Ep panel as an outgassing source has been studied and reported. (Refs. 1 and 2) In the present study, the attention is focused on the moisture content that affects the dimension stability of a Gr/Ep panel.

The moisture desorption rate from a Gr/Ep panel is governed by diffusion processes, which are represented by a diffusion equation (Ref. 3). The desorption rate is proportional to the concentration gradient at the surface. The desorption rate is the outgassing flux at the surface, which can be calculated from the moisture distribution across the thickness of the panel. The diffusion model was developed for the cases where the panel outgasses from one side or from both sides of the panel. In the 1-sided case, the non-outgassing side is insulated and the concentration gradient is zero at the surface. It takes longer to reach the desired moisture content level if the panel is outgassing on one side only. In the 2-sided case, the concentration is assumed to be symmetric in either half thickness.

The diffusion coefficient depends strongly on the temperature. An integration of the diffusion coefficient over time will account for the variations in temperature during this time period (Ref. 4). A comparison of the desorption rate with varied temperature and with constant temperatures shows the effects of the temperature history. The model has been applied successfully to predict the pressure inside a spacecraft payload where the Gr/Ep desorption is the driver of the internal pressure. The predicted results correlated well with the pressure measurements taken during a thermal vacuum test and verified the diffusion outgassing model. The model was later used to determine the required desorption time when

high voltage components in the payload enclosure can operate safely, for both thermal vacuum test and on-orbit operations.

## SYMBOLS

|                  |  |
|------------------|--|
| C                | concentration (g/cm <sup>3</sup> )                   |
| C <sub>avg</sub> | average concentration (g/cm <sup>3</sup> )           |
| D                | diffusion coefficient (cm <sup>2</sup> /sec)         |
| D <sub>0</sub>   | initial diffusion coefficient (cm <sup>2</sup> /sec) |
| E                | activation energy (cal/g-mole)                       |
| h                | total panel thickness (cm)                           |
| j                | surface outgassing flux (g/cm <sup>2</sup> -sec)     |
| R                | universal gas constant (1.9872 cal/g-mole K)         |
| t                | time (sec)   |
| t*               | integrated diffusion coefficient (Eq. 3)             |
| T                | temperature (K)                                      |
| x                | distance across thickness (cm)                       |

## METHOD OF SOLUTIONS

### Diffusion Flux Model

The outgassed molecules from a Gr/Ep face sheet panel are primarily H<sub>2</sub>O molecules. The outgassing flux is governed by a diffusion process through the thickness of the panel. There are various diffusion processes in the nature, but the model used here follows the Fick's law of diffusion with constant diffusion constant. Flux of outgassed molecules is proportional to the concentration gradient, while the concentration, C, is governed by the one-dimensional diffusion equation, shown below.

$$\frac{\partial C}{\partial t} = D \frac{\partial^2 C}{\partial x^2} \quad (1)$$

$$j = D \left[ \frac{\partial C}{\partial x} \right]_{x=h/2} \quad (2)$$

As the temperature changes, the outgassing rate on the surface of a Gr/Ep panel varies, because the value of diffusion coefficient D(T,t) changes. The concentration distribution C(x,t) depends on the outgassing history of the panel. In order to account for the past outgassing history of the panel, a transformation in the diffusion equation is proposed (Ref. 4). Let t\* be defined as follows.

$$t^*(t) = \int_0^t D(\tau) d\tau \quad (3)$$

Introducing the parameter  $t^*$  to replace  $t$  in the diffusion equation, the new diffusion equation becomes

$$\frac{\partial C}{\partial t^*} = \frac{\partial^2 C}{\partial x^2} \quad (4)$$

The diffusion equation now is independent of the diffusion coefficient, which has been normalized to unity in the equation. The solutions of Eq. (4) for a flat plate are available in the literature (Ref. 5).

### Concentration and Surface Flux

For an infinite plate outgassing to both sides, the concentration  $C$  is given below in Eq. (5), where  $0 \leq x \leq h$ . Eq. (2) is then applied to obtain the outgassing rate  $j$  at the surface, shown in Eq. (6).

$$C = \frac{4 C_o}{\pi} \sum_{n=0}^{\infty} \frac{1}{(2n+1)} e^{-(2n+1)^2 \pi^2 t^* / h^2} \sin\left(\frac{(2n+1) \pi x}{2h}\right) \quad (5)$$

$$j = -\left[D \frac{\partial C}{\partial x}\right]_{x=h} = \frac{4 D C_o}{h} \sum_{n=0}^{\infty} e^{-(2n+1)^2 \pi^2 t^* / h^2} \quad (6)$$

Similar solutions can be derived for an infinite plate which outgasses from one side only. In this case, the plate is assumed to be at  $2h$  thick, while the computation space is limited to  $0 \leq x \leq h$ . The surface at  $x=0$  is insulated, and the surface at  $x=h$  is open to vacuum. The solutions for concentration and the outgassing flux at  $x=h$  are listed as follows.

$$C = \frac{4 C_o}{\pi} \sum_{n=0}^{\infty} \frac{(-1)^n}{(2n+1)} e^{-(2n+1)^2 \pi^2 t^* / 4h^2} \cos\left(\frac{(2n+1) \pi x}{2h}\right) \quad (7)$$

$$j = -\left[D \frac{\partial C}{\partial x}\right]_{x=h} = \frac{2 D C_o}{h} \sum_{n=0}^{\infty} e^{-(2n+1)^2 \pi^2 t^* / 4h^2} \quad (8)$$

The average concentration across the thickness  $h$  of the plate can be obtained by integrating the concentration, given by Eq. (5) or Eq. (7) as the case may be. The average concentration for a 2-sided plate is shown in Eq. (9), and that for the 1-sided plate in Eq. (10).

$$C_{avg} = \frac{8 C_o}{\pi^2} \sum_{n=0}^{\infty} \frac{1}{(2n+1)^2} e^{-(2n+1)^2 \pi^2 t^* / h^2} \quad (9)$$

$$C_{avg} = \frac{8 C_o}{\pi^2} \sum_{n=0}^{\infty} \frac{1}{(2n+1)^2} e^{-(2n+1)^2 \pi^2 t^* / 4h^2} \quad (10)$$

## Diffusion Coefficient

The diffusion coefficient  $D$ , is a function of temperature. An exponential model for diffusion coefficient has been proposed (Refs. 3, 4, and 6). The model of  $D$  is shown in Eq. (11). The coefficients,  $D_0$  and  $E$ , can be determined from measured material outgassing data.

$$D = D_0 e^{-E/RT} \quad (11)$$

## DESCRIPTION OF THE HONEYCOMB PANEL

The Attitude Reference Platform (ARP) is the structural base where precision guidance instruments, such as control gyro, star sensor, and laser reflectometer, are mounted. The ARP requires high degree of dimensional stability for pointing accuracy. A scientific satellite may have several ARP's. The ARP is made of a composite panel with M55J/954-3 graphite epoxy face sheets and an aluminum honeycomb core. Figure 1 shows a typical ARP panel with cutouts and mounting inserts. Figure 2 shows an exploded view of the panel blank. The Gr/Ep face sheets vent to the exterior and to the cells of the honeycomb core in this application.

The loss of moisture in the Gr/Ep face sheet causes dimension changes of the platform and pointing accuracy on orbit. In order to minimize the dimension change, the initial moisture content is reduced through thermal vacuum (TV) bakeout. The diffusion outgassing model was applied to predict the moisture content, concentration distribution, and surface desorption rate of the panel, as a function of time and temperature in the TV bakeout. Results from the model provide the basis to design the TV bakeout temperature and duration or to determine the time required to deplete the moisture on orbit.

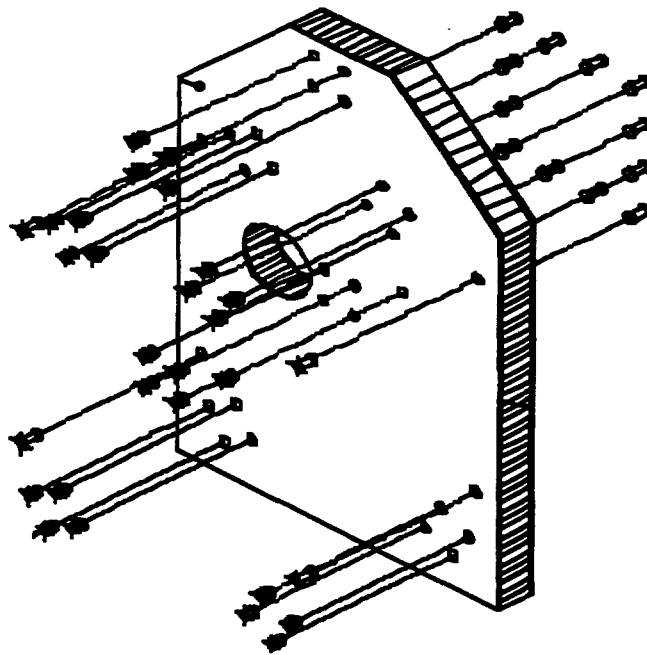


Fig. 1 Panel substrate of the Attitude Reference Platform.

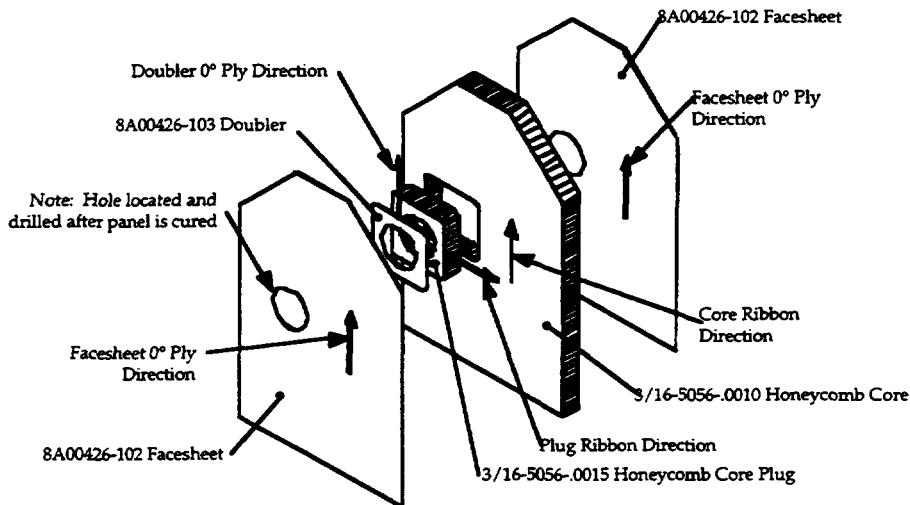


Fig. 2 Exploded view of the panel blank, showing the graphite epoxy face sheet panels.

## PREDICTED RESULTS

### Measurement of the Diffusion Coefficient

The measured data for M55J/954-3 composite material show that the values of  $D$  are  $3.19 \times 10^{-9}$   $\text{cm}^2/\text{sec}$  at  $20^\circ\text{C}$  and  $5.43 \times 10^{-9}$   $\text{cm}^2/\text{sec}$  at  $65^\circ\text{C}$ . Based on these data, the value of  $D_0$  and  $E$  in Eq. (11) are calculated. The diffusion coefficient of M55J/954-3 is expressed as follows.

$$D = 1.7335 \times 10^{-7} e^{-2326.26/1.9872T} \quad (12)$$

Figure 3 shows the diffusion coefficient for M55J/954-3 composite material as a function of temperature. The solid line in the figure shows the diffusion coefficient for M55J/954-3, while the dashed line is for another Gr/Ep material (K13C2U/954-3) as a reference.

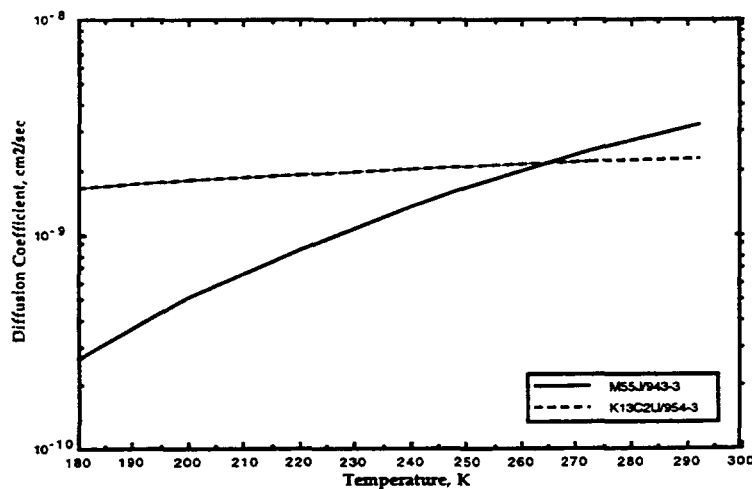


Fig. 3 Diffusion coefficients of Gr/Ep materials versus temperature.

## Predicted Results for On-Orbit Outgassing

The diffusion process is applied to the ARP facesheet, which is 64 mils thick and has an initial moisture content of 0.002 by weight. In order to maintain dimension stability, the desired target level is 1/10 of this initial moisture content.

The temperature profile of the ARP facesheet after launch can be calculated with a thermal model. Figure 4 shows the temperature profile of a nominal case. In this case, the temperature drops rapidly from ground level ambient temperature to a fluctuating final temperature. The average final temperature of the facesheet is  $-33^{\circ}\text{C}$  (240K). This temperature is adopted as the nominal case. A hot case has also been considered, where the final average temperature is 250K.

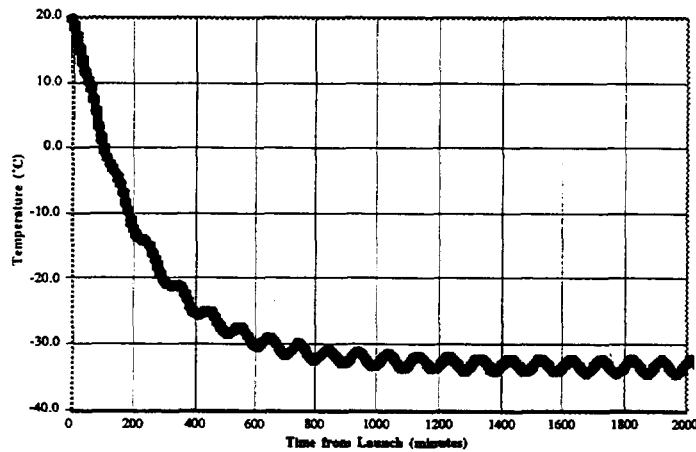


Fig. 4 ARP temperature after Launch.

The diffusion outgassing model was used to compute the moisture concentration profiles of the facesheet panel. The concentration profiles at selected time intervals for the nominal 1-sided and 2-sided models are shown in Figures 5 and 6. The average concentration across the thickness of the plate is computed by integrating the concentration profile at each time interval. For the nominal case, the time required to reach 1/10 of the initial average concentration is 197 days for the 1-sided case, and 49 days for the 2-sided case. For the hot case of 250K, the concentration profiles are shown in Figures 7 and 8. The time required to reach 1/10 of the initial average concentration is reduced to 170 and 43 days for the 1-sided and the 2-sided case, respectively.

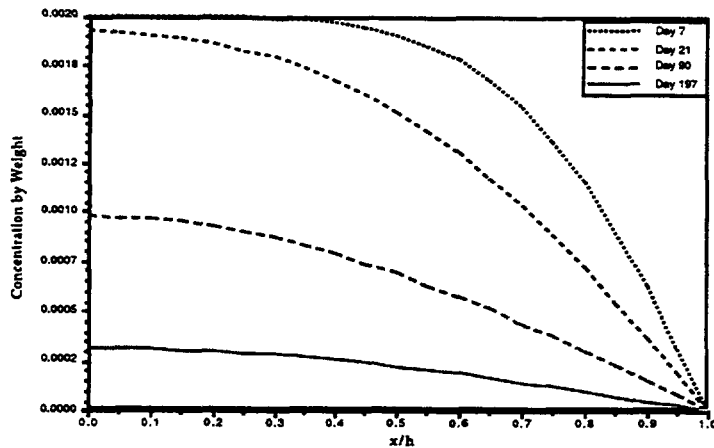


Fig. 5 Concentration profiles for the one-sided plate at 240K.

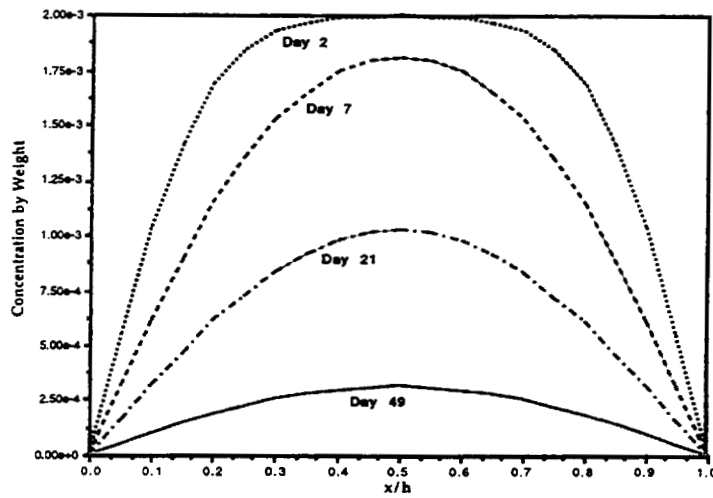


Fig. 6 Concentration profiles for the two-sided plate at 240K.

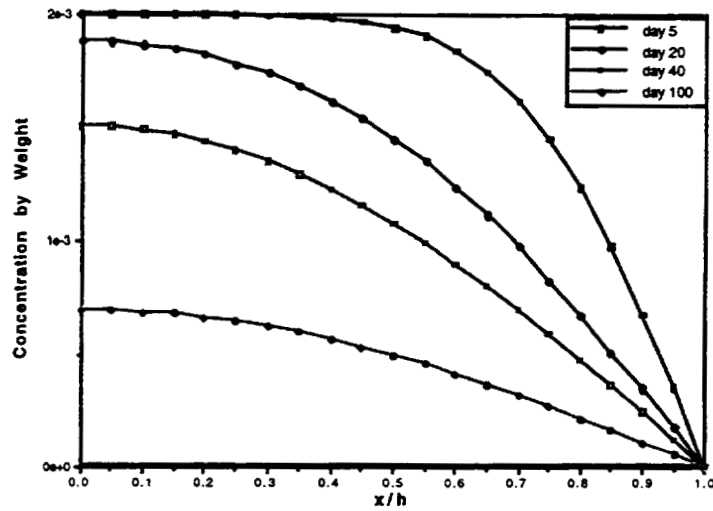


Fig. 7 Concentration profile for a one-sided plate at 250K.

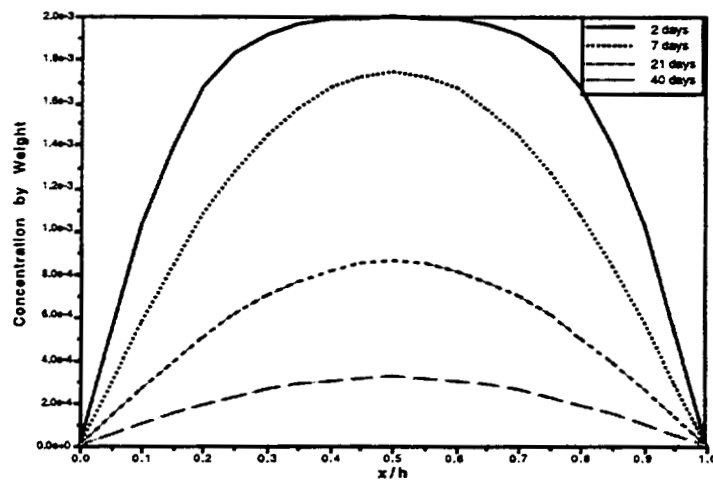


Fig. 8 Concentration profile for a two-sided plate at 250K.

Since the time required to reach 1/10 of its initial concentration varies for the 1-sided model is roughly four times that of the 2-sided model, it is necessary to determine which model is appropriate here. The key is the difference between the water vapor pressure and the ambient pressure. If the water vapor pressure is higher than the ambient pressure next to the inner panel surface, the water molecules will vent to the ambience freely, just like the outer surface, and the 2-sided model will be appropriate to predict the moisture content.

The pressure inside the honeycomb core is vented out to the ambience fairly quickly. An earlier study showed that the pressure in the honeycomb core of a radiator panel would reach  $10^{-7}$  torr after 12 hours on orbit (Ref. 7). The water vapor pressure at low temperature is found to be 4.6 torr at 273K and drops to 0.29 torr at 243K (Ref. 8). The pressure in the honeycomb core is several orders of magnitude lower than the water vapor pressure at these temperatures. The water moisture in the facesheet will diffuse freely from the inner side bonded to the honeycomb core, just like the outer side which is exposed to space environment. The two-sided diffusion solution is appropriate.

The inverse problem of determining the required temperature for a given time can also be solved with the diffusion model. Let the final target moisture be 10% or 5% of its original value, and the desorption duration be 30 days. The required bakeout temperatures for the 1-sided and 2-sided panel are predicted. Table 1 summarizes the results.

Table 1 Required temperatures to reach moisture targets

| Diffusion Model | Target moisture content in 30 days |                  |
|-----------------|------------------------------------|------------------|
|                 | 10%                                | 5%               |
| 2-Sided         | 267K (21.2°F)                      | 285.5K (54.5°F)  |
| 1-Sided         | 390.5K (243.5°F)                   | 431.5K (317.3°F) |

### Predicted Results for Bakeout Outgassing

In a thermal vacuum bakeout, the temperature varies with time to simulate the on orbit thermal conditions. In a particular scenario, the temperature varies between 40°F and 100°F. The temperature profile is shown in the bottom part of Figure 9. The figure also shows the surface outgassing fluxes of the 1-sided model for constant temperatures and varied temperature profile. The parallel curves represent the outgassing flux at constant 40°F, 70°F, and 100°F.

The outgassing flux for the varied temperature case demonstrates interesting features of the diffusion outgassing model. When the temperature rises to 100°F, the outgassing flux rises above the flux of constant 100°F. This can be explained by reasoning that the moisture content is higher in the varied temperature case when the panel was subjected to lower temperature. The situation is reversed when the temperature is lowered to 70°F and 40°F later. The outgassing flux is lower than that of constant temperature cases. This is because the panel is depleted of its moisture faster during the high temperature outgassing period. This comparison shows how the outgassing flux of a Gr/Ep panel depends on its prior outgassing history. The panel possesses a memory of the outgassing process.

Table 2 summarizes the results of outgassing flux for both 1-sided and 2-sided models. Note that the outgassing rate at constant 100°F is higher than that at 40°F initially. As time elapses, the outgassing rate at 100°F becomes lower than that at 40°F, because the moisture is depleted faster at the higher temperature and the moisture concentration has a flatter distribution. This is especially evident in the 2-sided case. The outgassing flux model has been used to predict the pressure of satellite enclosure during thermal vacuum tests. The predicted results correlated well with the measured data and validated the outgassing model (Ref. 1).

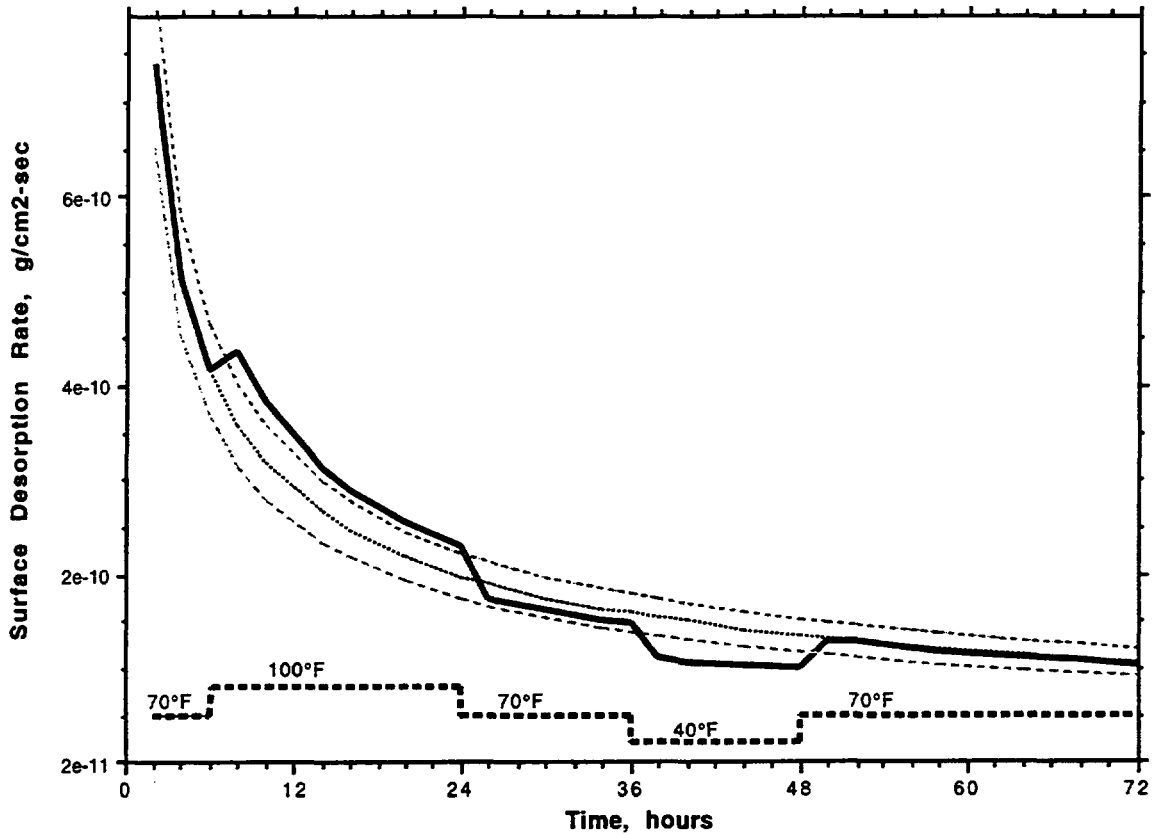


Fig. 9 The desorption rate with variable temperatures.

Table 2 Surface outgassing rate of the 64-mil Gr/Ep panel

| Time, day | Outgassing Mode | Varying Temperature | Constant 40°F (277.4K) | Constant 70°F (294.1K) | Constant 100°F (310.8K) |
|-----------|-----------------|---------------------|------------------------|------------------------|-------------------------|
| 1         | 1-sided         | 2.491E-10           | 1.938E-10              | 2.185E-10              | 2.431E-10               |
| 1         | 2-sided         | 2.185E-10           | 1.938E-10              | 2.185E-10              | 2.431E-10               |
| 2         | 1-sided         | 1.195E-10           | 1.370E-10              | 1.545E-10              | 1.719E-10               |
| 2         | 2-sided         | 1.545E-10           | 1.370E-10              | 1.545E-10              | 1.719E-10               |
| 10        | 1-sided         | 6.882E-11           | 6.128E-11              | 6.907E-11              | 7.680E-11               |
| 10        | 2-sided         | 5.606E-11           | 5.518E-11              | 5.606E-11              | 5.411E-11               |
| 30        | 1-sided         | 3.639E-11           | 3.408E-11              | 3.646E-11              | 3.740E-11               |
| 30        | 2-sided         | 6.932E-12           | 1.064E-11              | 6.934E-12              | 4.067E-12               |
| 45        | 1-sided         | 2.455E-11           | 2.488E-11              | 2.459E-11              | 2.301E-11               |
| 45        | 2-sided         | 1.446E-12           | 3.100E-12              | 1.446E-12              | 5.838E-13               |

(unit: g/cm<sup>2</sup>-sec)

## CONCLUDING REMARKS

A diffusion flux model was developed to compute the outgassing characteristics of a graphite epoxy panel. The model computes concentration profiles, average moisture contents, and the diffusion flux at the surface. The diffusion coefficient was modeled with an exponential function where the coefficients were determined from measured outgassing data. An integrated diffusion coefficient was used in the diffusion model to account for the outgassing history of the Gr/Ep panel.

The diffusion flux model can be used to verify the methods and processes to reach the desired moisture contents in a Gr/Ep panel with a given time period. The options include raising the temperature of the panel on orbit, bakeout on ground and dry air purge, reducing the thickness of the panel, and using the material with a higher diffusion coefficient.

## REFERENCES

1. P. W. Knopf, A. L. Lee, and A. P. Glassford, "Prediction and Test Correlation of Venting from a Satellite Enclosure with Temperature-Dependent Outgassing," AIAA Paper 93-2875, July 1993.
2. P. W. Knopf and A. L. Lee, "Application of Temperature-Dependent Venting Simulation for Early Orbit Operation," AIAA Paper 95-0685, January 1995.
3. R. B. Bird, W. E. Stewart, and E. N. Lightfoot, *Transport Phenomena*, 1960.
4. M. A. Peterson and D. W. Delaney, "Chamber Transient Venting Analyses," LMMS Internal Memo, July 15, 1991.
5. H. S. Carslaw and J. C. Jeager, *Conduction of Heat in Solids*, The Clarendon Press, 1959.
6. M. A. Peterson and D. W. Delaney, "Baseline Venting Analysis," LMMS Internal Memo, March 6, 1991.
7. A. L. Lee, "Honeycomb Radiator Panel Venting," TSS-561, Nov. 27, 1996.
8. R. C. Weast, S. M. Selby, and C. D. Hodgman, *Handbook of Chemistry and Physics*, 45th Edition, The Chemical Rubber Co., 1964, pp. D-91.

# STATISTICAL EVALUATION OF MOLECULAR CONTAMINATION DURING SPACECRAFT THERMAL VACUUM TEST

Philip Chen, Randy Hedgeland, Alex Montoya,  
Juan Roman-Velazquez, and Jamie Dunn  
Goddard Space Flight Center  
Greenbelt, MD 20771

Joe Colony  
Mantech Systems Engineering Corporation  
Seabrook, MD 20706

Joseph Petitto  
Naval Surface Warfare Center  
Indian Head, MD 20640

## ABSTRACT

The purpose of this paper is to evaluate the statistical molecular contamination data with a goal to improve spacecraft contamination control. The statistical data was generated in typical thermal vacuum tests at the National Aeronautics and Space Administration, Goddard Space Flight Center (GSFC). The magnitude of material outgassing was measured using a Quartz Crystal Microbalance (QCM) device during the test. A solvent rinse sample was taken at the conclusion of each test. Then detailed qualitative and quantitative measurements were obtained through chemical analyses. All data used in this study encompassed numerous spacecraft tests in recent years.

## INTRODUCTION

Outgassing from polymeric materials is a major molecular contamination source for spacecraft. Rigorous contamination control efforts in the selection of materials, cleaning of sub-assemblies, and integration procedures is necessary in order to minimize material outgassing and accomplish an acceptable overall cleanliness. Among all efforts, high temperature thermal vacuum bakeout is considered as one of the most effective methods in reducing the material outgassing in order to achieve acceptable on-orbit performance.

During the thermal vacuum tests, many monitoring devices were applied to measure the outgassing levels. Devices such as a Residual Gas Analyzer (RGA), pressure gauge, and QCM were commonly used tools. These devices provided valuable "fingerprint" information for the conditions of the chamber and the test components. At the conclusion of each test, cold finger<sup>[1]</sup> and scavenger plate samples were typically taken for further chemical analyses using infrared spectroscopy and mass spectrometry. Individual test data from the monitoring devices and analyses have been widely applied in evaluating the component conditions and identifying outgassing species for contamination control purposes. However, a statistical approach to correlate the data is not currently available.

An effective approach to spacecraft contamination control may be accomplished by a systematic method based upon statistical material outgassing data. It is imperative to monitor, evaluate, and correlate the contamination data in order to improve overall spacecraft contamination control. Relevant test data

from Hubble Space telescope (HST) and other satellites is presented to support the approach of a statistical evaluation of molecular outgassing as an effective spacecraft contamination control process.

## MOLECULAR CONTAMINATION INSTRUMENTATIONS

### Quartz Crystal Microbalance

The Thermoelectric Quartz Crystal Microbalance (TQCM) and M-2000 control unit system measures and records condensable mass that deposits on a piezoelectric crystal. Extreme accuracy was obtained by comparing the exposed measurement crystal to an encapsulated reference crystal located in the same TQCM head. A computer controlled thermoelectric device provides a high degree of crystal temperature control, which was vital for accurate frequency measurement. Two TQCM sensing units were used, 10 MHz or 15 MHz.

The dimension of the TQCM was 5 cm (2 in) diameter x 25.5 cm (10 in) length. The mass sensitivity was  $4.43 \times 10^{-9}$  g/cm<sup>2</sup>-Hz for the 10 MHz unit and  $1.97 \times 10^{-9}$  g/cm<sup>2</sup>-Hz for the 15 MHz unit. The crystal temperature was operated between -50 and +100 °C within  $\pm 0.1$  °C accuracy. One or more TQCM sensing units were installed in a thermal vacuum chamber. The chamber was pumped down to a test pressure of 1.33 mPa ( $10^{-5}$  torr) or less, at which point the TQCM was turned on and set for the appropriate operating temperature. As the test articles outgassed and materials condensed on the TQCM sensing crystal, the crystal frequency increased directly proportional to the amount of deposition from test article outgassing.

The function and control of a Cryogenic Quartz Crystal Microbalance (CQCM) was similar to that of a TQCM. The CQCM with mass sensitive piezoelectric crystals were operated between -268 and 127 °C.

### Residual Gas Analyzer

The RGA was used to measure the partial pressures of ionized molecules over a mass range of 1 to 300 atomic mass units (AMU) where the best sensitivities were below 100 AMU. Using a combined Radio Frequency (RF) and electrostatic field formed by two metal rods, the RGA scanned the mass range and detected the partial pressures of each element or compound fraction. The RGA probe was located in the thermal vacuum facility and was oriented to maximize the detection of the outgassing species. After the facility pressure reached 13.3 mPa ( $10^{-4}$  torr), the instrument was activated. An alternate technique was to use the micro-sampling valve at high chamber pressure. Monitoring and recording of the vacuum environment was via a display meter and printer. The data was stored and recalled upon command. An integrated programmable data system with dual disk drives allowed flexibility in scanning, monitoring, storing, printing, and recalling the data. Three models (MKS PPT 200EM, MKS PPT 100F, and Leybold C100F) were available for various test conditions.

### Cold Fingers

Cold fingers are small stainless steel cylinders which were mounted in the test volume of each thermal vacuum chamber. The size of the cold finger was 5.0 cm diameter x 10.0 cm height with a surface area of 142 cm<sup>2</sup> nominal. The cold finger was operated during the last 8 hours of the test at an operating temperature of -196 °C (-321 °F). At this cold temperature, condensable vapors were collected by the cold finger and analyzed after the test. In some cases, a large cold plate (scavenger plate) was used to collect the condensable materials. The cold finger was maintained at liquid nitrogen (LN<sub>2</sub>) temperature during test and maintained until the chamber was backfilled to 80 kPa (600 torr).

The cold finger was thoroughly cleaned before the test. After the test, the cold finger was warmed and again rinsed with spectroscopic-grade isopropyl alcohol. The rinse sample was collected in a clean

bottle and sent to the Materials Engineering Branch for chemical analysis. Scavenger plates were operated at LN<sub>2</sub> temperature throughout the test and then rinsed and analyzed in the same manner.

### **Witness Mirrors**

Aluminum coated witness mirrors are used primarily to collect outgassed materials in the thermal vacuum chambers and placement within the chamber was not critical in collecting condensable matter. To determine the quantity of material on the mirror, reflective ultraviolet measurements were made prior to test, and then compared to post-test measurements for reflectivity changes. The mirror was placed inside the thermal vacuum chamber (or other environment) and allowed to remain in that location for the duration of the test. In most cases, the mirror's temperature followed the thermal vacuum chamber temperature profile. For large accretions (greater than 10% change in reflectivity) the mirror was sent to the Materials Engineering Branch for chemical analysis of the non-volatile residue (NVR).

The mirror size was 5 cm x 5 cm (2 in x 2 in) with 600 to 800Å of aluminum coated on one side and layered with 250Å of Magnesium Fluoride (MgF<sub>2</sub>). Typical measurement wavelength ranges recorded were 1216Å, 1608Å, and 2000Å with ± 2% measurement error. The operating temperature range of the mirrors was between -190 and +100 °C (-310 to +212 °F).

### **Fourier Transform Infrared Spectrometer (FTIR)**

The infrared spectrometer instrument was used to obtain Fourier transform data processing to produce transmission spectra. The Materials Engineering Branch FTIR was a Nicolet 710SX research grade instrument used for the identification of organic functional and transmission characteristics of materials from 4000 to 400 cm<sup>-1</sup> with a resolution of 4 cm<sup>-1</sup>. Infrared spectra were produced by measuring the amount of infrared radiation which a material absorbed at different wavelengths. These measurements were then compiled and a "fingerprint" spectrum was produced showing all the absorption bands throughout the infrared region.

### **Gas Chromatography/Mass Spectrometry (GC/MS)**

A gas chromatograph interfaced with a quadrupole mass spectrometer was used to analyze the cold finger residue. The GC/MS had an analysis range of 1 to 1000 AMU. By factoring the instrument parameters along with the type and length of column used in the GC, a precise identification of a compound was made. The system that collected most of the cold finger data was a Nermag R10-10C mass spectrometer interfaced with a Varian 3300 gas chromatograph.

### **CONTAMINATION DATA COLLECTION**

The thermal vacuum chambers were operated by the Environmental Test Engineering and Integration Branch at GSFC. The test articles along with their test fixtures were placed in a chamber where a QCM detected the deposition of mass. A Temperature Controlled Witness Mirror (TCWM) and a metallic cylindrical "cold finger" were utilized to collect the contaminant for further study.

The QCM and witness mirror were positioned, usually as close as possible to the test article, to fill the QCM's field-of-view. The QCM, the witness mirror, and the walls of the vacuum chamber were kept at specific conditions. At the end of the test, the cold finger was rinsed and the solvent was collected for chemical analysis. The cold finger was evaporated in air and the total amount of residue was determined. FTIR analysis was then performed on the residue. Since the residue was frequently a mixture of various compounds, the FTIR analysis was used as a screening test to identify the various classes of compounds

present in the sample. The residue was analyzed using GC/MS to obtain a more precise identification of each component.

### Statistical QCM data

Statistical QCM data were obtained from the tests between November 1995 and January 1997. The types of the tests were thermal vacuum, thermal balance, and bakeout. About 200 thermal tests were performed in this time period. There were only 167 tests with complete QCM and cold finger data for this statistical study. Test articles included the flight materials, thermal blanket, solar array, electronic boxes, harness, cables, flight support hardware, instruments, and full spacecraft complements. Major projects such as: HST, Tropical Rainfall Measuring Mission (TRMM), Cassini Composite Infrared Spectrometer (CIRS), Mars Observer Laser Altimeter (MOLA), Geostationary Operational Environmental Satellite (GOES), Fast Auroral Snapshot Explorer (FAST), X-ray Timing Explorer (XTE), and Transition Region and Coronal Explorer (TRACE) were included in the data reduction.

During the thermal vacuum tests, recorded QCM readings were strongly influenced by the collection temperature and environmental parameters of the thermal vacuum chamber. Therefore, the relationships among QCM temperatures, chamber shroud temperatures, and QCM readings were critical elements to be studied. These factors were changed frequently to reflect the test conditions stated in the thermal vacuum test procedures. For a meaningful comparison, only data prior to the activation of the cold finger was compiled. As shown in Table 1, 167 QCM data points were reported for various temperature ranges. Under normal tests, QCMs were kept at  $-20^{\circ}\text{C}$  for easy operations and best readings. For the majority of the thermal vacuum tests (156 tests), QCM temperatures were maintained at  $-20^{\circ}\text{C}$ . For these tests, only regular TQCMs were needed. Less than 7% of the time (11 tests), QCMs were held below  $-50^{\circ}\text{C}$ . Under these occasions, colder QCMs were used to simulate actual hardware conditions in order to understand the potential of the molecular deposition. For the test requiring the temperature as cold as  $-135^{\circ}\text{C}$ , a CQCM was needed.

Table 1 QCM Temperatures

| QCM Temperatures ( $^{\circ}\text{C}$ ) | Number of Tests |
|---|-----------------|
| -135                                    | 1               |
| -50 to -70                              | 10              |
| -20                                     | 156             |
|   | 167             |

During the thermal vacuum tests, the shroud temperatures greatly affected the temperature profiles and material outgassing. In these 167 tests, the shroud temperatures were maintained between  $-175$  and  $100^{\circ}\text{C}$  to provide proper temperature conditions for the test articles. As shown in Table 2, there were 42 tests with the shroud temperature below  $-20^{\circ}\text{C}$ , 7 tests with a range of  $-20$  and  $25^{\circ}\text{C}$ , 65 tests with a range of  $25$  and  $90^{\circ}\text{C}$ , and 53 tests above  $90^{\circ}\text{C}$ . The distribution of the shroud temperature reflected the nature of the tests. Normal thermal vacuum tests were operated between  $-20$  and  $90^{\circ}\text{C}$ . During the bakeout or chamber certification, the temperature of the shroud was raised to approximately  $100^{\circ}\text{C}$  to promote the material outgassing and chamber cleaning. Chamber temperatures higher than  $100^{\circ}\text{C}$  were prohibited to prevent severe outgassing from the chamber wall or test articles. Cold chamber shroud, functioned like a large scavenger plate, and thus isolated chamber outgassing from test articles outgassing. Liquid or gaseous nitrogen was used to cool the shroud for the below room temperature operation.

Table 2 Thermal Vacuum Chamber Shroud Temperatures

| Shroud Temperatures (°C) | Number of Tests |
|--------------------------|-----------------|
| < -20                    | 42              |
| -20 to 25                | 7               |
| 25 to 90                 | 65              |
| > 90                     | 53              |
|                          | 167             |

Both 10 MHz and 15 MHz QCMs were commercially available. Each type of QCM had a unique mass sensitivity depending upon the manufacturer. The baseline for the thermal vacuum tests at GSFC was the 10 MHz QCM. For this study, the values of the 15MHz QCM were converted to the 10 MHz QCM. Table 3 shows the actual or the equivalent readings of a 10 MHz QCM for all 167 tests taken prior to the activation of the cold finger. There were 22 tests with the QCM readings below 1 Hz/hr, which was the minimum sensitivity of a QCM. Two significant factors existed for tests with QCM readings of less than 1 Hz/hr. The negligent QCM readings indicated either the test articles were required to meet a very stringent requirement or the tests were performed at low temperatures. The majority of the QCM readings were within 2 to 250 Hz/hr which illustrated the goal of reducing test article outgassing during the thermal vacuum tests. The tests with QCM readings around 300 Hz/hr represented the bakeout or chamber certification. The QCM value of 300 Hz/hr was a general criterion for a hardware bakeout process that the chamber was guaranteed to meet. For the post chamber certification, the thermal vacuum chambers were required to meet the 300 Hz/hr cleanliness level.

Table 3 QCM Readings

| QCM Readings (Hz/hr) | Number of Tests |
|----------------------|-----------------|
| < 1                  | 22              |
| 2 to 50              | 65              |
| 50 to 250            | 24              |
| 250 to 300           | 37              |
| > 300                | 19              |
|                      | 167             |

#### Statistical cold finger chemical analysis data

In addition to the statistical QCM data, the statistical chemical analysis data were also obtained. Upon receiving the cold finger sample, the Materials Engineering Branch's laboratory performed the chemical analyses using the FTIR and GC/MS techniques. NVR results from these chemical analyses provided the quantity of the molecular contaminants, identified various outgassing species, and in some cases confirmed contamination sources. Table 4 shows the quantity of the NVR collected during the cold finger period. The amount of the NVR was directly proportional to the molecular outgassing inside the thermal vacuum chamber after the activation of the cold finger. There were 31 tests with the NVR values of less than 0.1 mg. A small NVR (<0.1 mg) always indicated a low outgassing nature of the test articles. For example, some HST hardware were required to be baked out to below 1 Hz/hr. Most of the NVR values after normal thermal vacuum tests were below 0.5 mg. Typical NVR values after the chamber bakeout and certification were around 1.0 mg because of the high temperature.

NVR values of 2.0 mg and higher suggested problems associated with the test articles and/or thermal vacuum chambers. One example was that a high concentration of hydrocarbons was constantly detected when the temperature of the chamber shroud was 100°C or higher. These hydrocarbons were associated with the lubricating oils, machining oils, and greases used on various parts of the thermal vacuum chamber. The other example was due to the malfunction of the cooling system of the cold finger. The cold finger sample was inadvertently activated at the beginning of the thermal vacuum test, and exceeded the normal 8-hour operation period.

Table 4 Cold Finger Results

| NVR (mg)   | Number of Tests |
|------------|-----------------|
| < 0.1      | 31              |
| 0.1 to 0.5 | 52              |
| 0.5 to 1.2 | 49              |
| > 1.2      | 35              |
|            | 167             |

#### Cold finger chemical species

Besides the NVR values, principal chemical species were identified from the chemical analysis. The chemical species with their frequency of occurrences are shown in Table 5. There were more than 40 identifiable chemical species commonly detected during the thermal vacuum tests at GSFC.

A plasticizer is a high-boiling molecular compound or softening agent, usually liquid, added to a polymer to facilitate processing or to increase flexibility or toughness. Some commercial plasticizers use complex mixtures of phthalate esters. Di-(2-ethylhexyl) phthalate (DEHP) is used primarily as one of several plasticizers in polyvinyl chloride (PVC) polymers to make them flexible. Some PVC can contain up to 50% by weight of plasticizers. DEHP was the most observed plasticizer of GSFC's cold finger samples. Dibutyl phthalate (DBP) and Butyl benzyl phthalate (BBP) also function as plasticizers for many rubbers and a wide range of other synthetic resins. In addition, di-(2-ethylhexyl) adipate, di-(2-ethylhexyl) azelate, and di-(2-ethylhexyl) sebacate were also frequently outgassing compounds from the polymeric materials. Triphenyl phosphate (TPP) and 2-butoxy ethanol phosphate 3:1 are common flame retardant compounds added to the polymeric materials either as plasticizers or as an anti-wear additive. TPP was found to be outgassed from the flight hardware as the additive to the TRMM thermal blankets.

Room-temperature vulcanizing (RTV) silicone adhesives and sealants are designed for a wide range of sealing, bonding, and protection for spacecraft applications. Therefore, adhesive material of silicones were easily detectable during the thermal vacuum tests. There were 88 occurrences of either methyl silicones, methyl phenyl silicones, fluorinated silicones, or silicones. On one sample, methyl silicones was detected because a piece of pink polyester tape with a silicone adhesive was inadvertently placed on the thermal blanket. This blanket was removed from a test fixture hardware, the pink polyester tape was removed, and the fixture was cleaned with a solvent prior to installing a new thermal blanket on the fixture. Methyl silicones were also identified to be released from silicone grommets used in the assembly of the electrical connectors, from silicone foam, from Furon Chorlastic R-10404, or from Thermobond used for the heat sink on the circuit boards. Fluorosilicone material, ZZ-R-765, was identified as part of the assembly of the electric connectors (the insulator material) used on the flight hardware.

Table 5 Occurrence Frequency of Chemical Species

| Chemical Species                               | Number of Occurrences |
|--|-----------------------|
| <i>Plasticizer</i>                             |                       |
| Di-(2-ethylhexyl) phthalate                    | 159                   |
| Butyl benzyl phthalate                         | 98                    |
| Di-(2-Ethylhexyl) adipate                      | 74                    |
| Di-(2-Ethylhexyl) sebacate                     | 70                    |
| Di-(2-Ethylhexyl) azelate                      | 66                    |
| Phthalate ester                                | 46                    |
| Triphenyl phosphate (TPP)                      | 40                    |
| Dibutyl phthalate                              | 31                    |
| Didecyl phthalate                              | 19                    |
| 2-butoxy ethanol phosphate 3:1                 | 18                    |
| Diocetyl phthalate                             | 10                    |
| 2-Mercaptobenzothiazole (MBT)                  | 6                     |
| Azelate ester                                  | 4                     |
| Butylbenzenesulfonamide                        | 1                     |
| <i>Elastomers</i>                              |                       |
| Methyl silicones                               | 52                    |
| Methyl phenyl silicones                        | 25                    |
| Silicones                                      | 9                     |
| Fluorinated silicones                          | 2                     |
| <i>Polymers and Adhesives</i>                  |                       |
| Bis-phenol-A(Epoxy)                            | 45                    |
| Aromatic amine (uralane)                       | 21                    |
| Unknown phthalimide (epoxy)                    | 14                    |
| Methyl-benzenediamine (epoxy)                  | 13                    |
| Methylene diphenol (Primer 9924)               | 12                    |
| Unknown amine (epoxy)                          | 9                     |
| Aliphatic amine (epoxy)                        | 7                     |
| Polyurethane curing agent                      | 5                     |
| Acrylic adhesive                               | 1                     |
| <i>Other Compounds</i>                         |                       |
| Saturated & unsaturated hydrocarbons           | 167                   |
| Palmitic acid                                  | 114                   |
| Detergent derivatives                          | 67                    |
| Stearic acid                                   | 51                    |
| DC704 diffusion pump oil                       | 20                    |
| Calcofluor (Fluorescent tracking compound)     | 20                    |
| Myristic acid                                  | 18                    |
| Phthalic anhydride                             | 14                    |
| Benzoic acid                                   | 4                     |
| Tetraethylene glycol di-2-ethylhexanoate       | 3                     |
| Lauric acid                                    | 3                     |
| 2-Hydroxy 4-methoxy benzophenone (antioxidant) | 2                     |
| Erucamide                                      | 1                     |
| Tri-(allyl) cyanurate                          | 1                     |

Caprolactam (Nylon-6 bagging contaminate) did not appear in any cold fingers while Tri-(allyl) cyanurate was only detected once. These highly volatile compounds were normally vaporized before the activation of the cold finger. As a result, these compounds were detected in large quantities in the scavenger plate samples which were activated earlier to preserve volatile chemical species. In contrast, Bis-phenol-A was less volatile and was only found in certification samples because it was derived from the epoxy chamber coatings at high temperature. Bis-phenol-A was a major outgassing species from the TRMM beta cloth. Methylene diphenol most likely came from Chemglaze 9924 wash primer used with polyurethane coating materials on the flight hardware.

Occasionally an aromatic amine from the curing agent in various Uralanes was detected from the test samples. For example, Uralane 5753LV with CAB-O-SIL was used as a staking compound on a piece of flight hardware. Final analysis could not define whether the curing agent was excessively added to the mixture or whether the polyurethane was not cured completely before the thermal vacuum test.

Saturated & unsaturated hydrocarbons were the most common chemical species. The butoxy compound, possibly from the detergent used for cleaning the chambers, was detected when the chamber temperature was high and the amounts of other residues were low. Fatty acids such as palmitic acid, myristic acid, stearic acid, and lauric acid were frequently found in the test. They were often natural organic oils commonly used in polymers, antistatic agents, and general handling contaminants (including fingerprints). They were soluble in alcohol and were easily removed by a simple solvent cleaning.

Calcofluor, a fluorescent tracking compound, was observed 20 times during all tests. This was an additive usually found in polyurethane conformal coatings. The percentages added to the conformal coating usually varied from tenths of a percent to a few percent. DC704 diffusion pump oil occurred 20 times during the evaluation period. Specifically there were 11 times for chamber 237, 5 times for chamber 243, and 4 times for chamber 238. Even though DC704 was no longer used at GSFC, traceable quantities of the compound still appeared in the cold finger analysis. The presence of DC704 was a strong indication that the hardware was contaminated during previous thermal vacuum tests conducted at vendor facilities because GSFC's Chambers 237, 238, and 243 used Santovac diffusion pump oil. This indicated that thermal vacuum chambers equipped with diffusion pumps and DC704 were still common in the aerospace industry. Tetraethylene glycol di-2-ethylhexanoate was a unique chemical species which was detected only in Chamber 290.

### **Major cold finger chemical species**

In each chemical analysis, as high as 15 chemical species were identified and listed according to their relative quantities within the test sample. In general the top 3 chemical species represented the most significant outgassing components during the thermal vacuum tests. A summary of 11 common chemical species were found to be among the top 3 of all identified chemical compounds (refer to Table 6). As shown in Table 6, saturated & unsaturated hydrocarbons (164 times) and DEHP (140 times), butoxy compound (34 times), and methyl silicones (22 times) were major chemical species. Even though the butoxy compound and methyl silicones were less frequent in the overall samples surveyed, i.e. Table 5, they were identified as significant chemical species as shown in Table 6. Therefore, the summary list in Table 6 identified the significance and relative quantity of the common chemical species.

### **COMPARISON WITH EARLY CHEMICAL ANALYSIS DATA**

Extensive chemical analyses were performed at GSFC from 1970 to 1978 and a total of 1163 data points were reported by Colony<sup>[2]</sup> in 1979. In the report, individual materials were incorporated into their

Table 6 Occurrence Frequency of Major Cold Finger Chemical Species

| Chemical Species                           | Top 3 |
|--|-------|
| 1. Saturated & unsaturated hydrocarbons    | 164   |
| 2. Di-(2-ethylhexyl) phthalate             | 140   |
| 3. Butoxy compound (detergent derivatives) | 34    |
| 4. Methyl silicones                        | 22    |
| 5. Palmitic acid                           | 21    |
| 6. Phthalate ester                         | 16    |
| 7. Methyl phenyl silicones                 | 14    |
| 8. Di-(2-ethylhexyl) adipate               | 13    |
| 9. Bis-phenol-A (epoxy)                    | 10    |
| 10. Triphenyl phosphate (TPP)              | 9     |
| 11. Di-(2-ethylhexyl) azelate              | 9     |

generic classes along with the frequency and percentage. Esters were the leading generic class of compounds found in the early survey, followed by hydrocarbons and methyl silicones. As shown in Table 7, the chemical classes of the 70s consisted of 36% esters, 23% aliphatic hydrocarbons, 16 % methyl silicones, 5.7% aromatic silicones, 4.7% antioxidants, 2.8% aromatic hydrocarbons, 2.2% polyurethane derivatives, 1.1% organic acids, and 9% other materials. Within the classes, DEHP was the most often found individual species in large outgassing samples. The compound TPP appeared in 1972-1973 and then not again until 1977. The use of di-(2-ethylhexyl) azelate increased radically in 1976 and 1977 and disappeared after 1977.

Table 7 GSFC Chemical Analysis Data Comparison

| Chemical Classes            | Percentage (%) |                                     |       |
|-----------------------------|----------------|-------------------------------------|-------|
|                             | 1970-1978      | 1995-1997<br><u>All Occurrences</u> | Top 3 |
| 1. All esters               | 36             | 47.2                                | 41.4  |
| 2. Aliphatic hydrocarbons   | 23             | 12.4                                | 32.7  |
| 3. Methyl silicones         | 16             | 4.5                                 | 4.8   |
| 4. Aromatic silicones       | 5.7            | 1.9                                 | 2.8   |
| 5. Antioxidants             | 4.7            | 0.1                                 | 0.0   |
| 6. Aromatic hydrocarbons    | 2.8            | 0.0                                 | 0.0   |
| 7. Polyurethane derivatives | 2.2            | 2.5                                 | 0.8   |
| 8. Organic acids            | 1.1            | 14.1                                | 5.2   |
| 9. Other materials          | 9              | 17.3                                | 12.3  |

Based upon all occurrences, the chemical classes of 1995-1997 consisted of 47.2% esters, 12.4% aliphatic hydrocarbons, 4.5 % methyl silicones, 1.9% aromatic silicones, 0.1% antioxidants, 2.5% polyurethane derivatives, 14.1% organic acids, and 17.3% other materials. However, based upon the top 3 species, the chemical classes of the 90s changed to 41.4% esters, 32.7% aliphatic hydrocarbons, 4.8 % methyl silicones, 2.8% aromatic silicones, 0.8 polyurethane derivatives, 5.2% organic acids, and 12.3% other materials. Esters and hydrocarbons remained as the leading generic classes. However, the usage of methyl silicones was reduced. Antioxidants and aromatic hydrocarbons did not appear on the top 3 list indicating the reduction of the usage in spacecraft materials. DEHP continued to be the most often found

individual species in outgassing samples. Both TPP and di-(2-ethylhexyl) azelate appeared frequently and showed 9 times each on the top 3 list.

In summary, the esters, aliphatic hydrocarbons, and methyl silicones accounted for 75% of the outgassing problems in the 70s. In comparison, these 3 species account for 64% (based upon all occurrences) or 79% (based upon top 3) of the outgassing problems in the 90s. This comparison also demonstrated that even though more polymeric materials were incorporated into spacecraft now than in the 70s, they were pre-treated to prevent high concentrations of outgassing species. This actually reduced the levels of species that were seen in the cold finger samples (For example, the decrease in methyl silicone levels).

## CONTAMINATION DATA CORRELATION

At the end of the thermal vacuum tests, the QCM readings were used to provide test termination criteria. These readings illustrated the dynamic outgassing behavior of the test articles and thermal vacuum chamber conditions. However, the QCM was not capable of determining the outgassing species unless an extensive Thermogravimetric Analysis (TGA) procedure was performed. This may not always be possible with long chain hydrocarbons or high AMU species. Therefore, the TGA was applied only for very specific test conditions during the thermal vacuum tests. On the contrary, the NVR values from the cold finger tests was not transient. The NVR values provided a collected information of the quantity and chemical constituents of the cold finger sample. Utilizing the combined QCM and NVR information helped provide a better understanding of the thermal vacuum tests. In addition, the correlation of the QCM readings from thermal vacuum tests and NVR values from the cold finger tests helped provide a trend of all thermal vacuum tests.

As shown in Figure 1, the NVR values are plotted against the QCM values. Data with QCM values higher than 350 Hz/hr or NVR values larger than 3.0 mg were not selected. These data points were excluded due to incompleteness, inconsistency, chamber failure, or abnormal high outgassing condition. All QCM readings were reasonably separated into two major groups according to their thermal vacuum shroud temperatures. Large variations of some data points were probably caused by the QCM locations and chamber temperature changes. Generally, the QCM values of the cold shroud tests ( $-20^{\circ}\text{C}$  or below) were less than 50 Hz/hr and the NVR values were below 1.0 mg. For the warm shroud tests (above room temperature), the main range of the NVR values was between 0.1 and 2.0 mg. And the majority of the QCM values were below 300 Hz/hr. For data point with the same QCM value, the cold shroud tests generated a higher NVR value than that of the warm shroud.

At GSFC, the QCM requirement of the post-test chamber certification was 300 Hz/hr. As shown in Figure 1, only a few of the certifications have the QCM values higher than 300 Hz/hr, i.e. non-certified. However, for those non-certified chambers, the 300 Hz/hr was achieved prior to the next thermal vacuum test cycle. The range of the NVR for all certified chambers was between 0.3 to 2.5 mg. It was safe to assume that the chamber was certified if the NVR was below 1.0 mg limit.

## CONCLUSIONS

To understand material outgassing under thermal vacuum conditions, it was advantageous to continuously monitoring the chamber conditions by the QCM and cold finger. The QCM and cold finger provided complementary information for both qualitative and quantitative contamination assessments. Chemical analysis also provided interesting information such as either the unique evidence of contamination

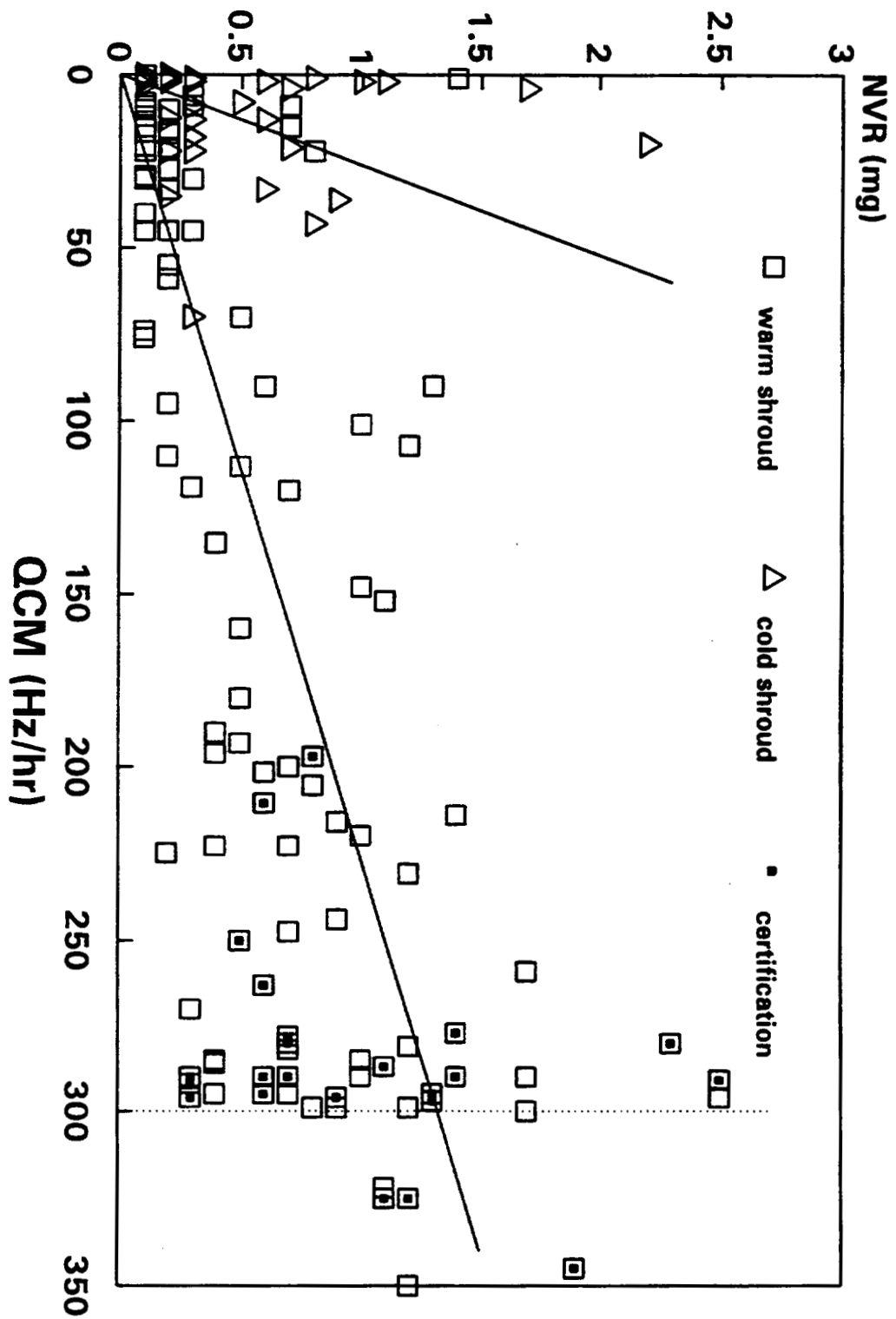


Figure 1 Thermal vacuum QCM values and chemical analysis NVR results

transfer (DC704 diffusion pump oil) or unique signature of a chamber (Tetraethylene glycol di-2-ethylhexanoate).

The conditions of the chamber shroud were very important for a successful thermal vacuum test. Test conditions were influenced by the shroud temperatures. For bakeout or chamber certification, the shroud temperature was raised to a maximum temperature to expedite outgassing. On the contrary, the cold shroud served as a cold sink that could provide a favorable clean environment for the test articles. Therefore, it was important to understand the status of the chamber conditions and monitor by way of the QCM and cold finger.

During the thermal vacuum test, the QCM and chamber shroud temperatures strongly affected the QCM readings. The placement of the QCMs in the thermal vacuum chamber was also an important factor of QCM results. QCMs performed adequately for the majority of the thermal vacuum tests when maintained at a stable temperature of  $-20^{\circ}\text{C}$ . The QCM value of 300 Hz/hr was a general criterion for the bakeout and chamber certification at GSFC. Typical NVR values after the chamber bakeouts and certifications were around 1.0 mg. Therefore, from a statistical point of view, it was reasonable to assume that the chamber was certified if the NVR was below 1.0 mg limit. A small NVR ( $<0.1$  mg) always indicated the low outgassing nature of the test articles. A high NVR ( $>2.0$  mg) indicated problems associated with the test articles and/or thermal vacuum test chambers.

The chemical analysis was not only effective in determining the outgassing potential, but also useful in assessing the conditions of the facility. The variation of NVR collected from a particular chamber provided the long-term conditions of the thermal vacuum chamber and its accessories. The continuous appearance of high NVR values and/or specific chemical species indicated the need for chamber recertification.

DEHP, hydrocarbons, and silicones were the most common chemical species in outgassing samples in the 70s as well as in the 90s. The evidence of these phthalate esters and hydrocarbons indicated their extensive use in many polymers and lubricants. The detergent derivative of butoxy compound appeared often whenever the temperature of the chamber shroud was raised above  $70^{\circ}\text{C}$ . Due to its wide applications, silicones, continue to be detected in the cold finger samples. The comparison of current and previous GSFC chemical analysis data showed the variations of material usage, material development, process changes, test concepts, and test approaches.

The statistical approach allowed for a parametric correlation of QCM and NVR values obtained from thermal vacuum tests. As expected from the correlation, the reduction in outgassing has been observed on the QCM and supported by NVR results. The correlation is not definitive, but it helps in determining the degree of success of an established contamination control approach. A precise determination is difficult to derive because of the dynamic changes in materials used in the manufacturing processes that affect outgassing and NVR results.

## REFERENCES

1. ASTM E-834, "Standard Practice for Determining Vacuum Chamber Gaseous Environment using a Cold Finger", American Society for Testing and Materials, 1985.
2. Colony, J. A., "Trends in Materials' Outgassing Technology", NASA Technical Memorandum 80585, November 1979.

## Challenging Pneumatic Requirements for Acoustic Testing of the Cryogenic Second Stage for the new Delta III Rocket

Andrew T. Webb  
Mantech Systems Engineering Corporation  
Goddard Space Flight Center

### ABSTRACT

The paper describes the unique pneumatic test requirements for the acoustic and shock separation testing of the Second Stage for the new Delta III Rocket at the Goddard Space Flight Center in Greenbelt, Maryland. The testing was conducted in the 45,000 ft<sup>3</sup> (25-foot wide by 30-foot deep by 50-foot high) Acoustic Facility. The acoustic testing required that the liquid oxygen (LOX) and liquid hydrogen (LH<sub>2</sub>) tanks be filled with enough liquid nitrogen (LN<sub>2</sub>) to simulate launch fuel masses during testing. The challenge for this test dealt with designing, procuring, and fabricating the pneumatic supply systems for quick assembly while maintaining the purity requirements and minimizing costs.

The pneumatic systems were designed to fill and drain the both LOX and LH<sub>2</sub> tanks as well as to operate the fill/drain and vent valves for each of the tanks. The test criteria for the pneumatic sub-systems consisted of function, cleanliness, availability, and cost. The first criteria, function, required the tanks to be filled and drained in an efficient manner while preventing them from seeing pressures greater than 9 psig which would add a pressure cycle to the tank. An LN<sub>2</sub> tanker, borrowed from another NASA facility, served as the pre-cool and drain tanker. Pre-cooling the tanks allowed for more efficient and cost effective transfer from the LN<sub>2</sub> delivery tankers. Helium gas, supplied from a high purity tube trailer, was used to pressurize the vapor space above the LN<sub>2</sub> pushing it into the drain tanker. The tube trailer also supplied high pressure helium to the vehicle for valve control and component purges. Cleanliness was maintained by proper component selection, end-use particle filtration, and any on-site cleaning determined necessary by testing. In order to meet the availability / cost juggling act, products designed for LOX delivery systems were procured to ensure system compatibility while off the shelf valves and tubing designed for the semiconductor industry were procured for the gas systems.

### INTRODUCTION

In the Spring of 1997, Goddard Space Flight Center (GSFC) and Mantech Systems Engineering Corporation (MSEC) met with Boeing (McDonnell Douglas at the time) to discuss the testing of the second stage of their new Delta III launch vehicle. Their testing required the use of Goddard's large, 45,000 ft<sup>3</sup> Acoustic Facility to run qualification tests on the new second stage design.

Many challenges faced the combined test team such as obtaining a Space Act Agreement for doing a commercial test at a government facility, physically supporting and fitting the second stage into the acoustic cell, scheduling, designing and fabricating the cryogenic and pneumatic interfaces, and the time constraints. This paper addresses the cryogenic and pneumatic challenges that were encountered for this test.

What made the test unique was the requirement to simulate launch conditions in the LOX and LH<sub>2</sub> tanks using LN<sub>2</sub> as the working fluid during the acoustic and shock separation testing. Temporary, high purity storage and supply systems for LN<sub>2</sub> and helium were going to be needed to load and off-load almost 5000 gallons of LN<sub>2</sub> into the fuel tanks on the second stage. The following sections describe the design, fabrication, integration, testing, and performance of the cryogenic and pneumatic systems for the Delta III Second Stage Acoustic and Shock Separation tests conducted at Goddard Space Flight Center in February and March of 1998.

## TEST CRITERIA

This test required the second stage be tested with the vehicle vertical, cryogenic temperature and mass in LOX and LH<sub>2</sub> tanks, control of second stage fill/drain and vent valves, and connections made using the vehicles umbilical panel. All components connected to the vehicles propulsion system were required to be suitable for LOX service.

The requirements for the LN<sub>2</sub> were that of Mil-P-27401C, grade B, Type I nitrogen with 100 micron absolute particle filtration. The GSE helium for the pneumatic valves was required to meet or exceed MIL-P-27407 with 25 micron absolute particle filtration supplied at a pressure of 650 psig. The LOX tank would require 3400 gallons of LN<sub>2</sub> to simulate the mass at launch and the LH<sub>2</sub> tank would require 1400 gallons. The Fill System was requested to fill the tanks in about 2 hours without exceeding one fourth of the tank burst pressure, thereby avoiding a pressure cycle on the tanks. The tanks were to be drained quickly without requiring a pressure cycle if possible.

## DESIGN APPROACH

The approach that Goddard's Environmental Test Branch adopted was to assemble a team and assign a team leader during the proposal phase that would follow the test from proposal to completion. Preliminary designs were compiled in the proposal stage. Some of the early decisions evaluated LN<sub>2</sub> sources, LN<sub>2</sub> disposal, condensation of water, nitrogen versus helium for pushing LN<sub>2</sub> out of tanks, etc.. Detailed design and component selection could not happen until the Space Act Agreement was signed in October 1997.

The key to success in any design is obtaining correct, detailed information as early as possible in the design. This was accomplished by visiting the manufacturing plant to obtain dimensions, confirm orientations, and to discuss proposed design with those most familiar with the equipment. The detailed design started by developing a process and instrumentation (P&ID) drawing based on the Boeing test plan and sequence of operations. Component selection and procurement were based on function, availability and cost.

### Conceptual Phase (Early Decisions)

Preliminary system design and analysis, meetings with the customer, and teamwork led to some effective decisions early in the project that proved instrumental in finishing under budget. Good analysis in the proposal (conceptual phase) provided a good foundation for the technical as well as the schedule and cost details. Some of the more critical decisions for this project are described below.

#### *LN<sub>2</sub> Supply*

No LN<sub>2</sub> taps existed in or near the acoustic facility. Piping from one of the existing tanks at our site would have required an LN<sub>2</sub> pump to provide the pressures and flow rates needed to fill the tanks. Temporary supply tanks with the capacity needed for this test would require concrete foundations in our parking lot area. Local gas suppliers were contacted and none of them had tankers we could park at our facility. Filling directly from delivery trucks was possible but the suppliers did not want the "used" LN<sub>2</sub> at the end of the test. Goddard team members networked and located portable LN<sub>2</sub> tankers at two other NASA centers that could be borrowed. The team pursued this option because it also provided a place to collect the LN<sub>2</sub> after the test.

#### *LN<sub>2</sub> Disposal*

Now that we had a vessel to drain the LN<sub>2</sub> into following a test, we had to determine what to do with the "used" LN<sub>2</sub>. If the purity of the tanker was verified, then it was proposed that the "used" LN<sub>2</sub> be re-used to pre-cool the supply lines and second stage tanks for the next fill operation and use a delivery from our local supplier for topping off the tanks.

## *Helium Tanker*

High pressure helium was required for the vehicles' pneumatic valves and low pressure helium gas was required for several GSE purges around the second stage. In addition, large volumes of gas were going to be required for pushing the LN<sub>2</sub> out of the second stage tanks. Because there was no requirement for gaseous nitrogen and helium does not collapse at LN<sub>2</sub> temperatures, helium was chosen early on as the gas used to push the LN<sub>2</sub> out of the LOX and LH<sub>2</sub> tanks. These factors drove the decision to use a tube trailer of high purity, high pressure helium and a manifold system that would be used for the vehicle valve control, vehicle purges, and tank draining.

## *Flex Lines*

Flex lines were chosen for several reasons. The first being that they facilitate rapid integration of the second stage to a system that was installed prior to the start of the test. The second fundamental reason was that flex lines provide the isolation of the second stage from its' support fixture and from the building piping sysetms. The flex lines that were used had to be designed to dissipate electrical energy to eliminate any build up of static electricity. The disadvantages to using flex lines mostly revolved around the difficulty in cleaning convoluted shapes as well as greater pressure drops per foot of pipe.

## **P&ID Drawing**

The Process and Instrumentation Diagram (P&ID) drawing was used to put the written requirements graphically onto paper detailing the piping systems as well as the instrumentation details. This was the tool used on this project to identify the components and the piping necessary to satisfy the Boeing test plan. The pipe sizes, component names, general relationships of equipment, etc. are portrayed in this fashion. A copy of the drawing is included at the end of this document.

## **Component Selection**

Component selection followed after the start of the P&ID drawing but continued in a parallel effort as the design was finalized. Some of the components were to be used with LN<sub>2</sub> at cryogenic temperatures and some were to be used with high purity helium gas but all components were to be cleaned for oxygen service. This terminology, "cleaned for oxygen service," was found to mean many things to different suppliers. All of the components we purchased were tested either individually or as a system for total hydrocarbons measured as methane and for water contamination. The most difficult component to locate was the 100 micron absolute particle filter for cryogenic service at high flow rates and low pressure drops.

## **FABRICATION**

Due to the use of flex lines, the external piping and the control console could be fabricated before the second stage had arrived at the test facilities. This design approach allowed for a smaller crew that could work sequentially through the task and thereby be dedicated to the task for its duration.

## **Purity Testing**

The first step was to determine if the supplied components met the purity requirements. Those requirements are outlined below:

- |                                     |                          |                                   |
|-------------------------------------|--------------------------|-----------------------------------|
| • H <sub>2</sub> O, water vapor     | < 11.5 ppm <sub>v</sub>  | per Mil-P-27401C, Grade B, Type I |
| • THC, Total hydrocarbon as methane | < 5.0 ppm <sub>v</sub>   | per Mil-P-27401C, Grade B, Type I |
| • NVR, Non-Volatile Residue         | < 3.0 mg/ft <sup>2</sup> | per Mil Std 1330, Oxygen Cleaning |

The majority of the components met the requirements while several did not. Two different methods were used to test for purity. The first technique, an alcohol rinse of 1 square foot of surface area, was designed to sample for the non-volatile residue (NVR). The alcohol was evaporated at room temperature and then analyzed using an FTIR infrared spectrometer. The

second technique looks for contamination in the gaseous phase. A flame ionization detector (FID) was used to analyze for hydrocarbon contamination with sensitivity in the parts per billion (ppb) range and a hygrometer was used to analyze the water vapor contamination with sensitivity in the parts per billion (ppb) range.

## **Component Cleaning**

The type of cleaning employed depended on the contamination that was found on the component. Hydrocarbon and particulate contamination was found in the 2-inch type L, ACR copper tubing used for the LN<sub>2</sub> lines. Alcohol soaked, lint-free, cleanroom wipes were attached to a ram and pushed through the lengths of copper until no evidence of contamination was visible. The line was then rinsed with alcohol and blown down with filtered nitrogen gas. The flex hoses procured with oxygen service cleaning showed hydrocarbon contamination. Flushing with isopropyl alcohol, followed by purging with dry nitrogen gas for 24-hours brought the tubing well within specification for both types of testing.

## **Develop Clean Brazing Technique**

Since the inside of the copper tube could not be rinsed or cleaned after brazing, several brazing techniques were tried and evaluated to determine which would provide the better internal surface integrity. The standard technique used at our facility for cryogenic soldering of copper consists of using flux with the silver solder. This technique heavily oxidizes the internal surfaces. For more critical applications, the internal volume is purged with nitrogen gas while soldering. The concern was with the flux and any potential reactions with the nitrogen at the elevated temperatures of silver soldering. A technique was developed using a silver brazing alloy containing copper phosphorous that does not require flux since the flux gas created when heated etches the copper oxides and allows the silver solder to flow and bond with the copper. The internal surfaces were purged with argon gas while soldering and until the joint had cooled. This technique produced solder joints showing no traces of flux or oxidation and that met all the purity requirements with minimal gas purging.

## **Fabrication of Piping System**

Upon arrival of the 4000 gallon LN<sub>2</sub> tanker borrowed from Marshall Space Flight Center, MSEC's Pressure Systems Recertification group evaluated the tanker and found it to meet the applicable codes. The tanker was then pressurized with high purity nitrogen gas and tested for THC and H<sub>2</sub>O contamination. The installation of the LN<sub>2</sub> piping started with nitrogen purge maintained during the installation phase. Before opening the LN<sub>2</sub> tanker to the rest of the piping system, the LN<sub>2</sub> system piping was pressure tested per ANSI B31.3 and then certified for THC and H<sub>2</sub>O contamination.

When ready, the 70,000 ft<sup>3</sup> helium tube trailer was delivered. The delivered purity was 99.999% indicating that it had no more than 10 ppm<sub>v</sub> of anything but helium. The tube trailer was sampled and tested for THC and H<sub>2</sub>O contamination to baseline the source gas. High pressure helium was piped to the control console using stainless steel tubing and compression fittings. The helium system was pressure tested then certified for purity.

The control console contained all of the critical instrumentation. It was fabricated on the bench during periods of inclement weather. All connections to the console were via flex lines which allowed for easy positioning of the console for various operations.

## **SYSTEM INTEGRATION**

The mobile support fixture (MSF) was sent ahead of the vehicle and was erected at our facility. After the fixture had been structurally tested, the interconnecting piping from the GSE flex line connection to the vehicle interface flex line was installed. This piping would allow for more rapid integration of the second stage to the GSE piping systems once installed in the acoustic facility.

Upon arrival of the second stage at Goddard, it was placed in the MSF. Some of the vehicle interface flex hoses were mated at the vehicle but capped until the rest of the system could be purged with helium. The site visit during the design phase was pivotal in ensuring all of the connections mated without any surprises. After the fixture was moved to the

acoustic cell, the control console and the LN<sub>2</sub> systems were connected to the piping on the MSF. The remainder of the vehicle connections were made after the piping systems had been purged and then leak tested up to the point of connection. The final connections were made and then the LOX and LH<sub>2</sub> tanks were leak tested and purge with helium.

## SYSTEM PERFORMANCE

The filling, draining, and feedback systems performed as designed and met all of the customers' requirements. The calculated flowrates were achieved, the ability to control the ullage pressure in the tanks using helium was stable, and the amount of LN<sub>2</sub> consumed for each test was significantly reduced. In addition, the condensation of ambient water vapor on the uninsulated exterior surfaces of the tanks did not present the water problem anticipated when warming up the tanks.

### LN<sub>2</sub> Filling / Draining

The use of the portable LN<sub>2</sub> tanker to pre-cool the supply lines, the LOX tank and the LH<sub>2</sub> tank worked well. Using the pressure building coil to build head pressure in the portable tanker allowed for flow rates around 50 gallons per minute (gpm). This technique allowed finer control when first introducing LN<sub>2</sub> into the tanks while trying to maintain LOX and LH<sub>2</sub> tank pressures less than 9 psig. We found that once, the bottom of the uninsulated tank was covered with LN<sub>2</sub>, that the flow rate could be throttled full open without causing the pressure to increase. Flow rates of up to 100 gpm were achieved when using the delivery trucks' high pressure LN<sub>2</sub> pumps. Fill times of 100 minutes were safely achieved.

Draining the LH<sub>2</sub> Tank worked very well using 8 psig of head pressure and gravity because the fill/drain connection was at the bottom of the tank. The LOX tank had to be drained through the fill line which enters the tank from the top and has a dip tube that extends to the bottom of the tank. At head pressures of 9 psig, the flow was estimated at 20 gpm. The decision reached was to drain the LOX tank using the design tank pressure which increased the flow to over 50 gpm. When the LOX tank reached gas break, the 4000 gallon fill/drain tanker was full. One of the unanticipated events was the time required ( $\approx$  17 hours) to boil off the remaining LN<sub>2</sub> in the LOX tank even though it was an uninsulated aluminum vessel.

### Level Sensing

Type 'T' thermocouples were taped to the aluminum surfaces of the tanks at their bottoms, middles, and tops. These thermocouples were a very effective and inexpensive way to indicate level in this application. The upper or top thermocouples were placed at the height on the tank calculated for the expected mass of LN<sub>2</sub> required. The measured amount of LN<sub>2</sub> pumped into each tank correlated very closely to the expected amount when the thermocouple indicated that LN<sub>2</sub> was at the appropriate level.

## CONCLUSIONS

Forming a good team in the early phases of a test in order to identify and understand the test criteria was the key element to adhering to the fundamentals of the proposal and maintaining both the schedule and cost constraints. Taking the time in the beginning to design the system to meet the criteria led to some decisions that formed the basis of the final system. One of the design highlights that saved fabrication costs and integration time was the use of flex lines at optimum locations so that large sections of piping could be fabricated and tested independent of whether some other phase of the task was on schedule. The use and re-use of the LN<sub>2</sub> from the fill drain tanker proved to be beneficial in several ways. It was used to pre-cool the LN<sub>2</sub> lines and vehicle tanks while maintaining low pressures during initial cool down of the tanks. Re-using the LN<sub>2</sub> saved not only consumable costs but also solved the problem of where to dispose the LN<sub>2</sub> following a test.

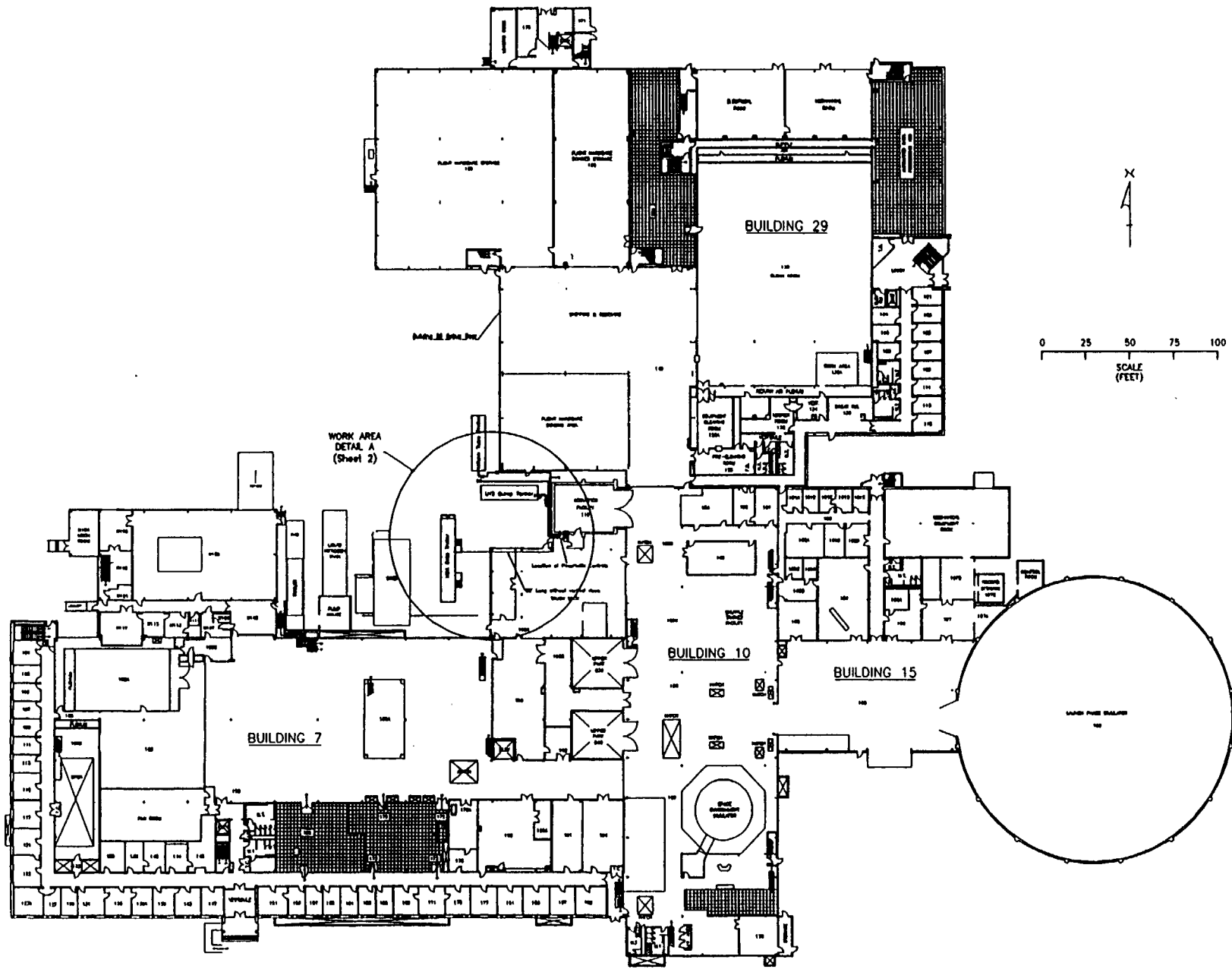


Figure 1: Goddard Space Flight Center Environmental Test Complex

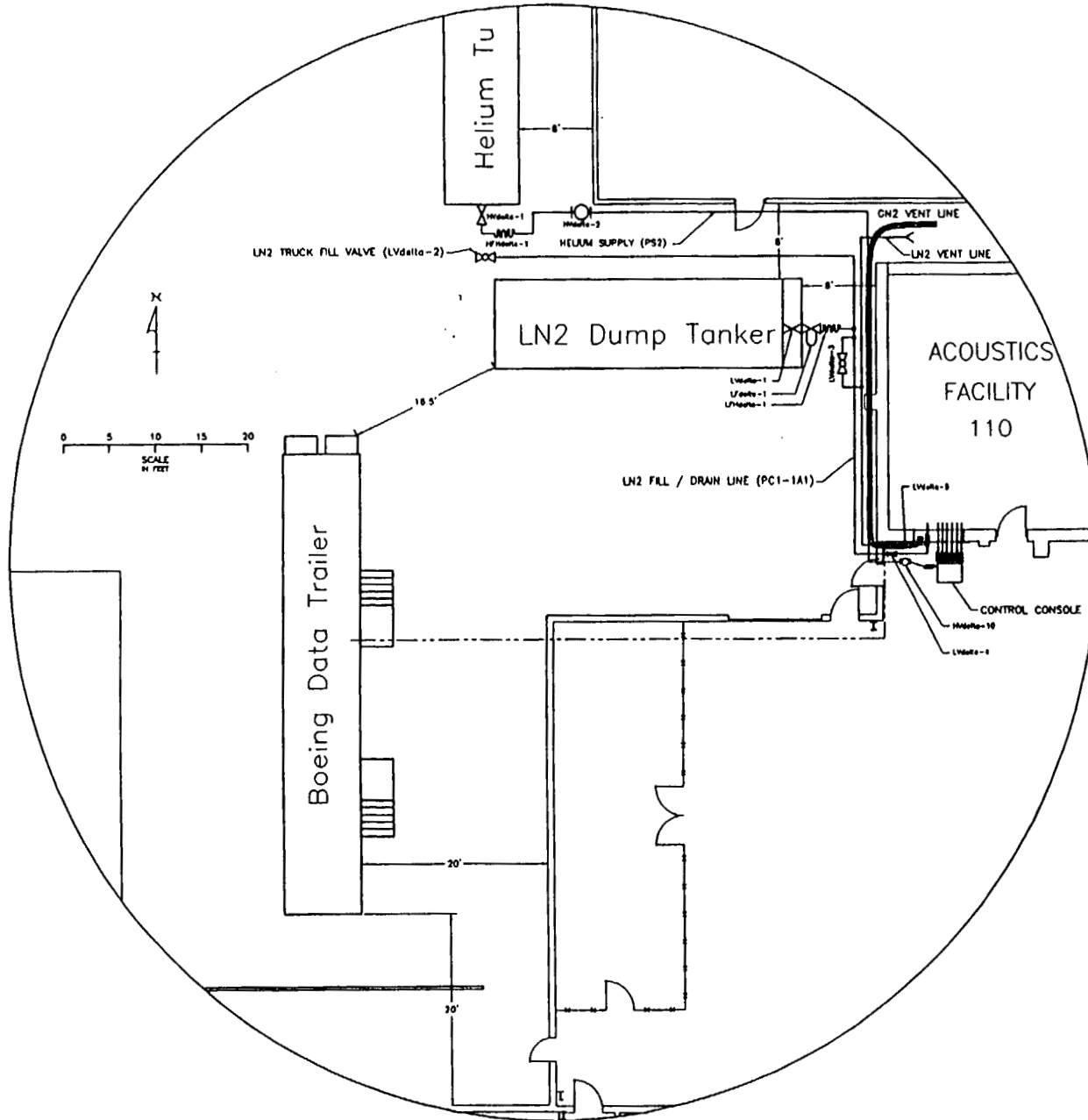


Figure 2: General Test Configuration

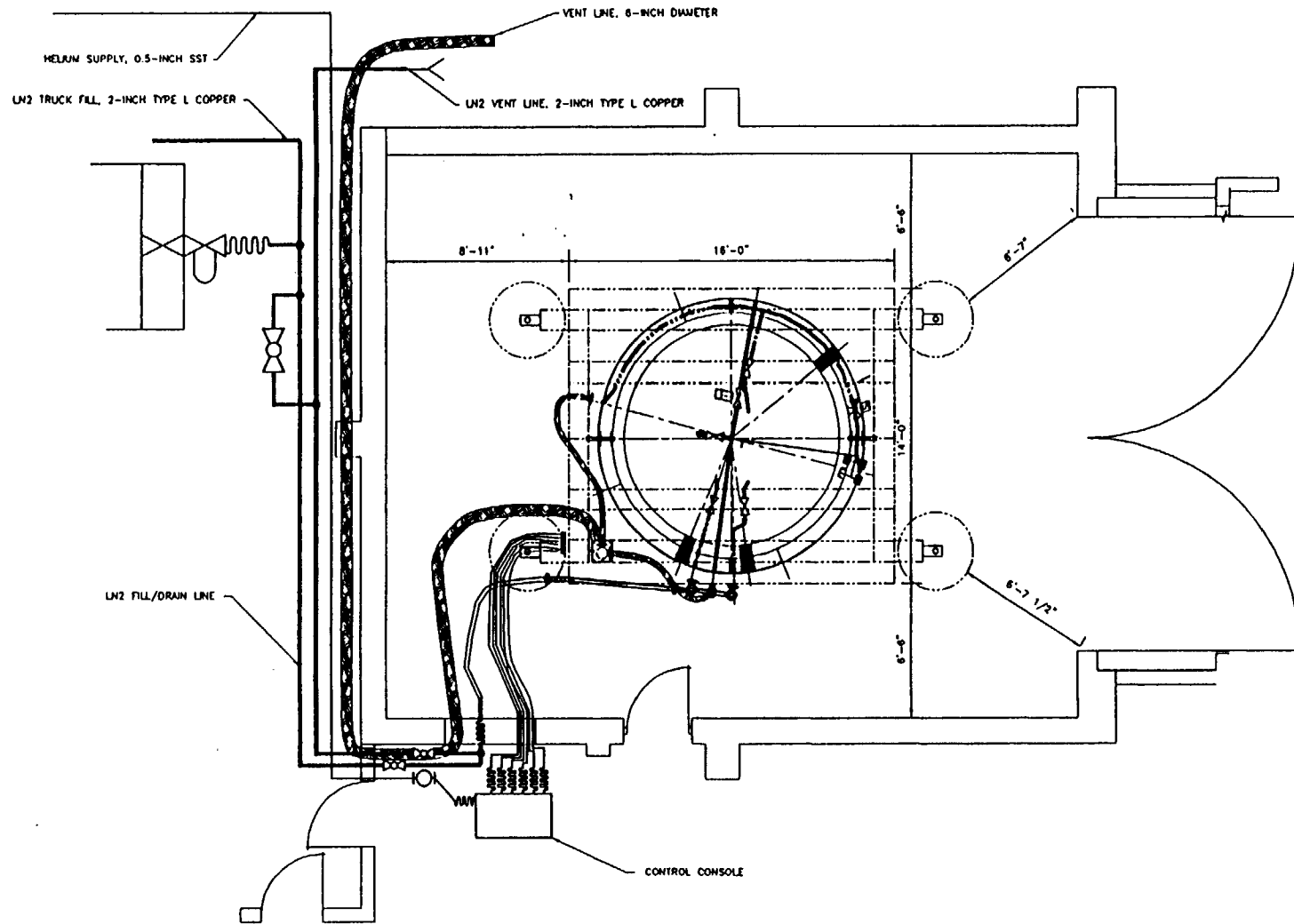
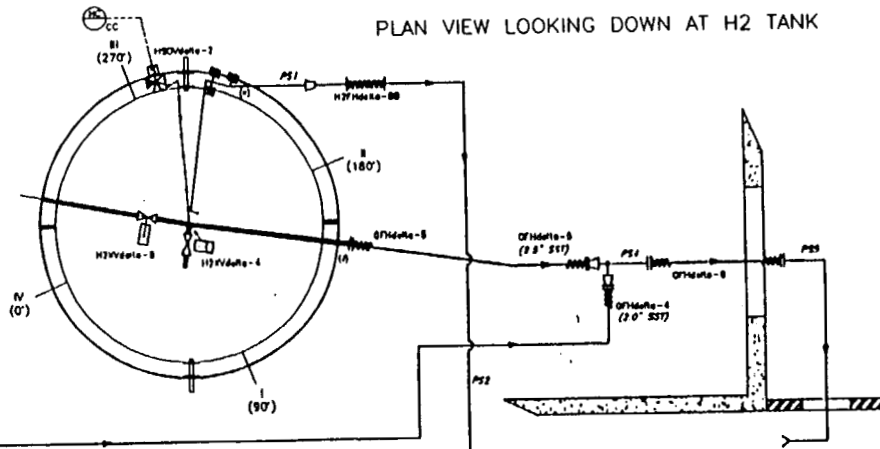


Figure 3: Plan View of the Piping Configuration in the Acoustic Test Cell

PLAN VIEW LOOKING DOWN AT H2 TANK



PPHG LEGEND

| ID  | SIZE | MATL   | PRESS RATING | MATL GRADE | MATERIAL SPECIFICATIONS         | CLEANING SPECIFICATION |
|-----|------|--------|--------------|------------|---------------------------------|------------------------|
| PC1 | 3.0  | COPPER | 180          | TYPE L     | 2.125 OD, 0.070 WALL ACR COPPER | 03 CLEANED             |
| PC2 | 1.5  | COPPER | 150          | TYPE L     | 1.825 OD, 0.060 WALL ACR COPPER | 03 CLEANED             |
| PC3 | 0.75 | COPPER | 80           | ACR        | 0.78 OD, 0.041 WALL ACR COPPER  | 03 CLEANED             |
| ID  | SIZE | MATL   | RATING       | GRADE      | MATERIAL SPECIFICATIONS         | SPECIFICATION          |
| PS1 | 0.35 | SST    | 2400         | 304L       | 0.75 OD, 0.035 WALL SEAMLESS    | 03 CLEANED             |
| PS2 | 0.50 | SST    | 2400         | 304L       | 0.90 OD, 0.048 WALL SEAMLESS    | 02 CLEANED             |
| PS3 | 1.5  | SST    | 1800         | 304L       | 1.5 OD, 0.048 WALL SEAMLESS     | 02 CLEANED             |
| PS4 | 0.8  | SST    | 150          | 304L       | 0.8 OD, 0.125 WALL ASA TEE      | N/A                    |
| PS5 | 0.0  | SST    | 0            | 18-8       | HVAC CYLINDRICAL DUCTING        | N/A                    |

INSULATION LEGEND

| ID | MATERIAL | THICKNESS | MATERIAL SPECIFICATIONS              |
|----|----------|-----------|--------------------------------------|
| M1 | ARMAFLEX | 0.75      | CLOSED CELL REFRIGERATION INSULATION |

PLAN VIEW LOOKING DOWN AT LOX TANK

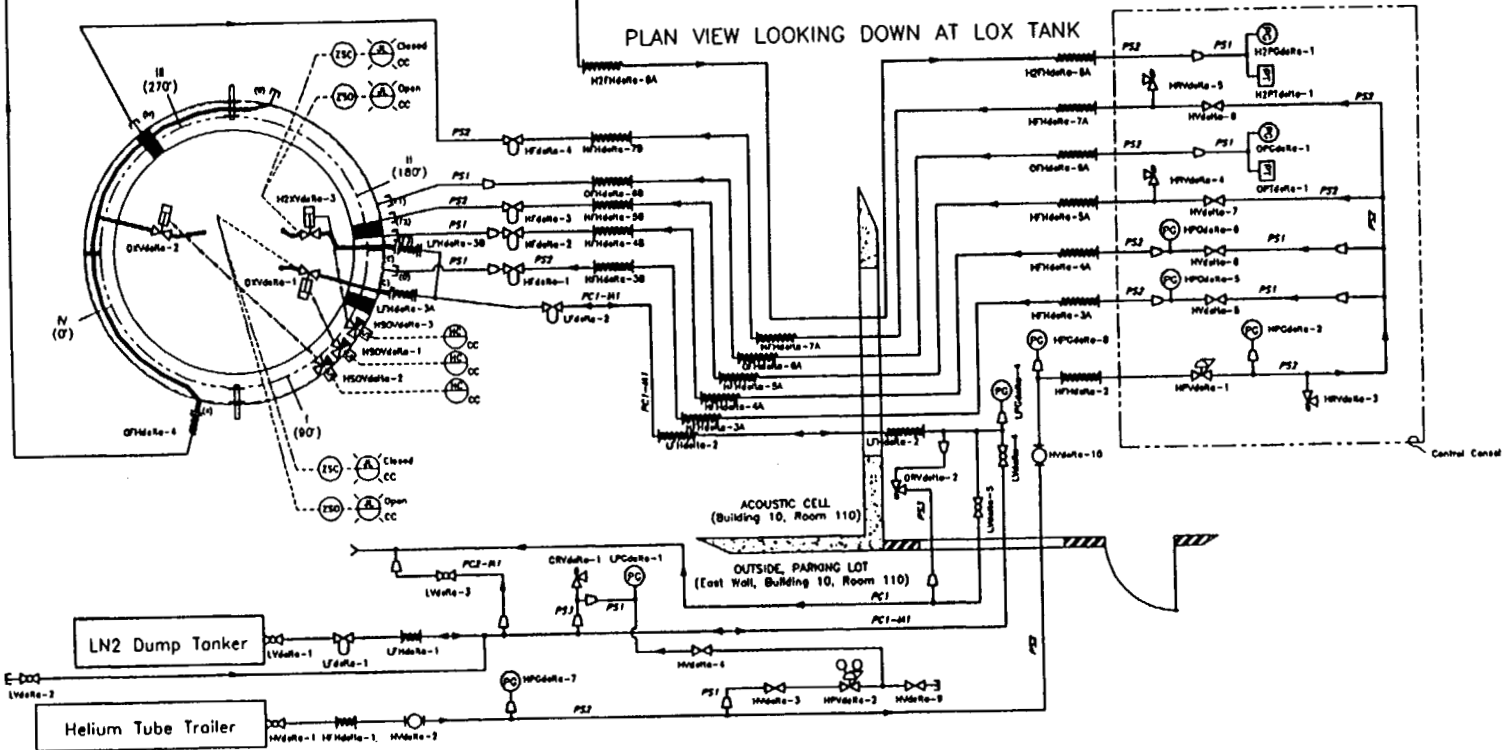
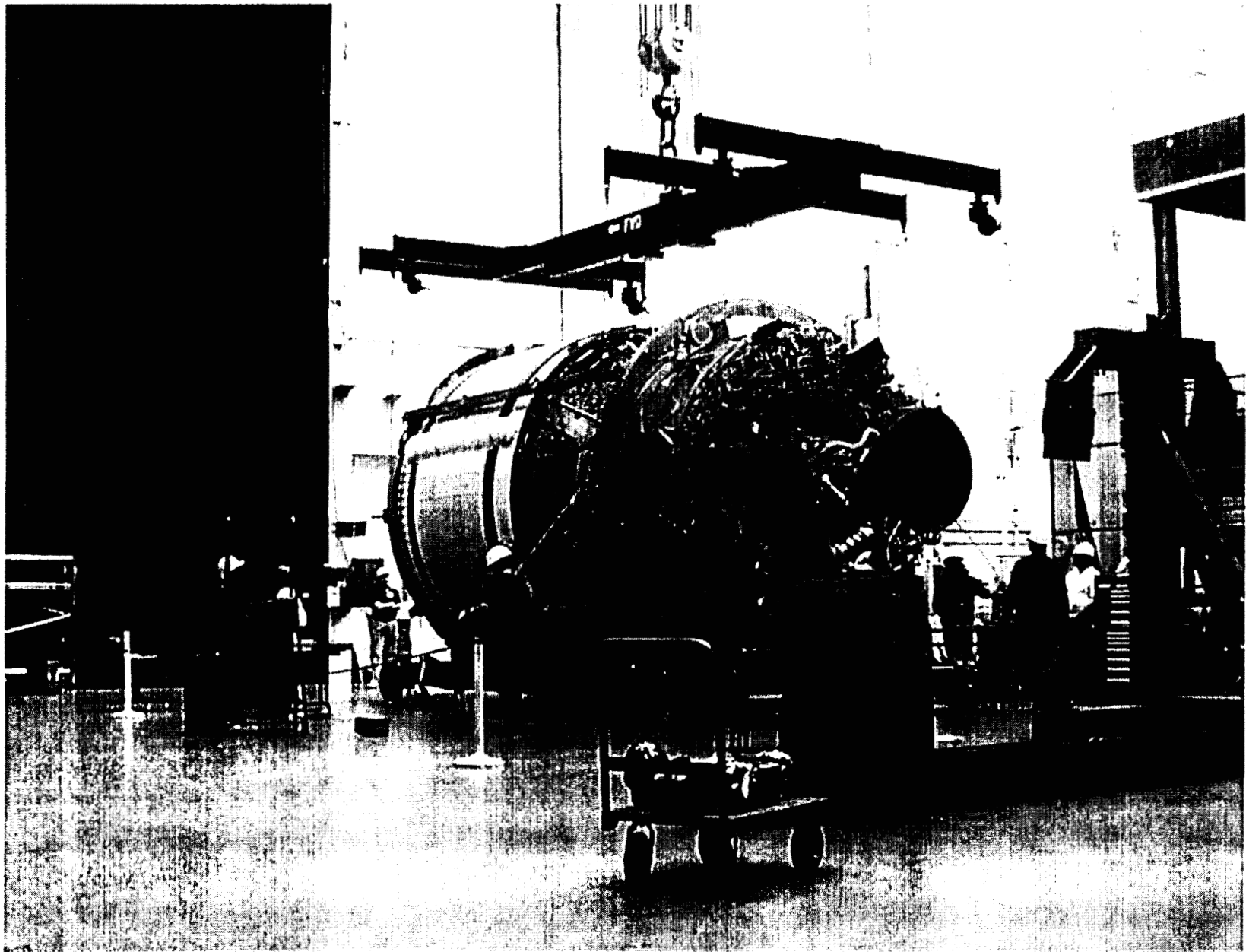


Figure 4: Process and Instrumentation Diagram for the Pneumatic Systems



**Figure 5: Delta III Second Stage After Arrival at Goddard Space Flight Center**

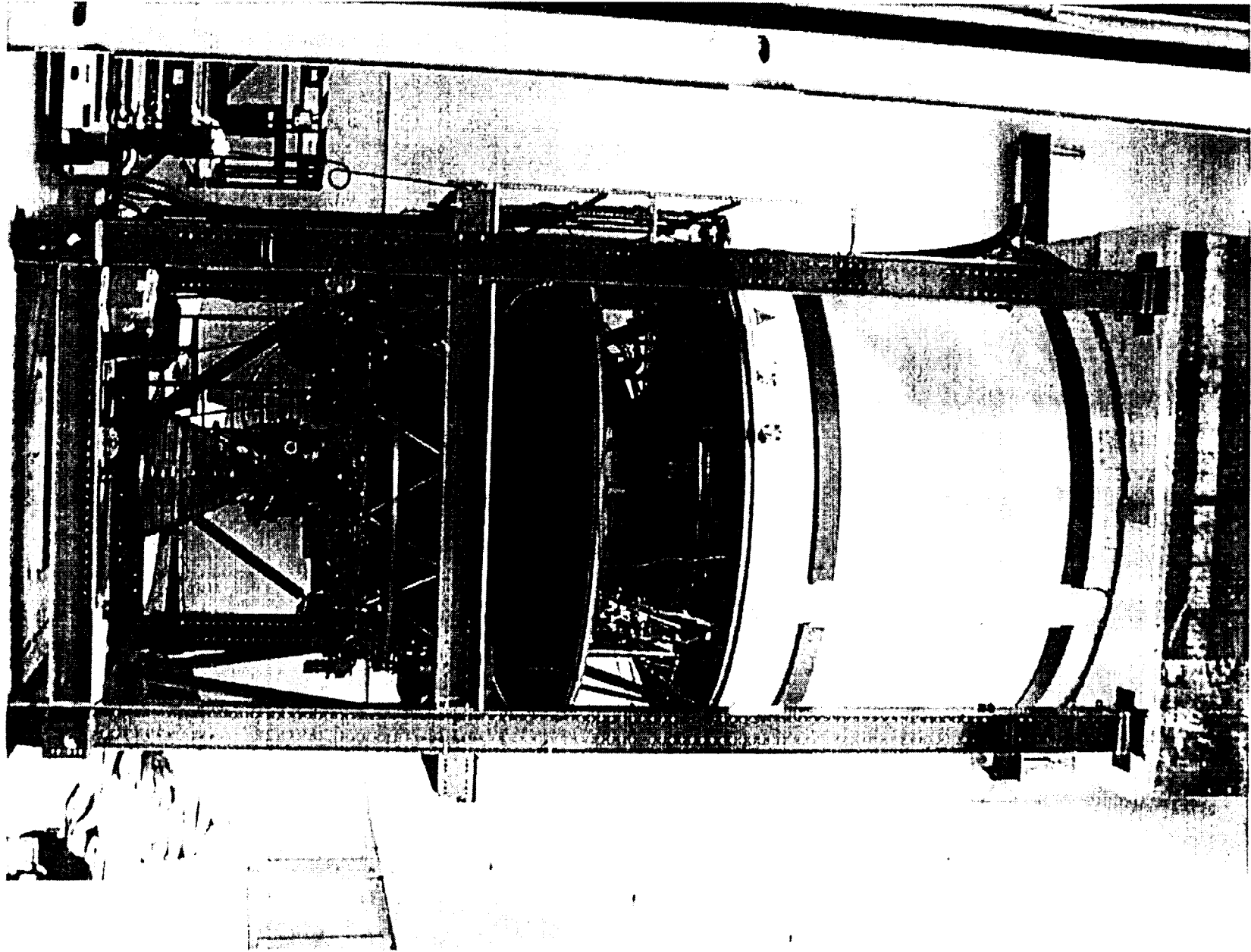


Figure 6: Delta III Second Stage and Mobile Support Fixture Configured in the Acoustic Cell



# POTENTIAL AND LIMITATIONS OF THE MODAL CHARACTERIZATION OF A SPACECRAFT BUS STRUCTURE BY MEANS OF ACTIVE STRUCTURE ELEMENTS \*

Anton M. Grillenbeck and Stephan A. Dillinger  
IABG mbH, Einsteinstrasse 20, D-85521 Ottobrunn, Germany

## ABSTRACT

Theoretical and experimental studies have been performed to investigate the potential and limitations of the modal characterization of a typical truss spacecraft bus structure by means of active structure elements. The aim of these studies was to test and advance tools for performing an accurate on orbit modal identification which may be characterized by the availability of a generally very limited test instrumentation, autonomous excitation capabilities by active structure elements and a zero-g- environment. The NASA LaRC CSI Evolutionary Model Testbed provided an excellent object for the experimental part of this study program.

## INTRODUCTION

Modal identification of orbiting structures requires several technological and methodological questions to be solved. The need for on-orbit modal identification arises from the size of orbiting structures which cannot be assembled and tested on earth, from systems with adaptive control, and as well as from the impact of a 0-g environment on the structural behavior. Technological questions like the sensor and exciter design, the signal processing and transmission are not addressed here. The focus of this paper are methodological questions related to complex spacecraft structures, in particular:

- optimum exciter and sensor placement reflecting the limited resources on board
- the modal identification potential of different types of forcing functions for active structure elements like piezo-ceramic struts
- and the applicability of existing modal parameter extraction algorithms.

Theoretical and experimental investigations on these topics were performed in 1996 on the NASA LaRC CEM3 testbed to study and to compare, from an engineering point of view, suitable and promising approaches for a modal characterization of such structures. A part of the results of these experimental investigations, with the focus on piezo-ceramic struts and on random and sinusoidal forcing functions, is presented in this paper.

Parallel to these investigations, some structure identification experiments on small-sized structures were executed on-orbit or were under preparation like the US experiment MACE during a shuttle mission in 1995 (ref. 1), and the French-Russian CASTOR project which initially was foreseen to be performed on MIR in 1996 (ref. 2), but finally was postponed to later this year. These flight experiments focused on specific problem solving related to system identification and active control or active damping, respectively.

## SYMBOLS AND ABBREVIATIONS

|      |   |
|------|---|
| CEM3 | CSI Evolutionary Model Testbed, Phase 3 |
| CSI  | Controls Structures Interaction         |
| EOS  | Earth Observing System                  |
| FE   | Finite Element                          |
| FRF  | Frequency Response Function             |
| MIV  | Mode Indicator Value                    |
| MPC  | Mode Phase Collinearity                 |

---

\* The work was supported by Deutsche Gesellschaft für Luft- und Raumfahrt (DLR)

## EXPERIMENTAL TEST SET-UP

The CEM3 testbed, as described in ref. 3, was made available by NASA LaRC for the experimental investigations on basis of a letter of intent between NASA and the German DLR. This structure initially was devoted to the development and testing of CSI technologies associated with typical earth science and remote sensing platforms. The CEM3 testbed was of particular interest for the eight-satellite Earth Observing System (EOS) as it was used to support system identification and CSI technology development experiments that were to be employed on the EOS AM-1 spacecraft (see ref. 4). Therefore, the primary objective of the CEM3 was to simulate the overall on-orbit dynamic behavior of the EOS AM-1 spacecraft, and it provided an excellent object for the envisaged investigations.

The CEM3 testbed consisted of a spacecraft bus, two flexible appendages, simulating the EOS low-frequency solar array and the high gain antenna, gimballed instrument simulators, and dummy masses to simulate both science instruments and spacecraft subsystems. The appendage simulating the solar array consisted of a deployable mast and a variable tip weight. This weight was off-loaded by a suspension cable, connected to the tip mass. The structure simulating the high gain antenna comprised a flexible boom and a rigid tip weight.

The primary structure (see Figure 2) was based on four truss system longerons, six truss bulkheads, diagonal struts, and payload towers. The payloads on the EOS AM-1 spacecraft were modeled on the CEM3 testbed using either a discrete ring mass, or three 2-axis gimbals with an attached mass each. In total 11 of the 19 payloads of the EOS AM-1 were modeled.

The CEM3 was suspended from 5 cables attached to advanced suspension devices for the simulation of the free-free zero-g spacecraft environment. The interactions between the suspension modes and the testbed flexible modes were minimized in order to correctly simulate free-free dynamics, and to realize a realistic interaction between the spacecraft bus and the appendages what was critical for the low-frequency control experiments. The rigid-body suspension mode frequencies were tuned to frequencies lower than 0.25 Hz.

Making use of this structure for this study, modal identification was performed both with conventional means by using up to four external electrodynamic exciters, in order to obtain a reference experimental modal model, and with internal excitation by simultaneously using up to four out of six installed piezo-ceramic actuators which replaced corresponding struts of the spacecraft bus structure. These actuators were designed to directly interface the node balls of the truss structure and to replace either a longitudinal or a diagonal strut. The actuators were equipped with one force transducer to measure the axial strut force, and with strain gauges to measure the total elongation respectively compression of the active strut, as well as the enforced deformation of the piezo device. At the two interfacing node balls of an active element, accelerometers were installed to measure the relative axial displacement of the two actuator interfaces (see Figure 1 for the measurement installations at the active element, and Figure 3 for a photo of the integrated active struts).

According to a preliminary FE-model that was available for the preparation of the experiment, 53 eigenmodes were expected in the frequency range up to 50 Hz, namely the six rigid-body modes below 0.25 Hz, about 8 appendage modes with rigid-body interaction of the spacecraft bus structure in the range from 0.7 Hz to about 20 Hz, and global and local elastic modes of the payloads and the bus structure above 20 Hz. In order to save time and to avoid overloading of the critical appendage modes, the experiments underlying this study were frequency band limited from 20 Hz to 50 Hz.

## PLACEMENT OF EXCITATION DEVICES AND OF THE MEASUREMENT SENSORS

Theoretically, the absolute minimum of the number of sensors is equal to the number of modes in the frequency range of interest, since according to the orthogonality criterion applied to the measured modes, it is still possible to distinguish between the individual modes.

According to this approach, Link et. al. (ref. 5) developed a procedure based on the assumption that a given analytical model describes the real structure in an appropriate manner. The basic idea is that the most linear independent rows of the modal matrix indicate degrees-of-freedom that should be chosen as measurement degrees-of-freedom. Hence they form the smallest possible modal matrix providing a MAC-matrix with minimized off-diagonal terms, i.e. among all possible sets this set is the best one to distinguish between the individual mode shapes.

This procedure was applied to the CEM3 using its preliminary FE model. The locations of the 53 measurement sensors obtained by using the most linear independent approach are given in Figure 4. The MAC Criterion was applied to the analytical mode shapes. The computation was first based on the full set of analysis degrees-of-freedom, and then on the set of degrees-of-freedom considered here. Both MAC-matrices were compared and it was found that on basis of the analytical modal matrix they do hardly differ. It was interesting whether this result would be confirmed by experiment.

The set of sensors, to be used for the measurements was selected such that it included the ones of the minimum set as identified by the most linear independence approach. However, for an experimental validation of this approach, a total number of some 180 sensors were distributed over 80 locations. Mainly 2 and 3-axial measurements were used in order to be able to distinguish the measured modes and interpret them by just inspecting them visually. Another important aspect for the enlarged set of sensors was that the reliability of the available preliminary FE-model was not ensured, and during testing, it turned out that the final hardware configuration showed some important differences to the model assumptions.

Two sets of exciters and exciter locations were prepared for the experimental investigation. The first set consisted of 4 electrodynamic external exciters which should provide a reference measurement for the subsequent modal investigations with the active elements. The second set consisted of 6 struts with integrated piezo-ceramic active elements which replaced 3 longerons and 3 diagonal struts of the original structure close to the attachment structure of the gimballed payload platforms. It was foreseen to install the two sets of excitation means to the test article at a time and to keep them throughout all the measurements to avoid any change of the test article's dynamic characteristics.

The location of the external excitation points is shown in Figure 6. This selection was based on the result of a previous modal identification test which was performed to investigate the optimum choice of external exciter locations (ref 6). It turned out, that the excitation of the CEM3 structure at hard structure points with six exciters acting according to the six rigid-body degrees-of-freedom provided sufficient excitation for all modes of the CEM3 including the rigid-body modes and the appendage-bus interaction modes. In order to reduce the instrumentation effort for the planned experiment, from this set four external excitation points were selected which proved to excite at least 85% of all elastic modes satisfactorily. In so far, it was ensured that an optimum basis for the reference modal test with the external exciters could be achieved.

The locations of the active strut elements were selected according to locations of high strain energy. This information was obtained from the preliminary FE-model. However, due to the available measurement equipment, only locations at the lower section of CEM3 could be chosen. Hence, the selected locations as indicated in Figure 6 focused primarily on the suspension modes of the gimballed instrument platforms. However, it was expected that in addition to these platform suspension modes, at least all global modes could be excited.

## TEST PERFORMANCE AND TEST DATA EVALUATION

In order to have a reference to modal model that was obtained by using conventional external excitation and in order to achieve a comprehensive and consistent data set, the following testing steps were performed:

- Multi-point burst random measurements with the 4 external exciters (reference modal test).
- Single- and multi-point burst random measurements with excitation at one, two or four active struts.
- Single-point stepped sine measurements with one active strut each.
- Single-point excitation with exponentially decaying sinusoids using one active strut each.

During all these testing steps, the test article and the installed test equipment remained unchanged.

In so far, mainly classic excitation functions were used. In order to improve the energy input to selected target modes, exponentially decaying sinusoids were applied additionally. The excitation functions of this technique consisted of a sum of decaying sinusoids with frequencies that corresponded to the eigenfrequencies of the target modes. The expected advantage of these functions was that a small number of interesting target modes could be excited at a time while focusing the energy input just to these target modes. The idea to use decaying sinusoids was to excite neighboring frequency lines as well, making standard estimation algorithms for the determination of frequency response functions applicable. It was intended to use the standard polyreference method throughout the evaluation of the test data, unless additional tools would have been necessary. For the exponentially decaying sinusoids, the standard tools turned out to not provide results with sufficient quality. Since the studies with other analysis tools are not finished yet, they have not been included in this paper.

The frequency range of interest was limited to 20 to 50 Hz in order to focus on methodological aspects, to avoid long testing times that would have been needed to investigate the very low frequencies of the appendages, and to suppress additional efforts concerning the safety of the test article.

## ASSESSMENT OF THE RESULTS

### Reference Modal Model

Due to the thorough preparation of the reference test, very good modal results were achieved. First, the reciprocity checks proved an excellent consistency of the measured frequency response functions. Then, by modal analysis, in the frequency range from 20 to 50 Hz, 28 elastic modes were identified, 17, respectively 5 of them were rated excellent ( $MIV > 0.9$ ,  $MPC > 0.95$ ), respectively good ( $MIV > 0.8$ ,  $MPC > 0.9$ ), the remainders turned out to be either isolated local modes of CEM3 (typically with one significant response location only) or unexpectedly strong coupled modes of the CEM3 structure with the free-free suspension cables. The only problem to solve with the data set was to separate out about 20 further pure suspension cable modes. For the identified elastic CEM3 structure modes, the MAC-check revealed an excellent result with only few correlation between the identified modes as indicated by maximum non-diagonal MAC values of 0.1 to 0.3, with the exception of two modes with strong coupling with the suspension cables. When repeating this MAC test with the optimum set of 53 sensors, a comparatively good result was achieved (see Figure 7).

### Suitable References for the FRFs of the Internally Excited Structure

For the calculation of FRFs usually the measured responses are referenced to the applied forces which theoretically can be considered independent from the structure dynamics. However, when using the measured forces of the active struts as a force reference to calculate FRF for the tests with active structure excitation, it became obvious that wrong modal characteristics would be obtained in the subsequent modal analysis. The reason is, that in contrast to the external excitation, the measured forces at the internal excitation means are composed of the force response of the adjacent structure to the enforced elongation and compression induced by the active element, and of the dynamic loading of the structure due to modal deformation at resonance. This is of major importance since the active structure elements intentionally were placed at locations which were supposed to yield high elastic strain at several elastic modes of the structure.

The physical explanation may be given with Figure 8: The measured strut force and the corresponding (scaled) elongation of the strut as derived from the accelerations of the two strut interface points are shown. They were obtained from a single-point burst random measurement with an active strut. The physical reference selected for these functions was the externally enforced elongation of the piezo. In case of no interference with the structure dynamics, only constant real force and anti-phase constant real deformation is expected, like in the frequency range around 15 Hz, provided that local inertia of the active element can be neglected (this is justified here since the longitudinal resonance of the active strut is at much higher frequency). In the case when a resonance of the structure is being excited by the active element, the resonant structure responses have to be in quadrature to the excitation such that the damping forces are balanced. This easily can be seen in Figure 8. Physically, the excitation is the enforced elongation of the active element which can be considered as real function with respect to the reference since it must be independent from the structure. Then, at resonance, imaginary strut forces and corresponding in-phase imaginary strut deformation can be observed which correspond to the elastic mode shape. It is important here that with random excitation, the structure is excited such that it can vibrate nearly independent from the excitation forces.

As indicated in Figure 8, the superposition of the modal strut forces and the enforced strut forces may result in zeroes of the force function in between of the structure resonances. If this force function was used for the calculation of the FRFs for a subsequent modal analysis, a pole would be generated which however would not correspond to a physical mode of the structure, resulting in misleading modal parameters.

Following this explanation, a suitable reference function is the enforced physical elongation of the active element or as an alternative, if the transfer function to the physical elongation is known, even the driving signal of the power amplifier of the active element could be used. In order to finally prove this approach, a reciprocity check was performed between the reference measurement with the external exciters and the measurements with the active elements.

## Reciprocity Checks

When performing a reciprocity check between the FRFs of the externally excited structure with corresponding FRFs of the internally excited structure, it has to be considered that the internal excitation actually acts on two loading points, namely the at the two interface points of the active element to the structure (see Figure 5). Consequently, the reciprocity check has to be formulated as follows: The difference of the response accelerations due to the external excitation at the two active strut's interface points, referenced to the external excitation, has to be compared to the response at the external excitation point due to the internal excitation, referenced to the driving elongation of the active element. An example of such a reciprocity check is shown in Figure 9 which was obtained from the multi-point random tests with internal respectively external excitation.

In order to improve this reciprocity check, it turned out to better use the strut response force at the active element due to the external excitation instead of the difference of the response accelerations for the following reason: For external excitation, the internal strut force must be proportional to the strut's strain which is manifest in the difference of the accelerations. The direct measurement of the strut force, however, gives more accurate results than calculating the difference of the two measured accelerations since comparatively large elastic deformations of the spacecraft bus structure superimpose a rigid-body vibration on the active strut which also are measured by the accelerometers.

Making this approach, the reciprocity check looks nearly perfect, proving that the driving elongation of the active element was a suitable reference for calculating the FRF in this test case with internal excitation. The apparent small differences in the resonance frequencies can be attributed to the different excitation levels achieved during the tests with internal respectively external excitation. Moreover, in the frequency range above 35 Hz, it seems that the internal excitation means can - under the circumstances applied here - provide even better excitation of specific modes than with the chosen external excitation.

## Random Test with Active Elements

According to the result of the reciprocity check, good modal results were achieved from the multi-point random test using the active elements. In the frequency range between 20 and 50 Hz, 26 modes were extracted, 13 of them were rated excellent (MIV > 0.9, MPC > 0.95, with MAC better than 0.9 to the modes of the reference test) and 4 were rated good (MIV > 0.9, MPC > 0.95, MAC better than 0.85). The result of the cross-MAC check for the mode shapes obtained from both external and internal excitation with multi-point random, and by using the optimum set of 53 sensors, is shown in Fig. 10. This result emphasizes that for this experimental set-up, a good modal identification was possible with internal active elements. However, for the calculation of generalized mass values, the calibration between the enforced strain and the resulting force has to be known.

For the ten remaining modes which did achieve neither good ratings nor good correlation to the modes of the reference set, it has to be considered, that the selected locations of the active struts were not the optimum set for all structure modes in the frequency range of interest, since some practical restrictions for the selection of the locations had to be observed. But all modes which were selected target modes for the locations of the active struts according to the distribution of the strain energy were found with excellent quality ratings. This shows that the chosen active strut locations according to the distribution of the strain energy was suitable for this type of modal identification.

## Step Sine Test with Active Elements

In contradiction to the multi-point random test, the step sine test did not yield valid FRFs by using the same references as during the random test. They did not yield the correct phase behavior at resonances of the structure. Instead of a phase shift of 180 degrees at isolated resonances, 360 degrees were observed, making the application of the standard modal analysis tools impossible, since two identical modes would be extracted for each physical structure mode.

The reason for the unusual shape of the FRFs is shown in Figure 11: In contradiction to the random test (see Figure 8), the structure now strictly follows the enforced sinusoidal elongation of the active strut, such that only an in-phase vibration of the structure with respect to the strut force is possible, i.e. there is a phase lock at zero degrees between the driving elongation, which is equivalent to 180 degrees of the active element's force, and the structure's response. It seems that this behavior is determined by the high stiffness of the active struts with respect to the stiffness of the structure. In case of a negligible actuator stiffness, the actuator would behave like two external

exciters which would follow the deformation of the structure, however, their force would balance the in quadrature damping forces at the structure's resonances.

Nethertheless, the structure gets into resonance at its eigenfrequencies as indicated in Figure 11. For maintaining a structure vibrating at resonance, however, the damping of the structure has to be balanced. This requirement is not explained with the available measurements. As a consequence, more information about the internal behavior of the active elements would be necessary to completely describe the dynamic characteristics of the complete system.

However, the modal results that can be obtained from this step sine tests are the resonance frequencies and the mode shapes. In this case, the cross-MAC values to the well established modes of the reference modal model were between 0.9 and 1. Nethertheless, this outcome seems to be not attractive enough with respect to the much longer testing times needed compared with a multi-point random test which directly led to FRFs suitable for the available standard analysis tools.

## CONCLUSIONS

It has been demonstrated, that the dynamic characteristics of a truss structure can be investigated by using integrated active elements like piezo-ceramic struts to excite the structure, and by using a limited number of sensors which were located according the most linear independence approach. It turned out that even some discrepancies between the preliminary model and the actual hardware did not significantly effect the quality of the identification results.

The placement of active struts at locations with high modal strain turned out to be effective for the excitation of the corresponding modes. However, the selection of the excitation functions and the choice of a suitable reference is important for the suitability of the acquired FRF data for standard modal analysis tools. It seems that this choice is dependent on the behavior of the actuators inside the test structure, and it is determined by the stiffness of the actuator with respect to the adjacent structure. Further investigations on this subject are in progress.

## REFERENCES

1. Glease, R.M., Miller, D.W., "Derivation of 0-g structural control models from analysis and 1-g experimentation", AIAA-95-1121-CP
2. Bousquet, P.W., Dancet, Y., Guay, P., Mercier, F., "CASTOR: Ground Test Results", Conference on Spacecraft Structures, Materials & Mechanical Testing, Noordwijk, 1996, ESA-SP-386, pp 191 - 198
3. Gronet, M.J., Davis, D.A., Tan, M.K., "Development of the CSI Phase-3 Evolutionary Model Testbed", NASA Contractor Report 4630, October 1994
4. Maghami, P.G., Gupta S., Elliott, K.B., Joshi, S.M., Walz, J.E., "Experimental Validation of an Integrated Controls-Structures Design Methodology for a Class of Flexible Space Structures", NASA Technical Paper 3462, November 1994
5. Link, M., Schedlinski C., "An Approach to Optimal Pick-Up and Exciter Placement", Report 1995
6. Troidl, H., "Dynamic Tests on the NASA LaRC CSI Evolutionary Model Testbeds", IABG Report B-TR-V028, December 1995

## FIGURES

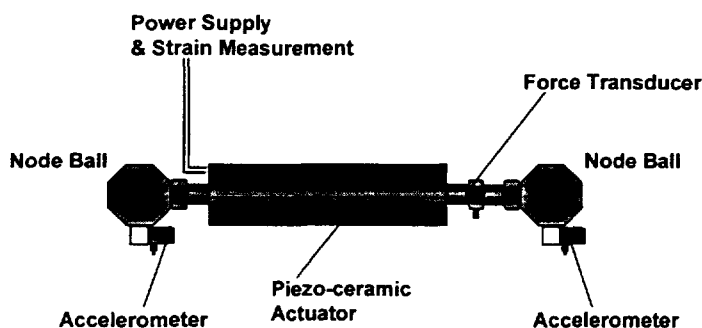


Fig. 1: Sketch of a piezo-ceramic actuator

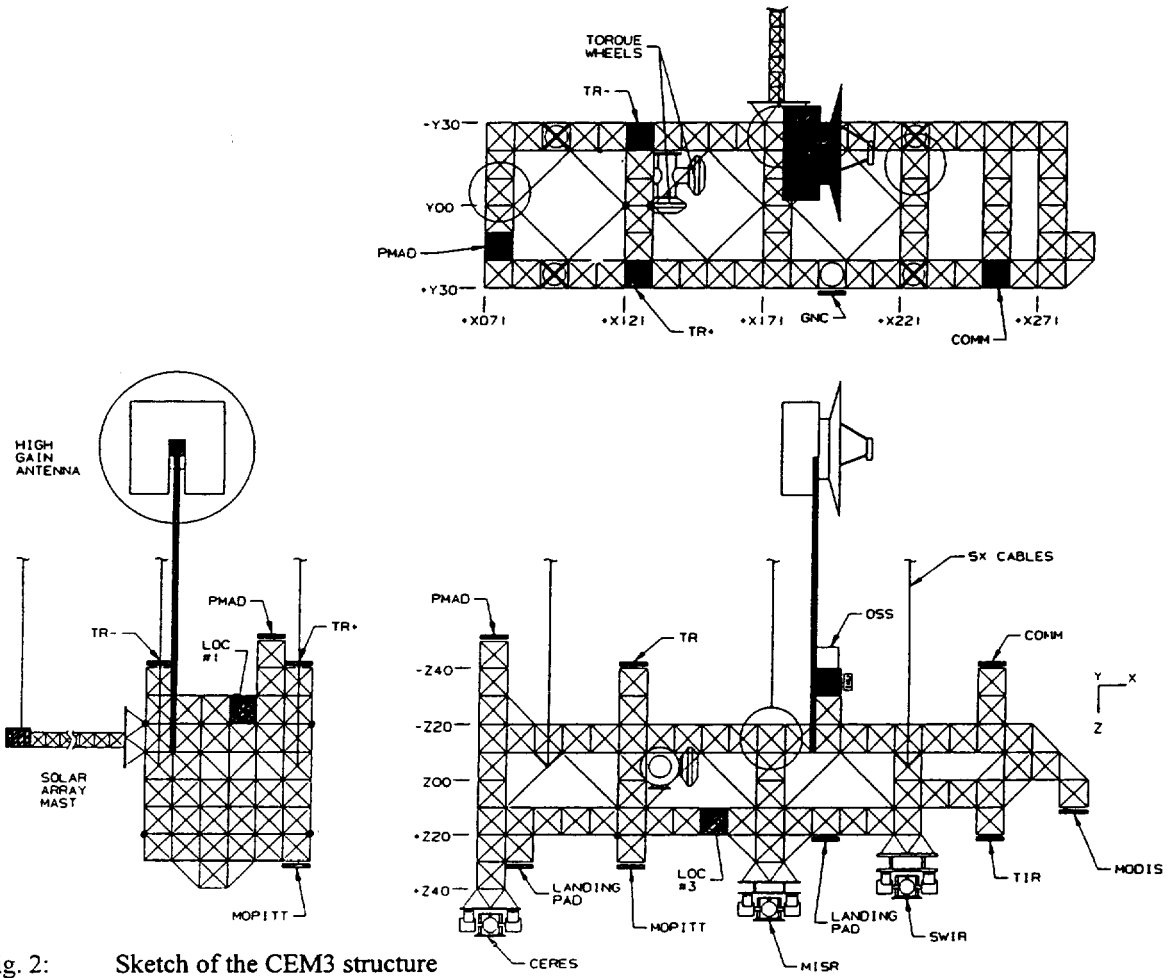


Fig. 2: Sketch of the CEM3 structure

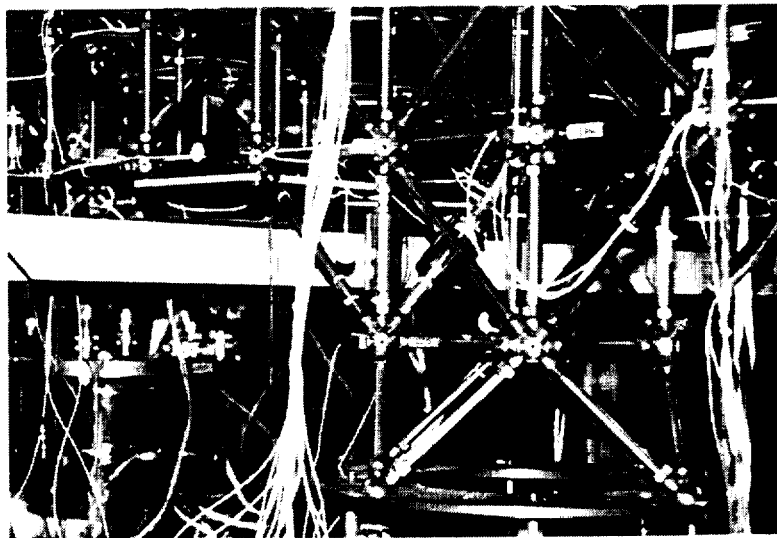


Fig. 3: Photo of two integrated active struts (longeron and diagonal in the center of photo)

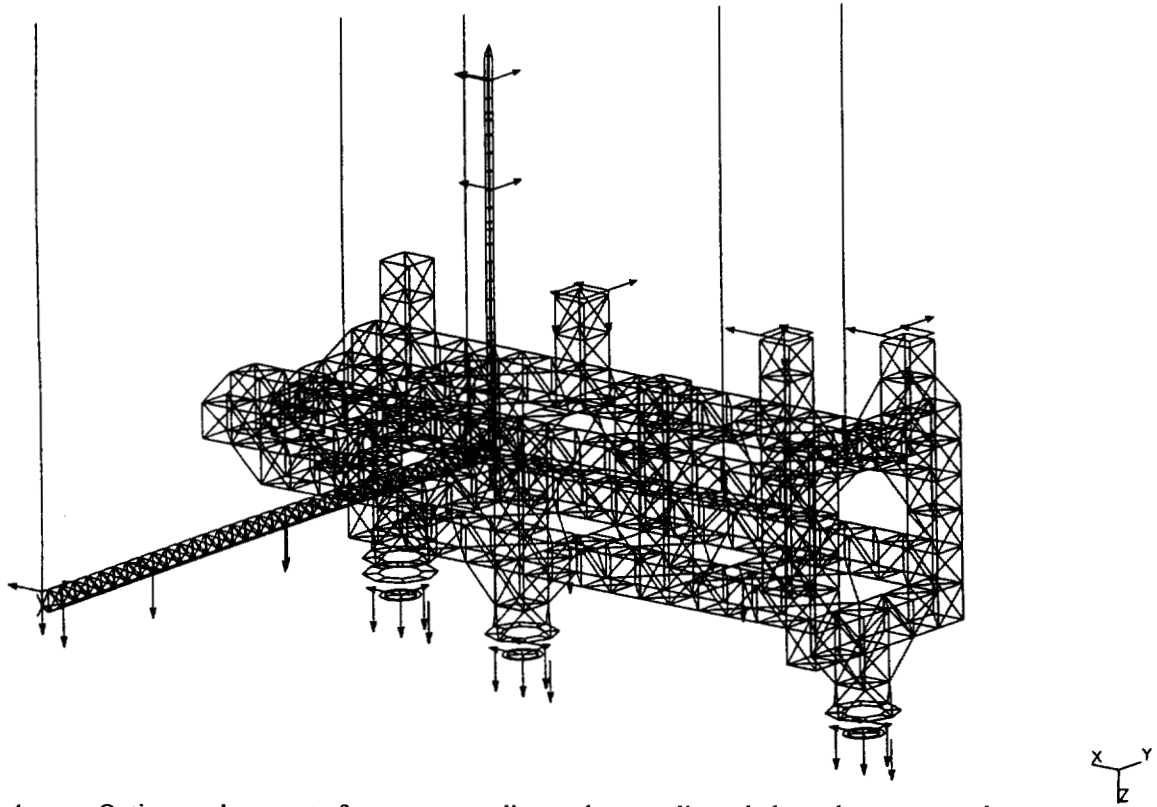


Fig. 4: Optimum placement of sensors according to the most linear independence approach, arrows indicate the sensors of the optimum set

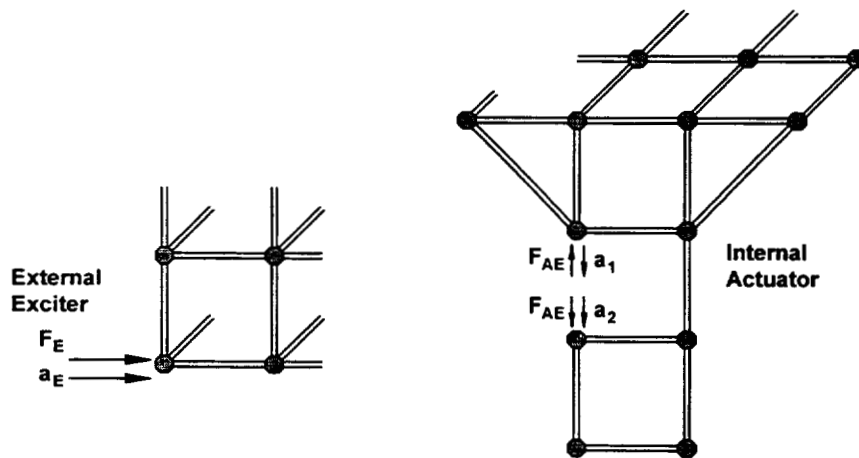


Fig. 5: Approach for the reciprocity check between external and internal excitation

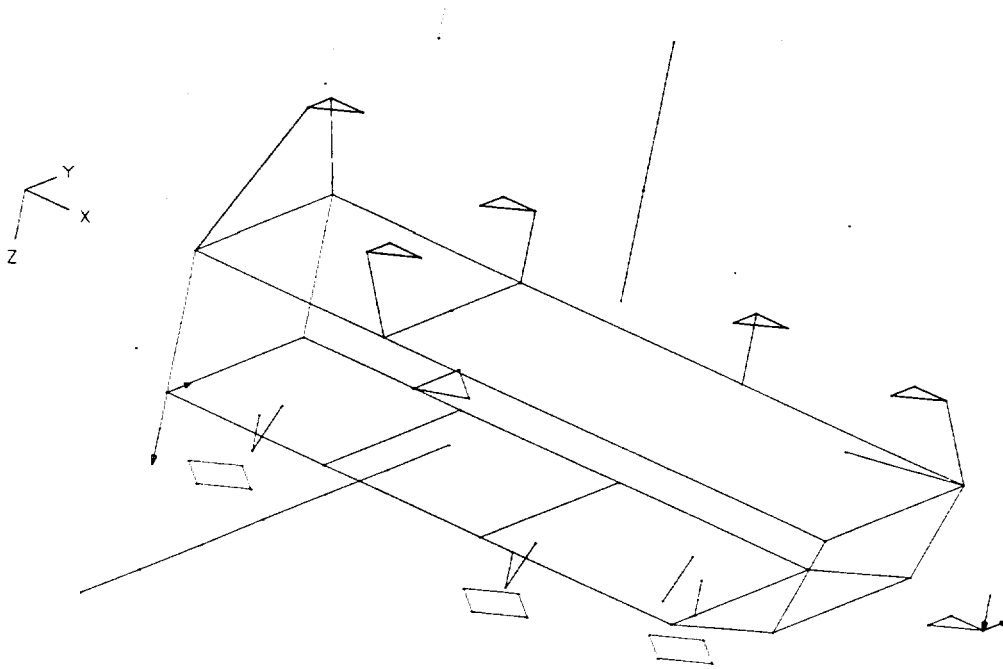


Fig. 6: Location of the external exciters (black arrow) and of the internal active struts (V-shaped red lines)

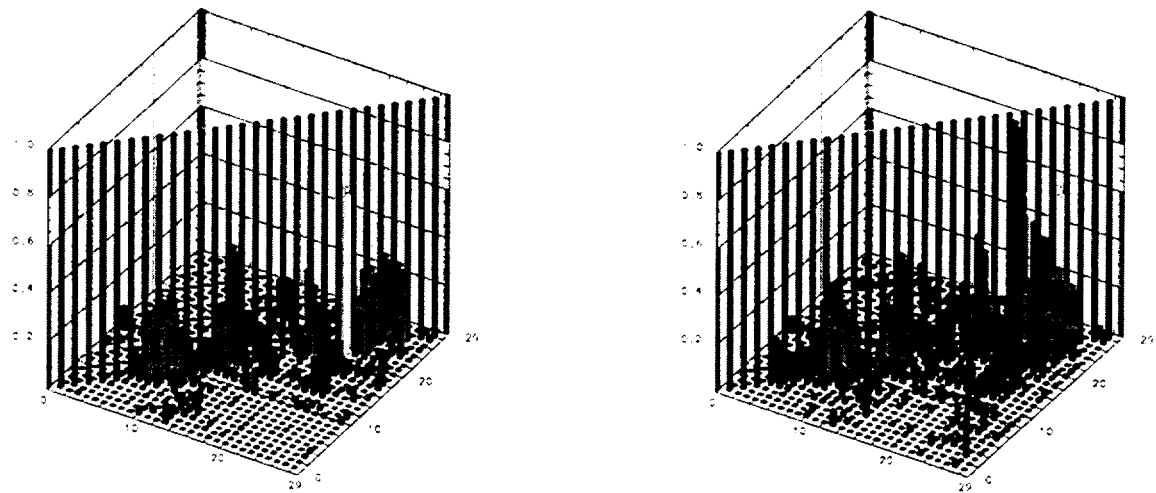


Fig. 7: MAC-Matrices for the reference measurement using the full measurement set of sensors (left) and the optimum set of sensors (right)

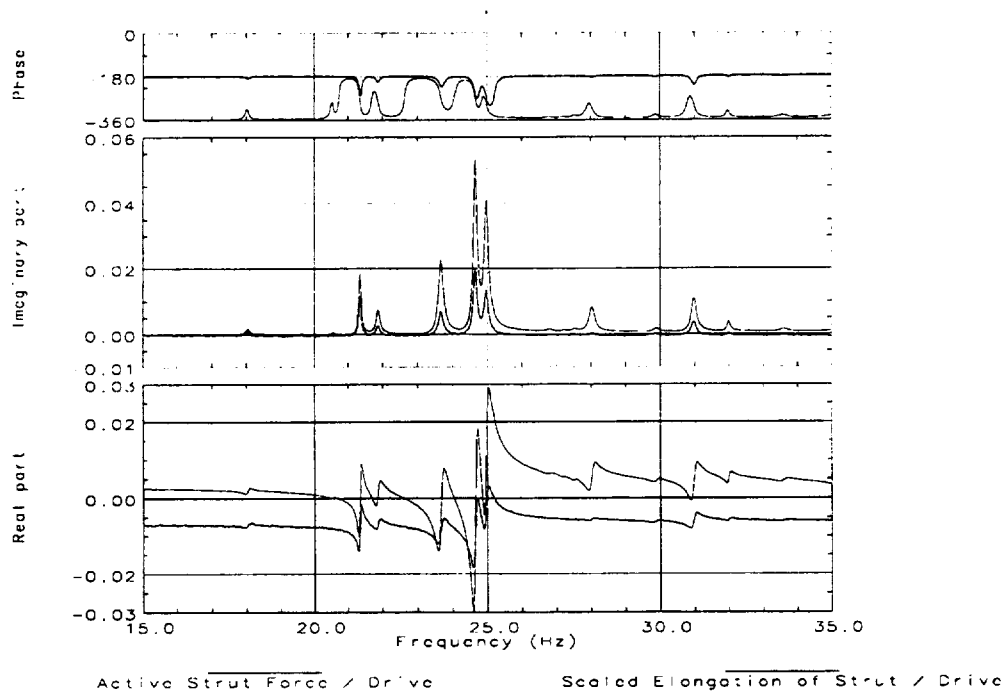


Fig. 8: Superposition of external excitation forces with internal dynamic resonance responses during active strut excitation (random test)

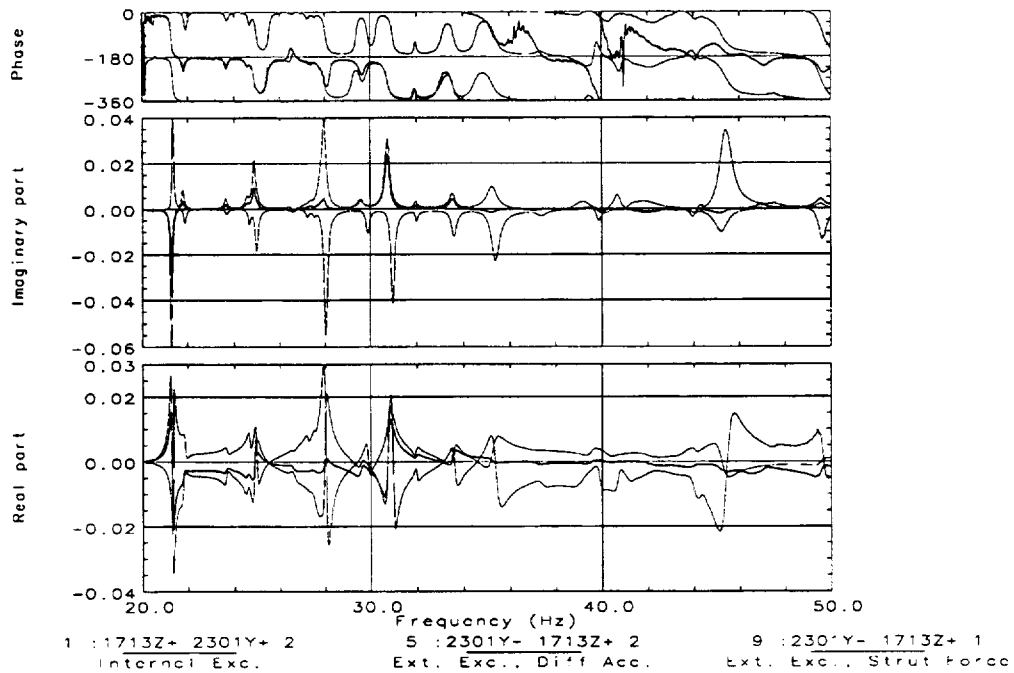


Fig. 9: Example reciprocity check using internal respectively external excitation (random test)

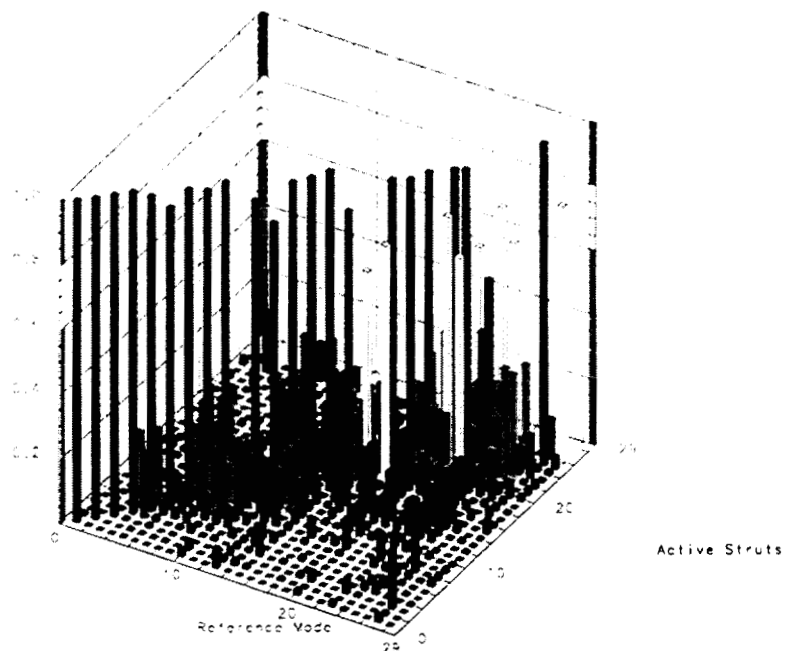


Fig. 11: Cross-MAC between the reference modal model and the multi-point-random modal results using the optimum set of sensor locations

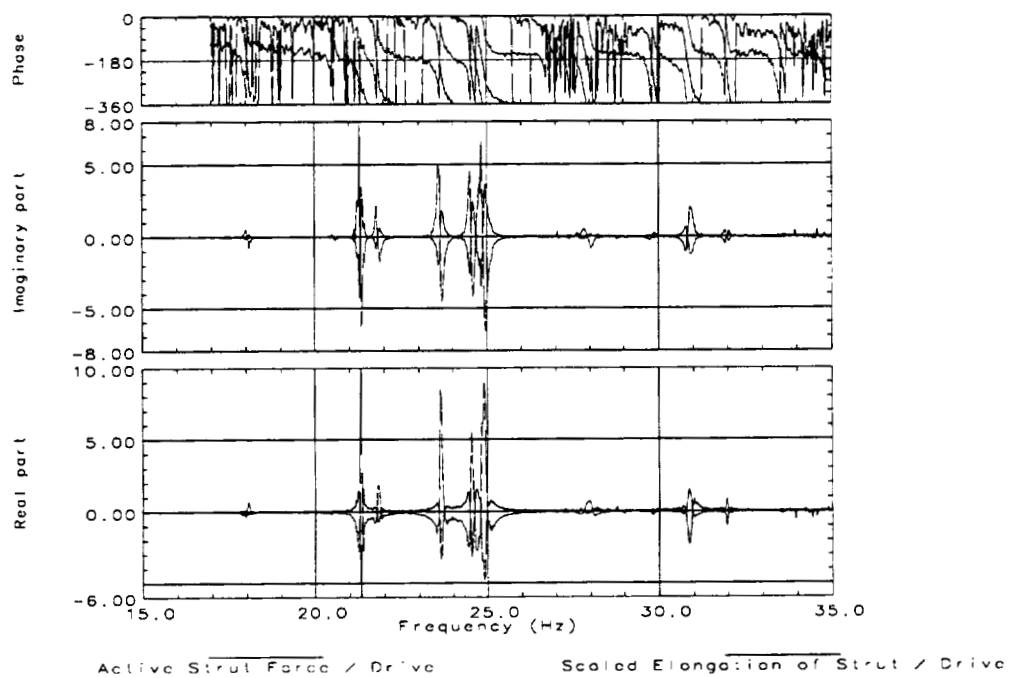


Fig. 12: Response functions obtained from the step sine test with the active elements using the same reference as during the random test



# MECHANICAL FLIGHT QUALIFICATION TESTING OF THE ADVANCED COMPOSITION EXPLORER OBSERVATORY

Teresa M. Betenbaugh

The Johns Hopkins University Applied Physics Laboratory

## ABSTRACT

The Advanced Composition Explorer (ACE) Observatory is a National Aeronautics and Space Administration (NASA) Explorer mission with the primary purpose of determining the composition of energetic solar and galactic particles. With a cost cap of \$141 million, measures were taken to reduce development costs of the observatory. As a part of this effort, a protoflight test program was used to qualify the ACE Observatory. This paper describes the overall mechanical flight qualification program which included vibration, acoustic, shock, and mass properties testing. The ACE project requirements, objectives of the test program, and verification of the project requirements are discussed.

## MISSION DESCRIPTION

The ACE Observatory was launched on a Delta II 7920-8 launch vehicle on August 25, 1997 from the Cape Canaveral Air Station in Florida. In December of 1997, ACE arrived at its destination, the Earth-sun libration point (L1), where the gravitational pull of the Earth and the Sun are balanced. Nearly a million miles from earth, ACE provides a platform for measuring accelerated particles from the Sun and interstellar and galactic sources. Study of the composition of these particles will help scientists to understand the evolution of the universe. A secondary mission of ACE is to provide advance warning of geomagnetic storms that can overload power grids, disrupt communications on Earth, and present hazards to astronauts.

The ACE mission is managed by the Explorer Project Office of NASA/Goddard Space Flight Center (GSFC) and the science payload is managed by the California Institute of Technology (Caltech). The Johns Hopkins Applied Physics Laboratory (APL) was responsible for the ACE spacecraft design and integration, observatory environmental testing, and launch operation support.

## OBSERVATORY MECHANICAL DESCRIPTION

The ACE Observatory is depicted in Figures 1 and 2. The spacecraft primary structure is a 56 inch wide by 30 inch tall closed octagon structure, consisting of an internal aluminum frame covered with aluminum honeycomb panel decks. The Observatory Attach Fitting (OAF) is a 9 inch aluminum cylinder which attaches the octagon to a 5624 Delta Payload Attach Fitting (PAF) with a clampband. The majority of the instrument payload is mounted to the top (+z) deck. Two instruments, the spacecraft terminal boards, and the power, attitude determination and control, and command and data handling subsystems are mounted to the side decks. The lower (-z) deck houses the majority of the radio frequency subsystem and the Spacecraft Loads and Acoustics

Measurements payload. With the exception of the thrusters which are mounted on the  $\pm x$  sides of the  $\pm z$  decks, the propulsion subsystem is attached to the  $-z$  deck and is enclosed by the octagon structure. 430 lbs. of hydrazine is contained in the four conospheric titanium tanks that make up the propulsion subsystem. Four 34 inch by 59 inch deployable aluminum honeycomb solar panels are hinged from the  $\pm x$  and  $\pm y$  sides of the  $+z$  deck and are restrained to the  $-z$  deck during launch with pin-puller mechanisms. A 60 inch titanium boom attaches a magnetometer to the end of each of the  $\pm y$  solar panels. The  $+z$  end of each boom is restrained to the  $\pm y$  solar panels for launch with a pin-puller mechanism. Pyrotechnic devices actuate the pin-pullers, which release solar panels and booms. Preloaded torsion springs deploy and center the solar panels and booms to their appropriate positions.

## **TEST REQUIREMENTS**

### **Flight Requirements**

The Delta II flight events produce loads from steady state and dynamic environments. The steady state environment produces a maximum thrust acceleration at the end of the first stage burn, or "main engine cut off" (MECO). The dynamic environments produced by the Delta II are sinusoidal vibration, acoustics, and shock. The sources of the sinusoidal environment are liftoff transients, pre-MECO oscillations, and engine ignition and shutdown. A spacecraft random vibration environment is generated by launch vehicle acoustics.

The spacecraft must be designed to produce fundamental frequencies above 12 Hz in the lateral axes and 35 Hz in the thrust axis to prevent dynamic coupling of spacecraft and launch vehicle low frequency structural modes. Verification of spacecraft strength and stiffness was required by the ACE program office. Orbital Launch Services (OLS) and McDonnell Douglas Aerospace (MDA, now Boeing) recommended structural loads testing to maximum expected flight levels multiplied by a factor of 1.25 (protoflight level), sinusoidal vibration and acoustics testing to maximum expected flight levels +3dB (protoflight level), and shock (clampband separation) testing to maximum expected flight levels.

### **Alignment and Attitude Control Requirements**

The pointing accuracy of the ACE instrument payload required that ACE Observatory be spin stabilized with a principal spin axis misalignment less than or equal to 0.2 degrees. A spin axis moment of inertia 1.05 times larger than the lateral moments of inertia was needed to maintain stability of the spinning observatory.

## **TEST OBJECTIVES**

The objectives of the ACE Observatory mechanical flight testing program were to demonstrate that the observatory was qualified for flight aboard a Boeing Delta II 7920-8 launch vehicle and to verify that the observatory mass properties met the science alignment and mission attitude control requirements.

In an effort to reduce cost and schedule, a protoflight testing program was used to qualify the ACE Observatory. Tests were performed on instruments, components and some subsystems prior to final integration to minimize the risk involved with a prototype program.

## **VERIFICATION TESTING**

Prior to observatory integration, structural loads and vibration testing were performed individually on the ACE instruments, the spacecraft components, an engineering model of a solar panel with magnetometer boom, and the spacecraft primary structure with integrated propulsion subsystem. A bend test was conducted on a solar array qualification panel, and an acoustic test was performed on one flight solar array. Acoustic, shock, and mass properties testing were performed on the fully flight configured observatory.

### **Instrument and Spacecraft Component Verification**

#### **Structural Loads and Sinusoidal Vibration Testing**

The structural loads and sinusoidal vibration testing requirements were combined into a three-axis sine sweep vibration test for the ACE instruments and spacecraft components. A frequency response analysis was performed on a finite element model of the ACE Observatory to generate instrument and component level sine sweep test specifications. Sinusoidal test requirements from the Delta II Payload Planners Guide<sup>1</sup> and maximum expected flight levels from MDA were used as acceleration inputs to the finite element model. The resulting test specifications were later revised following a sine sweep vibration test of the spacecraft structure/integrated propulsion subsystem. Vibration testing of ACE instruments and components took place from 1995 through 1996.

#### **Random Vibration Testing**

The initial random vibration specifications for the ACE instruments and spacecraft components were generated by Goddard Space Flight Center engineers by scaling the acoustic responses of similar types of spacecraft structures to the expected acoustic environment for Delta II with an eight foot fairing. These specifications were later revised based on responses from the spacecraft primary structure/propulsion subsystem vibration test, and acoustic structural responses for similar APL spacecraft (Delta 180, Midcourse Space Experiment, Near-Earth Asteroid Rendezvous). As an

added measure of protection for the delicate ACE instruments, force limiting<sup>2</sup> was incorporated under the direction of Terry Scharton of The Jet Propulsion Laboratory. Vibration testing of ACE instruments and components took place from 1995 through 1996.

## **Solar Array and Magnetometer Boom Verification**

### **Structural Loads and Sinusoidal Vibration Testing**

A three-axis sine sweep vibration test to represent the sinusoidal environment and structural loads requirements was developed to test an engineering model of a solar array and magnetometer boom with their hinge mechanisms. The inputs were derived from a frequency response analysis performed on a finite element model of the ACE Observatory. The engineering model, pictured in Figure 3, consisted of an aluminum honeycomb panel similar to the flight solar panels, with aluminum pieces epoxied to the panel to represent the mass of the solar cells. A flight like magnetometer boom with a magnetometer mass simulator was attached with a flight spare hinge assembly to the solar panel engineering model. Two other flight spare hinge assemblies attached the panel to flight spare mounting brackets, which were mounted to the vibration fixture. Flight spare snubber and clevis pin assemblies attached the lower end of the panel to the vibration fixture. Vibration testing of the solar array and magnetometer boom engineering model took place in May 1996.

### **Random Vibration Testing**

The random vibration specifications for the solar panel/magnetometer boom engineering model were derived from the instrument/component specifications. Random vibration testing of ACE instruments and components took place in May 1996.

### **Stiffness Verification and Solar Cell Adhesive Bond Test**

A bend test of a solar array qualification panel was performed to verify the substrate stiffness and to ensure adequate bond strength of the solar cell adhesive. The panel was bent to a radius of curvature equivalent to what is expected in launch. The bend test took place in October 1995. Following the bend test, the ACE/Delta II coupled loads model was updated to reflect the actual solar array stiffness.

### **Acoustic Testing**

Prior to APL's acceptance of the solar arrays from the vendor, one flight solar array was tested to protoflight acoustic levels in April 1996.

### **Deployment Testing**

Deployment testing of the solar array/magnetometer boom assembly was performed in May 1996 for the engineering model assembly and in July 1997 for the

flight assemblies. The assembly was rotated such that the axis of rotation aligned with the gravitational axis. The assembly was then g-negated by supporting the end of the panel/magnetometer boom with an overhead crane. The panels and booms were sequentially released to allow full deployment to occur. Flight assembly testing is pictured in Figure 4.

## Spacecraft Structure/Propulsion Subsystem Verification

### Structural Loads and Sinusoidal Vibration Testing

To minimize the risk to the delicate ACE instruments, the ACE primary flight structure with integrated propulsion subsystem was load tested prior to instrument integration. To expedite the testing, the structural loads and sinusoidal vibration testing requirements were combined into a three axis sine sweep test for the spacecraft primary structure with integrated propulsion subsystem. The sine sweep vibration specification and limit load test factors recommended by OLS and MDA are shown in Tables 1 and 2 below.

| Table 1   |                             |                    |                             |
|---|-----------------------------|--------------------|-----------------------------|
| Protoflight Sinusoidal Sweep Vibration Test                       |                             |                    |                             |
| for ACE Spacecraft Structure/Propulsion Subsystem and Observatory |                             |                    |                             |
| Thrust Axis (Z)   |                             | Lateral Axes (X,Y) |                             |
| Frequency (Hz)  | Acceleration (zero to peak) | Frequency (Hz)     | Acceleration (zero to peak) |
| 5 to 6.2  | 0.5 in. (d.a.)              | 5 to 100           | 0.7 g                       |
| 6.2 to 100  | 1.0 g                       |                    |                             |
| Rate = 4 octaves/min  |                             |                    |                             |

| Table 2   |                  |         |
|---|------------------|---------|
| Worst Case Test Limit Load Factors                |                  |         |
| (Limit Load Factors X 1.25)                       |                  |         |
| for ACE Spacecraft Structure/Propulsion Subsystem |                  |         |
|   | Liftoff/Max Aero | MECO    |
| Lateral   | ±3.0 g           | -       |
| Axial   | +3.0 g           | +10.1 g |

(+ indicates compression at the launch vehicle interface)

Since the axial limit loads for both Liftoff/Max Aero and MECO are compressive loads, the axial loads applied by the vibration table could be reduced by one g. The  $\pm 3.0$  g lateral,  $+3.0$  g axial Liftoff/Max Aero load case was represented by lateral vibration testing using an equivalent lateral load of  $4.0$  g. Only  $2.0$  g needed to be applied to get the  $3.0$  g thrust test level. Since lateral axis vibration will be used to represent Liftoff/Max Aero, a higher lateral load had to be applied to envelope a combined lateral and thrust (compression) load case at the ACE/Delta separation plane. The maximum compressive running load at the ACE/Delta separation plane can be calculated as follows:

$$\text{Maximum Compressive Running Load} = \frac{(\text{Lateral Factor})(\text{S/C Wt})(\text{S/C Thrust CG})}{\pi(\text{PAF Radius})^2} + \frac{(\text{Axial Factor})(\text{S/C Wt})}{2\pi(\text{PAF Radius})}$$

(Notes: The S/C Thrust CG is with reference to the ACE/Delta separation plane. The PAF Radius is measured at the separation plane.)

The Lateral Load Factor necessary to produce an equivalent compressive running load is calculated as follows:

$$\text{Lateral Load Factor} = \frac{(\text{Max Compressive Running Load})(\pi)(\text{PAF Radius})^2}{(\text{S/C Wt})(\text{S/C Thrust CG})}$$

|                |   |             |
|----------------|---|-------------|
| Lateral Factor | = | 3.0 g       |
| S/C Wt         | = | 1731 lbs.   |
| S/C Thrust CG  | = | 25.5 inches |
| PAF Radius     | = | 28 inches   |
| Axial Factor   | = | 2.0 g       |

Using the previous values, a Lateral Load Factor of  $4.0$  g is calculated.

The  $10.1$  g MECO load case was represented by axial sine sweep vibration testing of  $9.1$  g.

The test article depicted in Figure 5 consists of the ACE spacecraft flight primary structure, the integrated flight propulsion subsystem, mass simulators representing instruments and spacecraft components, and a Delta II test Payload Attach Fitting (PAF) in the thrust axis (Z) test configuration. The mass simulator weights were configured such that the spacecraft weight totaled or exceeded the maximum allowable weight of  $1731$  lbs. The propulsion subsystem prior to integration is pictured in Figure 6. The propulsion subsystem tanks were filled with Olin (now Primex) provided water and pressurized with dry nitrogen to  $150$  psid.

Vibration testing of the ACE primary structure/propulsion subsystem was performed from October 11 through 18, 1995. The primary structural modes of the ACE structure/propulsion subsystem mounted on the Delta II PAF are summarized in Table 3. The fundamental lateral modes of the spacecraft were used to generate the lateral load factor of  $4.0$  g. The spacecraft had two thrust modes, one of the  $+Z$  deck at  $45$  Hz and one of the remaining primary structure at  $105$  Hz. Rather than trying to generate the limit load at two

different frequencies, a large input at a low, non-resonant, frequency was used to achieve the 9.1 g load factor at the spacecraft center of gravity. The full level sine sweep specifications along with the equivalent loads generated in the structure/propulsion subsystem are shown in Tables 4 through 9.

| Mode Description  | Frequency (Hz) |
|-------------------|----------------|
| Spacecraft RY     | 40             |
| Spacecraft RX     | 41             |
| +Z Deck Thrust    | 45             |
| Spacecraft Thrust | 105            |

| Frequency (Hz)       | Acceleration (zero to peak) |
|----------------------|-----------------------------|
| 5-35                 | 0.7 g                       |
| 38-47                | 0.6 g                       |
| 50-100               | 0.7 g                       |
| Rate = 4 octaves/min |                             |

| Location                            | Load Factor (g's) |
|-------------------------------------|-------------------|
| +Z Deck                             | 5.8               |
| Side Decks                          | 4.2               |
| -Z Deck                             | 2.5               |
| Propulsion Tanks                    | 3.8               |
| OAF                                 | 1.6               |
| <b>Spacecraft Center of Gravity</b> | <b>4.5</b>        |

| Table 6<br>ACE Primary Structure/Propulsion Subsystem<br>Full Level Y Axis Sine Sweep Vibration Inputs |                             |
|--|-----------------------------|
| Frequency (Hz)   | Acceleration (zero to peak) |
| 5-34   | 0.7 g                       |
| 37-46  | 0.55 g                      |
| 49-100   | 0.7 g                       |
| Rate = 4 octaves/min   |                             |

| Table 7<br>ACE Primary Structure/Propulsion Subsystem<br>Equivalent Load Factors at 41 Hz for Y Axis 0.55 g Input |                   |
|---|-------------------|
| Location  | Load Factor (g's) |
| +Z Deck   | 5.8               |
| Side Decks  | 4.1               |
| -Z Deck   | 2.3               |
| Propulsion Tanks  | 4.3               |
| OAF   | 1.4               |
| <b>Spacecraft Center of Gravity</b>   | <b>4.6</b>        |

| Table 8<br>ACE Primary Structure/Propulsion Subsystem<br>Full Level Z Axis Sine Sweep Vibration Inputs |                             |
|--|-----------------------------|
| Frequency (Hz)   | Acceleration (zero to peak) |
| 5-6.2  | .5 " Double Amplitude       |
| 6.2-16   | 1.0 g                       |
| 21   | 10.5 g                      |
| 26-39  | 1.0 g                       |
| 42-48  | .5 g                        |
| 51-58  | 1.0 g                       |
| 63-90  | .25 g                       |
| Rate = 4 octaves/min   |                             |

| Table 9<br>ACE Primary Structure/Propulsion Subsystem<br>Equivalent Load Factors at 21 Hz for Z Axis 10.5 g Input |                   |
|---|-------------------|
| Location  | Load Factor (g's) |
| +Z Deck   | 9.3               |
| Side Decks  | 9.1               |
| -Z Deck   | 8.9               |
| Propulsion Tanks  | 9.4               |
| OAF   | 9.7               |
| <b>Spacecraft Center of Gravity</b>   | <b>9.2</b>        |

The sine sweep input specifications were notched to ACE/Delta II Coupled Loads levels to protect the propulsion subsystem tanks. Sixty-one spacecraft response acceleration channels were recorded. Following this vibration test, the ACE/Delta II coupled loads model was refined to represent the measured structural dynamics.

### Random Vibration Testing

Launch vehicle acoustics is the only significant source of random vibration for a Delta II payload. Since there are no significant high frequency random vibration inputs at the spacecraft/launch vehicle interface, a random vibration environment is not specified in the Delta II Payload Planners Guide<sup>1</sup>. A spacecraft level random vibration test is not necessary if protoflight acoustic testing is performed. However, the random vibration specification shown in Table 10 was used to provide a workmanship test of the spacecraft structure and propulsion subsystem. This specification was developed using a base drive random specification published in the General Environmental Verification Specification for STS & ELV Payloads, Subsystems, and Components<sup>3</sup>, together with acoustic response data from Midcourse Space Experiment (MSX) and Delta 183 programs.

| Table 10<br>ACE Primary Structure/Propulsion Subsystem<br>Workmanship Random Vibration Test Inputs |                          |
|--|--------------------------|
| Frequency (Hz)   | PSD Level                |
| 100  | 0.002 g <sup>2</sup> /Hz |
| 100-300  | +7.4 dB/oct              |
| 300-700  | 0.03 g <sup>2</sup> /Hz  |
| 700-2000   | -3.2 dB/oct              |
| 2000   | 0.01 g <sup>2</sup> /Hz  |
| Overall Amplitude = 6.0 g rms<br>Duration=60 seconds   |                          |

Three axis random vibration was performed on the primary structure/propulsion subsystem, with acceleration response limits set to protect the propulsion subsystem tanks. Sixty-one spacecraft response acceleration channels were recorded.

### **Observatory Verification**

The mechanical verification program for the observatory consisted of protoflight sinusoidal vibration testing, a random vibration survey, protoflight acoustic testing, clampband separation and solar array and magnetometer boom release shock testing, and observatory spin balance and mass properties measurements.

### **Sinusoidal Vibration Testing**

The sinusoidal vibration testing requirements for the ACE Observatory are the same as for the spacecraft structure, and are shown in Table 1. Since the spacecraft primary structure, propulsion subsystem, instruments and spacecraft components had been previously load tested, observatory structural loads testing was not required.

The X axis vibration test configuration of the fully flight configured observatory is shown in Figure 7. The propulsion subsystem tanks were filled with 431 lbs. of Olin (now Primex) provided water and pressurized with dry nitrogen to 150 psid.

Vibration testing of the ACE Observatory occurred from January 29 through February 7, 1997. The sinusoidal vibration inputs to the base of the PAF are displayed in Tables 11 through 13. Notches to the input specification and limits to some response channels were incorporated to protect the instruments, propulsion subsystem, and solar arrays. The notch and response limit levels were above the minimum levels permitted by the ACE/Delta coupled loads analysis. The primary structural modes of the ACE Observatory mounted on the Delta II PAF are summarized in Table 14.

| Table 11<br>ACE Observatory<br>Full Level X Axis Sine Sweep Vibration Inputs |                             |
|--|-----------------------------|
| Frequency (Hz)   | Acceleration (zero to peak) |
| 5-35   | 0.7 g                       |
| 38-47  | 0.6 g                       |
| 50-100   | 0.7 g                       |
| Rate = 4 octaves/min   |                             |

| Table 12<br>ACE Observatory<br>Full Level Y Axis Sine Sweep Vibration Inputs |                             |
|--|-----------------------------|
| Frequency (Hz)   | Acceleration (zero to peak) |
| 5-32   | 0.7 g                       |
| 36-46  | 0.6 g                       |
| 49-56  | 0.7 g                       |
| 60-66  | 0.45 g                      |
| 70-80  | 0.2 g                       |
| 85-100   | 0.1 g                       |
| Rate = 4 octaves/min   |                             |

| Table 13<br>ACE Observatory<br>Full Level Z Axis Sine Sweep Vibration Inputs |                             |
|--|-----------------------------|
| Frequency (Hz)   | Acceleration (zero to peak) |
| 5-6.2  | .5 " Double Amplitude       |
| 6.2-58   | 1.0 g                       |
| 58-100   | 0.2 g                       |
| Rate = 4 octaves/min   |                             |

| Table 14<br>Primary Structural Modes of ACE Observatory on Delta II 5624 PAF |                |
|--|----------------|
| Mode Description   | Frequency (Hz) |
| +Y Solar Array Flexure   | 15             |
| +X Solar Array Flexure   | 22             |
| Spacecraft RX  | 42             |
| Spacecraft RY  | 43             |
| +Z Deck Thrust   | 45             |
| Spacecraft Thrust  | 100            |

Sixty-one spacecraft response acceleration channels were recorded. The primary modes of the observatory were very close to those observed in the ACE primary structure/propulsion subsystem vibration test.

### Random Survey Vibration

The October 1995 primary structure/propulsion subsystem random vibration test generated significant response accelerations throughout the spacecraft structure and propulsion subsystem. Spacecraft panel responses for the workmanship random vibration began to approach what was expected from the protoflight acoustic test. The goal of the observatory random vibration test was to submit the observatory to a workmanship random vibration only, since protoflight vibration would be covered in the observatory acoustics test. The random vibration survey levels shown in Table 15 were considered to be adequate

in generating a sufficient workmanship structural response in the observatory. Sixty-one spacecraft response acceleration channels were recorded.

| Table 15<br>ACE Observatory<br>X ,Y and Z Axis Random Survey Vibration Test |                           |
|---|---------------------------|
| Frequency<br>(Hz)   | PSD Level                 |
| 100-2000  | 0.0001 g <sup>2</sup> /Hz |
| Overall Amplitude = 0.4 g rms<br>Duration=60 seconds                        |                           |

## Acoustic Testing

The ACE Observatory in its acoustic test configuration is shown in Figure 8. The acoustic test requirements for a Delta II payload in an eight foot fairing are shown in Table 16<sup>1</sup>. These protoflight levels represent maximum expected flight levels +3 dB. The observatory acoustic test was performed on March 11, 1997 in the Goddard Space Flight Center Acoustic Chamber. Sixty-one spacecraft acceleration responses were recorded. Generally, the random vibration response of the spacecraft decks was lower than the random vibration levels specified for the instruments and spacecraft components. The ACE Observatory seemed to provide more damping than previous APL spacecraft. The water filled propulsion tanks may have contributed to this higher damping.

| One-Third Octave Center Frequency (Hz)  | Protoflight Levels (dB) |
|---|-------------------------|
| 31.5  | 123.5                   |
| 40.0  | 125.0                   |
| 50.0  | 126.5                   |
| 63.0  | 128.0                   |
| 80.0  | 130.0                   |
| 100.0   | 131.0                   |
| 125.0   | 132.5                   |
| 160.0   | 133.5                   |
| 200.0   | 134.5                   |
| 250.0   | 135.5                   |
| 315.0   | 137.5                   |
| 400.0   | 139.0                   |
| 500.0   | 141.0                   |
| 630.0   | 138.0                   |
| 800.0   | 135.0                   |
| 1000.0  | 133.0                   |
| 1250.0  | 131.5                   |
| 1600.0  | 130.5                   |
| 2000.0  | 129.5                   |
| 2500.0  | 128.5                   |
| 3150.0  | 127.0                   |
| 4000.0  | 125.5                   |
| 5000.0  | 124.5                   |
| 6300.0  | 123.5                   |
| 8000.0  | 122.5                   |
| 10000   | 121.5                   |
| OASPL = 147.6 dB<br>Duration = 1 min<br>SPL Reference: $2.0 \times 10^{-5} \text{ N/m}^2$ |                         |

## Shock Testing

The primary sources of shock to the ACE Observatory are the PAF clampband separation shock and the solar array and magnetometer boom release shock. The maximum expected clampband shock at the Delta 5624 PAF interface is shown in Table 17.

| Table 17<br>5624 Payload Attach Fitting<br>Spacecraft Interface Shock Environment<br>Maximum Flight Levels |                            |
|--|----------------------------|
| Frequency<br>(Hz)  | Peak Acceleration Response |
| 100  | 50 g                       |
| 900-3000   | 3000 g                     |
| Q = 10<br>(Clamp Preload = 3900 lbs)   |                            |

The observatory shock test was performed on March 17 and 18, 1997 in the Goddard Space Flight Center Acoustic Chamber. Separation shock was performed by MDA initiation of the clampband bolt cutter. The observatory was suspended by a crane, allowing the PAF to drop onto foam. The PAF separation initiated the spacecraft separation switch, which activated the solar array pin-puller release. The  $\pm X$  arrays were released first, followed by the  $\pm Y$  arrays. After this sequence, the magnetometer pin-pullers were actuated by spacecraft command. The ACE Observatory in its post-shock configuration is shown in Figure 9. Shock responses with  $Q=10$  were plotted for 32 locations on the observatory. Peak responses are summarized in Tables 18 through 21.

| Table 18<br>ACE Observatory Shock Test<br>Delta 5624 PAF Clampband Separation Shock Peak Responses |                            |
|--|----------------------------|
| Location   | Peak Acceleration Response |
| +Z Deck  | 90 g max above 3000 Hz     |
| Side Decks   | 300 g max above 2000 Hz    |
| -Z Deck, edge  | 500 g max above 3000 Hz    |
| -Z Deck, center  | 200 g max above 2000 Hz    |
| -Z Deck, propulsion tank bracket   | 600 g above 1000 Hz        |
| Magnetometer   | 100 g max above 1000 Hz    |
| Q = 10<br>(Clamp Preload = 3900 lbs)   |                            |

| Table 19<br>ACE Observatory Shock Test<br>±X Solar Array Pin Puller Shock Peak Responses |                            |
|--|----------------------------|
| Location   | Peak Acceleration Response |
| -X Deck, center  | 300 g max above 2000 Hz    |
| -X Deck, near pin puller   | 600 g max above 2000 Hz    |
| -Z Deck, center  | 300 g max above 2000 Hz    |
| -Z Deck, propulsion tank bracket   | 300 g max above 1000 Hz    |
| +X Solar Array corner  | 400 g above 150 Hz         |
| +X Solar Array, near clevis  | 500 g max above 1000 Hz    |
| Q = 10   |                            |

| Table 20<br>ACE Observatory Shock Test<br>±Y Solar Array Pin Puller Shock Peak Responses |                            |
|--|----------------------------|
| Location   | Peak Acceleration Response |
| +Z Deck, edge  | 120 g max above 2000 Hz    |
| -Y Deck, center  | 200 g max above 2000 Hz    |
| -Z Deck, center  | 200 g max above 2000 Hz    |
| -Z Deck, propulsion tank bracket<br>(closer to Y side)                                   | 1000 g max above 1000 Hz   |
| +Y Solar Array corner  | 450 g above 150 Hz         |
| +Y Solar Array, near snubber   | 300 g max above 2000 Hz    |
| Magnetometer   | 200 g max above 2000 Hz    |
| Q = 10   |                            |

| Table 21<br>ACE Observatory Shock Test<br>Magnetometer Boom Pin Puller Shock Peak Responses |                            |
|---|----------------------------|
| Location  | Peak Acceleration Response |
| +Y Solar Array corner   | 2000 g max above 1000 Hz   |
| +Y Solar Array, near snubber  | 600 g max above 2000 Hz    |
| +Y Magnetometer   | 500 g max above 3000 Hz    |
| Q = 10  |                            |

### Spin Balance and Mass Properties Measurements (GSFC)

The ACE Observatory spin balance and mass property measurements were performed in the Goddard Space Flight Center Acoustic Chamber from March 27 through April 4, 1997.

The flight configured observatory, minus solar arrays and magnetometer booms, is shown mounted on the GSFC Mass Properties Measurement Facility (MPMF) in Figure 10. The propulsion tanks were filled to a flight weight of 431 lbs. with water plus nitrogen pressurant. Due to instrument weight increases late in the program, the observatory was unbalanced prior to the addition of balance weights. The GSFC spin table could not accommodate a large payload center of gravity offset, so calculated balance weights were attached to the observatory prior to the first GSFC spin. The observatory was balanced in six spins with residual products of inertia ( $P_{xz}$ ,  $P_{yz}$ ) of 200 lb-in<sup>2</sup> (the accuracy of the GSFC spin facility). A principal axis misalignment of 0.07

degrees from the ACE spin axis was calculated for the launch configuration. The maximum orbit configuration (deployed solar arrays and booms) principal axis misalignment permitted by the flight operations team is 0.2 degrees. This 0.2 degrees includes not only spin axis measurement inaccuracies, but deployment misalignments and calculation errors for the orbit configuration balance. Spin balance operations resulted in the addition of 16.79 lbs. of balance weights on the +Z deck and 15.99 lbs. of balance weight on the -Z deck. The final balance weights were very close in magnitude and location to what was predicted from calculations.

Following the observatory spin balance, observatory mass property measurements were made. CGX, CGY, IZZ, PXZ, and PYZ were measured for the "wet" spin axis configuration. The propulsion tanks were then emptied and CGX, CGY, IZZ, PXZ, and PYZ were measured for the "dry" spin axis configuration. A product of inertia increase of 200 lb-in<sup>2</sup> and a lateral center of gravity shift of almost 0.01 inch was measured for the "dry" configuration. The difference between the "wet" and "dry" measurements indicated that the observatory would be slightly unbalanced when the propulsion tanks were empty. CGZ, IXX, and IYY of the "dry" observatory minus solar arrays and booms were then measured on the MPMF as shown in Figure 11. The observatory was attached to a "yoke" fixture, enabling the alignment of the X and Y axes with the table spin axis.

Centers of gravity measurements were made for the solar arrays in October 1996, and for the magnetometer booms in January 1997. The solar arrays and booms were supported on two ends, one end being placed on a scale (Figures 12). After weighing each solar array and boom, the center of gravity could be calculated using statics. Using the mass property measurements of the solar arrays, magnetometer booms, and observatory, the ACE Observatory mass properties were calculated for launch and orbital configurations. These mass properties are presented in Table 22.

Table 22

ACE Mass Properties Following GSFC Spin Balance, 4/24/97

| Launch Configuration (Non-spinning with 1G acceleration): |                     |              |                | Orbital Configuration (Beginning of Life): |                     |              |                |
|---|---------------------|--------------|----------------|--|---------------------|--------------|----------------|
| Weight =  |                     | 1658.82 lbs. | 752.30 kg.     | Weight =                                   |                     | 1658.82 lbs. | 752.30 kg.     |
| CGX =   | 0.01 in.            | 0.00 ft.     | 0.02 cm.       | CGX =                                      | 0.01 in.            | 0.00 ft.     | 0.04 cm.       |
| CGY =   | 0.00 in.            | 0.00 ft.     | 0.00 cm.       | CGY =                                      | 0.00 in.            | 0.00 ft.     | 0.00 cm.       |
| CGZ =   | 25.78 in.           | 2.15 ft.     | 65.49 cm.      | CGZ =                                      | 28.01 in.           | 2.33 ft.     | 71.15 cm.      |
| IXX =   | 849288.19 lb-in**2  | 183.33 sfs.  | 249.38 kg-m**2 | IXX =                                      | 1163851.29 lb-in**2 | 251.24 sfs.  | 341.75 kg-m**2 |
| IYY =   | 846109.49 lb-in**2  | 182.65 sfs.  | 248.45 kg-m**2 | IYY =                                      | 914603.72 lb-in**2  | 197.43 sfs.  | 268.56 kg-m**2 |
| IZZ =   | 1085365.15 lb-in**2 | 234.29 sfs.  | 318.70 kg-m**2 | IZZ =                                      | 1578715.12 lb-in**2 | 340.79 sfs.  | 463.56 kg-m**2 |
| PXY =   | -428.04 lb-in**2    | -0.09 sfs.   | -0.13 kg-m**2  | PXY =                                      | -760.79 lb-in**2    | -0.16 sfs.   | -0.22 kg-m**2  |
| PXZ =   | -197.11 lb-in**2    | -0.04 sfs.   | -0.06 kg-m**2  | PXZ =                                      | 243.01 lb-in**2     | 0.05 sfs.    | 0.07 kg-m**2   |
| PYZ =   | -19.37 lb-in**2     | 0.00 sfs.    | -0.01 kg-m**2  | PYZ =                                      | 10.70 lb-in**2      | 0.00 sfs.    | 0.00 kg-m**2   |
| Launch Configuration (Spinning with 0G acceleration):     |                     |              |                | Orbital Configuration (End of Life):       |                     |              |                |
| Weight =  |                     | 1658.82 lbs. | 752.30 kg.     | Weight =                                   |                     | 1227.82 lbs. | 556.83 kg.     |
| CGX =   | 0.01 in.            | 0.00 ft.     | 0.02 cm.       | CGX =                                      | 0.02 in.            | 0.00 ft.     | 0.05 cm.       |
| CGY =   | 0.00 in.            | 0.00 ft.     | 0.00 cm.       | CGY =                                      | 0.00 in.            | 0.00 ft.     | 0.00 cm.       |
| CGZ =   | 26.23 in.           | 2.19 ft.     | 66.62 cm.      | CGZ =                                      | 29.25 in.           | 2.44 ft.     | 74.29 cm.      |
| IXX =   | 845836.04 lb-in**2  | 182.59 sfs.  | 248.37 kg-m**2 | IXX =                                      | 1098052.45 lb-in**2 | 237.03 sfs.  | 322.43 kg-m**2 |
| IYY =   | 842657.34 lb-in**2  | 181.90 sfs.  | 247.43 kg-m**2 | IYY =                                      | 848804.75 lb-in**2  | 183.23 sfs.  | 249.24 kg-m**2 |
| IZZ =   | 1085365.15 lb-in**2 | 234.29 sfs.  | 318.70 kg-m**2 | IZZ =                                      | 1478050.74 lb-in**2 | 319.06 sfs.  | 434.01 kg-m**2 |
| PXY =   | -428.04 lb-in**2    | -0.09 sfs.   | -0.13 kg-m**2  | PXY =                                      | -760.79 lb-in**2    | -0.16 sfs.   | -0.22 kg-m**2  |
| PXZ =   | -203.00 lb-in**2    | -0.04 sfs.   | -0.06 kg-m**2  | PXZ =                                      | 212.56 lb-in**2     | 0.05 sfs.    | 0.06 kg-m**2   |
| PYZ =   | -19.27 lb-in**2     | 0.00 sfs.    | -0.01 kg-m**2  | PYZ =                                      | 9.32 lb-in**2       | 0.00 sfs.    | 0.00 kg-m**2   |

## Spin Balance (KSC)

After the GSFC spin balance, 9 out of 10 instruments were removed from the observatory and reconfigured. A second spin balance at the Boeing spin facility at the Kennedy Space Center (KSC) was recommended since the balanced configuration had been changed. The final spin balance took place from August 4 through 6, 1997 (three weeks prior to launch). The fully flight configured observatory, fueled with 434 lbs. of hydrazine and nitrogen pressurant, is shown in Figure 13. The launch configuration of the observatory was balanced in one spin operation with the addition of 0.32 lbs. on the +Z deck and 0.37 lbs. on the -Z deck. The products of inertia were 1 lb-in<sup>2</sup> for Pxz and 4 lb-in<sup>2</sup> for Pyz, resulting in a calculated principal axis misalignment of 0.001 degrees. Since the solar arrays and booms are not identical in weight or center of gravity, 0.76 lbs. of balance weights were added to the +Z deck and 0.37 lbs. of balance weights were added to the -Z deck to balance the orbit configuration. After the spin balance was complete and the official observatory weight measurement was made by Boeing, the observatory mass properties were updated. The final mass properties, shown in Table 23, result in a principal axis misalignment of less than 0.02 degrees for the orbital beginning of life configuration.

**Table 23**  
**ACE Mass Properties Following KSC Spin Balance, 8/13/97**

| Launch Configuration (Non-spinning with 1G acceleration): |                     |              |                | Orbital Configuration (Beginning of Life): |                     |              |                |
|---|---------------------|--------------|----------------|--|---------------------|--------------|----------------|
| Weight =  |                     | 1668.16 lbs. | 756.54 kg.     | Weight =                                   |                     | 1668.16 lbs. | 756.54 kg.     |
| CGX =   | -0.01 in.           | 0.00 ft.     | -0.02 cm.      | CGX =                                      | 0.00 in.            | 0.00 ft.     | 0.00 cm.       |
| CGY =   | 0.00 in.            | 0.00 ft.     | -0.01 cm.      | CGY =                                      | 0.00 in.            | 0.00 ft.     | 0.00 cm.       |
| CGZ =   | 25.80 in.           | 2.15 ft.     | 65.52 cm.      | CGZ =                                      | 28.01 in.           | 2.33 ft.     | 71.15 cm.      |
| IXX =   | 853491.32 lb-in**2  | 184.24 sfs.  | 249.72 kg-m**2 | IXX =                                      | 1175056.44 lb-in**2 | 253.66 sfs.  | 343.81 kg-m**2 |
| IYY =   | 850724.42 lb-in**2  | 183.64 sfs.  | 248.91 kg-m**2 | IYY =                                      | 919244.72 lb-in**2  | 198.43 sfs.  | 268.96 kg-m**2 |
| IZZ =   | 1091892.18 lb-in**2 | 235.70 sfs.  | 319.48 kg-m**2 | IZZ =                                      | 1591966.88 lb-in**2 | 343.65 sfs.  | 465.79 kg-m**2 |
| PXY =   | -129.41 lb-in**2    | -0.03 sfs.   | -0.04 kg-m**2  | PXY =                                      | -461.66 lb-in**2    | -0.10 sfs.   | -0.14 kg-m**2  |
| PXZ =   | -402.22 lb-in**2    | -0.09 sfs.   | -0.12 kg-m**2  | PXZ =                                      | 93.97 lb-in**2      | 0.02 sfs.    | 0.03 kg-m**2   |
| PYZ =   | -65.15 lb-in**2     | -0.01 sfs.   | -0.02 kg-m**2  | PYZ =                                      | 45.32 lb-in**2      | 0.01 sfs.    | 0.01 kg-m**2   |
| Launch Configuration (Spinning with 0G acceleration):     |                     |              |                | Orbital Configuration (End of Life):       |                     |              |                |
| Weight =  |                     | 1668.16 lbs. | 756.54 kg.     | Weight =                                   |                     | 1234.47 lbs. | 559.85 kg.     |
| CGX =   | -0.01 in.           | 0.00 ft.     | -0.02 cm.      | CGX =                                      | 0.00                | 0.00 ft.     | 0.00 cm.       |
| CGY =   | 0.00 in.            | 0.00 ft.     | -0.01 cm.      | CGY =                                      | 0.00                | 0.00 ft.     | 0.00 cm.       |
| CGZ =   | 26.24 in.           | 2.19 ft.     | 66.64 cm.      | CGZ =                                      | 29.25               | 2.44 ft.     | 74.28 cm.      |
| IXX =   | 850002.32 lb-in**2  | 183.49 sfs.  | 248.70 kg-m**2 | IXX =                                      | 1108851.83          | 239.36 sfs.  | 324.44 kg-m**2 |
| IYY =   | 847235.42 lb-in**2  | 182.89 sfs.  | 247.89 kg-m**2 | IYY =                                      | 853040.10           | 184.14 sfs.  | 249.59 kg-m**2 |
| IZZ =   | 1091892.18 lb-in**2 | 235.70 sfs.  | 319.48 kg-m**2 | IZZ =                                      | 1490674.35          | 321.79 sfs.  | 436.16 kg-m**2 |
| PXY =   | -129.41 lb-in**2    | -0.03 sfs.   | -0.04 kg-m**2  | PXY =                                      | -461.66             | -0.10 sfs.   | -0.14 kg-m**2  |
| PXZ =   | -397.00 lb-in**2    | -0.09 sfs.   | -0.12 kg-m**2  | PXZ =                                      | 94.54               | 0.02 sfs.    | 0.03 kg-m**2   |
| PYZ =   | -62.39 lb-in**2     | -0.01 sfs.   | -0.02 kg-m**2  | PYZ =                                      | 45.67               | 0.01 sfs.    | 0.01 kg-m**2   |

## SUMMARY

Mechanical flight qualification testing of the ACE Observatory was completed from October 1995 through August 1997. ACE was launched on a Delta II 7920-8 vehicle on August 25, 1997, and is currently on station at the Earth-Sun libration point L1. The launch accelerations and sound pressure levels measured by the Goddard Spaceflight Center Spacecraft Loads and Acoustics Measurements payload were below the maximum expected levels predicted by the launch vehicle contractor, MDA. According to the mission operations crew, ACE successfully survived the launch vibration, acoustic, and shock environments and has a stable 5 rpm spin with a 0.1 degree principal axis misalignment.

## ACKNOWLEDGEMENTS

Contributions from many individuals lead to the success of the ACE Observatory mechanical qualification test program. Ted Sholar, supervisor of the APL Space Department Mechanical Analysis group, provided input and support in all the test efforts. Vibration testing was conducted by the APL Vibration Test Laboratory (Bob Tomkiewicz, Craig Hughes, Leon Garvin, Harold Fox). Observatory spin balance, acoustic testing, and shock testing were conducted at the Goddard Spaceflight Center (Dan Worth, Don Baker, Bob Denhardt, K. C. Shah, Wyatt Rinker). Final spin balance operations were supported by the Boeing spin balance facility at Kennedy Space Center (Randy Hicks).

## REFERENCES

1. MDC H3224C, Commercial Delta II Payload Planners Guide, McDonnell Douglas Commercial Delta, Inc., Huntington Beach, California, October 1993.
2. Scharton, T., "Monograph on Force Limited Vibration Testing", NASA RP-1403, May 1997.
3. GEVS-SE, General Environmental Verification Specification for STS & ELV Payloads, Subsystems, and Components, NASA Goddard Space Flight Center, Greenbelt, Maryland, January 1990.

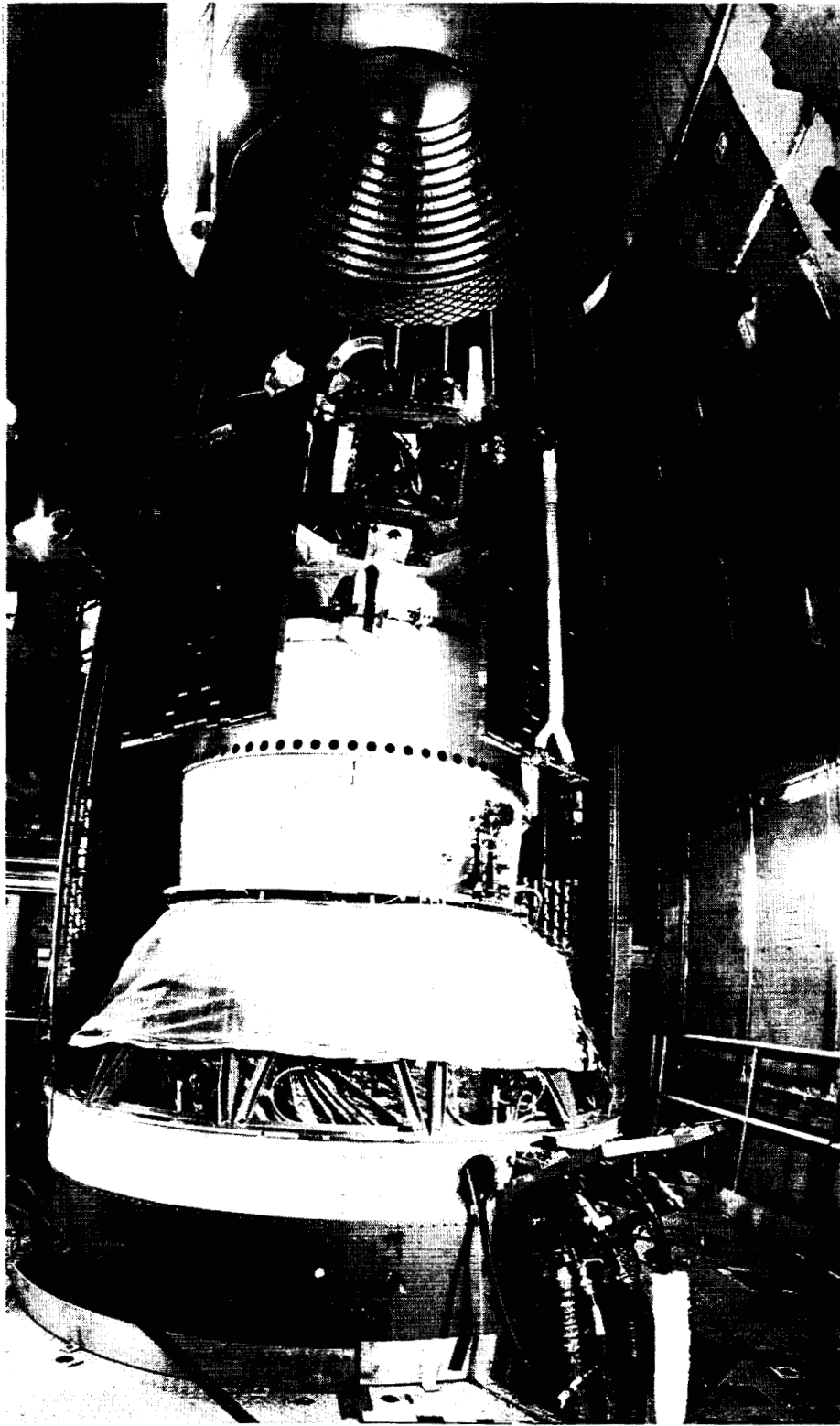


Figure 1. ACE Observatory in Delta II Fairing.

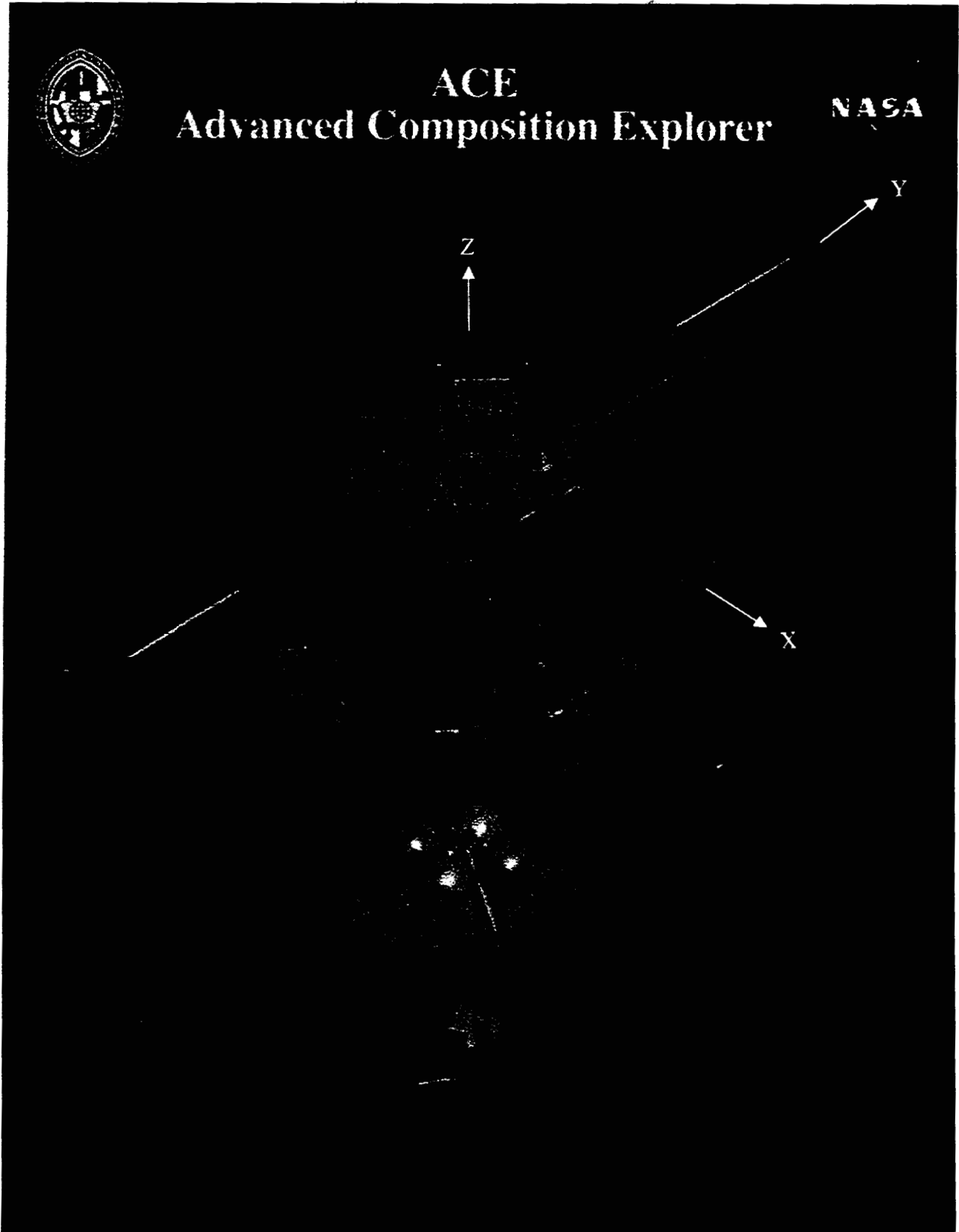


Figure 2. Exploded View of ACE Observatory.

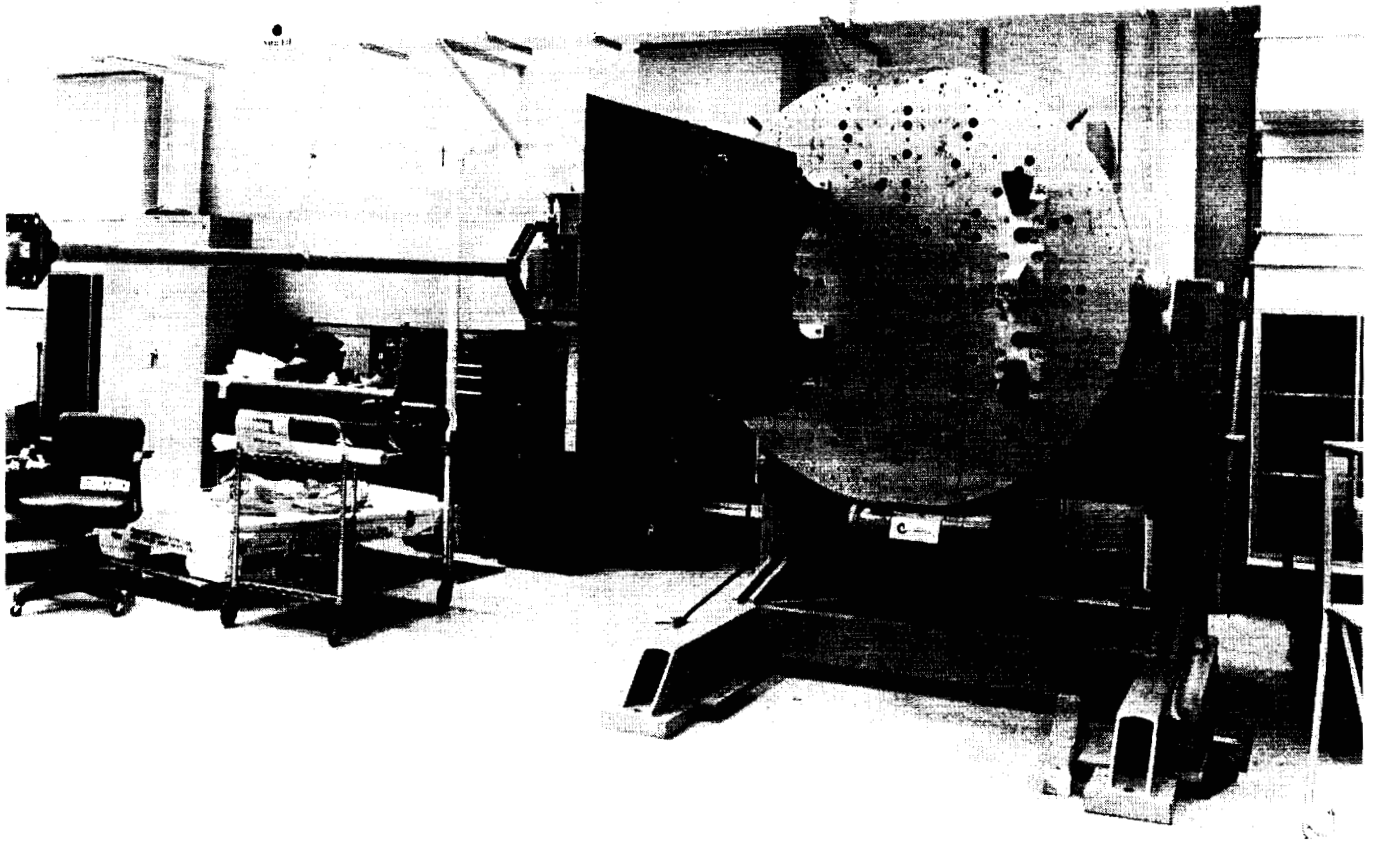


Figure 3. ACE Solar Array/Magnetometer Boom Engineering Model Deployment Test.

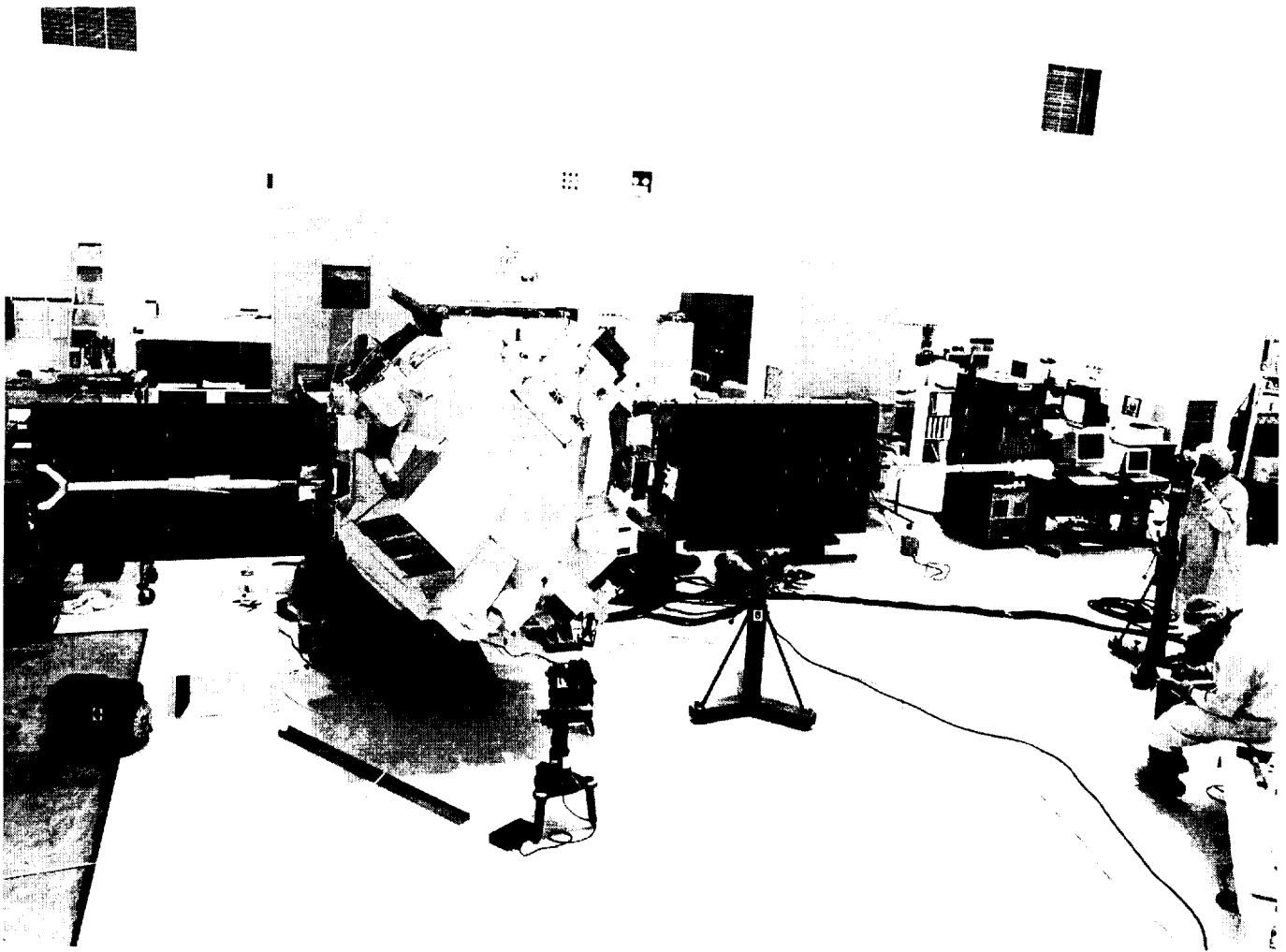


Figure 4. ACE Solar Array/Magnetometer Boom Flight Unit Deployment Test.

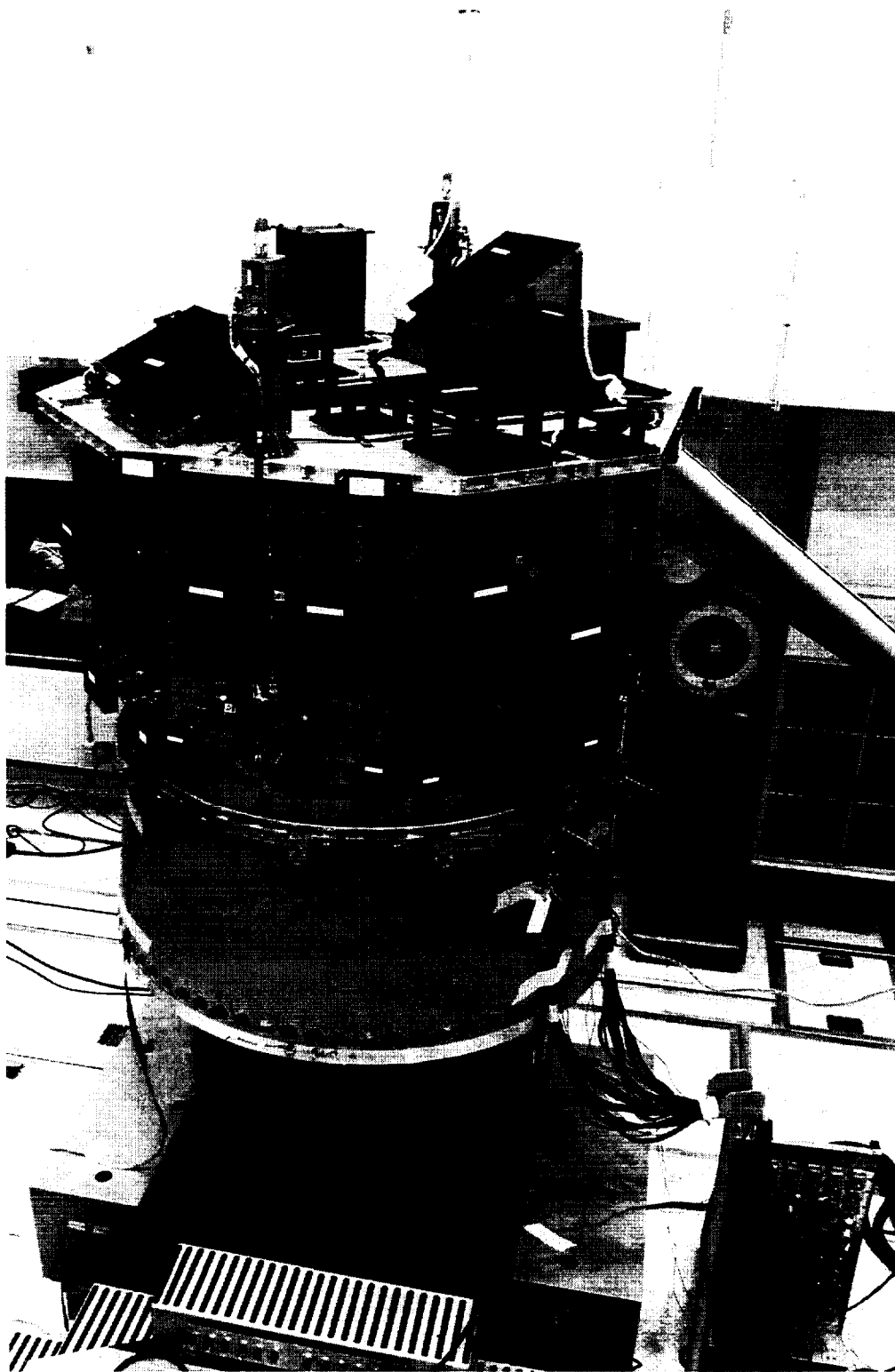


Figure 5. ACE Spacecraft Primary Structure/Propulsion Subsystem Vibration Test.

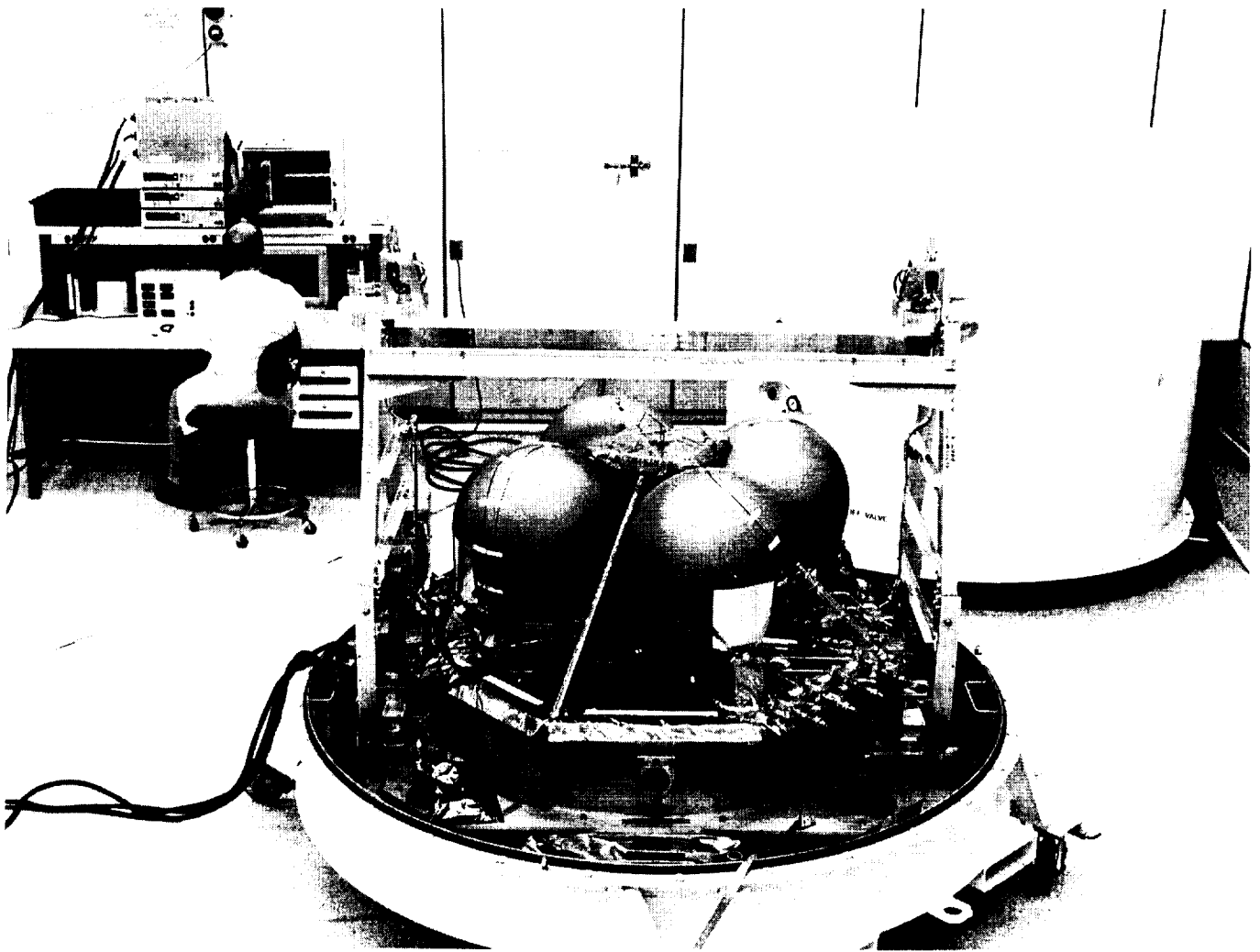


Figure 6. ACE Propulsion Subsystem in Shipping Container.

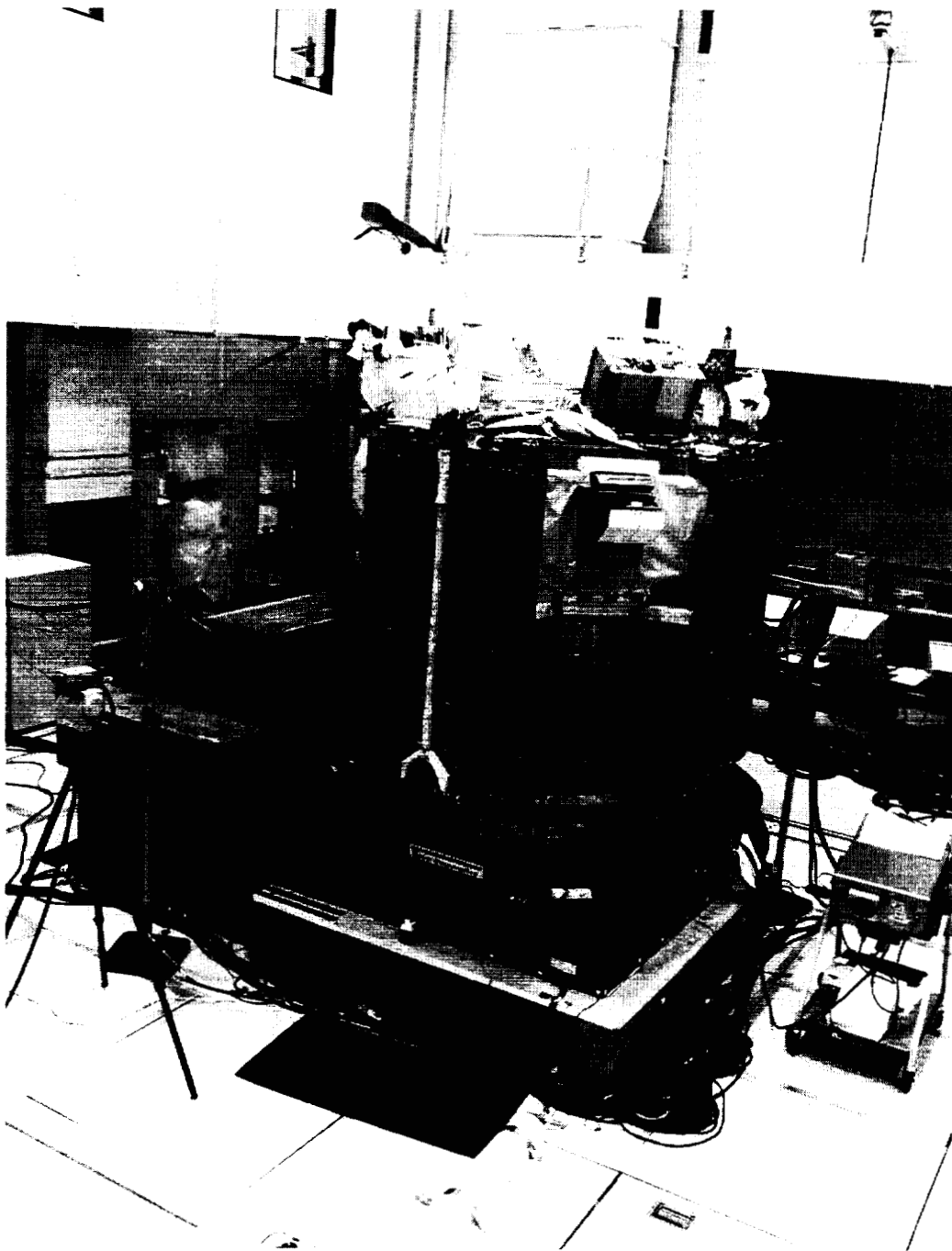


Figure 7. ACE Observatory Vibration Test, X Axis Configuration.

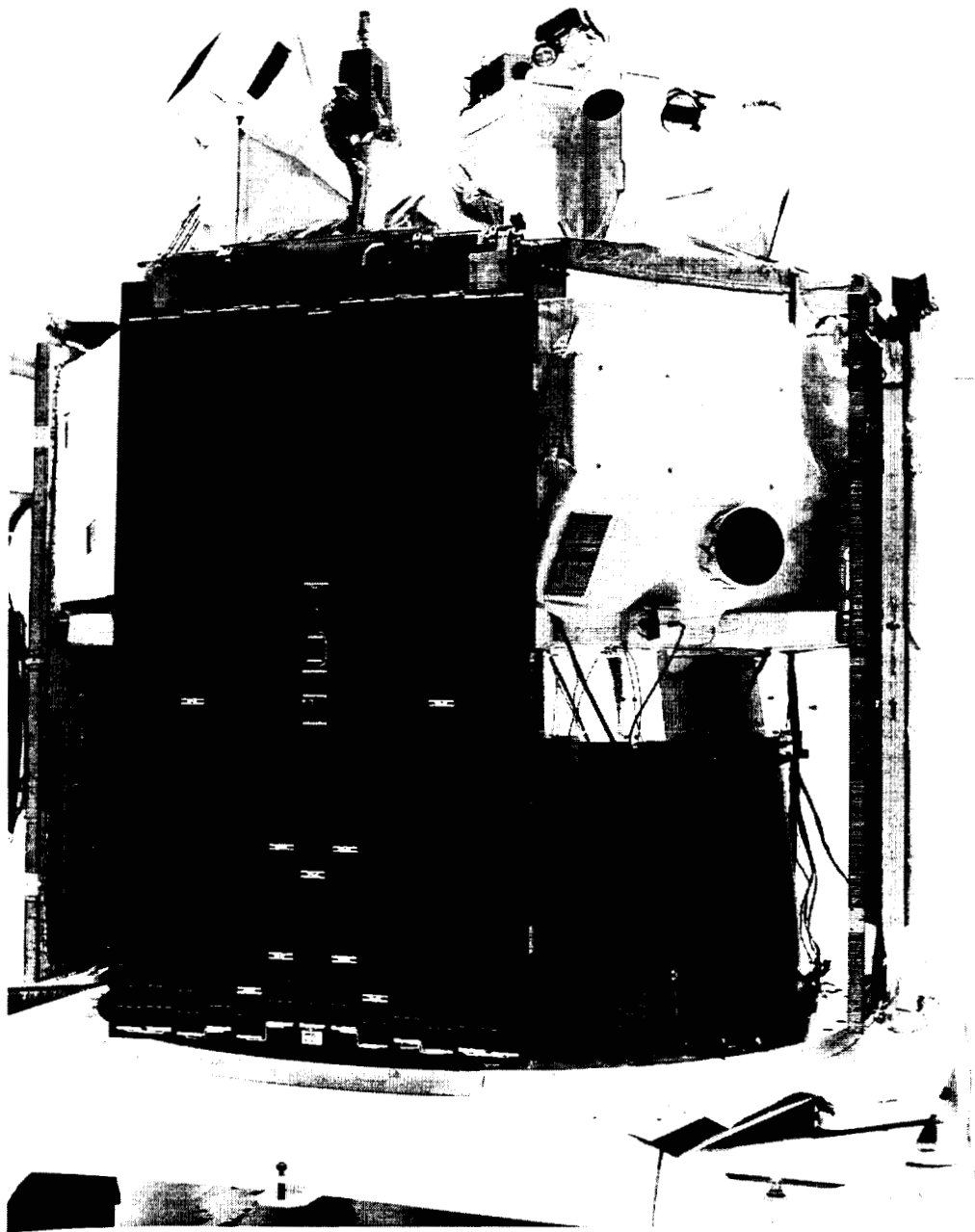


Figure 8. ACE Observatory Acoustic Test.

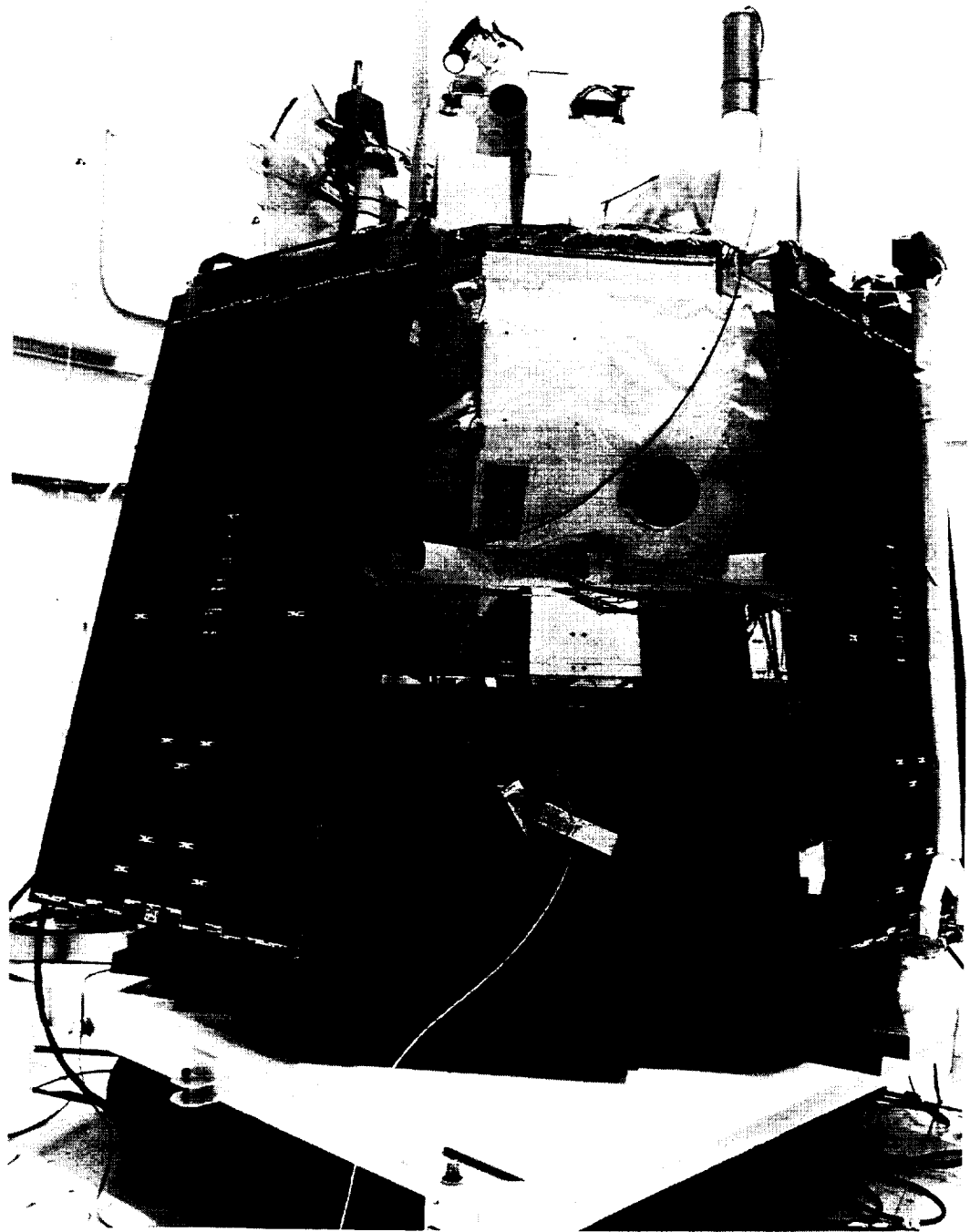


Figure 9. ACE Observatory Shock Test.

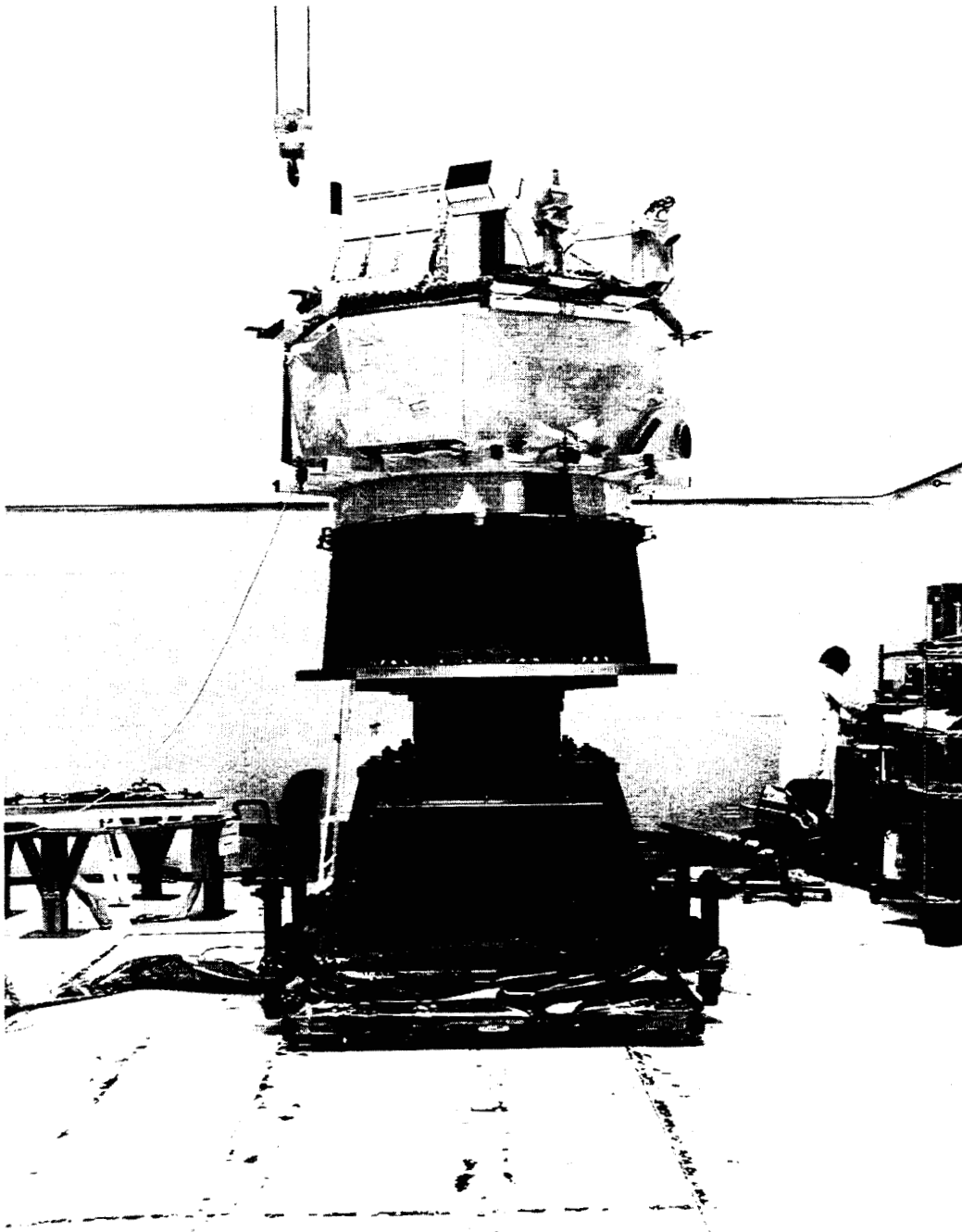


Figure 10. ACE Observatory Spin Balance/Mass Properties Measurements at GSFC, Spin Axis Configuration.

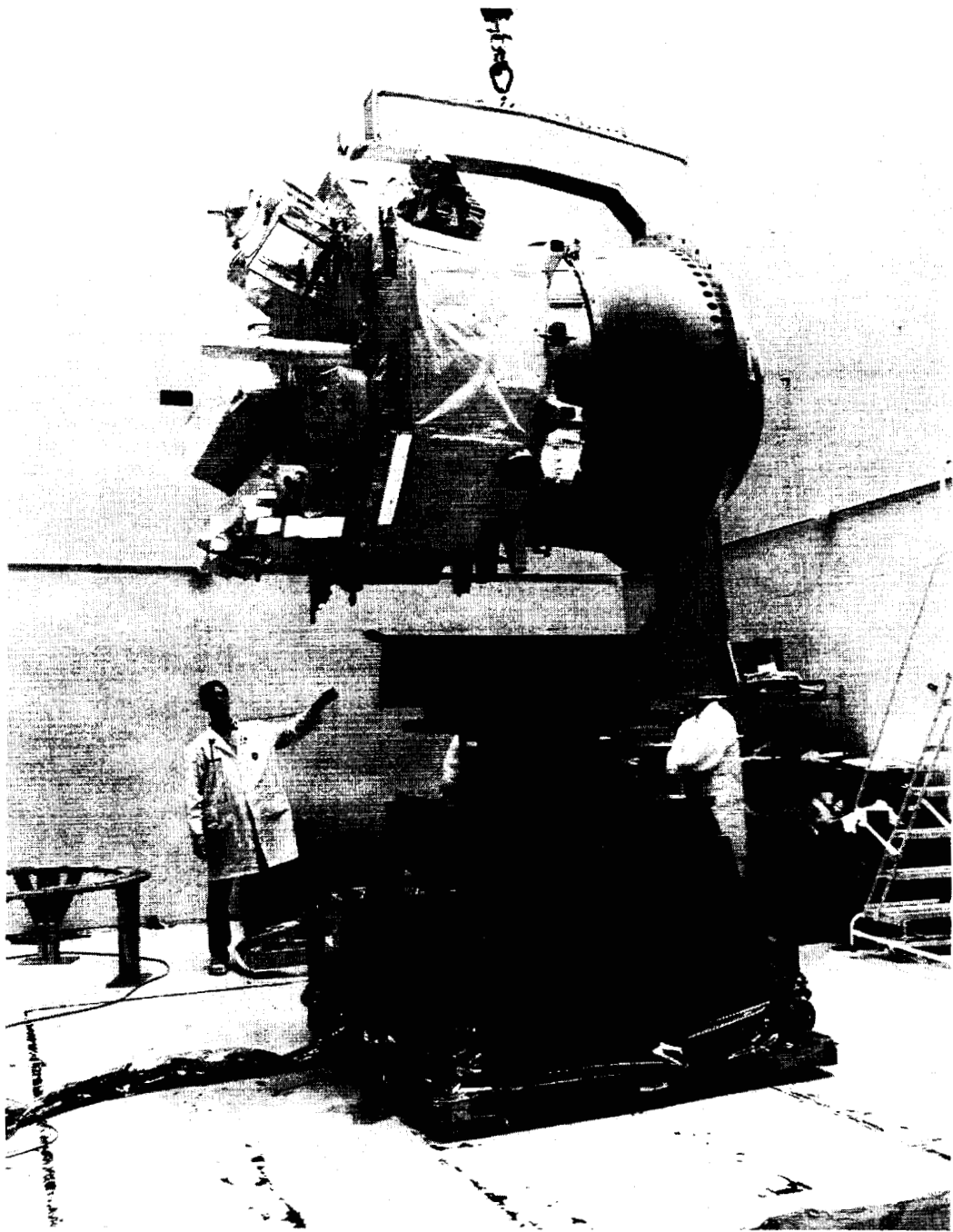


Figure 11. ACE Observatory Mass Properties Measurements at GSFC Lateral Axis Configuration.

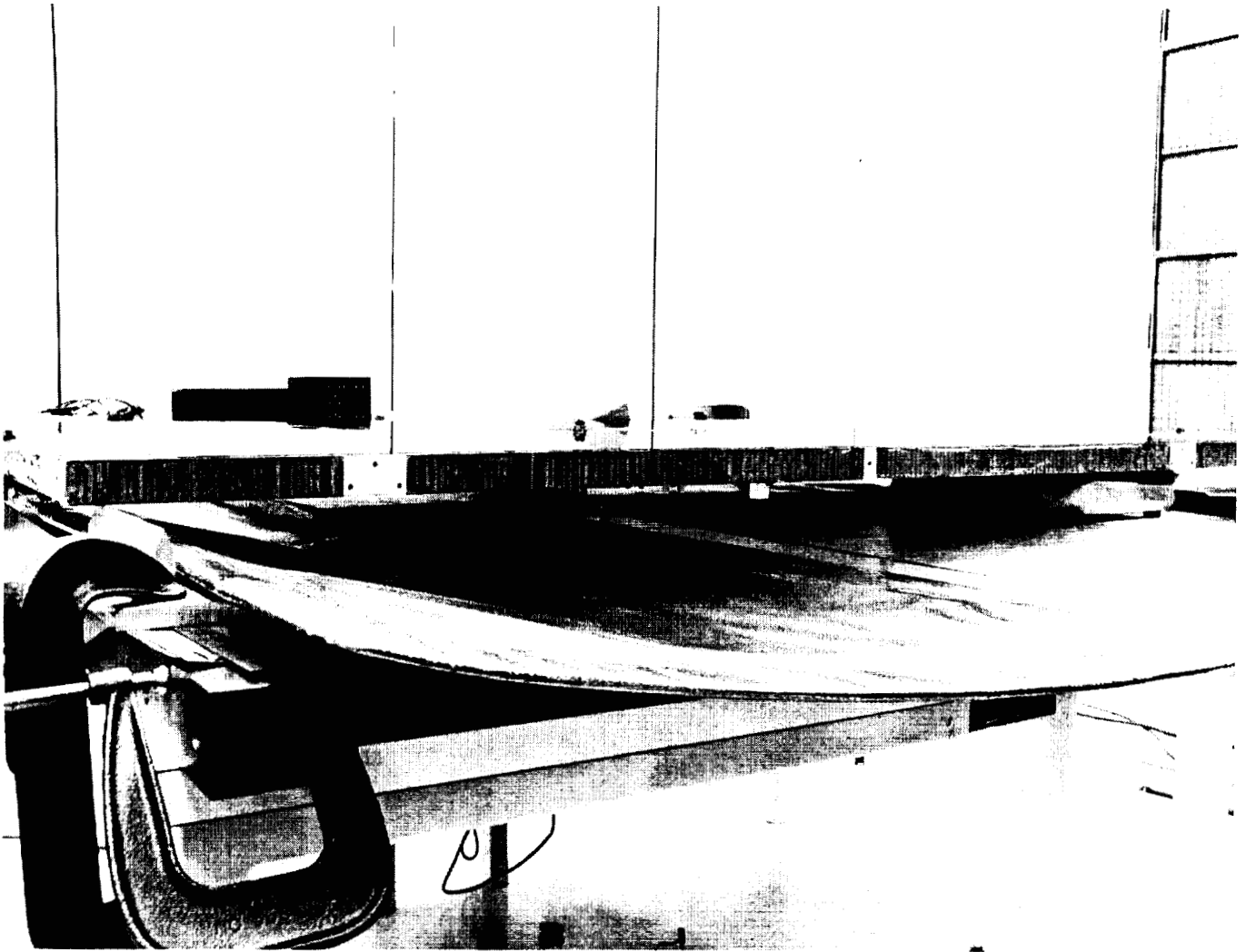


Figure 12. ACE Solar Array Center of Gravity Measurement.

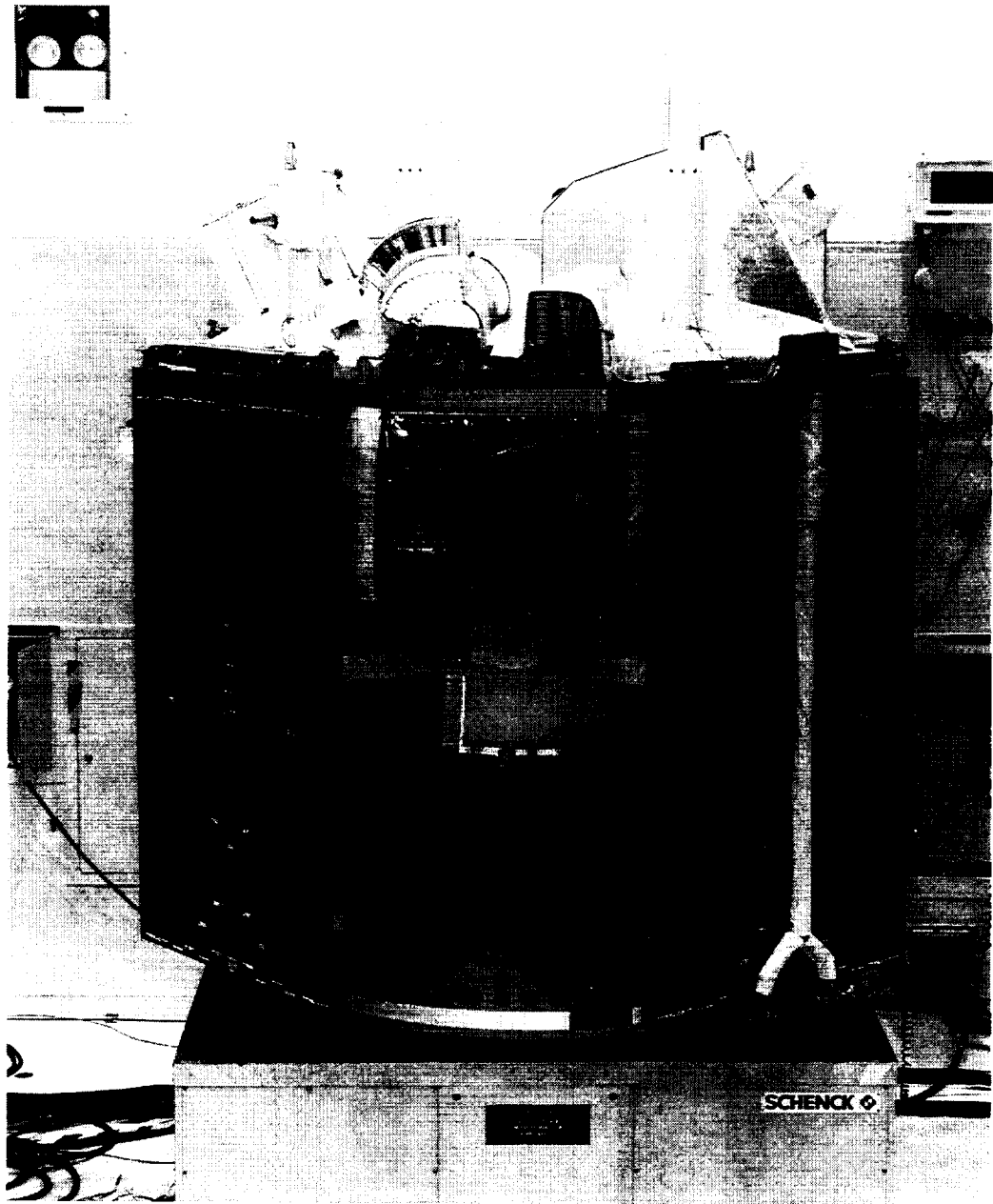


Figure 13. ACE Observatory Spin Balance at KSC.

**STRUCTURAL WELD LEAK TESTING  
IN SUPPORT OF THE INTERNATIONAL SPACE STATION  
NODE 1, AIRLOCK AND LABORATORY FLIGHT ELEMENTS**

Steve Underwood, Angela Holt  
Boeing Defense and Space Group  
International Space Station Program  
Huntsville, Alabama

**ABSTRACT**

Developmental testing on the detector probe method of helium leak detection was performed in support of the International Space Station program (ISS) at Marshall Space Flight Center (MSFC), in Huntsville AL. The test evaluated detector probe sniffing techniques, head designs, optimum sizes and linear head speeds used to detect a known leak approximately  $1E-4$  accs helium. The test resulted in detector probe head design and fabrication for leak testing pressurized vessel external surfaces, and also in the development of the detector probe head design and test procedure used to test all structural welds on Node 1, Airlock, and Laboratory flight elements.

In support of the ISS structural weld leak test, a helium mixing test was performed to evaluate the helium mixing method required to obtain a uniform helium concentration during testing of these modules, as a known helium concentration is necessary to accurately determine leak rates. Testing was performed in a 2500 cubic foot pressure vessel located at MSFC. Mixing fans were positioned internal to the pressure vessel, and oxygen sensors were mounted in the vessel top, middle and bottom areas in order to evaluate helium concentrations. The vessel was pressurized to 14.7 psig with 100% helium, vented to atmospheric pressure, pressurized back to 14.7 psig helium then vented back to atmospheric pressure. The test demonstrated that a uniform helium concentration can be obtained without mixing fans, and resulted in the elimination of oxygen monitors and mixing fans in the flight articles during weld and seal leak tests.

The leak tests of the structural welds on the ISS Node 1, Airlock, and Laboratory flight elements were successfully completed in 1996 and 1997.

**INTRODUCTION**

The ISS modules are comprised of machined and formed aluminum panels welded together. Leak testing of the module welds and structural skin was proposed, and the helium detector probe testing was one of the possible test methods. Developmental tests were performed in April of 1995 to evaluate the suitability of detector probe testing on the module welds and skin, and to evaluate the design of the test aids used to increase the sensitivity of the sniffer test.

## MODULE WELD DEVELOPMENTAL TESTING

The developmental test setup simulated a leak in a module weld. The ISS modules have two different sizes of welds:  $\frac{3}{4}$ " wide and  $\frac{1}{2}$ " wide. The development test utilized two sample weld plates - one with each weld size - approximately two feet long by 9 inches wide. A  $\frac{1}{4}$ " hole was drilled through each weld, and a  $\frac{1}{2}$ " ID x 2" long tube was welded to the plate back side centered over the hole. This tube stub was connected to the helium standard leak. Figure 1 shows a weld test plate.

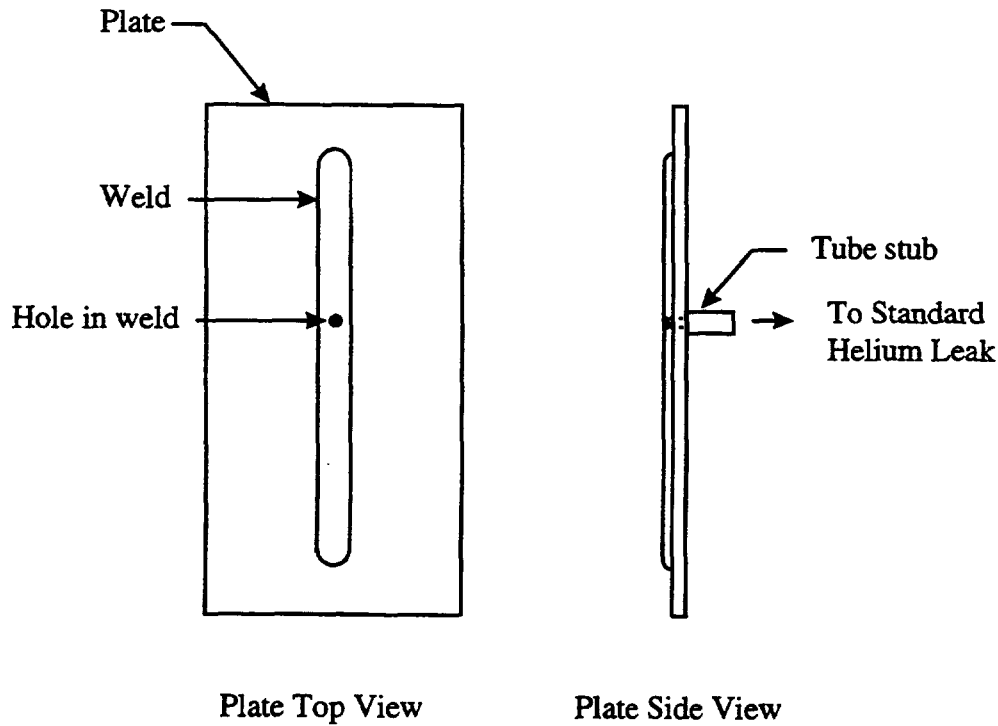


Figure 1: Weld Test Plate

A sniffer head was built to fit over the sniffer probe tip and approximate the shape of the weld to be tested. The head was built with several concentric pieces of tygon tubing pushed together, then hand-carved to fit the weld shape. Figure 2 shows the weld sniffer head design.

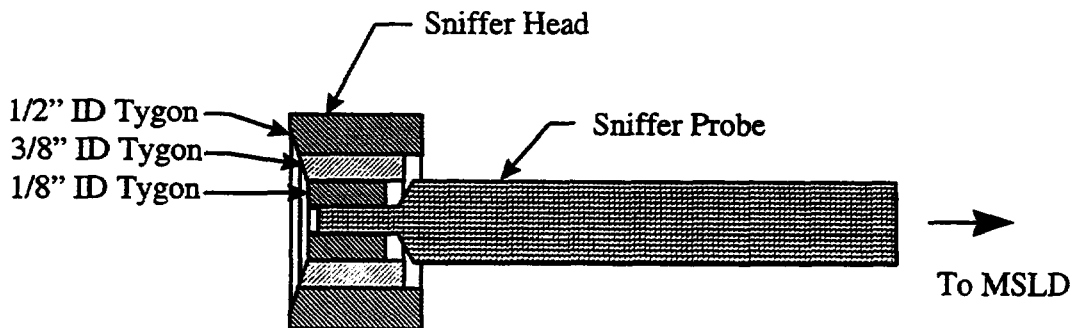


Figure 2:  $\frac{1}{2}$ " Weld Sniffer Head

The mass spectrometer leak detector (MSLD) used for the test was a direct flow turbo-pumped portable leak detector. The sniffer probe was a throttle valve type connected to the MSLD with 1/2" I.D. rubber hoses of either 6' or 20' length.

The test conduct consisted of passing the sniffer probe over a 9.7E-5 accs helium leak (connected to the weld plate) at varying speeds and recording the MSLD background and then the maximum MSLD output. First the probe was held over the leak, then it was moved at speeds of 1-5 feet/minute. The probe heads contacted the weld as they were moved across, which held the distance from the probe tip to the weld to 1/8" by the sniffer head design.

A bare probe (without the sniffer head) was also tested at speeds of 0, 2, and 5 feet/minute. The probe was held 1/8" from the surface of the weld. Test results are summarized in Figure 3.

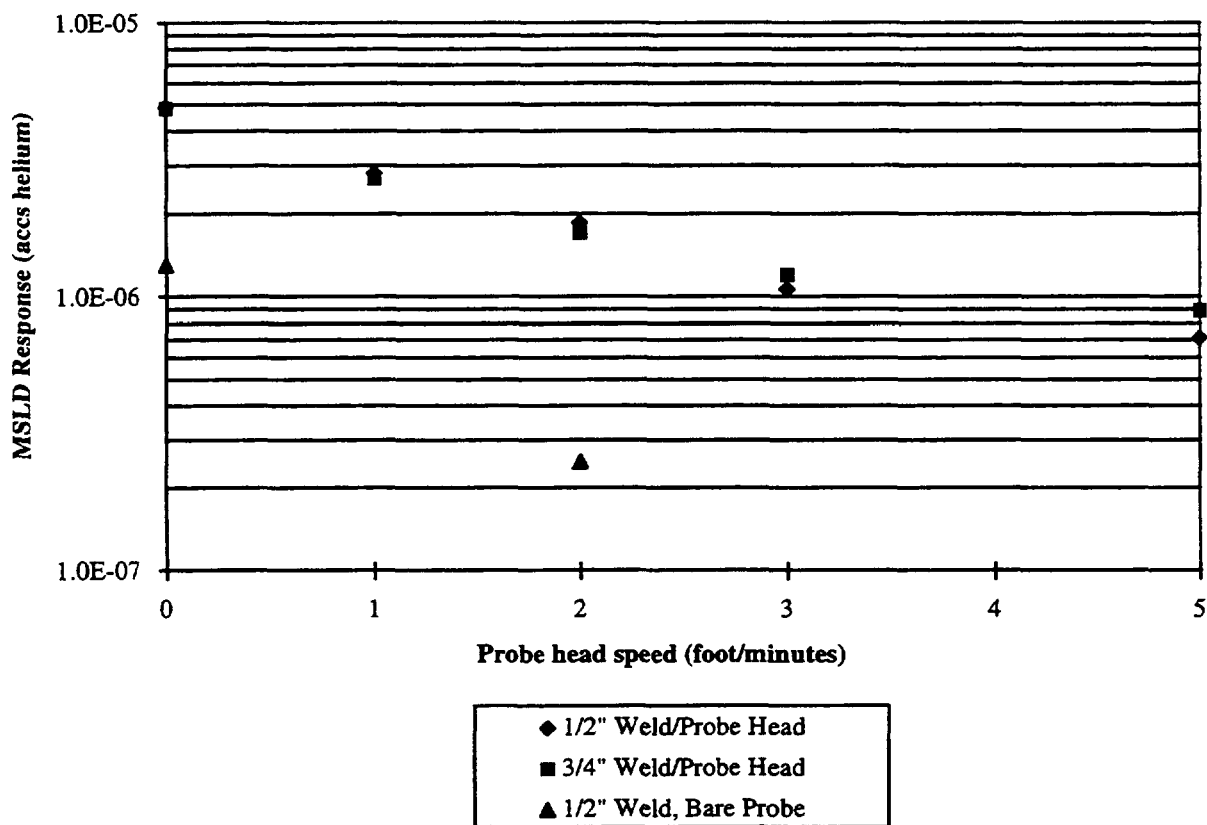


Figure 3: Weld Sniffer Developmental Test Results

Test data points are the MSLD output minus the background and are the average value of three passes of the sniffer probe. As expected, the MSLD output with the probe head was higher than with the bare probe. There was no MSLD response from the bare probe at a speed of 5 feet/minute. The response time was about 3 seconds in all cases. The test demonstrated that the test sensitivity and the probe head design were adequate to meet the ISS weld leak rate requirement.

## MODULE SKIN DEVELOPMENTAL TESTING

For the developmental testing of the module skin leak test, the test setup was similar to the weld leak test, but the test plate was a flat plate with a  $\frac{1}{4}$ " hole in it welded to a  $\frac{1}{2}$ " tube stub. The plate was connected to a helium standard leak. 2" and 4" diameter sniffer probe heads were machined out of solid teflon stock. The probe head design is shown in Figure 4. The probe head was connected to the tip of the sniffer probe with a small piece of tygon tubing.

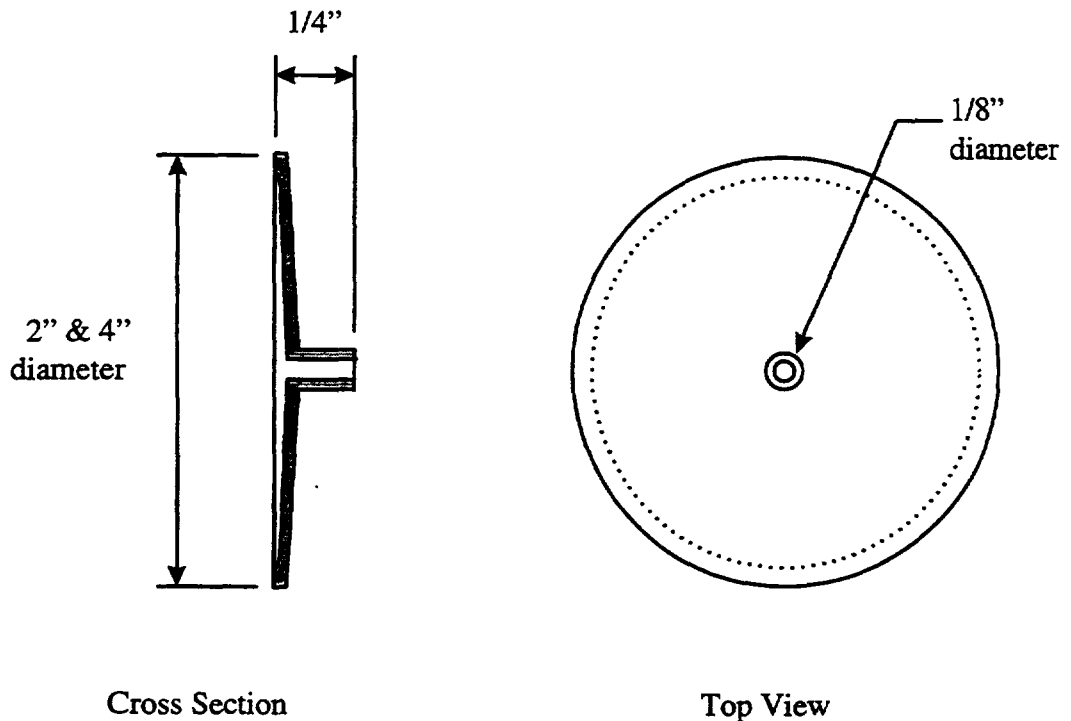


Figure 4: Module Skin Sniffer Probe Head Design

The test consisted of moving each sniffer probe head over the leak at varying speeds. Also varied was the position of the probe head over the leak. Tests were run passing the center of the probe head over the  $9.7E-5$  accs helium leak, and also passing the inside edge of the probe head over the leak. The 20' hose was used to connect the sniffer probe to the MSLD. Test results are summarized in Figure 5.

Test data points are the average value of two passes of the sniffer probe. The test data showed that the leak was detected even at the fastest speed of 20 feet/min. The response time for both the 2" and 4" probe head centered over the leak was 2 seconds. For the 2" probe head edge over the leak, the response time was 3 seconds, and it was 6 seconds for the 4" probe head edge.

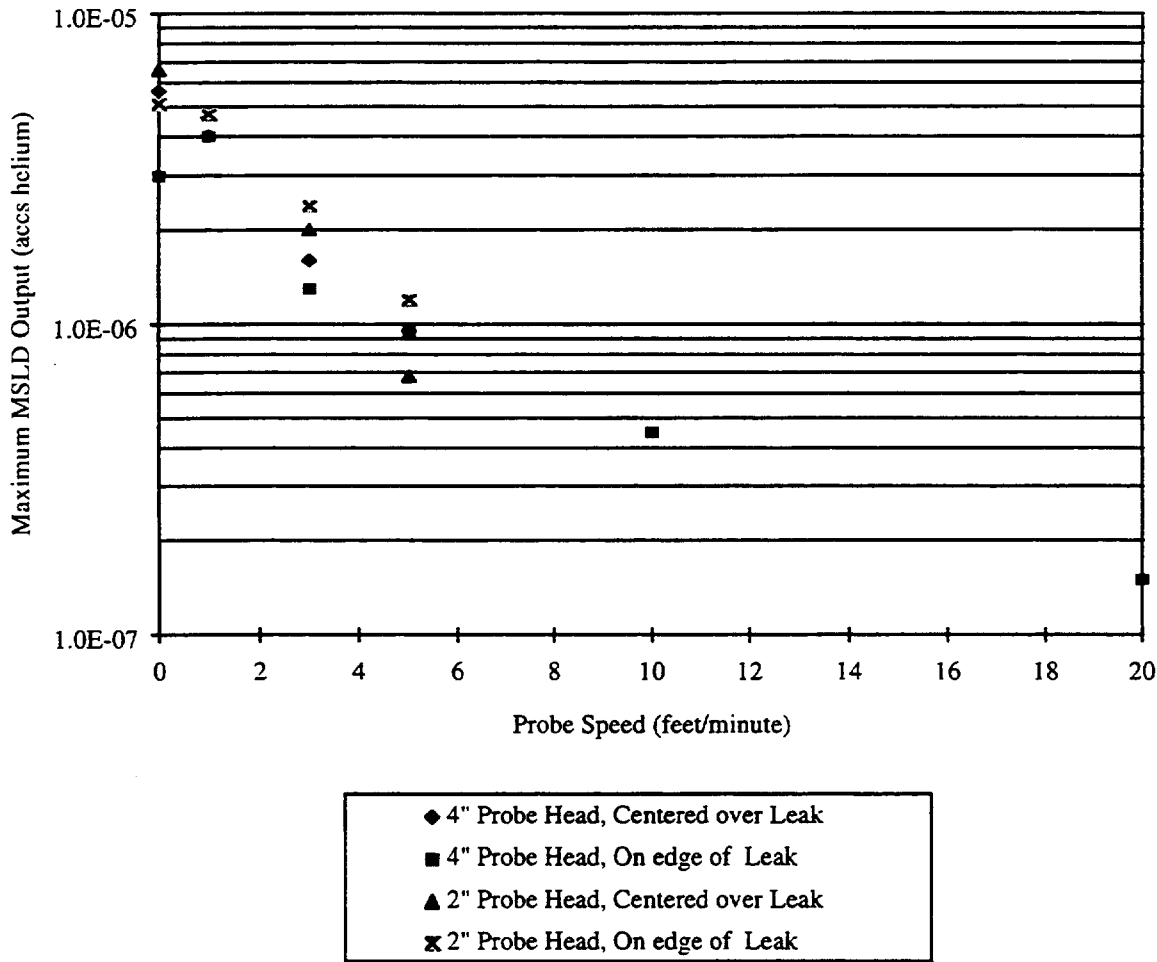


Figure 5: Module Skin Developmental Test Results

## HELIUM MIXING TEST

In order to determine how to ensure an even helium concentration during module weld/skin leak tests, a helium mixing test was performed in a module similar in shape and volume to the ISS Resource Node structure. The test was performed in February of 1996 in the Module Leak Rate Test Pressure Vessel, a 22 foot long, 14 foot diameter, and 2500 cubic foot volume module.

Two mixing fans were installed internal to the pressure vessel for mixing helium after it was introduced. The fans were mounted at the extreme top and bottom on opposite ends of the vessel. Oxygen sensors were positioned at different levels within the vessel to evaluate the mixing method. Helium concentrations were determined by measuring the oxygen concentration as it was displaced. (The test setup is shown in Figure 6.)

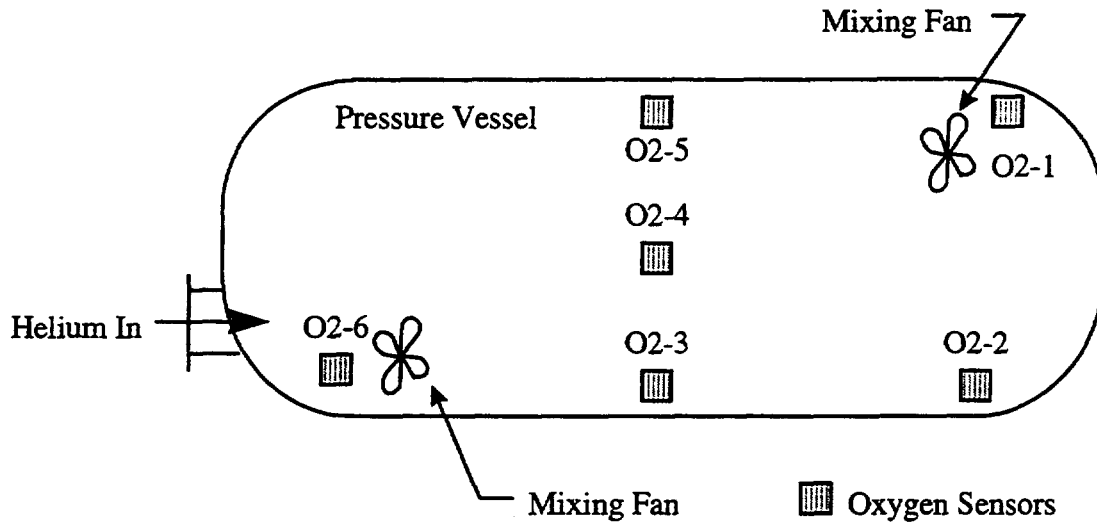


Figure 6: Helium Mixing Test Setup

Before helium was introduced into the pressure vessel, the oxygen sensors all read 20.9 % volume. The theoretical oxygen concentration was 20.99 % volume. With the mixing fans off, the vessel was pressurized to 14.7 psig with 100% helium. The sensors measured accurately only at their calibration pressure (ambient pressure), so the module was vented to 0 psig before measuring the oxygen concentrations. The theoretical oxygen concentration was 10.8 % volume, and the oxygen sensor readings were as follows:

O2-1 10.5 % Volume  
 O2-2 10.0 % Volume  
 O2-3 10.0 % Volume  
 O2-4 10.5 % Volume  
 O2-5 10.5 % Volume  
 O2-6 10.6 % Volume

The mixing fans were powered on for 10 minutes, and the sensor readings remained unchanged. With the mixing fans off, the module was again pressurized to 14.7 psig with helium, and then vented to 0 psig. Oxygen monitor readings were as follows:

O2-1 5.25 % Volume  
 O2-2 5.0 % Volume  
 O2-3 5.0 % Volume  
 O2-4 5.0 % Volume  
 O2-5 5.25 % Volume  
 O2-6 5.0 % Volume

The theoretical oxygen concentration is 5.25 % Volume. The module was left at this concentration without the mixing fans for 15 hours, and the oxygen concentration remained unchanged. The decision was made to eliminate the mixing fans for the flight module leak tests, but to use the oxygen monitors to verify the helium concentration during testing.

## **FLIGHT ARTICLE MODULE WELD/SKIN LEAK TESTING**

Following the development testing, the decision was made to forego the leak testing of the module skin, as the possibility of leaks through the skin's parent material was determined to be minimal. A total module-level leak test was later added to the program which would detect leakage through the module skin.

The module weld leak tests were performed on the Resource Node 1, US Laboratory Module, and Airlock Module in 1996 and 1997. The sniffer probe heads evaluated in the developmental test were used. For the flight article tests, the welds were marked and identified (with tape) in 1 foot increments, and the modules were pressurized to 12-14.7 psig for a 87% helium concentration.

Portable counter-flow Leybold UL200 MSLDs were used in conjunction with Quicktest 100 diaphragm pumps which enabled the use of 75 foot sniffer hoses. The response time, even with the long hoses, was 1-2 seconds. The weld test plates were used, fitted with certified helium standard sniffer leaks that provided leak rates slightly less than  $1E-4$  sccs helium. The sniffer probes were "calibrated" by passing the probe head over the leak and recording the background, maximum MSLD reading, and response time. Calibration of the sniffer probe was performed prior to start of sniffing, a minimum of every hour thereafter, whenever sniffer probe operators were changed, and before shutting down the test.

The linear probe head speed used for the module weld tests was 1 foot/minute. This speed was slower than the developmental test indicated was required, but was chosen because of the high dependence of the manual operation of the sniffer probe. The speed was measured with a stop watch for the calibration and for every foot of weld tested, to ensure that operators maintained the required sniffer probe sensitivity throughout the tests.

Prior to the start of the weld sniffing, a "gross test" was performed to sniff module hatches, penetrations, and pressurization line joints to ensure that leaks from the test setup did not interfere with weld testing. Because all such leaks were not easily reparable, some were bagged with plastic to lower the helium background in the area. It was still necessary in some areas of the modules to use air while sniffing to purge helium away from the welds being tested.

## **SUMMARY AND CONCLUSION**

The tests performed demonstrated the advantage of sniffer probe heads over a bare probe. The probe heads increased test sensitivity and reduced test time. The sniffer probe calibration test plates developed ensured a continued uniformity of sniffing technique throughout testing. Adequate helium mixing was obtained in the modules without the use of fans. The developmental tests resulted in the acceptance of over a thousand feet of International Space Station structural welds.



A NEW THERMAL VACUUM FACILITY  
FOR HUGHES SPACE AND COMMUNICATIONS AT EL SEGUNDO, CALIFORNIA

Robert N. Watson  
Pitt-Des Moines Incorporated

Gregory F. Proulx  
Hughes Space and Communications

**ABSTRACT**

A new thermal vacuum test facility has been recently completed at the Hughes Space and Communications Company in El Segundo, California. The facility was designed, fabricated, installed and tested as a turn-key project by Pitt-Des Moines Inc. The chamber has a 12.19 meters by 14.48 meters (40 feet by 47 feet, 6 inches) flat floor and a half-cylindrical roof with a diameter of 12.19 meters (40 feet). One end of the chamber has a full cross section door, equipped with a translating motor for horizontal motion. The chamber is provided with six 1.89 meters (48 inches) cryopumps to obtain an ultimate pressure of  $3 \times 10^{-7}$  Torr (Clean-Dry-Empty). The thermal shroud is designed to operate at a maximum of  $-179\text{ }^{\circ}\text{C}$  ( $-290\text{ }^{\circ}\text{F}$ ) with an internal heat input of 300 kW using liquid nitrogen. The shroud is also designed to operate at any temperature between  $-156\text{ }^{\circ}\text{C}$  ( $-250\text{ }^{\circ}\text{F}$ ) and  $121\text{ }^{\circ}\text{C}$  ( $+250\text{ }^{\circ}\text{F}$ ) using gaseous nitrogen, and heat or cool at a rate of  $1.1\text{ }^{\circ}\text{C}$  ( $2\text{ }^{\circ}\text{F}$ ) per minute. A removable internal liquid nitrogen panel allows the test envelope to be subdivided to support test of two items simultaneously.

**INTRODUCTION**

In January of 1998, Pitt-Des Moines Inc. completed work on a new thermal vacuum test facility for Hughes Space and Communications Company. The vacuum chamber and associated equipment were installed in a new addition to an existing building at Hughes' El Segundo, California facility. The chamber was designed as a general purpose facility for thermal vacuum testing of satellites and complements existing capabilities at the Integrated Satellite Factory. The new chamber has a dedicated bulk  $\text{LN}_2$  storage and is functionally independent of the other chambers. The chamber and support equipment are operated from either a local control room in a mezzanine adjacent to the chamber, or a from a centralized multi-chamber control room in another part of the building.

The facility consists of the chamber and four support systems: vacuum system, thermal system, control system and utility system. The chamber incorporates the vacuum boundary elements, including penetrations and doors, the personnel and equipment access bridges, and the internal rails and hardpoints for mounting test articles and support equipment. The vacuum system comprises the external equipment required to evacuate the chamber, repressurize it and purge it for personnel entry.

The thermal system includes the internal shroud and LN<sub>2</sub> and GN<sub>2</sub> equipment necessary for establishing the desired thermal environment in the chamber. The control system includes the logic controller subsystem and the control and data acquisition subsystem. Utility systems include LN<sub>2</sub> and GN<sub>2</sub> distribution subsystems, primary and backup power distribution subsystems, cooling water distribution subsystems, and the instrument air distribution subsystem. This paper will provide an overview of each of these systems, including the operational features and performance requirements.

## **CHAMBER SYSTEM**

### **Chamber**

The vacuum chamber for the facility [Figure 1] is in the shape of a mailbox, with a flat operating floor, vertical side walls and a cylindrical roof. The test envelope floor is 10.67 meters (35 feet) wide by 13.72 meters (45 feet) long and is flush with the elevation of the surrounding laboratory floor. To match these floor elevations, the chamber is mounted on concrete pedestals in a pit formed into the foundation for the building addition. The chamber is rigidly attached to the pedestals and the foundation structure. The test envelope is 12.19 meters (40 feet) high at the centerline and 6.86 meters (22 feet, 6 inches) high at the junction with the side walls. The actual size of the vacuum envelope is 12.19 meters (40 feet) wide, 14.48 meters (47 feet 6 inches) long and 13.72 meters (45 feet) high, which permits a 0.76 meters (2 feet, 6 inches) space between the shroud and the chamber wall for maintenance.

The chamber shape provides several operational and construction advantages. The flat floor minimizes wasted internal volume and allows simpler chamber and internal shroud supports. It also minimizes the distance between the test article and external support equipment. The flat vertical side walls also simplify penetrations of the chamber walls.

### **Main Door**

Access to the chamber is provided through an o-ring sealed door on the west end of the chamber. The PDM FLEX-SEAL door flange system was used to accommodate the size of the door and its square lower corners without costly field machining. The door is motorized and mounted on a rail system that permits it to translate outward (west) and then south. The door system consists of three motor-driven screw jacks that provide east-west door motion and a motor-driven rail drive to move the door in the north-south direction. Limit switches on the system provide door position information to the facility programmable logic controller (PLC), which automatically sequences the door motion. The PLC also provides interlocks with the oxygen sensing system to prevent door opening if a safe oxygen atmosphere is not present. When fully open, the main door provides complete access to the full cross section of the chamber. The door system is also equipped with an actuated seismic restraint, which secures the door in the full open position.

### **Personnel Doors**

To permit convenient personnel access without opening the 105-ton main door, the chamber has two personnel doors. The doors are located in the northwest and southeast walls of the chamber at the elevation of the main laboratory floor. The latch systems for each are equipped with a key system to prevent opening of either personnel door if an unsafe environment exists inside and to prevent

initiation of chamber vacuum pumps with personnel inside. The shroud system also has internal doors, which are aligned with the chamber doors, to permit entry into the test envelope.

### **Access Bridge**

A bridge [Figure 2] is provided to span the main door handling trench and provide access for test article carts to the chamber test envelope. The bridge is raised and lowered by a hydraulic system connected to a local panel. This panel allows operation of both the bridge system and the main chamber door. Limit switches on the system provide information to the PLC to automatically sequence operation of the bridge and to coordinate it with the movements and position of the main door. The surface of the bridge has four rails for test article carts, which align with rails outside and inside the chamber.

### **Internal Rails**

Four full length internal rails [Figure 3] are provided along the length of the internal shroud floor for support of test articles. The rails consist of two flat plates and two inverted angles and are aligned with those on the bridge and the external laboratory floor. They are supported independently from the shroud floor with structural members connected to the bottom chamber. Each pair of rails is designed to support a 89.1 kN (20,000 pound) load distributed on four wheels.

### **Internal Monorail**

To provide additional capability to handle test equipment inside, the chamber is equipped with a 17.8 kN (4,000 pound) capacity overhead monorail [Figure 4], which runs the full length of the chamber ceiling. A manually operated chain drive hoist runs along the monorail and is stored outside the chamber during tests. A removable rail extension is mounted outside the main door opening to permit moving loads from outside to inside the chamber. Because the monorail is thermally isolated from the chamber wall and the shroud system, it is equipped with a heater system to warm it to ambient temperature at the conclusion of a test.

### **Internal Hardpoints**

Twenty-one hardpoints each with an access port through the shroud plane provide lifting points for internal rigging. Each hardpoint is designed to support a 13.4 kN (3,000 pound) load and provides a flat 203 mm by 203 mm (8 inch by 8 inch) plate with four mounting holes.

### **Penetrations**

The chamber is provided with more than 139 penetrations, located primarily on the north, south and east ends of the chamber [Figure 5]. Those on the north wall and in the roof of the south wall support the instrumentation, power and control of the test article, and range from 305 mm (12 inches) to 38 mm (1.5 inches). The balance of the penetrations are related to systems required for chamber and shroud system operation. The largest of these is 1321 mm (52 inches) in diameter for each of the six cryopumps.

## VACUUM SYSTEM

The vacuum system provides the equipment to evacuate the chamber to the following design conditions:

- $3.0 \times 10^{-7}$  Torr with the chamber clean, dry and empty
- $5.0 \times 10^{-6}$  Torr with the shrouds operating at 394 K (250 °F)
- $5.0 \times 10^{-6}$  Torr with a passive gas N<sub>2</sub> load of 0.5 Torr-liter/sec

It also includes the systems to return the chamber to a safe condition for personnel entry at atmospheric pressure.

### Rough Vacuum Pumping

The roughing segment of this system utilizes two three-stage roughing skids that each provide 50% of the required pumping capacity. Each system consists of two roots-type blowers backed by a mechanical pump. The skids are mounted in a mechanical equipment room south of the chamber. The line connecting the chamber to the skids contains a liquid nitrogen-cooled trap to prevent oil migration from the pumps into the chamber. A high vacuum gate valve is installed at the chamber penetration for isolation of the rough vacuum system during high vacuum pumping of the chamber. A warm gaseous nitrogen inlet line can introduce gas into the roughing line at the trap to assist in the warming of the trap after use.

### High Vacuum Pumping

The high vacuum pumping system consists of cryopumps, turbomolecular pumps and a water vapor pumping panel.

#### *Cryopumps*

The high vacuum pumping system is equipped with six 1219 mm (48 inch) cryopumps, each with a high vacuum gate isolation valve. The cryopumps are mounted on the flat south face of the chamber near the midheight of the chamber. The chamber shroud in the area of the cryopumps is a chevron-type extrusion, which provided good conductance to the test volume. Connected to the cryopumps are the following support systems:

- liquid nitrogen supply to the internal shield
- roughing line
- high pressure helium lines to the expander
- heated gaseous nitrogen supply for regeneration
- ambient nitrogen supply for removal of liquid nitrogen from the internal shield
- instrument connections for monitoring shroud and cold head temperatures

The liquid nitrogen supply for the internal shield is drawn from a high pressure central supply tank at 1.05 MPa (150 psi) outside of the building. Liquid is subcooled prior to supply to the cryopumps by passing it through a heat exchanger in an ambient pressure subcooler tank used for the thermal shroud system. Liquid level control is performed by a temperature control valve on the inlet side of the cryopump. Boiloff gas is piped to a central vent system and vent stack outside the building. The roughing system for the cryopumps consists of a shared two stage skid with a roots-type blower and a mechanical backing pump. The skid is mounted in the mechanical room and piped to each

cryopump mounted on the chamber. High pressure helium gas for the cryopump expanders is supplied by flex hoses from the compressors mounted on a platform adjacent to the cryopumps. Regeneration system gaseous nitrogen is piped from the building supply system through an in-line heater and into the cryopumps.

To warm-up a cryopump for regeneration or shutdown, ambient temperature gaseous nitrogen is supplied to the inlet side of the internal shield system. By adding of nitrogen at this point, all liquid nitrogen in the shield is forced out into the central vent system.

#### *Turbomolecular Pumps*

Also included in the system are two turbomolecular pumps, each rated for 1500 liter/second capacity. Both pumps have a refrigerated cold trap and high vacuum gate isolation valve between them and the chamber. Each is backed by a mechanical pump mounted on a platform a short distance from the pump. The pumps are vertical axis downflow machines mounted on chamber penetrations on either end of the array of cryopumps.

#### *Water Vapor Panel*

To pump water vapor without imposing a load on the cryopumps, an internal LN<sub>2</sub> cooled panel is provided near the location of the cryopumps. The panel is mounted on moveable supports to permit it to be cleaned. It also has a drip pan to catch contaminants after it is warmed up following a test.

### **Repressurization System**

The repressurization system permits the chamber to be returned to atmospheric pressure using gaseous nitrogen or laboratory room air. Using nitrogen, the rate can be varied from 1 Torr per minute to 25 Torr per minute. The system provides a connection between the vacuum chamber and the building gaseous nitrogen distribution system or between the vacuum chamber and the room air. The nitrogen and room air piping combine into a common inlet pipe leading into the chamber. The system elements include a flow control valve and an in-line filter on the nitrogen branch, a HEPA filter in the room air leg, and valving to permit selection of media and isolation during chamber high-vacuum operation. The facility PLC system provides interlocks to prevent actuation of the system when the cryopumps are in operation, or other times when actuation will jeopardize a test in progress.

### **Purge System**

The chamber purge system is designed to remove the gaseous nitrogen used for repressurization and replace it with room air with a safe oxygen level. It consists of a low pressure blower, which draws room air through the chamber and exhausts to a vent outside the building. High vacuum gate valves permit isolation of the purge ducting from the chamber during high-vacuum operation. A HEPA filter, which is shared with the air branch of the repressurization system, removes unwanted particulates from the purge flow entering the chamber.

The chamber oxygen monitoring system consists of three separate analyzers independently drawing samples from the chamber test envelope and from the area behind the shroud surfaces. High vacuum valves on each loop provide isolation of the systems from the chamber during a test. Interlocks in the PLC system prevent opening of the main or personnel doors if unsafe oxygen levels are present inside the chamber.

## THERMAL SYSTEMS

The thermal environment of the chamber can be established at any steady state temperature from 94 K (-290 °F) to 394 K (250 °F) using the internal shroud panels and either LN<sub>2</sub> or GN<sub>2</sub> flows. Controlled temperature ramps can also be accommodated using GN<sub>2</sub> at rates up to 1.1 K/sec (2 °F/sec). The system is designed to absorb internal distributed heat loads of up to 300 kW when in the LN<sub>2</sub> mode and 50 kW when in the GN<sub>2</sub> mode.

The overall system flow [Figure 6] illustrates the two modes of operation. In the steady-state LN<sub>2</sub> mode, subcooled<sup>1</sup> liquid nitrogen is circulated through the 10 shroud zones using a parallel flow arrangement. Each of the zones is equipped with outlet control valves on the LN<sub>2</sub> branch to permit automatic flow control using the facility PLC system. In the GN<sub>2</sub> mode, conditioned gaseous nitrogen from six dense gas generator skids is circulated through the zones. Flow and temperature control is achieved by varying the output from the gas generator skids, also under PLC control. The main elements of this system are discussed further below.

### Thermal Shroud

The shroud system consists of zone subassemblies fabricated from aluminum extrusions, which have integral flow passages. High conductance extrusions are used in the area of the high vacuum pumping systems. Lower conductance extrusions are used in the balance of the system. The zone subassemblies are mounted on supports anchored to the chamber walls which permit the required thermal movements during cooling and heating. The zone attached to the chamber main door is designed to move with the door during actuation. The floor zones are supported from the chamber floor and have sufficient strength to permit loads from personnel and equipment. The shrouds are mounted a distance of 0.76 meters from the inside surface of the chamber walls to permit personnel access behind the shrouds for cleaning and maintenance activities.

An additional removable shroud panel is provided to permit dividing the chamber volume into two east and west test areas for two simultaneous test articles. This shroud is designed to be supplied with LN<sub>2</sub> only.

The main shroud system [Figure 7] is divided into 10 physical zones. Each zone is independently controllable when in the LN<sub>2</sub> mode. When in the GN<sub>2</sub> mode, four of the zones are supplied in parallel with the other zones, which provides six independently controllable zones. Provisions exist for future expansion to permit 10 controllable zones when in the GN<sub>2</sub> mode.

### LN<sub>2</sub> System

Liquid nitrogen for the shrouds is provided by the LN<sub>2</sub> subcooler skids located in the mezzanine south of the chamber. The circulation skid contains two pumps for developing the required system pressure and for circulating the liquid through the shroud zones. The pumps are equipped with variable frequency drives (VFD) which permit system turn-down in periods of low heat load in the chamber, and allow the associated savings of LN<sub>2</sub> consumption. On the second skid is the subcooler vessel that contains a heat exchanger submerged in an ambient pressure saturated, LN<sub>2</sub> bath. A secondary heat exchanger is also provided in the bath to precool the LN<sub>2</sub> coming from the central LN<sub>2</sub> supply at 1.05 MPa (150 psi), and at saturation temperature, for use in the GN<sub>2</sub> dense gas generators and for makeup

---

<sup>1</sup> Liquid at temperature well below the saturation boiling point at the elevated pressure of the closed loop

to the main subcooled loop. The pumps and all actuated valves on the subcooler skids are controlled by the facility PLC system. Vacuum jacketed distribution piping is used for the closed loop between the subcooler skid and the shroud zones inside the chamber.

### **GN<sub>2</sub> Dense Gas Generators**

The GN<sub>2</sub> required for shroud conditioning is supplied by six dense gas generator skids. Each contains a cryogenic turbine circulator, an electrical heater and a LN<sub>2</sub> injection mixer. The circulator is also equipped with a variable frequency drive that permits infinite speed control. Each skid has a local PLC which controls turbine speed, loop density/pressure, LN<sub>2</sub> injection rate and electrical power to the heater. The local PLCs are digitally linked to the facility PLC system for operator control from the remote control room. Due to the direct LN<sub>2</sub> injection approach used with these skids, pressure control requires periodic venting of the loops to a centralized GN<sub>2</sub> vent system. This system passes vent GN<sub>2</sub> to a stack situated outside of the chamber building. Closed loop distribution piping of the conditioned GN<sub>2</sub> to and from the shrouds is mechanically insulated.

### **Auxiliary Internal LN<sub>2</sub> Zones**

To support miscellaneous cooling needs inside the chamber, eight LN<sub>2</sub> supply zones are provided at ports inside the chamber. Each zone is supplied by the high pressure 1.05 MPa (150 psi) LN<sub>2</sub> central system after a pressure step down to 594 KPa (85 psi). Level control is provided by an inlet-side temperature control valve. Discharge vent gasses are piped to the central GN<sub>2</sub> vent system and the stack outside the building.

### **LN<sub>2</sub> Removal System**

All LN<sub>2</sub> using equipment in the facility is provided with a GN<sub>2</sub> driven liquid removal system. The most important use of this is the liquid removal system for the shroud zones, which permits rapid switches from LN<sub>2</sub> to GN<sub>2</sub> mode. Ambient temperature GN<sub>2</sub> is injected into the shroud zone in a manner that drives liquid out of the system through low-point drains. Removed liquid is sent to a dump tank located outside the building where it boils off to the GN<sub>2</sub> vent stack. With this system, a transition from shroud LN<sub>2</sub> mode to GN<sub>2</sub> mode can be achieved in 60 minutes or less.

## **CONTROL SYSTEM**

The Thermal Vacuum Facility chamber systems are controlled and monitored by a Personal Computer (PC) based Supervisory Control and Data Acquisition System (SCADA). The SCADA system consists of Personal Computer Operator Stations or Human Machine Interfaces (HMIs), Programmable Logic Controllers (PLCs) and all the hardware and software configurations providing a complete Thermal Vacuum Facility control platform. A block diagram for the system is shown in Figure 8.

### **Programmable Logic Controller System**

The Thermal Vacuum Facility control system interlocks, sequencing, loop process control, algorithms, and field device input/output functions are performed by the PLCs. The PLC system includes hot back-up or redundant main processors, local and remote input/output racks, inter-rack communication modules, field input/output cards and a peer-to-peer PLC communication network. The field devices, solenoid valves, limit switches, thermal shroud thermocouples, motor control circuit

starters, etc., are wired and terminated in field marshaling panels containing the PLC input/output racks and cards. The field marshaling panels are all connected in parallel to the PLC input/output field bus. The Thermal Units and LN<sub>2</sub> supply system each contains PLCs and local Operator Interface Terminals (OITS). This configuration allows local operation of these subsystems and remote control by the main PLCs via the peer-to-peer communication network.

### **Supervisory Control and Data Acquisition System**

The PCs provide the interface to the process and support monitoring and control through graphic displays. The SCADA or HMI software resides at the PC level. The PCs have customized SCADA software utilizing graphic displays to effectively communicate to the operator's equipment status and process state. Three operator terminals have been installed providing system flexibility and redundancy. Two stations are located near the chamber in the first floor mezzanine electrical room; the third station resides in the overall facility Central Control Room (CCR). The CCR station is also equipped with a 40-inch monitor that displays the overall facility status. The PCs stations are configured to communicate to the PLCs via the standard Ethernet network protocol.

### **Instrumentation**

The Thermal Vacuum Facility is provided with various types of sensors for control and monitoring system performance. The primary sensors used to monitor shroud status are type "T" thermocouples. The thermocouples are strategically located on the shroud surfaces to monitor the overall shroud performance. The chamber and equipment vacuum status utilizes Convectron, (Granville-Phillips trademark), and Bayard-Alpert type ionization gauges for monitoring and control functions. The thermal and vacuum sensors are displayed and recorded by the facility SCADA system.

## **SUPPORT SYSTEMS**

### **LN<sub>2</sub> Supply**

The LN<sub>2</sub> supply is provided from four 13,000-gallon bulk storage tanks. Each tank is capable of independent pressure control to support the 45 and 150 psi LN<sub>2</sub> feeds required for chamber operation. The tanks can be configured to supply the high or low pressure feed manifolds with up to three of the four available bulk storage tanks. Each tank can be isolated from the system or reconfigured during test without affecting test operations. The system reconfiguration flexibility is designed to optimize the bulk storage reserves in support of the different usage profiles required to assure uninterrupted operation.

### **GN<sub>2</sub> Supply**

Two ambient air vaporizers that are each capable of generating 66,000 SCFH for 8 hours continuous operation provide the GN<sub>2</sub> supply. The primary purpose of the GN<sub>2</sub> supply is to handle the purge requirement during standard or emergency warm-ups of the shrouds and provide backup to the instrument air in the event of a complete power failure.

### **Power Distribution**

The power distribution system for the Thermal Vacuum Chamber is provided by a free-standing 480 VAC motor control center (MCC), a 208/120 VAC power panel and a Uninterruptable

Power Supply (UPS) system. The normal and emergency electrical loads are supplied via these systems. The electrical loads are programmed within the PLC to prevent inadvertent operation of equipment during a power outage. The SCADA system is powered by the UPS system. The UPS will provide continuous power to the control system to allow monitoring of the Thermal Vacuum Chamber during a power outage until emergency power is established.

## **CONCLUSIONS**

The new thermal vacuum facility completed by PDM has proved to be a useful and reliable addition to the Hughes El Segundo installation. The primary lessons learned from the construction of the facility include:

- The mailbox chamber shape, used by PDM on most recent vacuum chambers, continues to be convenient, space-saving arrangement for test operations.
- The large size of the chamber and the ability to subdivide it into two independent test zones will enable Hughes to accommodate new, larger size spacecraft and increase overall test productivity.
- The use of the 0.76 meters (30 inches) distance between the shroud panels and the wall of the chamber proved to be very useful in maintaining the shroud and in the routing of instrumentation cabling.
- The use of variable frequency drives (VFD) on the LN<sub>2</sub> circulation pumps have contributed to low LN<sub>2</sub> consumption during test operation.
- The digital control system with CRT-based operator interface has proved to be a flexible, cost effective and space-saving approach over large fixed control panels with conventional switches and indicator lights.

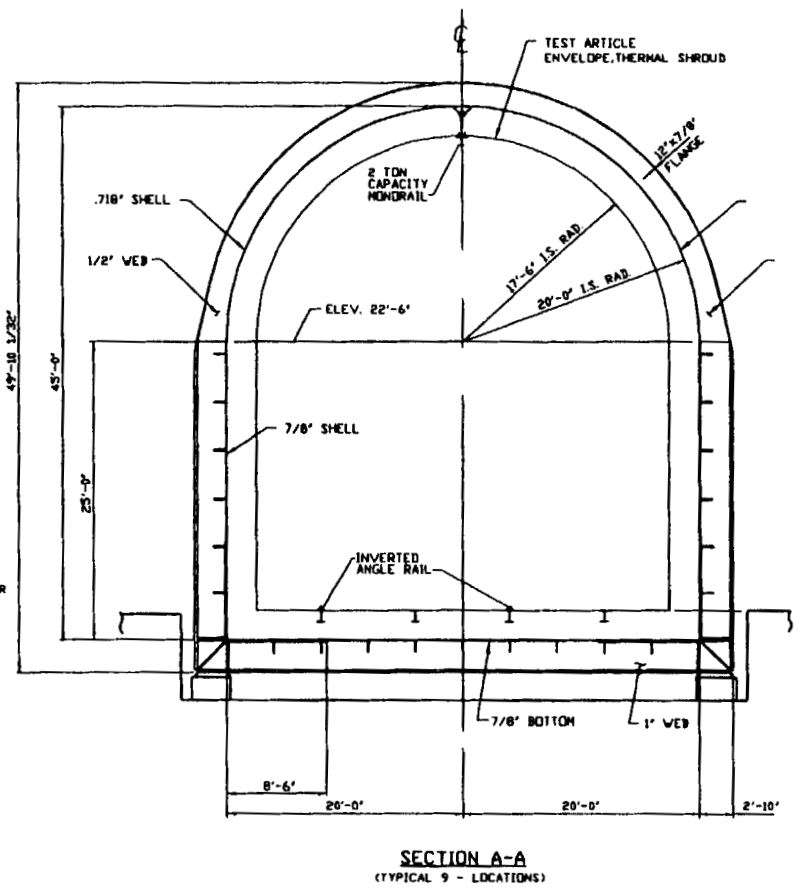
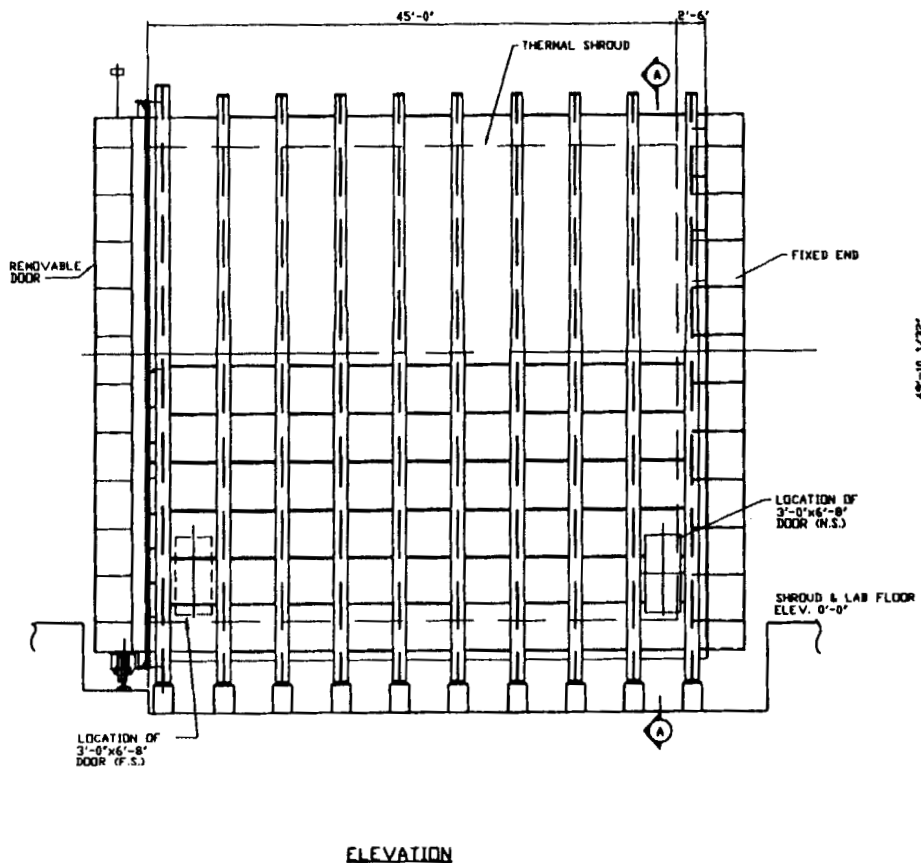


FIGURE 1: CHAMBER GENERAL ARRANGEMENT

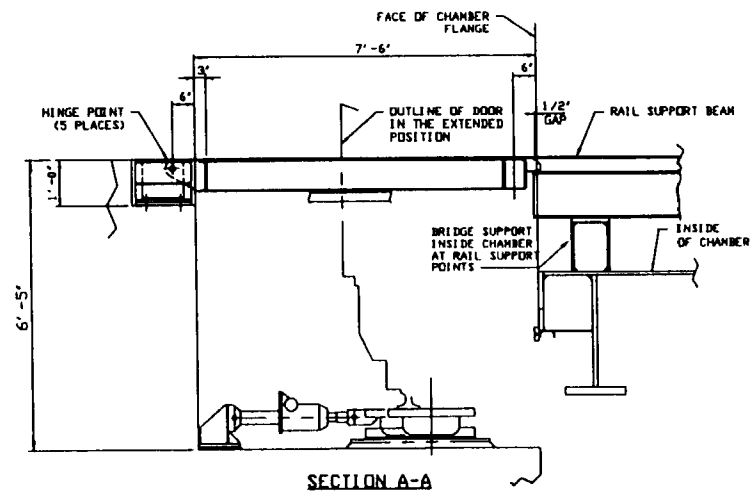
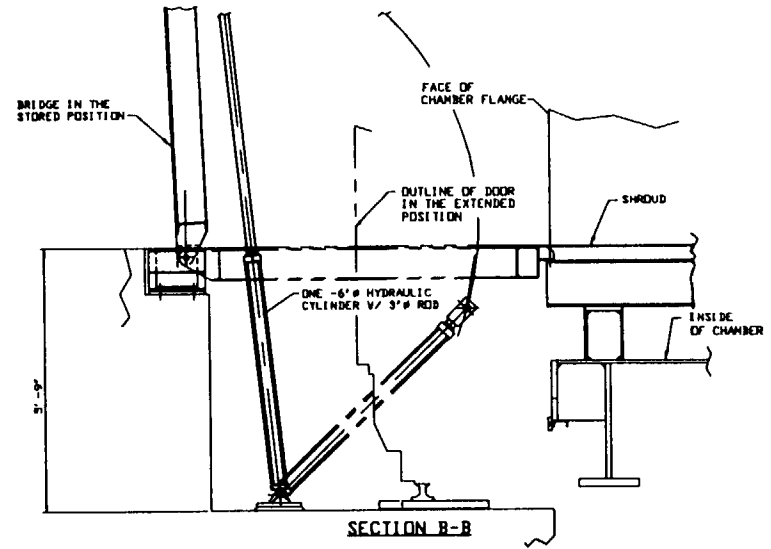
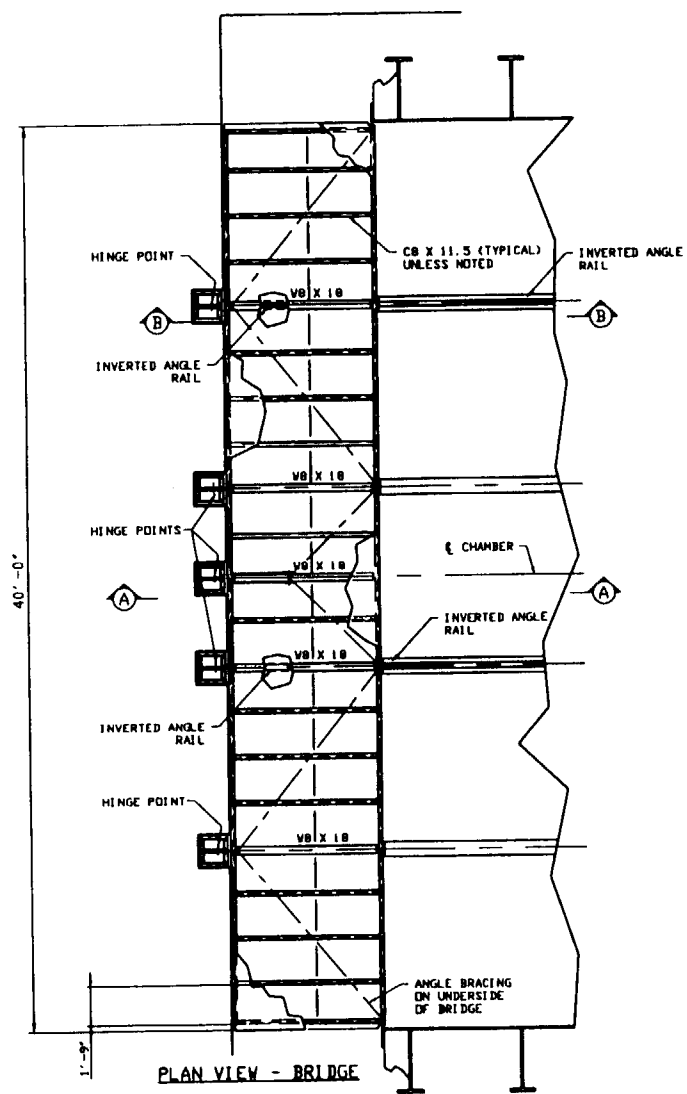


FIGURE 2: BRIDGE ARRANGEMENT

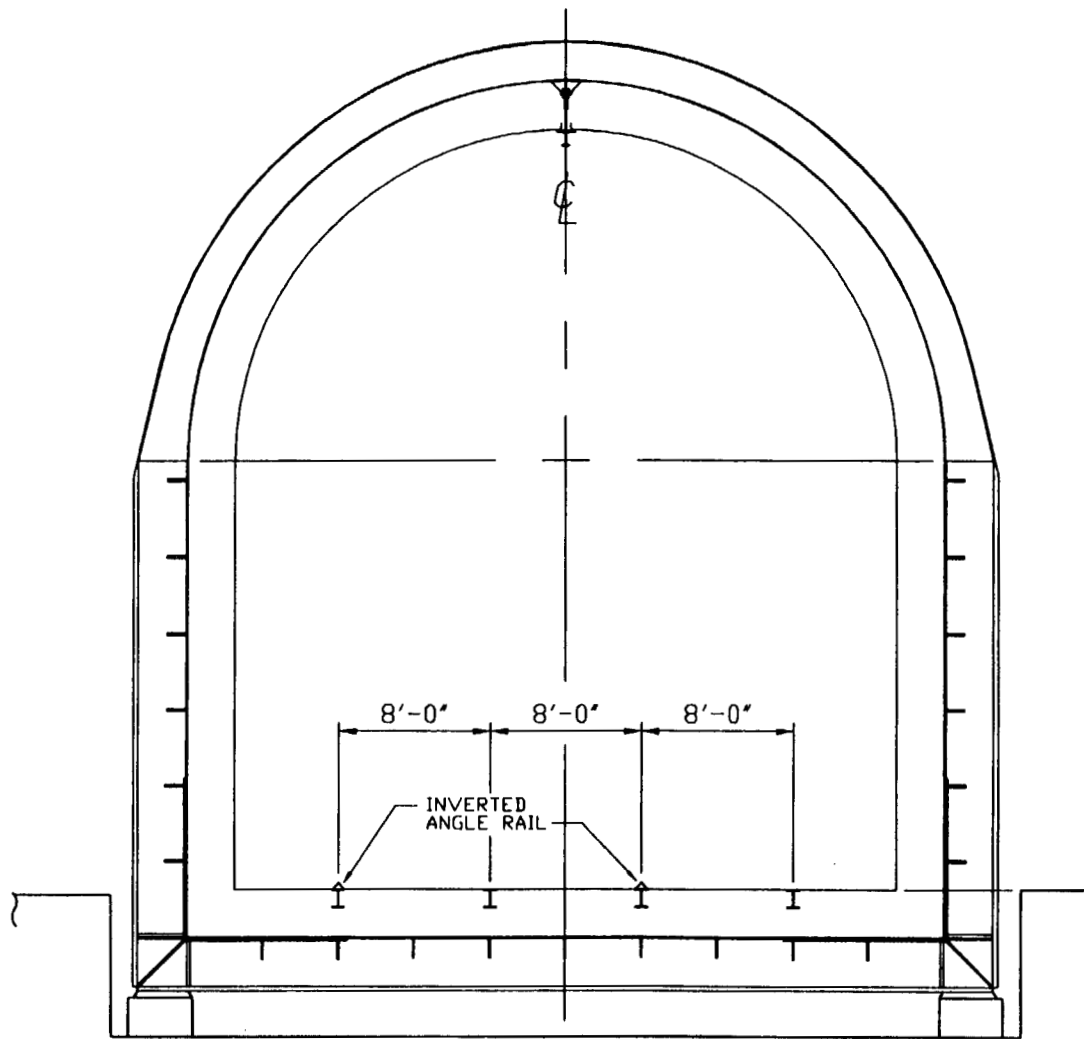
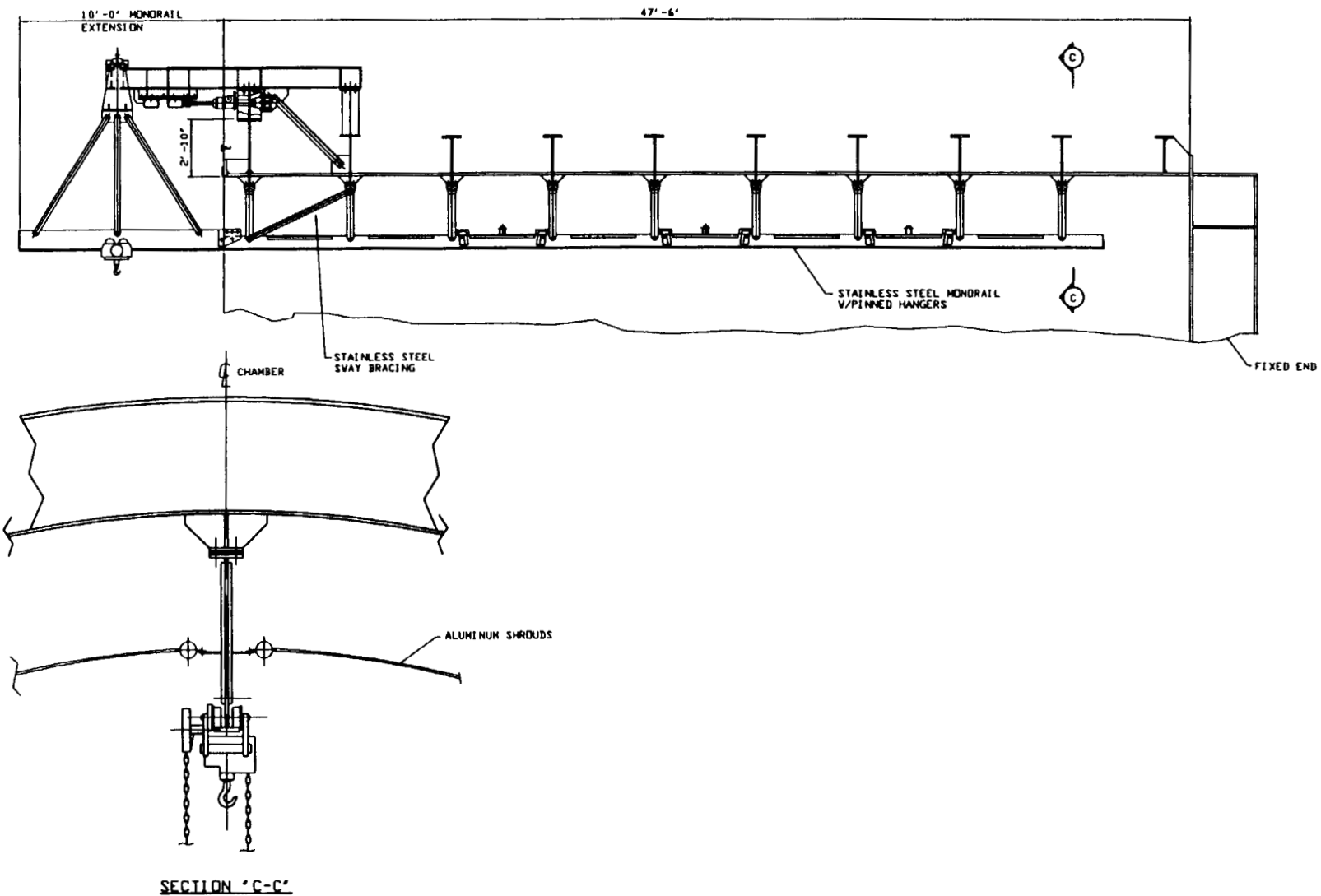


FIGURE 3: INTERNAL RAIL ARRANGEMENT



125

**FIGURE 4: INTERNAL MONORAIL ARRANGEMENT**

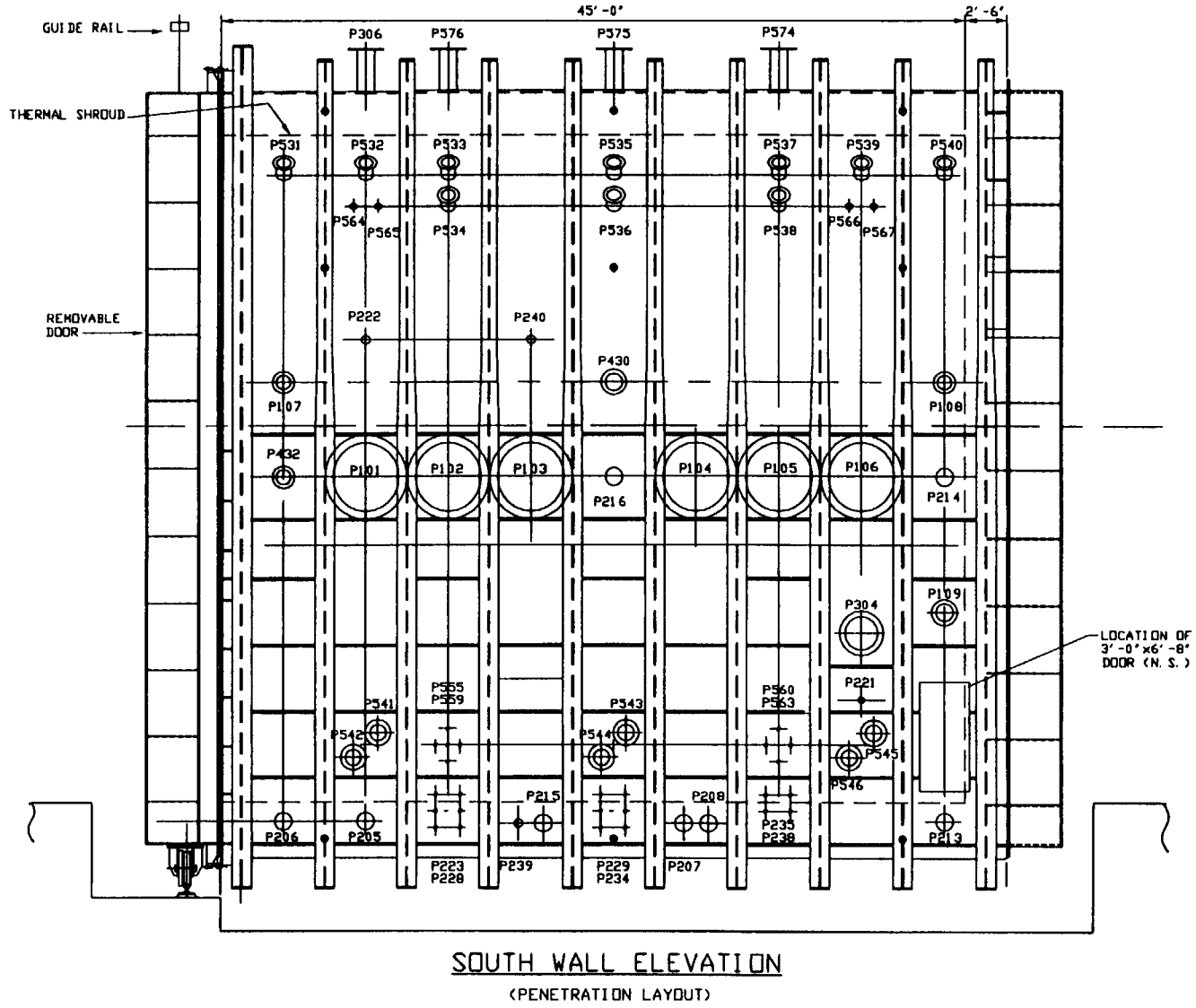


FIGURE 5: PENETRATION ARRANGEMENT



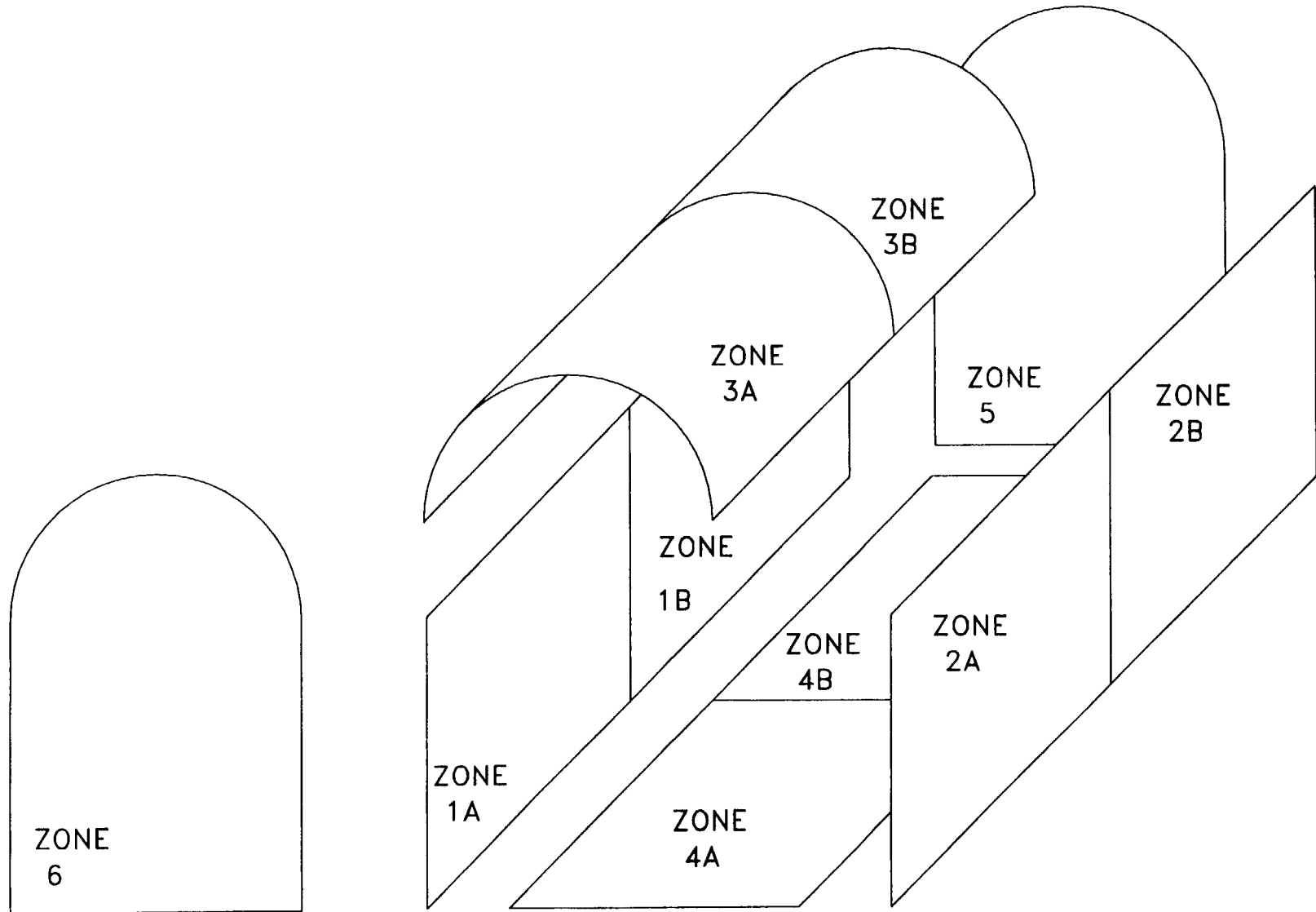


FIGURE 7: SHROUD ZONE ARRANGEMENT

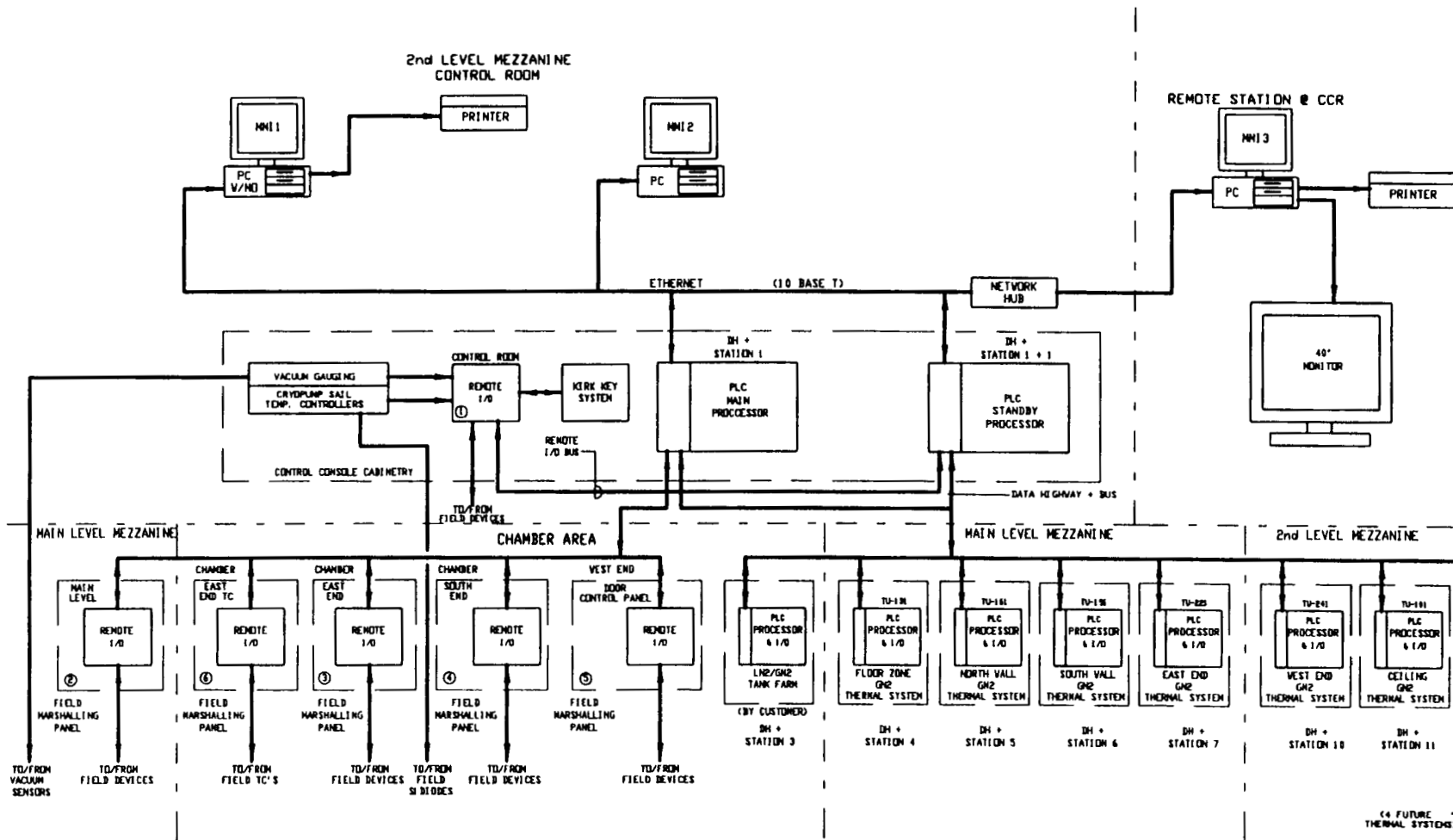


FIGURE 8: CONTROL BLOCK DIAGRAM



# LEAK RATE TESTING OF THE INTERNATIONAL SPACE STATION HATCH IN A THERMAL VACUUM ENVIRONMENT

Angela Holt, Steve Underwood  
Boeing Defense and Space Group  
International Space Station Program  
Huntsville, Alabama

## ABSTRACT

The International Space Station (ISS) Hatch successfully passed extensive leak rate qualification testing in a thermal vacuum environment. Testing was performed at Marshall Space Flight Center in the 10 foot diameter by 12 foot tall "Sunspot" vacuum chamber. As the Hatch was thermally cycled through its analytically predicted temperature extremes, leak rate tests were performed on all of the Hatch seals using helium mass spectrometer leak detectors. The test setup was designed to provide for maximum test sensitivity and simultaneous leak testing of multiple seals in order to reduce test flow times. The test was part of the Qualification program for the Hatch used on the ISS Nodes, Laboratory, Habitation, and International flight elements.

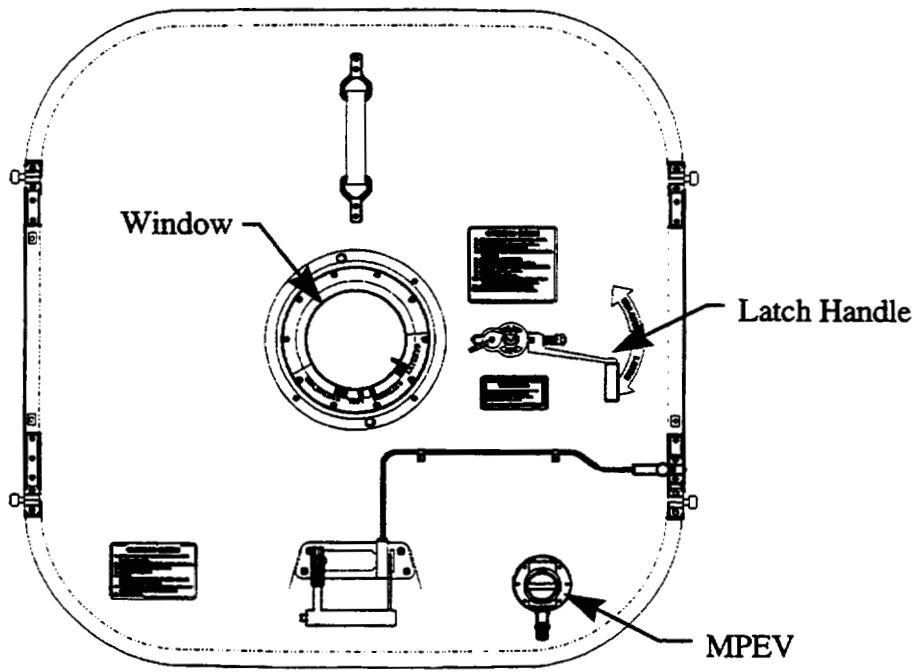
## INTRODUCTION

Due to the expected longevity of the program and the limitations on resupply gas, the ISS leak rate requirements are stringent and testing on the ground is extensive. The leak rate requirement for the entire ISS assembly is less than two pounds of air a day, and for each module is approximately one tenth of a pound of air a day. Potential leakage paths to space include feedthrough penetrations through which fluids and power pass to different areas on the station, Common Berthing Mechanisms (CBMs) that mate the various modules together, and windows that allow crew observations of external activities and space. This paper focuses on another leakage path, the hatches that provides crew access to the ISS modules.

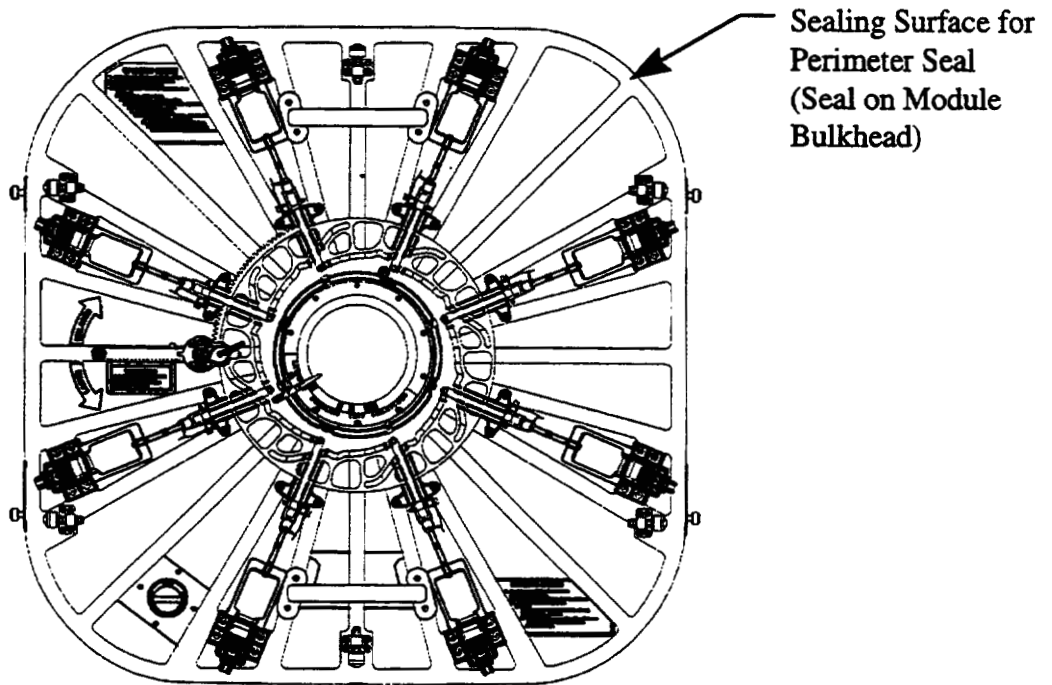
Throughout this paper, references will be made to certain sides of the Hatch assembly. The external side will sometimes be referred to as the Outboard or Extravehicular Activity (EVA) side while the internal side will sometimes be referred to as the Inboard or Intravehicular Activity (IVA) side. The EVA side is the side that will face away from the modules toward space if so exposed and the IVA side will face toward the modules.

## INTERNATIONAL SPACE STATION HATCH

ISS modules include at least one common Hatch, and the Node modules have six hatches each. When two modules are connected, the hatches between them will generally be open, however, for an unused port the Hatch is exposed to the vacuum of space. The leakage requirements for Hatch seals range from  $3E-4$  to  $1E-2$  sccs helium and are verified by testing on the ground. The aluminum Hatch seals to the module via a Perimeter Seal, a two-beaded silicone rubber molded seal with a stainless steel substrate. This seal is installed on the module bulkhead, and seals the outer perimeter of the Hatch when the Hatch is latched. (See Figure 1 for an illustration of the Hatch. Figure 2 shows cross sections of the Hatch seals.)



Hatch Internal View



Hatch External View

**Figure1: International Space Station Hatch**

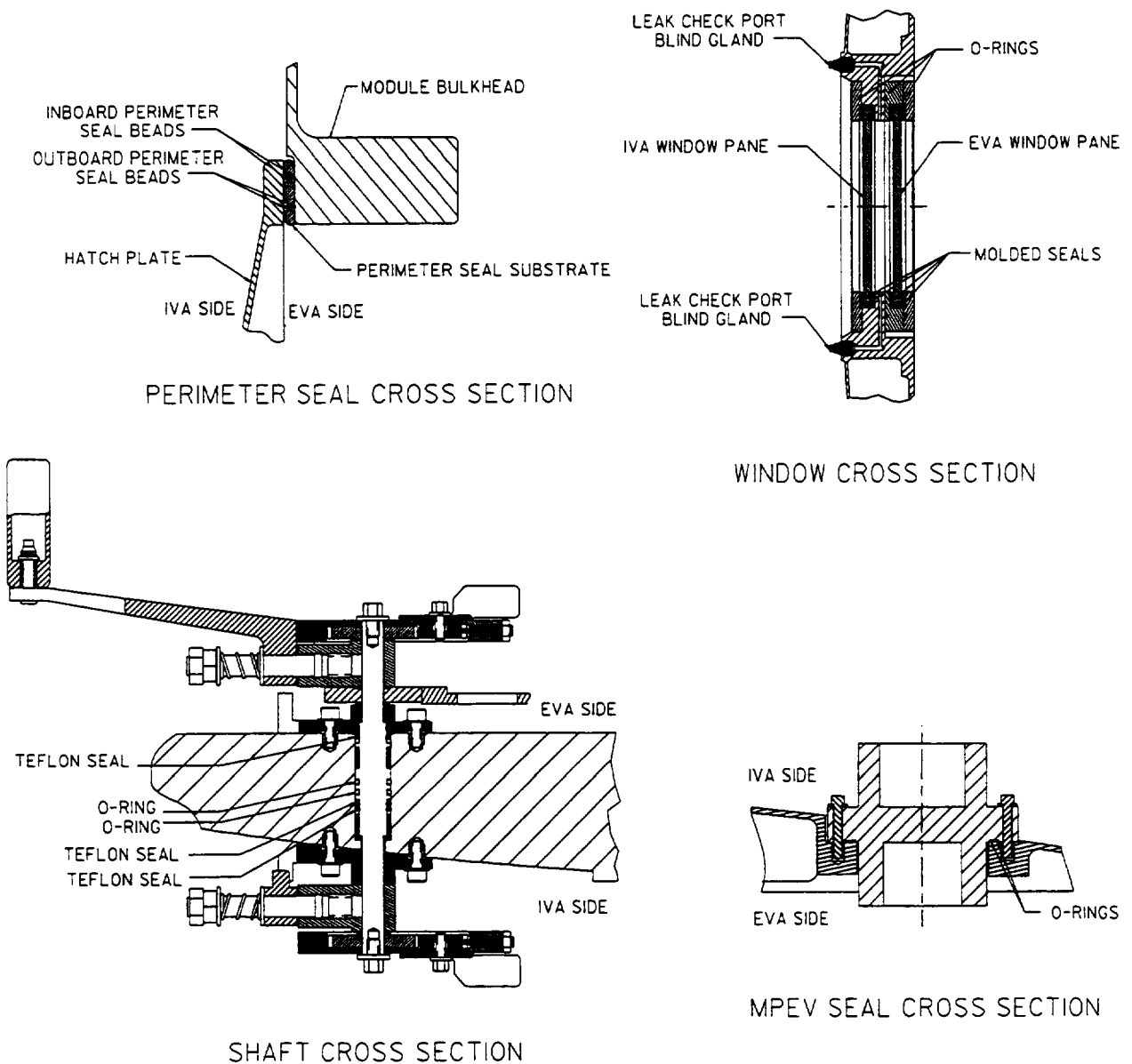


**Figure 2: Hatch Seals**

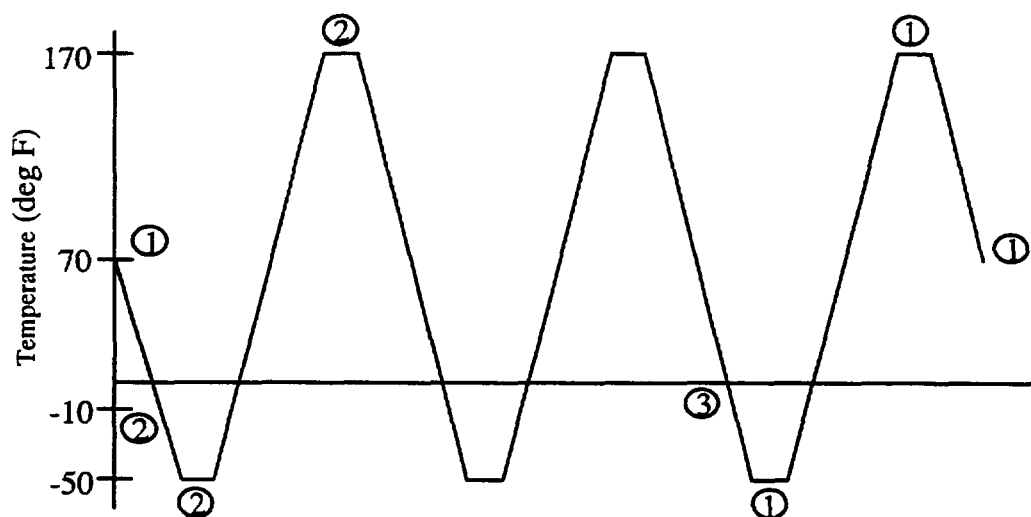
Two Leak Check Ports on the module bulkhead provide access to the volume between the two Perimeter Seal beads. These ports are located on opposite sides of the Hatch, and are used for leak testing the Perimeter Seals. The ports are plugged with "Blind Glands" during flight/orbit, and are replaced with test adapters for ground testing.

The Hatch has an eight-inch diameter double-paned window at its center. The window assemblies are sealed using silicone O-rings and one-beaded silicone rubber molded seals. The window has two Leak Check Ports located on the Window frame 180° apart. The Hatch has a Manual Pressure Equalization

Valve (MPEV), used to equalize pressure across the Hatch prior to use. The MPEV has two silicone O-rings in its flange. The Hatch Shaft runs through the Hatch plate and attaches to the handles that allow the Hatch to be opened from the IVA or EVA side. The Shaft design incorporates viton O-rings and teflon seals. (At the time of the test, the hatch shaft seal design had two O-rings and one teflon seal; the current design has two O-rings and three teflon seals.)

### THERMAL VACUUM TEST

Completion of the Thermal Vacuum test was a major milestone for the Qualification program of the ISS Hatch. The purpose of this test was to verify that the Hatch assembly maintained structural integrity and performance characteristics after exposure to the thermal vacuum environment. Hatch assembly test temperatures were defined as -10 °F to 170 °F for complete Hatch operation, and -50 °F to +170 °F for pressure containment. Leak tests were performed at ambient temperature and at the different temperature extremes throughout three thermal cycles. (Figure 3 shows the thermal cycles and leak tests.)



#### Leak Rate Tests:

- ① Complete Hatch Assembly (All Seals)
- ② Perimeter Seals Only
- ③ Shaft Seals Only

**Figure 3: Thermal Cycles and Leak Tests**

All Hatch seals were tested during the thermal vacuum testing, except for the MPEV through-valve seals and the Leak Check Port Blind Gland Seals. The Qualification MPEV was not available to support the test, so a mass-simulated blank-off plate was used in its place. The MPEV has since undergone component-level Thermal Vacuum Qualification testing as part of MPEV vendor's qualification program. The Blind Glands were also qualified in a separate test.

## DESCRIPTION OF LEAK TEST FIXTURES AND PLUMBING

The Qualification Hatch was latched to an adapter plate during the thermal vacuum testing. The adapter plate simulated the module bulkhead and retained the perimeter seal. A pressure dome provided the close-out to simulate a pressurized module. The test setup schematic is shown in Figure 4. The Hatch adapter plate provided the Leak Check Ports that allowed access to the volume between

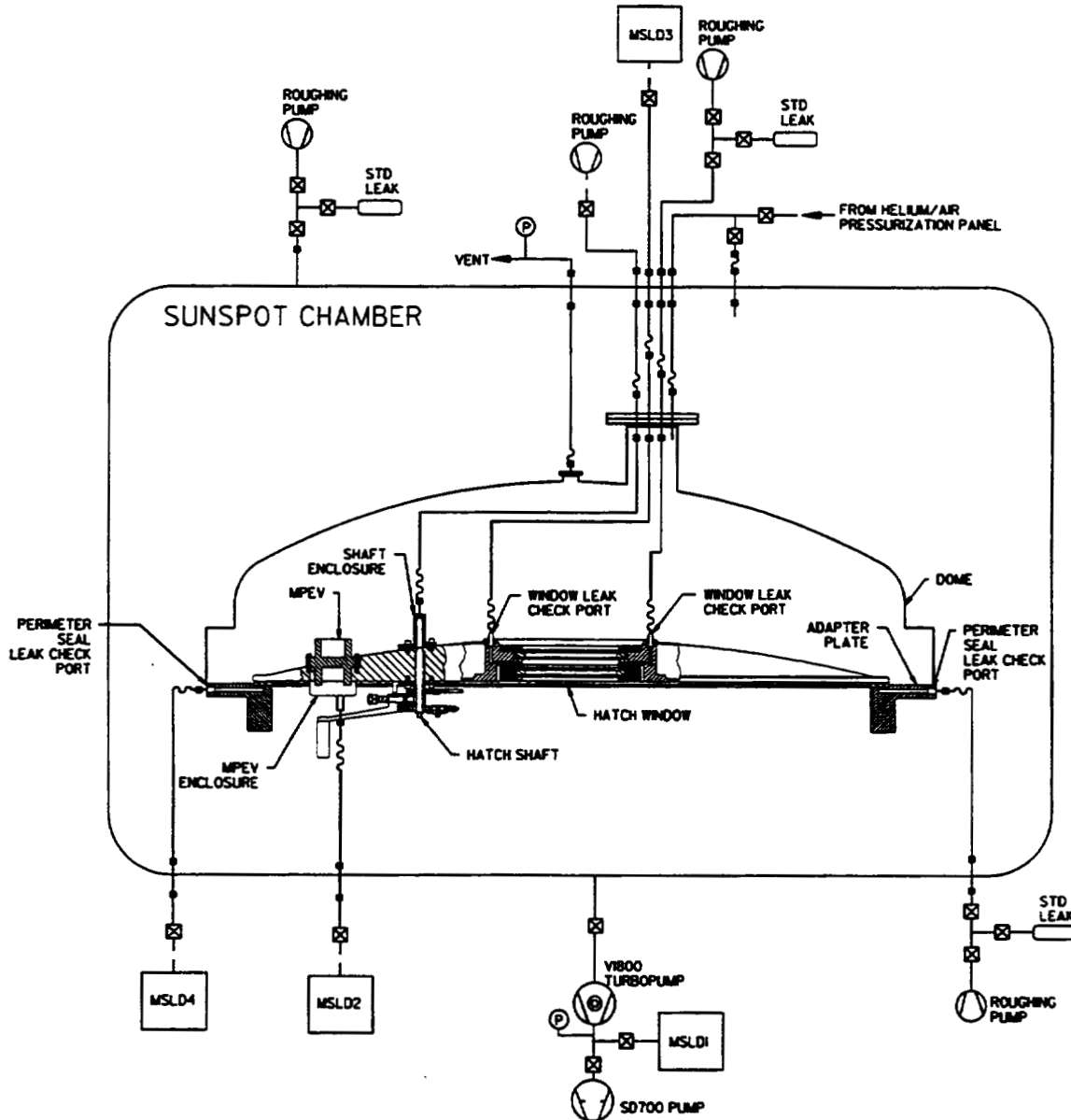


Figure 4: Hatch Thermal Vacuum Leak Test Setup

the Perimeter Seals. These ports were connected to stainless steel flex hoses and plumbed through the chamber feedthrough plate. The Leak Check Ports on the Hatch Window frame were similarly plumbed through the Hatch Dome, then through to the chamber exterior.

In order to test the Shaft seals, an enclosure was designed to fit over the Shaft on the IVA side of the Hatch. To install the enclosure for the test, the Hatch IVA handle had to be removed, but this did not impact either the Hatch operation or the Shaft sealing capability. An enclosure over the MPEV blankoff was designed to fit over the MPEV EVA side, because the EVA side has a flat surface with bolt holes that could easily accommodate the enclosure. The enclosures for the Shaft and the MPEV both sealed to the Hatch with silicone O-rings, and were both plumbed with stainless steel tubing and flex hoses to the chamber exterior.

All chamber plumbing was stainless steel tubing or flex hoses, and metal gaskets were used in joints wherever possible. Thorough helium leak tests were performed on all of the test plumbing as it was built up and installed into the chamber.

## **LEAK TESTING VIA THE SUNSPOT VACUUM CHAMBER ENVIRONMENT**

MSFC's Sunspot Space Simulation Chamber is a 10 foot diameter by 12 foot tall top-loading vacuum chamber capable of a 1E-6 to 1E-7 torr vacuum. The chamber is pumped by a refrigerator cryopump, CVI's Torrmaster Model TM1200, and an auxiliary turbomolecular pump (Varian V1800) backed by a roughing pump. The turbopump foreline was temporarily modified to allow the installation of a portable leak detector which was used to back the turbopump, thus sampling the chamber environment. The turbopump alone could not hold the chamber at a low vacuum, so the chamber cryopump was left pumping on the chamber during the leak testing. This did not have noticeable impact on sensitivity, because helium is not efficiently pumped by a cryopump.

Developmental testing was performed prior to the Qualification test to evaluate the test setup for quantitative leak testing of the chamber volume. The leak detector used on the chamber was a Leybold UL200, a counter-flow leak detector whose higher inlet pressure made it acceptable for the turbopump foreline pressure of 1E-2 torr. A three-valve manifold was installed on the side of the chamber and was used in conjunction with a roughing pump to evacuate the helium leaks used to determine the chamber sensitivity. The manifold for the standard leaks was located as far as was practical from the MSLD and turbopump. Helium leaks used for the test were Vacuum Technology Incorporated's (VTI's) pressurized permeation and capillary leaks in sizes ranging from 1E-5 to 1E-3 sccs helium.

Once the chamber was pumped down to a stable pressure, the leak detector was valved onto the turbopump foreline. Then the valve to the backing pump was slowly closed, while the foreline pressure was monitored to ensure that it did not rise above 100 millitorr, the maximum desired foreline pressure. Once the leak detector was fully backing the turbopump, a system calibration was performed in which the helium leak was evacuated by a roughing pump, then valved onto the chamber. This procedure was referred to as the "chamber calibration". Response and cleanup results from a typical chamber calibration with a 1.4E-5 accs helium leak are shown in Figure 5. The data showed that leak testing of the chamber volume in this configuration resulted in an excellent response time. Sensitivity of the chamber was approximately 1E-10 accs/division, which meant that with a typical starting background of 1000 divisions, a leak of size 1E-7 sccs helium or greater could be detected.

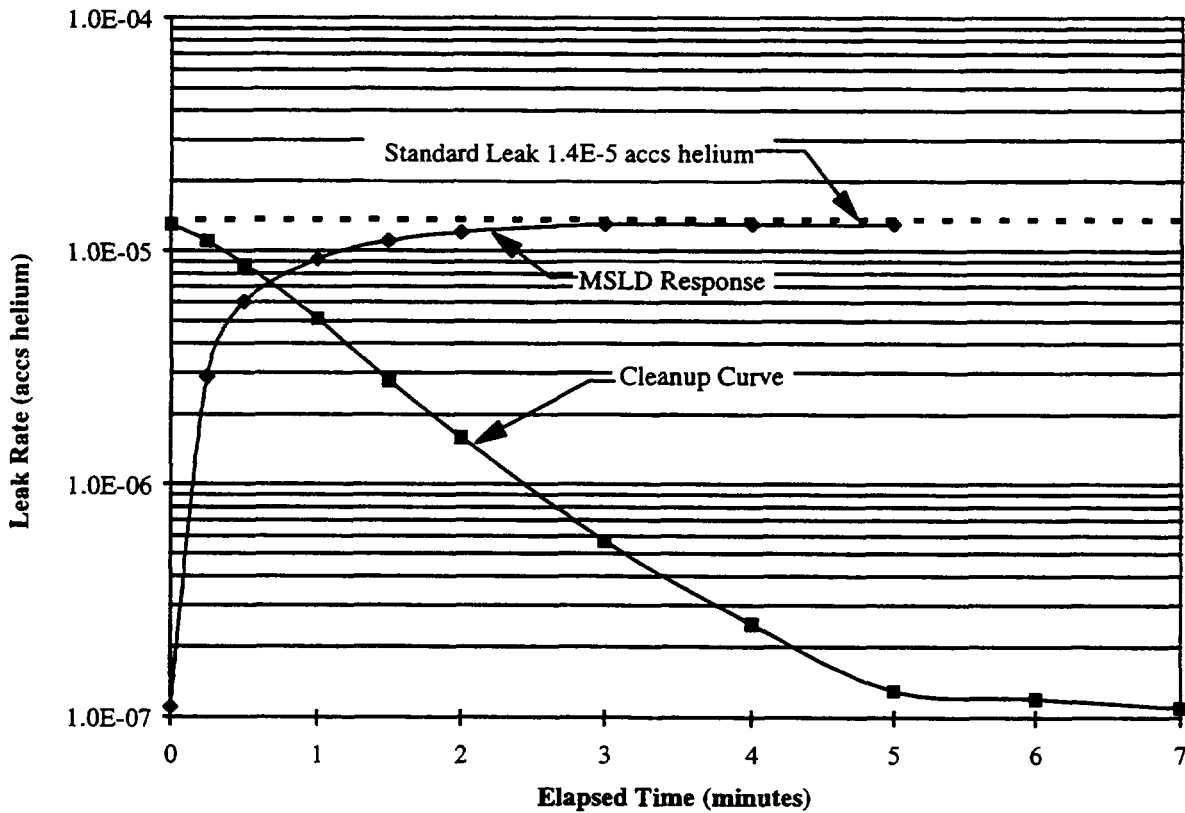


**Figure 5: Sunspot Chamber Calibration Curve**

## TEST CONDUCT

The thermal vacuum test began on May 23, 1996 and ended on June 3, 1996. During the initial pumpdown of the chamber and during subsequent temperature shifts, the pressure in the dome volume was equalized with the chamber pressure. Prior to leak test start, the dome was pressurized to 14.7 psia with high quality/purity air. Ambient pressure in the dome was required to expose the Hatch to the space-like pressure deflections. Chamber pressure was maintained at 1E-5 torr or less during the tests, with an average pressure of approximately 5E-6 torr.

All of the seals were not tested during each leak test in the test flow, as additional tests of the Perimeter Seals and Shaft Seals were required. An outline of the procedure for a complete test of all the Hatch seals follows. The order of seal testing was chosen in an attempt to optimize chamber helium background, which would rise as testing continued, and to shorten test time.

The tests of the first three seals, the Shaft, the Outboard Window, and the Outboard Perimeter seal, require the MSLD to sample the chamber volume. The MSLD connected to the chamber turbopump foreline was started, calibrated, and brought on line to the turbopump foreline. The SD700 backing pump was valved off. After the initial pumpdown of the chamber, a leak test was performed on the chamber itself: a helium tracer probe was used to spray helium on all chamber feedthroughs and

leakage paths. A chamber calibration was performed to obtain the chamber sensitivity; then the leak was closed and the background was allowed to return to its original value.

The enclosure over the IVA side of the Hatch Shaft was evacuated with a roughing pump. Then the pump was valved off and replaced with a jumper from the helium/air pressurization panel. The MSLD background reading was recorded, and the Shaft enclosure was backfilled with helium to 14.7 psia. The Shaft's three seals in series made permeation of the shaft an impracticably long operation (about 12 hours at ambient temperature) so the thermal vacuum test of the shaft was limited to "through" leakage only. This meant that the leak rate was only observed for a few minutes (a minimum of three minutes) to determine if there was leakage around the seals, as opposed to permeation through the seals, which has a considerably longer response time. A year after the Hatch Thermal Vacuum Test, a Shaft Thermal Vacuum Qualification Test was performed to completely qualify the Shaft seal design.

For the leak test of the Outboard Window seals, the volume between the Hatch Window panes was evacuated with a roughing pump. The volume was then pressurized with helium to 14.7 psia, and the seals allowed to permeate. There are four seals in the Outboard Window assembly, but several are in parallel, so that the permeation time for the test, at less than an hour, was relatively short. Following this test, the volume between the panes was again evacuated, and the chamber background allowed to drop before proceeding to the next test.

The Outboard Perimeter Seal was tested by evacuating the volume between the perimeter seal beads with a roughing pump, and then pressurizing the volume with helium to 14.7 psia. Once the seal was permeated, the helium was evacuated from between the seal beads. Another chamber calibration was then performed to ensure that there had been no loss in chamber sensitivity. Then the MSLD connected to the chamber turbopump was valved off and shut down.

The tests of the remaining three seals, the Inboard Window, the Inboard Perimeter, and the MPEV flange, required the dome volume to be pressurized with helium while three separate MSLDs sampled the inter-seal volumes of the window and perimeter seals and the MPEV enclosure. Before the helium was applied to the dome, calibrations were performed for each of the seals to be tested. These calibrations were performed simultaneously to reduce the test duration. The enclosure over the MPEV was connected directly to an MSLD outside the chamber. No system calibration was performed on the MPEV enclosure, so the MSLD sensitivity (determined by connecting an external helium standard leak to the MSLD prior to test) was used in the subsequent leak rate calculations.

The test of the Inboard Window assembly seals required connection of the volume between the window panes to an MSLD via one of the two Window Leak Check Ports. The other Window Leak Check Port was connected to a three valve manifold used to evacuate a standard leak. The volume between the panes was evacuated with the MSLD, then the standard leak was valved onto the volume to get the system sensitivity, which was used later for the Inboard Window leak rate calculations. Once the standard leak was valved off, the background returned to its initial value.

The volume between the Perimeter Seals was calibrated in the same manner as the Window Seal inter-volume. After the calibrations were performed, the Hatch Dome was evacuated to a maximum pressure of 10 torr via a roughing pump outside the chamber, then it was pressurized to 14.7 psia with helium. Leak rate data was recorded on the three separate MSLDs until each seal was stable.

Following this leak test, the Hatch Dome was evacuated, then equalized with the chamber pressure in preparation for heating or cooling to the next temperature extreme.

## **TEST RESULTS**

Leak rate data, consisting of the test requirements and test results, is summarized in Table 1. The data shows that the Inboard Window failed its leak rate requirement in the -50 °F case. Following the completion of the third thermal cycle, the source of the leakage was discovered to be a gouge on the sealing surface of the Leak Check Port, and was not associated with the Inboard Window seals. The leak was repaired by application of epoxy to the leaky fitting. As an added precaution, an enclosure was installed over the Window frame that allowed helium to be applied to the Window seals exclusive of the leak check ports. The -50 °F case was then repeated for the Inboard Window seals, and a successful leakage rate of 1.1E-6 sccs helium was obtained.

Another test anomaly was a failure of the Shaft seals in the -50 °F cycle. Although the Shaft passed the total leak rate requirement, the quick helium response time indicated that there was excessive through leakage of the shaft seals. As a result of this test the Shaft design was modified to incorporate two more teflon seals, for a total of five seals. The resultant design change was qualified in the Hatch Shaft Seal Qualification Test in August-September of 1997.

## **CONCLUSIONS**

Optimal test sensitivity was obtained on the cryo-pumped chamber by installing the MSLD on the turbopump foreline. There was no detrimental loss in chamber due to the use of the chamber cryo-pumps. The Hatch Thermal Vacuum Qualification Test demonstrated that full assemblies can be tested in such a way that the individual components can be evaluated during one test. The leak rate tests were a successful example of complex quantitative leak rate testing in a large vacuum chamber.

**Table 1: Leak Rate Test Results**

| Hatch Cycle                             | Hatch Temp (deg F) | Inboard Perimeter Seal (sccs he) | Outboard Perimeter Seal (sccs he) | Shaft Seals (sccs he) | MPEV Flange Seals (sccs he) | Inboard Window Seals (sccs he) | Outboard Window Seals (sccs he) |
|---|--------------------|----------------------------------|-----------------------------------|-----------------------|-----------------------------|--------------------------------|---------------------------------|
| Leak Rate Requirement (sccs helium)     | All                | 1.0E-02                          | 1.0E-02                           | 2.7E-04               | 5.4E-02                     | 1.6E-03                        | 1.6E-03                         |
| Baseline Ambient                        | 70                 | 1.2E-03                          | 1.2E-03                           | No through leakage    | 1.7E-05                     | 1.6E-05                        | 1.8E-04                         |
| First Cycle Cold (Perimeter seals only) | -10                | 5.6E-04                          | 4.5E-04                           | -                     | -                           | -                              | -                               |
| First Cycle Cold (Perimeter seals only) | -50                | 1.0E-04                          | 2.2E-04                           | -                     | -                           | -                              | -                               |
| First Cycle Hot (Perimeter seals only)  | 170                | 2.8E-03                          | 3.3E-03                           | -                     | -                           | -                              | -                               |
| Third Cycle Cold (Shaft seals only)     | -10                | -                                | -                                 | No through leakage    | -                           | -                              | -                               |
| Third Cycle Cold                        | -50                | 1.9E-04                          | 1.6E-04                           | 2.7E-05               | 4.5E-03                     | 3.2E-02                        | 2.0E-05                         |
| Third Cycle Hot                         | 170                | 2.5E-03                          | 3.3E-03                           | 4.8E-06               | 7.7E-05                     | 2.2E-05                        | 4.3E-04                         |
| Third Cycle Ambient                     | 70                 | 1.3E-03                          | 1.4E-03                           | No through leakage    | 6.0E-05                     | 2.2E-05                        | 1.8E-04                         |

## INTERNATIONAL SPACE STATION NODE 1 HELIUM ACCUMULATION LEAK RATE TEST

Steve Underwood, Angela Holt  
Boeing Defense and Space Group  
International Space Station Program  
Huntsville, Alabama

### ABSTRACT

Developmental testing in support of the International Space Station program was performed which verified the methodology, accuracy and sensitivity for the International Space Station (ISS) Node 1 flight article leak test. The testing was performed in the Space Station Processing Facility (SSPF) located at Kennedy Space Center (KSC), and it evaluated the accumulation test technique of quantifying the leak rate of a pressurized test article located in a container of known volume, the Multiple Mission Support Equipment (MMSE) canister. Three calibrated leaks provided known helium concentrations into the canister over time. The calibrated leaks selected for the test provided helium flow rates which represented the overall Node makeup gas allocation and the approximated Node leakage rate based on individual component testing previously performed. The calibrated leaks were introduced through an access door penetration located at one end of the MMSE canister. A gas chromatograph thermal conductivity analyzer was used to measure the helium concentrations taken from six sample lines distributed inside the canister. As a result of testing, the helium accumulation technique was selected as the method for determining the Node 1 flight article leak rate. The Node 1 element-level leak test was conducted March 11-19, 1998, in the SSPF.

### INTRODUCTION

The ISS Node 1 is an interconnecting module for the US Laboratory, Airlock and other ISS modules. With 160 penetrations through the module structure for power, data, and fluid pass-throughs and six hatches, the Node has many potential leakage paths to space. All leakage paths were leak tested as the Node was built up, but an overall element level test was required in order to verify that the Node met its leak rate requirement of .117 pounds of air per day. A helium accumulation test was proposed, with the Node pressurized to 14.7 psig with 50% helium enclosed in the MMSE canister. A developmental test was performed in September of 1997 to validate the proposed test method.

### ACCUMULATION DEVELOPMENTAL TEST

For the developmental test, three different sizes of helium standard leaks were connected to the MMSE canister and allowed to accumulate in the canister volume. The leaks selected for the test provided helium flow rates which represented the overall Node makeup gas allocation, (1.5 sccs helium), and two smaller leaks of .23 sccs helium and .023 sccs helium. A gas chromatograph thermal conductivity analyzer was used to measure the helium concentration in parts per million helium, and was plumbed to six sample ports distributed inside the MMSE canister. The canister was outfitted with two fans located at opposite ends. See Figure 1 for the test setup configuration.

The first series of tests consisted of separately valving on the three different leaks and taking periodic samples of the MMSE canister helium background. The canister fans were on for these tests. The 1.5 sccs helium leak and the .23 sccs helium leak were valved onto the canister for 20 hours. Every four hours, samples were taken from each of the six ports and analyzed by the gas chromatograph. The .023 sccs helium leak was valved on to the canister for 70 hours, with data collected every 10-12 hours. Test results are compared with the theoretical results in Figure 2. The test results plotted were the average of the six samples taken. The tests demonstrated that the accumulation method using the MMSE canister could be used to accurately quantify a 0.023 sccs helium leak within 17% (worst case average).

### **NODE 1 FLIGHT ARTICLE ACCUMULATION TEST**

In March of 1998 the Node 1 flight article was installed into the MMSE canister for its element-level acceptance test. The test setup is shown in Figure 3. The Node 1 was fully outfitted for flight, except for one inter-module ventilation port feedthrough that had been removed and replaced with a penetration for the test plumbing. First a characterization test was performed that was similar to the earlier developmental tests, with the same three leaks introduced into the canister while the Node 1 was unpressurized. The Node 1 was pressurized to 14.7 psig for a 50% helium concentration. Helium that leaked from the Node into the canister was collected periodically and analyzed by the gas chromatograph. The Node was de-pressurized to 0 psig and a final calibration was performed using a .023 sccs helium leak. Test results are summarized in Figure 4. The values for the Node 1 pressurization with helium were adjusted for the 50% helium concentration in the module. Node 1 leakage was determined to be .005 pounds per day of air.

### **CONCLUSIONS**

The test demonstrated the ability to leak test space station modules in an atmospheric environment by the use of the accumulation test method. The test sensitivity was verified with standard leaks before and after the Node was pressurized with helium. The helium accumulation test resulted in verification that Node 1 leakage was 23 times below its requirement.

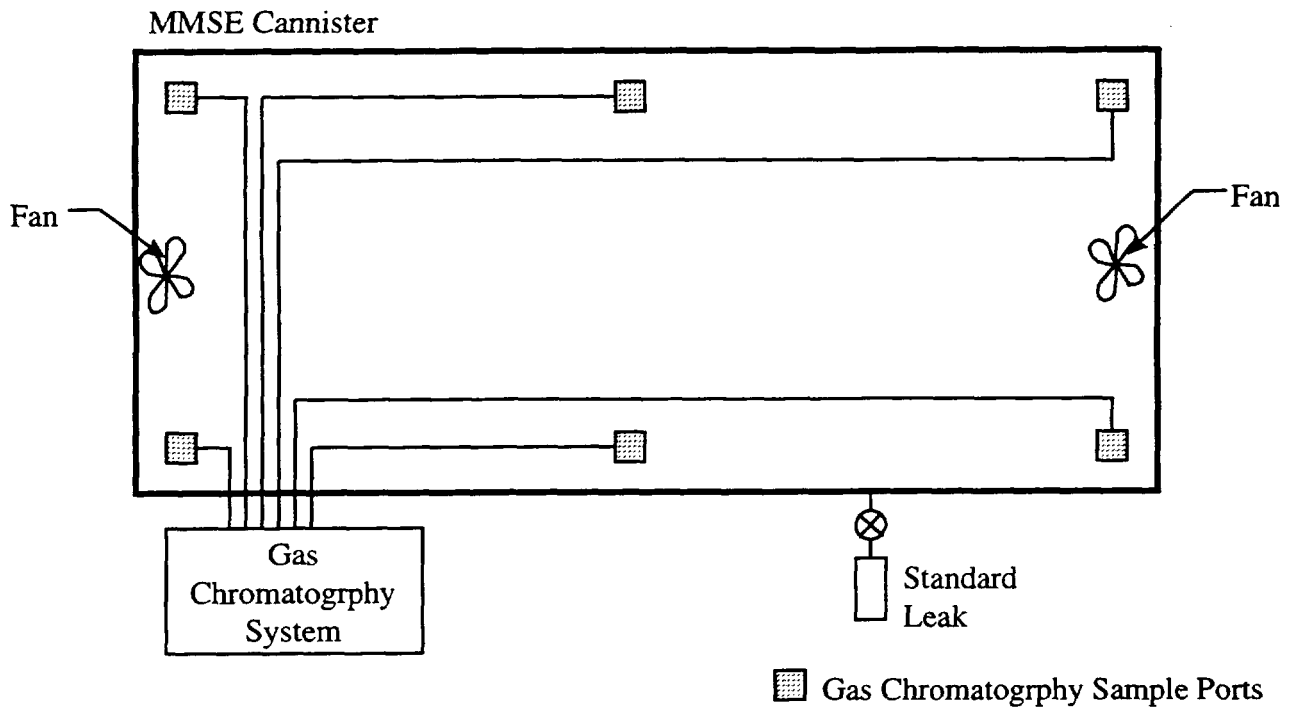


Figure 1: Accumulation Developmental Test Setup

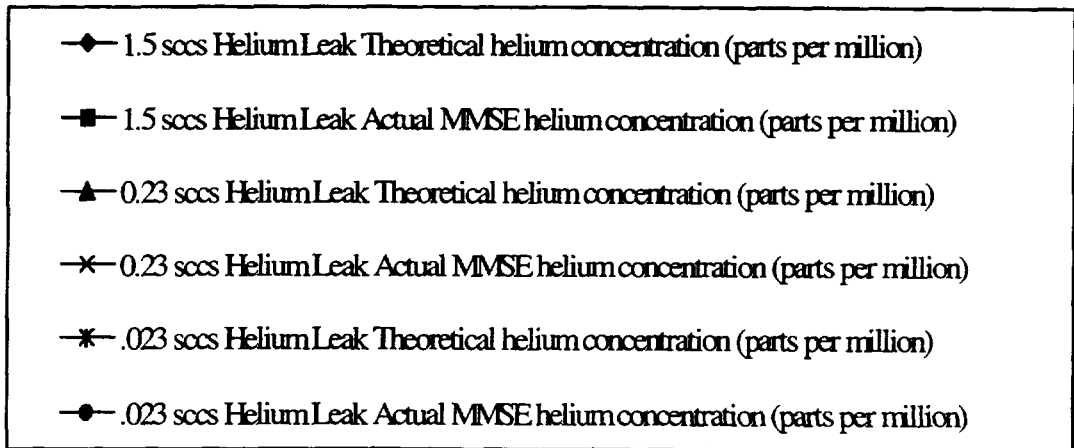
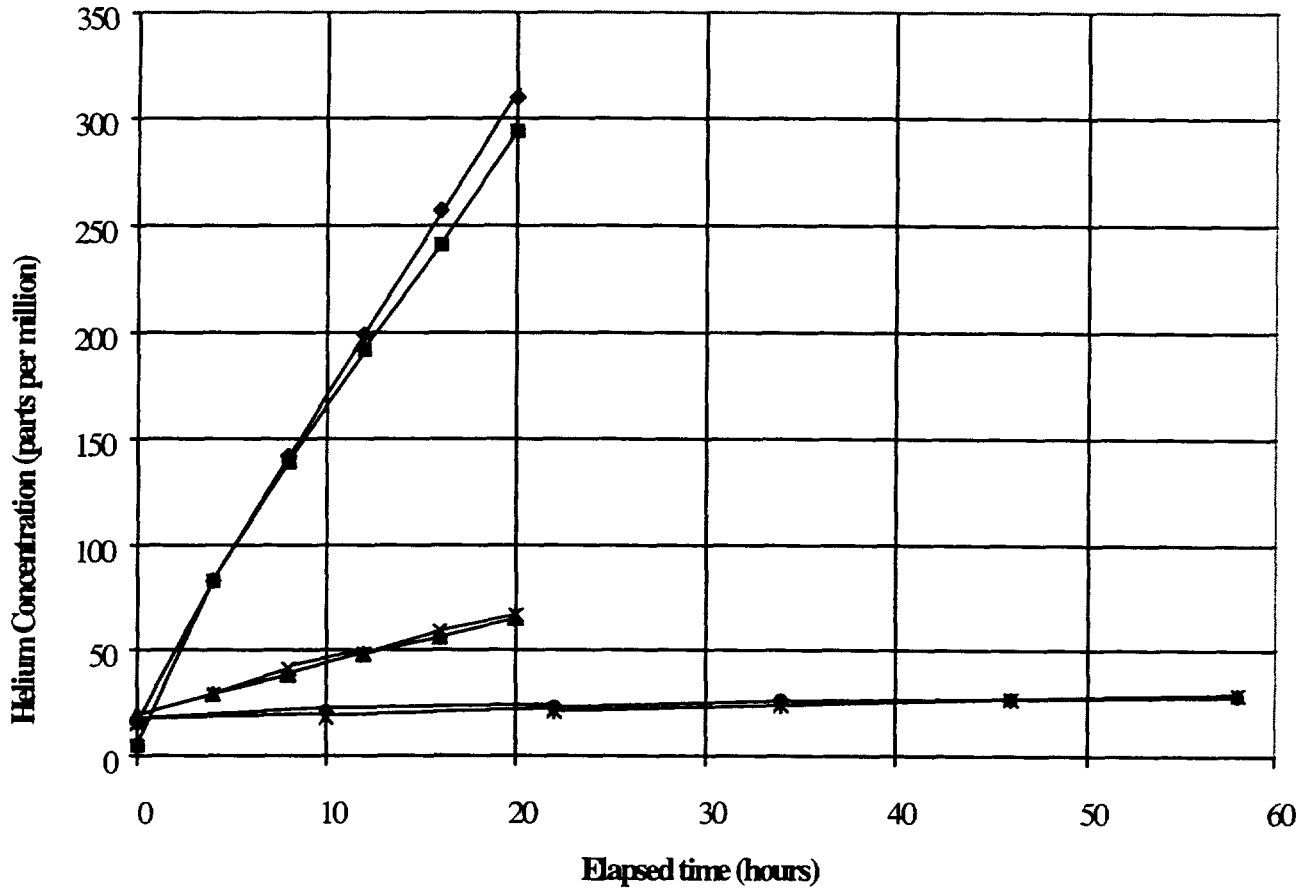


Figure 2: Dev Test Results

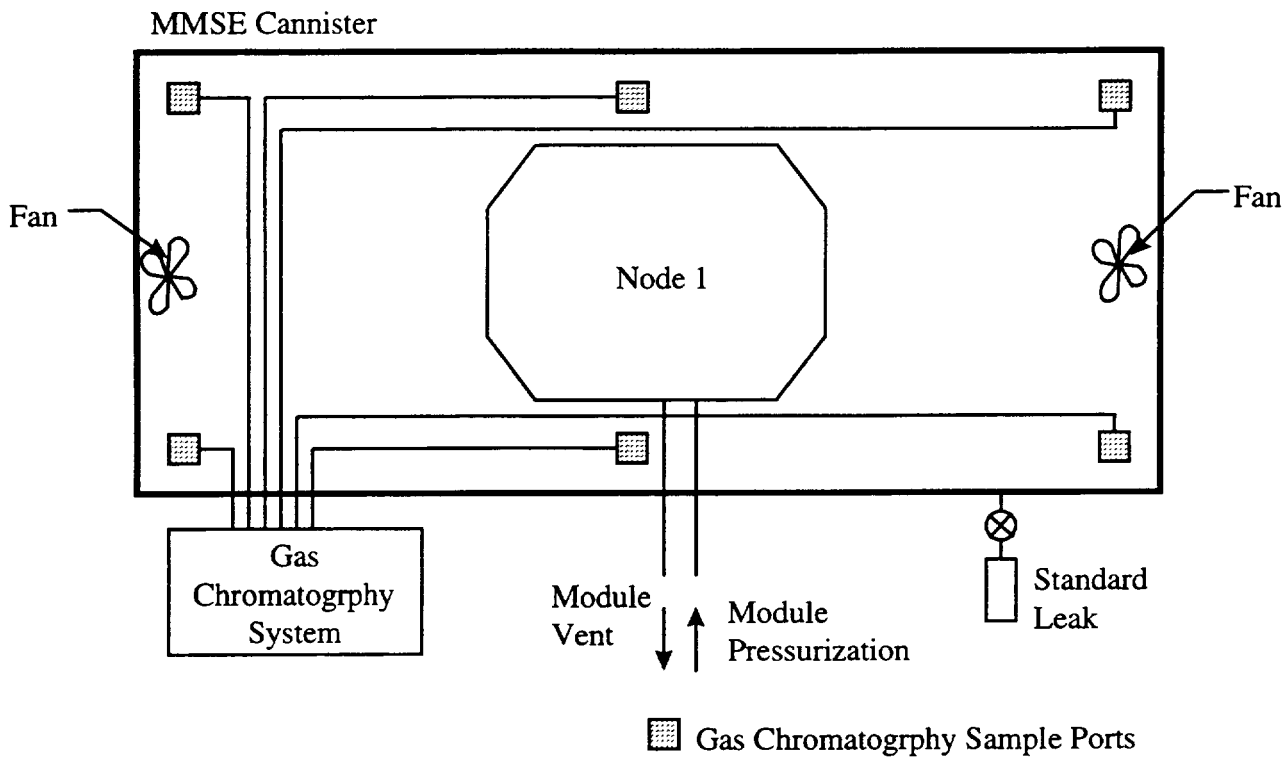


Figure 3: Node 1 Accumulation Test Setup

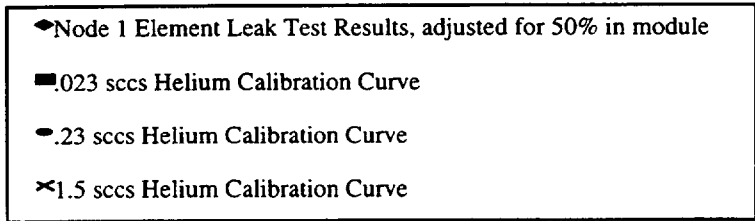
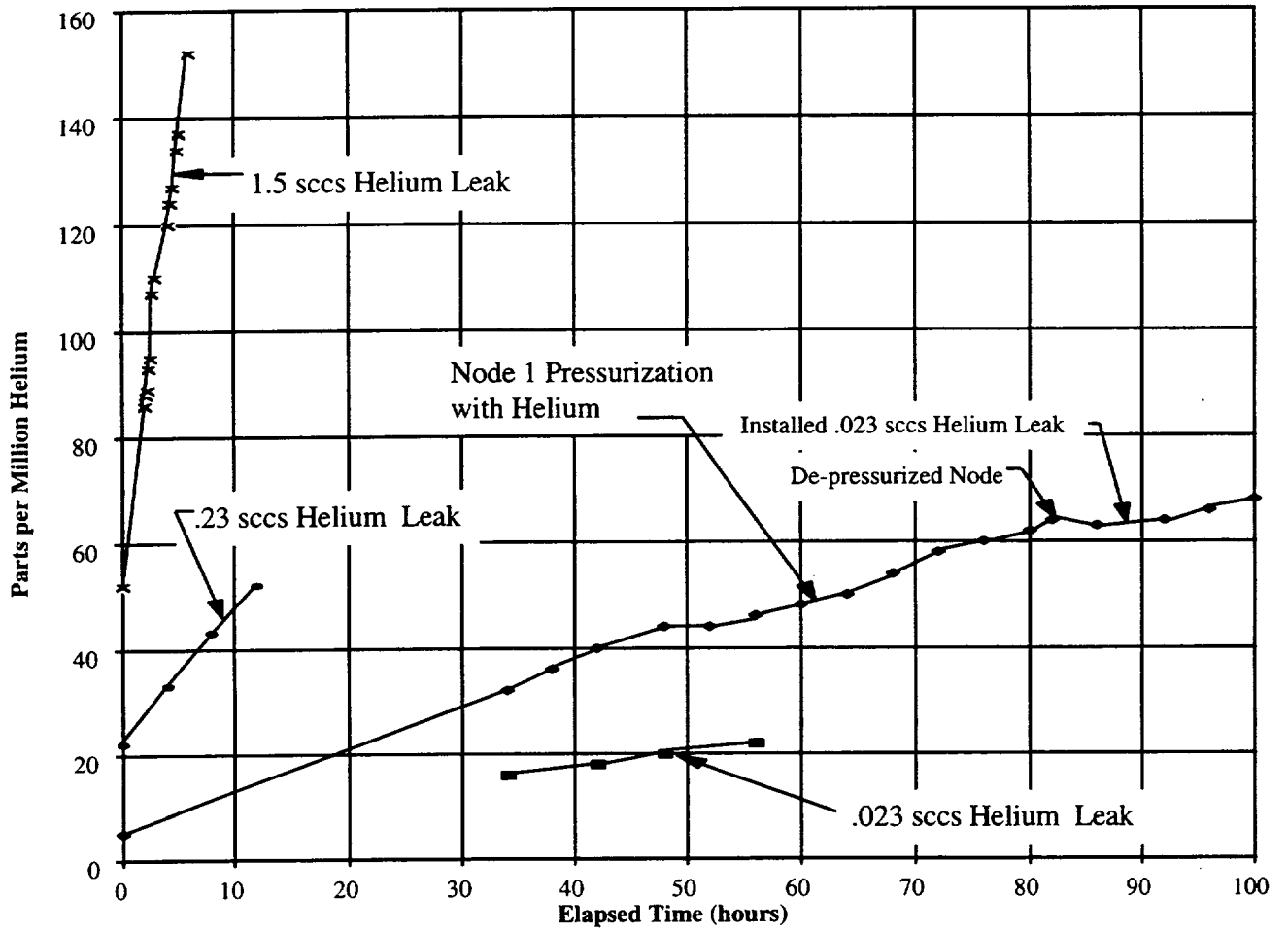
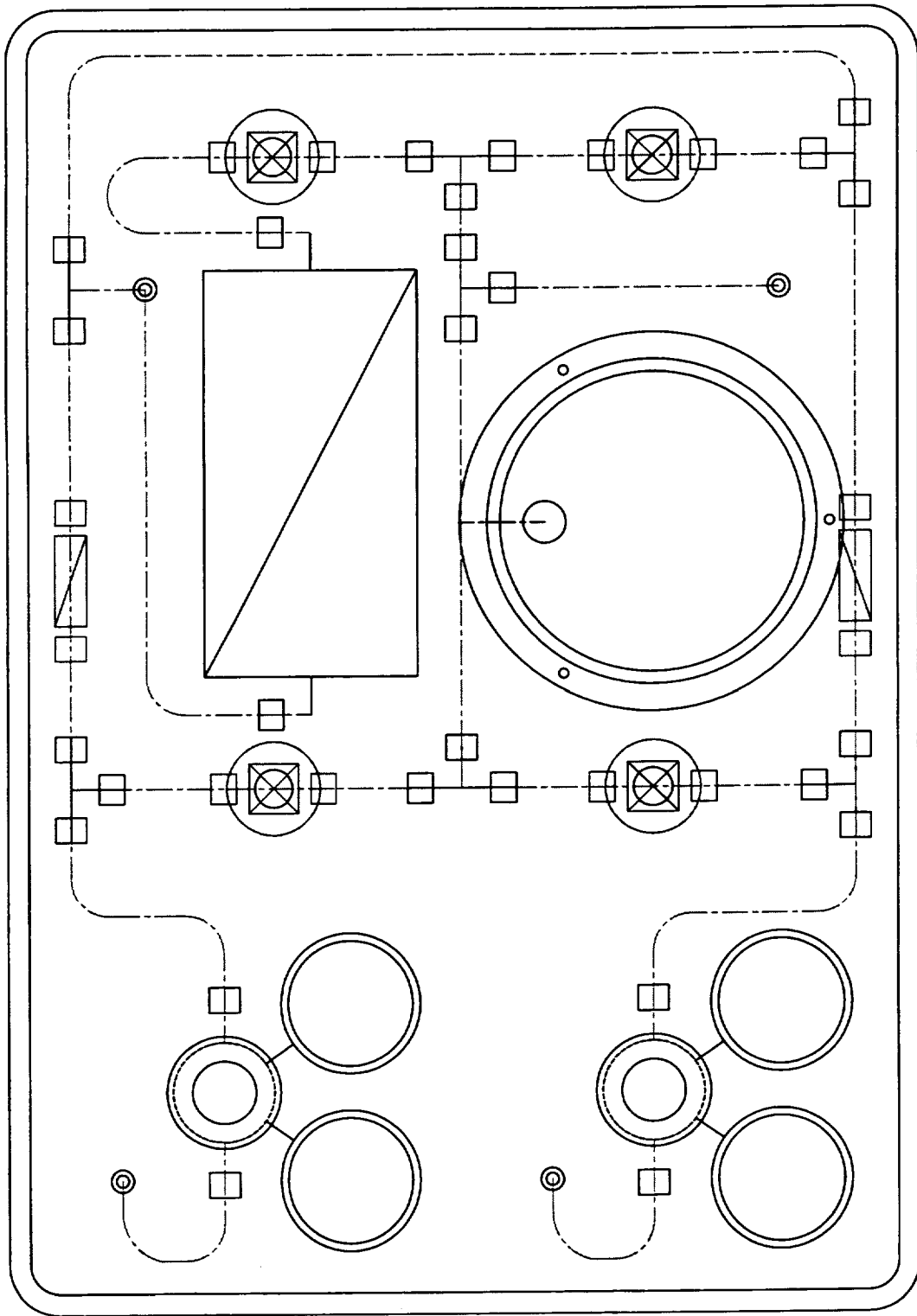


Figure 4: Node 1 Accumulation Test Results





# CABLE BUNDLE WIRE DERATING

Ray A. Lundquist and Dr. Henning Leidecker  
NASA Goddard Space Flight Center

## ABSTRACT

The allowable operating currents of electrical wiring when used in the space vacuum environment is predominantly determined by the maximum operating temperature of the wire insulation. For Kapton insulated wire this value is 200°C. Guidelines provided in the Goddard Space Flight Center (GSFC) Preferred Parts List (PPL) limit the operating current of wire within vacuum to ensure the maximum insulation temperature is not exceeded. For 20 AWG wire, these operating parameters are:

- 3.7 amps per wire
- bundle of 15 or more wires
- 70°C environment
- vacuum of  $10^{-5}$  torr or less

To determine the behavior and temperature of electrical wire at different operating conditions, a thermal vacuum test was performed on a representative electrical harness of the Hubble Space Telescope (HST) power distribution system. This paper describes the test and the results.

## BACKGROUND

The HST Power Distribution Units (PDUs) are the primary distribution points of electrical power for the HST electrical system. The PDUs accept high power, fused, solar array/battery power from the Power Control Unit (PCU), fuse this power into lower current services, and distribute it to all the HST loads.

The output services from the PCU use either 16 AWG or 20 AWG wiring, depending on load requirements that were set two decades ago. The wire used within the PDU is Kapton-insulated, multistranded, silver-coated copper wire. The maximum temperature for this kind of wire is 200°C, set by the insulation. (Connections are either crimped, or are heat-sunk such that the connections remain well below the melting temperature of solder, 183°C.) The specification for the wire is MIL-W-81381/17-20-4.

A recently proposed design modification would increase to as much as 6.0 Amps the current through a section of an individual 20 AWG wire; there are four such wires in a bundle of 28 wires. This produces a possible conflict with the GSFC Preferred Parts List

(PPL). The PPL specifies that the maximum current through a single 20 AWG wire be 3.7 Amps when that wire is present in a bundle of 15 wires or more, in a vacuum, and in an environment whose ambient temperature is 70°C.

However, the PDU wiring of concern is operating in an environment whose nominal temperature is 12°C, and whose maximum temperature is 25°C: not 70°C. In addition, most of the other wires in the bundle (24 of the 28) will be carrying no more than 3 Amps at any time: not all 28 wires will be simultaneously loaded to 6.0 Amps. Thus, it is not clear that the recommendation of the PPL applies, since it is clear that the precise conditions do not apply. Other guideline documents were also consulted, but offered no clear guidance. Finally, estimating the temperature rise using a radiative transfer model is not an option since neither the surface emissivity of these wires, nor the heat current coupling between the wires, are known to the required accuracy.

To determine if the operating conditions described above will present a potential failure point, or even a hazard, a thermal vacuum test was performed under conditions designed to match the actual operating conditions to the greatest extent possible.

## **TEST SET-UP**

A bundle was constructed using the same wire and assembly procedures that had been used to construct the PCU bundle. In particular, the Kapton insulation was matched in color, to match the radiative properties of that used in the PCU bundle. The bundle is two feet in length, and contains a total of 28 wires. One wire was zigzagged back and forth to create the “background” bundle of 24 wires, and another wire was zigzagged to create the four “foreground” wires of present interest. This arrangement ensured that the same foreground current passed through each of the foreground wires, and the same background current passed through each of the background wires.

Four thermocouples were used, located about every six inches along the bundle, but no closer than six inches from either end of the bundle. These were type T thermocouples, with 30 AWG wire diameter. Each thermocouple was placed next to a selected wire being measured, and fastened with lacing cord. To provide a measure of the bulk temperature of the wires being measured, 7 mil aluminum tape was wrapped around the bundle and the thermocouple. A Kapton tape over-wrap of the aluminum tape was provided to maintain the thermal properties similar to the Kapton wire insulation. Two thermocouples were fastened to an outer wire (background), and two were fastened to an inner wire (foreground).

The wires were collected into a bundle so that each wire retains its relative position radially within the bundle, as one moves from one end to the other. (The wires were not “woven” into a braid or a rope.) In particular, the foreground wires are at (or near) the radial center, everywhere from one end of the bundle to the other. Cable ties were used

every four inches along the bundle and tensioned using a Panduit Tie-Wrap tool with a setting of 4. The bundle was placed into the thermal chamber, in a nearly vertical orientation; thus, the thermocouples are classified as “top” and “bottom” in the table, rather than “left” and “right.”

Figure 1 shows the test set-up and the schematic location of the thermocouples.

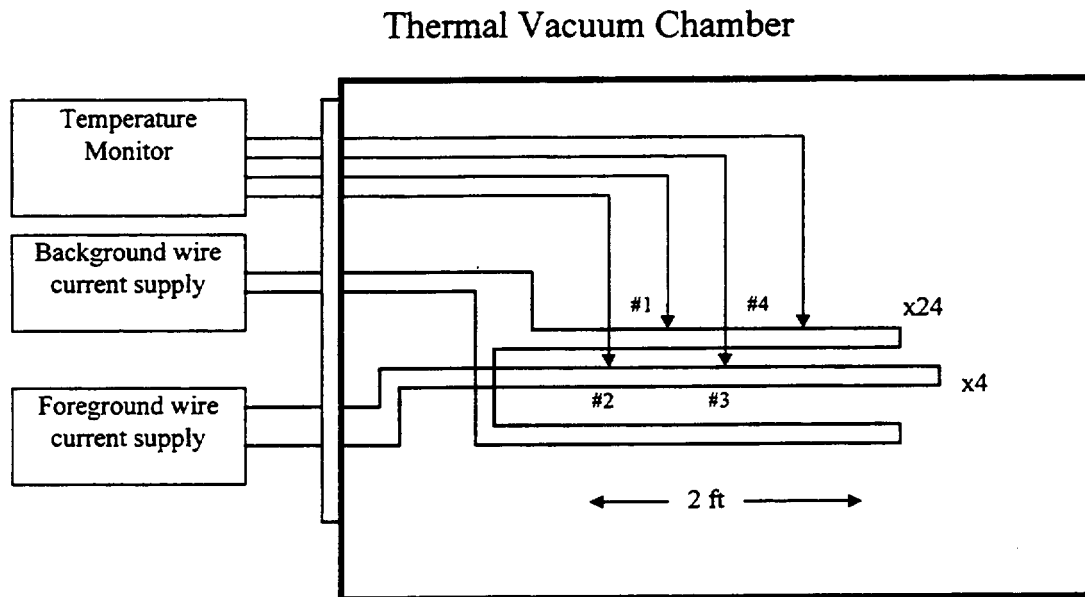


**Figure 1 – Thermocouple Locations During Thermal Vacuum Test**

Note: The figure depicts the wires installed in the thermal vacuum chamber in a horizontal configuration. This is for ease of drawing only. The wire bundle was actually installed in the thermal vacuum chamber in a vertical configuration as shown in Figure 2.

Figure 2 displays a photograph of the set-up in the thermal vacuum chamber.



**Figure 2 – Photograph of Thermal Vacuum Chamber**

## **TEST RESULTS**

The effects of three parameters were measured: the temperature of the thermal vacuum chamber's shroud, the foreground current driving the 4 wires of special interest to this study, and the background current driving the 24 enclosing wires.

Values were set and then held constant for each of these parameters until the steady state temperatures could be estimated. The values of the parameters, and the history of the four temperatures, are shown in Figure 3. Inspection shows that these temperatures approach steady state values for each set of test parameters, with a time constant (the time to achieve ~70% of the steady state value) of about 15 minutes. Estimates of the steady state values are given in Table 1.

Thermocouples #1 and #4 measure apparently equivalent locations: we would expect their temperatures to be identical except for differences in the construction of the bundle. We would expect the same from thermocouples #2 and #3. In fact, the difference  $T(\#1) - T(\#4)$  ranges from  $5^{\circ}\text{C}$  to  $27^{\circ}\text{C}$ , and the difference  $T(\#2) - T(\#3)$  ranges from  $1^{\circ}\text{C}$  to  $6^{\circ}\text{C}$ .

| Cylinder Temperature<br>$^{\circ}\text{C}$ | Background Current<br>Amps | Foreground Current<br>Amps | TC #1<br>Outside<br>Top | TC#2<br>Inside<br>Top | TC#3<br>Inside<br>Bottom | TC#4<br>Outside<br>Bottom |
|--|----------------------------|----------------------------|-------------------------|-----------------------|--------------------------|---------------------------|
| 0  | 1                          | 4                          | 18                      | 32                    | 31                       | 13                        |
| 0  | 1                          | 6                          | 38                      | 68                    | 65                       | 32                        |
| 0  | 1                          | 8                          | 61                      | 113                   | 108                      | 38                        |
| 0  | 3                          | 4                          | 56                      | 73                    | 71                       | 41                        |
| 0  | 3                          | 6                          | 71                      | 104                   | 100                      | 49                        |
| 0  | 3                          | 8                          | 92                      | 147                   | 141                      | 63                        |
| 12   | 1                          | 4                          | 29                      | 44                    | 41                       | 22                        |
| 12   | 1                          | 6                          | 44                      | 76                    | 71                       | 32                        |
| 12   | 1                          | 8                          | 67                      | 121                   | 116                      | 46                        |
| 12   | 3                          | 4                          | 63                      | 80                    | 78                       | 49                        |
| 12   | 3                          | 6                          | 77                      | 111                   | 107                      | 57                        |
| 12   | 3                          | 8                          | 97                      | 152                   | 147                      | 70                        |
| 25   | 1                          | 4                          | 39                      | 54                    | 51                       | 33                        |
| 25   | 1                          | 6                          | 53                      | 85                    | 81                       | 42                        |
| 25   | 3                          | 6                          | 85                      | 119                   | 115                      | 65                        |
| 25   | 3                          | 8                          | 105                     | 160                   | 155                      | 78                        |
| 70   | 3.7                        | 3.7                        | 122                     | 140                   | 137                      | 109                       |

**Table 1 – Experimental Data**

The temperature of individual wires is affected by the extent of “openness” versus “tightness” of the bundle, which affects the thermal coupling of the individual wires. This effect is more important for wires on the outside of the bundle than for wires in the inside. We are most interested in the temperature of the inner wires, and these are well determined for our present purposes. We shall use the averages of thermocouples #1 and #4, and of #2 and #3.

To the extent that the properties of the wires do not depend on temperature, and that the temperature differences between the outer wires and the shroud are relatively small (on an absolute temperature scale), then the temperature increases above the shroud’s temperature should be the same for each shroud temperature. Table 2 displays the foreground temperature (computed as the average of thermocouples #2 and #3), minus the temperature of the shroud.

| Foreground Current | Shroud Temperature °C | Foreground Wire Temperature Minus Shroud Temperature For Background Current °C |       |
|--------------------|-----------------------|--|-------|
|                    |                       | 1 Amp  | 3 Amp |
| 4 Amp              | 0                     | 32°C   | 72    |
|                    | 12                    | 31   | 67    |
|                    | 25                    | 28   | ---   |
| 6 Amp              | 0                     | 67   | 102   |
|                    | 12                    | 62   | 97    |
|                    | 25                    | 58   | 92    |
| 8 Amp              | 0                     | 111  | 144   |
|                    | 12                    | 107  | 138   |
|                    | 25                    | ---  | 133   |

**Table 2 – Experimental Data With Shroud Temperature Dependence Removed**

The entries in each box are in the vertical order:  $T(\text{shroud}) = 0^\circ\text{C}$ ,  $12^\circ\text{C}$ , and  $25^\circ\text{C}$ , respectively. Also, “---” means that the parameters were not included in the test. To a first approximation, the values do not depend on the temperature of the shroud. To a second approximation, there is a clear (if small) downward trend with increasing shroud temperature. This is caused in part by the temperature dependence of the electrical resistance of the wire, and in part by end effects, which, while small, are not completely absent. The  $12^\circ\text{C}$  shroud temperature values are fit with an average error of about 5% by the expression

$$T_{\text{Foreground}} = T_{\text{Shroud}} + \frac{1.5^\circ\text{C}}{\text{Amp}^2} * I_{\text{foreground}}^2 + \frac{4.8^\circ\text{C}}{\text{Amp}^2} * I_{\text{Background}}^2$$

which has the expected theoretical form. On the one hand, this equation, with just two parameters, usefully summarizes 16 test results. On the other hand, a better fit would capture the dependence on the shroud’s temperature: inspection of Table Two shows that the coefficients drop steadily with increasing shroud temperature. This would introduce other parameters, perhaps only one more, if the main dependence is caused by the change of resistivity with temperature (which is the same for both foreground and background wires).

The coefficient of the background current is larger (3.2 times larger) than the coefficient of the foreground current. There are 24 background wires, and 4 foreground wires (a factor of 6 times more); but the foreground wires are more tightly coupled to each other than to the typically more distant background wires, and this reduces the effect of the

background wires on the foreground wires. Thus, the observed ratio of the current-coefficients is plausible.

The thermal vacuum test included the special case  $I(\text{foreground}) = I(\text{background}) = 3.7$  Amp. This was not included in data set used to obtain the fitted expression. Using the expression, we compute  $T(\text{foreground}) = T(\text{shroud}) + 86^\circ\text{C}$ , while the experimental value is  $69^\circ\text{C}$ . The computational value is  $170^\circ\text{C}$ , or 25% greater than the observed value. This difference would decrease sharply if the decrease of the coefficients with increasing temperature were to be included, since the coefficients represent the behavior at  $12^\circ\text{C}$ , and this last test used a shroud temperature of  $70^\circ\text{C}$ .

The test results show that the recommendation of the PPL keeps all wires under their rated maximum temperature, as it should.

The values of the coefficients of the fitting equation must depend on the emissivity of the insulation, and so must not be used to predict the behavior of other sorts of wire. It might prove possible to usefully estimate this effect, so that an approach like this one could be used to compliment guidebook recommendations. The form of the fitting equation should be general: the temperature rise of any wire above that of the shroud must be a linear combination of the squares of the currents through the other wires.

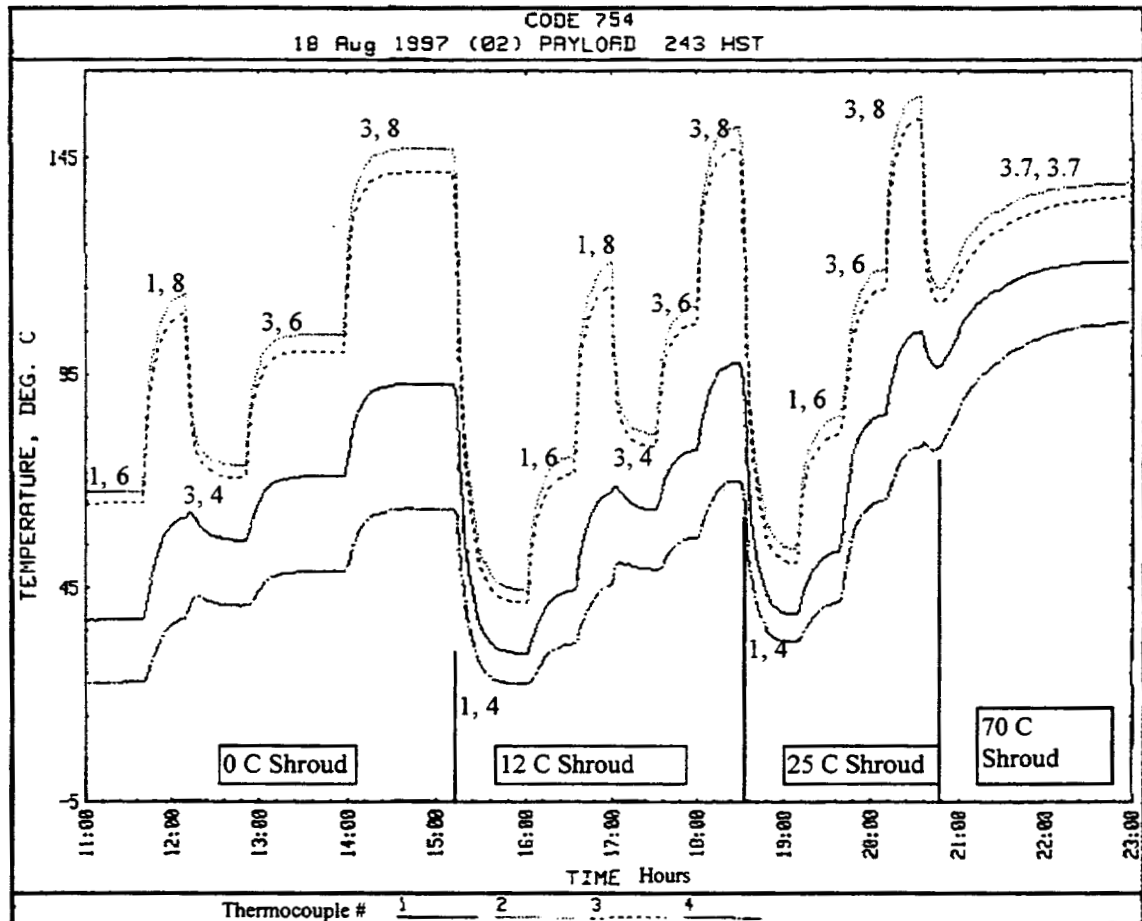


**Figure 3 – Wire Bundle Temperature History**

Notes: The numbers in the figure are the currents carried by the foreground and background wires. The first number is the background current: the current carried by 24 wires in the test bundle. The second number is the foreground current: the current carried by 4 wires in the bundle. For example, “3, 8” designates 3 Amps on the 24 background wires, and 8 Amps on the 4 foreground wires.

## CONCLUSION

There is a high level of confidence that the wires within the PDU of the HST will not exceed or approach their maximum operating temperature. This is true even when as much as 8 Amp is passing through the subject wires, if no more than 3 Amp is passing through the remaining wires, and the PDU is no hotter than 25°C.

Under the conditions named in the PPL, some wires reached a maximum temperature of 140°C, which is safe.

A variety of test data were brought under the control of a single equation with two parameters. The form of this equation is general, and should apply to other wire bundles as well. Experiments are presently required to determine the parameters.



ENVIRONMENTAL TESTING AT DIFFERENT LEVELS OF THE SEVIRI PAYLOAD OF THE ESA  
"METEOSAT SECOND GENERATION " PROGRAM.

Pierre Jamotton, Isabelle Tychon, Isabelle Domken, David Demaret, Henri Balbeur,  
Olivier Teller and Antonio Cucchiaro

Facility Department  
CENTRE SPATIAL DE LIEGE Université de Liège ( Belgium )

## 1. ABSTRACT

In the frame of the European Space Agency " METEOSAT SECOND GENERATION " meteorological program, the "Centre Spatial de Liège ", which is part of the University of Liège ( Belgium ), has been in charge of recreating in its facilities the main thermal constraints of the mission; and this at four levels :

- At the detector level
- At the Passive Cooler Assembly level ( with and without detectors )
- At the payload level

Three of these tests have already been performed successfully. From the Facility point of view, we present here the relevant testing philosophies used to meet the specifications, the related problems, solutions and results.

## 2. INTRODUCTION

The first METEOSAT SECOND GENERATION (MSG) satellite is planned to be launched in 2000. As the first generation of the Meteosat satellites ( MOP ), it is mainly an Infra-Red and Visible Imager. Compared to the first generation of the METEOSAT satellites (MOP), MSG is about twice bigger in term of number of channels, height and diameter. The cooling of the experiment is provided by a passive radiator facing the Deep Cold Space.

In the frame of this program, CSL is in charge of the testing of four different parts of the payload, with different thermal environments and cooling systems i.e:

a) the Focal Plane Optics (FPO), the I/R detectors are calibrated at 85 and 95 (K), before and after cycling them from 328K down to 70K. The visible detectors are calibrated at 248K and cycled from 328K down to 233K. They are cooled conductively.

A vibration campaign has also been integrated in this cycle.

b) the Passive Cooler Assembly ( PCA ) including the Sunshield and a two stages radiator, is tested with regards to its mechanical stability and thermal performances. To simulate space conditions, it is cooled radiatively by means of an Helium plate (called "Deep cold space"). The main specifications for this plate are a total hemispherical emittance greater than 0.95 at 20K, and a temperature lower than 25K with a heat load of 400W. Liquid Nitrogen shrouds are surrounding the set-up.

c) the Passive Cooler Assembly and the detectors ( FPCA ) are calibrated at their nominal temperature. The cooling power is provided by the same Helium plate simulating the deep cold space.

d) the whole payload, called SEVIRI ( for Spinning Enhanced Visible & InfraRed Imager ), see figure 1, is thermally and optically calibrated. Up to 19 temperature regulated channels are used, and the space is again simulated by the Deep Cold space.

These tests are necessary for at least 3 reasons:

- verify and fit the thermal model
- check that the hardware can support space conditions
- calibrate the instrument under flight conditions

As the geometry and requirements for the different parts are specific, different systems have been developed and used for the related tests.

### 3. CSL PREMISES

From a long time, CSL (former IAL Space) has been involved in the manufacturing and/or optical calibration of space instruments (FOC, GIOTTO, MOP, HIPPARCOS, ISO, EIT, SILEX, GOMOS, XMM, XMM-OM, MSG, IMAGE,...). Different facilities are used to perform the test campaigns.

#### 3.1. Vacuum Chambers

To simulate the space environment, five large vacuum chambers (from 1 to 200 [m<sup>3</sup>]) are owned by CSL ( ref. 1 ). The particularity of these chambers is that they are all equipped with a stable optical bench. These benches are physically insulated from the surrounding and mounted on seismic blocs. The residual micro-vibrations are of the order of 1 [μg] -around the limit of sensibility of the seismic accelerometers- except around the resonant frequencies where the levels are around several tenth of [μg].

Classically, the secondary vacuum of several 10<sup>-6</sup> [mbar] is obtained by turbomolecular and cryogenic pumping. The vacuum chambers are all in clean area of class 100 following FED-STD-209E. Particular contamination is monitored by Particle Fall Out (PFO) measurements, airborne contamination is monitored by a Royco particle counter and molecular contamination is monitored by witnesses and mass spectrometer.

#### 3.2. N<sub>2</sub> Thermal Control

To reproduce the space thermal conditions, copper shrouds are installed around the instruments and thermally regulated. The temperature range is about 120 to 333 [K]. The stability is about ± 0.1[K] and the absolute accuracy about ± 0.5 [K].

The system is able to perform automatic cycling of different shapes like saw teeth or trapezoid profiles.

To achieve these performances, a specific thermal system has been developed at CSL ( ref 2 ). A computer controls a LN<sub>2</sub> evaporator, delivering GN<sub>2</sub> at boiling temperature and constant pressure. This cold gas is injected in warm GN<sub>2</sub>. The mixing rate controls the gas temperature. The temperature of the regulated panel inside the vacuum chamber is driving the whole process through a PID algorithm.

The computer is also able to drive electrical power supplies with other PID loops to control the temperature at different points via heaters.

For example, in the vacuum chamber called FOCAL 5 (  $\varnothing$  5 [m] ) see figure 2, in which SEVIRI is tested, 10 GN<sub>2</sub> channels and 8 electrical channels are used. One more electrical regulated channel with a separate PID controller, and 4 LN<sub>2</sub> channels, are also used for this test.

### 3.3. Helium System

For the ISO telescope testing ( ref.3 ), a Koch 1630 Helium liquefier/refrigerator has been installed at CSL. This machine has the particularity of providing either cold gas around 4.2 [K] or liquid or both. Typical figures are a production of 50 [l LHe h<sup>-1</sup>] or a power of 200 [W] at 4.4 [K].

The FOCAL 5 chamber is linked directly to the gaseous and liquid loops. Several years ago, in the scope of the MOP testing, another vacuum chamber called FOCAL 2 (  $\varnothing$  2 [m] ) has been equipped with LHe system, the liquid being provided by Dewars. Now a third vacuum chamber called FOCAL 3 (  $\varnothing$  3 [m] ) is also connected to the gaseous loop. But as it is installed far from the Helium liquefier/refrigerator (about 60 m), special care has been taken for the transfer lines in order to keep enough Helium mass flux at the Deep Cold Space level.

## 4. FOCAL PLANE OPTICS ( FPO )

### 4.1. Description and Specifications

MSG is looking to Earth at different wavelengths. Basically, there are 4 visible channels, and 8 InfraRed channels. The detectors and their closed optics have to be calibrated. These detectors are set on two plates fixed on the Passive Cooler Assembly.

The visible detectors are set on a plate called WIRO/VHRO (Warm InfraRed Optical bench/Visible High Resolution Optical bench). The thermal requirements are :

| Phase                  | T [K] |
|------------------------|-------|
| Reference measurements | 248   |
| Cycle hot phase        | 333   |
| Cycle cold phase       | 228   |

The IR detectors are installed on a plate called CIRO (Cold InfraRed Optical bench). The thermal requirements are :

| Phase                  | T [K]    |
|------------------------|----------|
| Reference measurements | 85 or 95 |
| Cycle hot phase        | 333      |
| Cycle cold phase       | 70       |

### 4.2. Test Set-up

The detectors plates (see figure 3) are set on specific baseplates. A three stage regulation system is used for each plate :

- 1) the fine detectors temperature regulation is done via heaters on the plates and PID algorithms;
- 2) the baseplates themselves are temperature controlled also by heaters and PID algorithms;
- 3) the “cooling power” is provided by heat sinks controlled several ten degrees under the baseplate set point. Copper straps are used as thermal link between the heat sinks and the baseplates.

The customer is in charge of the control of the detectors and the CIRO baseplate. The WIRO/VHRO baseplate and both heat sinks are controlled by CSL.

For the WIRO/VHRO, a GN<sub>2</sub> channel from the thermal system provides the heat sink. The gas is used either for warm or cold phases. The heat sink is always 10 to 20 [K] colder than the baseplate.

The CIRO heat sink is an Helium heat exchanger. It is made of a copper plate with 30 [m] of copper pipe brazed on it. Cold Helium gas is provided by a Dewar. A siphon inside the Dewar is taking gas over the liquid phase, and driving it through the liquid phase to cool it to the LHe temperature. The gas flow is regulated by a heater. Boiling liquid inside the Dewar induce an overpressure of the order of 50 [mbar]. This pressure is balancing the pressure drop for the related mass flow.

The decision of flowing GHe instead of LHe has been driven by two reasons :

- 1) the relatively high temperatures of the heat exchanger (60 [K] in cycling, 75 and 85 [K] in reference measurements)
- 2) the number of cool down phases (7 per test).

At the outlet of the heat exchanger the temperature of the GHe is very close to the specified temperature. Comparing the enthalpies at atmospheric pressure we find :

| Phase  | T [K] | H [J g <sup>-1</sup> ] | H – H(4.2)<br>[J g <sup>-1</sup> ] |
|--------|-------|------------------------|------------------------------------|
| Liquid | 4.2   | 10.0                   | -20.7                              |
| Gas    | 4.2   | 30.7                   | 0                                  |
| Gas    | 60    | 327.0                  | 296.3                              |
| Gas    | 75    | 428.8                  | 398.1                              |
| Gas    | 85    | 436.2                  | 405.5                              |

The loss of the latent heat of vaporisation is leading to an increase of the Helium consumption of 5 to 7 [%]. On the opposite, trying to perform the cool down with liquid is very difficult. The liquid reaching hot parts of the line is flashing to gas inducing large overpressure. As the pressure in the Dewar is limited to 500 [mbar], it is necessary to pump out the lines at the cool down to ensure reasonable cool down time.

The trade-off between the Helium consumption and the ease of use of the system led us to prefer the gaseous solution.

The warm phases are obtained by stopping the Helium flow. The CIRO baseplate is warmed by the regulation heaters and the conductive straps are used to drive power to the heat exchanger. By this way, the detectors are always at a higher temperature than the heat exchanger, to avoid molecular contamination.

### 4.3. Test Results

Typical temperature results are :

| Phase  | Item          | Spec [K] | Detec t [K] | Base pl [K] | Sink [K] |
|--------|---------------|----------|-------------|-------------|----------|
| Ref. 1 | CIRO          | 85       | 85          | 85          | 74       |
|        | WIRO/<br>VHRO | 248      | 248         | 248         | 228      |
| Ref. 2 | CIRO          | 95       | 95          | 95          | 84       |
|        | WIRO/<br>VHRO | 248      | 248         | 248         | 228      |

|            |               |     |     |     |     |
|------------|---------------|-----|-----|-----|-----|
| Cold Cycle | CIRO          | 70  | 70  | 70  | 60  |
|            | WIRO/<br>VHRO | 228 | 228 | 228 | 203 |
|            |               |     |     |     |     |
| Hot Cycle  | CIRO          | 333 | 333 |     | 330 |
|            | WIRO/<br>VHRO | 333 | 333 | 333 | 318 |
|            |               |     |     |     |     |

The mean Helium consumption is about 3 to 4 [l LHe h<sup>-1</sup>]. The cool down time is about 6 [h] while the warm up time, due to the requirement of keeping the Helium heat exchanger colder than the CIRO plate, is about 8 [h].

The feeding Dewar is a fixed 100 [l] one. The refill is done with another 100 [l] Dewar. The temperature perturbation, using such a "serial" Dewar system, is a slight cooling of the heat exchanger, counterbalanced by the PID system of the CIRO detector. The parallel solution is not used because the induced perturbation is a warm up instead of an overcooling, leading to measurement perturbations.

It must be pointed out that, for one thermal cycle, one full Dewar is enough. The refill is then done at the start of the cool down. So the liquid loss, due to the isenthalp expansion during the transfer, is not wasted but used for the cool down.

## 5. PASSIVE COOLER ASSEMBLY ( PCA )

### 5.1. Description and Specifications

The MSG detectors are cooled radiatively by the Passive Cooler Assembly ( ref. 4 ). It is composed of the Sunshield Assembly and the Radiator Assembly as shown in figure 4.

The Sunshield is mainly a solar reflector, shielding the radiator from the sunlight. But its outer edge ring is covered with Optical Solar Reflectors ( OSR ) to drive heat from the sunshield to the deep cold space.

The Radiator is a two stage passive one. As it is holding both detector plates (CIRO and WIRO/VHRO), there is a strong alignment specification through the whole temperature range of use, i.e. from ambient, before launch and during decontamination phases, to cryogenic in nominal use.

Thus the main objectives of the test are :

- 1) check the thermal design by reaching the predicted temperature when looking to the deep cold space,
- 2) check the alignment through the whole temperature cycle.

To reproduce the flight conditions, surrounding shrouds fed with LN<sub>2</sub> are used. The supporting frame is controlled by heaters to simulated the heat fluxes. The deep cold space is simulated by an Helium cooled plate. The total hemispherical emittance of the Helium plate should be better than 0.95.

The alignment requirements are :

|                                |       |        |
|--------------------------------|-------|--------|
| Tilt out of plane              | ± 30  | [μrad] |
| Rotation about revolution axis | ± 250 | [μrad] |
| Lateral translation            | ± 60  | [μm]   |

The thermal requirements are :

| Phase           | Item       | Load [W] | T [K] |
|-----------------|------------|----------|-------|
| Cool down       | LN2 shroud | < 500    | < 100 |
|                 | He panel   | 200      | < 25  |
| Hot Operating   | LN2 shroud | < 500    | < 100 |
|                 | He panel   | 200      | < 25  |
| Decontamination | LN2 shroud | < 500    | < 100 |
|                 | He panel   | 400      | < 100 |

## 5.2. Test Set-up

The LN<sub>2</sub> shrouds are classical copper panels, with a copper pipe brazed on it. As they are fed with LN<sub>2</sub>, there is no problem to keep them around 90 [K].

The deep cold space is simulated by an assembly of two copper plates, each with a copper pipe brazed on it as shown in figure 5. The diameter of these plates is 1630 [mm], leading to an active area of around 2 [m<sup>2</sup>]. The lower one is fed with LN<sub>2</sub> and is a thermal shield for the upper one fed with cold Helium. The Helium is provided by the KOCH 1630 liquefier/refrigerator. The gaseous refrigeration loop, providing 4.4 [K], gas is used.

The temperature monitoring is made by cryogenic diode sensors. They are home made and calibrated at the CSL low temperatures laboratory to perform the measurement from 4.2 to 300 [K] ( ref .5 ).

The distribution of the copper pipe on the plate is important for thermal homogeneity reasons. During the decontamination phase, most of the heat load is coming from the outer edge of the Sunshield Assembly where the OSR's are glued, while the Radiator is mainly in view of the centre of the Helium plate. As the radiator is the most sensitive part, the temperature distribution is then of more importance in the centre of the plate, and of less importance at the outer diameters.

At the inner part of the plate ( $\varnothing < 1200$  [mm]), the pipe is brazed , alternating in and out flow to make a sort of heat exchanger. This insure a good homogeneity in temperature. The outer diameters are brazed in serial, as the temperature increase with diameter is less important.

To achieve the emittance specification, several coatings have been tested. Then the geometrical factor has been increased by using an open honeycomb glued on the copper plate.

The Helium plate is made of a 2 [mm] thick copper plate. On it a 10 [mm] thick aluminium honeycomb is glued with Stycast 2850 FT. The cell dimension is 0.25 [inch]. The open honeycomb side is then coated with MAP PU1 paint. Measurements has been done at CSL ( ref 6 ) and the total hemispherical emittance between 90 and 15 [K] is about 0.98.

The stability is checked by direct measurements with a theodolite in target or autocollimating mode. The theodolite is set on the top of the vacuum chamber. The targets are glued on the reference points and on the detector plates. As the stability of the mirror fixation on the CIRO plate was doubtful at cold temperature, a dummy CIRO plate was polished to be itself the autocollimation mirror.

## 5.3. Test Results

Only the facility thermal results will be discussed here. The thermal performance of the PCA itself is very close to the prediction.

The fluid flows are controlled manually by adjusting needle valves on the line or on the liquefier/refrigerator in the case of the He loop.

Typical temperature results are :

| Phase | LN <sub>2</sub> Shrouds |               |               |
|-------|-------------------------|---------------|---------------|
|       | Load<br>[W]             | T mean<br>[K] | DT max<br>[K] |
| All   | 500                     | 88.2          | 8.0           |

| Phase           | Deep Cold Space He Plate |               |               |
|-----------------|--------------------------|---------------|---------------|
|                 | Load<br>[W]              | T mean<br>[K] | DT max<br>[K] |
| Start Cool Down | < 400                    | 7.9           | 6.0           |
| End Cool Down   | 50                       | 4.5           | 0.5           |
| Hot Operation   | < 200                    | 6.8           | 4.0           |
| Decontamination | 400                      | 16.3          | 5.6           |

No major problems were encountered, the liquefier/refrigerator ran for 12 days without problem. In the field of the emittance measurement, attempts were made to start the liquefaction loop in parallel with the used refrigeration loop.

Due to warm gas in the liquefaction loop, the perturbation was too large and the attempts were stopped. Thus we learned that, to use both loops, it is necessary to start liquefaction before starting the gas refrigeration loop.

The cool down time for the Helium plate to 10 [K] is about 8 [hours] while the cool down time for the CIRO plate to 80 [K] takes five days in three steps.

## 6. FOCAL PASSIVE COOLER ASSEMBLY ( FPCA ) and SEVIRI

### 6.1. Description and Specifications

During the Passive Cooler Assembly tests the detectors are replaced by dummy ones. After checking the thermal and stability performances, the detectors are mounted on the CIRO and WIRO/VHRO plates. It is then necessary to test them at their operating temperatures in the FPCA test.

After this test, the optics are integrated over the focal plane and cooler assembly. The optics are composed of a telescope and a scanning mirror. The alignments are checked and the optical calibration under a thermal environment close to the flight environment is achieved.

From a thermal point of view, the FPCA test set-up is only using a part of the SEVIRI set-up.

For SEVIRI, the temperature distribution of the surroundings is complex. Radiative surroundings and conductive interfaces for the Main Unit, the Sunshield and the Electronics must be regulated independently. The thermal influence of the satellite through the optical aperture has also to be simulated by a thermal baffle called the Aperture Thermal Simulator (ATS). The GSE requires also two LN<sub>2</sub> lines and one regulated GN<sub>2</sub> line.

Typical thermal requirements are :

| <b>Item</b>       | <b>T min<br/>[°C]</b> | <b>T max<br/>[°C]</b> |
|-------------------|-----------------------|-----------------------|
| Main Unit + X I/F | + 3                   | + 36                  |
| Main Unit + Y I/F | - 12                  | + 30                  |
| Main Unit – Y I/F | - 12                  | + 31                  |
| Sunshield I/F     | - 22                  | + 32                  |
| Upper Shrouds     | - 20                  | + 25                  |
| Lower Shrouds     | - 18                  | + 31                  |
| ATS + X           | + 10                  | + 46                  |
| ATS – X           | + 9                   | + 41                  |
| Electronic PU     | - 20                  | + 50                  |
| Electronic MDU    | - 20                  | + 50                  |
| Electronic FCU    | - 20                  | + 50                  |

The Deep Cold Space Helium plate has mainly the same thermal specifications as for the PCA test, i.e. being under 25 [K] during the whole test, and under 50 [K] with the 400 [W] heat load during the decontamination phase.

## 6.2. Test Set-up.

All these constraints lead to a system with 24 temperature control loops. They can be divided into different types :

- 1) Helium loop :
  - the Deep Cold Space panel;
- 2) GN<sub>2</sub> regulated channels :
  - the 5 upper shrouds,
  - the 4 lower shrouds,
  - the OGSE integrating sphere;
- 3) Full LN<sub>2</sub> loops :
  - the Deep Cold Space guard,
  - the electrical regulation heat sink,
  - the 2 OGSE black bodies;
- 4) Regulated heaters with heat sink :
  - the 3 Main Unit I/F, - the 3 electronic units;
- 5) Regulated heaters without heat sink :
  - the 2 ATS zones, - the Sunshield I/F.

To give an idea of the dimensions, the height of the thermal shrouds is about 2.8 [m] while the bottom area is a 2.5 \* 2.2 [m<sup>2</sup>] rectangle.

The Helium and LN<sub>2</sub> loops are controlled manually by adjusting needle valves. GN<sub>2</sub> loops and electrical heaters are regulated by the thermal system computer with PID laws. Exception is done for the Sunshield I/F that is regulated with an independent regulator.

The same Deep Cold Space is used for all the tests. For planning questions, a second assembly has been manufactured to allow parallel testing of the FPCA set-up in FOCAL 3 while the SEVIRI set-up is under integration in FOCAL 5 see figure 6.

One must note that, if integration periods can overlap, the vacuum periods must be separated, as far as the liquefier/refrigerator is at its maximum rate during cool down or decontamination phases.

Alignment measurements are also done through a combined theodolite-autocollimator set-up from the top of the vacuum chamber.

### 6.3. Test Results

The SEVIRI STM test has already been performed. In parallel, a FPO test was done, and liquid Helium was successfully produced while running the refrigeration loop.

The Deep Cold Space results are very similar to the PCA test, and mainly all the requirements are met.

## 7. CONCLUSIONS

About 20 years ago, IAL Space, renamed CSL now, tested the radiometer of the first Meteosat satellite. At this time, an open honeycomb black coated was also used, fed with liquid Helium provided by the University of Liège.

From this time on, in collaboration with pr. R. Blanpain<sup>†</sup> from the University of Liège, a Helium liquefier/refrigerator has been connected to the vacuum chambers. The Helium gas is used in closed loops, i.e. compressed, purified and liquefied before used again.

This system allows the testing of large space instruments in the cryogenic range, sometimes with special solutions.

## 8. REFERENCES

1. M. HENRIST, A. CUCCHIARO, I. DOMKEN, J.P. MACAU, The Space Simulation Facilities at IAL Space, proc. of the 16<sup>th</sup> Space Simulation Conference, Albuquerque, NM, 1990, NASA CP 3096
2. O. TELLER, A. CUCCHIARO, P. JAMOTTON, Development of a Thermal Regulation System for Space Simulation, to be published.
3. A. CUCCHIARO and al. , Development of a Cryogenic Laboratory for the Testing of the ISO Optical Subsystem, 24<sup>th</sup> International Conference on Environmental Systems, SAE-941275, 1994, Friedrishafen, G.
4. H. PETERSEN, F.J.H.M. TEUNISSEN, H.BARBOSA VAZQUEZ, Passive Cryogenic Cooler for MSG SEVIRI Design and Performance, 6<sup>th</sup> European Symposium on Space Environmental Control Systems, 20-22/05/97, Noordwijk, NL.
5. A. CUCCHIARO, R. BLANPAIN, C. JAMAR, ISO Thermometry Phase B Report, doc. SR-IAL-ISO-87002, IAL Space, 1987.
6. P.JAMOTTON, A. CUCCHIARO, D. DEMARET, H. BALBEUR, Measurement of the Total Hemispherical Emittance of Different Surfaces at Temperature from 4.4 to 200 [K], 6<sup>th</sup> European Symposium on Space Environmental Control Systems, 20-22/05/97, Noordwijk, NL.

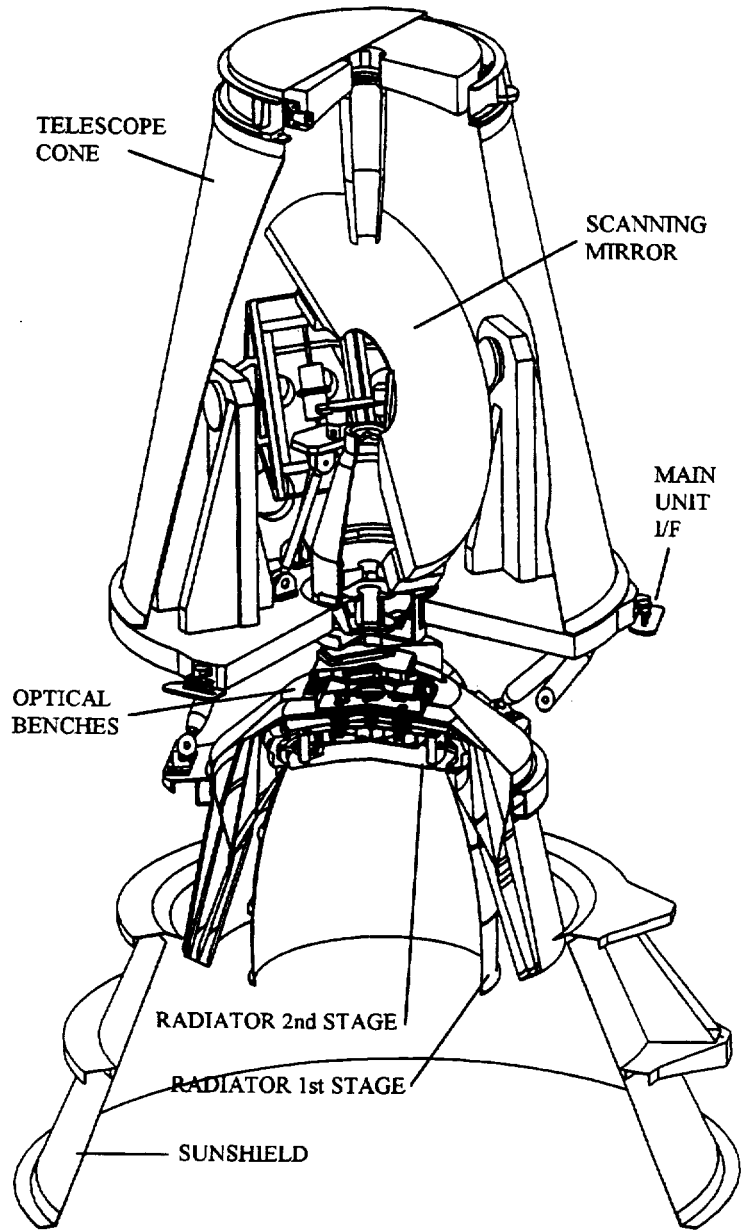


Figure 1. SEVIRI Overview

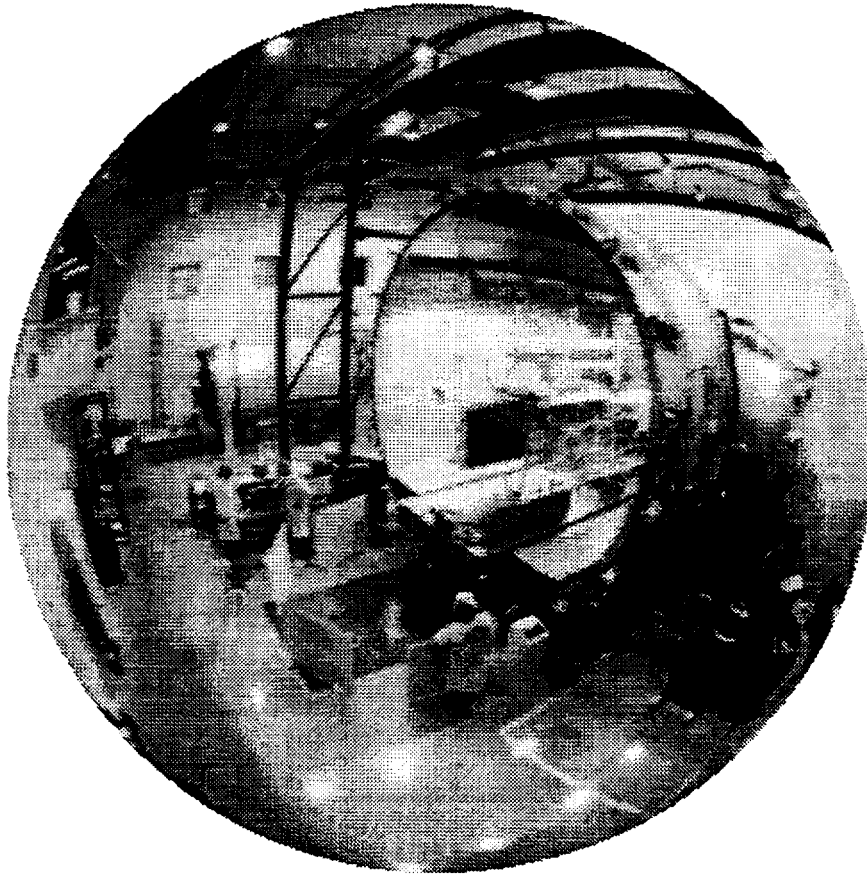


Figure 2. CSL FOCAL 5 Overview

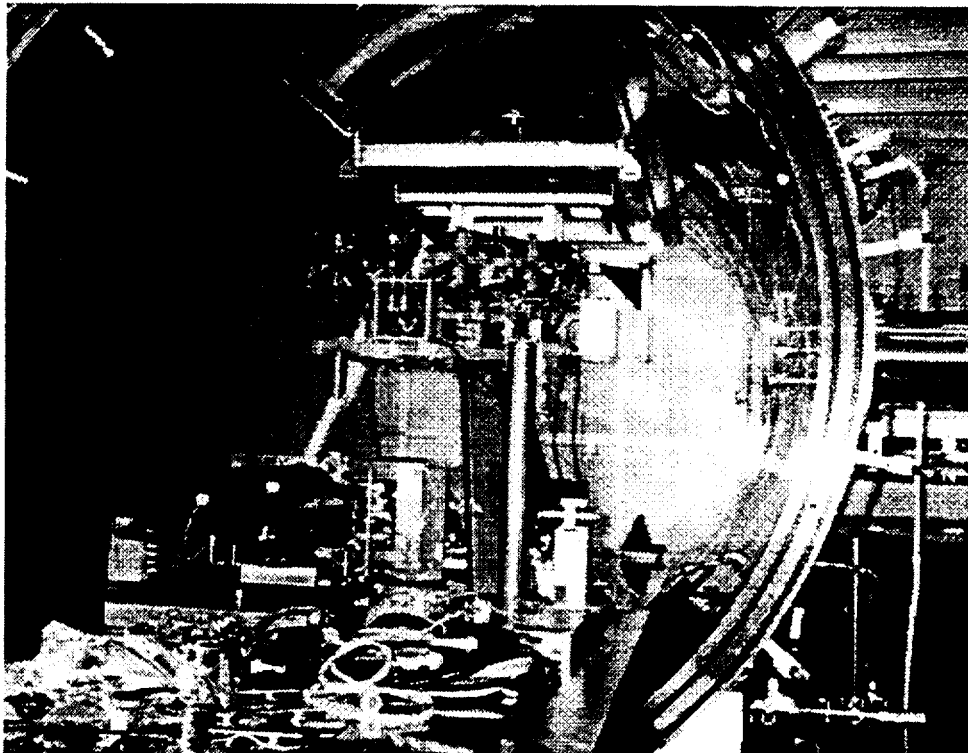


Figure 3. FPO Set-up Overview

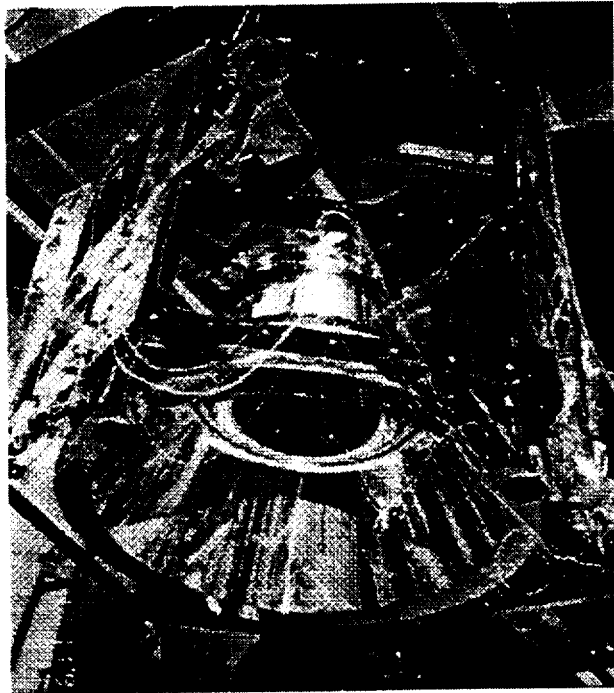


Figure 4. PCA Assembly.

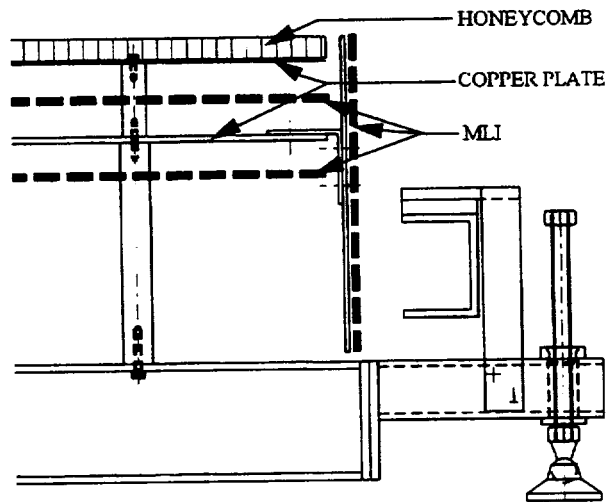


Figure 5. DCS geometry.

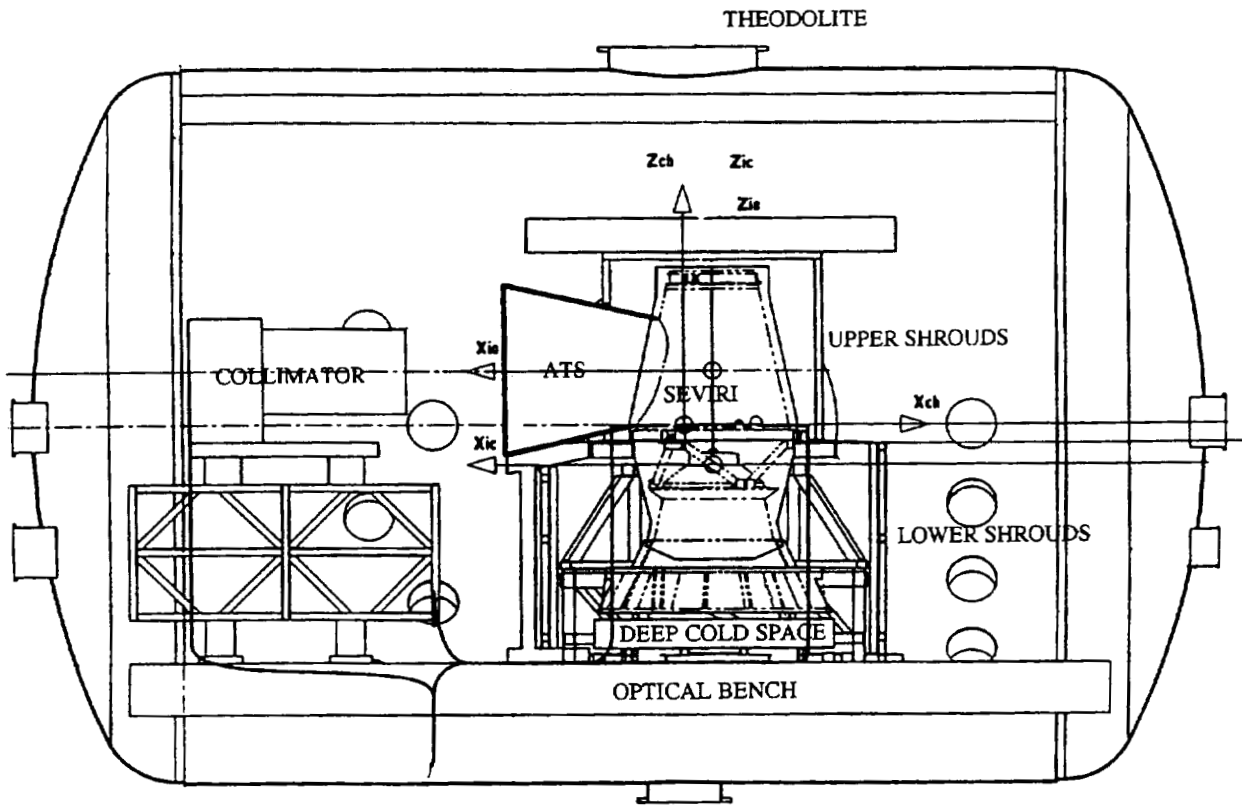


Figure 6. SEVIRI test configuration.



THERMAL VACUUM TESTING OF  
THE MARS SURVEYOR PROGRAM AND STARDUST SPACECRAFT

William N. Breeden III  
Lockheed Martin Astronautics  
Denver, Colorado

ABSTRACT

Following the success of the Mars Global Surveyor (MGS), Lockheed Martin Astronautics (LMA) in Denver, CO was awarded two more contracts by NASA to produce spacecraft under the faster, better, cheaper initiative. The first contract, the Mars Surveyor Program (MSP), includes two vehicles, an orbiter and a lander. The Orbiter will launch on December 10, 1998 and move in to orbit around Mars on September 23, 1999. The lander will launch on January 3, 1999 and land on the Martian surface on December 3, 1999. The second contract, Stardust, is the space mission that will fly close to a comet and, for the first time ever, bring cometary material back to Earth for analysis.

In support of these two programs, four system level thermal vacuum tests were performed in 1998, three for MSP and one for Stardust. The MSP Orbiter was tested in LMA's 8.8m x 19.8m (29' x 65') solar thermal vacuum chamber. The MSP Lander was tested in two configurations. The Lander was tested in its cruise configuration in LMA's 8.8m x 19.8m (29' x 65') solar thermal vacuum chamber. The landed configuration was performed in LMA's 5.5 m x 6.1m (18' x 20') thermal vacuum chamber. The Stardust spacecraft will undergo one test in LMA's 5.5 m x 6.1m (18' x 20') thermal vacuum chamber.

INTRODUCTION

This paper will discuss the four system level thermal vacuum tests conducted for the MSP and Stardust spacecraft. For each test, this paper will present the test objectives, test configuration, test profile, and test results. As the paper indicates, meeting the cost and schedule constraints of these two faster, better, cheaper programs required designing tests around existing capabilities and test fixtures to the extent possible.

The next sections will present a brief mission overview of the two programs and a brief description of the system level thermal vacuum testing performed for each. The Mars Surveyor Program will be discussed first followed by Stardust.

### Mission Overview of Mars Surveyor Program

The Mars Surveyor Program (MSP) is the next generation of spacecraft to be sent to Mars. The program consists of both an orbiter and a lander. The two will be launched separately on Delta launch vehicles. The MSP mission will build on the knowledge gained by the Mars Global Surveyor and Mars Pathfinder missions. The MSP orbiter, which has been named the Mars Climate Orbiter, will launch in December 1998 and arrive at Mars 10 months later. Following a series of aerobraking maneuvers, the orbiter will achieve a stable orbit around Mars, and then use atmospheric instruments and cameras to provide detailed information about the surface and climate of Mars. The MSP lander, which has been named the Mars Polar Lander, will launch in January of 1999, one month after the orbiter. It will land near the southern polar cap on Mars. The lander is equipped with cameras, a robotic arm and instruments to measure the Martian soil composition. Two small microprobes on the lander will penetrate into the Martian subsurface to detect water ice.

The two MSP spacecraft, the orbiter and the lander, obviously will be subjected to very different environments. This meant that at least two different system level thermal vacuum tests would be necessary. Furthermore, the lander is exposed to two very different environments. The environment during the cruise stage of the mission is very different from the landed environment. As a result, a total of three system level thermal vacuum tests were conducted in support of MSP:

1. MSP Orbiter Thermal Vacuum
2. MSP Lander Cruise Stage Thermal Vacuum
3. MSP Lander Landed Thermal Vacuum

### Mission Overview of Stardust

Stardust is the fourth of NASA's Discovery missions. It is a comet sample return mission. This will be the first sample return mission from beyond the Earth-Moon system. Stardust will launch in 1999 onboard a Delta launch vehicle. The mission will collect interstellar dust in 2000 and 2002, and then encounter Comet P/Wild 2 in 2004. It will collect comet dust and possibly obtain high resolution images of the comet's nucleus. The Sample Return Capsule (SRC) will return to Earth in 2006 with cometary and interstellar dust.

The Stardust spacecraft will undergo a single system level thermal vacuum test.

## TEST FACILITIES AND EQUIPMENT

### Space Simulation Lab Equipment

The following chambers and equipment were utilized in support of thermal vacuum testing for these spacecraft:

Large Thermal Vacuum Chamber: The 8.8m dia x 19.8m high top loading chamber is cylindrical in shape. It is a high vacuum, chamber capable of being evacuated to a pressure of  $1 \times 10^{-5}$  torr or less. It has a work space of 7.9m x 14.0m. The chamber is equipped with a thermal shroud which can be flooded with LN<sub>2</sub> or controlled with GN<sub>2</sub> between -155°C and 38°C.

4.8m dia Solar Simulator: The 4.8m Solar Simulator system is part of the 8.8m dia x 19.8m high thermal vacuum chamber. The system is capable of producing a cylindrical test volume 4.8m diameter and 4.8m high with high fidelity and variable intensity. It is an off-axis, collimated beam system

capable of .35 to 1.4 solar constants, with beam uniformity of +/- 5%. The beam is spectrally filtered for close air mass zero solar spectral match.

Two Axis Gimbal: The Gimbal is a stainless steel support structure that is 3.8m high and has a support beam 6.4m long. The position of a test article mounted to the gimbal turntable can be controlled in two axes. The beam can tilt the test article at varying speeds from .018 RPM to 3 RPM. The turntable can rotate 360° at varying speeds from .018 RPM to 3 RPM both forward and reverse. The structure is capable of supporting a dynamic load of 2268 kg and has a maximum moment capability of 2268 kg at 1.2m = 27,120 nm. The gimbal system is computer driven to provide programmable control to both axes.

Thermal Environment Simulator (TES): The TES is a thermally controlled enclosure. The enclosure is 11m high and has an octagonal cross section which measures 4.9m across. The TES has a total of 56 independently controlled temperature zones. Each zone consists of a panel of multiple heated louvers. The louvers can be rotated between 0° and 90° to allow the test article mounted inside the enclosure to view either the closed louvers which can be controlled between +121°C and -157°C or the chamber shroud. The 48 side panels are easily removed from the TES and can be operated independently from the system. Each side panel measures approximately 1.8m x 1.8m. The TES is six sections high. The top two sections of the TES can be removed as a unit.

5.5m x 6.1m Thermal Vacuum Chamber: The 5.5m x 6.1m chamber is a high vacuum, chamber capable of being evacuated to a pressure of  $1 \times 10^{-5}$  torr or less. It has a work space of 4.9m x 5.6m. The chamber is equipped with a thermal shroud which can be flooded with LN2 or controlled with GN2 between -157°C and +121°C.

#### Program Owned Test Fixtures

In addition to the lab's resources, several existing program owned test fixtures were utilized. These fixtures were originally built for the MGS program. These include the following:

Gimbal Interface: This interface plate mounts to the launch vehicle interface of the spacecraft. It was originally designed to mount the MGS to the two axis gimbal. It was also used to mount the MGS to the spin table for spin balancing the spacecraft.

Aft Cooling Plate: This thermally controlled plate mounts inside the gimbal interface and creates the desired thermal environment for the aft end of the spacecraft. The plates are heated with heater tape or cooled with LN2.

Gimbal Cryo Shields: These two thermally controlled plates mount to the gimbal on either side of the spacecraft. They were originally designed to shield the spacecraft from the thermal effects of the gimbal. The plates are heated with heater tape or cooled with LN2.

Planet Simulator: The simulator consists of four thermally controlled plates. Each plate measures 1.5m x 1.5m. Together they form a 3m x 3m temperature controlled sink. The plates are heated with heater tape or cooled with LN2.

### MSP ORBITER THERMAL VACUUM TEST

#### Test Objectives

The objectives of the MSP Orbiter thermal vacuum test were as follows:

1. Validate the thermal behavior of the MSP spacecraft in all bounding mission states except aerobraking.

2. Validate integrated spacecraft functionality by performing the following:
  - a. Perform two spacecraft functional tests.
  - b. Perform thermal "transient" cases.
  - c. Validate heater set-points to the maximum extent possible.
3. Gather PMIRR/Spacecraft integrated performance data in a space-like environment.
4. Gather MARCI/Spacecraft integrated performance data in a space-like environment.
5. Provide a medium for removal of all residual IPA from propulsion system.
6. Provide an overall system level thermal workmanship test.

Test Configuration

The MSP orbiter thermal vacuum test was performed in the 8.8m x 19.8m chamber. Two separate mission phases, cruise and mapping, as well as a cruise safing configuration were simulated. The spacecraft was mounted to the Two Axis Gimbal utilizing the Gimbal Interface that was built for MGS. This configuration allowed the orbiter to be positioned at the appropriate sun angle for each phase of the mission. This test also utilized the Planet Simulator that was designed and built for MGS. During the mapping sequence, the planet environment was simulated by this system. In order to reduce the thermal effects of the Two Axis Gimbal, three thermally controlled plates from the MGS test were used. These were the aft cooling plate and the two gimbal cyroshields. Each of these plates was capable of being heated or flooded with LN<sub>2</sub>. Figure 1 shows a top view of the test configuration. Figure 2 shows a side view of the test configuration with the gimbal oriented in the initial position for the first phase of the test.

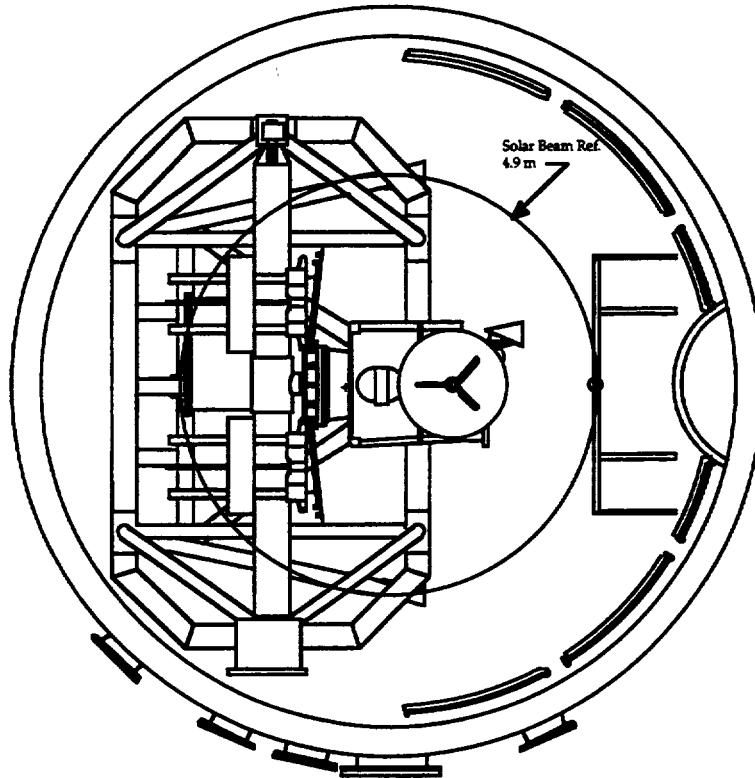


Figure 1 - MSP Orbiter Thermal Vacuum Test Configuration - Top View

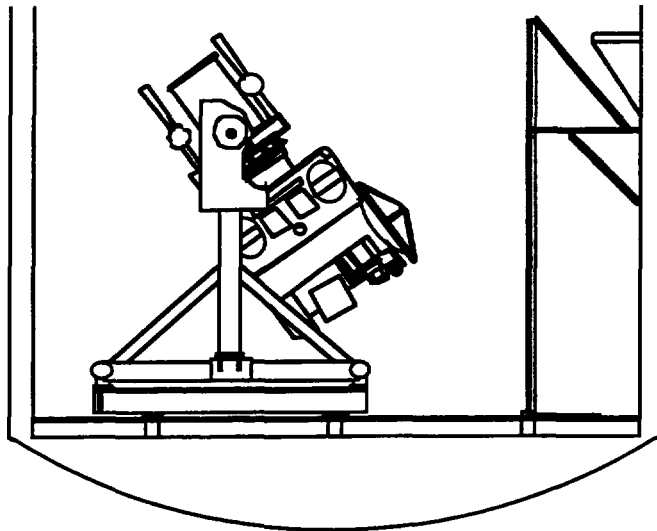


Figure 2 - MSP Orbiter Thermal Vacuum Test Configuration  
Initial Position - 144° Inner/Outer Cruise Stage, Case 1 and 2

Test Profile

The deep space environment was created by flooding the chamber shroud with LN<sub>2</sub> and evacuating the chamber to a minimum of 1x10<sup>-5</sup> torr. The intent of the test was to simulate two distinct mission phases; cruise and mapping. During each phase, the gimbal was used to obtain the correct spacecraft orientation relative to the solar beam. The solar intensity was varied, and the planet simulator was used to simulate the environmental effect of the Martian planet during the mapping phase. During each phase, the spacecraft was powered to a state which is nominally associated with that particular phase of the mission. Figure 3 shows the test profile. The test required five different orientations of the spacecraft. These orientations are shown in figure 4

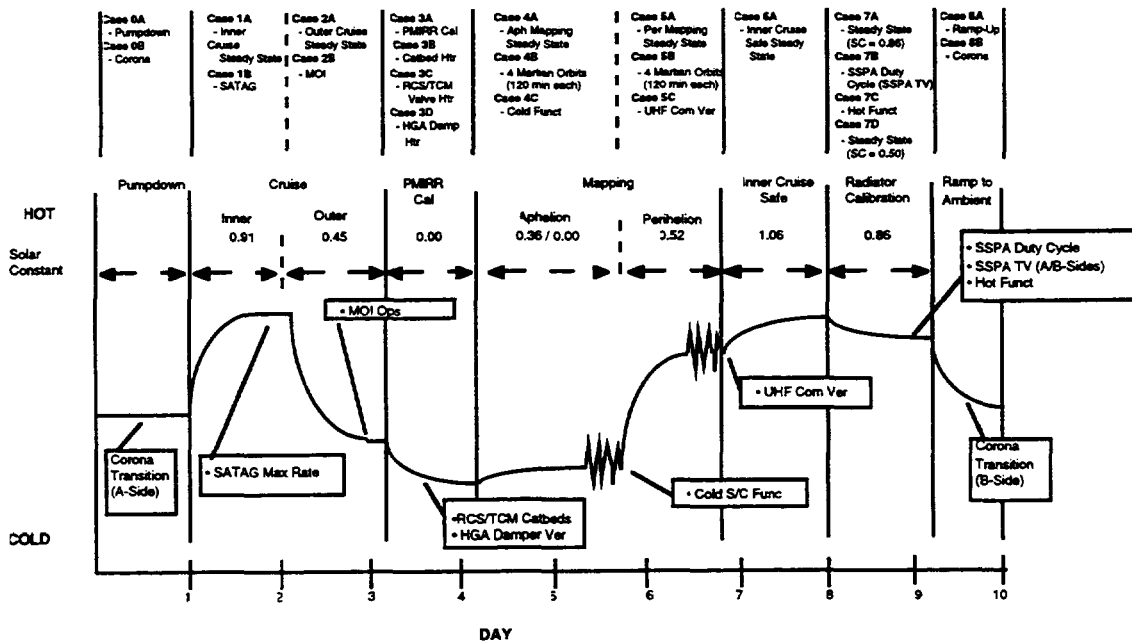
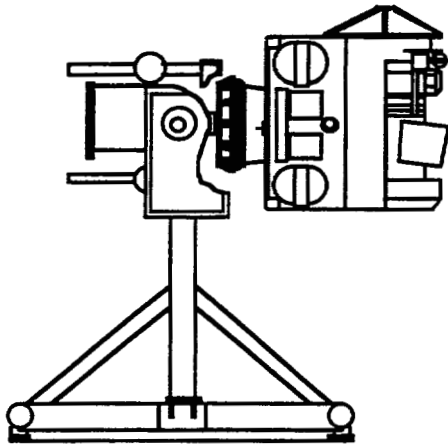
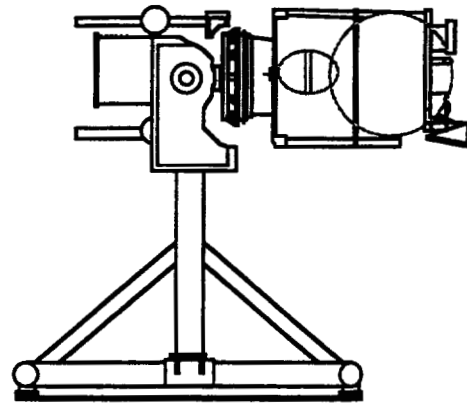


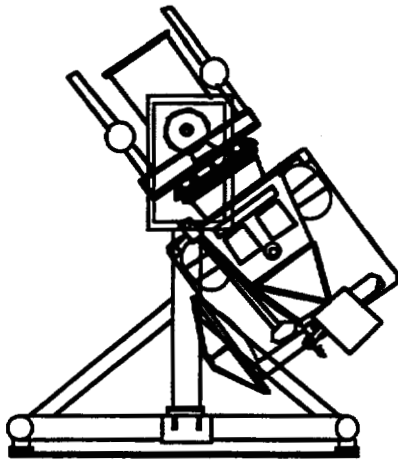
Figure 3 - MSP Orbiter TV Test Profile



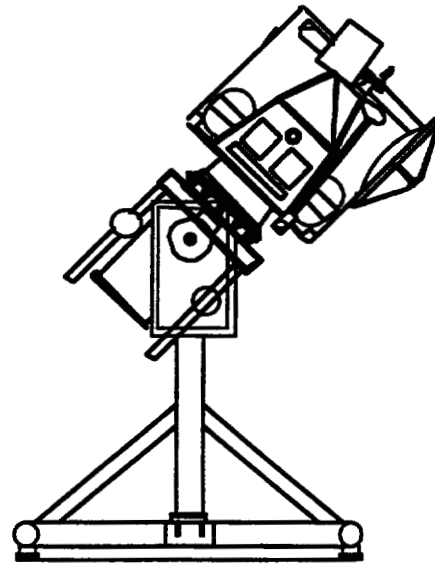
Second Position - 90° PMIRR Calibration Stage, Case 3



Third Position - 90° Aphelion/Perihelion Mapping Stage, Case 4 and Case 5



Fourth Position - 144° Inner Cruise Safe Stage, Case 6



Fifth Position - 45° Radiator Calibration Stage, Case 7

Figure 4 - MSP Orbiter TV Spacecraft Orientations

### Test Results

The initial MSP orbiter test began on April 13, 1998. The test was returned to ambient on April 24, 1998. During this initial test, an anomaly occurred involving the PMIRR instrument. After determining the cause of the failure, a partial re-test was run from April 27, 1998 to April 30, 1998. Including pumpdown and return to ambient operations, the initial test ran for 264 hours, and the re-test ran for an additional 67 hours.

## MSP LANDER CRUISE STAGE THERMAL VACUUM

### Test Objectives

The objectives of the MSP Lander Cruise Stage thermal vacuum test were as follows:

1. Acquire thermal data that will sufficiently validate the thermal behavior of the MSP Lander while in the cruise configuration for all bounding mission states.
2. Validate integrated spacecraft functionality by performing the following:
  - a. Perform two spacecraft functional tests.
  - b. Perform thermal "transient" cases.
  - c. Validate heater set-points to the maximum extent possible.
  - d. Validate spacecraft sensitivity to heatshield temperature variation.
3. Provide an overall system level thermal workmanship test.

### Test Configuration

The MSP Lander Cruise Stage thermal vacuum test was performed in the 8.8m x 19.8m chamber. A single mission phase, the cruise phase, was simulated. The spacecraft was placed on a stand with its heatshield removed. This assembly was installed inside the top two sections of the TES. The lid of the TES was removed in order to allow the beam of the solar simulator to irradiate the spacecraft. The appropriate sun angles for inner and outer cruise were simulated with the solar simulator and supplemented IR radiation from the TES. The chamber configuration for this test is shown in figure 5.

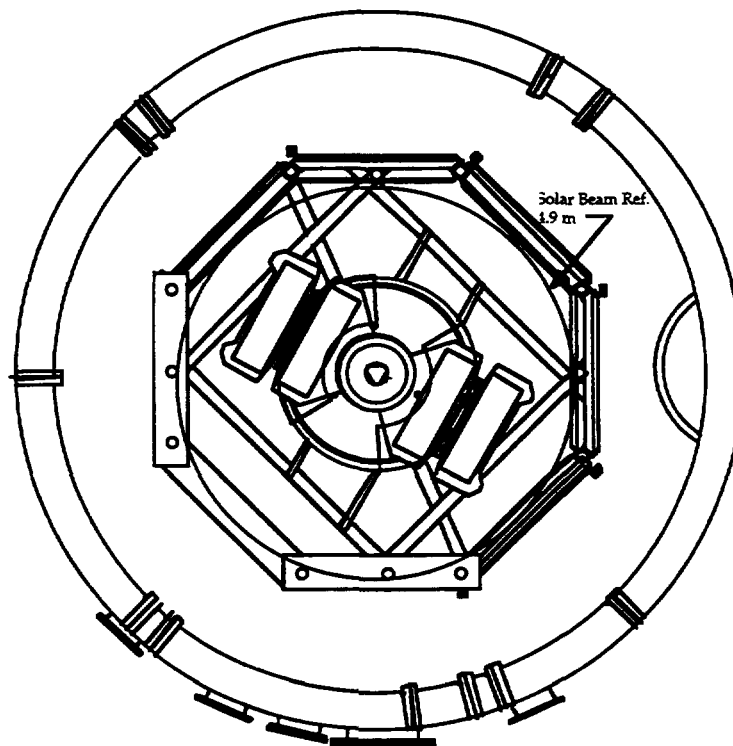


Figure 5 - MSP Lander Cruise Stage Thermal Vacuum Test Configuration - Top View

## Test Profile

The deep space environment was created by flooding the chamber shroud with LN<sub>2</sub> and evacuating the chamber to a minimum of 1x10<sup>-5</sup> torr. The intent of the test was to simulate the cruise portion of the lander mission. During each cruise phase, the proper environment was created by varying the intensity of the solar simulator and supplementing the solar beam with additional IR energy from the TES. Figure 6 shows the test profile.

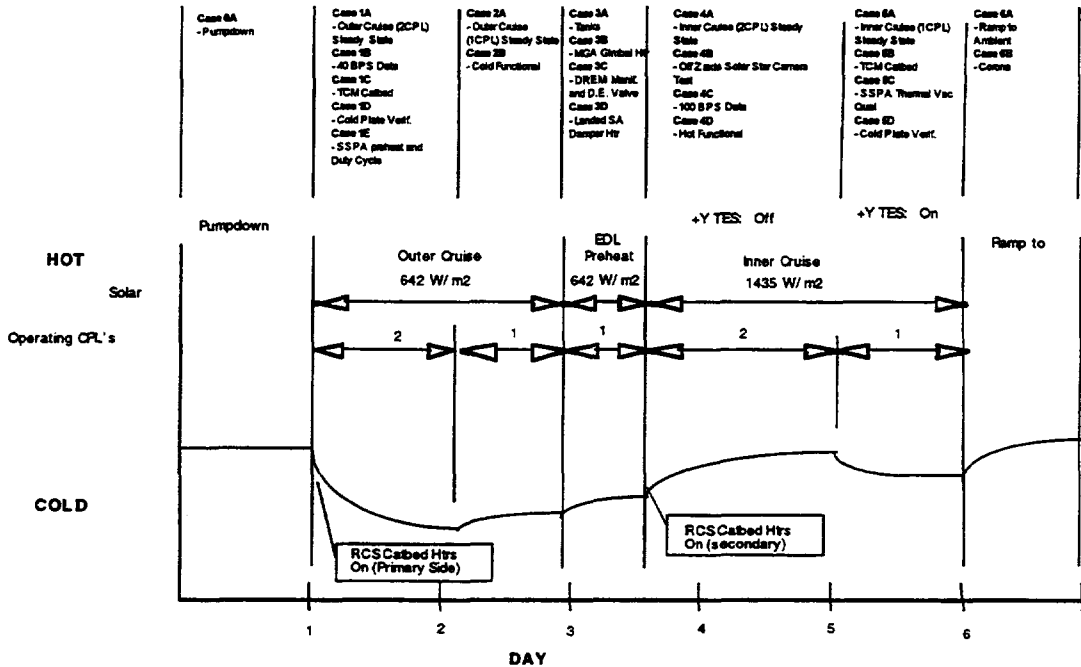


Figure 6 - MSP Lander Cruise Stage Thermal Vacuum Test Profile

## Test Results

The test began on May 17, 1998. The test led to the discovery of a problem with a critical component of the spacecraft's thermal control system. The Capillary Pumped Loops (CPL) failed to function as designed. The test was returned to ambient on May 19, 1998, 72 hours after starting. As a result of the failed CPLs, the lander's thermal control system was redesigned to utilize a passive thermal control scheme. The cruise stage was scheduled to be re-tested following this modification.

At the time this paper was written, the thermal vacuum test of the spacecraft's new configuration had not been conducted. In the new test, the heat shield will be installed and the spacecraft will be suspended in the 8.8m x 19.8m chamber as shown in figure 7. The solar simulator will again be utilized, but the TES will not be used. Testing is scheduled to be run in early September of 1998.

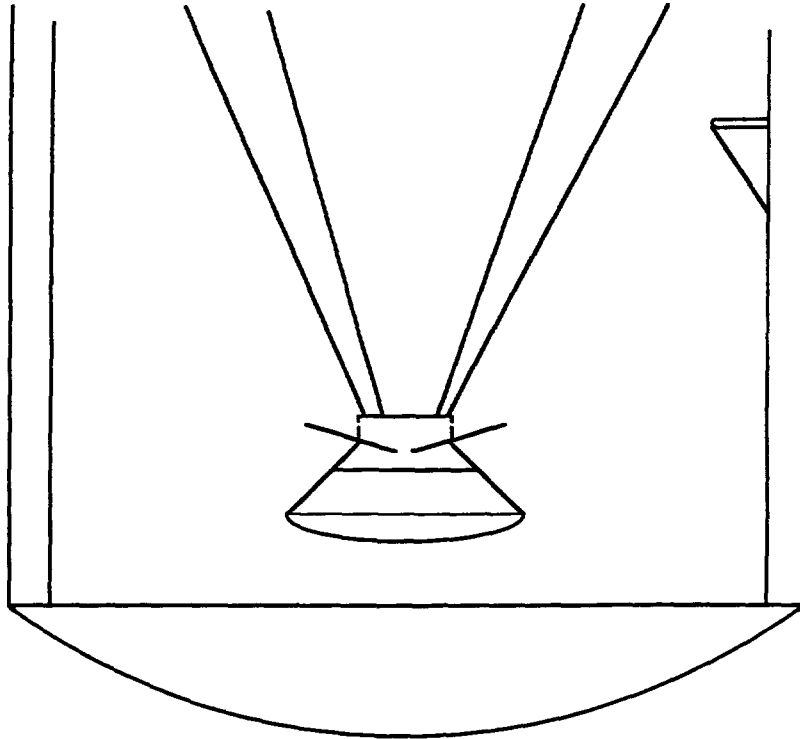


Figure 7 - MSP Cruise Stage Planned Re-test Configuration

## MSP LANDER LANDED THERMAL VACUUM

### Test Objectives

The objectives of the MSP Lander Landed thermal vacuum test were as follows:

1. Acquire thermal data that will sufficiently validate the thermal behavior of the MSP Lander in all of the major mission states.
2. Validate integrated spacecraft functionality in the Martian environment by performing flight-like sequences or other functional tests.
3. Validate heater set-points to the maximum extent possible.
4. Provide an overall system level thermal workmanship test.
5. Validate thermal design margin as a function of the vehicle performance in the Martian environment.
6. Validate science and spacecraft power consumption models at the hot and cold environments.

### Test Configuration

The MSP Lander Landed Thermal Vacuum test was performed in the 5.5m x 6.1m chamber. The Martian surface environment was created by driving the shroud to a sky temperature of  $-133^{\circ}\text{C}$ , back-filling the chamber with  $\text{GN}_2$  to 8 torr, and simulating the solar irradiance with six TES panels which enclosed the spacecraft. The TES panels were controlled to simulate temperature ranges from  $-30^{\circ}\text{C}$ , representing a hot Martian day, to  $-75^{\circ}\text{C}$ , representing a cold Martian day. The chamber remained at 8 torr for the majority of the test. During high pressure thermal balance cases, the pressure was raised to 20 torr. Figure 8 and figure 9 show the test configuration.

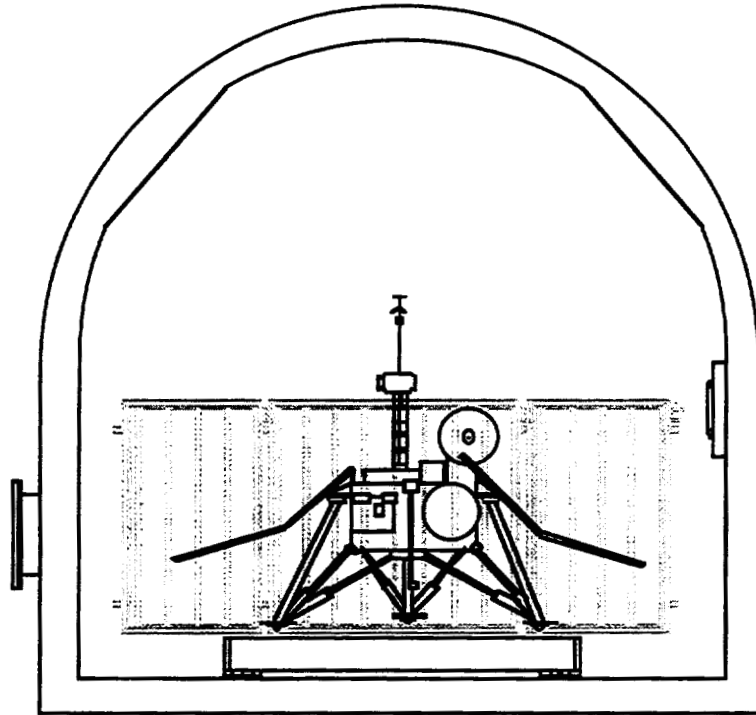


Figure 8 - MSP Lander Landed Thermal Vacuum Test Configuration - End View

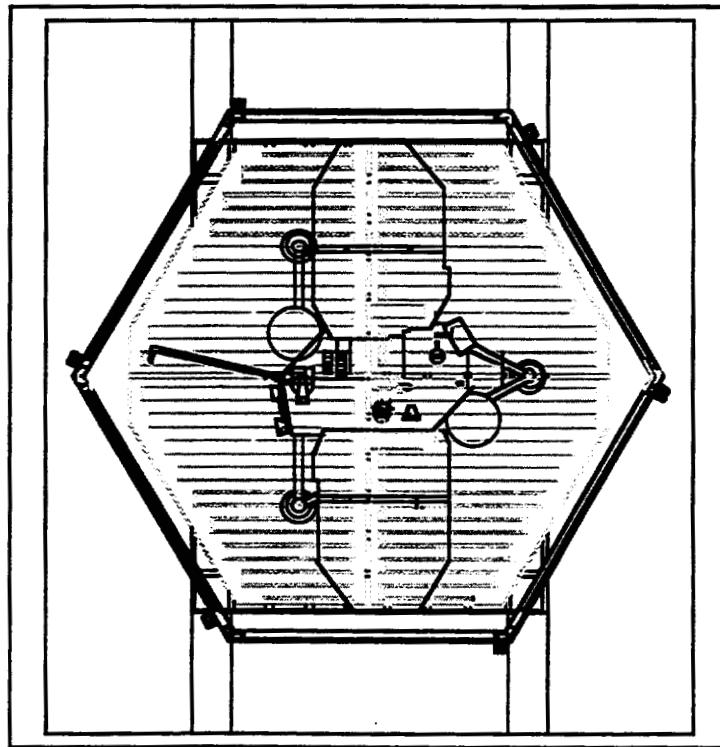


Figure 9 - MSP Lander Landed Thermal Vacuum Test Configuration - Top View

## Test Profile

As previously stated, the Martian surface environment was created by driving the shroud to the anticipated sky temperature of  $-133^{\circ}\text{C}$ , simulating the Martian atmosphere by back-filling the chamber with  $\text{GN}_2$  to 8 torr, and simulating the solar irradiance with six independently controlled TES panels. The Lander was operated through a "hot" Martian day and several "cold" Martian days. Figure 10 shows the test profile.

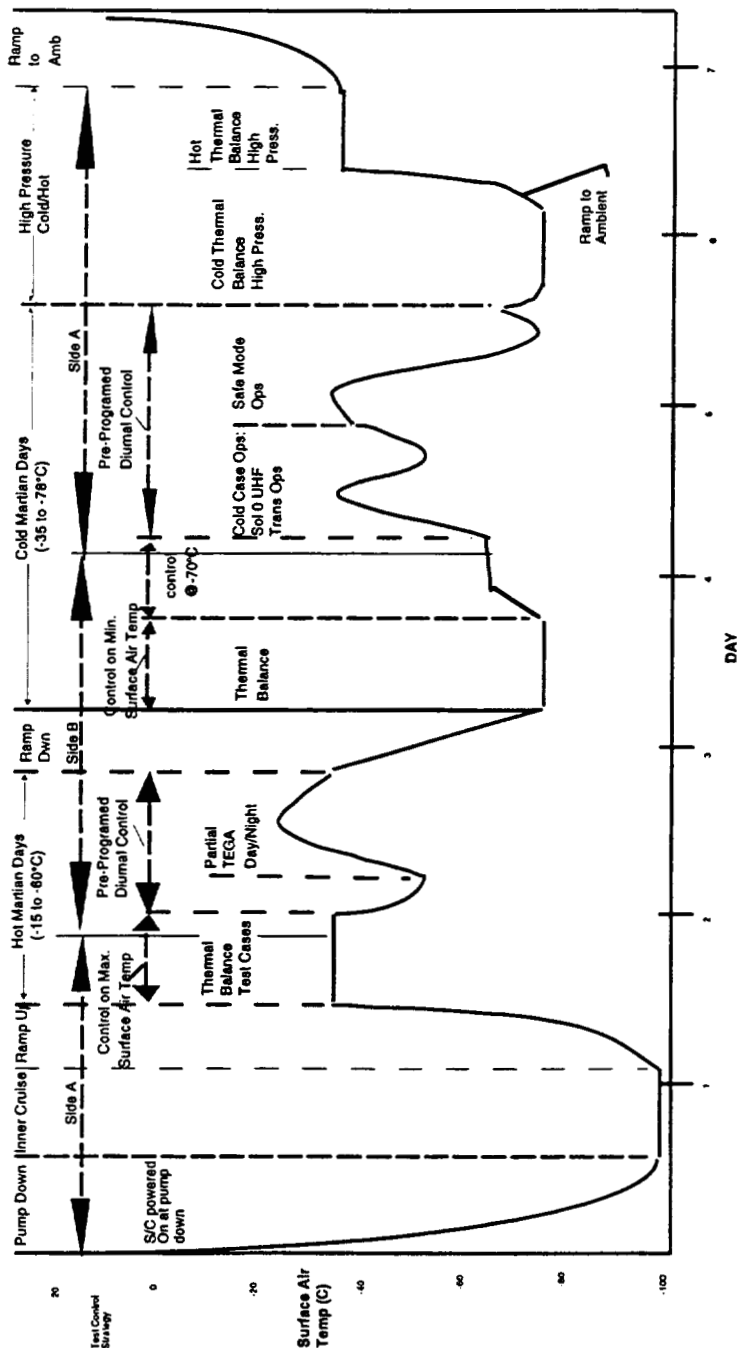


Figure 10 - MSP Lander Landed Thermal Vacuum Test Profile

## Test Results

The test of the MSP Lander in its landed configuration began on July 26, 1998. Testing was successfully completed on August 2, 1998. The total test duration including pumpdown and return to ambient activities was 168 hours.

## STARDUST THERMAL VACUUM

### Test Objectives

The objectives of the Stardust thermal vacuum test were as follows:

1. Acquire thermal data that will sufficiently validate the thermal math model predictions of the thermal behavior of the Stardust spacecraft in all of the major mission states.
2. Validate integrated spacecraft functionality and the performance of the flight thermal subsystem.
3. Validate heater set-points to the maximum extent possible.
4. Provide a medium for removal of all residual IPA from the propulsion subsystem.

### Test Configuration

The Stardust Thermal Vacuum test will be performed in the 5.5m x 6.1m chamber. The spacecraft will be tested in a vertical orientation. It will be mounted to the chamber's air bearing cart using the MGS Gimbal Interface. The MGS Aft Cooling Plate and Gimbal Cryo Shields will serve as the +X sink panel and will be controlled from -180°C to 50°C. The solar arrays will be replaced by solar array simulators. The simulators will be designed to produce a temperature of -120°C to 90°C. The MGS Planet Simulator will serve as a +Z sink panel which will provide the thermal heating to simulate the hot spacecraft environment. The panel will be controlled from -120°C to 90°C. The test configuration is depicted in figure 11 and figure 12.

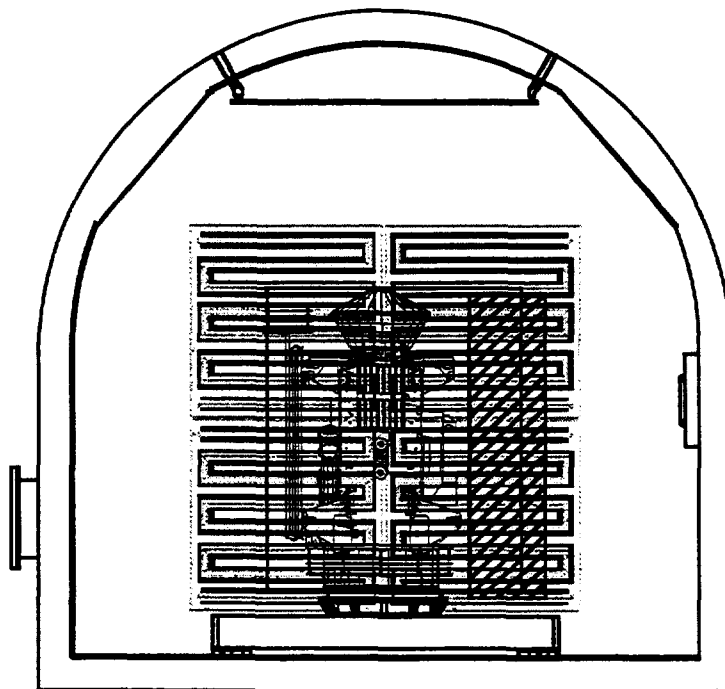


Figure 11 - Stardust Thermal Vacuum Test Configuration - End View

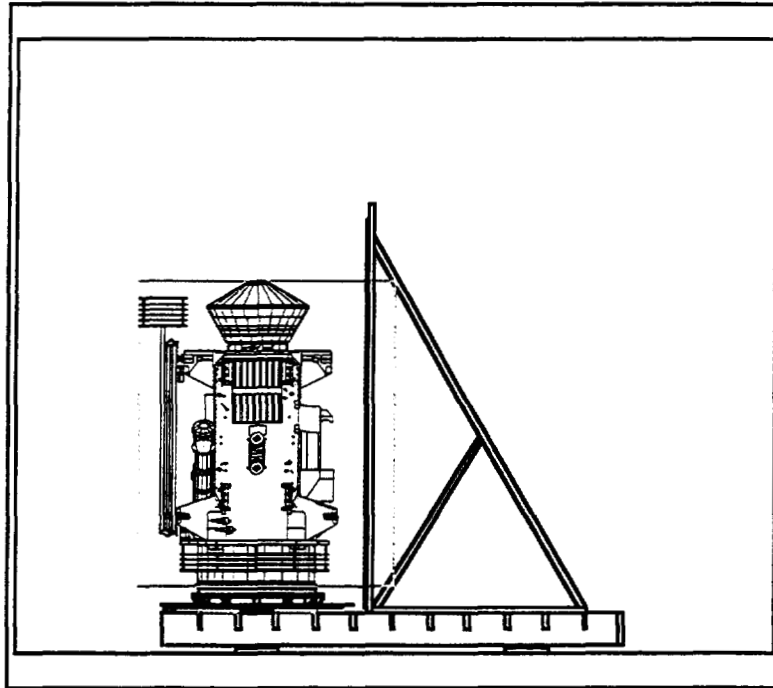
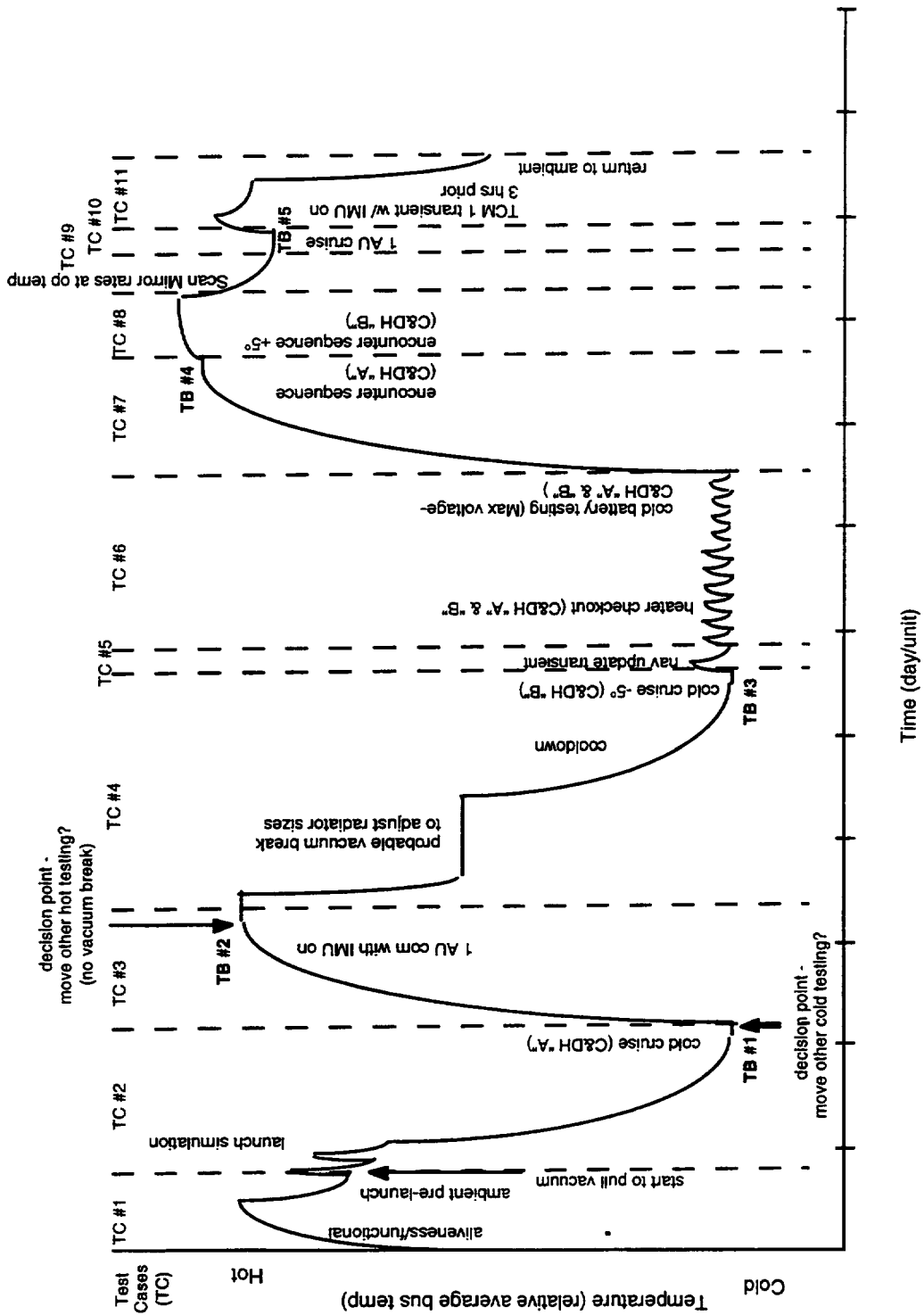


Figure 12 - Stardust Thermal Vacuum Test Configuration - Side View

#### Test Profile

The deep space environment will be created by flooding the chamber shroud with LN<sub>2</sub> and evacuating the chamber to  $5 \times 10^{-5}$  torr or less. The intent of the test is to simulate mission phase flight operations. The proper environment will be created by using the sink panels and simulators. Figure 13 shows the test profile.



**Test Results**

As of the date of this paper, the Stardust System Level Thermal Vacuum had not been run. The test is currently scheduled to be run in September of 1998.

## CONCLUSION

Performing thermal vacuum testing of spacecraft under the faster, better, cheaper initiative presents a great challenge. Conducting test programs for multiple spacecraft concurrently makes the task all the more difficult. By utilizing existing facility capabilities and designing tests around existing test fixtures, the challenge can be met. This often requires compromise on the part of program thermal engineers. By heavily relying on the work done to support the Mars Global Surveyor, Lockheed Martin Astronautics successfully designed spacecraft level thermal vacuum tests for the MSP Program and Stardust spacecraft that were faster, cheaper, and better.



# A NEW METHOD FOR THERMAL VACUUM TESTS TELECOMMUNICATION SPACECRAFT THE SIMULATION OF THERMAL SINK

Jean-Louis MARCÉ  
Joseph MERLET  
Yannick CHARLES  
INTESPACE<sup>(1)</sup>

B. POULAIN  
Matra Marconi Space France<sup>(2)</sup>

J. GAYRARD  
Centre National  
d'Études Spatiales<sup>(3)</sup>

TOULOUSE, France

## ABSTRACT

The solar simulation chamber has some limitations well known : diameter of solar beam, performance of attitude simulator, of thermal generator, value of irradiation. Their investment costs are high and there is a strong strength : the reduction of test cost which implies to mix functional tests with thermal balance test.

A new method is described in this paper which overcomes these difficulties. This method is called simulation of thermal sink.

The paper presents :

- The comparison between various simulation methods in thermal vacuum test versus the requirements of test of telecommunication spacecraft with a conclusion of the interest of the simulation of thermal sink.

- The studies which lead to a prototype of a thermal generator. Various design choices are explained and justified. In particular, the thermo-hydraulic studies of the shroud which simulates the thermal sink have allowed an optimisation of the pressure drop, the thermal gradient and the geometry of the fluid loop.

- The specification prototype of the thermal generator, its implementation on the SIMMER facility, the results of assessment tests.

- The design of the operational thermal generator and the final implementation.

## INTRODUCTION

Apart from standard validation needs for the thermal control of a telecommunications satellite related firstly to competitiveness constraints (the need to reduce costs of using test means, limitation of the duration and grouping of vacuum thermal and vacuum-sunlight tests), and secondly to special needs (verification of payload performances in the winter and summer seasons, the satellite at the equinox, batteries and antennas), changes in thermal well simulation test methods are related to the development of new identified needs such

as compensation for flux received by the satellite at the end of its life or simulation of transients compatible with radio frequency test needs not covered by existing classical means.

It is unrealistic to design an equipment that satisfies all the previously developed needs. In most cases, validation of the thermal control involves a simple simulation of flux on the North/South walls, the purpose then being to compensate for external powers absorbed by the satellite (in practice heating at a given power or increasing to a given temperature) rather than reproducing the cause, for example using an artificial sun.

The general specifications for this type of equipment compatible with the needs mentioned above are:

### In terms of control

To control the satellite by temperature or by flux in order to simulate an environment similar to flight conditions required by the customer.

### In terms of homogeneity

Equipment of this type must be capable of producing sufficient flux to avoid introducing hot points on the radiator, the value of the homogeneity remaining to be defined in the design specification.

### In terms of calibration

The simulation of fluxes absorbed by satellite N/S radiators involves a precise calibration of the test facility, setting up a correspondence between a regulating value in the equipment (for example a voltage) and either:

- the flux absorbed at OSR radiators for control by flux,
- the temperature of the radiators for control by temperature.

### Permanent and transient status simulation

The simulation of transient statuses caused by eclipses requires the ability to reproduce flux losses absorbed by

(1) 18 avenue E. Belin - 31029 Toulouse cedex 4 - France - Tél : 33 (0)5 61 28 11 11 - Fax : 33 (0)5 61 28 11 12

(2) 31 avenue des Cosmonautes - 31402 Toulouse cedex 4 - France - Tél : 33 (0)5 62 19 62 19 - Fax : 33 (0)5 62 19 55 10

(3) 18 avenue E. Belin - 31401 Toulouse cedex 4 - France - Tél : 33 (0)5 61 27 31 31 - Fax : 33 (0)5 61 27 31 79

the radiators as similar as possible to losses during eclipses. This point does not need to be considered in this case.

### **In terms of modularity**

This specific feature is a result of economic needs (test equipment to be reused on other Telecommunication Satellite programs).

### **EQUIPMENT USED**

Several methods (infrared lamps, Calrods, plates with temperature controlled by a fluid, local heaters, etc.) can be considered for Vacuum-Thermal tests in which the objective is to compensate for an effect or to heat. The importance of the advantages and disadvantages of each will depend on the context (see selection below); these methods can easily be combined on North/South walls, (see figure 1 attached).

The method is selected based on three criteria, considering constraints related to the satellite, the test equipment, and the test. Although constraints related to the satellite depend on its geometry such that it is impossible to determine one preferred method, it is apparent that the use of regulated plates is the most efficient way of controlling the temperature, calibration, definition, qualification, repetitiveness and precision of the test equipment. Calrods are also good for control by temperature, they have precision and can provide a more modular solution, like lamps (with the additional advantage of lower thermal inertia).

For constraints related to the test, regulated plates are the best way of solving problems related to thermal modeling, reliability, contamination, end of life simulation, precision of emitted fluxes, positioning with respect to the satellite, and equipment reuse. Calrods appear to be best when there is a large number of areas, and lamps are the last choice particularly due to possible contamination and poor precision of emitted fluxes.

Due to the simple geometry of North/South walls on telecommunication satellites and constraints related to the test equipment or the test, the preferred choice will be the method using temperature regulated plates located in a chamber reproducing space vacuum conditions.

Nodal thermohydraulic modeling of the two types of plates is done using the ESACAP software, and the results are summarized in table 1 in terms of pressure loss and local temperature uniformity.

Several submodels were placed inside the ESACAP model in order to identify the temperature variation

within the shield itself. A coupled network using pressures as state magnitudes, was used to determine the variation of pressure losses taking account of the very large variations of fluid properties.

The nodal breakdown of a tube was done by nesting, and the behavior of several successive tubes was studied. All solutions were studied considering a large number of tubes in order to clearly identify the behavior of the area under a high flux density. Thermohydraulic calculations related to the choice of the operating mode were made using the Excel software.

### **MAIN RESULTS**

Therefore, the problem to be solved consisted of choosing a plate geometry, defining the industrial architecture, and a thermohydraulic operating mode for the fluid loop.

#### **Choice of fluid** (see figure 3 attached)

The operating temperature range (100 K - 300 K) naturally imposes nitrogen gas as the fluid.

#### **Choice of the plate geometry**

Two plate geometries could be adopted; firstly a geometry with "hairpin" fluid circulation (coil type with one input/output), or secondly a geometry based on tubes supplied in parallel (n inputs / n outputs). Another important parameter is the position of the flux with respect to the fluid circulation in the regulated plate.

Table 1 summarizes the main thermohydraulic results derived from the ESACAP model.

The results summarized in the above table clearly show that the spatial non-homogeneity of the temperature and the rib effect depend on:

- the type of circulation of nitrogen gas (circulation in hairpin or tubes supplied in parallel);
- the position of the flux with respect to the tubes (flux perpendicular or parallel to the tubes).

#### *Choice of the gas circulation type*

Although the thermal performances (rib effect/temperature difference between area with high flux and area with low flux) are approximately equal (with a slight advantage for plate tubes being supplied in parallel), an examination of the pressure losses induced by a "hairpin" circulation shows that this option is unrealistic due to the size of the circulating pump

necessary to control the fluid loop. Therefore, it was decided to supply the plate using tubes in parallel, branch connected to a manifold at the top and bottom.

*Position of flux compared with gas circulation*

An examination of the local temperature uniformity shows significantly better results when the flux in the critical area is perpendicular to the gas circulation tubes.

**Choice of the industrial architecture**  
(see figure 2 attached)

Four solutions were proposed in the presentation of the various possible solutions that could satisfy the needs:

- Solution 1

in which a direct connection is made to an existing thermal generator, using it as a source at 100 K, the temperature increase being supplied by heat exchangers and electric heaters placed in series.

- Solution 2

in which a source at 100 K independent of the existing network is used, the temperature increase being supplied as above by heat exchangers and electric heaters placed in series.

- Solution 3

in which independent 100 K - 300 K thermal generators are used. The previous equipment is eliminated (each circuit includes only the generator associated with its thermal shield).

- Solution 4

in which a single 100 K - 300 K thermal generator is used for the six areas, the thermal generator then being used at the lowest temperature of the six areas, the temperature increase being supplied as in cases 1 and 2 by heat exchangers associated with electric heaters.

The thermohydraulic design of the various solutions identified a solution making use of independent thermal generators based on the following technical criteria:

- Thermal performances (margins, controllability by area, modularity, temperature uniformity)
- Instrumentation
- Control system (Control and regulation loop, ease of use, operation)
- Product assurance.

**Choice of the operating mode for the fluid loop**

After the industrial architecture is chosen, the need can be solved using two different philosophies. The fluid

loop can operate either at imposed pressure (with tank) or at constant density.

*Operation at constant pressure*

The working pressure is fixed (for example by the pressure in the supply tank), and the density of the gas is allowed to vary as a function of the temperature. Heating is done by heaters located in the gas flow, cooling is done either by direct injection of liquid nitrogen (which requires a pressure control loop in addition to the temperature control), or by a liquid nitrogen / nitrogen gas exchanger.

In this operating mode, the fluid speed and therefore the pressure loss varies proportionally to the temperature. Therefore, the power of the circulation fan becomes an important factor in the increase in liquid nitrogen consumption.

The following table summarizes the main results of this operating mode with the following calculation assumptions:

- Speeds are calculated in a tube in the cryogenic shield.
- The calculated pressure loss takes account of the cryogenic shield and 60 m of a DN 100 line.
- The flow is adjusted to give a difference equal to 6°C at the shield terminals. For example, the calculation may be made on an area with a satellite power of 3000 W (severe case).

| T (K) | Flow (kg/s) | V (m/s) Shield | Rho (kg/m <sup>3</sup> ) | h (W/m <sup>2</sup> /K) | Pressure loss mbars | Pfan (W) | mLN2 (kg/s) |
|-------|-------------|----------------|--------------------------|-------------------------|---------------------|----------|-------------|
| 100   | 0.451       | 4.7            | 7.01                     | 107.41                  | 40.92               | 527      | 0.017       |
| 150   | 0.473       | 7.61           | 4.54                     | 118.06                  | 69.69               | 1451     | 0.017       |
| 200   | 0.477       | 10.32          | 3.38                     | 126.37                  | 95.73               | 2703     | 0.018       |
| 260   | 0.479       | 14.01          | 2.5                      | 133.47                  | 130.88              | 5017     | 0.021       |
| 300   | 0.48        | 15.66          | 2.24                     | 137.06                  | 146.67              | 6283     | 0.022       |

Comments:

- The maximum consumption of LN2 is at 300 K.
- The large variation in speed between operation at 100 K and operation at 300 K causes very large differences in the pressure loss that make the design of the circulating pump unrealistic at 300 K.

### Operation at constant density

| T (K) | P (bars) | Flow (kg/s) | Rho (kg/m <sup>3</sup> ) | V (m/s) Shield | h (W/m <sup>2</sup> /K) | Pressure loss (mbars) | Pfan (W) | m.L N2 (kg/s) |
|-------|----------|-------------|--------------------------|----------------|-------------------------|-----------------------|----------|---------------|
| 100   | 3.66     | 0.435       | 12.5                     | 2.54           | 105.57                  | 21.33                 | 148      | 0.0158        |
| 150   | 5.49     | 0.459       | 12.5                     | 2.69           | 116.47                  | 23.9                  | 176      | 0.011         |
| 200   | 7.33     | 0.467       | 12.5                     | 2.73           | 125.11                  | 24.81                 | 186      | 0.0093        |
| 240   | 8.79     | 0.471       | 12.5                     | 2.76           | 132.43                  | 25.32                 | 191      | 0.0082        |
| 300   | 10.99    | 0.474       | 12.5                     | 2.77           | 136.24                  | 25.62                 | 194      | 0.007         |

Under the same calculation assumptions, the maximum consumption of LN2 is at 100 K and is 30% lower than the maximum consumption with operation at constant pressure.

Note that at 300 K, the consumption is three times less than with the constant density operating mode.

The following comments are applicable for approximately the same temperature uniformity on the regulated plates (difference of 1% on the convection exchange coefficient between operation at constant pressure and operation at constant density):

The fact of working at constant density introduces a slight speed variation in the shields and pressure losses five times lower than with operation at constant pressure, which means that the effective fan power can be much lower.

Secondly, in order to limit the speed in shields, and therefore pressure losses, and therefore the fan power and consequently the consumption of LN2, the GN2 circuit needs to be pressurized as high as possible (highest possible density, while keeping a working pressure of less than 12 bars in the circuit).

#### Selected operating mode

Therefore, the selected solution will be based on a thermal generator operating at constant density. The proposed solution is achieved using an LN2/GN2 exchanger (vaporization of liquid nitrogen), the temperature increase being achieved by heaters placed in the gas flow. The exchanger is a tubular, multi-pass exchanger with grille.

The GN2 temperature varies between 100 K and 300 K, the pressure varying from 3.6 bars to 11 bars.

The fan controlling circulation of nitrogen gas is a centrifugal fan (standard) placed in a gas tight chamber with a thermal barrier between the turbine and the drive motor.

Comments on the choice of an exchanger compared with direct injection:

Cooling may be achieved in two different ways; either by a liquid / gas heat exchanger or by direct injection of liquid nitrogen in the gas flow; there are advantages and disadvantages in each of these solutions.

Direct injection is preferable for systems in which required transient responses are fast, however it is essential to ensure that the available tank is capable of adding gas at a pressure 2 to 3 bars higher than the circuit. Since this circuit is open, additional pressure regulation is necessary. The heat exchanger can work at low pressure and recover 20% (compared with injection at 12 bars) more energy from the latent heat of nitrogen vaporization. Furthermore, no pressure regulation is necessary since the circuit is closed, and moreover it is more suited to systems with low thermal inertia which is the case for this type of test.

#### Method validation conditions

Method validation conditions do not cause any problems and simply involve adding radiation transfers between the regulated plate and the area of the test specimen that it concerns, to the test mathematical model.

The test conditions are as follows: space chamber shield at ambient temperature.

Vacuum of  $10^{-5}$  mbars in the chamber, with a radiator simulating the North or South wall of the satellite. Validation requires knowledge of local uniformity of the plate temperature (rib effect), the global uniformity (inlet/outlet fluid temperature), and the temperature stability.

In tests under transient conditions (drop from 300 K to 100 K and rise from 100 K to 300 K), the sensitive parameters are:

- Respecting the rate of variation of the shields,
- Not exceeding the set value

These parameters are sufficient to validate the behavior of the regulated plate.

### CONCLUSION

While satisfying new identified needs for validation of the thermal control of telecommunication satellites, this thermal well simulation test method avoids the need to use solar flux simulation when it is not necessary (study to be carried out on precise needs) while including all functional tests (including radio frequency tests) and thermal balancing tests. These needs are generally related to a cost reduction policy.

| Circulation scheme<br>Flow 0.47 kg/s                               | Rib effect<br>°C  | Gas inlet /<br>outlet | Temperature offset<br>between areas                     | Pressure loss on<br>DP shield |
|--|---|-----------------------|---|-------------------------------|
| Non-homogenous T flux<br>Hairpin shields                           | Low flux 1.5°C<br>High flux 4°C   | 4.5°C                 | Low flux 5°C<br>High flux 5.5°C<br>DT max. = 3°C        | 0.38 bars                     |
| Non-homogenous<br>parallel flux<br>Hairpin shields                 | Low flux 1°C<br>High flux 4°C   | 4.5°C                 | Low flux 4°C<br>High flux 13°C<br>DT max. = 10°C        | 0.38 bars                     |
| Non-homogenous T flux<br>Shields without hairpin                   | Low flux 0.4°C<br>High flux 2.18°C  | 4.35°C                | Inlet outlet<br>one tube 3.99°C<br>DT max. = 10.2°C     | 0.014 bars                    |
| Non-homogenous<br>parallel flux<br>Shields without hairpin         | Low flux 0.5°C<br>High flux 2.58°C<br>Contiguous area<br>(transition) 6.8°C | 4.4°C                 | Low flux 2.05°C<br>High flux 2.2°C<br>DT max. = 21.57°C | 0.014 bars                    |
| Homogenous flux<br>shields without hairpin<br>300 W/m <sup>2</sup> | 0.5°C   | 2.74°C                | 2.8°C   | 0.014 bars                    |

Table 1: Summary of thermohydraulic results

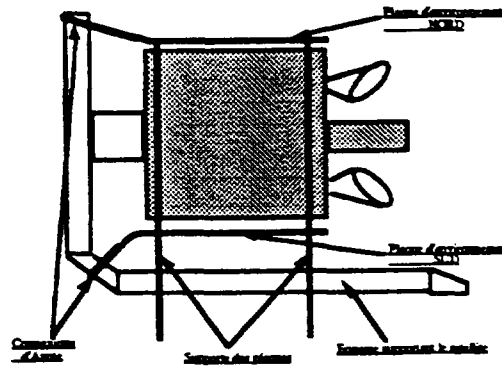
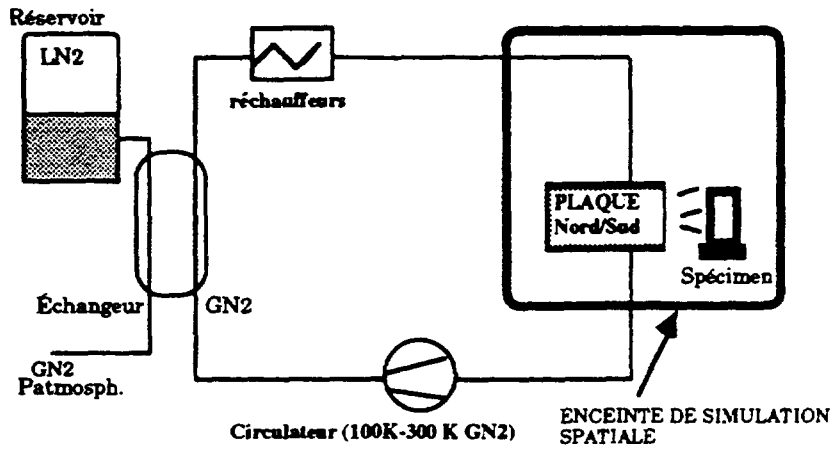
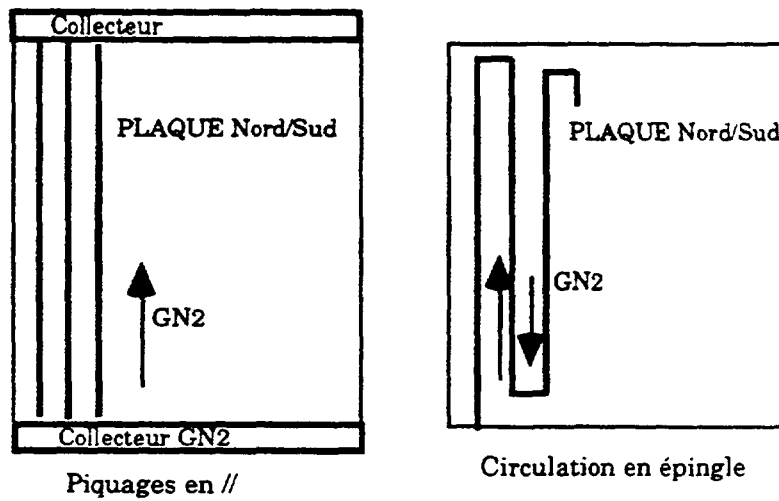


Fig. 1: Test configuration in a simulation chamber

**Fig1: Configuration d'essai dans l'enceinte de simulation**



**Fig. 2: Industrial architecture**



**Fig. 3: Regulated plate geometry**

## ATOMIC OXYGEN EFFECTS ON SEAL LEAKAGE

John R. Christensen, Steve D. Underwood  
Boeing Defense and Space Group  
International Space Station Program  
Huntsville, Alabama

Rachel R. Kamenetzky, Jason A. Vaughn  
NASA MSFC EH-12

### ABSTRACT

Common Berthing Mechanism (CBM) provides the structural interface between separate International Space Station (ISS) elements, such as the Laboratory and Node modules. The CBM consists of an active and a passive half that join together with structural bolts. The seal at this interface is the CBM-to-CBM molded seal. The CBM-to-CBM interface is assembled on orbit, thus the seals can be exposed to the space environment for up to 65 hours. Atomic Oxygen/Vacuum Ultraviolet radiation (AO/VUV) in space is a potential hazard to the seals. Testing was conducted to determine the effect on leakage of the CBM-to-CBM seal material exposed to AO/VUV. The sealing materials were S383 silicone and V835 fluorocarbon material. Control samples, which were not exposed to the AO/VUV environment, were used to ensure that if any changes in leakage occurred, they could be attributed to the AO/VUV exposure. After exposure to the AO/VUV environment the leakage increase was dramatic for the fluorocarbon. This testing was a major contributing factor in selecting silicone as the CBM-to-CBM seal material.

### INTRODUCTION

The International Space Station (ISS) is designed to allow long term continuous scientific experiments to be performed in the zero gravity environment of space. ISS consists of pressurized modules approximately 15 feet in diameter. The modules have attachment locations to allow the construction of ISS in stages. These attachment locations are accessed by berthing an active CBM (ACBM) to a passive CBM (PCBM). The ACBM is a ring of approximately 80 inches in diameter with various mechanisms attached (bolts, latches, guides, pins, etc.). The PCBM is also a ring of approximately 80 inches in diameter with nuts, guides, sockets, etc. attached. The ACBM contains all the powered components, the PCBM contains only non-powered components, including the CBM-to-CBM face seal. The CBM-to-CBM face seal consists of an aluminum metal retainer with rubber molded in the metal with heat and pressure. The ACBM and PCBM rings have flanges of approximately 3.5 inches that provide the seal surfaces for the CBM-to-CBM seal. The CBM-to-CBM interface is a field interface (i.e. the interface is put together on-orbit). The environment that the seals can experience prior to berthing the interface includes AO/VUV. Subsequent to this environmental exposure the seals need to provide atmospheric sealing for the berthed interface.

Many factors were analyzed in determining the material for this field interface. Factors included temperature, vacuum compatibility, AO/VUV stability, permeation, sealing force, and

mechanical damage resistance. Silicone and fluorocarbon were initially selected as seal materials. Silicone material is generally better suited for low temperature effects, while fluorocarbon material generally provides good mechanical damage protection with low permeation. In order to evaluate the performance of both silicone and fluorocarbon seals exposed to the ISS environment, ground testing was conducted in which the seals were exposed to simulated AO/VUV under vacuum. Leak testing on o-rings was conducted pre and post exposure to monitor sealing performance. Various compression's were tested to simulate the gapping of the CBM-to-CBM interface. This paper presents the results of the seal leak testing.

## TEST DESCRIPTION

The seals tested were o-rings in a dovetail groove. The seals were obtained from the same vendor that manufactures the CBM-to-CBM seals. The seals were S383 silicone and V835 fluorocarbon material. Control samples were used, which were not exposed to the AO/VUV environment. The control samples were used to ensure that if any changes in leakage occurred, it could be attributed to the appropriate cause (i.e. AO/VUV exposure).

Sample set up was as shown in figures 1 and 2. Leak testing was conducted per reference 1, Helium Mass Spectrometer Hood Test. O-ring samples were size -214 o-rings in a standard dovetail groove. The o-rings were not removed from their grooves until all testing was complete, to ensure that the o-rings saw minimal handling.

The seals were exposed to a synergistic effect of both atomic oxygen and vacuum ultraviolet radiation (AO/VUV) in the Atomic Oxygen Beam Facility (AOBF) located at NASA Marshall Space Flight Center. The exposure assembly is shown in figure 3 and the AO/VUV exposure system (AOBF schematic) is shown in figure 4. The Atomic Oxygen Beam Facility (AOBF) produces a 5 eV neutral atomic oxygen beam by placing a metal plate in contact with a magnetically (3 to 4 kilogauss) confined atomic oxygen plasma. The atomic oxygen plasma is produced by a radio frequency (RF) driven lower hybrid plasma source. A magnetron supplies 2kW of power at a frequency of 2.45 GHz to the center pin to produce the plasma. Because of the facility geometry, the atomic oxygen plasma is magnetically confined such that a 1 cm (0.39 in.) diameter. plasma column is produced on centerline of the test chamber. The plasma column interacts with an electrically biased metallic plate. The bias applied to the plate accelerates ions from the plasma to the plate. During the acceleration process, the ions gain energy equal to the difference in the plasma potential and the neutralizer plate bias. Once the ions hit the plate, they collect an electron from the metal lattice and become neutral. Following collision with the neutralizer plate, the atoms are reflected towards the test specimen at a fraction of their pre-collision energy. The fraction of energy lost by the reflected atoms is a function of the type of material used to make the neutralizer plate. Because the energy of the reflected atom depends on the plasma potential, which is inherently subject to slight variations, not all atoms will be accelerated by the same potential difference. Thus, the reflected atoms will have a slight energy distribution.

The atomic oxygen flux produced by the AOBF system ranges from  $5 \times 10^{15}$  atoms/sec-cm<sup>2</sup> to  $1.7 \times 10^{16}$  atoms/sec-cm<sup>2</sup>. During production of the atomic oxygen plasma, the system produces electromagnetic radiation. This radiation is produced primarily during the dissociation and ionization process. Attempts to identify and quantify the radiation using a photodiode with appropriate narrow band filters indicated that the primary radiation line was 130 nm, the atomic oxygen resonant peak in

the VUV region. The VUV intensity was determined to be nearly 200 times the sun's intensity averaged over the duty cycle. In order to eliminate possible magnetic interactions, appropriate shielding is placed around the diode.

Sample size for the AOBF is limited to 15.24 cm (6 in.) diameter. Thermocouples monitor the increase in sample temperature due to heat radiating from the neutralizer plate and magnets. Sample temperature ranges from 50 to 60 degrees C (122 to 140 F) depending on the duty cycle.

The AO exposure requirements come from reference 2, "The PCBM shall withstand a ram AO fluence of  $5.0E21$  atoms per  $cm^2$  per year for the on-orbit exposure duration. PCBM surfaces exposed less than 30 days shall withstand  $4.4E19$  atoms per  $cm^2$  per day AO ram fluence." The integrated ultraviolet irradiance at one astronomical unit is 118 Watts per square meter.

The maximum predicted hours of on-orbit exposure for the CBM-to-CBM seal is 65 hours for Pressurized Mating Adapter 2 (PMA2), the next most exposure is PMA3 at 25 hours.

## **TEST CONDUCT**

### **Sample preparation**

1. Inspected seals for defects and seal groove for radial scratches.
2. Inspected groove and seal for contamination (performed in a flow bench). Cleaned with ethyl alcohol or denatured alcohol.
3. Installed seal into groove (performed in a flow bench).
4. Measured crown height.
5. Inspected exposed seal and seal surface for contamination (performed in a flow bench). Cleaned with ethyl alcohol or denatured alcohol as required.
6. Assembled fixture with no shim, verified no gap with feeler gauge on outside of seal (performed in a flow bench).
7. Installed helium containment hood (performed in a flow bench).
8. Attached fixture to leak detector.
9. Calibrated system.
10. Performed leak test.
11. Disassembled fixture to allow for next shim installation (performed in a flow bench).

The initial condition was performed for no gap, then steps 6-11 were repeated with a .007" shims, then .010" shims for silicone and .015" shims for fluorocarbon. The same sample was tested at all three gaps against the same sealing surface before going to next sample. The sample was oriented the same during each test.

## **TEST FLOW**

### **Non-lubricated samples**

1. Baseline leak tested fluorocarbon and silicone samples.
2. Exposed fluorocarbon and silicone samples to AO/VUV.

3. Leak tested fluorocarbon and silicone samples.
4. Exposed silicone samples to additional AO/VUV.
5. Leak tested silicone samples.

### **Lubricated samples**

(new samples different from non-lubricated samples)

1. Lubricated samples with a wet shiny appearance, with no clumps. Braycote 601 lubricant was used.
2. Silicone samples were compressed five times each and the lubrication track on the sealing surface was removed between each compression. This was to simulate multiple on-orbit berths (Pressurized Mating Adapter 2 (PMA2) has a maximum of 6 berths).
3. Baseline leak tested fluorocarbon and silicone samples.
4. Exposed fluorocarbon and silicone samples to AO/VUV.
5. Leak tested fluorocarbon and silicone samples.

## **RESULTS**

### **Non-lubricated**

The non-lubricated samples test results are shown in table 1. Baseline leakage is tabulated for the three different compression values, and then the post exposure leakage is shown, and finally the exposure environment. The silicone samples were exposed to additional AO/VUV. Additional exposure leakage values and exposure environment are also tabulated in table 1. Equivalent hours of exposure for the fluorocarbon seals was 18 to 23 hours and 10 to 181 hours for the silicone samples. Compression values are  $\pm 3\%$  accuracy and VUV values listed are minimum values. The post exposure leakage indicates that the fluorocarbon had a dramatic increase in leakage. Post exposure visual examination of the fluorocarbon samples revealed a gray ash appearance, which was not present in the control sample. Plots of leak rate versus equivalent exposure time for the silicone samples (figures 5 and 6) are included. A second order linear regression line for the data indicates excellent linear correlation. Control samples were sample number 3, and indicated excellent repeatability of leak testing. As expected the less compression that the seals experienced resulted in higher leakage.

### **Lubricated**

The lubricated samples test results are shown in table 2. Baseline leakage is tabulated for the three different compression values, and then the post exposure leakage is shown, and finally the exposure environment. Equivalent hours of exposure for the silicone samples was 43 to 45 hours and 10 to 12 for the fluorocarbon samples. Compression values are  $\pm 3\%$  accuracy and VUV values listed are minimum values. The post exposure leakage indicates that the fluorocarbon had a dramatic increase in leakage. Post exposure visual examination of the fluorocarbon samples revealed a gray ash appearance, which was not present in the control sample. Plots of leak rate versus equivalent exposure time for the silicone samples (figures 5 and 6) are included. Silicone samples reveal a small degradation of leakage and following the exposure. The lubricated samples generally have less leakage degradation. Control samples were sample number 3, and indicated excellent repeatability of leak testing. As expected the less compression that the seals experienced resulted in higher leakage.

## CONCLUSIONS

The non-lubricated silicone S383 leakage degradation varies linearly with the amount of AO/VUV exposure. This linear relationship can be used for exposures less than 181 hours for S383 silicone. Silicone exposure should be minimized to ensure that leakage will not exceed requirements. Fluorocarbon V835 was dramatically effected by AO/VUV exposure and should not be used in space flight for maintaining pressure when exposed to this environment.

## REFERENCES

1. *ASME Boiler and Pressure Vessel Code*, Section V, Article 10, 1992.
2. *Prime Item Development Specification for Passive Common Berthing Mechanism*, S683-28943 paragraph 3.2.5.18, rev D.

201

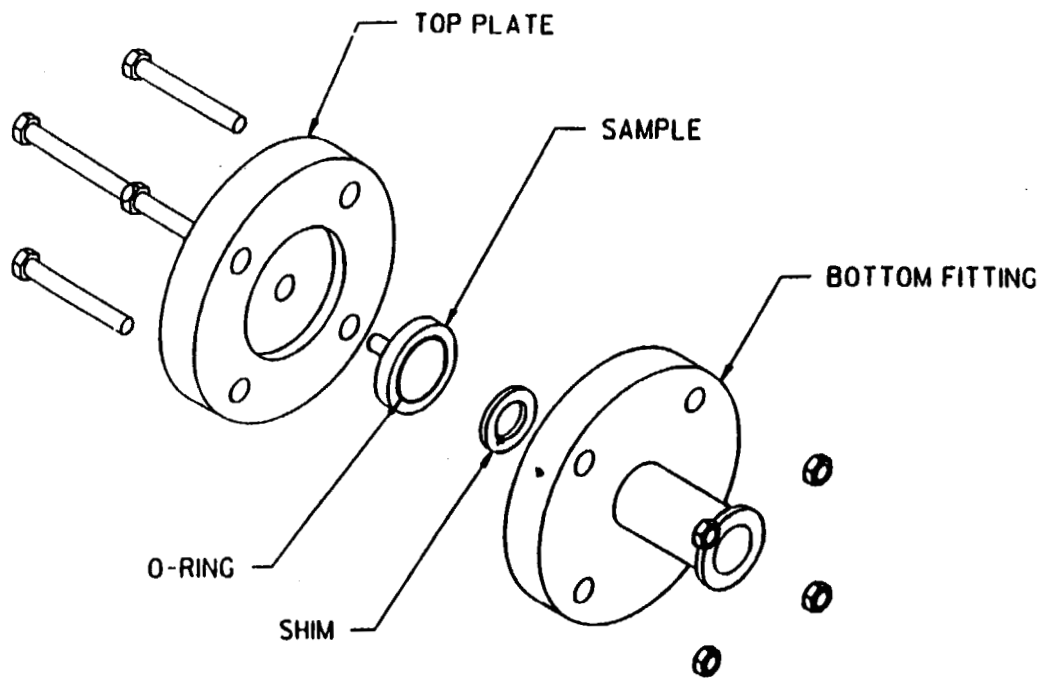


**FIGURE 1**  
Exploded View of Sample  
scale: none

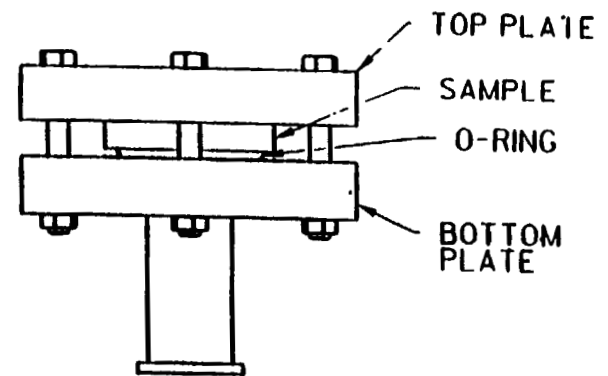


**Figure 2**  
Assembly of Sample  
scale: none

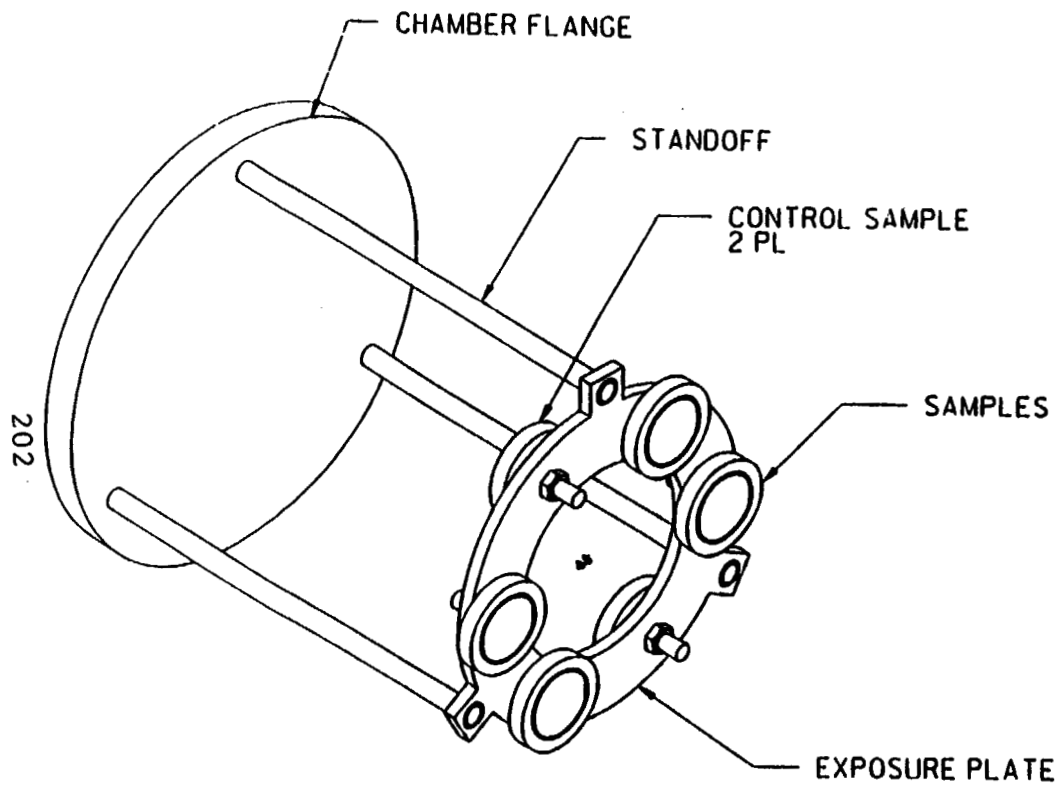


**Figure 3**  
**Exposure Assembly**  
scale: none

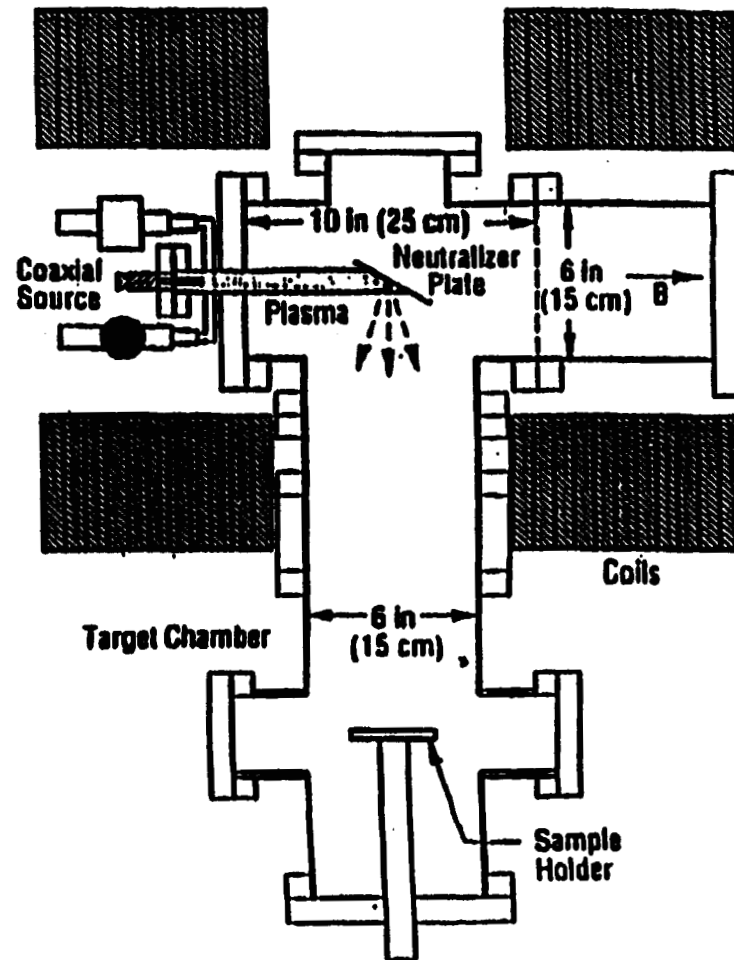


**Figure 4**  
**AO/VUV Exposure System**  
scale: none

**Table 1 Non-Lubricated Seals**

| Pre-exposure Baseline Leakage (atm cc/sec He) |                                     |                  |                                 |           |               |                       |           |               |                       |
|---|-------------------------------------|------------------|---------------------------------|-----------|---------------|-----------------------|-----------|---------------|-----------------------|
| Sample Identification                         | Leak Rate                           | % Compression    |                                 | Leak Rate | % Compression |                       | Leak Rate | % Compression |                       |
| Fluorocarbon 1                                | 2.20E-06                            | 16.0             |                                 | 2.60E-06  | 11.0          |                       | 1.10E-05  | 5.0           |                       |
| Fluorocarbon 2                                | 2.30E-06                            | 16.0             |                                 | 2.60E-06  | 11.0          |                       | 6.20E-06  | 5.0           |                       |
| Fluorocarbon 3                                | 1.70E-06                            | 16.0             |                                 | 3.90E-06  | 11.0          |                       | 1.20E-05  | 5.0           |                       |
| Silicone 1                                    | 1.80E-05                            | 12.0             |                                 | 2.30E-05  | 7.0           |                       | 2.60E-05  | 4.0           |                       |
| Silicone 2                                    | 1.60E-05                            | 14.0             |                                 | 2.20E-05  | 9.0           |                       | 2.60E-05  | 7.0           |                       |
| Silicone 3                                    | 2.70E-05                            | 13.0             |                                 | 3.20E-05  | 8.0           |                       | 3.70E-05  | 6.0           |                       |
| Exposure 1 Environment                        |                                     |                  |                                 |           |               |                       |           |               |                       |
| Sample Identification                         | AO Fluence (atoms/cm <sup>2</sup> ) | Equivalent Hours | VUV (watts-hrs/m <sup>2</sup> ) |           |               |                       |           |               |                       |
| Fluorocarbon 1                                | 4.24E+19                            | 23.1             | 2729.0                          |           |               |                       |           |               |                       |
| Fluorocarbon 2                                | 3.44E+19                            | 18.8             | 2214.1                          |           |               |                       |           |               |                       |
| Fluorocarbon 3                                | 0.0                                 | 0.0              | 0.0                             |           |               |                       |           |               |                       |
| Silicone 1                                    | 1.88E+19                            | 10.3             | 1210.0                          |           |               |                       |           |               |                       |
| Silicone 2                                    | 1.95E+19                            | 10.6             | 1255.1                          |           |               |                       |           |               |                       |
| Silicone 3                                    | 0.0                                 | 0.0              | 0.0                             |           |               |                       |           |               |                       |
| Post-exposure 1 Leakage                       |                                     |                  |                                 |           |               |                       |           |               |                       |
| Sample Identification                         | Leak Rate                           | % Compression    | % Change in Leak rate           | Leak Rate | % Compression | % Change in Leak rate | Leak Rate | % Compression | % Change in Leak rate |
| Fluorocarbon 1                                | 1.90E-03                            | 16.0             | -86263.6                        | 2.70E-03  | 11.0          | -103746.2             | 5.40E-03  | 5.0           | -48990.9              |
| Fluorocarbon 2                                | 1.10E-03                            | 16.0             | -47726.1                        | 1.50E-03  | 11.0          | -57592.3              | 3.60E-03  | 5.0           | -57964.5              |
| Fluorocarbon 3                                | 1.00E-06                            | 16.0             | 41.2                            | 3.30E-06  | 11.0          | 15.4                  | 1.20E-05  | 5.0           | 0.0                   |
| Silicone 1                                    | 1.90E-05                            | 12.0             | -5.6                            | 2.60E-05  | 7.0           | -13.0                 | 3.70E-05  | 4.0           | -42.3                 |
| Silicone 2                                    | 3.00E-05                            | 14.0             | -87.5                           | 3.10E-05  | 9.0           | -40.9                 | 7.40E-05  | 7.0           | -184.6                |
| Silicone 3                                    | 1.60E-05                            | 13.0             | 40.7                            | 2.00E-05  | 8.0           | 37.5                  | 2.30E-05  | 6.0           | 37.8                  |
| Exposure 1 and 2 Environment                  |                                     |                  |                                 |           |               |                       |           |               |                       |
| Sample Identification                         | AO Fluence (atoms/cm <sup>2</sup> ) | Equivalent Hours | VUV (watts-hrs/m <sup>2</sup> ) |           |               |                       |           |               |                       |
| Silicone 1                                    | 2.70E+20                            | 147.3            | 17378.2                         |           |               |                       |           |               |                       |
| Silicone 2                                    | 3.32E+20                            | 181.1            | 21368.7                         |           |               |                       |           |               |                       |
| Silicone 3                                    | 0.0                                 | 0.0              | 0.0                             |           |               |                       |           |               |                       |
| Post-exposure 1 and 2 Leakage                 |                                     |                  |                                 |           |               |                       |           |               |                       |
| Sample Identification                         | Leak Rate                           | % Compression    | % Change in Leak rate           | Leak Rate | % Compression | % Change in Leak rate | Leak Rate | % Compression | % Change in Leak rate |
| Silicone 1                                    | 5.00E-05                            | 12.0             | -177.8                          | 6.40E-05  | 7.0           | -178.3                | 1.80E-04  | 4.0           | -592.3                |
| Silicone 2                                    | 1.40E-04                            | 14.0             | -775.0                          | 4.30E-04  | 9.0           | -1854.5               | 8.60E-04  | 7.0           | -3207.7               |
| Silicone 3                                    | 1.50E-05                            | 13.0             | 44.4                            | 1.90E-05  | 8.0           | 40.6                  | 2.20E-05  | 6.0           | 40.5                  |

203

**Table 2 Lubricated Seals**

| Pre-exposure Baseline Leakage |                                     |                  |                                 |           |               |                       |           |               |                       |  |  |
|-------------------------------|-------------------------------------|------------------|---------------------------------|-----------|---------------|-----------------------|-----------|---------------|-----------------------|--|--|
| Sample Identification         | Leak Rate                           | % Compression    |                                 | Leak Rate | % Compression |                       | Leak Rate | % Compression |                       |  |  |
| Fluorocarbon 1                | 2.10E-06                            | 15.0             |                                 | 3.00E-06  | 10.0          |                       | 4.00E-06  | 4.0           |                       |  |  |
| Fluorocarbon 2                | 2.40E-06                            | 15.0             |                                 | 3.00E-06  | 10.0          |                       | 3.90E-06  | 4.0           |                       |  |  |
| Fluorocarbon 3                | 1.90E-06                            | 15.0             |                                 | 2.90E-06  | 10.0          |                       | 3.00E-06  | 4.0           |                       |  |  |
| Silicone 1                    | 1.90E-05                            | 11.0             |                                 | 2.40E-05  | 5.0           |                       | 2.60E-05  | 3.0           |                       |  |  |
| Silicone 2                    | 1.80E-05                            | 11.0             |                                 | 2.20E-05  | 5.0           |                       | 1.80E-05  | 3.0           |                       |  |  |
| Silicone 3                    | 1.10E-05                            | 10.0             |                                 | 2.40E-05  | 5.0           |                       | 2.60E-05  | 2.0           |                       |  |  |
| Exposure 1 Environment        |                                     |                  |                                 |           |               |                       |           |               |                       |  |  |
| Sample Identification         | AO Fluence (atoms/cm <sup>2</sup> ) | Equivalent Hours | VUV (watts-hrs/m <sup>2</sup> ) |           |               |                       |           |               |                       |  |  |
| Fluorocarbon 1                | 1.82E+19                            | 9.9              | 1171.4                          |           |               |                       |           |               |                       |  |  |
| Fluorocarbon 2                | 2.24E+19                            | 12.2             | 1441.7                          |           |               |                       |           |               |                       |  |  |
| Fluorocarbon 3                | 0.0                                 | 0.0              | 0.0                             |           |               |                       |           |               |                       |  |  |
| Silicone 1                    | 8.20E+19                            | 44.7             | 5277.8                          |           |               |                       |           |               |                       |  |  |
| Silicone 2                    | 7.90E+19                            | 43.1             | 5084.7                          |           |               |                       |           |               |                       |  |  |
| Silicone 3                    | 0.0                                 | 0.0              | 0.0                             |           |               |                       |           |               |                       |  |  |
| Post-exposure 1 Leakage       |                                     |                  |                                 |           |               |                       |           |               |                       |  |  |
| Sample Identification         | Leak Rate                           | % Compression    | % Change in Leak rate           | Leak Rate | % Compression | % Change in Leak rate | Leak Rate | % Compression | % Change in Leak rate |  |  |
| Fluorocarbon 1                | 4.70E-04                            | 15.0             | -22281.0                        | 3.50E-03  | 10.0          | -116566.7             | 1.60E-03  | 4.0           | -39900.0              |  |  |
| Fluorocarbon 2                | 7.30E-04                            | 15.0             | -30316.7                        | 1.00E-03  | 10.0          | -33233.3              | 2.20E-03  | 4.0           | -56310.3              |  |  |
| Fluorocarbon 3                | 1.50E-06                            | 15.0             | 21.1                            | 2.10E-06  | 10.0          | 27.6                  | 2.30E-06  | 4.0           | 23.3                  |  |  |
| Silicone 1                    | 3.10E-05                            | 11.0             | -63.2                           | 4.10E-05  | 5.0           | -70.8                 | 4.20E-05  | 3.0           | -61.5                 |  |  |
| Silicone 2                    | 2.30E-05                            | 11.0             | -27.8                           | 4.00E-05  | 5.0           | -81.8                 | 4.40E-05  | 3.0           | -144.4                |  |  |
| Silicone 3                    | 1.80E-05                            | 10.0             | -63.6                           | 2.20E-05  | 5.0           | 8.3                   | 2.60E-05  | 2.0           | 0.0                   |  |  |

Figure 5  
Silicone Sample 1

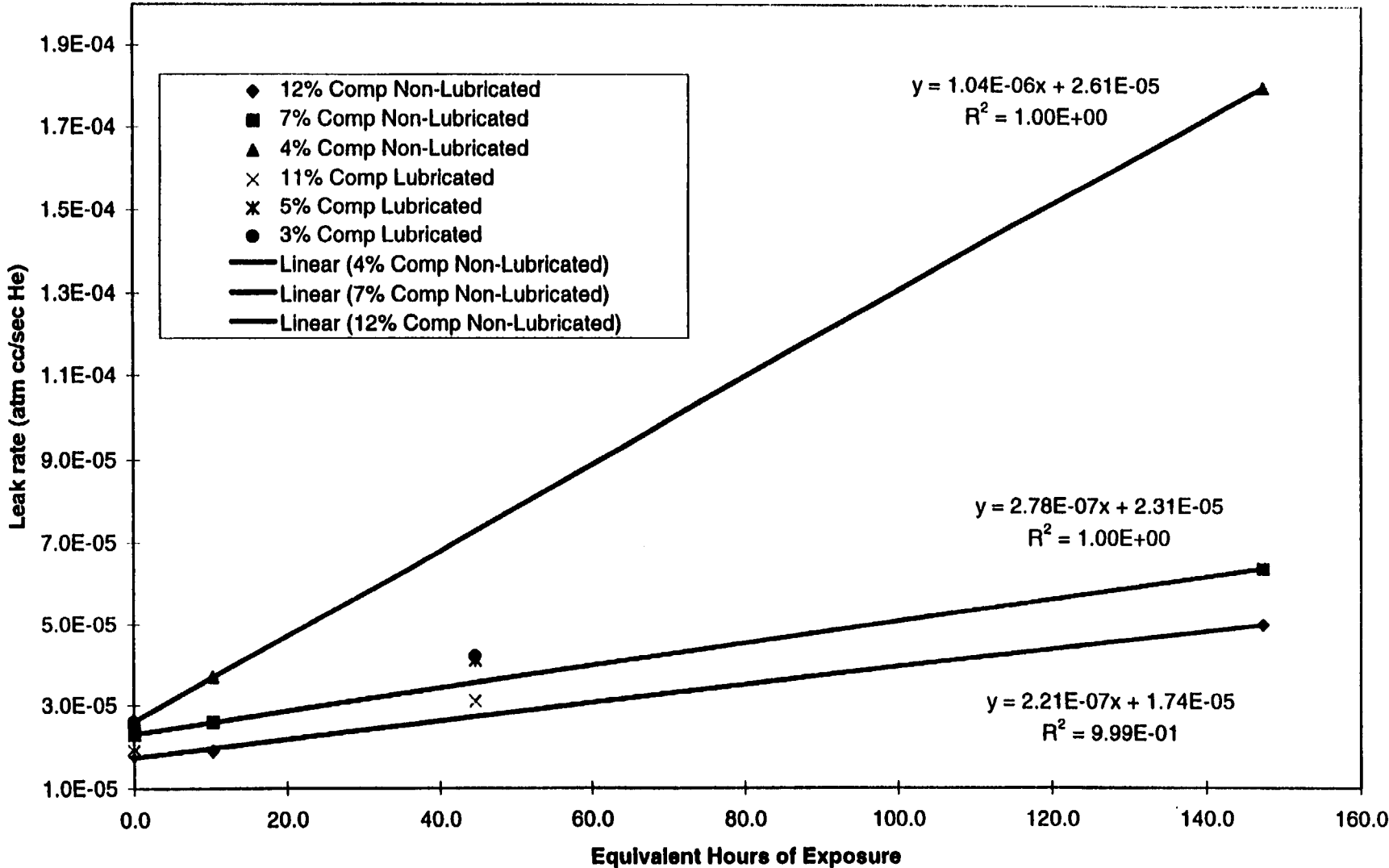
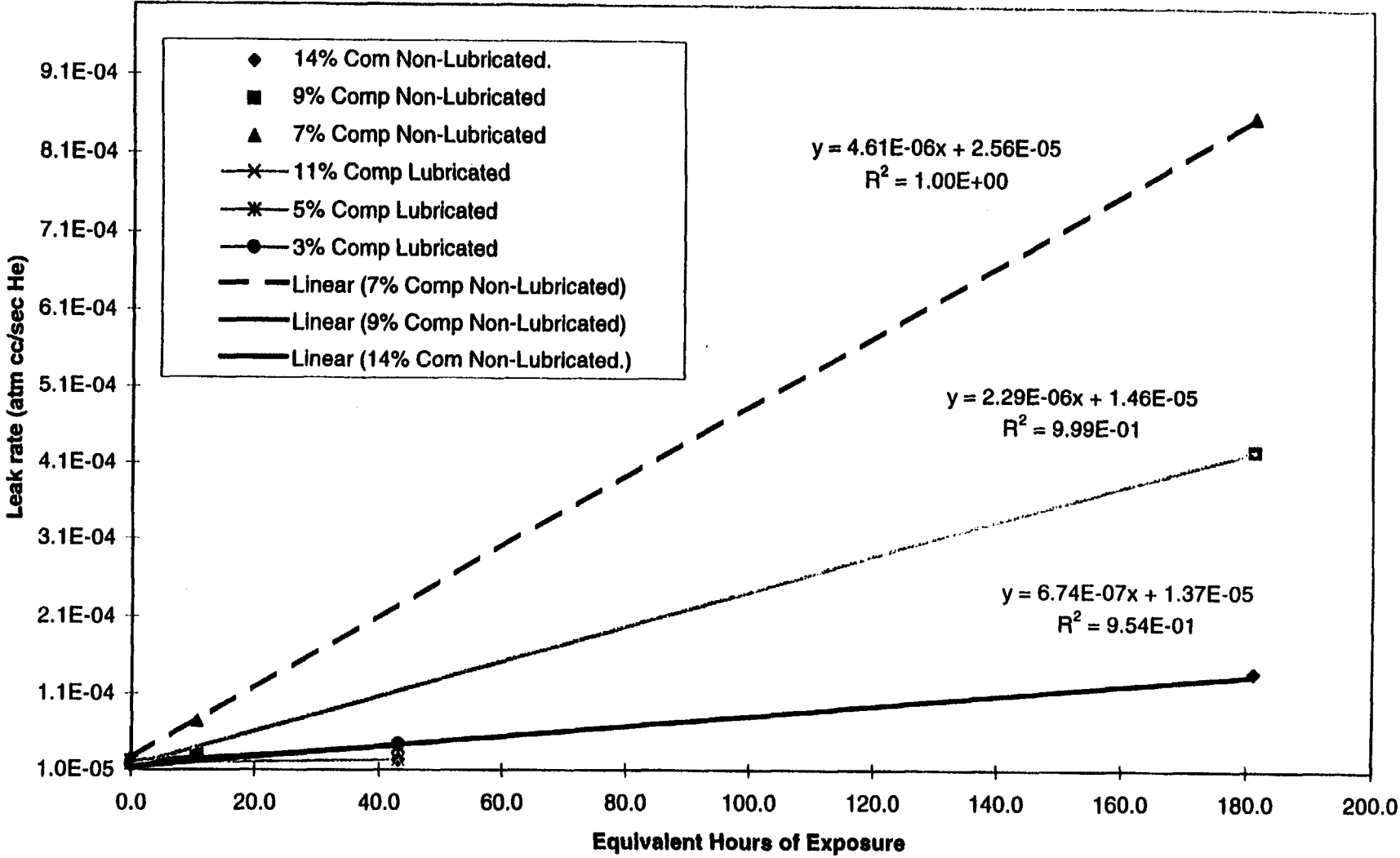


**Figure 6**  
**Silicone Sample 2**



## RADIATION INDUCED DEGRADATION OF WHITE THERMAL CONTROL PAINT

D.L. Edwards, J.M. Zwiener, G.E. Wertz, J.A. Vaughn, R.R. Kamenetzky,  
M.M. Finckenor

Physical Sciences and Environmental Effects Branch, NASA, MSFC, AL 35812  
M.J. Meshishnek

Mechanics and Materials Technology Center, Technology Operations, The Aerospace Corporation,  
El Segundo, CA 90245-4691

### ABSTRACT

This paper details a comparison analysis of the zinc-oxide pigmented white thermal control paints Z-93 and Z-93P. Both paints were simultaneously exposed to combined space environmental effects and analyzed using an in-vacuo reflectance technique. The dose applied to the paints was approximately equivalent to 5 yr in a geosynchronous orbit. This comparison analysis showed that Z-93P is an acceptable substitute for Z-93. Irradiated samples of Z-93 and Z-93P were subjected to additional exposures of ultraviolet (UV) radiation and analyzed using the in-vacuo reflectance technique to investigate UV activated reflectance recovery. Both samples showed minimal UV activated reflectance recovery after an additional 190 equivalent Sun hour (ESH) exposure. Reflectance response utilizing nitrogen as a repressurizing gas instead of air was also investigated. This investigation found the rates of reflectance recovery when repressurized with nitrogen are slower than when repressurized with air.

### INTRODUCTION

The Marshall Space Flight Center (MSFC) Space Environmental Effects Branch conducted a series of space environmental effects exposure tests to requalify a new potassium silicate binder used in the production of white thermal control paints Z-93 and YB-71. This requalification program was a joint effort between MSFC, the Air Force Space and Missile System Center, The Aerospace Corporation, NASA's Lewis Research Center, Wright Laboratory, and several other Government and industry facilities.

Z-93 was originally flight qualified with a potassium silicate binder (PS7) from Sylvania. Sylvania discontinued production of PS7 and a new vendor, PQ Corporation, was located to provide the potassium silicate binder denoted as K2130 (ref. 1). The Air Force sponsored and funded this effort at the Illinois Institute of Technology Research Institute (IITRI), and The Aerospace Corporation was the technical lead of this program to requalify three paints, Z-93, YB-71, and S13G/LO-1. The paints using the potassium silicate binder PS7 are denoted as Z-93 and YB-71, while the paints using the K2130 binder are denoted as Z-93P and YB-71P. The S13G/LO-1 paint utilizes a room-temperature vulcanized, silicone, binder. Testing on this paint was not performed at MSFC.

The task performed by the MSFC Space Environmental Effects Branch was a comparison analysis of the two aforementioned paints utilizing the original (PS7) and new (K2130) binders. Two samples per test would be simultaneously exposed to combined space environmental effects (CEE). One of these samples would have the PS7 binder and the other would have the K2130 binder.

This paper describes the CEE test facility used to requalify the white thermal control paint Z-93P and discusses the comparison analysis of Z-93 and Z-93P when simultaneously exposed to CEE. A post-exposure reflectance recovery phenomenon, bleaching, was observed and is discussed.

### DESCRIPTION OF THE FACILITY

The Space Environmental Effects Branch at MSFC operates the CEE test system, which provides the unique capability to expose materials to a simultaneous or sequential simulated space radiation environment and perform in-vacuo reflectance measurements. The simulated space environment consists of protons, low-energy electrons, high-energy

electrons, vacuum ultraviolet (VUV), and near ultraviolet (NUV) radiation. The CEE test chamber is shown in Figure 1. This test system is composed of all Conflat™ metal seals and is maintained at a base pressure of  $5 \times 10^{-8}$  torr with four ion pumps. High-energy electrons and protons propagate through the vacuum from the National Electrostatics Corporation accelerators to the test chamber through two separate beam lines, each equipped with a beam profile monitor and Faraday cups. Each beam line Faraday cup is remotely moved into and out of the charged particle beam path.

The test chamber has a Faraday cup array, and each Faraday cup in the array is oriented to collect charge from a specific charged particle source (see Fig. 1). A temperature-controlled sample holder transports two 1-in diameter samples in the horizontal plane from the sample exposure position to the integrating sphere for in-vacuo reflectance measurement. The sample holder was maintained at 21 °C for this comparison test to reduce any sample heating effects.

During CEE exposure, the samples are rotated so the sample normal is +45° off the horizontal plane to allow them to be simultaneously exposed to all sources. High-energy electrons and protons impinge the sample surface at a 45° angle of incidence. The NUV irradiation also impinges at a 45° angle to the sample surface. The VUV and low-energy electrons impinge the sample at angles of 35° and 55°, respectively.

## CONTAMINATION

A previous test, which subjected a trial Z-93 sample to a low dose of CEE, indicated the presence of a surface contaminant. That sample was prepared by AZ Technology. Figure 2 shows the detrimental effects of a photodeposited surface contaminant on Z-93. This Z-93 sample was exposed to a low dose of CEE's detailed in Table 1. After the exposure, an in-vacuo reflectance spectrum of the Z-93 sample was obtained. The CEE test chamber was repressurized with air to ambient pressure before the acquisition of the in-air reflectance spectra, also shown in Figure 2.

The Z-93 sample was placed in a standard sample holder and kept on a shelf in the laboratory. A reflectance spectrum was taken after 5,160 hr of ambient exposure. The data shown in Figure 2 indicate that the reflectance of this specific contaminant on Z-93 will not immediately recover when exposed to air, but low levels of surface contaminate on Z-93 will slowly recover reflectance with prolonged ambient exposure.

Supporting indicators, which showed that a contaminant was present, were rapid loss of VUV intensity and rapid reduction of electron flux from the electron flood gun. A visible contaminant layer was observed accumulating on the VUV source window; however, this layer was removed with solvent cleaning (methyl-ethyl ketone, acetone, and ethyl alcohol). The VUV intensity was reestablished after the contaminant layer was removed. The reduction of electron flux, from the electron flood gun, was not recoverable due to extensive contamination on the firing unit. The initial electron flux could not be restored even after extensive cleaning of the firing unit. The initial electron flux was eventually restored by removing the contaminated firing unit and installing a new electron flood gun firing unit. The contaminated firing unit was sent to the factory for refurbishment.

The CEE test system was cleaned, decontaminated, and verified to be contamination-free using techniques developed by the MSFC Space Environmental Effects Branch (ref. 2). Figure 3 shows the reflectance spectrum of the Z-93 sample utilized in the contamination-free verification test. This sample was exposed to 1,156.5 EHS of NUV and 50 KeV electrons at a fluence of  $3.53 \times 10^{15}$  electrons/cm<sup>2</sup>. After the exposure, the test chamber was repressurized with air and a reflectance spectrum was obtained after 15 min in air. Figure 3 indicates the Z-93 sample experienced a reflectance recovery when air was used as a repressurant. This phenomenon is discussed below.

## EXPOSURE SEQUENCE

Two white thermal control paint samples were obtained from IITRI: a Z-93 sample, number A-042 of batch R155 with the PS7 binder; and a Z-93P sample, number X-11 of batch S044 with the K2130 binder. The goal of this test was to expose these two samples to a 5-yr equivalent geosynchronous Earth orbit (GEO) dose of electron radiation. NUV and VUV exposure equivalent to 5 yr in GEO could not be performed without requiring extensive testing times. The NUV and VUV exposures were included to provide a testing environment approaching that of the natural space environment.

The simulated 5-yr GEO electron fluence was determined by calculating the dose-depth profile (obtained by using the Integrated Tiger Series 3 software (ref. 3)) for a 5-mil thick Z-93 sample. The dose-depth profile is shown in Figure 4.

The Z-93 and Z-93P samples were placed in the CEE test chamber and a pre-exposure in-vacuo reflectance measurement was taken when the vacuum level in the chamber reached  $8 \times 10^{-7}$  torr. The NUV and VUV exposures were initiated, after the pre-exposure measurement was obtained, with both sources providing nominally 2 UV Suns intensity on the samples. The VUV intensity was measured over the wavelength range from 120 to 200 nm. The NUV intensity was measured over the wavelength range from 250 to 400 nm. The samples were continuously exposed to NUV and VUV throughout the test, and the intensities were maintained at nominally 2 UV Suns. Sample exposure to 50- and 200- KeV electrons varied in duration from day to day; however, the beam current for each source was maintained at  $1 \text{ nA/cm}^2$  during each electron exposure. In-vacuo reflectance measurements were obtained periodically throughout the duration of this test. The CEE exposure portion of the test was terminated after 3 wk of exposure, with a total dose of 953.5 ESH of NUV and VUV, 50 KeV electrons at a fluence of  $1.2 \times 10^{15}$  electrons/cm<sup>2</sup>, 200-KeV electrons at a fluence of  $7.35 \times 10^{14}$  electrons. Figure 5 shows the reflectance of the two samples degraded similarly during this investigation.

## REFLECTANCE RECOVERY INVESTIGATION

Previous data (Fig. 3) indicate that a reflectance recovery process will occur when Z-93 type paints are damaged with space environmental effects then repressurized with air. The term "bleaching" refers to those optical property recovery processes induced after introduction of gasses. A bleaching effect is a type of recovery process generally associated with exposure to air or some other gas containing oxygen. Figure 3 shows a bleaching effect after the Z-93 sample was irradiated and then repressurized with air as a fill gas. "Recovery process" refers to those processes that produce an increase in the reflectance of a material after the material experienced a decrease in reflectance due to space environmental exposure.

An attempt was made to back-fill the CEE test chamber with nitrogen, from liquid nitrogen boil-off, at a rate sufficient to monitor reflectance changes as a function of pressure. The nitrogen leak valve utilized lacked the required sensitivity for this procedure to be implemented, so the reflectance was measured as a function of time. The in-vacuo reflectance system was configured to monitor the sample reflectance at 600 nm, chosen because reflectance recovery is measurable at this wavelength (Fig. 3). The sample analyzed was Z-93P. Figure 6 shows that over a 10-min nitrogen back-fill time, the reflectance at 600-nm wavelength recovered by about 47 percent. After 10 min of nitrogen back-fill, the test chamber reached atmospheric pressure. Reflectance measurements of the Z-93 and Z-93P samples were obtained after a total of 113 hr in a dark closed nitrogen environment, with an interim measurement taken after 41 hr to determine if nitrogen produced any bleaching effects. Results indicate that extended exposure to a dark closed nitrogen environment produces little change in reflectance beyond the first 10 min of nitrogen exposure (Fig. 7)

After the reflectance spectra was obtained for the Z-93 and Z-93P samples, which remained in a dark closed nitrogen environment for 113 hr, the samples were removed from the CEE test system and measured, in air, by the laboratory portable spectroreflectometer (LPSR). The transit time, in air, between the dark closed nitrogen environment of the CEE test chamber and the LPSR measurement was approximately 15 min. Results are also shown in Figure 7. After this measurement in air, the samples were placed in a standard sample holder and kept in a dark environment for 510 hr. Figure 7 shows that the samples experienced a slight recovery during the 510 hr in the dark ambient environment.

## CONCLUSIONS

The IITRI-manufactured samples of Z-93 and Z-93P were exposed to equivalent doses of NUV, VUV, 50-KeV, and 200-KeV electrons. This test shows similar degradation in both samples when subjected to equivalent space environmental effects exposure. A conclusion is that Z-93P is a suitable replacement for Z-93.

During the course of this test, many observations were made concerning the response of Z-93 to a simulated space environment in addition to documenting the reflectance degradation of Z-93 and Z-93P in the simulated 5-yr GEO dose. Figure 2 shows that low levels of a surface contaminant photofixed on Z-93 does not experience rapid reflectance recovery when exposed to air. The reflectance of Z-93 with a low level surface contaminant will partially recover with prolonged exposure to air. Figures 5 and 7 show that the reflectance of Z-93, without a surface contaminant layer, will rapidly recover reflectance when exposed to air.

The nitrogen back-fill test was performed to determine if the bleaching effects, commonly observed when back-filled with air, could be eliminated or reduced and thus provide a guideline to measure sample reflectance ex-vacuo with some credibility. The results show that Z-93 samples experience a recovery in solar alpha of approximately 52 percent when back-filled and maintained in a dark closed nitrogen environment for 113 hr. It should be noted that this 52-percent recovery of solar alpha was observed after a specific CEE exposure was applied to the Z-93 sample. This specific dose was 953.5 ESH of NUV and VUV,  $1.2 \times 10^{15}$  electrons/cm<sup>2</sup> at 50 KeV, and  $7.35 \times 10^{14}$  electrons/cm<sup>2</sup> at 200 KeV. Another Z-93 sample was exposed to a CEE of 1,156.5 ESH of NUV and  $3.53 \times 10^{15}$  electrons/cm<sup>2</sup> at 50 KeV then repressurized with air. The solar alpha of this sample recovered by 71 percent after 15 min in air, as shown in Figures 3 and 7. Figure 8 summarizes the change of Z-93 and Z-93P solar alpha during this test. Solar alpha of both Z-93 and Z-93P increased with increasing CEE, and solar alpha recovered as the samples were exposed to nitrogen and, later, air. These results indicate that nitrogen repressurization can decrease the rate of reflectance recovery and, therefore, has a potential use in obtaining credible reflectance measurements ex-vacuo. The authors emphasize that this specific use of nitrogen, as a repressurant, requires further development.

## REFERENCES

1. Babel, H.W. et al.: *Selection, Rationale, Application, Optical Properties and Life Verification of Z-93 for the Space Station*, August 1994.
2. NASA TM-108518, *Radiation Induced Degradation of the White Thermal Control Paints Z-93 and Z-93P*, October 1996.
3. *Integrated Tiger Series 3.0*, Oak Ridge National Laboratory, Radiation Shielding Information Center, CCC-467, 1994.

TABLE 1. Dose applied to the Z-93 sample shown in Fig. 2.

| Source            | Fluence  |
|-------------------|--|
| NUV               | 150 ESH at 2 UV Suns                           |
| VUV               | 150 ESH at 2 UV Suns                           |
| 700 KeV protons   | $5 \times 10^{13}$ protons/cm <sup>2</sup>     |
| 200 KeV protons   | $6.3 \times 10^{13}$ protons/cm <sup>2</sup>   |
| 100 KeV protons   | $6.2 \times 10^{13}$ protons/cm <sup>2</sup>   |
| 200 KeV electrons | $1.1 \times 10^{14}$ electrons/cm <sup>2</sup> |
| 50 KeV electrons  | $1.9 \times 10^{14}$ electrons/cm <sup>2</sup> |

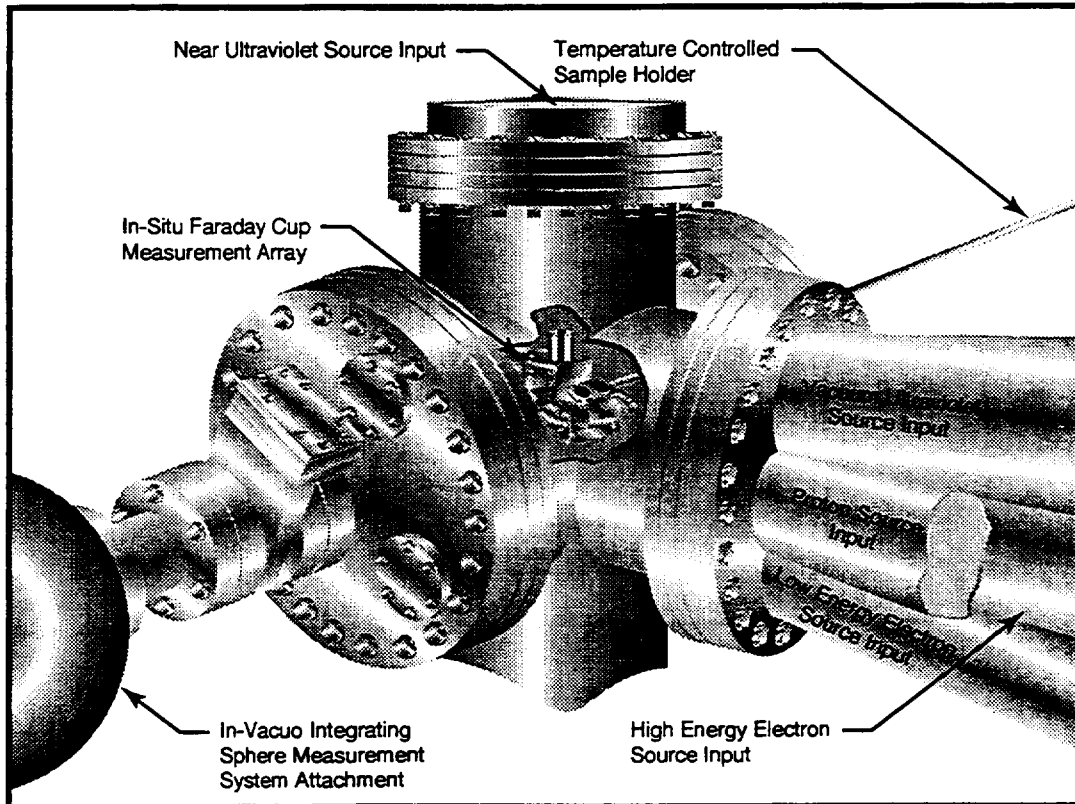


FIGURE 1. CEE test chamber

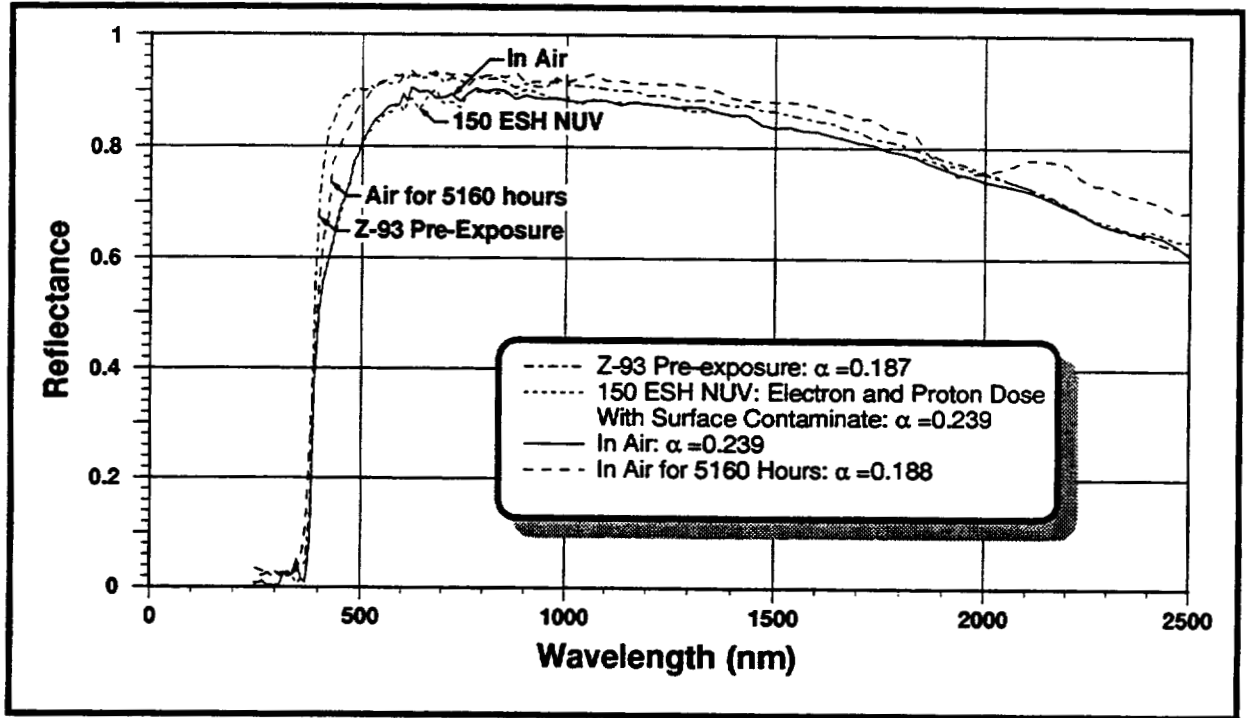


FIGURE 2. Reflectance spectra showing photodeposited surface contaminant on Z-93 accumulated during a low dose CEE exposure.

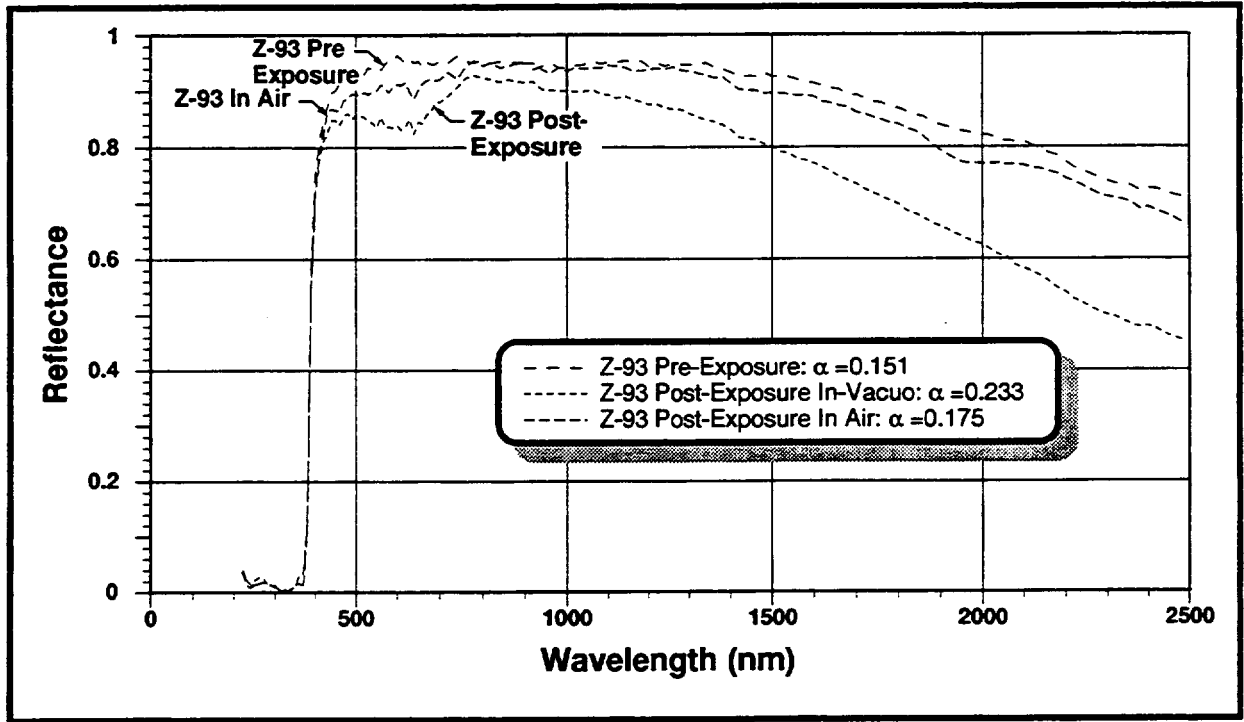


FIGURE 3. In-vacuo reflectance spectra of Z-93 exposed to CEE and repressurized with air.

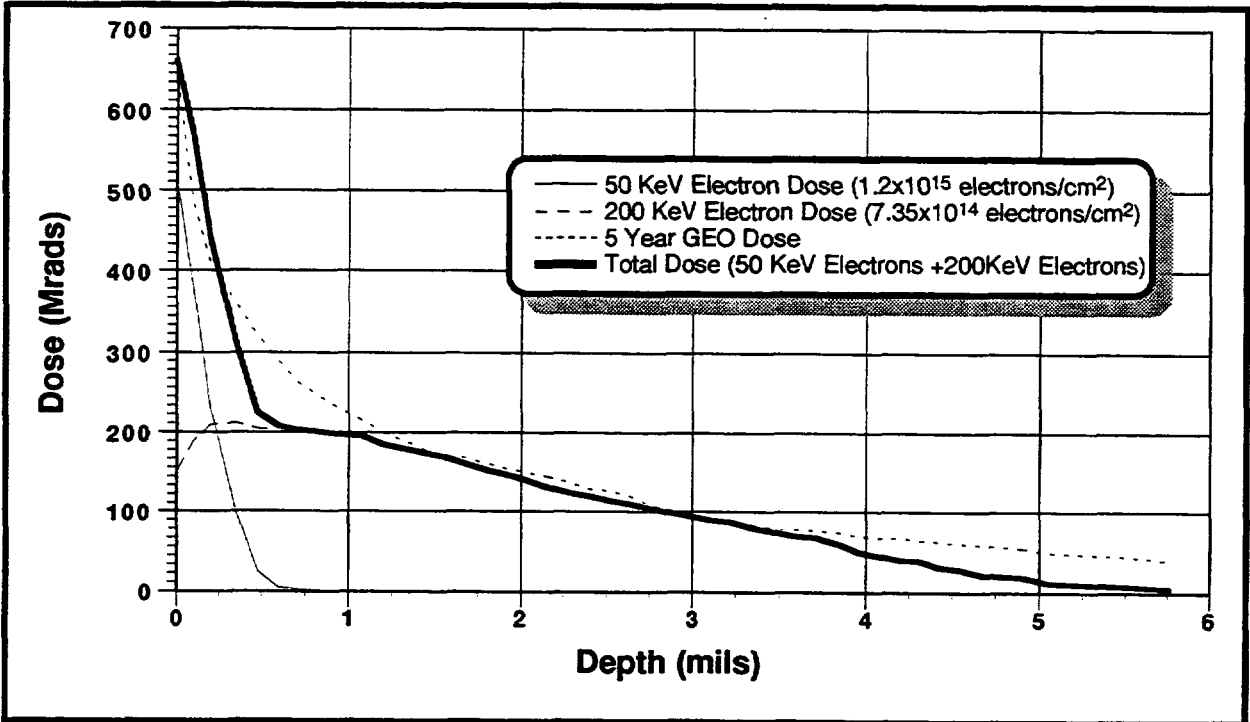


FIGURE 4. Dose-depth profile for Z-93 with a dose of to 50 KeV electrons at a fluence of  $1.2 \times 10^{15}$  electrons/cm<sup>2</sup>, 200 KeV electrons at a fluence of  $7.35 \times 10^{14}$  electrons/cm<sup>2</sup> and a 5-yr GEO dose.

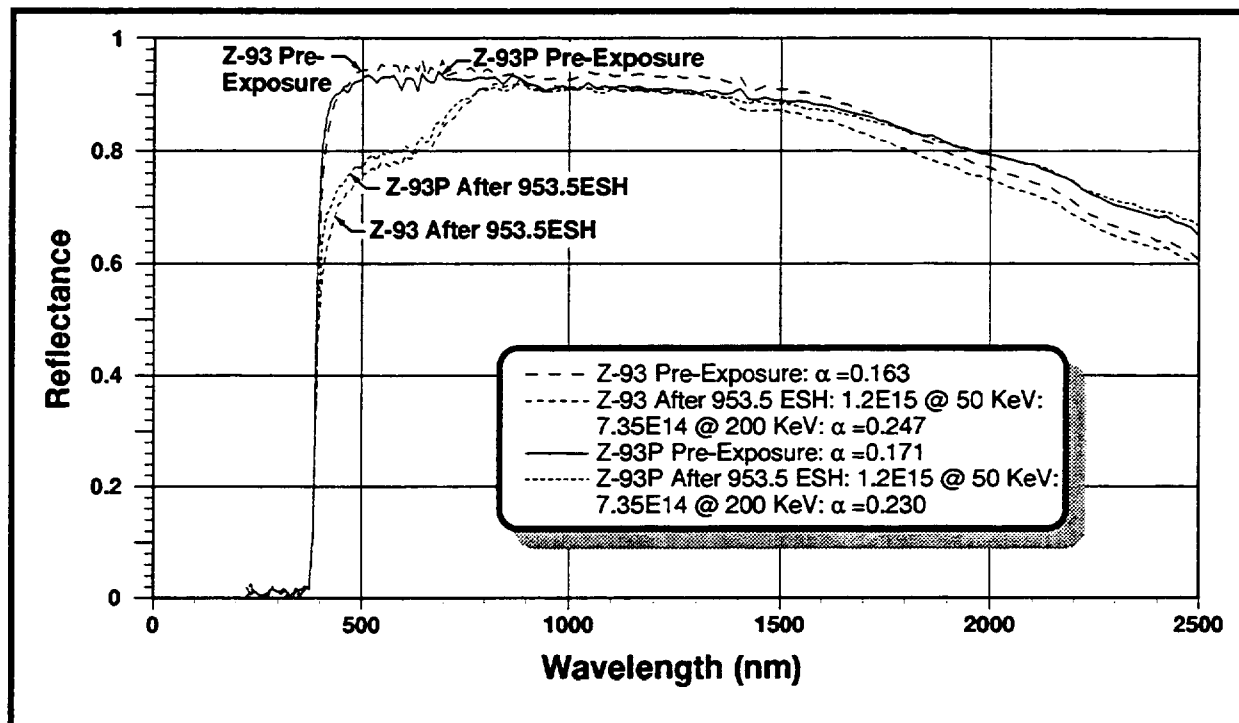


FIGURE 5. In-vacuo reflectance spectra of Z-93 and Z-93P after a cumulative dose of 953.5 ESH of NUV and VUV, 50-KeV electrons at a fluence of  $1.2 \times 10^{15}$  electrons/cm<sup>2</sup> and 200-KeV electrons at a fluence of  $7.35 \times 10^{14}$  electrons/cm<sup>2</sup>.

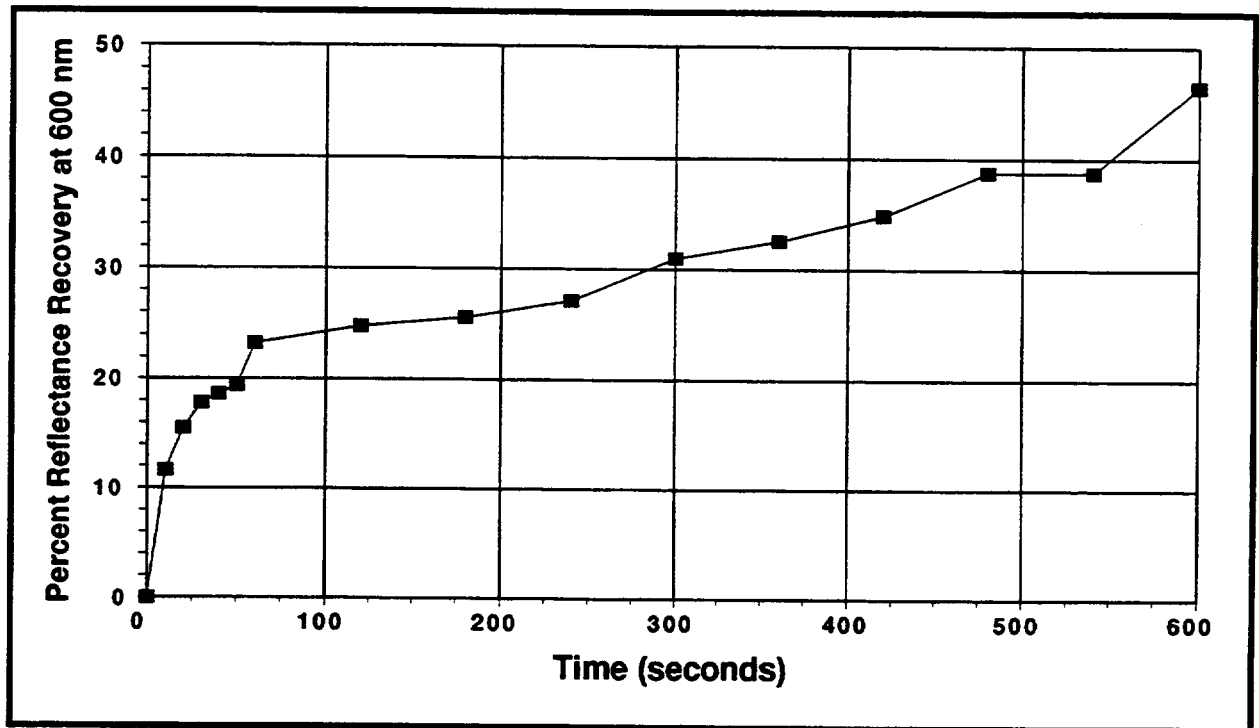


FIGURE 6. Data showing the percent reflectance recovery at 600 nm of the Z-93P sample during repressurization with nitrogen.

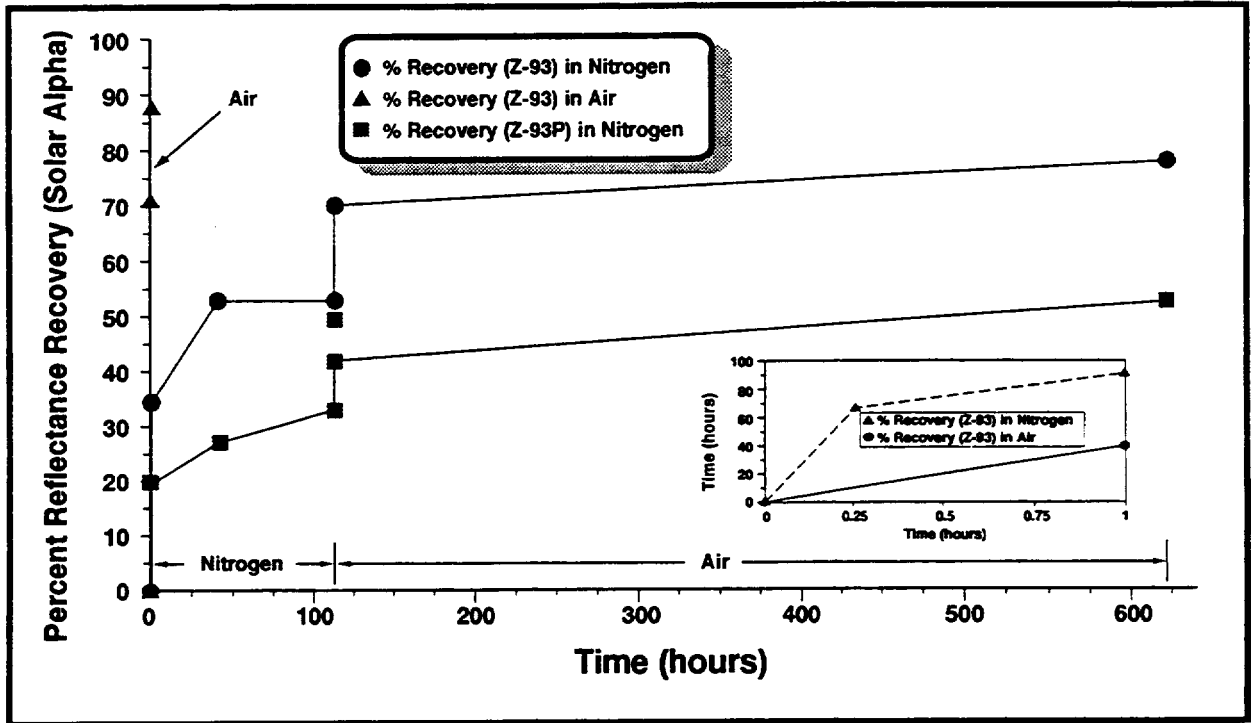


FIGURE 7. Reflectance of Z-93 and Z-93P after 1, 41, and 113 hr in a closed nitrogen environment then exposed to air for a total of 510 hr. This graph shows that the rate of reflectance of the Z-93 solar alpha was less when nitrogen was used as a repressurizing gas.

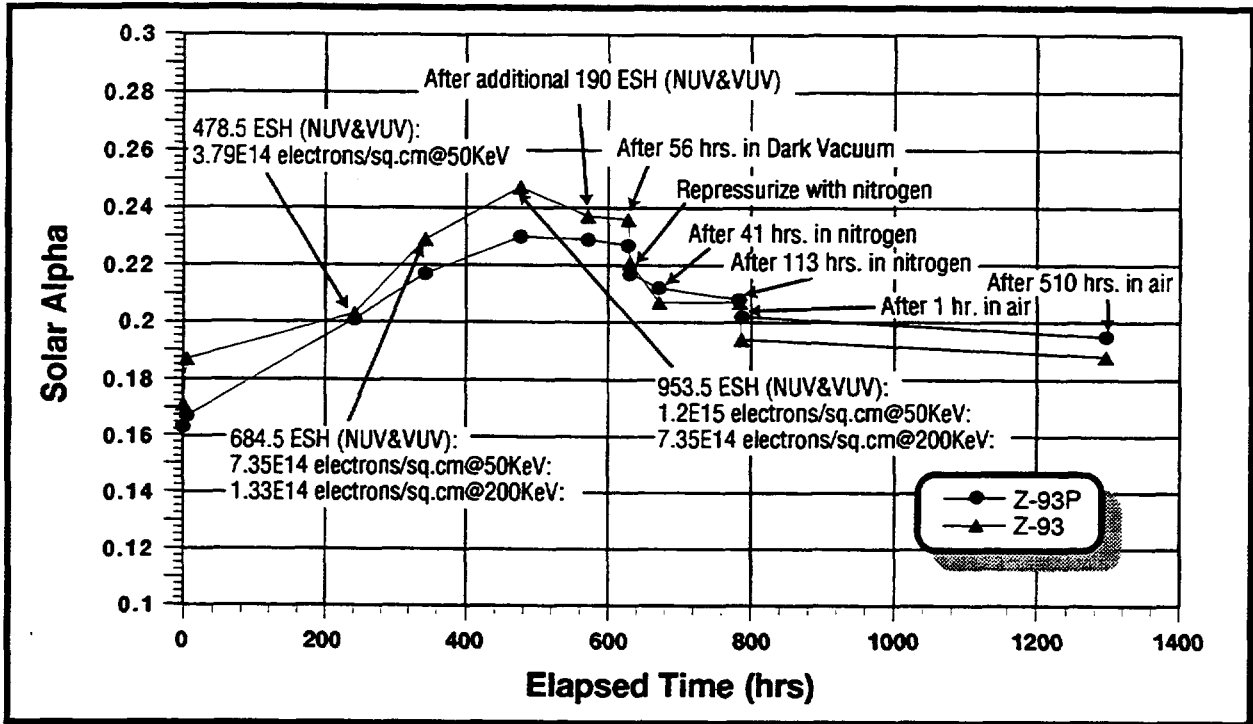


FIGURE 8. Summary of Z-93 and Z-93P solar alpha change during the CEE test.

## ON-ORBIT TEFLON® FEP DEGRADATION

Jacqueline A. Townsend, Patricia A. Hansen  
NASA/GSFC  
Greenbelt, Maryland 20771  
301-286-6685  
jacqueline.a.townsend.1@gsfc.nasa.gov  
patricia.a.hansen.2@gsfc.nasa.gov

Joyce A. Dever  
NASA/LeRC  
Cleveland, Ohio 44135  
joyce.a.dever@lerc.nasa.gov

### ABSTRACT

During the Hubble Space Telescope (HST) Second Servicing Mission (SM2), degradation of unsupported Teflon® FEP (fluorinated ethylene propylene), used as the outer layer of the multi-layer insulation (MLI) blankets, was evident as large cracks on the telescope light shield. A sample of the degraded outer layer was retrieved during the mission and returned to Earth for ground testing and evaluation. The results of the Teflon® FEP sample evaluation and additional testing of pristine Teflon® FEP led the investigative team to theorize that the HST damage was caused by thermal cycling with deep-layer damage from electron and proton radiation which allowed the propagation of cracks along stress concentrations, and that the damage increased with the combined total dose of electrons, protons, UV and x-rays along with thermal cycling. This paper discusses the testing and evaluation of the Teflon® FEP.

### INTRODUCTION

The Hubble Space Telescope was launched into Low Earth Orbit (LEO) in April 1990 with a mission to spend 15 years probing the farthest and faintest reaches of the cosmos. Crucial to fulfilling this promise is a series of servicing missions to upgrade scientific capabilities. During the First Servicing Mission (SM1) in December 1993, MLI blankets were retrieved and analyzed in ground-based facilities. These studies revealed that the outer layer of the MLI, aluminized Teflon® FEP, was beginning to degrade. Close inspection of the Teflon® FEP revealed through-thickness cracks in areas with the highest solar exposure and stress concentration. Mechanical tests showed significantly decreased ultimate strength and elongation (2).

During the Second Servicing Mission (SM2) in February 1997, astronauts observed and documented severe cracking in the outer layer of the MLI blankets on both solar facing and anti-solar facing surfaces (1). During the repair process, a small specimen of the outer layer was retrieved from the Light Shield (LS) region and was returned for ground-based analysis. In addition, as part of an instrument installation, a sample of the bonded Teflon® FEP radiator surface was returned on the Cryogen Vent Cover (CVC).

Since the damage to the outer layer was so severe at SM2, a Failure Review Board was convened to, among other tasks, determine the mechanism of the damage. There were three phases to that investigation: document the condition of the MLI on the telescope; analyze the retrieved specimens; perform simulated environmental exposures. This paper summarizes the results of the first two phases and draws overall conclusions about the failure mechanism.

## HUBBLE SPACE TELESCOPE

### Thermal Control Materials

#### *Description*

The Hubble Space Telescope uses several thermal control materials to passively control temperatures on-orbit. The two primary types are MLI blankets and radiator surfaces (Figure 1).

MLI blankets were used on over 80 percent of the external surface area of HST. The top (space-exposed) layer of these blankets was 127  $\mu\text{m}$  (0.005 in) FEP with roughly 100 nm of vapor deposited aluminum (VDA) on the back (FEP/VDA). Next there were 15 layers of embossed 8.17  $\mu\text{m}$  (0.00033 in) double-aluminized Kapton<sup>®</sup>. The inner-most layer was 24.5  $\mu\text{m}$  (0.001 in) single aluminized Kapton. The embossing pattern reduced layer-to-layer conduction, making spacers unnecessary. The blankets were closed out on all four sides with a taped cap section, and the layers were tied together intermittently throughout the blanket using spots of acrylic transfer adhesive film. Where the blankets were cut to fit around features (handrails, standoffs, etc.) the blanket was closed out again by taping the cap section. In addition, the blankets were vented with "X" cuts and the outer layer was reinforced using aluminized Kapton<sup>®</sup> scrim tape. The entire blanket was attached to the space craft with Velcro<sup>®</sup> stitched to the inner layer.

The radiator surfaces were simply perforated silver Teflon<sup>®</sup> tape bonded directly to the aluminum vehicle substrate. The space-exposed surface was 127  $\mu\text{m}$  (0.005 in) FEP with roughly 100 nm of vapor deposited silver (VDS) on the back (FEP/VDS). The silver side was coated with Inconel and finally with an acrylic adhesive. This material was purchased in rolls (4 in. width) with the adhesive already applied. The tape was applied in sections, and a Teflon<sup>®</sup> wand was used to minimize air entrapment and ensure a good bond. Damaged tape was replaced as necessary as the telescope was built.

#### *Retrieved Specimens*

Specimens of these thermal control materials were retrieved during the servicing missions. Table 1 provides the labels and descriptions of the specimens that will be discussed in this paper. No material was saved when the telescope was built, therefore no control material existed from the same production lot. The blanket shop at Lockheed Martin Missiles and Space (LMMS) provided a full-build MLI blanket in April 1997 to be used as the control sample for this experiment.

Complete MLI blankets were removed from the HST magnetometers during SM1. The magnetometers were roughly cubic, and the covers had surfaces that received various solar exposures. A complete analysis of the damage at SM1 was performed by Zuby, de Groh, and Smith following the mission (2). For the purpose of comparison with SM2 damage, a specimen of the top layer was cut from the section that received the middle range of solar exposure. When possible, SM1 results reported in this paper were taken from the earlier analysis of this section of the magnetometer covers. When an analysis had not been completed following SM1, the analysis was performed on this section along with the analysis of the SM2 specimen.

During SM2, a specimen from the outer layer of the MLI, shown in Figure 2, was taken from the upper light shield (LS) region of the telescope. The roughly triangular specimen was tightly curled, forming several rolled layers (Figure 2). The astronaut cut the specimen from right to left, with a change in the initial direction as the astronaut realized he was cutting through the roll of the specimen. In Figure 3 the specimen is shown flat with the cracks identified. The specimen was stored in a reclosable polyethylene bag and stowed in a mid-deck locker for the duration of the mission.

In addition to the outer layer MLI specimen, a radiator specimen was retrieved during SM2. As part of an instrument installation, a cryogen vent cover (CVC) was removed and returned to Earth at project request. The outside of the CVC (radiator surface) had been exposed to the orbital environment and provided good data for the thermal degradation of the radiator surfaces.

TABLE 1: SPECIMEN NAMES AND DESCRIPTIONS

| Specimen Name | Description  |
|---------------|--|
| Pristine      | Outer layer MLI (FEP/VDA) from LMMS, received 4/15/97                      |
| SM1 MSS       | Outer layer MLI (FEP/VDA) from magnetometer cover, retrieved at SM1, 12/93 |
| SM2 LS        | Outer layer MLI (FEP/VDA) from light shield region; retrieved at SM2, 2/97 |
| SM2 CVC       | Radiator surface (FEP/VDS) from cryogen vent cover; retrieved at SM2, 2/97 |

### Environment

The Hubble Space Telescope was deployed at an altitude of 598 km and an orbit inclination of 28.5 degrees. The telescope is oriented such that one side (+V3) faces the sun throughout its orbit, although the telescope does pitch and roll in order to maintain focus on a target object. This means that one side of HST (+V3) receives direct sunlight at all times when HST is not in the Earth's shadow, and the other side (-V3) only receives sunlight reflected from the Earth's surface (albedo). The other surfaces of the telescope receive varying amounts of sunlight depending on how much time is spent pointing in a given direction (1).

The exterior surfaces of HST are exposed the orbital environment which includes solar radiation, charged particles (trapped particles and plasma), atomic oxygen, and temperature extremes. Solar exposure, including near ultraviolet radiation (UV), vacuum ultraviolet radiation, and soft x-rays from solar flares, may cause surface damage in polymeric materials such as Teflon<sup>®</sup> FEP. Trapped electrons and protons (particle radiation) may cause molecular changes in the bulk of the material, changing the mechanical properties. Atomic oxygen can erode the surface through chemical reactions with gaseous oxide products. Temperature extremes and thermal cycling can enhance the rate of damage from other environmental factors, and in Teflon<sup>®</sup> FEP they can affect the molecular structure (1-4).

Table 2 contains a summary of the environmental exposure each of the retrieved specimens received in terms of fluence and, when appropriate, absorbed dose. The dose-versus-depth profile for each type of radiation was calculated, and the absorbed doses at 25.4 μm (0.001 in) and 127 μm (0.005 in) are included in Table 2. The total absorbed dose of ionizing radiation, included in the table, is the dose due to x-rays and trapped charged particles.

### Observations

#### *First Servicing Mission (SM1)*

The first servicing mission took place in December 1993, 3.6 years after the telescope was deployed. During the mission itself, the only damage noticed was on the -V3 (anti-sun) side. Some cracks were apparent near the NASA logo, and they were attributed to the mismatch in the coefficient of thermal expansion of the materials in the MLI and the logo. However, close examination of the retrieved magnetometer covers revealed some localized (less than 4 cm), through-thickness cracks in areas that experienced the highest solar exposure and stress concentration (2).

The exterior of the telescope was photographed extensively during the mission, although not all surfaces were documented. At that time, it appeared that most of the MLI was intact, however,

a review of those images following the second servicing mission showed more damage. A significant fraction of the largest cracks at SM2 were visible as lines or wrinkles in the older images. Following SM1 it was impossible to tell that these were crack initiation sites, however, knowing that a crack had propagated through a region at SM2, the evidence of damage could be seen in the SM1 images.

TABLE 2: ENVIRONMENTAL EXPOSURES FOR RETRIEVED HST MATERIALS

| Environmental Factor  | Deposited Depth                  | SM1 MSS  | SM2 LS   | SM2 CVC                                       |
|---|----------------------------------|--|--|---|
| Duration  |                                  | 3.6 years  | 6.8 years  |   |
| Atomic Oxygen (sweeping ram)                                      |                                  | 1.56E20 atoms/c m <sup>2</sup>                         | 1.64E20 atoms/c m <sup>2</sup>                         |   |
| Thermal Cycles  |                                  |  |  |   |
| Number of Cycles  |                                  | 21,000   | 40,000   | 40,000  |
| Temperature Limits  |                                  | -100 to +50 °C   | -100 to 50 °C nominal<br>-100 to 200 °C curled         | -80 to -15 °C                                 |
| Equivalent Sun Hours (ESH)  |                                  | 11,339 (7% albedo)                                     | 33,638 (0% albedo)                                     | 19,308 (33% albedo)                           |
| VUV Dose (<180 nm, absorbed)                                      | 1 mil<br>5 mil                   | 2.185E6 krads<br>4.37E5 krads                          | 6.480E6 krads<br>1.296E6 krads                         | 2.490E6 krads<br>4.98E5 krads                 |
| X-ray Fluence   |                                  |  |  |   |
| 0.5 to 4 Å<br>1 to 8 Å  |                                  | 4.9 J/m <sup>2</sup><br>74 J/m <sup>2</sup>            | 9.0 J/m <sup>2</sup><br>142 J/m <sup>2</sup>           | 3.5 J/m <sup>2</sup><br>54.6 J/m <sup>2</sup> |
| X-ray Dose  |                                  |  |  |   |
| 0.5 to 4 Å<br>(24 to 3.1 keV)                                     | 1 mil<br>5 mil                   | 0.98 krads<br>0.59 krads                               | 1.8 krads<br>1.1 krads                                 | 0.69 krads<br>0.41 krads                      |
| 1 to 8 Å<br>(12 to 1.55 keV)                                      | 1 mil<br>5 mil                   | 59.1 krads<br>23.2 krads                               | 113.2 krads<br>44.4 krads                              | 43.4 krads<br>17.0 krads                      |
| Trapped Particle Fluence (> 40 keV)                               |                                  |  |  |   |
| Electrons<br>Protons  |                                  | 1.39E13 #/cm <sup>2</sup><br>7.96E9 #/cm <sup>2</sup>  | 2.13E13 #/cm <sup>2</sup><br>1.83E10 #/cm <sup>2</sup> |   |
| Trapped Particle Dose (> 40 keV)                                  |                                  |  |  |   |
| Electrons<br>Protons  | 1 mil<br>5 mil<br>1 mil<br>5 mil | 277 krads<br>71.6 krads<br>0.93 krads<br>0.75 krads    | 389 krads<br>95.9 krads<br>2.32 krads<br>1.87 krads    |   |
| Plasma Fluence (.1 to a few keV; absorbed dose in 1 mil < 1 krad) |                                  |  |  |   |
| Electrons<br>Protons  |                                  | 3.18E19 #/cm <sup>2</sup><br>1.11E19 #/cm <sup>2</sup> | 4.66E19 #/cm <sup>2</sup><br>1.63E19 #/cm <sup>2</sup> |   |
| Total Absorbed Ionizing Radiation<br>(trapped particles, x-rays)  | 1 mil<br>5 mil                   | 337 krads<br>96 krads                                  | 506 krads<br>142 krads                                 | 435 krads<br>115 krads                        |

*Second Servicing Mission (SM2)*

During SM2, the first damage was noticed on the +V3 side (sun side) with several large cracks in the light shield MLI outer layer. The largest crack, more than one meter long, is shown in Figure 4. Upon further visual inspection of the vehicle, additional cracks were apparent on all MLI surfaces, on both solar and anti-solar facing surfaces. Although the most striking damage occurred on the +V3 side, significant damage was observed all around the telescope. A program decision was made to reconfigure contingency MLI patches and use them to patch the worst of the damaged areas.

Prior to patching the corners of the Bay 8 MLI, the astronauts performed two tests: a Velcro® cycling test and a Teflon® FEP bend test. The Velcro® attaching the blanket to the spacecraft was cycled to determine its integrity. The astronauts reported that the Velcro® appeared to be securely fastened to the vehicle substrate and the hook seemed to hold the pile securely. The astronauts also bent a piece of the Teflon® FEP over on itself (VDA surface to VDA surface) to determine if manipulating it during the patching process would cause significant damage. The astronauts reported that the Teflon® FEP did not crack.

Images of the radiator surfaces revealed a mottled appearance. Significant increases in the solar absorptance of the silver Teflon® tape were obvious as dark patches distributed across the aft region of the telescope. Some tape strips were significantly worse than others, and the dark patches occasionally occurred in broad streaks along a section of tape.

The degradation of these thermal control materials was barely measurable as increased temperatures inside the equipment bays of the telescope. However, the telescope was designed with a large thermal margin, so at SM2 this small increase had no effect on telescope performance.

## ANALYSIS OF RETRIEVED MATERIALS

The SM2 flight specimens were fully documented using macro photography, optical microscopy, and scanning electron microscopy (SEM). Then the MLI specimens from SM1 and SM2 were characterized through exhaustive mechanical, optical, and chemical testing.

### Scanning Electron Microscopy (SEM) and Optical Microscopy

The first task was to document the SM2 LS specimen and assemble the four pieces received into the single specimen that was cut in orbit. Both SEM and optical microscopy were used in this effort. Once the original configuration had been determined, the edges were identified as either a deliberate cut, a handling artifact, or an on-orbit fracture (Figure 3). From this information, the fracture initiation site became apparent.

The fractures that resulted in the SM2 LS specimen initiated at an edge of the MLI that had been cut to fit around a handrail (Figure 2). From small defects in this cut edge, two fractures developed and propagated in orbit almost normal to one another, resulting in a roughly triangular specimen. The VDA was completely missing from the SM2 LS specimen in regions where the Teflon® FEP was bonded to the rest of the blanket, which included the region where the cracks initiated.

Although the blankets were relatively flat when deployed, photos of the SM2 LS specimen in orbit showed that it was tightly curled, with the space-exposed Teflon® FEP surface as the inner surface and the VDA exposed. This curling indicated a volume shrink gradient in the specimen. Based on the diameter of the curl (1.5 cm) the estimated strain difference between the outer and inner surface of the Teflon® FEP was ~1.5% (3).

SEM images of the initiation region showed clear differences between the scissors cut that occurred prior to launch or on orbit, the fractures that propagated while in orbit, and cracks from subsequent handling. The featureless nature of the orbital fracture is unique, and attempts to duplicate this smooth fracture with the SM2 specimen under bending or tensile stress resulted in fractures with more fibrous features. The inability to duplicate the featureless fracture indicated that the fractures propagated in orbit very slowly, in the presence of relatively low stress and under the influence of radiation and other environmental factors. This type of "slow crack growth" has never been studied in Teflon® FEP (3).

Homogeneous mud-like cracking (mud-tiling) and buckling of the VDA were also apparent in the SEM and optical images. A mismatch between the coefficient of thermal expansion (CTE) of the

Teflon<sup>®</sup> FEP and the VDA was most likely the cause. Tensile cracks developed in the aluminum from low cycle fatigue as the material cycled above room temperature, and buckling occurred when the material cycled below room temperature (3).

The mud-tiling of the metal backing was apparent in all of the specimens. In the SM2 CVC specimen, handling and processing procedures such as bending and pressing the FEP/VDS while adhesive bonding it to the spacecraft surface most likely created the cracks.

SEM images of the surface showed recession and texturing common in polymers exposed to a sweeping ram fluence of atomic oxygen.

### Mechanical Analyses

The most obvious indication of degradation in the retrieved specimens was found in the tensile test results. Table 3 (below) is a summary of the strength test results. In terms of strength, the SM2 LS specimen was obviously most degraded. The CVC SM2 specimen was less degraded, and the strength of the MLI SM1 specimen degraded the least. This ranking was most apparent in the elongation data.

TABLE 3: SUMMARY OF STRENGTH TEST RESULTS (3)

| Material | Yield Strength (MPa) | Ultimate Strength (MPa) | Elongation (%) |
|----------|----------------------|-------------------------|----------------|
| pristine | 13.8                 | 24.8                    | 340            |
|          | 14.3                 | 26.5                    | 360            |
|          | 14.3                 | 28.1                    | 390            |
| SM1 MSS  | 14.3                 | 15.4                    | 196            |
|          | 14.3                 | 16.6                    | 116            |
| SM2 CVC  | 11.0                 | 12.1                    | 25             |
|          | 15.4                 | 16.0                    | 25             |
|          | N/A                  | 11.0                    | 15             |
| SM2 LS   | N/A                  | 13.2                    | 0              |
|          | N/A                  | 2.2                     | 0              |

Bend testing was performed on the retrieved specimens from SM1 and SM2. Each small specimen was bent manually to 180 degrees around successively smaller mandrels (diameters from 9.19 to 3.56 mm). Following each bend, the specimen was examined with an optical microscope to detect crack length and features. As expected, the pristine material showed no cracking when bent around the smallest mandrel, a strain of 15 percent (4).

Each of the two SM2 LS samples formed a full-width crack when bent around the first or second large mandrel with the space-exposed surface in tension. Examination showed that this single, full-width crack went most of the way through the thickness of the sample, although the strain from the mandrel diameter was only 2 to 2.5 percent. SEM analysis of the fractures showed the fibrous features of a handling crack. Bending two other SM2 LS samples around the smallest mandrel with the space-exposed surface in compression did not produce cracks, even at the resulting 15 percent strain. This implied that the space-exposed surface was more brittle than the back surface (4).

The SM1 MSS specimens and the SM2 CVC specimens cracked quite differently from the SM2 LS specimens. Instead of a single, catastrophic crack, the specimens developed several very short, shallow cracks that eventually joined to form a long, jagged crack across the surface at much smaller mandrels (higher strain). Existing flaws from vent cuts or handling reduced the strain at which

cracks first appeared. Unlike the SM2 LS samples, these samples appeared to retain considerable ductility (4).

The surface micro-hardness of the retrieved specimens were measured by Nano Instruments using their patented Continuous Stiffness Measurement technique. All of the space-exposed specimens showed an increased hardness at the surface that decreased with depth. By 500 nm, the hardness of all the exposed specimens was indistinguishable from that of pristine at 500 nm. Although the SM1 materials seemed to show a trend of increasing hardness with increasing solar exposure, the SM2 materials, which had the highest solar exposure, did not follow this trend (4).

### Optical Analyses

Significant effort was spent in determining the appropriate method for measuring the solar absorptance ( $\alpha_s$ ) of the flight materials. Because of the mud tiling and the delamination of the metal coatings, traditional methods gave results that either over- or under-estimated the changes to the solar absorptance (5). The reflectance of the specimens was measured using a Cary 5E UV-Vis-NIR Spectrophotometer with an integrating sphere (ASTM E490, E903). A 99.9 percent reflective standard was placed behind the specimens while the measurements were made to minimize transmitted light through metal delamination sites.

Table 4 contains a summary of the solar absorptance data of the retrieved specimens. Since there were no control specimens from the HST lot, increases were reported with respect to pristine for the FEP/VDA specimens (SM1 MSS and SM2 LS). For the SM2 CVC specimen the post-flight increases were reported with respect to data found in literature for the solar absorptance of FEP/VDS ( $\alpha_s < 0.09$ ).

TABLE 4: SOLAR ABSORPTANCE ( $\alpha_s$ ) OF RETRIEVED SPECIMENS (5)

| Sample       | # of Samples | Metallized FEP   |          | FEP Alone (metal removed) |          |
|--------------|--------------|------------------|----------|---------------------------|----------|
|              |              | $\alpha_s$       | Increase | $\alpha_s$                | Increase |
| Pristine     | 6            | $0.12 \pm 0.002$ | -        | $0.01 \pm 0.001$          | -        |
| Post Flight: |              |                  |          |                           |          |
| SM1 MSS      | 2            | 0.22             | 0.10     | 0.03                      | 0.02     |
| SM2 LS       | 2            | 0.20             | 0.08     | 0.07                      | 0.06     |
| SM2 CVC      | 2            | 0.125            | -0.04    | -                         | -        |

For the SM2 LS specimen, most of the 0.08 solar absorptance increase of the material was attributed to increases in the solar absorptance of the Teflon<sup>®</sup> FEP, rather than to cracking in the VDA. With the VDA removed, the solar absorptance of the SM2 LS specimen was still 0.06 higher than pristine. No clear correlation was found between solar absorptance increase and equivalent solar hours (ESH).

Literature values for solar absorptance of pristine FEP/VDS were found between 0.06 to 0.09. The increase in the solar absorptance of the SM2 CVC specimen was attributed to darkening of the acrylic adhesive that was used to bond the material to the spacecraft. During the bonding process, the material was repeatedly bent and deformed, which created the mud tiling cracks in the silver deposit. The adhesive bled through these cracks in the silver and was exposed to sunlight. Acrylic adhesives are known to darken when exposed to UV (1, 6).

In these measurements, the amount of darkening varied widely as a function of the crack size and density. In localized regions of the SM2 CVC, the solar absorptance was as high as 0.14 and as low as 0.115. The average value is reported in Table 4. The average solar absorptance of the

FEP/VDS on the aft region of the telescope was estimated at 0.14 based on the temperature limits of HST.

## Chemical Analyses

The chemical composition was studied using Time-of-Flight Secondary Ion Mass Spectrometry (TOF-SIMS), Fourier Transform infrared microscopy ( $\mu$ -FTIR), Attenuated Total Reflectance infrared microscopy (ATR/FTIR), and X-ray Photoelectron Spectroscopy (XPS).

Time-of-Flight Secondary Ion Mass Spectrometry (TOF-SIMS) was used to determine the ion composition of the first mono-layer (0.3 nm) of the specimens and to image ion intensities on the cross sections (6). For pristine Teflon<sup>®</sup> FEP, the most common fragmentation point was at the bond between CF<sub>2</sub> molecules, and some minor contamination of the surface was found.

The SM2 LS specimen had the most evidence of chemical changes. The surface was highly oxidized, and there was weak evidence of surface de-fluorination. The cross-section analysis showed that this damage only penetrated to a depth of 5-10  $\mu$ m; from 10-110  $\mu$ m deep the material appeared similar to the pristine Teflon<sup>®</sup> FEP. Some silicon-containing surface contamination was also found (6).

The TOF-SIMS analysis of the SM2 CVC specimen revealed strong evidence of de-fluorination on the surface. Although oxygen was detected in a few of the low-mass fragments, unlike the SM2 LS specimen, most ions did not contain oxygen. Analysis of the cross section showed a spectrum very similar to pristine Teflon<sup>®</sup> FEP, indicating that the de-fluorinated region was on the very surface of the specimen. Very few silicon-containing contaminants were found on this surface.

The SM1 MSS specimen most closely resembled the pristine. There was some evidence of oxidation and de-fluorination, but not to the extent present in either of the other two flight specimens. Silicon-containing contaminants were detected on the surface (6).

Fourier Transform infrared microscopy ( $\mu$ -FTIR) analysis was performed as described in reference 7, to detect crystallinity changes and oxidation. The testing conducted for this effort did not confirm that this  $\mu$ -FTIR method can detect crystallinity changes. So, although this method showed no significant differences in the crystallinity of the of the pristine, SM1 MSS, SM2 LS or SM2 CVC specimens, the test was inconclusive. Also, only SM1 MSS showed significant oxidation in the first 3 to 5  $\mu$ m of the material (6).

X-ray Photoelectron Spectroscopy (XPS) was performed on the MLI SM2 and CVC SM2 specimens and a pristine specimen. The analysis depth of the XPS is roughly 10 nm; a change in the ratio of carbon to fluorine (C/F) was defined as damage. The C/F ratio of pristine Teflon<sup>®</sup> FEP was 8.05 with an oxygen concentration of 0.2 atom percent. The SM2 CVC specimen appeared to be the most damaged with a measured C/F ratio of 6.3, and an oxygen concentration of 1.9 atom percent. A typical region of the SM2 LS specimen had a C/F ratio of 6.8 with an oxygen concentration of 0.8 atom percent. A region of the SM2 LS specimen that appeared contaminated was the least damaged with a measured C/F ratio of 7.9, an oxygen concentration of 1.5 atom percent, and a trace contaminant of either silicone or hydrocarbon (6).

## Molecular Structure Analyses

X-ray Diffraction (XRD) was used to detect changes in the crystallinity of the returned MLI specimens from SM1 and SM2, and the results are summarized in Table 5. The pristine specimen had a crystallinity of 28-29 percent. Specimens with various ESH returned during SM1 showed a crystallinity of 28-32 percent. These measurements were within the uncertainty of the instrument, so

SM1 MSS samples had a crystallinity that was indistinguishable from pristine. The SM2 LS samples showed a significant increase, with a crystallinity of 46-47 percent (6).

The density of the specimens was found using a density gradient column. This data was then converted to crystallinity values using a table provided by DuPont. These results are also summarized in Table 5 (below). The calculated crystallinity of the SM1 specimens were indistinguishable from pristine material at 50 percent. The crystallinity of the MLI SM2 specimen was higher, at 65 percent (6).

Although there were differences between the absolute value of the crystallinity determined using XRD and the density method, the change in crystallinity is identical. Both methods show an increase in crystallinity of 15 percent. The different absolute values of the two methods was not surprising because the principles involved were so different. Based on literature data comparing XRD to various methods, a difference in absolute crystallinity of up to 14 percent is not uncommon (6).

TABLE 5: SUMMARY OF CRYSTALLINITY RESULTS

| Sample             | ESH            | XRD      |                   | Density Gradient Column      |                   |
|--------------------|----------------|----------|-------------------|------------------------------|-------------------|
|                    |                | # Tested | Crystallinity (%) | Density (g/cm <sup>3</sup> ) | Crystallinity (%) |
| Pristine 5 mil FEP | 0              |          |                   | 2.1400                       | 50                |
| Pristine FEP/VDA   | 0              | 6        | 28-29             | 2.1394                       | 50                |
| SM1 MSS            | 4,477          | 1        | 30                | 2.1375                       | 49                |
|                    | 6,324 or 9,193 | 1        | 29                | 2.1381                       | 50                |
|                    | 9,193 or 6,324 | 1        | 32                | 2.1381                       | 50                |
|                    | 11,339         | 2        | 29-30             | 2.1378                       | 50                |
|                    | 16,670         | 1        | 32                | 2.1406                       | 50                |
| SM2 LS             | 33,638         | 2        | 46-47             | 2.1836                       | 65                |

Solid-State Nuclear Magnetic Resonance (NMR) was performed at the University of Akron on pristine Teflon<sup>®</sup> FEP and MLI specimens from SM1 and SM2 to detect changes in chemical species and morphology. NMR performed on the pristine material showed a CF<sub>3</sub> abundance of 7.5 percent. Analysis of the SM1 MSS specimen detected no significant changes in chemistry or morphology. However, the analysis of the SM2 LS specimen showed evidence of changed morphology. The results indicated that the SM2 specimen had undergone chain scission, and that either an increased crystallinity or cross-linking also occurred. No quantitative analysis was feasible.

## DISCUSSION

The mechanical properties of specimens that were returned from the second servicing mission were significantly degraded. Curling in the SM2 LS specimen indicated a volume shrinkage gradient through the thickness, and bend test results confirmed that the space-exposed surface was more embrittled than the inside surface. Fractographic examination of the cracks that occurred in orbit indicated that they propagated very slowly under relatively low stress in the presence of radiation or other environmental effects. Similar featureless fracture surfaces were found in the few localized cracks in the SM1 MSS specimens as well. This "slow crack growth" phenomenon has never been studied in Teflon<sup>®</sup>.

Crack patterns in the vapor deposited metal coatings on the back of the thermal control materials resembled homogeneous mud cracks. This "mud tiling" can be caused by thermal cycling or handling. When the material was bonded, as with the radiator surfaces on HST, the adhesive bled through these cracks in the metal and darkened in the presence of ultraviolet radiation, increasing the solar absorptance.

The chemical analysis techniques used did not yield consistent results. TOF-SIMS data (analysis depth of 0.3 nm) indicated that the SM2 LS specimen was the most damaged, with oxygen-containing ions dominating the mass spectra. The XPS data (analysis depth of 10 nm) indicated that the SM2 CVC specimen was most changed, with the lowest C/F ratio. Infrared microscopy (analysis depth of 3  $\mu\text{m}$ ) was inconclusive with respect to crystallinity, although some contamination was found on the SM1 MSS specimen. The differences may have been simply a function of the analysis depths and sensitivities of the different techniques. Limited attempts to determine the chemical composition deeper into the bulk of the material with these techniques found no changes below 10  $\mu\text{m}$ . Therefore, it is unlikely that composition changes (e.g. de-fluorination, oxidation) can explain the changes to the bulk properties observed in the retrieved specimens.

The decreased elongation in the retrieved specimens, as evidenced by the tensile and bend test results, demonstrated the material's loss of plastic deformation capability. This, coupled with the decreased ultimate tensile strength indicated a reduced molecular weight in the returned Teflon<sup>®</sup> FEP. This implied that chain scission, rather than crosslinking, was the dominant damage mechanism in the retrieved materials. The density measurements and XRD analysis of the SM2 LS specimen revealed a 15 percent increase in crystallinity. The NMR analysis confirmed that both chain scission and increased crystallinity occurred in the SM2 LS specimen and found no change in the bulk molecular structure of the SM1 MSS specimen.

There are two possible explanations for the differences in the bulk property measurements of the SM1 and SM2 retrieved materials. The first, and simplest, is different degrees of damage. NMR and XRD both measure the bulk of a material. It is possible that, although some damage had obviously occurred, at SM1 the damage was not sufficient to be detected by these two techniques. The strength testing did reveal that the SM1 MSS specimen had decreased elongation and ultimate tensile strength, indicating chain scission. However, the damage was not as severe as at SM2.

The second explanation comes from the curling of the SM2 LS specimen. Based on the solar absorptance and emittance of the FEP/VDA, when the top layer was flat it cycled between -100 and +50  $^{\circ}\text{C}$ . Once the specimen curled such that the aluminum was exposed, the thermal properties changed significantly. With the aluminum exposed the specimen cycled between -100 and +200  $^{\circ}\text{C}$ . This higher temperature limit was only experienced by the SM2 LS specimen, not by the SM1 MSS specimen. High temperature thermal cycling can affect the crystallinity, and if the temperature is severe enough it can induce chain scission (8). Further testing is currently under way to determine the effects of high temperature thermal cycling on the SM1 MSS specimen.

Additionally, the astronaut observation following the "bend test" in orbit revealed that a damaged region that did not curl maintained more ductility in orbit than the curled SM2 LS specimen exhibited in the ground testing. That qualitative difference could be from either the different temperatures experienced by the Bay 8 specimen and the SM2 LS specimen or from changes that occurred after the SM2 specimen was exposed to atmosphere. Further testing is required to understand the effects of atmosphere on vacuum irradiated Teflon<sup>®</sup> FEP.

With these analyses completed, the changes to the material were relatively well understood, however, what had caused these changes was not apparent.

The documentation of the condition of the blankets in various locations around HST during the two servicing missions was revealing. At the first servicing mission, there were very few macroscopic cracks. A few were discovered near the NASA logo on the anti-solar-facing side of the spacecraft, and a few were found on close examination of the returned materials from the solar-facing side. However, in general, the outer layer of the MLI blankets appeared to be intact (1,2). During SM2, cracks all around HST were visible to astronauts and in photographs. The damage

appeared to be worse on the solar-facing side of HST, but the MLI on the anti-solar side was also significantly damaged.

Note that the anti-solar-facing side of HST only received Earth albedo sunlight, equivalent to roughly 10 percent of the solar-facing equivalent solar hours (ESH) (1). This meant that at SM1 the solar-facing surfaces of HST had received five times more ESH than the anti-solar facing surfaces had received at SM2. If any component of the ESH was the dominant damaging environmental factor, the damage to the solar-facing side should have been far worse at SM1 than the anti-solar facing surfaces. The photographic evidence of HST clearly contradicts this supposition and casts strong doubt on the idea that any component of the solar spectrum could be solely responsible for the damage observed on HST.

Because the damage to HST did not appear to coincide with ESH, components of the space environment that are more closely homogeneous were suspect. The likely candidates were electron and proton fluences and thermal cycling. Experiments were carried out at NASA Goddard Space Flight Center (GSFC) to explore the combined effects of radiation and thermal cycling, and the results are described elsewhere in this volume (9).

The GSFC experiments showed that electron and proton radiation alone affected the tensile properties of the Teflon<sup>®</sup> FEP. The reduced ultimate strength and elongation was apparent at fluences comparable to the HST end-of-life (20 years). Subsequent thermal cycling between -100 and +60 °C reduced these properties further. These particle radiation exposures coupled with thermal cycling produced damage that most closely resembled the HST specimens. However, the study did not duplicate the degree of damage observed on the returned SM2 specimen with SM2 doses of radiation and thermal cycling at nominal limits (-100 to +50 °C) (9).

Since the thermal cycling following irradiation did affect the tensile properties of the materials, it is possible that the more extreme thermal cycling the SM2 LS specimen experienced produced more damage. Further testing is needed to determine what effect the high temperature cycling has on electron and proton irradiated Teflon<sup>®</sup> FEP.

## CONCLUSIONS

Analysis of the returned specimens showed that all of the retrieved specimens, SM1 MSS, SM2 LS and SM2 CVC, underwent chain scission. Evidence of increased crystallinity was found only in the SM2 LS specimen. Solar absorptance changes in the SM2 LS specimen were attributed to these changes in the Teflon<sup>®</sup> FEP and mud tiling in the VDA. Solar absorptance changes in the SM2 CVC specimen were attributed to mud tiling from handling and subsequent darkening of the acrylic adhesive.

The conclusions of the HST MLI Failure Review Board were based on the combined evidence of HST damage and data uncovered in ground-based experiments. The FRB concluded the following:

*The observations of HST MLI and ground testing of pristine samples indicate that thermal cycling with deep-layer damage from electron and proton radiation are necessary to cause the observed Teflon<sup>®</sup> FEP embrittlement and the propagation of cracks along stress concentrations. Ground testing and analysis of retrieved MLI indicate that damage increases with the combined total dose of electrons, protons, UV and x-rays along with thermal cycling.*

Tests continue in order to determine the effects of the higher temperature limit the MLI SM2 specimen experienced.

## ACKNOWLEDGMENTS

The analysts in the Materials Engineering Branch of NASA, Goddard Space Flight Center who performed tests are Diane Kolos, Len Wang (Unisys), Charles He (Unisys), Charles Powers, Bruno Munoz (Unisys), Alex Montoya, Mary Ayres-Treusdell, Tom Zuby (Unisys), and Mike Viens. Other GSFC contributors include Steve Brown, Claude Smith, Bob Gorman, Wanda Peters (Swales), Dave Hughes (Swales), and Jack Triolo (Swales). The fluence and dose calculations were performed by Janet Barth (GSFC) and Teri Gregory (Lockheed). Analysts at NASA, Lewis Research Center who performed tests are Kim de Groh, Bruce Banks, Don Wheeler, and Jim Gaier. The TOF-SIMS analysis was performed under contract by Mark Nicholas of Evans East. The Nano Indenter analysis was performed by Barry Lucas and Angela Gizelar of Nano Instruments, Inc. NMR analysis was performed by Matthew Espe and Daveen England of the University of Akron. The work of all these analysts and the contributions of the entire HST MLI Failure Review Board are gratefully acknowledged by the authors.

## REFERENCES

- 1) P.A. Hansen, J.A. Townsend, Y. Yoshikawa, J.D. Castro, J.J. Triolo, and W.C. Peters, "Degradation of Hubble Space Telescope Metallized Teflon<sup>®</sup> FEP Thermal Control Materials", Science of Advanced Materials and Process Engineering Series, 43, 570 (1998).
- 2) T. Zuby, K. de Groh, and D. Smith; "Degradation of FEP Thermal Control Materials Returned from the Hubble Space Telescope," NASA Technical Memorandum 104627, December 1995.
- 3) L. Wang, M. Viens, J. Townsend, "Mechanical Properties and Fractography of MLI FEP from the HST Second Service Mission", Science of Advanced Materials and Process Engineering Series, 43, 594 (1998).
- 4) J.A. Dever, K.K. de Groh, J.A. Townsend, L.L. Wang, "Mechanical Properties Degradation of Teflon<sup>®</sup> FEP Returned from the Hubble Space Telescope", NASA/TM-1998-206618
- 5) C. He and J.A. Townsend, "Solar Absorptance of the Teflon<sup>®</sup> FEP Samples Returned from the HST Servicing Missions", Science of Advanced Materials and Process Engineering Series, 43, 607 (1998).
- 6) J.A. Townsend, P.A. Hansen, J.A. Dever, Jack J. Triolo, "Analysis of Retrieved Hubble Space Telescope Thermal Control Materials", Science of Advanced Materials and Process Engineering Series, 43, 582.
- 7) A. Milintchouk, M. Van Eesbeek, F. Levadou and T. Harper, "Influence of X-ray Solar Flare Radiation on Degradation of Teflon<sup>®</sup> in Space" Journal of Spacecraft and Rockets, Vol. 34, No. 4, July-August, 1997.
- 8) H. F. Mark, "Degradation of Polymers in Hostile Environments", The Effects of Hostile Environments on Coatings and Plastics, American Chemical Society Symposium Series 229, 11.
- 9) J.A. Townsend, C.E. Powers, M.J. Viens, M.T. Ayers-Treusdell, B.F. Munoz, "Degradation of Teflon<sup>®</sup> FEP Following Charged Particle Radiation and Rapid Thermal Cycling", 20th Space Simulations Conference, NASA CP- , 1998. (Paper of this compilation.)

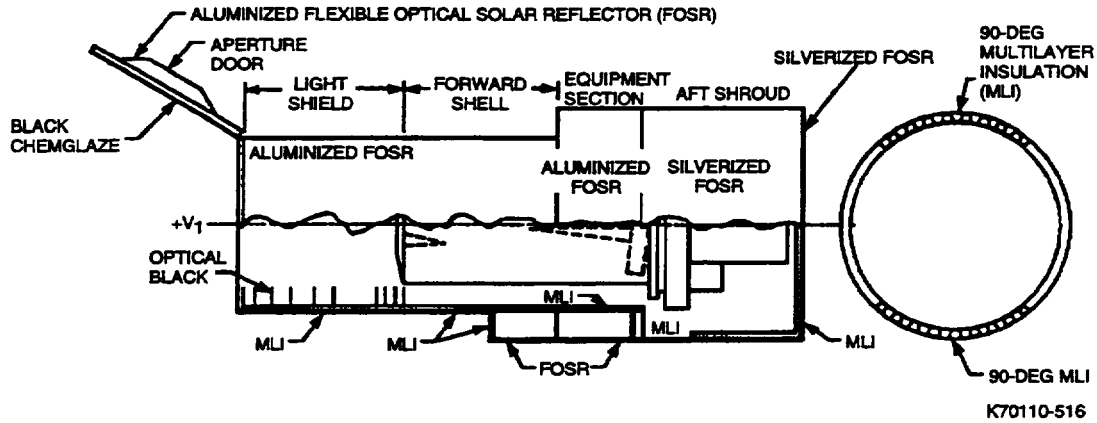


**FIGURE 1: LOCATION OF HUBBLE SPACE TELESCOPE THERMAL CONTROL MATERIALS**  
 In this image, Flexible Optical Solar Reflector (FOSR) is defined as metallized Teflon films used either as the top layer of MLI blankets or as tapes on radiator surfaces. MLI blankets were used on the entire Light Shield and most of the Forward Shell and Equipment Bays (Equipment Section). Tapes were used on the Aperture Door, a few locations on Equipment Bays, the entire Aft Shroud, and Aft Bulkhead (bottom of the telescope).



**FIGURE 2: SM2 LS SPECIMEN ON-ORBIT**  
 The top-center of this image shows the roughly triangular SM2 LS specimen on the Light Shield at SM2 prior to retrieval. A handrail and standoffs are apparent across the top of the image. The specimen is curled very tightly, so that it is detectable here as a triangular region where the next layer of the MLI is visible. The raised feature at the bottom edge of the triangular opening contains the entire specimen that covered this triangle prior to the damage. At the bottom of the image, the tip of the largest crack on HST is seen propagating vertically towards the top of the telescope. This large crack also opened to reveal the next MLI layer.

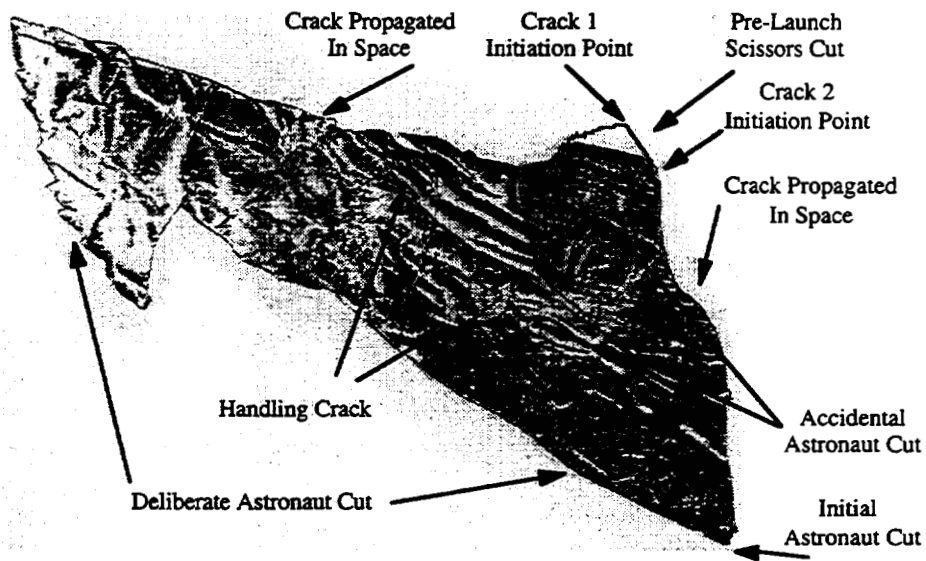


**FIGURE 3: SM2 LS SPECIMEN POST-RETRIEVAL**

The image above was taken during post-retrieval analysis, when the SM2 LS specimen was uncurled and placed between glass plates. The edges of the specimen are identified as scissors cut, handling crack, or orbit crack. The top-right corner of the specimen contains the crack initiation sites.



**FIGURE 4 (left):  
ASTRONAUTS PATCH HST  
LIGHT SHIELD DURING SM2**

This image shows two astronauts in the process of patching the Light Shield MLI during SM2. The astronauts give scale to the largest crack (more than one meter long) in the MLI at SM2. At this point the SM2 LS specimen had already been removed (left of top astronaut's arm).

x

**GROUND SIMULATION OF SPACE RADIATION EFFECTS ON NONMETALLIC  
MATERIALS:  
STATUS OF THE PROPOSED ISO STANDARD**

**Boris A. Briskman**

Obninsk Branch of Karpov Institute of Physical Chemistry, Russia

**Eugene N. Borson**

Consultant

**ABSTRACT**

Russia has proposed new international standard for the testing of nonmetallic materials to simulate space radiation effects.<sup>1</sup> The proposal was submitted to ISO (the International Organization for Standards) Technical Committee 20 (Aircraft and Space Vehicles), Subcommittee 14 (Space Systems and Operations) and was approved as Working Draft 15856 at the Los-Angeles meeting (1997). The second version of the draft was approved at the Beijing meeting (1998).

**INTRODUCTION**

Standards are still a critical part of product manufacturing and supply, even if the customer does not specify specific standards. Standards can improve efficiency, reliability, and reduce costs. However, standards can also be used to provide trade advantages to specific companies and nations. Within the U.S., standards organizations are required to invite all interested parties to participate in developing and reaching a consensus on a proposed standard.

International standards are under ISO (International Organization for Standardization) and the IEC (International Electrotechnical Commission). ANSI (American National Standards Institute) is the U.S. member of ISO.

International standards for space systems are in SC (Subcommittee) 14 (Space Systems and Operations) of TC (Technical Committee) 20 (Aircraft and Space Vehicles). AIAA (American Institute of Aeronautics and Astronautics) holds the secretariat for SC 14, for ANSI. WG (Working Group) 4 (Space Environment) in SC14 is responsible for the proposed standard on simulated space radiation testing of materials. Russia holds the secretariat for WG4.

In the world of international space business, it is advantageous to all participants to have a consistent and uniform approach to design, testing, and operations of space systems in order to reduce costs and implementation times and increase reliability and operational lifetimes. The objective of the ISO TC20/SC14 activity is reaching an international consensus on suitable space systems standards.

A suitable standard for testing under simulated space environments should contain the following:

- (1) A specified space environment that is the best representation of the true environment that can be agreed upon by international technical experts.
- (2) Guidelines on how to analyze for the effects of this standard environment on space systems, components, and materials.
- (3) Guidelines on how to test for the effects of the environment on space systems, components, and materials.

The space environment includes particulate and electromagnetic radiation as well as atmospheres of atomic oxygen, plasmas, and other gases. Meteoroids are also present. Induced environments, because of spacecraft, include temperature, electrostatic charging and discharges, debris, and contamination. Mission orbits and lifetimes determine the combined environments to which a space system is exposed.

The synergistic effects of combinations of environments complicate the analysis of effects and the simulation required to achieve satisfactory testing. To perform an exact simulation for a test would require that the true environment be reproduced both in magnitude and rate. It is impossible to reproduce the true space environment for ground tests of space system elements.

Simulation of the space environment for testing really means simulating the effects of the space environment for the particular mission and the component or material being tested. Only the factors that are important for determining the effects of interest need be simulated.

Another aspect of space simulation is the need to get data about the effects of a long mission within a time period that supports the design and testing of a space system. This requires that some factors and effects of the natural and induced environment be accelerated.

The following methodology is suggested for organizing space simulation tests:

1. Select the space environment factors for the specific mission and effects that are critical for performance and reliability.
2. Select the induced environment factors that can influence the effects that are under investigation.
3. Determine the factors that must be accelerated and the acceptable acceleration rates that will not adversely affect the results.
3. Factor parameters to be simulated for on-ground tests.

The elements of simulation for the natural space environment are shown in Figure 1 and for the induced space environment in Figure 2.

### **EXISTING STANDARDS**

There are no approved ISO standards specifying how to determine the response of spacecraft materials to the space radiation environment. However, the IEC (International Electrotechnical Commission) has the following standard:

IEC 544- "Electroinsulating Materials. Determination of Ionizing Radiation Influence", Parts 1 - 4.

Russia has a series of national standards related to space environment simulation. The Russian standards are listed below:

GOST 9.706 "Polymeric materials. Test methods for resistance to radiation aging".

GOST 25645.321 "Radiation resistance of polymeric materials. Terms and definitions".

GOST 25645.323 "Polymeric materials. Radiation test methods".

GOST 25645.331 "Polymeric materials. Demands to estimation of radiation resistance".

GOST R 25645.332 "Polymeric materials for spacecraft with nuclear reactor. Requirements for radiation tests".

GOST R 25645.338 "Polymeric materials for space technique. Requirements for far ultraviolet radiation stability tests".

Unfortunately, at this time these standards are not available in English.

We have a number of similar ASTM standards in USA:

- E 512 "Standard Practice for Combined, Simulated Space Environment Testing of Thermal Control Materials with Electromagnetic and Particulate Radiation"
- E 349 "Terminology Relating to Space Simulation"
- E 490 "Solar Constant and Air Mass Zero Solar Spectral Irradiance Tables"
- E 491 "Practice for Solar Simulation for Thermal Balance Testing of Spacecraft"
- E 1027 "Standard Practice for Exposure of Polymeric Materials to Ionizing Radiation"
- E 1420 "Standard Practice for Specifying Polymeric Materials for Service in Ionizing Radiation Environments"

Nonmetallic materials used on spacecraft are affected by electrons and protons in broad energy intervals, electromagnetic solar radiation (both the near and the far ultraviolet radiation), and X-ray radiation. The types and energies of the radiation define the ionization loss density, and the radiation response of nonmetallic materials depends from the last. The radiation spectrum defines the absorbed dose distribution, especially in the near surface layers.

With the aim of accelerated radiation test conduction it is necessary to achieve a steep rise in dose rate that often influences the value of radiation effect. So, the main requirement for the radiation tests is correct space environment simulation for the type of radiation, the spectrum, and the dose rate. The problem is complicated because the radiation response of different material properties depends on the manner of the approximation of the real operational conditions.

### **GENERAL PROVISIONS OF THE PROPOSED STANDARD**

This is the second version of the proposed international standard, "Space Environment Simulation for Radiation Tests of Materials. 1. Nonmetallic materials". It is the first part of a series of standards on space environment simulation for on-ground tests of materials. The following types of space radiation are included in this first document: charged particles (electrons and protons), solar ultraviolet radiation, and soft X-radiation of solar flares. The radiation affects the nonmetallic materials individually and jointly; so, synergistic effects must be considered. The simulation methods are used for reproducing the effects of the space environment for on-ground radiation tests of space engineering materials. Materials that are located on a surface of a space vehicle as well as behind shielding are considered.

The standard does not specify requirements for material specimen, methods of measuring their properties, components of radiation sources and vacuum systems, and preparing test reports. The users may address such items in national standards and specific system documentation. Also, the proposed standard does not include hazards and safety precautions. The users are responsible for providing safe conditions and meeting requirements of local and national safety standards.

### **SPACE RADIATION ENVIRONMENT**

The main sources of ionizing radiation in space are galactic and solar particle radiation, solar X-radiation with 1 to 10 nm wavelength, far ultraviolet radiation (FUV), and trapped charged particles of low energy in the radiation belts of the Earth.

Irradiance of the far (vacuum) ultraviolet on spacecraft in low earth orbits is about  $0.1\text{W/m}^2$  or 0.07% of the total solar electromagnetic radiation power. Irradiance of the near ultraviolet (NUV) radiation for the

same conditions is about  $118 \text{ W/m}^2$  or 8.7% of the total solar electromagnetic radiation power (see ASTM E 512). Spectra of these types of radiation are presented in ASTM E 490.

The components of some of these radiation sources and calculated values of absorbed doses on the vehicle surface and behind a shield are listed in Table 1<sup>2</sup> for low earth orbits. Spectra of electrons with minimal energy 100 keV and protons with minimal energy 500 keV are presented in the AE-8<sup>3</sup> and AP-8<sup>4</sup> models. Energy characteristics for protons at a geosynchronous orbit are presented in References 5 and 6 and for electrons in References 7 and 8.

The absorbed doses for the spacecraft surface are extrapolated because there are no standard models for the lower energy electrons and protons.

The main part of the solar X-ray radiation is in the energy range of 0.1 keV to 10 keV and results from solar flares<sup>9</sup>. The predominant energy contribution comes from photons with energies between 1 and 3 keV.

## STANDARD ORBITS

To provide a uniform methodology for space environment simulation, it is advisable to establish standard orbits for the spacecraft. Five standard earth orbits are recommended in the proposed standard and are contained in Table 2. The orbit designations reflect the Russian origination of the document, and some internationalization of the names probably is in order.

For the orbits not included in the Table 2 (such as higher Earth orbits, interplanetary missions, and other deep space flights), it is necessary to make special calculations including energy fluences. For corpuscular radiation, the reference values of the energy fluences are listed in Table 3. For each of the specified orbits, the spectra of electrons and protons are established.

For the MIR and POL orbits, the energy ranges are 50 keV - 5 MeV for electrons and 100 keV - 100 MeV for protons.

For the GEO, GLON and HEO orbits, the energy ranges are 1 keV - 5 MeV for electrons and 1 keV - 100 MeV for protons.

These values are independent of the origin of the charged particles. The energy fluence for each kind of radiation is specified in  $\text{J/m}^2$ . The initial data from models AE-8, AP-8, and models of the low energy parts of the electron and proton spectra (Refs. 5 and 6). The proposed set of standard spectra corresponds to the most widespread needs for the testing of spacecraft materials.

For FUV, the energy fluence is established using an irradiance of  $0.1 \text{ W/m}^2$ , and for NUV, the fluence is based on an irradiance of  $118 \text{ W/m}^2$ .

For simulating the space radiation environment for the testing of materials, standard orbital environments would be selected from the list in Tables 2 and 3. The selected orbit would be the one that is the closest to the actual orbit of the desired spacecraft.

The absorbed dose in the vehicle near-surface layers is determined mainly by low energy kinds of radiation (protons with energy up to 0.5 MeV, electrons with energy up to 100 keV, solar X-radiation, and FUV). The lower energy charged particles are not contained in the AE-8 and AP-8 models. The relative contribution, to the adsorbed dose, of the lower energy charged particles drops sharply into the depth of material, and the relative contribution of the high energy protons, electrons, and bremstrahlung increases.

Table 4<sup>10</sup> shows the adsorbed dose at various shielding depths for the Cosmos 1887 spacecraft.

### **CLASSIFICATION OF CHARACTERISTIC PROPERTIES OF SPACECRAFT MATERIALS**

Properties of materials can be divided into two general categories: surface properties and volume properties. Different regions of radiation spectra will affect surface and volume properties in varying degrees.

The surface properties include surface electrical conductivity, optical (reflectance, absorptance, emittance), adhesive (adhesion, adhesive strength) and tribotechnical characteristics (factor of friction, friction durability, wear resistance), and surface electrical charging.

Degradation of surface properties is determined by the low-energy part of corpuscular radiation (no more than 100 keV for electrons and 0.5 MeV for protons) and also by the whole spectrum of the solar X-radiation and UV. FUV is totally absorbed near the surface in nonmetallic materials (Russian standard GOST R 25645.338). The effects of longer wavelength UV depends upon the absorptance of the material at the specific wavelengths and the energies required to break chemical bonds.

Volume properties are determined by material characteristics averaged through the volume of a product. Degradation of the volume material properties is determined by the higher energy parts of a charged particle spectrum. The radiation damage of the materials located behind shielding of more than 10 mg/cm<sup>2</sup> thickness is also caused by higher energy parts of the spectrum. The rest of the material properties, listed in the normative documentation, make a group of volume characteristic properties.

To study the first group of properties a measure of radiation action should be taken equal to the energy fluence of corpuscular radiation, J/m<sup>2</sup>, proceeding from the above assessed absorption of more than 90% exposure energy in tens of μm thick near-the-surface layers and neglecting the absorption of bremsstrahlung energy in the same layers in comparison with that of corpuscular radiation (see Figure 3). The absorbed dose averaged over the product thickness is taken as a measure of radiation action to analyze the second group of properties, and it practically relates to a high-energy part of the spectrum. The same measure is applied to shielded materials.

This approach to selection of the radiation action measure is influenced by a scale effect, i.e. dependence of the material degradation on the thickness ratio of irradiated and unirradiated layers. Based on the experimental data on radiation creep and electrophysical properties of polymeric materials (Ref. 11), it is possible to conclude on propagation of the sizes of radiation defects outside the boundaries of irradiated layers, i.e. about the change of volume properties of a material during surface irradiation. Such «far action» in polymeric materials is estimated in one-two tens of μm for unloaded materials. So, the two-measure approach of radiation action is applicable to the products with more than 20 μm-thickness. The energy fluence is only a measure of radiation action on the products of less than 20 μm-thickness.

### **REQUIREMENTS FOR SIMULATION OF SOME RADIATION PARAMETERS**

The type of radiation, its spectrum and intensity are attributed to simulated parameters of space ionizing radiation.

#### **Simulation of the Type of Ionizing Radiation**

Impact of each kind of radiation for nonmetallic materials at the same values of absorbed energy, dose rate, and irradiation temperature is specific, i.e. the radiation effects differ both quantitatively and qualitatively. It is based on the features of radiation-chemistry processes, generated in a material, i.e. on

the different density of matter ionization. As a rule, it is desirable to conduct the tests of materials under the action of the same ionizing radiation as found in the space environment. The concern is to achieve the same surface property changes during ground testing as occurs in space. In a number of cases, as defined by the proposed standard, it is permissible to replace one kind of ionizing radiation by another if technically more feasible.

The lack of experimental and theoretical data on specific effects of low-energy protons and electrons, as well as of X-radiation and UV at the same absorbed dose, makes it difficult to replace one kind of radiation by another.

For protons and electrons of high energy, causing degradation of the material volume properties, it is possible to replace one kind of radiation by another. This approach is based on the examination of radiation-chemical yields dependence on the type of ionizing radiation for different organic material radiolysis species. Recommendations are contained in Russian standard GOST 9.706. Later, this approach was verified while investigating the effects of different types of radiation on polymeric materials in broad range of such materials and their properties<sup>12</sup>. Such replacement is possible by introducing special absorbed dose equivalence coefficients,  $k$ , with the values listed in Table 5.

In the course of simulation, the absorbed dose of simulated radiation (during test),  $D_1$ , is  $k$  times higher than a specific absorbed dose of natural radiation in space,  $D_2$ , i.e.

$$D_1 = kD_2 \quad (1)$$

Typical radiation sources for ground testing are monoenergetic. Therefore, to simulate the effects of the continuum of space irradiation on materials, it is generally necessary to use more than one monoenergetic source to simulate the correct absorbed dose vs depth in the material. For simulated radiation sources consisting of  $n$  components of one monoenergetic type of radiation, a maximum absorbed dose of the simulating radiation is established from the following expression:

$$D = \sum_{i=1}^n k_i D_{2i} \quad (2)$$

where  $D_{2i}$  is the absorbed dose from the  $i$ -th component of the simulated radiation;  $k_i$  is the appropriate absorbed dose equivalence coefficients from Table 5. This approach for ionizing radiation simulation is only applicable when maximum permissible changes of the material properties under radiation exposure are not more than the values listed in Table 6 for various classes of nonmetallic materials.

### Simulation of the Radiation Spectrum

The influence of ionizing radiation spectrum on radiation degradation of nonmetallic materials can have an effect for two reasons: a) different depth distribution of absorbed dose in a material; b) dependence of radiation-chemical yield on the LET (linear energy transfer or stopping power) value of radiation. As the difference in LET values for actual operational spectra of the same kind of radiation is small, we should take into account only the first reason.

The highest absorbed dose occurs in the near-the-surface layers; so, for the simulation of space corpuscular ionizing radiation, simulation based on spectrum is recommended for the testing of near surface properties of materials.

Figure 3 shows the absorbed dose vs depth for FEP film for three components of space radiation, soft background X-ray, charged particles at GEO, and Ly- $\alpha$  in the far ultraviolet.

Two methods for simulating the radiation spectrum of the charged particles are recommended:

- a) Use of several beams of quasi-monoenergetic charged particles with various energies;
- b) Conversion of a monoenergetic beam with the help of a sectioned foil, with the thickness varying from point to point under a certain law (thickness of the foil is about the size of free path of the particles).

In the first case the spectrum is adjusted by proper choice of intensities of separate radiation sources.

The assessment of reliable simulation of the radiation spectrum is made by introducing a certain numerical characteristic of depth distribution of an absorbed dose in a material, holding of which in the specific limits guaranties the reliability of the method.

For this purpose, it is recommended to use an exponent index of the absorbed dose depth distribution  $m$ , referred to the density of the material  $\rho$ . Such depth distribution can be presented as a sum of two exponents, as it is shown in Figure 4. The first exponent corresponds to a near-the-surface layer of 5 to 10  $\mu\text{m}$ -thickness, and the second exponent corresponds to a layer of from 10  $\mu\text{m}$  up to, as a minimum, 100  $\mu\text{m}$ -thickness.

The reference values of  $\mu/\rho$ , calculated for standard spectra of ionizing radiation, are given in Table 7.

For simulation, the absorbed dose-depth distribution curves for the tested material should be calculated to a depth of 100 to 150  $\mu\text{m}$  for both the space environment and test conditions. Then find the values of depth distribution criterion. Adjust the values of  $(\mu/\rho)$  for both types of conditions, varying the radiation source energy and the particle fluences.

Permissible difference between the absorbed dose depth distribution criteria for orbit flight and ground test is, in general, a complex function of material properties, values of absorbed dose, and dose rate. For the majority of nonmetallic materials, a linear response of optical property changes depends on not exceeding some specified dose. This response in a broad range of dose rates for irradiation in vacuum should change by not more than two times<sup>13</sup>. So, for the above adjustment procedure, the permissible difference between the  $(\mu/\rho)$  values is about 30%.

To calculate the absorbed dose depth distribution for electrons and protons both for space environment and ground radiation sources it is necessary to make use of just the same mathematical code and the same geometry of particle incidence. For the electrons, we recommend using the Tiger-P code (based on Monte Carlo methods) from the package ITS 3.0, Sandia National Laboratories,<sup>14</sup>. It is possible to use a stack of film dosimeters for measuring the absorbed dose-depth distribution.

### **Simulation of the Radiation Dose Rate**

The effects of radiation dose rate in polymeric materials are affected by the presence of oxygen in the environment. Damage results from oxidation. This dependence for materials irradiated in vacuum is not established<sup>15</sup> and<sup>16</sup>, i.e. irradiation in vacuum corresponds to reciprocity. These considerations are presented in standard IEC 544.2-79 and Russian standard GOST 9.701. The possible influence of dose rate for irradiation in vacuum may be associated with dissolved residual oxygen. So, for all kinds of accelerated radiation tests of nonmetallic materials in vacuum, a residual pressure not higher than  $10^{-2}$  to  $10^{-3}$  Pa is recommended. Also, accelerated radiation tests are only possible when preceded by conditioning the material samples in a high vacuum to remove dissolved oxygen.

The value of maximum dose rate (or rate of an energy fluence on a material surface) is determined by the allowable temperature increase of a sample. It is permissible to conduct accelerated tests for the effects of FUV exposure of nonmetallic materials at acceleration factors up to  $10^3$ . The maximum increase of the sample temperature due to radiation heating (including IR-region of spectrum) should not be greater than 30 K, if a phase transition of the material does not fall in this interval.

The range of operation temperatures on a surface of a space vehicle is taken to vary from  $-150\text{ }^\circ\text{C}$  up to  $+150\text{ }^\circ\text{C}$ . The operating temperature of the material should be considered when selecting test temperature requirements.

To measure radiation outgassing in accelerated tests with the acceleration factor up to  $10^3$  the factor of an absorbed dose reserve, equal to five, is established at a dose rate of no more than 1 mGy/s under operating conditions. This approach is based on the results of an investigation of radiation-chemical yield for species of chemical stage of radiolysis for a number of polymers during irradiation in vacuum (Ref. 12).

It is desirable for each kind of radiation to precede the tests by investigating the validity of reciprocity in the range of dose rates, defined by the acceleration factor, for one of the materials representing the series to be studied.

Another factor to consider in the simulated dose rate selection is the effect of electrical charging. Charge buildup may occur during accelerated testing although it would not happen in space. Surface charging can create an electrical field that repels incident, low energy, charged particles. Electrical charge buildup within the volume of a material can result in damage from electrical discharge.

### **Sources of Ionizing Radiation**

For simulating low-energy proton and electron effects in unshielded materials on a surface of space vehicles, it is recommended to use:

**Protons** - proton accelerators with energies from 10 keV to 2 MeV.

**Electrons** - electron accelerators with energies from 10 keV to 1 MeV.

To simulate FUV radiation effects for the same purpose, it is recommended to use sources of optical radiation in the range of 10 nm to 200 nm. Hydrogen and deuterium discharge lamps, and similar lamps filled with helium can be used following the recommendations in Russian standard GOST R 25645.338 and the USA standard ASTM E 512-94.

It is also possible to use resonant gas lamps filled with krypton ( $\lambda = 123.6\text{ nm}$ ) and xenon ( $\lambda = 147\text{ nm}$ ), gas-jet sources, and synchrotron radiation sources.

For simulation of NUV effects in the range of wavelength from 200nm up to 400 nm, it is desirable to utilize xenon arc lamps. It is also possible to use mercury-arc, mercury-xenon-arc, and carbon-arc lamps with necessary filtering of the simultaneously generated infrared radiation.

For the test of shielded materials in any case and for the radiation tests of volume properties of any materials, it is recommended to use the following:

**Protons** - proton accelerators with energies from 20 to 400 MeV.

**Electrons** - electron accelerators with the energies higher than 1 MeV.

**Bremstrahlung** - gamma-radiation  $^{60}\text{Co}$ .

To obtain a uniform field of protons with the mean energies of 0.5 to 1 MeV in the hydrogen rich materials, it is possible to use a neutron beam of a nuclear reactor filtered from accompanying gamma-radiation and thermal neutrons (Ref.17).

**Table 1.**  
**Absorbed Doses from Space Sources of Ionizing Radiation for Low Earth Orbits (Ref. 2)**

| Type of radiation                  | Energy, MeV                          | Annual dose, Gy (1 J/kg)           |                                    |
|------------------------------------|--------------------------------------|------------------------------------|------------------------------------|
|                                    |                                      | on surface                         | behind shield, 1 g/cm <sup>2</sup> |
| <b>Galactic Cosmic Rays (GCRs)</b> |                                      |                                    |                                    |
| Protons                            | 10 <sup>2</sup> - 10 <sup>3</sup>    | 0.01 - 0.1                         | 0.01 - 0.1                         |
| <b>Solar Particle Radiation</b>    |                                      |                                    |                                    |
| Protons                            | 20 - 10 <sup>3</sup>                 | 10 - 10 <sup>2</sup>               | 1 - 10                             |
| Electrons                          | 0.05                                 | 10 <sup>2</sup> - 10 <sup>5</sup>  | 0                                  |
| Bremstrahlung                      | 0.05                                 | 0.01 - 1                           | 0.01 - 1                           |
| <b>Inner Radiation Belt</b>        |                                      |                                    |                                    |
| Protons                            | 10 <sup>-3</sup> - 7·10 <sup>2</sup> | 10 <sup>8</sup>                    | 10 <sup>3</sup>                    |
| Electrons                          | 0.02 - 1                             | 10 <sup>10</sup>                   | 0                                  |
| Bremstrahlung                      | 0.02 - 1                             | 10 <sup>3</sup>                    | 10 <sup>3</sup> - 10 <sup>4</sup>  |
| <b>Outer Radiation Belt</b>        |                                      |                                    |                                    |
| Protons                            | up to 60                             |                                    |                                    |
| Electrons                          | 0.02 - 5                             | 10 <sup>9</sup> - 10 <sup>11</sup> | 10                                 |
| Bremstrahlung                      | 0.02 - 5                             | 10 <sup>3</sup> - 10 <sup>5</sup>  | 10 <sup>2</sup> - 10 <sup>4</sup>  |

**Table 2.**  
**Standard Orbit Parameters**

| NN | Designation | Orbit                | Altitude, km | Inclination, ° | Type of orbit                |
|----|-------------|----------------------|--------------|----------------|------------------------------|
| 1  | MIR         | MIR station          | 426          | 51.6           | Circular                     |
| 2  | GEO         | Geostationary        | 35 790       | 0              | Circular                     |
| 3  | GLON        | GLONASS vehicle      | 19 100       | 64.8           | Circular                     |
| 4  | HEO         | High-elliptic orbit  | 500-39 660   | 65             | Elliptical, 275 <sup>0</sup> |
| 5  | POL         | Standard polar orbit | 600          | 97             | Circular                     |

**Table 3.**  
**Energy Fluence of Corpuscular Radiation**

| NN | Orbit | Energy fluence, J/m <sup>2</sup> per year, 10 <sup>4</sup> |         |       |
|----|-------|--|---------|-------|
|    |       | Electrons  | Protons | Total |
| 1  | MIR   | 0.10   | 0.003   | 0.103 |
| 2  | GEO   | 98   | 3.8     | 102   |
| 3  | GLON  | 83   | 26      | 109   |
| 4  | HEO   | 49   | 6.8     | 56    |
| 5  | POL   | 0.23   | 0.01    | 0.24  |

**Table 4.**  
**Space Radiation Absorbed Dose at Various Shielding Depths on Satellite Cosmos 1887 (%) (from Ref. 11)**

| Type of Radiation          | Shielding depth, g/cm <sup>2</sup> |      |      |      |      |      |
|----------------------------|------------------------------------|------|------|------|------|------|
|                            | 0.1                                | 0.5  | 1.0  | 1.5  | 2.0  | 3.0  |
| Electrons                  | 99.2                               | 95.6 | 79.0 | 42.8 | 13.7 | 2.2  |
| Protons of radiation belts | 0.6                                | 2.7  | 11.8 | 30.0 | 42.5 | 34.0 |
| Protons of GCR             | 0.2                                | 1.7  | 9.2  | 27.2 | 43.8 | 63.8 |

**Table 5.**  
**Absorbed Dose Equivalence Coefficient**

| Type of Simulated Radiation          | Coefficient k for Simulated Radiation |       |           |         |
|--------------------------------------|---------------------------------------|-------|-----------|---------|
|                                      | Bremstrahlung                         | Gamma | Electrons | Protons |
| Bremstrahlung (E ≤ 100 keV)          | 1.0                                   | 1.5   | 1.5       | 2.0     |
| Gamma or bremstrahlung (E ≥ 100 keV) | 1.5                                   | 1.0   | 1.0       | 2.0     |
| Electrons (E ≥ 100 keV)              | 1.5                                   | 1.0   | 1.0       | 2.0     |
| Protons (E ≥ 200 keV)                | 1.5                                   | 2.0   | 2.0       | 1.0     |

**Table 6.**  
**Maximum permissible changes  $\delta$  of the properties of polymeric materials**  
**(percentage of the initial value)**

| Property of material   | Value of $\delta$ , %        |
|--|------------------------------|
| <b>Structural materials</b>  |                              |
| Strength at a break (bending, compression, shear)                                | -50                          |
| Relative elongation at a rupture   | from -50 up to +100          |
| Modulus of elasticity at tension   | -50                          |
| Impact viscosity   | -50                          |
| <b>Electrical insulation materials</b>   |                              |
| Specific volume and surface electrical resistance                                | -90                          |
| Tangent of dielectric loss angle in the range of frequencies $10^3 - 10^{10}$ Hz | From +50 up to +100          |
| Permeability of dielectric in the range of frequencies $10^3 - 10^{10}$ Hz       | From $\pm 10$ up to $\pm 30$ |
| Electric strength  | -50                          |

**Table 7.**  
**Depth Distribution Criterion of**  
**Absorbed Dose**

| NN | Standard Orbit | $(\mu/\rho)_1, \text{ cm}^2/\text{g}$ | $(\mu/\rho)_2, \text{ cm}^2/\text{g}$ |
|----|----------------|---------------------------------------|---------------------------------------|
| 1  | MIR            |                                       |                                       |
| 2  | GEO (1)        | $3.0 \cdot 10^3$                      | $1.22 \cdot 10^2$                     |
| 3  | GLON (2)       | $3.1 \cdot 10^3$                      | $0.53 \cdot 10^2$                     |
| 4  | HEO (2)        | $4.6 \cdot 10^3$                      | $0.46 \cdot 10^2$                     |
| 5  | POL (3)        | $4.2 \cdot 10^3$                      | $1.46 \cdot 10^2$                     |
| 6  | GEO (2)        | $2.5 \cdot 10^3$                      | $0.41 \cdot 10^2$                     |

**Notes:**

**For Kapton, assuming isotropic incidence.**

**For aluminum, assuming normal incidence.**

**For cerium glass, assuming isotropic incidence.**

Figure 1

Natural Space Environment Simulation Elements

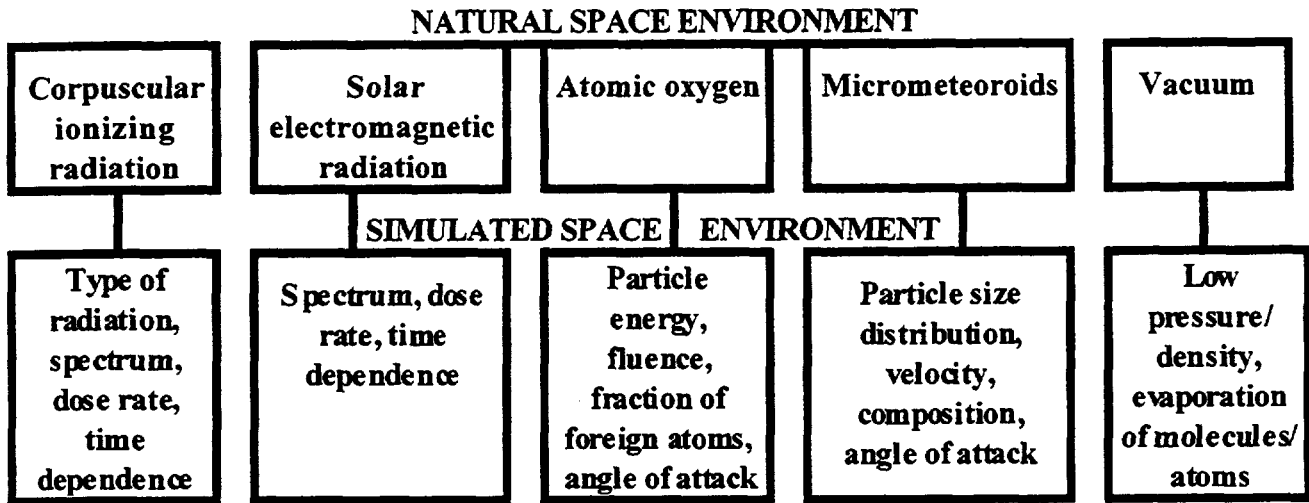
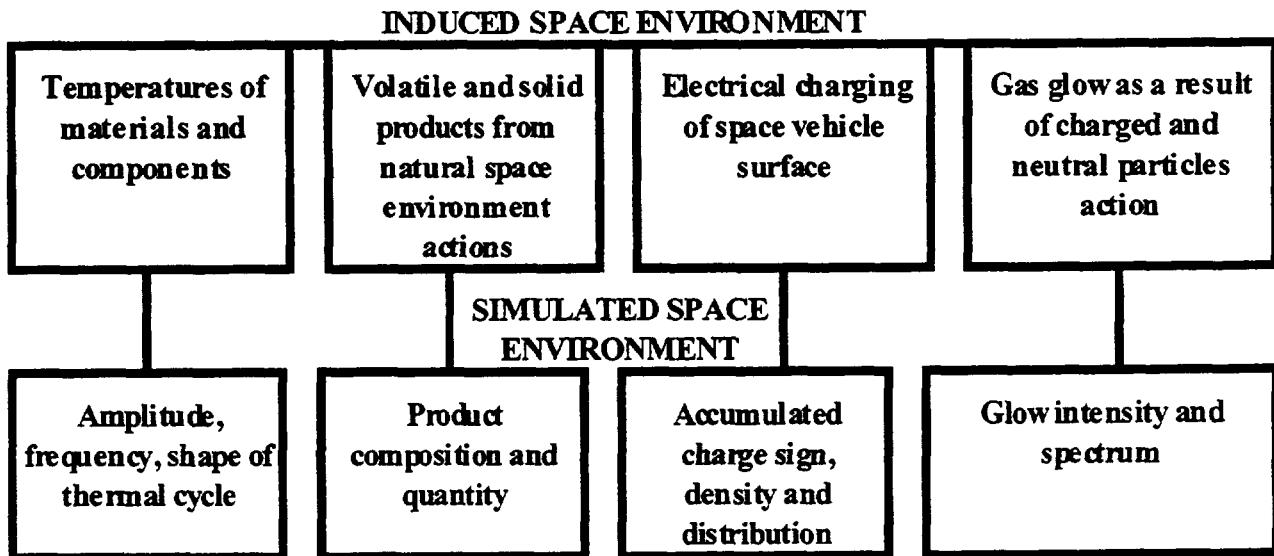
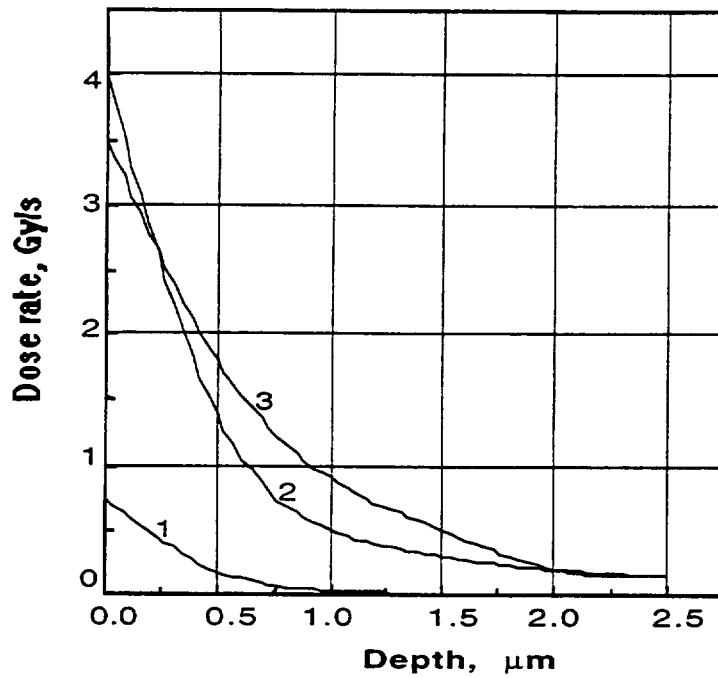


Figure 2

Induced Space Environment Simulation Elements





**Figure 3**  
**Absorbed Dose vs Depth in FEP Film**  
 1 - Soft background X-ray  
 2 - Charged particles at GEO  
 3 - Far ultraviolet (Ly- $\alpha$ )  
 Solar Activity Index,  $F_{0.7} = 170$

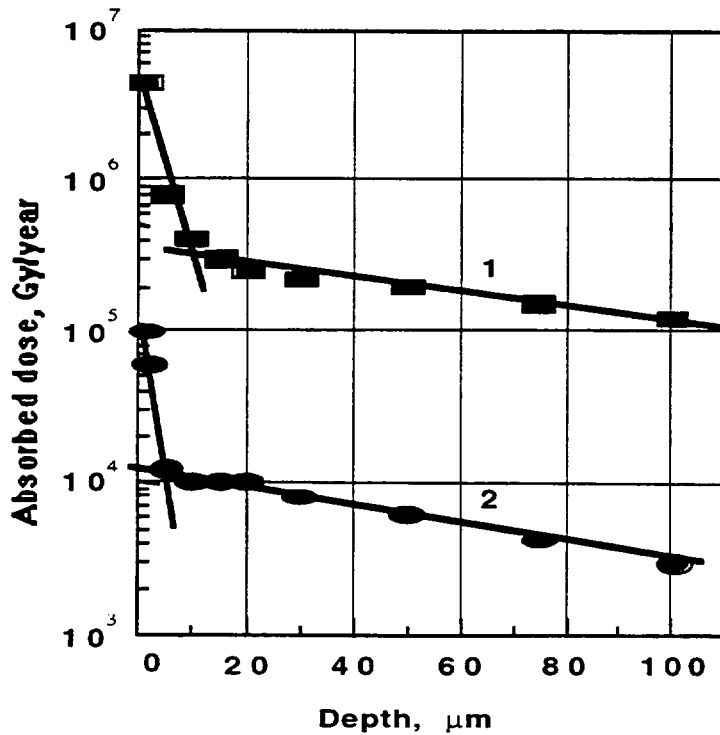


**Figure 4**  
**Absorbed Dose vs Depth for Kapton & cerium glass**  
 1 - Kapton, GEO orbit, inclination 0-160° Western longitude (Ref. 18).  
 2 - Cerium glass, polar orbit 800 km (Ref. 19).

## REFERENCES

- <sup>1</sup> Briskman B. A., Toupikov, V. I., Lesnovsky, E. N., "Space Environment Simulation at Radiation Tests of Materials. Draft of an International Standard", 7th International Symposium on Materials in Space Environment, ESA-SP-399, pp. 537-542, Toulouse, France, 16-20 June 1997.
- <sup>2</sup> Milinchuk, V. K.; Klinshpont, E. R.; & Tupikov, V. I., "Fundamentals of Radiation Resistance of Organic Materials", Ì., Energoatomizdat, 1986 (Russian).
- <sup>3</sup> Vette, J. I., "The AE-8 Trapped Electron Environment", NSSDC/WDCA-R&S 1-24 (1991).
- <sup>4</sup> Sawyer, D. M., & Vette, J. I., "AP-8 Trapped Proton Environment for Solar Maximum and Solar Minimum", NSSDC/WDCA-R&S 76-06 (1979).
- <sup>5</sup> Garrett, H. B.; Schwank, D. C.; & DeForest, S. E., J. Planet Space Sci., 1981, \_ 10, p. 1021-1044.
- <sup>6</sup> DeForest, S. E.; Garrett, H. B.; & Schwank D. C., J. Planet Space Sci., 1981, \_ 10, p. 1045-1060.
- <sup>7</sup> Pulliam, D. M.; Anderson, H. R.; Stammes, K.; & Rees, M. H. J., Geophys. Res., v. 86 (A4), 1981, pp. 2397-2404.
- <sup>8</sup> Anderson, J. F. & Smith, R. E., "Natural Orbital Environment Guidelines for Use in Aerospace Vehicle Development", NASA Technical Memorandum 4527, June 1994.
- <sup>9</sup> Milintchouk, A.; Van Eesbeek, M.; Holmes-Siedle, A.; & Levadou, F., "Degradation of Materials Under the Action of Soft X-Ray Radiation from Solar Flares", 7th International Symposium on Materials in Space Environment, ESA-SP-399, pp. 87-96, Toulouse, France, 16-20 June 1997.
- <sup>10</sup> Akatov, Yu. A., e.a., Nucl. Tracks Radiat. Meas., v. 17, \_ 2, 1990, p. 105-108.
- <sup>11</sup> Toupikov, V. I., e.a., Proceed. The Workshop «Methodologies for Ground Simulation of the Space Environment», Southampton, Great Britain, 1996, p. 11- 15.
- <sup>12</sup> Briskman, B. A., Milinchuk, V. K., Proceed. «1st All-Union Meeting. Dielectric materials in extreme environment», v.2. Suzdal, 1990, pp. 239-256 (Russian).
- <sup>13</sup> Bol'bit, N.M., e.a., Idem, pp. 59-63.
- <sup>14</sup> Radiation Safety Information, Computational Center, ORNL, Oak Ridge, Tennessee, USA, No 395, Nov. 1997.
- <sup>15</sup> Wilski, H, Rad. Phys. Chemistry, v. 29, No 1, 1987, p. 1-10.
- <sup>16</sup> Briskman, B. A., e.a., Chemistry of High Energy, v. 27, 1993, pp. 8-14 (Russian).
- <sup>17</sup> Briskman, B. A., e.a., Atomic Energy, 1990, v. 68, No 6, pp. 438 - 442 (Russian).
- <sup>18</sup> Haruvy, Y., Rad. Phys. Chem., 1990, v. 35, pp. 204-210.
- <sup>19</sup> Marco, J., e.a., Proceed. 6th International Symposium on Materials in Space Environment, ESTEC, Noordwijk, Netherlands, 1994, p. 77-82.

## DEGRADATION OF TEFLON® FEP FOLLOWING CHARGED PARTICLE RADIATION AND RAPID THERMAL CYCLING

Jacqueline Townsend, Charles Powers, Michael Viens, Mary Ayres-Treusdell  
Materials Engineering Branch, NASA Goddard Space Flight Center  
Greenbelt, Maryland 20771

Bruno Munoz  
Unisys Federal Systems at NASA Goddard Space Flight Center  
Greenbelt, Maryland 20771

### ABSTRACT

During the Second Servicing Mission (SM2) of the Hubble Space Telescope (HST) severe degradation was observed on the outer layer of the thermal control blankets. Astronaut observations and photographs revealed large cracks in the metallized Teflon® FEP (fluorinated ethylene propylene), the outer layer of the multi-layer insulation (MLI), in many locations around the telescope. In an effort to understand what elements of the space environment might cause such damage, pristine Teflon® FEP was tested for durability to radiation and thermal cycling. Specimens were subjected to electron and proton fluences comparable to those experienced by HST and were subsequently thermal cycled in a custom-built rapid thermal cycle chamber. Tensile tests of the specimens showed that radiation followed by thermal cycling significantly reduced the ultimate strength and elongation of Teflon® FEP.

### INTRODUCTION

The Hubble Space Telescope was deployed at an orbital altitude of 598 km (320 nmi) and 28.5° orbit inclination in April 1990. Two types of thermal control materials were used on HST: multi layer insulation (MLI) blankets and bonded radiator surfaces (1). MLI blankets were retrieved during the First Servicing Mission (SM1) in December 1993 and were analyzed in ground-based facilities. The analyses showed that the outer layer of the MLI, aluminized Teflon® FEP, had begun to degrade. When astronauts returned to the telescope in February 1997 for the Second Servicing Mission (SM2), they found severe cracking in the outer layer of the MLI blankets on both solar facing and anti-solar facing surfaces (1). The worst damage was patched, and a small outer-layer MLI specimen from the light shield was retrieved for testing.

The testing of the retrieved specimens following each servicing mission revealed a great deal about the type of damage the FEP sustained. At SM1, close inspection of the outer layer FEP revealed small, through-thickness cracks in regions with the highest solar exposure and stress concentration. Mechanical tests showed that the ultimate strength and elongation had reduced significantly (2). As evidenced by the cracking observed on the telescope MLI, the damage at SM2 was far more severe. By SM2, the material had undergone chain scission sufficient to cause the complete loss of the ability to plastically deform. The elongation had dropped to 0%, and the ultimate tensile strength had dropped by roughly 70%. In addition, fractographic examination of the cracks indicated that they were a type of slow crack growth, which is unusual in polymers (3).

With the testing of the retrieved specimens the type of damage was relatively well understood, however the cause of the damage was unclear. Environmental testing was done to determine what factor of the space environment might cause the observed degradation. Since the MLI damage occurred on all sides of the telescope, environmental factors that were relatively

homogeneous in the HST orbit were suspected. Trapped electrons and protons and thermal cycling were two such environmental factors (3).

Testing was carried out at NASA Goddard Space Flight Center to determine the effects of HST fluences of electrons and protons followed by thermal cycling. The initial purpose of the electron and proton radiation exposures was to determine the dose at which FEP would fragment with gentle contact. Specifically, at what servicing mission would the HST MLI outer layer fragment if astronauts tried to remove it or came into contact with it. The approach was to expose specimens of the material to increasing fluences of electrons and protons and then perform tensile tests to determine the changes to the yield and ultimate strengths. When initial testing revealed little change in the tensile test data at SM2 fluences, the decision was made to add thermal cycling to the test matrix. The modified test procedure and results are outlined in this paper.

## EXPERIMENTAL

### Materials

The MLI blankets on HST were composed of a top (space exposed) layer of 127  $\mu\text{m}$  (0.005 in) Teflon<sup>®</sup> FEP with roughly 1000 $\text{\AA}$  of vapor deposited aluminum (VDA) on the back (FEP/VDA) and fifteen underlying layers of 8.5  $\mu\text{m}$  (0.0003 in) embossed, double-aluminized Kapton<sup>®</sup>. The layers of the MLI were bonded together at the edges of the blanket assembly with an acrylic adhesive. Only the top layer of the blanket, the FEP/VDA, was damaged by the exposure (1). At the time the blankets were built, none of the FEP/VDA was saved for future testing. Therefore, no control material from that production lot was available.

New FEP/VDA was ordered from the blanket shop at Lockheed Martin Missiles and Space in July 1997 and was labeled "pristine". Twenty-eight tensile test specimens (ASTM D1822, Type L Die) were cut from a single sheet of the pristine FEP/VDA for this experiment. The orientation for all of the specimens was identical and parallel to the roll direction. The gauge dimensions of these specimens were: area, 0.127 mm x 3.18 mm; length, 19.05 mm.

### Environments

The fluences and doses for the various environmental factors on the HST surfaces are discussed elsewhere in this volume (4). An ideal experiment to simulate the damage observed on the HST would simulate the dose versus depth profile the orbital specimens experienced. However, the energies provided by the source used for this experiment were limited, making it difficult to match the profile. In addition, this experiment was intended to give a conservative estimate of the dose required to make it impossible to handle the material in orbit. Therefore, the decision was made to provide the entire HST fluence of electrons and protons (40 eV to 1 MeV) with 0.5 MeV electrons and 1 MeV protons. These energies provided a dose that was roughly constant through the depth of the specimen, slightly under exposing the front surface of the specimens and slightly over exposing the back surface.

### *Radiation*

The GSFC Radiation Effects Task Group exposed sets of three specimens to each of the fluences of electrons and protons listed in Table 1 (below). Each fluence was based on the estimated fluence at a specific HST servicing mission, with the end-of-life (EOL) defined as 20 years.

TABLE 1: FLUENCES FOR RADIATION AND THERMAL CYCLING

| Run | Protons<br>(1 MeV)<br>$\times 10^{10}/\text{cm}^2$ | Electrons<br>(0.5 MeV)<br>$\times 10^{13}/\text{cm}^2$ | Equivalent HST Fluence<br>Mission | HST Fluence<br>Years | Number of<br>Thermal Cycles<br>( $\pm 50$ ) |
|-----|--|--|-----------------------------------|----------------------|---|
| 1   | 1.956  | 1.949  | SM2                               | 6.8                  | -   |
| 2   | 2.771  | 2.740  | SM3                               | 9.6                  | 39,712                                      |
| 3   | 3.567  | 4.130  | SM4                               | 13.2                 | 56,304                                      |
| 4   | 5.861  | 6.040  | EOL                               | 20                   | 77,088                                      |
| 5   | 11.72  | 12.08  | 2xEOL                             | 40                   | 116,800                                     |
| 6   | 29.30  | 30.20  | 5xEOL                             | 100                  | -   |

*Thermal Cycling*

Following irradiation, some of the specimens were thermal cycled. Thermal cycling was carried out by the GSFC Materials Engineering Branch. The temperature limits of the thermal cycling were based on the nominal limits for the MLI outer layer in orbit. Based on the thermal properties of the FEP/VDA, the MLI outer layer of solar-facing surfaces reached +50 °C when in the sun, and dropped to -100 °C when in shadow (1). Although these limits changed when the MLI SM2 specimen curled and exposed the VDA, since most of the damaged surfaces on HST did not curl, these limits were used for the experiment.

The test samples were thermal cycled roughly 40,000 to 117,000 times between +50 and -100 °C. To accomplish this testing in a reasonable amount of time, liquid nitrogen (L N<sub>2</sub>) and a hot air gun were used (see Figure 1) to reduce the cycle period to approximately 15 seconds. The samples were cooled to below -100 °C by flowing LN<sub>2</sub> (as well as gaseous nitrogen) over the them. A phase separator attached to the end of the L N<sub>2</sub> inlet produced a L N<sub>2</sub> "mist" that flowed more evenly over the samples. The samples were then heated by use of a hot air gun. The entire setup was located inside a nitrogen-purged thermal chamber, so the hot air gun flowed gaseous nitrogen (N<sub>2</sub>) over the samples. This chamber was under constant N<sub>2</sub> purge to prevent moisture from condensing or freezing on the samples. The flow from the hot air gun was reflected off a metal plate onto the samples to diffuse the heat from the gun.

A solid state relay (SSR) was used to open and close a valve that controlled the flow of L N<sub>2</sub>. Another SSR was used to turn the hot air gun on and off. A square wave generator was used to toggle the SSRs. When the signal from the generator was one volt, the SSR controlling the L N<sub>2</sub> opened the valve and the SSR controlling the hot air gun was turned off. When the signal from the generator was zero volts, the SSR controlling the L N<sub>2</sub> closed the valve and the SSR controlling the hot air gun was turned on. The signal from the generator was conditioned through two amplifiers (one for each SSR) before reaching the SSRs.

The duty cycle of the square wave was adjusted to achieve the desired thermal cycle. For most of this testing, the L N<sub>2</sub> valve was open about 38 percent of the cycle and the hot air gun was on for the remaining 62 percent of the cycle. The samples were taped and clamped to the test fixture. Several thermocouples were mounted to the test fixture holding the samples and directly to a control sample to monitor temperature and to adjust the duty cycle of the square wave.

**Procedure**

Tensile test specimens were punched and sent to the Radiation Effects Task Group for electron and proton exposure. Specimens were exposed in sets of three to each of the fluences in Table 1.

Following irradiation, one specimen was thermal cycled. The other two were tensile tested to determine the effect of the radiation alone on the tensile properties. Following thermal cycling, the specimens were tensile tested. An unexposed control specimen was tensile tested along with each set to verify the repeatability of the tensile test procedure. Tensile tests were performed on an Instron 1125 with a 44 N (10 lb) load cell and a strain rate of 2.7 to 6.7 m/m/min.

## RESULTS AND ANALYSIS

### Data

The yield and ultimate strengths and elongation data are summarized in Table 2 (below). The loads and elongation can be calculated using the gauge dimensions in the Materials section. A typical load versus extension (stress versus strain) curve can be found in Figure 2.

TABLE 2: TENSILE TEST RESULTS FOLLOWING RADIATION AND THERMAL CYCLING (11)

| Run                    | Radiation Fluence (years) | Thermal Cycles | Yield Strength (MPa) | Ultimate Strength (MPa) | Elongation at Failure (%) |
|------------------------|---------------------------|----------------|----------------------|-------------------------|---------------------------|
| Control (10 specimens) | 0                         | 0              | 14.2 ± 0.2           | 25.1 ± 0.3              | 356 ± 8                   |
| 1                      | 6.8                       | 0              | 14.0                 | 23.2                    | 345                       |
|                        |                           | 0              | 14.5                 | 25.9                    | 329                       |
|                        |                           | 0              | 13.9                 | 25.4                    | 377                       |
| 2                      | 9.6                       | 0              | 13.5                 | 20.2                    | 314                       |
|                        |                           | 0              | 13.8                 | 21.0                    | 321                       |
|                        |                           | 39,000         | 14.3                 | 17.6                    | 284                       |
| 3                      | 13.2                      | 0              | 13.8                 | 19.9                    | 301                       |
|                        |                           | 0              | 13.8                 | 21.5                    | 280                       |
|                        |                           | 56,804         | 14.4                 | 18.0                    | 267                       |
| 4                      | 20                        | 0              | 13.8                 | 19.5                    | 301                       |
|                        |                           | 0              | 13.8                 | 19.0                    | 280                       |
|                        |                           | 77,088         | 14.3                 | 15.4                    | 192                       |
| 5                      | 40                        | 0              | 13.8                 | 18.2                    | 293                       |
|                        |                           | 0              | 13.8                 | 16.9                    | 263                       |
|                        |                           | 116,800        | 14.9                 | 14.3                    | 132                       |
| 6                      | 100                       | 0              | 13.5                 | 14.3                    | 233                       |
|                        |                           | 0              | 13.7                 | 13.4                    | 180                       |

### Analysis

The data indicate that yield strength was unchanged by the electron and proton radiation (Figure 3). Following irradiation, although the values were consistently lower than the control, most were still within two standard deviations of the control value. Since the sample set was so small, it was impossible to determine if the consistently lower values were indicative of any real change due to the radiation exposure. There was slight evidence that subsequent thermal cycling increased the yield strength. This was particularly evident in exposure set 5 (40 year fluence and 116,800 thermal cycles) with a yield strength of 14.9 MPa; the control value was 14.2 ± 0.2 MPa.

Yield strength represents the ability of a material to deform elastically. Changes to the yield strength could indicate changes in the crystallinity or crosslinking of the polymer, and the crystallinity of FEP is known to increase with elevated temperatures. However, the crystallinity of the specimens could not be measured directly because of the specimen size and the nature of tensile testing.

The ultimate tensile strength (UTS) was significantly reduced following both irradiation and subsequent thermal cycling. At the 20 year HST end-of-life fluence of electrons and protons the ultimate strength had decreased by 23 percent. Following thermal cycling, the ultimate strength had decreased by 39 percent. Although a UTS reduction could not be resolved in the first exposure set (6.8 year fluence, no thermal cycling), the UTS decreased with each subsequent exposure, and thermal cycling always reduced it further (Figure 4). A similar trend was noted in the elongation values.

As with the returned HST specimens, the changes to the bulk FEP were most apparent in the elongation data. With the 20 year EOL fluence of radiation, the elongation had decreased by 18 percent. The additional thermal cycling decreased the elongation by a total of 46 percent. No decrease in elongation was apparent in the first exposure set, however, similar to the UTS, the elongation decreased with each subsequent exposure, and thermal cycling reduced it further (Figure 5).

Elongation measures the material's plastic deformation capability. In polymers, plastic deformation is a function of chain entanglements and chain length. The decreased elongation of these specimens, coupled with the decreased UTS, indicated reduced molecular weight (chain scission). The simplest techniques to measure molecular weight cannot be used with FEP because it is rather inert. As with the crystallinity, it was impossible to measure the molecular weight of these specimens by other techniques due to the sample size and the nature of tensile testing.

Figures 3, 4 and 5 show the tensile properties (yield strength, UTS, and elongation) versus exposure duration. In addition to the values from this experiment, these graphs have the data from the retrieved HST specimens. From these graphs it is clear that the while irradiation and thermal cycling decreases the UTS and elongation, HST-equivalent fluences did not produce the degree of damage that was observed in the retrieved specimens.

The specimen retrieved during SM2 had curled while in orbit, exposing the underlying VDA to the sun. Once the aluminum was exposed, the material cycled from -100 to +200 °C with each 90 minute orbit (1, 3). Cycling through a much higher temperature limit could easily affect both the nature and the degree of the damage. However, since most of the damaged surfaces on HST did not curl, the nominal limits were chosen for the experiment. Further tests are needed to determine the effect of the higher temperature cycling, however it is likely that cycling through a higher temperature would increase the damage.

It is worth noting that some differences between the damage caused by these exposures and that caused by orbital exposures may have occurred because these exposures were sequential rather than simultaneous. The synergism between various factors in the orbital environment can often produce damage that is very different from what is produced by the individual factors. Although the synergistic damage is often worse than that caused by individual factors, there are a few combinations that actually mitigate the damage. This is another area that requires further investigation before any conclusions can be drawn about whether a simultaneous exposure would increase the damage.

## CONCLUSIONS

This experiment showed that electron and proton irradiation alone affected the tensile properties of the Teflon® FEP. The reduced ultimate strength and elongation were apparent at fluences comparable to the HST end-of-life (20 years). Subsequent thermal cycling between -100 and +50 °C reduced these properties further. These particle radiation exposures and thermal cycling produced chain scission in the FEP, damage that resembled the HST retrieved specimens. However, the study did not duplicate the degree of damage observed on the returned SM2 specimens with SM2 fluences of radiation and thermal cycling at the nominal limits.

The HST Multi Layer Insulation Failure Review Board used these data, along with data from other simulations and retrieved specimens to conclude that thermal cycling with deep-layer damage from electron and proton radiation are necessary to cause the observed Teflon® FEP embrittlement and the propagation of cracks along stress concentrations. It is believed that the damage increases with the combined total dose of electrons, protons, UV and x-rays along with thermal cycling (4).

#### ACKNOWLEDGMENTS

The HST Multi Layer Insulation Failure Review Board, chaired by Patricia Hansen, provided the analysis of the retrieved HST specimens and enabled this investigation. Steve Brown and Claude Smith of the Radiation Effects Task Group (GSFC) performed the electron and proton exposures in a timely and effective manner. Henning Leidecker (GSFC), Mike Meshishnek (Aerospace) and Wayne Stuckey (Aerospace), provided assistance in determining the dose versus depth profiles of the HST exposures and the simulations. Janet Barth (GSFC) provided the fluence calculations for the HST orbit. The authors gratefully acknowledge the contributions of all these individuals.

#### REFERENCES

1. P.A. Hansen, J.A. Townsend, Y. Yoshikawa, J.D. Castro, J.J. Triolo and W.C. Peters, "Degradation of Hubble Space Telescope Metallized Teflon® FEP Thermal Control Materials", Science of Advanced Materials and Process Engineering Series, 43, 570.
2. T. Zuby, K. DeGroh, and D. Smith; "Degradation of FEP Thermal Control Materials Returned from the Hubble Space Telescope," NASA Technical Memorandum 104627, December 1995.
3. J.A. Townsend, P.A. Hansen, J.A. Dever, Jack J. Triolo, "Analysis of Retrieved Hubble Space Telescope Thermal Control Materials", Science of Advanced Materials and Process Engineering Series, 43, 582.
4. J.A. Townsend, P.A. Hansen, J.A. Dever, "On-Orbit Teflon® FEP Degradation", 20th Space Simulations Conference, NASA CP- , 1998. (Paper of this compilation.)
5. H. F. Mark, "Degradation of Polymers in Hostile Environments", The Effects of Hostile Environments on Coatings and Plastics, American Chemical Society Symposium Series 229, 11.

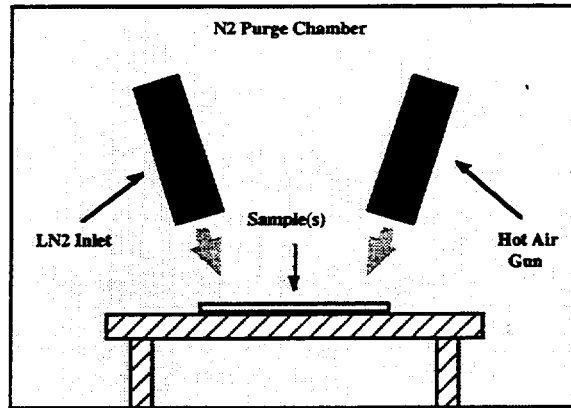


FIGURE 1: SCHEMATIC DIAGRAM OF HIGH-SPEED THERMAL CYCLING SETUP

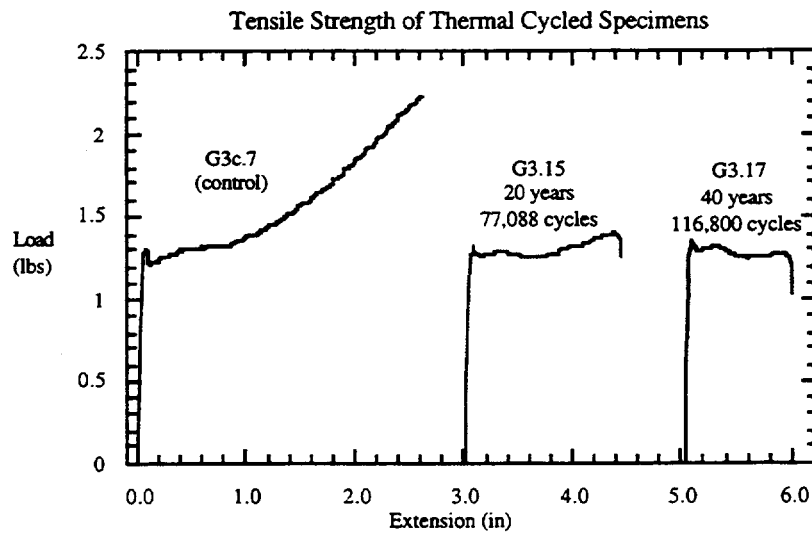


FIGURE 2: TYPICAL TENSILE TEST CURVES - Control Specimen, 20 Year Radiation With 77,088 Thermal Cycles, And 40 Year Radiation With 116,800 Thermal Cycles

FIGURE 3: Yield Strength Versus Exposure Duration

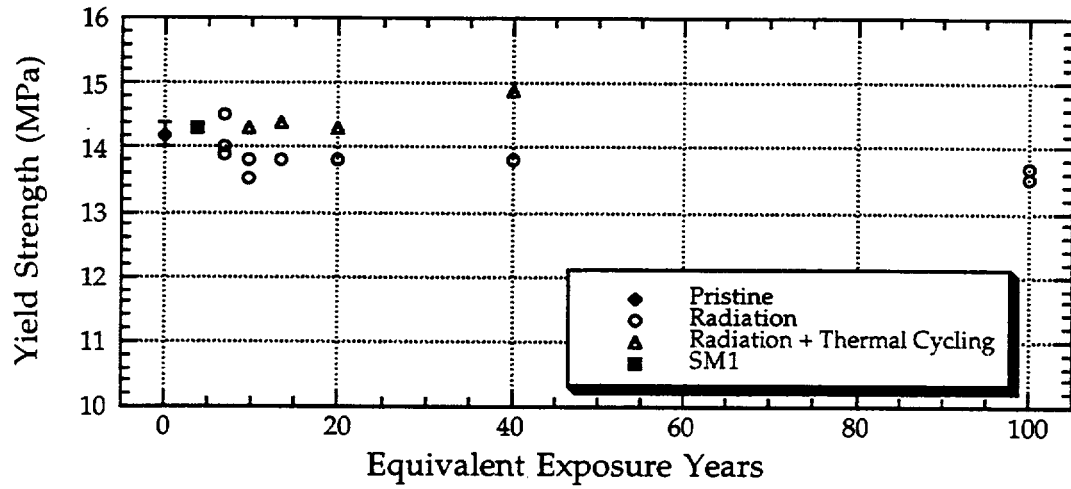


FIGURE 4: Ultimate Strength Versus Exposure Duration

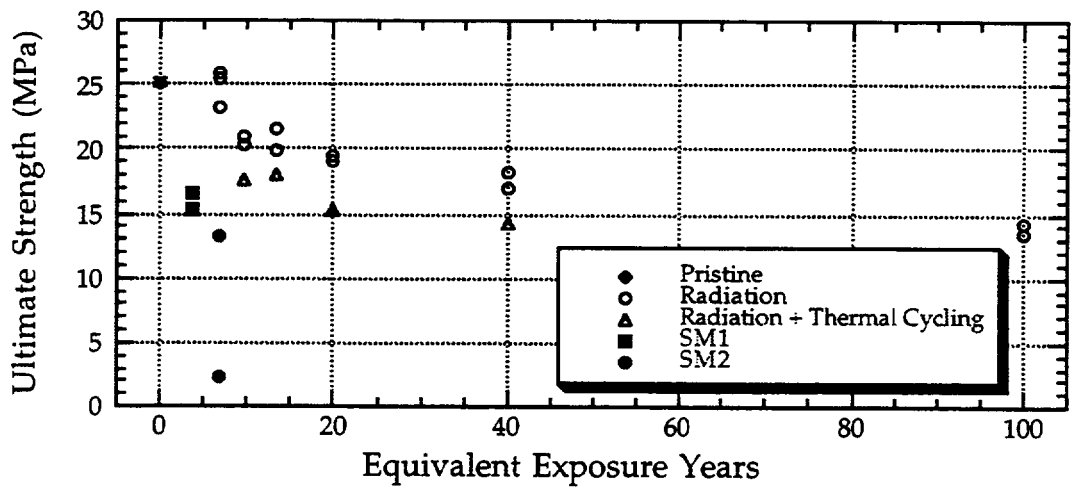
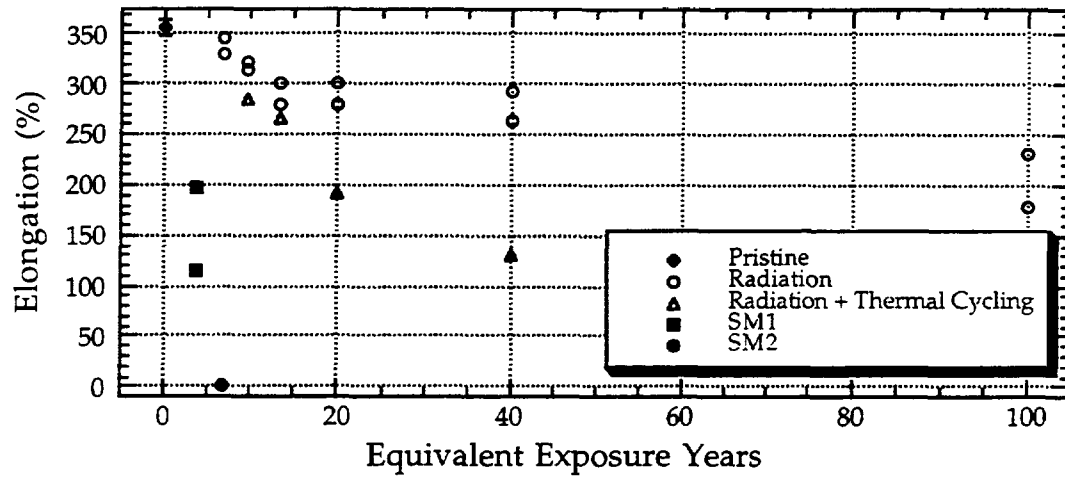


FIGURE 5: Elongation at Failure Versus Exposure Duration





# EFFECT OF X-RAYS ON THE MECHANICAL PROPERTIES OF ALUMINIZED FEP TEFLON®

James R. Gaier

NASA Lewis Research Center, Cleveland, OH 44135

Michael R. Brinkmeier and Elizabeth M. Gaier  
Manchester College, North Manchester, IN 46962

## ABSTRACT

Pieces of the multilayer insulation (MLI) that is integral to the thermal control of the Hubble Space Telescope (HST) have been returned by two servicing missions after 3.6 and 6.8 years in orbit. They reveal that the outer layer, which is made from 5 mil (0.13 mm) thick aluminized fluorinated ethylenepropylene (FEP) Teflon®, has become severely embrittled. Although possible agents of this embrittlement include electromagnetic radiation across the entire solar spectrum, trapped particle radiation, atomic oxygen, and thermal cycling, intensive investigations have not yielded unambiguous causes. Previous studies utilizing monoenergetic photons in the 69-1900 eV range did not cause significant embrittlement, even at much higher doses than were experienced by the HST MLI. Neither did x-rays in the 3 to 10 keV range generated in a modified electron beam evaporator. An antidotal aluminized FEP sample that was exposed to an intensive dose from unfiltered Mo x-ray radiation from a rotating anode generator, however, did show the requisite embrittlement. Thus, a study was undertaken to determine the effects of x-ray exposure on the embrittlement of aluminized FEP in hopes that it might elucidate the HST MLI degradation mechanism. Tensile specimens of aluminized 5 mil thick FEP were exposed to a constant fluence of unfiltered x-ray radiation from a Mo target whose maximum energy ranged from 20-60 kV. Other samples were annealed, thermally cycled (100×) between 77-333 K, or cycled and irradiated. Tensile tests and density measurements were then performed on the samples. Only the samples which had been irradiated had the drastically reduced elongation-to-break, characteristic of the HST samples. Thermal cycling may accelerate the embrittlement, but the effect was near the scatter in the measurements. Annealing and thermal cycling had no apparent effect. Only the samples which had been irradiated and annealed showed significant density increases, likely implicating polymer chain scission and annealing.

## INTRODUCTION

Effective thermal control of spacecraft is essential to their long-term operational success. To that end, strategies have been developed which reflect the heat load of the sun and yet emit infrared in the shadow. One of the most effective strategies is multi-layer insulation (MLI) in which there are several reflective layers (such as double sided aluminized Kapton®) with a transparent emitting layer on the outer surface (such as single sided silvered or aluminized FEP Teflon®). These materials are used extensively on the Hubble Space Telescope (HST).

The HST was first deployed on April 25, 1990 at an altitude of 614 km. On December 4, 1993 it was serviced to correct the optical flaw in its primary mirror and to upgrade its electronics. Servicing mission 1 (SM1) retrieved parts of the MLI which had been exposed to the environment for 3.6 years. This included covers on two magnetometer electronics boxes which jutted out from the surface of the light shield. Different sides of the boxes were exposed to slightly different environments with solar exposures ranging from 4,500 to 16,700 equivalent sun hours (ESH). Surprisingly, cracks which extended completely through the surface of the metallized FEP were observed.<sup>1</sup> This cracking led to an investigation into its possible causes.

When the HST was serviced a second time (SM2) on February 15, 1997, the damage to the MLI was markedly worse. This was in spite of the fact that the HST had encountered a substantially lower flux of atomic oxygen since SM1. Cracks in the FEP layer of the MLI that were tens of cm long and curled to expose the inner layers were clearly visible to the astronauts (Figure 1). The most heavily damaged sections of the MLI were removed and covered with patches. However, it was evident that the damage was increasing. NASA established a failure review board to determine the cause of the damage, predict the condition of the MLI at the next servicing mission, and to recommend MLI replacement materials for the third servicing mission, scheduled for 1999.

The orbital environment of the HST includes electromagnetic radiation across the entire solar spectrum, high energy electron and protons that have been trapped in the Earth's magnetic field, thermal cycles ranging from -100 to +50 °C on the solar facing surfaces, and from -200 to -10 °C on the anti-solar surfaces, and energetic atomic oxygen, all of which are candidates to be agents of the degradation. Despite three years of intensive study by researchers throughout NASA, no unambiguous cause of the FEP failure has been identified.<sup>1,2,3</sup> To replicate the chemical, thermal, and radiation environment experienced by HST has proved daunting, and

to date no tests under realistic simulation conditions have been able to replicate the extent of damage to the material. It is the object of this study to study one aspect of the HST environment, x-ray exposure, and to determine how it affects the mechanical properties of FEP, in the hopes of beginning to unravel the complex web of interactions.

That the x-ray environment might be involved was first suggested by Milintchouk, et al.<sup>4</sup> They argued that ultraviolet radiation would only alter the surface, because its penetration depth is so low. Although many x-ray have such a large penetration depth that they would not deposit sufficient energy to cause damage, photons in the soft x-ray regions (0.1 to 10 keV) have penetration depths similar to the thickness of the materials (0.13 mm or 0.005 in). The source of these soft x-rays would be solar flares. HST saw more solar flares than the Long Duration Exposure Facility (LDEF), which might explain why the HST MLI was so much more heavily damaged than similar materials that were exposed on LDEF, which had logged more hours in space.<sup>4</sup> Previous studies using monochromatic radiation in the range of 69 to 1900 eV showed little or no embrittlement of the FEP even at doses greatly exceeding that experienced by HST.<sup>3</sup> Embrittlement was also not seen when mission level doses of x-rays in the 3 to 10 keV generated by a modified electron beam evaporator was used.<sup>2</sup> Discoloration of some of the samples raised issues about whether there might also be charged particles or heating in these tests as well as x-ray exposure.

For the initial tests to see whether x-rays would embrittle 5 mil thick aluminized FEP, x-rays were generated in a rotating anode generator with an excitation voltage of 50 kV, an excitation current of 60 mA, and an exposure time of 1 hour. Although this sample was not tensile tested, it was not obviously embrittled. The FEP sample returned from SM2 showed considerable surface cracking (Figure 2), and though this may have been caused by the flattening out of the curled sample rather than the damage *per se*, it was not seen in the irradiated sample. When FEP was irradiated for 5 hours (50 kV, 60 mA), the texture of the irradiated area changed it from a specular to a diffuse reflector. When this sample was kinked with two pairs of forceps, there was an audible snap. Photomicrographs showed a brittle failure with sharp edges which ends abruptly at the edge of the exposed region (Figure 3). To achieve the same photon fluence, but at lower energy, a sample was exposed to x-rays generated at 20 kV and 60 mA for 31.25 hr. After this exposure, all of the aluminum appeared to be removed from the irradiated part of the sample and a large crack, as well as a few secondary cracks, developed across the entire length of the irradiated region of the sample when it was gently removed from the sample holder (Figure 4). In addition, drops of an unidentified liquid began to appear on the surface of the FEP. The drops, which increased with time, formed at the cracks (Figure 5). SEM photos of the crack surfaces indicate a thin surface layer ( $\approx 5 \mu\text{m}$ ), a brittle failure region (20 - 120  $\mu\text{m}$ ), and a region of scalloped structures (0 - 120  $\mu\text{m}$ ) (Figure 6). At this point, a test program was designed that would quantify the brittleness of the material using elongation-to-failure in tension as an indicator.

## METHODS AND MATERIALS

Aluminized FEP Teflon<sup>®</sup> of 0.013 mm (0.005 in) thickness was purchased from Sheldahl Inc. (Northfield, MN) which has supplied the original HST MLI material. Tensile dog-bone specimens were punched out using an ASTM 638-95 Type V Punch and an Arbor press. The width of the narrow portion of the dog-bone was 3.18 mm and the gauge length was 9.53 mm. Specimens were punched out both parallel and perpendicular to the direction which the FEP was machined.

Elongation-to-failure was chosen as the critical criterion to measure. Samples recovered from HST had elongation-to-failure so low as to not be measurable, while under similar conditions pristine FEP has an elongation-to-failure of about 200 percent. A computer controlled tensile tester was designed and assembled onsite<sup>5</sup> based on a 5 lb load cell (Sensotech Model 11). The tensile tester and grips were designed and optimized specifically for these samples. The test procedure was based on the ASTM standard. Since FEP is particularly susceptible to creep, all dog-bones were strained at a constant rate of 0.0210 cm/sec (0.00827 in/sec). Stress-strain curves were analyzed and ultimate tensile strength, tensile modulus, and elongation-to-failure were recorded for each sample.

The source of the x-ray exposure was a Rigaku Rotaflex BEH rotating anode source equipped with a Mo target. The x-rays passed through a 0.40 mm thick Be window and 1.90 cm of air before striking the sample. The excitation potential across the anode was varied from 20 to 60 kV, resulting in Bremsstrahlung with a maximum photon energy ranging from 20 to 60 keV. There is also a resonant energy spike at the  $K_{\alpha}$  energy for Mo of 17.4 keV superimposed on the Bremsstrahlung. The approximate shape and spectral variation less the Mo  $K_{\alpha}$  spike is shown in Figure 7.<sup>6</sup> Since the photon intensity is also a function of excitation potential, the time must be adjusted if the total fluence from trial to trial is to remain constant. The assumption was made that the photon intensity varied as the square of the excitation potential and linearly with the excitation current.<sup>5</sup> X-ray exposure conditions are shown in Table I.

The integrated intensity of the x-ray beam was determined using an AXUV detector (International Radiation Detectors, Torrance, CA) operating with a 7.5 volt bias voltage. This detector is sensitive to radiation from 10 to at least 4000 eV. Detector current was measured for values of the excitation potential ranging from 20 to 60 kV, and excitation currents from 10 to 70 mA. The dark current was three orders of magnitude below the lowest value for the detector current and so was neglected. Over this energy range the x-ray intensity varied linearly with both excitation potential and current as is shown in Figure 8.

Another characteristic of the FEP on HST that changed during its space exposure was its density. Thus, the density of several samples was measured using a calibrated density gradient technique which has been described in detail elsewhere.<sup>7</sup> The density solvents used were carbon tetrachloride (CCl<sub>4</sub>) which has a density of 1.594 g/cm<sup>3</sup>, and bromoform (CHBr<sub>3</sub>) which has a density of 2.899 g/cm<sup>3</sup>. Neither of these would be expected to interact significantly with the FEP.

The particular SM2 sample tested had rolled up in cylinder with a diameter of several mm and was not in good thermal contact with HST (top tear shown in Figure 1). Additionally, the reflective aluminum layer was outward facing, and the emissive FEP layer was inward facing. Calculations indicate it had likely reached temperatures as high as 200 °C.<sup>8</sup> Thus, it is possible that the high temperatures seen by this particular sample were responsible for the increased embrittlement and density. So several samples were annealed in a oven at 200 °C in air for times ranging from 1.0 to 96.0 hr.

In addition to the high temperatures seen by that particular sample, the entire HST is thermally cycled as it travels in and out of the earth's shadow. Calculations have estimated thermal swings between -100 and +50 °C.<sup>2</sup> This would take the FEP through the lower of its two second order phase transitions, which occurs at -85 °C (the other occurs at +85 °C).<sup>9</sup> Thus, it was thought important to cycle some of the test specimens to temperatures below and above that phase transition. This was done by attaching them to a sample holder by pinching them in the very end of the samples, well away from the grip and test sections. The sample were then submerged in liquid nitrogen (-196 °C) for 30 s, and then placed in an incubator maintained at 60 °C for 330 s. This cycling was repeated for 100 cycles, well below the 21,000 thermal cycles experienced by HST<sup>2</sup>, but perhaps enough to see at least the beginning of degradation. Samples were included which had been previously exposed to the x-rays, and others were subsequently exposed to the x-rays.

## RESULTS AND DISCUSSION

The first issue to be addressed was whether the machine direction was correlated with the tensile properties. To this end ten samples of the aluminized FEP were cut parallel to, and ten perpendicular to the machine direction. The elongation to failure parallel to the machine direction was  $196 \pm 9$  percent, and that for samples cut perpendicular was  $187 \pm 11$  percent. These values were judged to be statistically insignificant by Student's t test, so a combined pristine elongation-to-failure of  $192 \pm 11$  percent was used throughout the rest of the study. For comparison, FEP returned from HST SM1 had an elongation-to-failure of 41 percent.<sup>2</sup>

The effect of annealing time at 200 °C on the percent elongation-to-failure is shown in Figure 9. Only one or two samples were tested at each anneal temperature, so the mean  $\pm$  standard deviation for the pristine samples are superimposed on this figure. The least squares fit through the data has a slope of 0.014 percent elongation per hour, well within the error of the measurements, and in the direction of decreasing brittleness. All of the data lie within one standard deviation of the mean of the pristine value, so there is no indication that annealing at 200 °C for as long as 96 hr embrittles the FEP.

The samples that were thermal cycled had an elongation-to-failure of  $195 \pm 6$  percent. Thus there was no effect on the elongation-to-failure for thermal cycling at the level of 100 thermal cycles from -196 to + 50 °C. HST was exposed to about 40,000 thermal cycles between launch and SM2. The fraction of degradation seen in 100 cycles would be dependent on the degradation kinetics. If 40,000 cycles or less caused a 200 percent change in elongation-to-failure in the HST MLI, and the degradation is linear, then 100 cycles might be expected to increase the elongation-to-failure by 0.5 percent, well within the error of the measurement. If, however, the degradation is exponential, then the elongation-to-failure would be expected to be about 85 percent. Since no degradation was observed, that puts limits on the extent of degradation attributable to thermal cycling alone.

Figure 10 presents the effect of x-ray exposure on the percent elongation-to-failure. All of these samples had significantly lower percent elongation-to-failure than the pristine value. In the exposure region where the maximum energy was 60 keV, the average percent elongation-to-failure dropped by an order of magnitude to  $27 \pm 6$  percent. In the exposure regions where the maximum photon energy was 40 keV elongation-to-failure was  $5 \pm 3$  percent. At a maximum photon energy of 20 keV, the decrease was  $2.0 \pm 1.3$  percent, a full two orders of magnitude less than the pristine value. FEP exposed to Mo K<sub>α</sub> x-rays (17.4 keV) generated using a graphite monochromator for about 24 hours had an elongation to failure of 206 percent, well within the pristine range.

The convolution of the spectrum emitted by the x-ray source and that absorbed by the FEP reveals that there is only a limited overlap region. Figure 11 compares the spectral fluence of the photons absorbed by the 20 kV and the 60 kV tests. It can be seen in this plot that the 20 kV tests resulted in much higher fluence of photons in the 3 to 15 keV region where FEP is susceptible to through-thickness damage. It also illustrates why the Mo characteristic radiation (17.4 keV) did not damage the FEP. An independent analysis by Banks et al. from a the electron beam x-ray generator which was run at 10 kV concludes that the 3-10 keV photons would be capable of inflicting the most damage.<sup>2</sup> Unlike this work, their high energy cut-off (10 keV) was dictated by the maximum energy of their x-ray source.

The fluence of x-rays being generated by the x-ray source over the experimental times was about  $10^5$  J/m<sup>2</sup>. This is three orders of magnitude higher than the fluences estimated for HST's exposure at SM2, which was about 250 J/m<sup>2</sup>.<sup>7</sup> Although the damage was more extensive in these tests than in the HST samples, antidotal tests indicated that there was minimal damage when FEP was exposed at equal fluence. Thus, it is not claimed that x-rays within the 3 to 15 keV region are solely responsible for the damage in the HST MLI. Rather, these tests indicate that there is a similar damage mechanism, probably polymer chain scission, at work in both instances.

The synergistic effects of soft x-ray exposure and thermal cycling were investigated both by thermal cycling samples and then exposing them to x-rays, and by exposing them to x-rays and then thermal cycling them. The results, shown in Table II, may indicate that thermal cycling has a small effect on the elongation-to-failure of these materials. The numbers of samples were small (3 to 4) and the results showed decreases near the scatter of the data. But Banks, et al., have also reported that more extensive thermal cycling may be implicated in the MLI degradation on HST, though the effect appears to be minor.<sup>2</sup>

The results of the density measurements are shown in Table III. The samples returned from the magnetometer shield during SM1 showed no increase in density over pristine (both at  $2.141 \pm 0.003$  g/cm<sup>3</sup>). The density of four samples were measured with solar exposure ranging from 4,500 to 16,700 equivalent sun hours, but they all had the same density. However, the density of the sample returned from SM2 was  $2.184 \pm 0.003$  g/cm<sup>3</sup>. This particular FEP sample was removed from a place on the MLI that had split and coiled up into a tight spiral with a radius of only a few mm. Calculation carried out at NASA Goddard Space Flight Center indicate that temperatures on this section may have reached as high as 200 °C.<sup>7</sup> It has been suggested by de Groh *et al.* that the density increase is caused by polymer chain scission within the FEP, followed by annealing, which allows the shortened chains to pack more densely.<sup>10</sup> The results of this study confirm those of de Groh. Merely annealing the FEP increased its density by as much as 1.0 percent. Irradiating the FEP far beyond the levels experienced by HST increased its density by 0.7 percent. However, if the FEP is first exposed to soft x-rays and then annealed, its density increases by nearly 2.7 percent. This increase in the irradiated and annealed FEP density supports chain scission as a degradation mechanism.

The percent crystallinity of the sample can be determined from the density.<sup>11</sup> It can be seen that the crystallinity is a strong function of the density. Thus, though there is a range of densities of only 2 percent in these samples, it corresponds to nearly a 20 percent range in the crystallinity. Thus even small density changes support a chain scission mechanism.

## CONCLUSIONS

A study has been carried out to study the effects of x-ray exposure of FEP Teflon on its brittle failure, as characterized by its elongation-to-failure. Elongation-to-failure was unchanged for machine direction, annealing to 200 °C for up to 96 hr, and up to 100 thermal cycles between -196 and 50 °C. However, it fell from  $192 \pm 11$  percent to  $27 \pm 6$  percent when exposed to Bremsstrahlung with a maximum photon energy of 60 keV,  $5 \pm 3$  percent at 40 keV, and to  $2.0 \pm 1.3$  percent at 20 keV. Modeling indicates that 5 mil (0.13 mm) thick FEP would be most sensitive to through thickness cracking when exposed to radiation from 3 to 15 keV. Lower energy radiation will be absorbed near the surface, and higher energy radiation will pass through with little interaction. Our experimental data confirm this model. The elongation-to-failure of samples irradiated by 20 keV maximum energy photons was an order of magnitude less than those irradiated by 60 keV maximum photons. Thermal cycling (100×) may accelerate the embrittlement when combined with irradiation, though the effect was near the scatter in the measurements. The density of FEP increases by about 1.0 percent when annealed at 200 °C for 24 hour. Irradiation with x-rays increases the density by about 0.7 percent. However, if the sample is irradiated and then annealed its density increases by about 2.7 percent. This observation supports a degradation mechanism where x-rays in the 3 to 15 keV range can be absorbed, causing chain scission and subsequent degradation of the flexibility of the polymer. If the polymer is then heated, the newly formed shorter chains can rearrange more efficiently which increases the crystallinity and so also the density.

degradation of the flexibility of the polymer. If the polymer is then heated, the newly formed shorter chains can rearrange more efficiently which increases the crystallinity and so also the density.

This study was motivated by the degradation of the HST multi-layer insulation. It has shown that the embrittlement of FEP to the extent observed on the MLI could be caused by scission of the polymer chains. It is not likely that x-rays in the 3 to 15 keV range are the sole agents of the degradation, since the fluences used in this study were three orders of magnitude larger than those calculated to be present on HST, though they may be a significant contributor. This might especially be the case if the free radicals which are formed during the chain scission persist for very long periods of time and propagate. There are, however, other agents within the HST environment that may cleave the polymer chains and lead to similar degradation.

## ACKNOWLEDGMENTS

The authors would like to thank B.A. Banks, J. A. Dever, and K.K. de Groh of the NASA Lewis Research Center for their helpful discussions during the course of this work, and A. Jalics of Cleveland State University and R. Hall of Saint Mary's College for tensile data used in the pristine FEP analysis. E.M.G. gratefully acknowledges the support of the NASA Lewis Research Center under Cooperative Agreement NCC3-317.

## REFERENCES

- 1) T.M. Zuby, K.K. de Groh, and D.C. Smith, "*Degradation of FEP Thermal Control Materials Returned from the Hubble Space Telescope*", NASA Technical Memorandum 104627 (1995).
- 2) B.A. Banks, K.K. de Groh, T.J. Stueber, and E.A. Sechkar, "*Ground Laboratory Soft X-Ray Durability Evaluation of Aluminized Teflon FEP Thermal Control Insulation*", NASA Technical Memorandum 207914 (1998).
- 3) J.A. Dever, J.A. Townsend, J.R. Gaier, and A.I. Jalics, "*Synchrotron VUV and Soft X-Ray Radiation Effects on Aluminized Teflon FEP*", *Materials and Process Affordability: Keys to the Future* 43(1) (Society for the Advancement of Materials and Process Engineering, Covina, CA, 1998) pp. 616-628.
- 4) A. Milintchouk, M. Van Eesbeek, F. Levadou, and T. Harper, "*Influence of X-Ray Solar Flare Radiation on Degradation of Teflon in Space*", *J. Spacecraft and Rockets*, 34(4) (1997) 542.
- 5) Designed and built by T.J. Stueber, M.J. Forkapa, and E.A. Sechkar, NYMA, Cleveland, OH.
- 6) B.D. Cullity, *Elements of X-Ray Diffraction*, 2nd Ed. (Addison-Wesley Publishing Company, Inc., Reading, MA, 1978).
- 7) J.R. Gaier, and M.E. Slabe, "*Density of Graphite Fibers*", *Carbon* 34(2), 1990, pp. 1-15.
- 8) J.A. Townsend, P.A. Hansen, J.A. Dever, and J.J. Triolo, "*Analysis of Retrieved Hubble Space Telescope Thermal Control Materials*", *Materials and Process Affordability: Keys to the Future* 43(1) (Society for the Advancement of Materials and Process Engineering, Covina, CA, 1998) pp. 582-593.
- 9) *Tetrafluoroethylene Polymers*, Vol 13, DuPont, p. 657.
- 10) K.K. de Groh, J.R. Gaier, R. Hall, and M.J. Norris, M. Espe and D. Cato, "*Effects of Heating on Teflon FEP Thermal Control Material from the Hubble Space Telescope*," in preparation, 1998.
- 11) *Teflon Fluorocarbon Resins: Mechanical Design Data* - DuPont Product Information.

**Table I -- X-Ray Exposure Conditions**

| Excitation Potential | Excitation Current | Time  |
|----------------------|--------------------|-------|
| kV                   | mA                 | hr    |
| 20                   | 70                 | 17.89 |
| 40                   | 70                 | 7.94  |
| 60                   | 70                 | 1.98  |

**Table II -- Thermal Cycling + X-Ray Radiation**

| Thermal Cycling | X-Ray Exposure | % Elongation to Failure |
|-----------------|----------------|-------------------------|
| none            | none           | 192 ± 11                |
| 100×            | none           | 195 ± 6                 |
| none            | 60 keV         | 27 ± 6                  |
| 100× before     | 60 keV         | 18 ± 0.5                |
| none            | 20 keV         | 2.0 ± 1.3               |
| 100× after      | 20 keV         | 1.5 ± 0.9               |

**Table III -- Density of Alumized 5 mil FEP Under Various Conditions**

| Material         | Density g/cm <sup>3</sup> | Crystallinity percent |
|------------------|---------------------------|-----------------------|
| pristine         | 2.141                     | 50.6                  |
| SM1              | 2.141                     | 50.6                  |
| annealed 1 hr    | 2.149                     | 53.2                  |
| 60 kV x-rays     | 2.157                     | 55.9                  |
| annealed 3 hr    | 2.159                     | 56.5                  |
| annealed 5 hr    | 2.160                     | 56.8                  |
| annealed 7 hr    | 2.160                     | 56.8                  |
| annealed 24 hr   | 2.163                     | 57.8                  |
| SM2              | 2.184                     | 64.7                  |
| x-ray + 1 hr ann | 2.193                     | 67.7                  |
| x-ray + 3 hr ann | 2.195                     | 68.4                  |
| x-ray + 5 hr ann | 2.197                     | 69.0                  |
| x-ray + 7 hr ann | 2.198                     | 69.4                  |

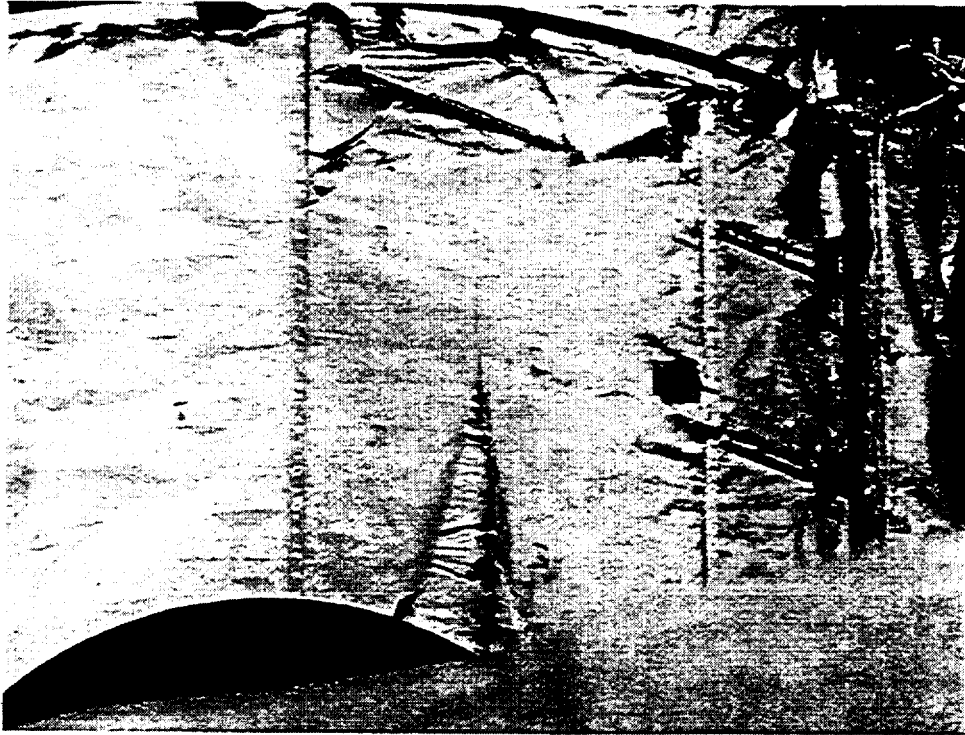


**Figure 1**— Damaged FEP outer layer in multi-layer insulation of Hubble Space Telescope.

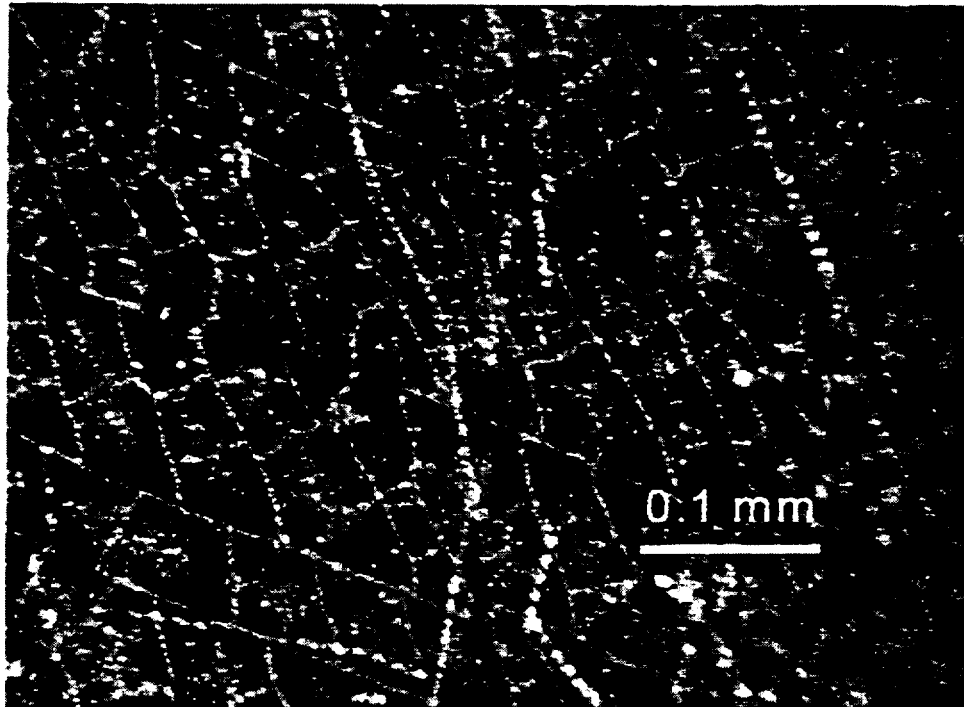


**Figure 2** – Surface cracks in FEP from MLI returned from HST during SM2.

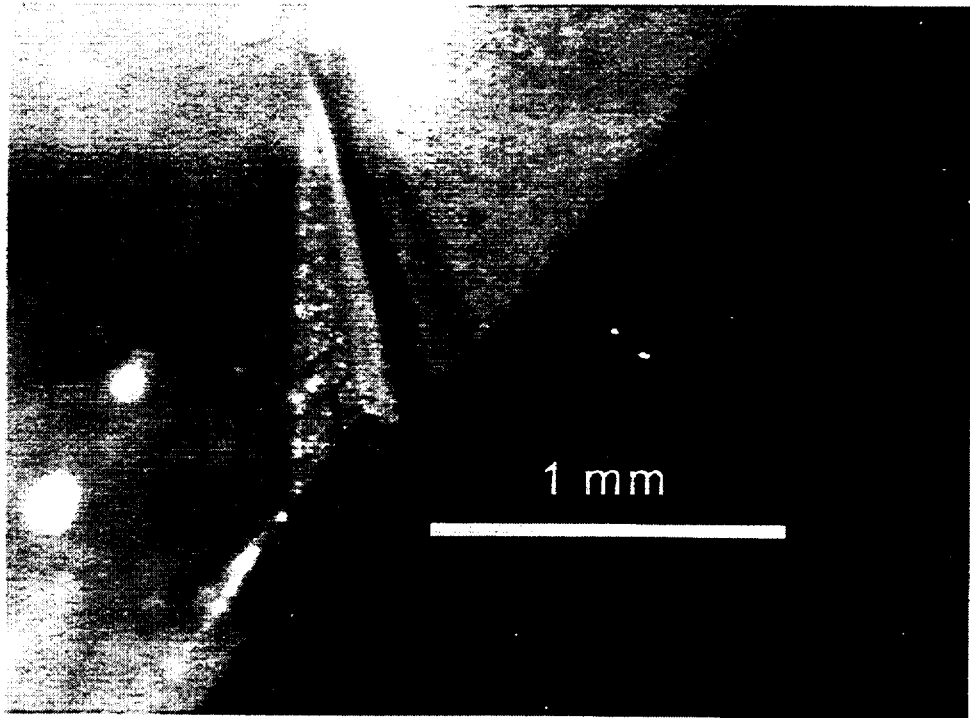


**Figure 3** – Brittle fracture in FEP after x-ray irradiation.

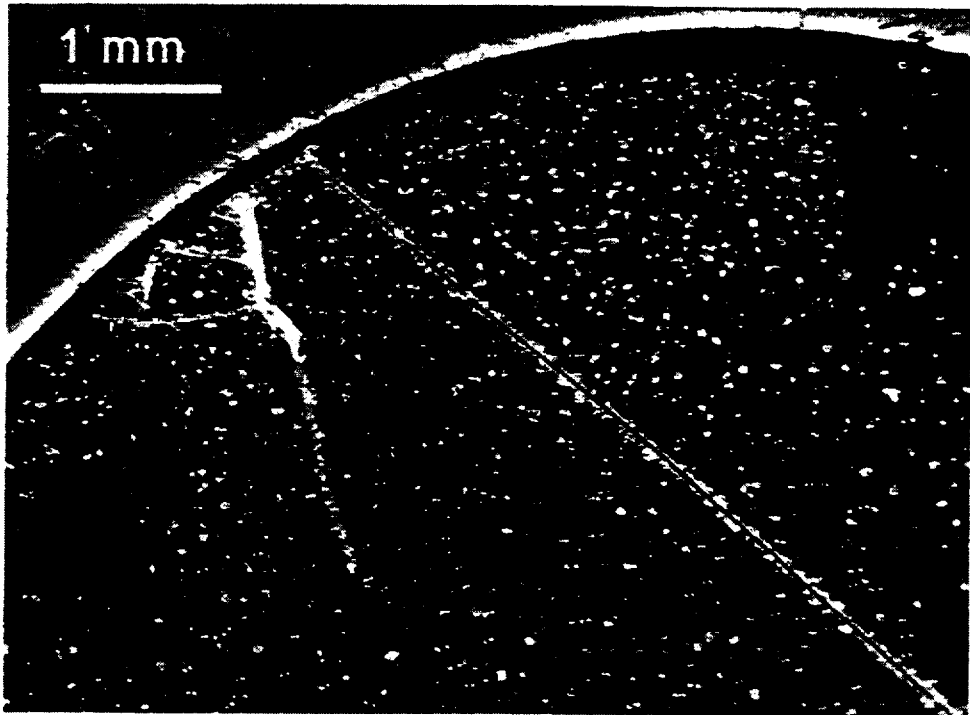


**Figure 4** – Brittle fracture of FEP after x-ray irradiation



Figure 5 – Liquid seeping from cracks in FEP induced by x-ray irradiation.

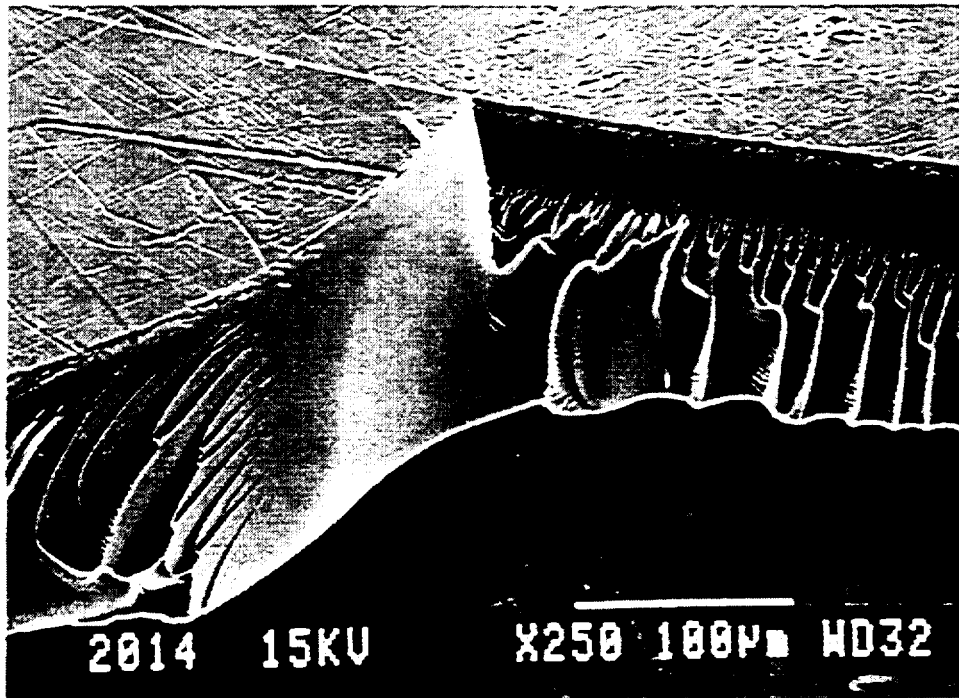
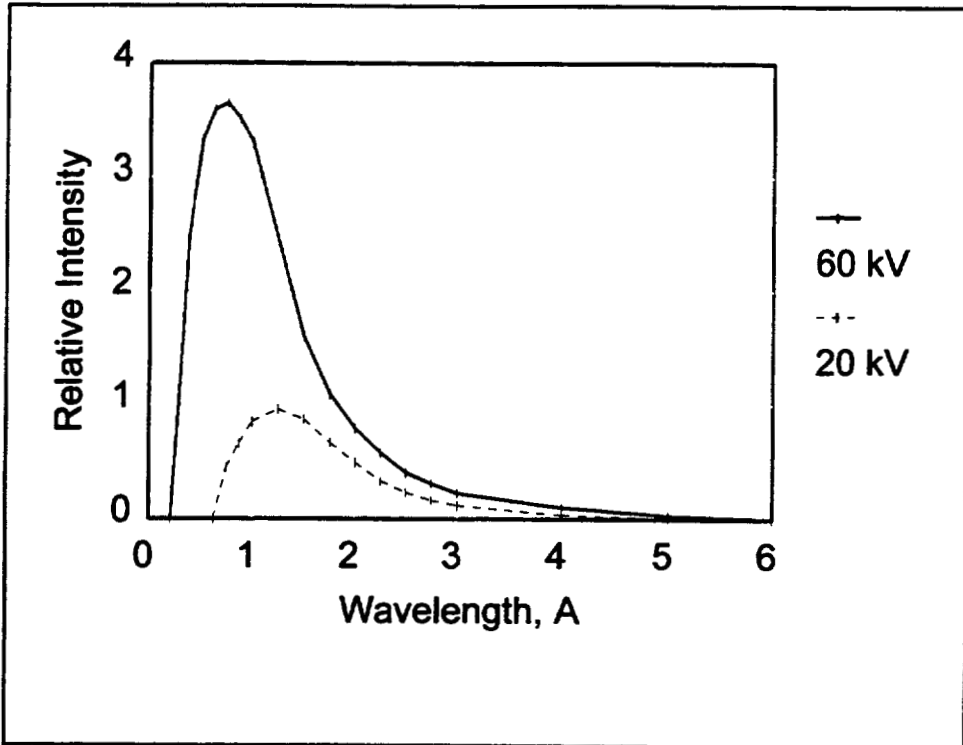
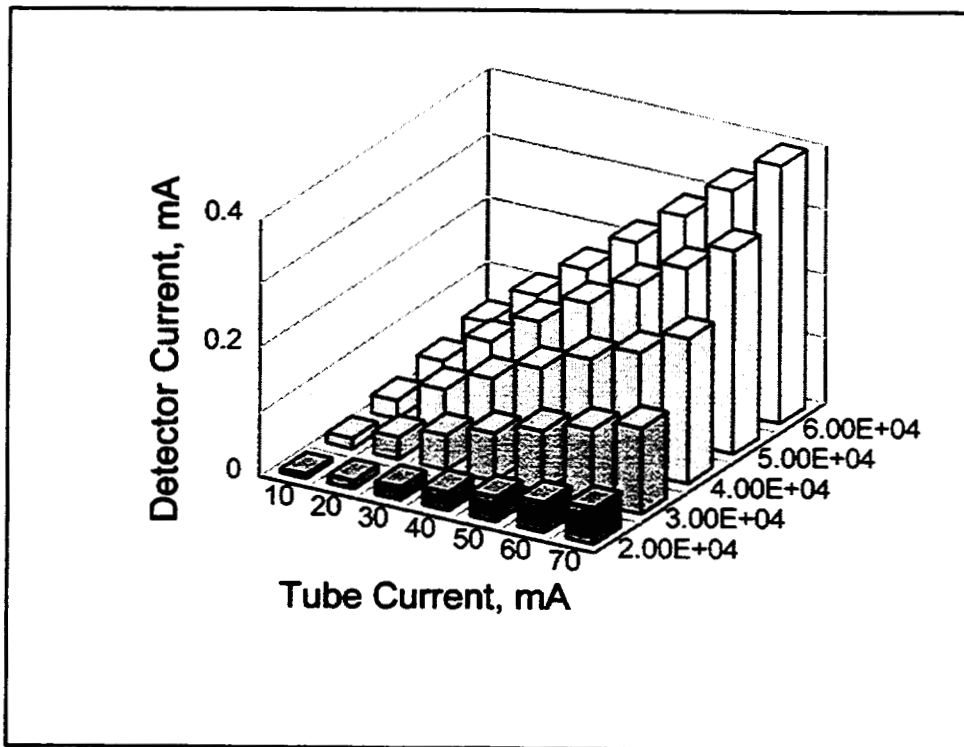


Figure 6 – Fracture surface of x-ray irradiation induced cracks in FEP.



**Figure 7** – Schematic x-ray spectrum of Bremsstrahlung emitted from a Mo target at excitation potentials of 20 and 60 kV.



**Figure 8** – AXUV detector current as a function of excitation current and voltage of the rotating anode x-ray source.

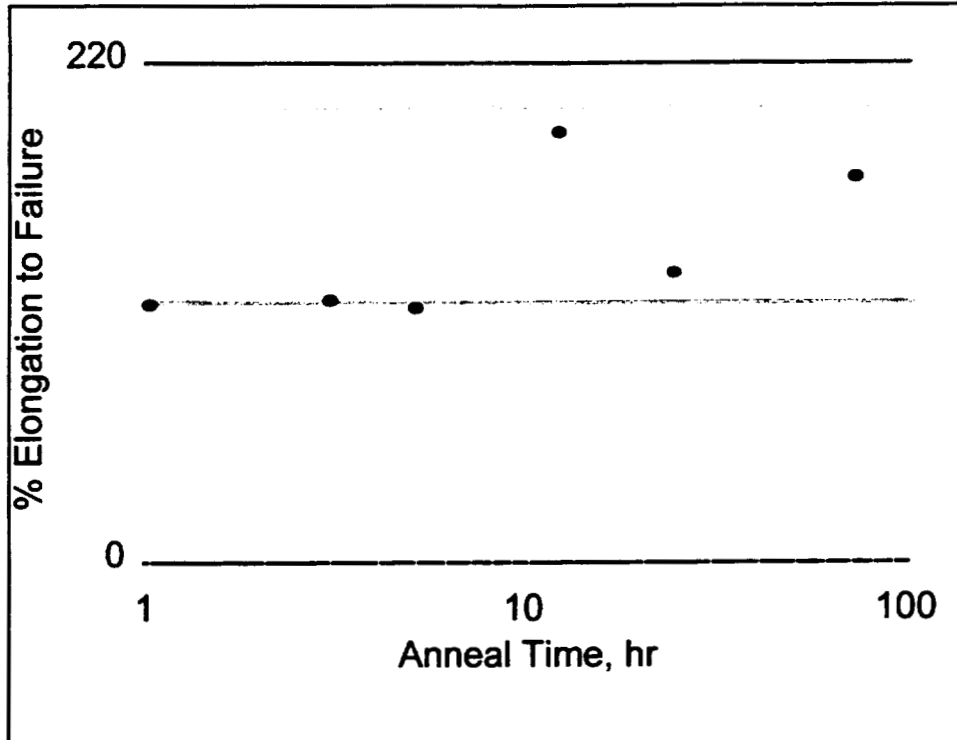


Figure 9 – Elongation to failure for 5 mil thick aluminized FEP as a function of anneal time in air at 200 °C. Grey lines give mean  $\pm \sigma$  for pristine FEP.

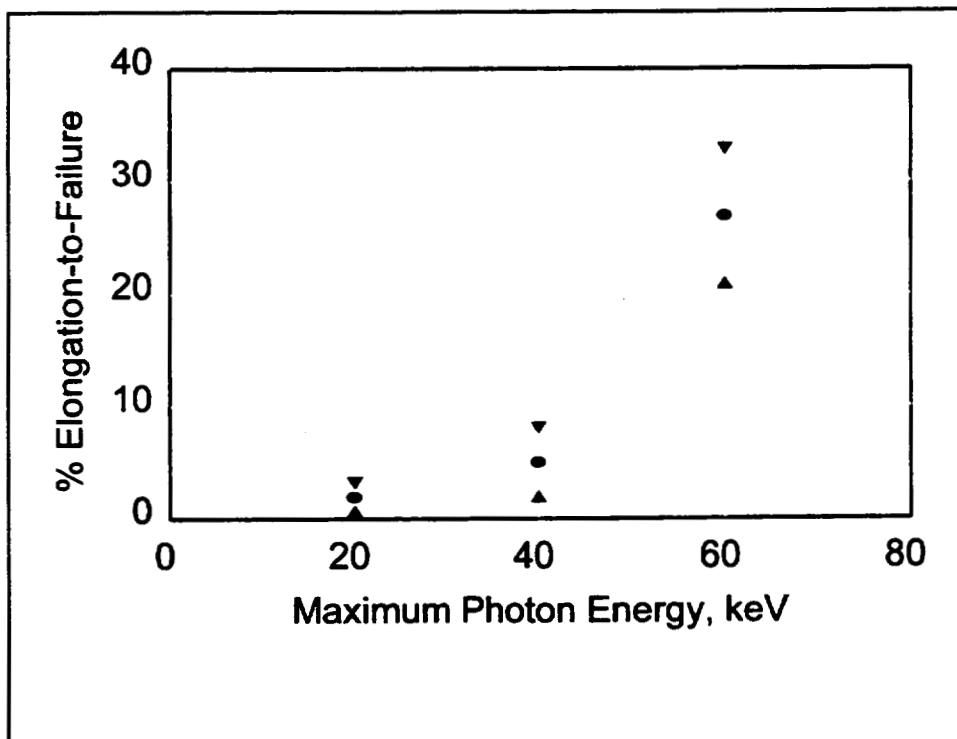
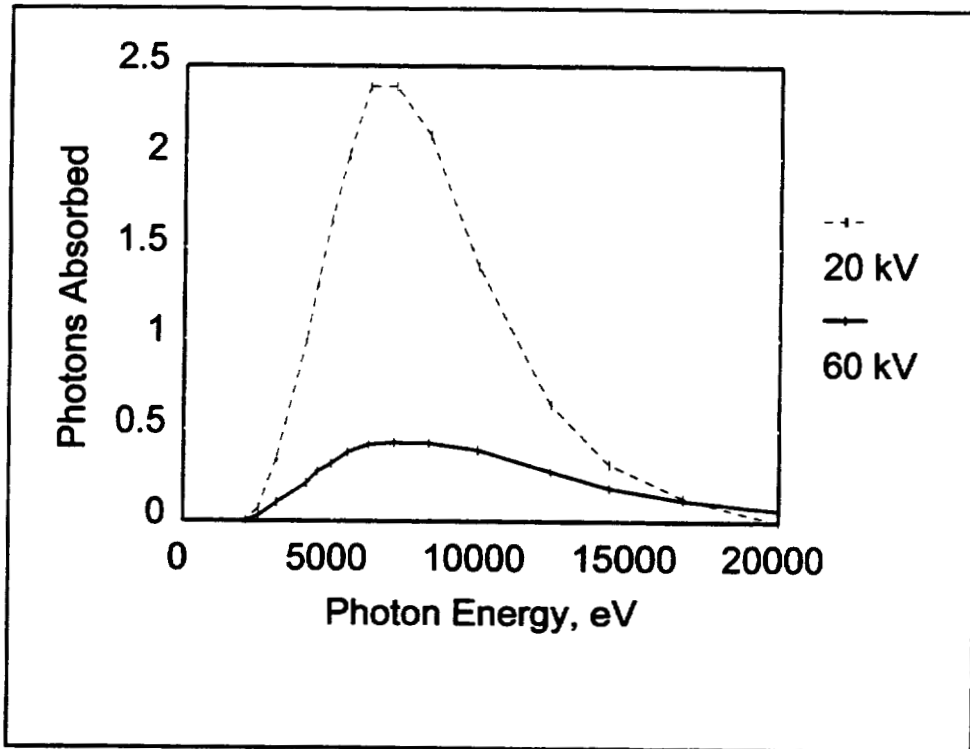


Figure 10 – Elongation-to-failure for 5 mil thick aluminized FEP exposed to  $10^5$  J/m<sup>2</sup> x-rays of various energies. Mean  $\pm \sigma$  is shown.



**Figure 11** – Convolution of emission spectrum of x-ray source with absorption spectrum of 5 mil FEP. The absorption on an arbitrary scale.

## THE ESA/ESTEC ENVIRONMENTAL TEST CENTRE'S NEW QUALITY ASSURANCE SYSTEM

Peter W. Brinkmann and Massimo Panicucci  
European Space Agency (ESA)  
European Space Research and Technology Centre (ESTEC)  
Noordwijk, The Netherlands

### ABSTRACT

During 1997, the ESA/ESTEC Environmental Test Centre underwent a major re-organisation, entrusting the responsibilities for maintenance and operation to an industrial consortium. As a consequence, the quality system had to be adapted to the new organisational structure and to the new allocation of tasks and responsibilities. After introducing the Test Centre and its facilities, the paper describes the new management structure and the modified quality system. In particular it addresses the interfaces between ESA/ESTEC and the industrial consortium and summarises the transition from the previous structure to the new organisation, during which activities and facilities were formally handed over to the consortium. It concludes with a preliminary assessment of the restructuring process.

### INTRODUCTION

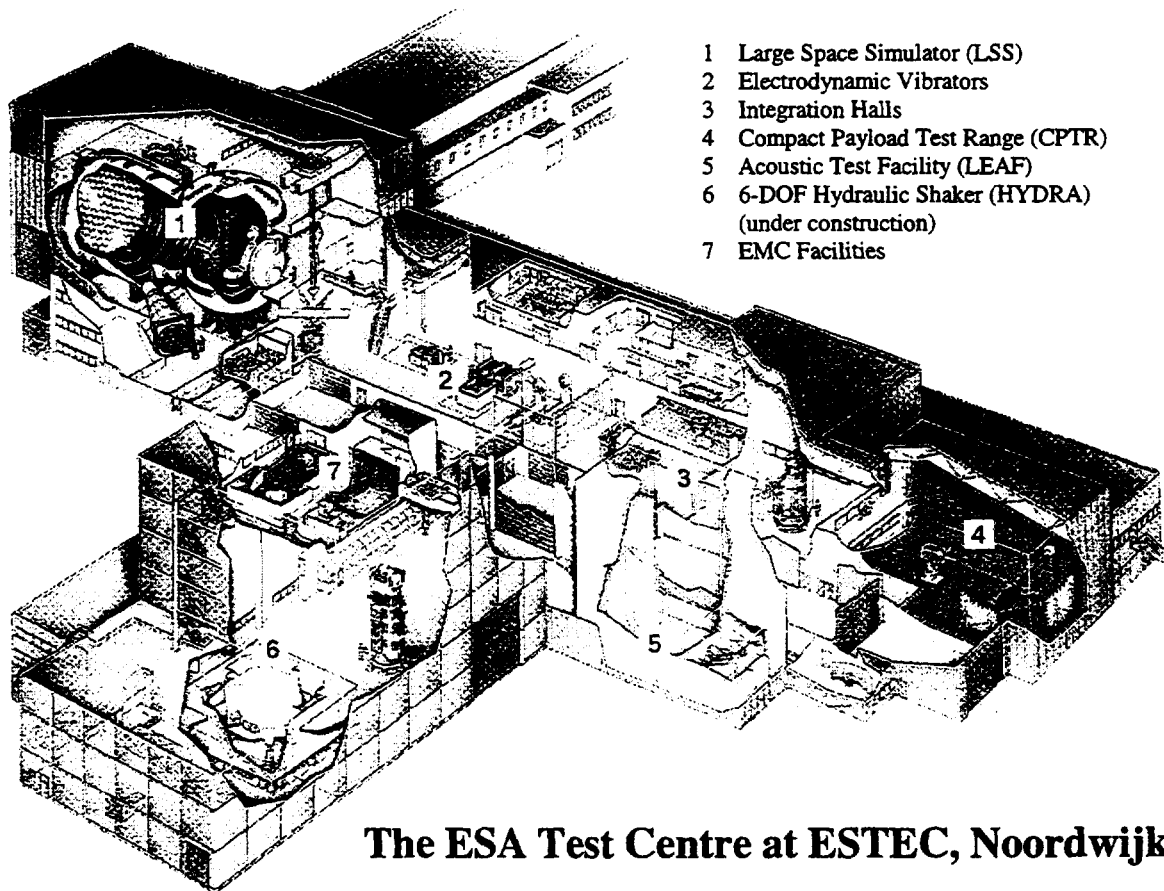
#### The Test Centre of ESA

The European Space Agency (ESA) has developed and maintains major environmental test facilities at its technology centre "ESTEC" in Noordwijk, The Netherlands.

The facilities and services of the ESTEC Test Centre have been developed primarily to support the Agency's own programmes, but can also be made available for non-ESA projects. Whilst the national Test Centres in Europe are equipped for environmental tests on small and medium-size spacecraft, the ESTEC facilities are compatible with the requirements of large spacecraft to be launched on Ariane-4 and Ariane-5. The facilities are compliant with the specific demands for testing space hardware, which requires extreme cleanliness conditions and high safety and reliability standards to avoid damage to or degradation of costly space hardware.

The ESTEC Test Centre has been designed in a way that allows a test article to be moved smoothly from one facility to the other by overhead cranes or on air-pallets. The advantage of this concept is that the complete series of environmental tests can be performed "under one roof" (i.e. without any outdoor transportation). There is therefore no need for reconfiguring the spacecraft between tests, thereby reducing the overall schedule as well as the risk of damage during handling and transportation. All test areas are air-conditioned and comply with Fed.Std.209 cleanliness

class 100,000 (class 10,000 and class 100 in limited preparation area). In addition to the test facilities and associated equipment, the ESTEC Test Centre provides data handling facilities, check-out rooms, storage areas as well as offices and meeting rooms for the users of the facilities.



**The ESA Test Centre at ESTEC, Noordwijk**

## **MANAGEMENT STRUCTURE AND QUALITY SYSTEM**

### **Transition Phase**

The ESTEC Testing Division has been responsible for the development, maintenance and operation of ESA's test facilities since 1967. For maintenance and operation activities the Testing Division has utilised the support of a contractor. The contractor's staff were integrated into the hierarchical structure of the Division, but all functions with key responsibilities were held by ESA staff. In 1997, the division was re-organised with the aim of increasing the flexibility for responding to varying workloads, to implement a clear split of responsibilities between ESA and the contractor and to become fully compliant with the latest European legislation. The contractor has been made fully responsible for the maintenance and operation of the test facilities.

The contractor was selected after a competitive tender action in 1996. A three-year contract, starting January 1<sup>st</sup>, 1997 was placed with the COMET consortium [IABG (D), ITS (F) and TERMA (DK)]. In particular, two of these companies, i.e. IABG and ITS, have directly relevant experience, because they operate the national environmental test centres in Germany and France, respectively.

The first quarter of 1997 was devoted to the setting-up of the contractor's on-site team and the familiarisation and training of the contractor's staff. This transition proceeded without any interruption of the test programme at the Centre. The new team was formed from key personnel drawn from the national centres and recruited from contractor's staff, who had already supported the test operations at ESTEC under the previous ESA regime. Familiarisation and training was primarily based upon "*on-the-job-training*", during the ongoing test programme. Between the first quarter of 1997 and the beginning of 1998, the responsibility for maintenance and operation of each individual test facility was successively transferred to COMET. These transfers were the subject of formal reviews and based on the contractor's evidence that the staff had the necessary qualifications and were adequately trained.

### **Responsibilities of ESA and Contractor**

After the transition phase lasting from January to March 1997, the new responsibilities were allocated as follows:

#### Responsibilities of ESA staff

- AIV support to ESA programmes during all project phases concerning model and test philosophy, programmatic and economic aspects.
- Test management and coordination between customers and contractor in order to ensure timely and correct execution of preparation, testing and reporting; this includes coordination of internal and external test support.
- Supervision of the contractor's activities in order to ensure full compliance with Agency rules and requirements for reliability, quality and safety.
- Facilitating project interfaces with the Coordinated European Facilities (IABG, ITS and CSL) for environmental testing of spacecraft hardware.
- Planning and cost control of all activities in the Division including test preparation, test, facility modifications, investments, engineering and workshop tasks.
- Maintaining know-how of facility technology and test methodology by performing studies and by preparing and controlling appropriate investments.
- Verifying implementation of PA/safety requirements for the Test Centre.
- Control of documentation and facility configurations.

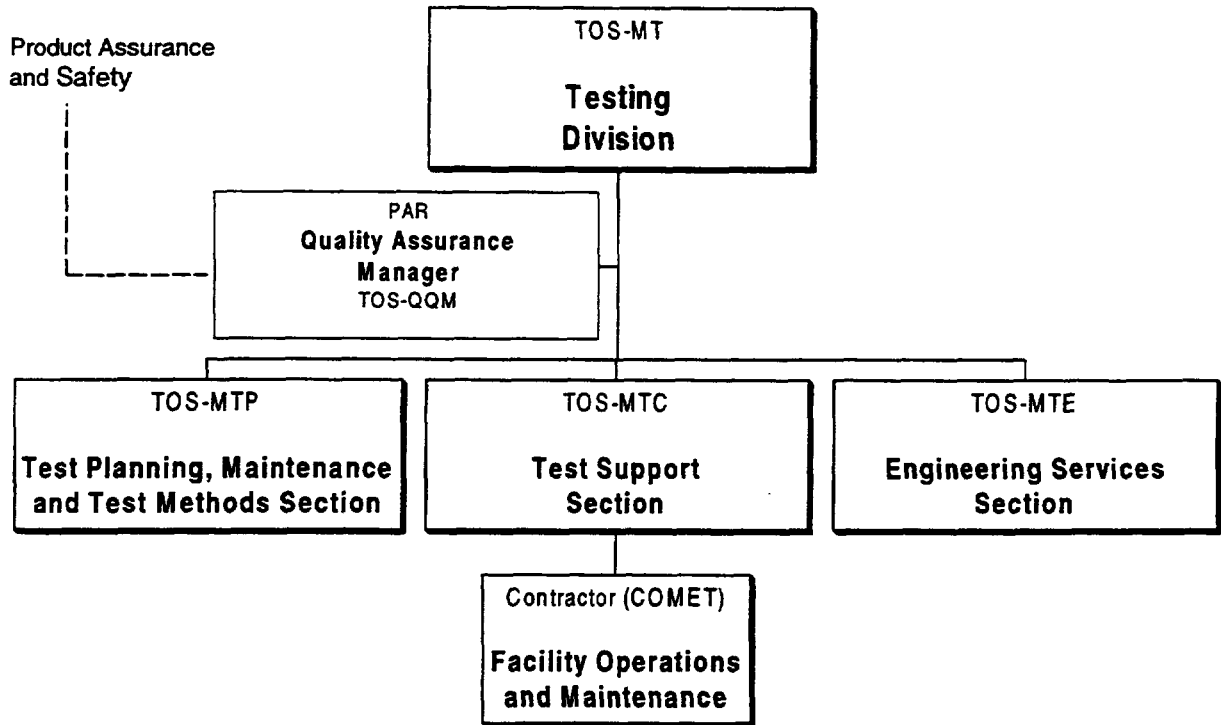
#### Responsibilities of the contractor (COMET)

- Execution of the maintenance of the test facilities, instruments and auxiliary equipment. The maintenance is executed in compliance with the requirements defined by and procedures approved by ESA, with the goal of ensuring that the facilities are kept

available for operations and do not degrade.

- Execution of test operations. This includes test preparation activities, management of engineering work to adapt the facility, performing all test operations during the test and all post test activities.
- Organisation and implementation of a training programme with the objective of retaining the necessary expertise for maintenance and operation of the facility.

The following diagram shows the new organisational structure of the Testing Division:



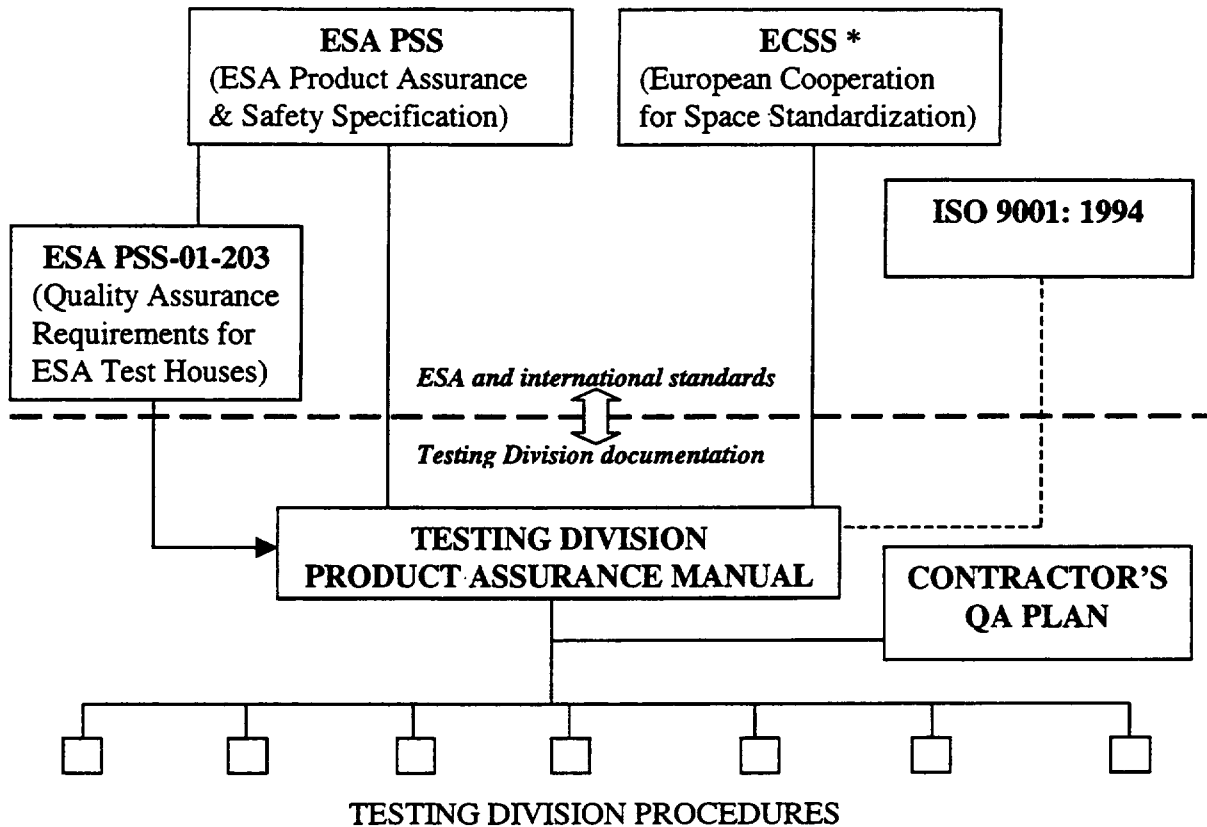
### Quality Assurance System of the Test Centre

The previous relationship between the user of the test facilities and the ESA Test Centre was characterised by the “Customer→ESA” model. This has now become a more complex “Customer→ESA→Contractor” model, where ESA still takes full responsibility for the contractor’s undertakings vis-à-vis the customer, although:

- The contractor executes the majority of the tasks.
- The contractor directly handles properties of ESA and interfaces with the customer’s equipment. The contractor’s performance has an important impact on the quality of the test results and the safety during test execution.
- The contractor’s manpower involvement in test execution is much larger than that of ESA.

## Quality Assurance Management / Policy / Organisation

Given that ESA is directly responsible for all services provided to its customers as well as for their quality and safety, it is the Agency's responsibility to give adequate confidence and visibility to its customers to demonstrate that all applicable contractual requirements are met. This visibility is provided by the existing documentation tree developed by ESA, as shown in the accompanying figure.



\* ECSS standards will gradually replace the ESA-PSS series

As far as the quality assurance system is concerned, ESA's main responsibilities are:

- To assess the effectiveness of the services supplied to the customer.
- To implement the requirements defined in the PA manual.
- To liaise with the customer with respect to PA and safety issues.
- To study, modify and develop the test facilities.
- To define the requirements for PA and safety, maintenance and calibration of facilities (and buildings).
- To perform the overall risk assessment and acceptance of the test operations.

The Test Centre QA policy is based upon the ESA Product Assurance and Safety Specifications (ESA PSS series) and is also compliant with the requirements of ISO 9001: 1994.

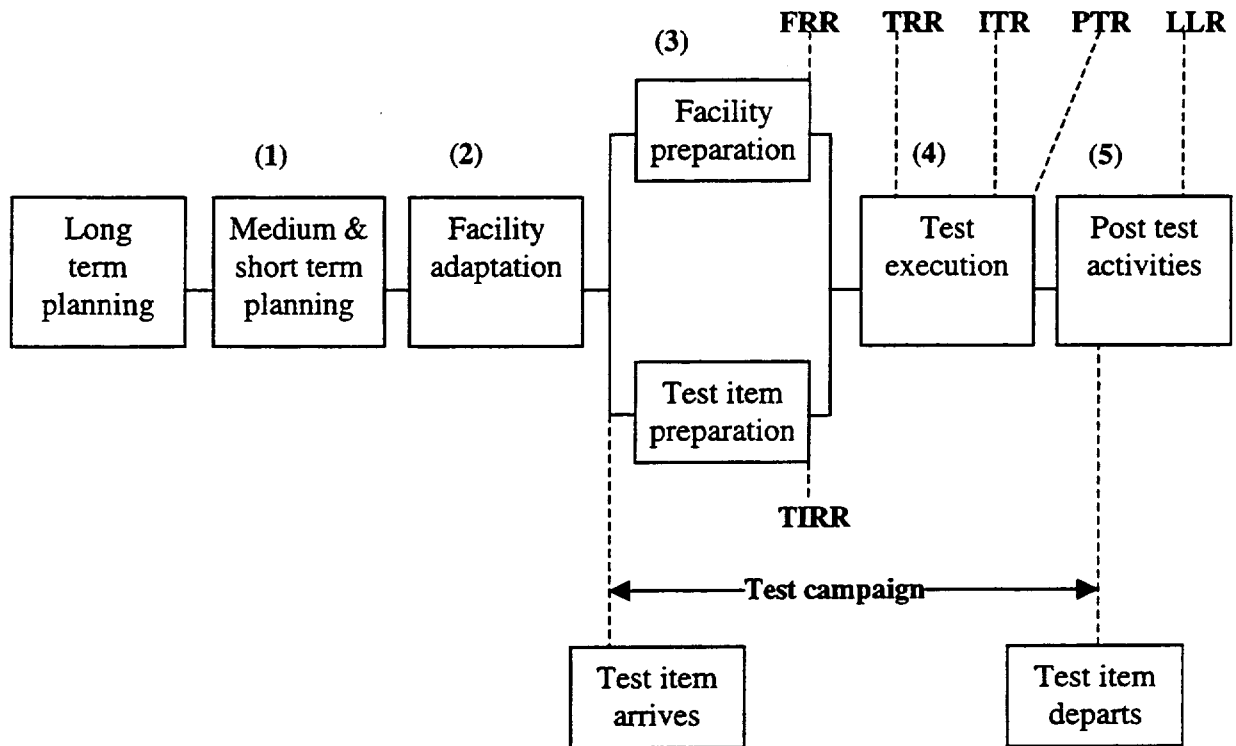
The Test Centre QA Manager reports hierarchically to the Head of the Product Assurance and Safety Department and functionally (and on a day-by-day basis) to the Head of the Testing Division. This ensures the necessary organisational freedom and authority. The Test Centre QA Manager receives support from his parent Department in specific QA disciplines like material, processes and contamination control. The contractor has nominated a full-time QA Manager. The contractor's QA organisation is defined in the contractor's QA plan.

#### The Quality Assurance Manual and Procedures

The Testing Division Product Assurance Manual describes the new QA organisation, the policy and the objectives. It was of primary importance to identify clearly in this manual the direct responsibilities, the preparation and testing process, the internal and external interfaces, the assurance functions and the related detailed procedures. In this context, the ESTEC Test Centre has developed a comprehensive set of quality system procedures, operational procedures and working instructions. All of these procedures are referenced in the relevant pages throughout the PA Manual. An example is shown in Attachment 1. The Manual also describes the testing process as well as the various interfaces between ESA and the contractor. These are summarised in Tables 1 to 5.

## The Preparation and Testing Process

The overall testing process, together with the associated reviews, is shown below.



### Acronyms

|             |  |
|-------------|--|
| <b>FRR</b>  | <b>Facility Readiness Review (internal review)</b>                             |
| <b>ITR</b>  | <b>Intermediate Test Review(s) (at the end of each test phase or test run)</b> |
| <b>LLR</b>  | <b>Lessons Learned Review</b>  |
| <b>PTR</b>  | <b>Post Test Review</b>  |
| <b>TIRR</b> | <b>Test Item Readiness Review *</b>  |
| <b>TRR</b>  | <b>Test Readiness Review *</b>   |

\* can be combined

Some process details, with emphasis on the QA involvement, are given below.

### (1) Medium and short term planning

When a test request is submitted, the suitability of the test facilities are evaluated as follows:

- Can the facility be used in the current configuration ?
- Are specific test support hardware or minor facility modifications required ?
- Are important modifications needed ?
- Is the procurement of a new facility necessary ?

## (2) Facility adaptation, modification and procurement of new facility

The test requirements (including the quality and safety requirements) are analysed and translated into the relevant technical specifications. Changes to the facility configuration are processed via a Change Request by the Configuration Control Board (see paragraph on “Configuration Management”). The relevant supporting safety and reliability analyses are updated, to assess any impact on the test operations and maintenance and to propose recommendations for risk reduction if necessary. The PA requirements for the procurement, upgrading/modification of test facilities (or their subsystems) are defined in the ESTEC Test Centre PA Manual. Those requirements are tailored from the ESA PSS and ECSS standards. In case of procurement of a new facility or instrumentation, a set of reliability and safety analyses is initiated (Ref. 1).

Depending on the complexity/criticality of the facility/system, a selection of the following RAMS (Reliability, Availability, Maintainability, Safety) analyses are carried out:

- FMECA (Failure Mode Effects and Criticality Analysis)
- Maintainability Analysis
- Hazard Analysis
- HAZOPS
- Fault Tree Analysis
- Operating Hazard Analysis

The output information from all analyses is compiled into a critical items and functions list containing information on components and functions which can have catastrophic or serious consequences due to hazards that are inherent in them, due to their own failures or due to other concerns. Additionally, action sheets are compiled and the implementation of actions is followed-up.

The most recent applications of the tailored concept for RAMS analyses in the ESTEC Test Centre were:

- Modification of the Large Space Simulator (LSS) Gimbal Stand
- Levelling System for the LSS
- Upgrading of the thermal vacuum chamber VTC 1.5
- Emergency shut-down system for LSS
- HYDRA (hydraulic shaker)
- Safety assessment of the CPTR

For the manufacturing phase the supplier is required to plan fabrication operations in coordination with inspections and tests (in compliance with the Design Verification Matrix). This planning is documented in a Manufacturing and Inspection Plan.

The installation, start-up and acceptance phases are defined in the relevant plans prepared by the supplier and approved by ESA. Finally, a formal Acceptance Review is performed by a board composed of ESA representatives (including the QA manager) and the supplier.

### (3) Preparation of the facility

The preparation of the facility is carried out by the contractor in accordance with the standard procedures or test specific procedures. At the end of the phase, prior to the formal Test Readiness Review (with the customer representatives), a Facility Readiness Review is held. Its main objectives are:

- To verify the adequacy of the maintenance/calibration status of the facility.
- To verify the adequacy of the personnel resources and qualification.
- To interpret the pre-test results, against test requirements.
- To confirm that open non-conformances have no negative effects on the safety/performance of the test.
- To confirm the cleanliness status of the facility and clean-rooms.

### (4) Test execution

The test is executed by the contractor according to approved and validated procedures. When the operation of the facility needs to be coordinated with the operation of the test item (e.g. during a solar simulation test) a so-called “Integrated Test Procedure” is prepared by the contractor together with the test customer. The QA manager is responsible for the test surveillance in particular when safety-critical operations are executed. When relevant, specific operation and safety procedures are drawn-up as defined in the paragraph on “Safety” below.

At the end of the test, a Post Test Review is held to confirm and verify test completion and authorise the starting of the post-test activities, which may include the removal of the test item from the facility.

### (5) Post test activities

The post test activities include:

- Preparation for the departure of the test item or the transfer to another facility/clean room.
- Lessons Learnt Review with the customer’s participation.
- Facility Data Report prepared by the contractor for the customer.

## **Safety**

The highest priority in the Test Centre is to ensure safety at all times to protect human life, customers' equipment, ESTEC property, facilities, equipment and to maintain an environment with no hazardous consequences. In order to assess the risk associated with a particular test campaign, information on hazardous items and operations is gathered at the earliest opportunity. To this end, the Test Centre's customer is required to provide information relevant to the possible presence of hazardous items and hazardous operations during the preparation and testing activities.

A standard questionnaire must be completed by the customer to gather the necessary information. This data package is used by the ESA QA Manager and the contractor for the preparation of the Specific Safety Procedures and, whenever necessary, for the risk assessment, test feasibility evaluation and facility hazard analysis. The questionnaire addresses, among others, the following aspects:

- Specific hazards to which personnel will be exposed during the operation (e.g. pyrotechnics, propellants, etc.).
- Identification of failure tolerances (e.g. redundancies, safety devices, inhibits) and means for verifying that they are in place and operational.
- Identification of any conditions which cause hazardous operations.
- Identification of the safety precautions to be taken for each activity, whether hazardous or not.
- Initial identification of the emergency/contingency actions for each hazardous operation.
- Recommendations for special provisions to be furnished by the ESTEC Environmental Test Centre.

The facility operation and safety procedures are prepared taking into account the baseline configuration of a facility and its nominal working conditions. They include:

### Facility Operations Procedure

The outcomes of the safety analyses (FMECA, Hazard Analysis, HAZOPS) performed on the facility are taken into account in the Operations Procedures. The hazardous conditions are identified and flagged within the procedure itself and the appropriate safety precautions are addressed.

### Facility Emergency Procedures and Facility Evacuation Procedures

The emergency actions to be taken in case of a failure of the facility are identified. The FMECA and HAZOPS recommendations are taken into account for the definition of appropriate actions to mitigate the consequences of a possible failure of the facility or its supplies.

## Safety Procedure for a Specific Test Campaign

The Test Centre prepares the specific safety procedures which include:

- Identification of the general facility operations and safety procedures.
- References for test item configuration and characteristics.
- Non standard test operations, facility configuration or facility operations.
- Questionnaire for the use of hazardous items, as completed by the customer.
- Facility and test item safety analyses (hazard analysis, FMECA, operating hazard analysis).
- Identification and classification of the “test specific” hazards and hazardous conditions.
- Test specific safety precautions and additional emergency and contingency actions.

## **Configuration Management**

The Configuration Management of the facilities is under ESA’s responsibility. The contractor is encouraged to propose modifications to the facilities which improve their performances and safety characteristics. The Configuration Management (CM) system is documented in the CM Manual and its supporting procedures. The CM system comprises:

- Configuration baseline identification, for hardware and software.
- Configuration control, to manage changes.
- Configuration accounting, to document the changes to baseline configurations.
- Configuration verification by means of audit and review.

The CM system applies to all documentation related to the ESTEC Environmental Test Facilities as well as to testing documentation. Customer CM requirements for a specific project may be applied, provided that they do not conflict with basic safety requirements or technical principles. Test specific items, test reports, etc., are not under configuration control. Configuration Management is administered by the Configuration Management Office (CMO). Changes are assessed and authorised by the Configuration Control Board (CCB), chaired by ESA.

## **Maintenance and Calibration of the Facilities**

The ESTEC Test Centre has developed a comprehensive set of maintenance and calibration procedures. The contractor has overall responsibility for the implementation of the maintenance and calibration programme, in compliance with the ESA requirements. A yearly maintenance plan is produced by the contractor and approved by ESA. Full visibility is given to ESA on the status of the maintenance and calibration programme and deviations are promptly reported. The ESA QA Manager has responsibility for monitoring the implementation of the maintenance and calibration programmes.

## **Non-conformance Control**

The ESTEC Test Centre maintains a documented non-conformance control system. It is designed to interface with customer systems when required. The non-conformance control system is under the responsibility of the ESA QA Manager. The system provides a disciplined approach to the identification and segregation of non-conforming items, the recording, reporting, review, disposition and analysis of non-conformances and the definition and implementation of corrective actions. Emphasis is placed on the prevention of recurrence of non-conformance by removing root causes. The non-conformances are processed by the ESA Material Review Board (MRB), chaired by the ESA QA manager and with mandatory participation of the contractor's QA Manager. In the case of minor non-conformances, ESA delegates its function to the contractor.

## **Internal Quality Audits**

Comprehensive, planned and documented Internal Quality Audits are carried out within the ESTEC Test Centre to verify that all activities, in particular those of the contractor, comply with planned arrangements and to determine that the QA system continues to be effective. Audits include examination of all operations and documentation, evaluation of actual operations against established requirements, recommendations for corrective and preventive actions and follow-up to assess the implementation of corrective actions. Audits are conducted of documented procedures and use is made of checklists to structure the audit task. The Internal Quality Audit programme is under the responsibility of the ESA QA Manager.

## **PRELIMINARY ASSESSMENT AND CONCLUDING REMARKS**

The re-organisation of the Testing Division and the transfer of responsibilities for maintenance and operation of the ESTEC Test Centre to the COMET industrial consortium has been a demanding and complex undertaking. The Test Centre is the largest in the ESA Member States and incorporates high performance facilities with a replacement value of about 200 million EURO. ESA staff, who had previously run these facilities with great motivation and pride, had to accept the new "hands-off approach", while still being fully responsible to the customer for test execution. The difficulties of adjusting to the new regime must not be underestimated. Despite the complexity of the process, the transition has been effected within a short time period and without any interruption of ongoing satellite test programmes. It is also worth noting that no degradation in safety or reliability has been identified in the test operations during the transfer process. The following elements have been prerequisites for this success:

- A well defined Safety Manual and a successfully operating Quality Assurance Manual, which was adapted to the new situation, provided good references for the new contractor.
- The new contractor had directly relevant know-how and provided staff with appropriate experience.
- The ESA staff supported the transfer of know-how very constructively during the transition period and thereafter.

A preliminary assessment has shown that the transfer process has been successfully completed. The contractor has established a qualified permanent on-site team, which is configured according to the basic workload for maintenance activities and test operations. Staff in the IABG and ITS test centres have been trained and can be called in when additional resources are needed temporarily to cope with the highly variable test load at ESTEC. This new approach keeps the fixed costs of the Test Centre low, whilst still maintaining a high degree of flexibility in terms of resource allocation.

## REFERENCES

1. Schäbe, H., "Reliability and Safety Analysis for the Large Space Simulator", *Third International Symposium on Environmental Testing for Space Programmes*, ESTEC, Noordwijk, The Netherlands, 25-27 June 1997, Proceedings SP-408 (ISBN 92-9092-315-6), pp. 281-287.

## TABLES

Table 1 : Interfaces on Quality Assurance and Safety

| Description of the activity   | ESA           | Contractor  |
|---|---------------|-------------|
| Preparation / maintenance of Test Centre PA Manual  | X             | I           |
| Preparation / maintenance of related QA procedures  | X             | S           |
| QA audits of contractor   | X             | S           |
| Personnel training and certification of contractor's staff  | →             | X           |
| Definition of QA requirements for new facilities, facility modifications and test support equipment                           | X             | I           |
| QA involvement during the design, manufacturing, testing and acceptance of new/modified facilities and test support equipment | X             | I           |
| Preparation and maintenance of contractor's QA plan   | →             | X           |
| Overall responsibility of non-conformance control   | X             | S           |
| Chairmanship of major non-conformance   | X             | I           |
| Verification of dispositions implementation and close-out of major non-conformance  | X             | S           |
| Chairmanship of minor non-conformance   | →             | X           |
| Verification of dispositions implementation and close-out of minor non-conformance  | →             | X           |
| Attendance to the Configuration Control Board   | X             | X           |
| Approval of documents for QA aspects  | X             |             |
| Cleanliness and contamination control   | →             | X           |
| Calibration control (including certificates)  | →             | X           |
| Maintenance control (including reports)   | →             | X           |
| Implementation of Quality Records procedure   | →             | X           |
| Access control  | →             | X           |
| Approval of facility safety and emergency procedures  | X             | X           |
| Approval of facility operation procedures, maintenance procedures, calibration procedures                                     | X             | X           |
| Surveillance of safety during maintenance activities  | →             | X           |
| Control of certification of items for handling and transportation   | →             | X           |
| Store control   | →             | X           |
| Spare parts definition and control  | →             | X           |
| Interface with customers for QA aspects, including QA plan  | X             |             |
| Review and analysis of customer's responses to the questionnaire on hazardous items   | X             | S           |
| Risk assessment of the test configuration   | X             | S           |
| Definition of specific safety procedures, safety devices and training   | X             | S           |
| Preparation of (writing) specific safety procedures, including dry-runs when necessary  | →<br>Approval | X           |
| Execution of dry-runs and training of emergency procedures  | →<br>Approval | X           |
| Approval of the emergency procedure during the specific test campaign   | X             | Preparation |
| Preparation of specific operating procedures  | Approval      | X           |
| Acceptance of customer's handling and lifting devices and MGSE  | X             | S           |
| Preparation of the Facility Readiness Review (FRR)  | →             | X           |
| Attendance of the FRR   | X<br>Approval | Chair       |
| Test surveillance   | →             | X           |
| Test surveillance on safety critical operations   | →             | X           |

X = Primary responsibility  
 → = Supervision, auditing, approval

S = Support  
 I = Implementation of relevant requirements

**Table 2 : Interfaces on Medium and Short Term Activities and Preparation of Test Facility**

| Description of the activity                                   | ESA           | Contractor |
|---|---------------|------------|
| Medium term report, monthly report, weekly report             | X             | I          |
| Preparation of test proposal                                  | →<br>Approval | X          |
| Test facility evaluation and selection                        | X             | S          |
| Opening of tasks to the contractor                            | X             | I          |
| Risk assessment of the test campaign                          | X             | S          |
| Preparation of test facility including specify safety devices | →             | X          |
| Preparation of the specific operation and safety procedures   | →<br>Approval | X          |
| Execution of the pre-tests and dry-runs                       | →             | X          |
| Preparation of the Facility Readiness Review                  | →<br>Approval | X          |

**Table 3 : Interfaces on Test Execution**

| Description of the activity   | ESA | Contractor |
|---|-----|------------|
| Integrated Test Procedure with customer   | →   | X          |
| Test operations according to procedure  | →   | X          |
| Interfaces with the test customer, including verification of the test procedure | X   | I          |

**Table 4 : Interfaces on Post Test Activities**

| Description of the activity                          | ESA           | Contractor |
|--|---------------|------------|
| Preparation for the departure of the test item       | →             | X          |
| Restoring the facility to its standard configuration | →             | X          |
| Lessons Learnt Review                                | X             | X          |
| Preparation of the Facility Operation Report         | →<br>Approval | X          |

**Table 5 : Interfaces on Maintenance and Calibration Activities**

| Description of the activity   | ESA           | Contractor |
|---|---------------|------------|
| Preparation/modification of maintenance and calibration procedures                              | →<br>Approval | X          |
| Preparation of the yearly maintenance plan  | →<br>Approval | X          |
| Updating/control of the maintenance and calibration databases                                   | →             | X          |
| Execution of the maintenance and calibration tasks according to approved procedures             | →             | X          |
| Regular reporting on the progress of the maintenance plan, including schedule and problem areas | →             | X          |

X = Primary responsibility  
 → = Supervision, auditing, approval

S = Support  
 I = Implementation of relevant requirements

## ATTACHMENT 1: EXAMPLE



### 3.3.3 Cleanliness and Contamination Control

Controls are applied within the Environmental Test Centre to maintain the **environmental characteristics** defined in part 2.4.5.

The general procedure referenced below defines the measures to ensure that **cleanliness and environmental characteristics are controlled at all time**. These measures include:

- Specification and monitoring of the conditioning equipment, the maintenance methods, the amount of equipment and number of personnel inside the controlled areas. Although the access to clean rooms is controlled, some activities may require, to limit the number of persons, present at the same time, within a specific area. This is achieved by controlling the access either to the clean room, or to a delimited area within it, by means of chains/barriers. A guard, posted at the entrance of the highly restricted area, is provided with a list of authorised persons and ensures, when the maximum number of persons is reached, that one is leaving the area before another may enter. Additional costs are supported by the user.
- Continuous monitoring of the key environmental parameters, temperature and humidity. Automatic warnings are given when the environmental specifications are exceeded ( by the Central Monitoring System, see description in the procedure at the bottom of this page).
- Design and selection of handling equipments and methods to avoid any contamination.
- For tests in vacuum chambers, adequate provisions for the selection of an approved material list , internally and/or by the customer ( see para 4.2.3 ).
- A strict cleaning regime throughout the test centre.
- Planned maintenance of the air conditioning equipment (see 5.3).
- Periodic training and briefing sessions on cleaning methods and requirements.
- Methods of verifications of the cleaning work.
- Implementation of the incoming inspection procedure, before entering the clean room areas.

| APPLICABLE INTERNAL PROCEDURES |  |             |
|--------------------------------|--|-------------|
| Document Number                | Document Title   | Responsible |
| YTO/NS/TEA/0759/C              | Regulations for incoming inspection of test items in test area       | MTP         |
| YTO/OPE/TEA/0970/C             | ESTEC Test Centre clean rooms cleaning procedure                     | Contractor  |
| YTO/NS/TEA/801/C               | Daily inspection   | Contractor  |
| YTO/OPE/BLDG/0748              | Operating instruction for the Test Floor Central Monitoring System   | Contractor  |
| MTT/STALSS/032/C               | LSS standard cleaning  | Contractor  |
| YTE/PI/CLD/0110                | Cleaning procedure for mechanical h/w to be used in clean room areas | MTE         |
| YTO/OPE/ALL/0792               | Procedure for the Test Floor Cleanliness survey                      | Contractor  |

# A HIGH ALTITUDE SPACE SIMULATION FACILITY TO STUDY EXHAUST PLUME INTERACTIONS AND CONTAMINATION

Andrew D. Ketsdever  
Air Force Research Laboratory  
Propulsion Directorate

Fred M. Lutfy, Stephen E. Vargo and E.P. Muntz  
University of Southern California  
Department of Aerospace Engineering

## ABSTRACT

Interest in realistic simulation of the space environment as applied to the study of spacecraft contamination and thruster plumes has led to the development of the CHAFF-4 facility. CHAFF-4 uses a multi-fin cryogenically cooled array (~20K) that completely envelops the interior of the chamber providing an available condensing surface area of 590 m<sup>2</sup>. The geometry of the array capitalizes on the fact that both neutral and ion species from spacecraft propulsion systems predominantly undergo diffuse reflections when impacting at angles normal to the surfaces they encounter. Preliminary figures of merit for the equivalent altitude possible for various propulsion systems vary between 150-350 km (depending on thruster type). The effective pumping speed is predicted to be between  $3 \times 10^7$  and  $1 \times 10^8$  liters/sec. The facility is expected to accommodate thruster power levels up to 3500 W without the use of supplementary liquid helium, although infrastructure permitting its use is available. Developmental considerations and design issues are discussed in view of basic principles of plume testing and contamination, in order to ensure the integrity of phenomena that are observed in the facility. Provisions for the simulation of high-speed LEO flow environments have been incorporated in the design, and the corresponding pumping requirements are well within the capabilities of CHAFF-4.

## INTRODUCTION

The interaction of spacecraft thruster plumes with a spacecraft and the ambient low-Earth orbit (LEO) environment is of interest to spacecraft mission planners for a wide variety of reasons. Although spacecraft propulsion systems are mission enabling, they can also be sources for particulate, molecular and radiation contamination on and near spacecraft surfaces [1,2]. In early 1995, the need for a national facility capable of performing meaningful LEO plume and contamination studies was identified by researchers at the University of Southern California and the Air Force Research Laboratory. One motivation was the present lack of a facility that could be used for ground-based studies of the many thruster interaction phenomena associated with the LEO high speed, rarefied flow environment. A second objective was to provide a facility that would be able to faithfully simulate the low pressures experienced by thrusters in space during operation. A matter of significance, particularly for electric thrusters such as Hall effect devices that operate based on a discharge directly exposed to the space environment. The same objectives are also of vital importance for meaningful contamination studies.

The complex interactions that propulsion systems encounter in space as well as the thruster's impact on satellite systems have brought about the need to test these devices in specially designed vacuum facilities. It is important to note

---

Support for this work was received from the Air Force Office of Scientific Research, the Army Research Office, and the University of Southern California. The authors would like to thank Dr. Keith Goodfellow for his advice and Robert Smith, Herb Llyod, Marc Young, Arthur Alves, Amanda Green, Matt Franklin and Mark Trojanowski for their efforts in helping construct this facility.

that there are few, if any, present-day vacuum facilities that were built with an infrastructure specifically tailored to address the concerns of contamination and plume diagnostic science. A notable historical exception was the JPL Molsink facility [3]. However, none of the current or past facilities provide a simulated LEO high-speed flow environment. More typical are vacuum vessels that maintain reasonable background pressures in order to allow the operation of various propulsion systems [4,5]. Such facilities are designed to determine operational constraints and parameters; however, they are not necessarily appropriate for detailed plume and contamination studies due to the relatively high background concentrations of propellant molecules.

Taking advantage of the relatively low operating costs of a university based facility, the David P. Weaver Collaborative High Altitude Flow Facility (CHAFF) was conceived as a place where synergistic government, university and industry research and preliminary development activities could be nurtured. The CHAFF is actually a complex of four high-altitude flow facilities as shown in Fig. 1. CHAFF-1 is a cryogenically pumped small plume and molecular beam facility. CHAFF-2 is for the study of high-altitude liquid vaporization phenomena. CHAFF-3 is a micropropulsion test chamber. CHAFF-4 is the new contamination and plume diagnostics LEO flow simulator. The realization of the CHAFF concept and the operation of CHAFF-4 are imminent. This paper documents the design considerations and the unique capabilities of the new CHAFF-4 facility.

Unlike thruster lifetime test chambers, CHAFF-4 was designed from its inception as a state-of-the-art contamination and plume diagnostics facility, including the presence of a high-speed external LEO flow environment. CHAFF-4 will enable researchers to measure intrinsic contamination footprints for a wide variety of electric as well as modest chemical thrusters (up to 5 g/sec flow rate). In addition, detailed and accurate near plume characterizations will be possible for the same variety of propulsion systems. Achieving the design conditions for CHAFF-4 is possible since the flux of reflected and sputtered material infiltrating the volume(s) of interest is drastically reduced. This was accomplished by developing a cryogenic array pumping system, which condenses thruster efflux by enhancing the probability of multiple interactions with cold surfaces (77 and 20 K) before most species can scatter back into the chamber interior.

The low background concentration of propellant fragments and the external high-speed flow capability make CHAFF-4 a unique facility. It is clear that one such facility is worth constructing. It will not be clear until spacecraft propulsion research results from CHAFF-4 are available whether or not there is a need for more than one such facility. It is for this reason that the original CHAFF concept was to make CHAFF-4 available to the community of government, university and industry investigators.

## EXHAUST PLUME AND CONTAMINATION STUDIES

The design of CHAFF-4 is derived from a few basic criteria that are outlined in this section. A convenient framework for the discussion are the principles of the rarefaction of exhaust plume interaction with background gases which were formulated by Muntz et al [6]. The thruster exhaust has two characteristic lengths, the mean free path  $\lambda_j$  of the exhaust gases in the background gas and the distance from the thruster,  $r_p$ , that is essentially free from the penetration of background gas into the exhaust gas plume. These characteristic lengths are most conveniently defined along the centerline of the exhaust plume. Exhaust plumes universally appear to be radial expansions from a source near the thruster exit (providing the observation is made at greater than say 10 diameters from the exit).

The characteristic plume dimensions  $\lambda_j$  and  $r_p$  are measured from the source and have the form

$$r_p = K_1 \frac{T_h}{V_{ex}^2} \quad (1)$$

$$\lambda_j = \frac{1}{\sqrt{2} \Omega_{jB} n_A} \quad (2)$$

where for SI units  $K_1$  is a constant of order  $10^7$ ,  $n_A$  is the atmospheric or background number density,  $\Omega_{jB}$  is the momentum transfer collision cross-section between the exhaust gas species and the atmosphere or background species,  $T_b$  is the propulsion system's thrust level in Newtons, and  $V_{EX}$  is the propellant's exhaust speed. Generally  $\lambda_j > \lambda_A$  primarily because  $\Omega_{jB} < \Omega_A$  where  $\lambda_A$  and  $\Omega_A$  refer to the atmosphere's mean free path and its average collision cross-section.

A plume Knudsen number can characterize the rarefied interaction between exhaust gases and the atmosphere which takes the form  $Kn_p = \lambda_j / r_p$ . If  $Kn_p \gg 1$ , the interactions can be considered as two separable molecular scattering events [6]. One is the effective stopping of the exhaust gases relative to the atmosphere in a distance  $\lambda_j$  and the other is the diffusive penetration of the atmospheric gases into the plume to a distance  $r_p$ .

It is instructive to cast the description of exhaust plume interactions outlined above into the framework of ground based thruster and plume investigations. Consider the atmospheric mean free path  $\lambda_A$ ; by 150 km, it is equivalent to the dimensions of any reasonable ground based facility. Since  $\lambda_j \geq \lambda_A$  for practically all circumstances of any significance, it is clear that full scale thruster investigations relating to complete plume-background interactions are not possible. However, providing  $r_p \ll \lambda_j$  as is the case for small nozzle thrusters or for electric thrusters, significant studies can be made of the near plume region (close to the thruster in analogy to the near wake region of re-entry vehicles). This is of course assuming that the thruster is not creating its own background gas in the facility. Thus, an initial requirement is that the facility provides an inner envelope that efficiently suppresses the reflection of thruster exhaust gases so that the large majority of background gas in the facility can be injected separately and be characteristic of the upper atmosphere, not products of the thruster exhaust gases. To accomplish this, the entire inner surface of the facility is designed as a pumping surface.

It is perhaps worthwhile to point out that for studying the basic operation of nozzle thrusters the penetration of background gas into the plume is in all cases far downstream of the thruster in terms of exit diameter ( $D_0$ ). That is  $r_p \gg D_0$  because of the necessity for maintaining continuum flow conditions in the nozzle expansion. As a consequence the background pressure and composition for studying nozzle thruster operating characteristics is not particularly critical.

For ion electric thrusters there is an entirely different situation. Note from Eq (1) that for a fixed thrust it is not surprising that the background gases are basically free to penetrate to the thruster exit in these devices. Thus, investigation of ion electric thruster operations in a facility is potentially more sensitive to facility induced background conditions. In fact such effects may be very subtle since the species (for example Xe) generated by the thruster in the facility is the same as the propellant. Consequently the effects of the background may be hard to discern.

For contamination studies, there are two important effects which must be minimize. First, it is important to minimize the effects of propellant gas reflections with chamber surfaces particularly in the backflow regions. Experimental results in this region can be dominated by propellant molecules which enter this region due to collisions with the chamber walls. Second, the effects of propellant molecules scattering from background gases must be negligible. This can only be accomplished by maintaining very low background pressures in the facility. Again to minimize these effects, the entire inner surface of the facility is designed as a pumping surface not only for increased pumping area but also to minimize surface scattering.

## HIGH ALTITUDE BACKGROUND DENSITY CONSIDERATIONS

For the study of spacecraft propulsion systems in a ground-based facility there are three basic propellant populations that need to be addressed;

- energetic ions (100 to 3000 eV) from Hall effect and conventional ion thrusters along with a smaller number of very fast neutrals resulting from charge exchange,
- cold neutrals from the unionized component of ion thrusters (up to 50% of mass flow) as well as from cold or resistojet thrusters,

- fast neutrals (~1 eV) from chemical or arc discharge thrusters.

One objective of the CHAFF-4 design effort was to achieve an extremely small background concentration of propellant gas. Consider the characteristics of a typical thruster test facility with an internal surface area that has some relatively modest fraction ( $f_p$ ) occupied by pump inlets or pumping surface. The exhaust mass flow of a thruster system is generally stopped and randomized by the facility's surfaces. The random motion of the scattered propellant molecules drives them into the pump inlets. The background number density of propellant  $n_{B,pr}$  can be calculated by the following expression

$$n_{B,pr} = \frac{\dot{M}_{EX} \left( \frac{T_p}{T_B} \right)^{\frac{1}{2}}}{\left[ \frac{m_{pr}}{4} \left( \frac{8kT_p}{\pi m_{pr}} \right)^{\frac{1}{2}} f_p A_s \right]} \quad (3)$$

where  $m_{pr}$  and  $T_p$  are the mass of the propellant molecule and the temperature of the propellant gas as it is driven to the pumping surface, respectively (for cryosorption pumps this is about 80 K).  $T_B$  is the background gas temperature and  $A_s$  is the chamber's surface area.

As one example, Randolph et al [7] suggest that for studies of stationary plasma thrusters reliable results can be obtained for  $n_b \leq 1.6 \times 10^{18} \text{ m}^{-3}$ . For near plume investigations they suggest  $n_b \leq 4 \times 10^{17} \text{ m}^{-3}$ . For other types of thrusters different criteria will apply. Clearly a critical point, at least for plume studies, is reached when the background mean free path  $\lambda_b \leq l_r$ , where  $l_r$  is the largest internal dimension of the facility.

For reasons such as investigations of back flow contamination, the effects of high-speed ambient flows on contamination, near plume characteristics, and thruster performance with flowing atmospheric species as the predominant background gas, it is important to maintain a very low propellant background gas concentrations relative to the ambient atmosphere. The task of simulating the atmospheric background gas for various altitudes is outlined in Table 1. Using propulsion system with a xenon mass flow of  $5 \times 10^{-6} \text{ kg/s}$ ,  $n_{B,pr}$  is calculated and compared to the ambient number density ( $n_a$ ) for the TRW (moderate size) [4], Hughes (large) [8], and CHAFF-4 [9] facilities as examples of state-of-the-art test chambers.

Table 1: Parameters of interest for state-of-the-art electric thruster test facilities.

| h<br>(km) | $n_a$<br>( $\text{m}^{-3}$ ) | $n_{B,pr}$ ( $\text{m}^{-3}$ ) |                      | $n_{B,pr}$ ( $\text{m}^{-3}$ ) |
|-----------|------------------------------|--------------------------------|----------------------|--------------------------------|
|           |                              | TRW                            | Hughes               |                                |
| 150       | $1 \times 10^{17}$           | $1.7 \times 10^{17}$           | $1.7 \times 10^{16}$ | $4 \times 10^{15}$             |
| 200       | $1 \times 10^{16}$           | $1.7 \times 10^{17}$           | $1.7 \times 10^{16}$ | $4 \times 10^{15}$             |
| 300       | $1 \times 10^{15}$           | $1.7 \times 10^{17}$           | $1.7 \times 10^{16}$ | $4 \times 10^{15}$             |

Note in Table 1 that the  $n_{B,pr}$  is equal to  $n_a$  at 200 km and is 17 times  $n_a$  at 300 km for the Hughes facility. In order to simulate the ambient atmosphere at 200 and 300 km (both operational satellite altitudes) in the Hughes facility, it would be necessary to increase the effective pumping speed by at least a factor of 10 and preferably by  $10^2$ , a rather substantial task.

The design of CHAFF-4 is an attempt to take a new approach to this problem. Consider the sketches in Figs. 2 and 3 that show schematics of the CHAFF-4 pumping system. The cut-out in Fig. 2 illustrates a cross section of the finned cryopanel, which are held at 20 K. A test thruster operates on the facility centerline producing radial flow that is nearly tangent to the radially arrayed fins. Both high-speed ions and the much slower neutrals impact the graphite surfaces on the LN<sub>2</sub> shield, the He coolant supply tubes, and the fin edges. Ions from electric propulsion plumes embed themselves in the graphite ejecting a carbon atom with a probability of about 0.03 [9]. The neutrals partially accommodate to the graphite surface and for the most part stick to the walls of the finned helium-cooled array. Some escape without cryosorbing and return to the interior of the facility as background gas. There is scattering from the finite thickness of the fins, which also returns a flux of propellant molecules to the chamber interior as background gas. Since the mean free path is large, these background gas molecules travel to some other portion of the pumping surface and condense. It is only those molecules that have a direction close to the normal of the two carbon coated surfaces that appear near the thruster as  $n_{B,p}$ .

## ATMOSPHERIC SIMULATION REQUIREMENTS

The interactions between spacecraft thruster plumes and the ambient environment have been of interest to many communities for the past several years. The CHAFF-4 provides an opportunity to simulate a variety of on-orbit phenomenon relating to thruster operation. Applications to material degradation, spacecraft contamination, gas-surface interactions and, in particular, atmospheric plume interactions (plume signatures) are all of interest. Of particular interest in low-Earth orbit (LEO) is the interaction of thruster plume species with atomic oxygen (AO) [10] and solar ultraviolet radiation (SUV). Ion electric thruster plume interactions with the ambient plasma environment have also been of interest recently [11]. The injection of background or simulated atmospheric species in CHAFF-4 can not be done efficiently by simply leaking a gas into the facility since it will be pumped very effectively by the cryogenic system. The injection into the facility can be accomplished by using a variant of a continuum source molecular beam. The continuum source creates a hypersonic beam of molecules from a differentially pumped, doubly skimmed free jet, nozzle, or ion source expansion (Fig. 3). The expansion can be generated by a variety of techniques that have been used for the production of energetic AO and ion beams as discussed in the following sections.

### The Simulation of Atmospheric AO

Atomic oxygen is the predominant species in LEO between 180 and 650 km altitude. AO primarily in the ground (<sup>3</sup>P) state, results from the photodissociation of molecular oxygen by SUV radiation. With typical number densities of  $10^9 \text{ cm}^{-3}$ , the flux of AO to surfaces normal to the satellite ram direction is approximately  $10^{15} \text{ cm}^{-2} \text{ sec}^{-1}$ . In the thermosphere (>80 km), AO is present at nearly thermal energies (~0.01 eV); however, the relative kinetic energy encountered during collisions with LEO spacecraft (traveling at 8 km/sec) is about 5 eV. Therefore, AO interactions with thruster plumes generally fall into three categories:

- (1) AO interactions with low energy (<10 eV), retro-fire plume species
- (2) AO interactions with high energy (>10 eV), retro-fire plume species
- (3) AO interactions with plume species of any energy in the anti-ram direction

For low energy, retro-fire plume studies, the energy of the atmospheric species (in this case AO) must be faithfully reproduced for accurate analysis. In this case, the AO energy of 5 eV becomes a significant fraction of the overall relative velocity of the collisional system, which tends to drive the chemical kinetic mechanisms. Chemical and electrothermal thrusters generate low energy plume species. However, the neutral species of a typical ion thruster are also at low energy. AO sources that can produce energies approaching 5 eV with adequate flux levels are generally complex and expensive systems [12,13].

For high energy, retro-fire or anti-ram plume studies, the energy of the atmospheric species is either unimportant (compared to the incident plume energy) or can be accurately simulated using thermal AO. This greatly simplifies the AO production scheme since energetic AO is not required; however, accurate simulation of anticipated flux levels is still important for studies trying to identify appropriate chemical kinetic mechanisms. Relatively simple microwave discharge production of AO can be used which provides thermal energies at appropriate flux levels [14].

An ideal AO source for plume related studies would be a tuneable energy, tuneable flux source like those initially investigated by Banks et al and his group at NASA Lewis Research Center and Ketsdever et al., [15,16]. Although the investigations into these systems were limited in scope, they showed the potential for tuneable energy atomic beams produced by energy selected, charge exchanged ions. With these systems, collisional energy dependent studies would be possible regardless of the thruster configuration or operating direction. Note that the anticipated mass flows associated with the use of high-speed atmospheric simulations are well within the pumping capabilities of CHAFF-4 (Table 1).

### **The Simulation of Ambient Plasma Constituents**

The simulation of the ambient plasma environment is accomplished using an ion source that operates on nearly any gas. The ions are produced using a microwave discharge and accelerated to the appropriate energy through electrostatic grids. Electrons can be added downstream of the ion acceleration to charge neutralize the plasma. The ion source is capable of energies ranging from 20 eV to 5 keV. Fluxes on the order of  $10^{15} \text{ cm}^{-2} \text{ sec}^{-1}$  are possible for nitrogen, oxygen and hydrogen discharge gases. Since the source operates on molecular gases such as  $\text{N}_2$ ,  $\text{O}_2$ , and  $\text{H}_2$ , the desired ion (either molecular or atomic) can be mass selected prior to introduction into the main facility.

## **CHAFF-4 CHAMBER DESIGN**

### **Summary of Design Objectives for CHAFF-4**

The following is both a summary and overview of the necessary operational parameters that need to be considered before a successful contamination and plume facility can be built. Such a facility should feature the elimination of backscattered molecules in the plume and backflow regions due to sputtering and reflection processes. It should be relatively straightforward to secure a specific thruster and associated optical diagnostics package. Additional access for non-intrusive diagnostic techniques is a design criterion that both maximizes flexibility and addresses unforeseen future needs. The facility must be relatively user friendly and cost effective. The CHAFF-4 design effort used the following specifications and constraints to satisfy the conditions detailed above:

- Minimize diagnostic complications from sputtered/reflected products to a level  $\ll 1\%$  of natural plume and backflow number densities by using a series of unique cryogenically cooled panels as well as careful material selection
- Actuation mechanism that is both precise and accurate on which a thruster and associated optical diagnostics package can be secured (sting)
- 3-axis non-intrusive optical imaging capability which can be adjusted during a test run
- Incorporate multiple optical ports of various sizes for diagnostics studies; laser-induced fluorescence (LIF), electron-beam fluorescence (EBF), quartz crystal microbalances (QCM), etc.
- Enhance quick turn-arounds to maximize efficient use of time
- Introduce O-atom, plasma and SUV generators to simulate LEO environment

### **CHAFF-4 Dimensions**

Since electric propulsion systems produce non-trivial ionization levels with associated energies of 100-1000+ eV, a chamber design must minimize complications due to fast-ion and neutral species. Ions impact surfaces and cause sputtered products to be released [7, 17, 18]. If it were technically feasible to have all propellant products condense on the first surface encountered, a plume facility would only need to be large enough to minimize stray electric field complications as well as allow for undisturbed plume and backflow regions in which to conduct studies. However, despite the use of extensive cryogenic panel systems, there is always a finite possibility that secondary products infiltrate the thruster's environment. Given the physical limit of any cryogenic array subjected to energetic ion bombardment, perhaps the simplest

way to help maintain the integrity of the regions of interest is to make the vacuum facility significantly larger than the thruster under study. CHAFF-4 is 6.1 m long with a 3 m diameter as shown in Fig. 4. Compared to existing thrusters, which can have exit diameters ( $D_e$ ) that are roughly a few tens of cm, CHAFF-4's dimensions dominate the relatively small propulsion systems. The closest distance that a thruster would be from the target wall is 3.5 m. Assuming a thruster diameter of 30 cm, the latter would have a maximum solid angle to the target wall that is roughly 0.023 sr. Consequently, there is only about a 1 in 300 chance that a backscattered molecule would find its way to the thruster's vicinity, assuming it managed to escape the cryogenic temperatures of the shield surfaces.

### Chamber Design

In comparison to other thruster evaluation chambers the CHAFF-4 is a moderate size facility. Figs. 3 and 4 show an outline of the CHAFF-4 chamber. On the back door, two 1.0 m diffusion pumps have been placed to remove incondensable gases from the facility (typically He and H<sub>2</sub>). An adjustable thruster support, which is referred to as the sting, is placed in the center of the casted door. The sting allows longitudinal movements of mounted thrusters and also carries a stepper motor optical system. Optical access to the interior of the chamber is made with several large (25 cm diameter), medium (10 cm) and small (7 cm) viewports. The number and location of these viewports have been selected to provide reasonable diagnostic flexibility. Two viewing stations were placed at one-third and two-third chamber length locations to provide for diagnostic measurements of thruster plumes in the chamber. Each station has three orthogonally placed 10 cm optical ports on the chamber. In addition to the 10 cm ports, each station has four 7 cm ports that are placed between the orthogonal ports. Quartz and Pyrex glass windows are used in these locations depending on the optical needs. Various vacuum, temperature, high-power, liquid and cryogenic feedthroughs are in place. The associated data acquisition/monitoring systems are implemented using two dedicated computers that are housed in a control room next to CHAFF-4. System monitoring areas will include panel temperatures, LHe/LN<sub>2</sub> levels, cryostat operation, chamber pressure and roughing pump status. Power failures and other complications that compromise the safe and efficient operation of CHAFF-4 will initiate automated shutdown procedures.

### Pumping System Design

#### Zyrianka 900 Diffusion Pumps

Conventional pumps are necessary to remove incondensable gases such as hydrogen and helium that the cryogenic pumping scheme discussed in the following sections can not pump from the system. Hydrogen and helium are present in the facility from normal atmospheric partial pressures but they can also be introduced as propellants in resistojet or arcjet studies or as atmospheric species. For this reason, the CHAFF-4 facility is conventionally pumped by two Zyrianka 900 diffusion pumps of Russian manufacture shown in Fig. 5. The general dimensions and operating characteristics of the Zyrianka 900 are given in Table 2. Diffusion pumps were chosen to conventionally pump the facility due to the high pumping speeds achievable and low cost per pumped volume. The major disadvantage to using oil diffusion pumps is the potential for chamber contamination from backstreamed pumping fluid.

Turbomolecular pumps, although capable of equivalent pumping speeds of molecular hydrogen and nitrogen, are extremely expensive when compared on a cost per pumping speed level. Oil cooled bearings on turbomolecular pumps can also be a source of oil contamination in the chamber although at relatively low levels as compared with diffusion pumps. Although cryosorption pumps are about half as expensive per pumping speed as turbomolecular pumps, they also have their limitations. Cryosorption pumps can not pump large flow rates of hydrogen and helium for extended periods of time without regenerative procedures.

However, the major feature of the Zyrianka 900 diffusion pump is the pumping fluid backstreaming rate of approximately 24 mg/hr over the inlet diameter. This is nearly an order of magnitude lower backstreaming rate than diffusion pumps of similar size manufactured elsewhere. Although testing is still on going with these pumps, it is conceivable that the pumps can be operated without the use of large cold traps, which are expensive and restrict pumping. The Institute of Thermophysics of the Russian Academy of Sciences has developed the Zyrianka series of pumps by optimizing the interactions of the oil vapor jets with the jet assembly and the pump condensing walls to minimize the backstreaming of the pumping fluid [19, 20]. As can be seen by point 9 in Fig. 5, the oil vapor ring jet from the first stage

is pointed toward the pump axis. The effect of this first stage jet configuration is to make the cooled outer casing an effective trap of the backstreaming oil vapor flow even at large expansion angles. A small water cooled trap is located on top of the ring jet staging to further reduce any oil backstreamed into the facility.

Table 2: Technical specifications of the Zyrianka 900 diffusion pump.

|                                     |  |
|-------------------------------------|--|
| Inlet Diameter (mm)                 | 932                                      |
| Height (mm)                         | 1360                                     |
| Pumping Speed (l/sec)               | Air 25000<br>Helium 42000                |
| Normal Operating Range (Torr)       | 5 x 10 <sup>-4</sup> to 10 <sup>-8</sup> |
| Pumping Fluid Backstreaming (mg/hr) | 24                                       |
| Warm-up Time (min)                  | 15                                       |
| Cooldown Time, Normal (min)         | 30                                       |
| Cooldown Time, Express (min)        | 3  |
| Operating Power (Watts)             | 14,000                                   |
| Water Cooling (l/hr)                | 600                                      |
| Weight (kg)                         | 260                                      |
| Lifetime to Major Service (hr)      | 20,000                                   |

#### Cryogenic Pumping

Another integral component of CHAFF-4's unique pumping scheme is a closed-loop gaseous helium refrigeration system. This system, which is referred to as the cryostat, provides a cryogenic source (20 K) for the inner CHAFF pumping surfaces. The cryostat is a refurbished 1950's refrigeration system that was originally designed for the transport of liquid hydrogen by Arthur D. Little, Inc. and Cambridge Corp. [21]. The cryostat is designed to maintain gaseous helium at 20K while handling a heat load of approximately 200W. The ability to operate CHAFF-4 using only liquid nitrogen and the cryostat provides a cost-effective means for the evaluation of low-power thrusters without the added cost of liquid helium. Fig. 6 shows the heat load curve for the cryostat at various shield temperatures. This curve represents a conservative estimate of the expected capability (75%). CHAFF-4's inner shield also incorporates a dedicated cryogenic system for liquid helium. This feature gives added flexibility for those occasions where greater heat loading and/or lower pumping temperatures are required.

#### Discussion of Finned Array Design

Although maximizing chamber size is the simplest way to help avoid the adverse impact reflected and sputtered species may have on the thruster's plume or backflow characteristics, more sophisticated design issues were considered with special attention given to a cryogenic finned array design and material selection. It is relevant to make some fundamental observations about the manner of pumping utilized in CHAFF-4. Conventional pumping systems making no use of cryogenic schemes have a fundamental pumping speed limit that can be approximated by

$$C = 12.1 \frac{D^3}{L} \quad (4)$$

where D and L are the tube diameter and length respectively expressed in cm and C is the conductance in liters/s. Eq. (4) is representative of molecules undergoing diffuse reflections with the walls of the pumping system in a free-molecular regime. The molecules consequently exit the volume when they encounter the pump inlet. It is important to note that Eq. (4) does not apply for the cryogenic system used in the CHAFF-4 facility. For instance, assume that all molecules emanating from a source within a vacuum facility condense on a cryogenic surface when it is first encountered. The effective pumping speed for such a system would essentially be limited only by the flow rate of the source (forgetting any heat load related surface temperature increase) and is independent of the classic concept of chamber conductance.

CHAFF-4 makes use of strategically oriented cryogenic fins that maximize the collision opportunities between propellant efflux and the cooling array. The geometry outlining the dynamics of this pumping system is shown in Fig. 7. The cryogenic array shown in Figs. 2 and 3 takes advantage of the fact that thermal neutral atoms and molecules undergo predominantly diffuse reflections with CHAFF-4 cryogenic surfaces. In the case of the significantly faster ions, the objective is to allow them to penetrate a surface (graphite) that minimizes sputtering and allows conduction of the deposited heat load.

For the cryogenic system used in CHAFF-4, the pumping speed is a parameter that stems from the unique geometry that emphasizes atom/cryogenic array collisions. The effective pumping speed of CHAFF-4 is fundamentally related to the available cryogenic fin area that is exposed to the plume species. Elevated pumping speeds equate to lower background densities and higher equivalent orbital altitudes. The following expression can be used to estimate the background number density in CHAFF-4

$$n_{\min} = 6.022 \times 10^{23} \frac{\dot{M}}{mA_p} \left[ \frac{\alpha}{\bar{V}_{\text{ion}}} + \frac{(1-\alpha)}{\bar{V}_{\text{neutral}}} \right] \quad (5)$$

where  $\dot{M}$  is the mass flow,  $m$  is molecular weight,  $\bar{V}$  is the representative speed of a particular specie impacting into a cryogenic surface,  $\alpha$  is the ionization fraction of propellant atoms and  $A_p$  is the effective cryogenic pumping area. Figures 8 and 9 represent anticipated simulation altitudes for various effective pumping area and ionization fractions respectively. The equivalent pumping speed for CHAFF-4 varies between  $3 \times 10^7$  and  $1 \times 10^8$  liters/s depending on effective propellant speed and exposed pumping area.

#### Description of cryogenic panel system

Cryogenic facilities have historically been constructed with the maximum pumping area that could be reasonably incorporated [22]. Although available pumping area is also a concern for CHAFF-4, the critical issue for a plume and contamination facility is minimizing sputtered and/or reflected products from the walls. Therefore, CHAFF-4's cryogenic shield arrays were designed to achieve both optimum pumping capability and, more importantly, reduce backscattered molecules to negligible levels.

CHAFF-4 has three aluminum cryogenic systems partitioned into four independent sections. Aluminum was chosen since the cost for using copper was roughly double. First, liquid nitrogen panels (LN<sub>2</sub>) thermally isolate the relatively hot chamber walls (300 K) from its interior (~20 K). The coverage of LN<sub>2</sub> shields will be significant (i.e. >99% of actual chamber wall area - Fig. 3). For a 72 m<sup>2</sup> LN<sub>2</sub> shields surface area and emissivity of 0.05 (polished aluminum), the associated heat load on the interior of the chamber due to the LN<sub>2</sub> shields is approximately 6 W. Second, the cryostat pumping facility will further reduce the interior shield temperature by flowing cooled gaseous helium through a series of tubes welded to the arrayed panels. This will enable a working temperature range between 20-35 K. The cryostat's heat load capacity is approximately 200 W at 20 K. This level of cryogenic cooling is more than adequate for ion engines and Hall-effect thrusters since the propellant of choice for these systems is xenon gas, which is very effectively pumped below -50 K [23,24]. However, in order to have the flexibility of testing the full range of thrusters (arcjets, resistojets and modest chemical types), a lower operating temperature needs to be possible for the inner-shield arrays. Consequently, there is an option to use liquid helium to reduce the cryogenic panel temperature (<10 K) to combat any complications that stem from elevated heat loading and/or pumping requirements. The liquid nitrogen shield system will take about 1 hour to cool down properly while the remaining cool down time from 77 K to ~20 K using the cryostat will take approximately 10-12 hours.

The shields are shown in various perspectives in Figs. 2 and 3. Using geometric considerations to minimize backscattered molecules was extremely important as shown in Fig. 7. By allowing most efflux atoms through to impact the liquid nitrogen panels, two important issues are addressed:

- First, the solid angle available to atoms sputtered and reflected to the interior of the chamber is greatly reduced. Consequently, a reflected/sputtered atom from the LN<sub>2</sub> shield has a high probability of interacting with another cold surface (25 K) before returning to the chamber's interior.

- Second, the liquid nitrogen panels effectively handle roughly 85% of the total heat load produced by thrusters, thereby allowing the cryostat's heat load capability to be used for pumping predominantly thermal atoms rather than wasting available power battling energetic species.

### Sting Design

It is anticipated that the elapsed time during which diagnostic data can be taken will typically extend for several hours. Therefore, it is important that flexibility be incorporated in CHAFF-4 to maximize data quality and quantity during limited operational test times. A hydraulically actuated sting, shown in Fig. 10, is incorporated in CHAFF-4 on which various thruster types can be secured. The sting allows longitudinal translations ( $\pm 1$  m) of the thruster with a projected accuracy of  $\pm 5$  mm. Three-dimensional optical diagnostic surveys are accomplished by utilizing a cryogenic temperature resistant stepper motor system attached to the sting. The latter will consist of one rotation and two translation axes ( $\pm 15$  cm). The flexibility of this system will greatly enhance scientific productivity during limited test times since a complete three-dimensional survey can be performed of the plume environment.

The sting arm itself will be shrouded in a liquid nitrogen cooled outer skin to minimize the adverse heat load on the inner cryogenic shield system. The shroud system will also allow for the radiative isolation of the rear and side quadrants of various thrusters further reducing adverse heating of the helium-cooled inner-shield system. The thruster shroud would be an option for research objectives that are not concerned about the backflow region.

Various feedthroughs designed for fiber optics,  $LN_2$ , power and gas requirements are incorporated at the end flanges of the sting. The respective cabling/tubing is positioned inside the sting with enough yield outside to allow uninterrupted service as the sting is actuated during a test. Finally, there is a contingency for floating the thruster potential relative ground to investigate the effect of spacecraft charging on operating and plume characteristics.

### CONCLUSIONS

Design objectives for the CHAFF-4 contamination and plume diagnostic facility have been outlined. The need to perform plume studies and obtain contamination footprints drove CHAFF-4 designers to pursue a different approach with respect to cryogenic pumping than is traditionally used. Development of an extensive multi-finned cryogenic shield system ( $590$  m<sup>2</sup> maintained between 20-35 K) results in significantly lower background densities than is typically found in facilities of this kind (with lower limits between  $5 \times 10^{14}$  and  $4 \times 10^{15}$  m<sup>-3</sup>). Equivalent test altitudes ranging between 150-350 km are possible depending on thruster operational specifications. The associated pumping speed is driven by the cryo-cooled surface area that interacts with propellant species and varies, depending on thruster type, between  $3 \times 10^7$  and  $1 \times 10^8$  liters/sec. The facility is cooled by a cryostat system that enables the testing of a range of thrusters, up to a power level of approximately 3500 W, without resorting to supplementary liquid helium. In addition, it is possible to introduce liquid helium for those occasions when it is warranted. An analysis to protect the facility against ion-driven sputtering erosion resulted in the use of strategically positioned graphite layers.

It will be necessary in the near future to perform detailed shakedown and performance tests to establish the actual operation envelope of CHAFF-4 and to validate the design principles. Finally, the greater goal for the Collaborative High-Altitude Flow Facility is to develop a detailed understanding of the complications and/or advantages inherently found in this type of facility, and to bring about more effective strategies for investigating space propulsion systems.

## REFERENCES

1. Boyd, I., Kannenberg, K., Kossi, K., Levin, D., and Weaver, D., "Modeling the plume contamination and emissions of an ammonia arcjet," AIAA paper 98-3505, Cleveland, OH, July 1998.
2. Ivanov, M., Markelov, G., Gimelshein, S., "Statistical simulation of reactive rarefied flows: numerical approach and applications," AIAA paper 98-2669, Albuquerque, NM, June 1998.
3. Stephens, J. P., "Space molecular sink simulator facility design", JPL Technical Report No. 32-901, March 1966.
4. McLean, C. H., Lesky, O., "Development of a helium cryopumped facility to evaluate Hall Effect Thrusters", IEPC-97-135, 25th International Electric Propulsion Conference, Cleveland, OH, August 1997.
5. Simpson, H.B., Wallace, N.C., "The lifetest of UK-10 ion thruster cathodes and neutralizers: implications for facility design", ESA SP-398, Aug., 1997.
6. Muntz, E.P., Hamel, B.B., Maguire, B.L., "Some characteristics of exhaust plume rarefaction", AIAA Journal, 8 (9), pp. 1651-1658, 1970.
7. Randolph, T., Day, M., Kim, V., Kaufman, H., Zhurin, V., Kozubsky, K., "Facility effects on SPT thruster testing", IEPC-93-093, 23rd International Electric Propulsion Conference, Seattle, WA, September 1993.
8. Hughes, [http://www.hughespace.com/hsc\\_pressreleases/98\\_01\\_14\\_edd.html](http://www.hughespace.com/hsc_pressreleases/98_01_14_edd.html), 1998.
9. Lutfy, F., Vargo, S., Muntz, E.P., Ketsdever, A., "The David P. Weaver Collaborative High Altitude Flow Facility's CHAFF-4 for studies of spacecraft propulsion plumes and contamination," AIAA paper 98-3654, Cleveland, OH, July 1998.
10. Vaghjiani, G., "Discharge flow-tube studies of O(3P)+N2H4 reaction", J. Chem. Phys., 104 (14), pp. 5479-5489, 1996.
11. Wang, J. and Brophy, J., "3-D Monte-Carlo Particle-in-Cell simulations of ion thruster plasma interactions", AIAA 95-2826, San Diego, CA, July 1995.
12. Caledonia, G., Krech, R., and Green, B., "A high flux source of energetic oxygen atoms for material degradation studies", AIAA Journal, 25 (1), pp. 59-63, 1987.
13. Orient, O., Chutjian, A., Murad, E., "Recombination reactions of 5-eV O(3P) atoms on a MgF2 surface", Phys. Rev. A, 41 (7), pp. 4106-4108, 1990.
14. Van Zyl, B., Gealy, M., "New molecular-dissociation furnace for H and O atom sources", Rev. Sci. Instrum., 57 (3), pp. 359-364, 1986.
15. Ketsdever, A., "The production of energetic atomic beams via charge exchange for the simulation of the low-Earth orbit environment", Ph.D. Dissertation, University of Southern California, 1995.
16. Ketsdever, A., Weaver, D., Muntz, E.P., "A facility to produce an energetic, ground state atomic oxygen beam for the simulation of the low-Earth orbit environment", NASA Conference Publication 3280, pp. 121-138, 1994.
17. Garner, Charles E., Brophy, John R., Pless, L.C., Barnett, John W., "The effect of nitrogen on xenon ion engine erosion", AIAA 90-2591, Orlando, Florida, 1990.
18. Sovey, J. S., Patterson, M. J., "Ion beam sputtering in electric propulsion facilities", AIAA-91-2177, Sacramento, CA, 1991.

19. Rebrov, A.K., "Gasdynamic and thermophysical optimization of the jet vacuum pumps", *Vuoto*, 20 (2), pp. 288-293, 1990.
20. Iliasova, N., Nedosekova, S., Rebrov, A., Skovorodko, P., and Roig, J., "Computational optimization of diffusion pump parameters", *Vacuum*, 55 (5-7), pp. 745-747, 1993.
21. Cambridge, Operating Manual for Refrigerated Transport Dewar. Cambridge Corp., Sept. 1952.
22. Dettleff, G. and Plahn, K. "Initial experimental results from the new DLR-high vacuum plume test facility STG," AIAA 97-3297, 1997.
23. Lide, D. R., CRC Handbook of Chemistry and Physics, CRC Press, Boca Raton, Florida, 1992.
24. Garner, Charles E., Polk, James R., Brophy, John R., Goodfellow, Keith., "Methods for cryopumping xenon", AIAA 96-3206, 1996.

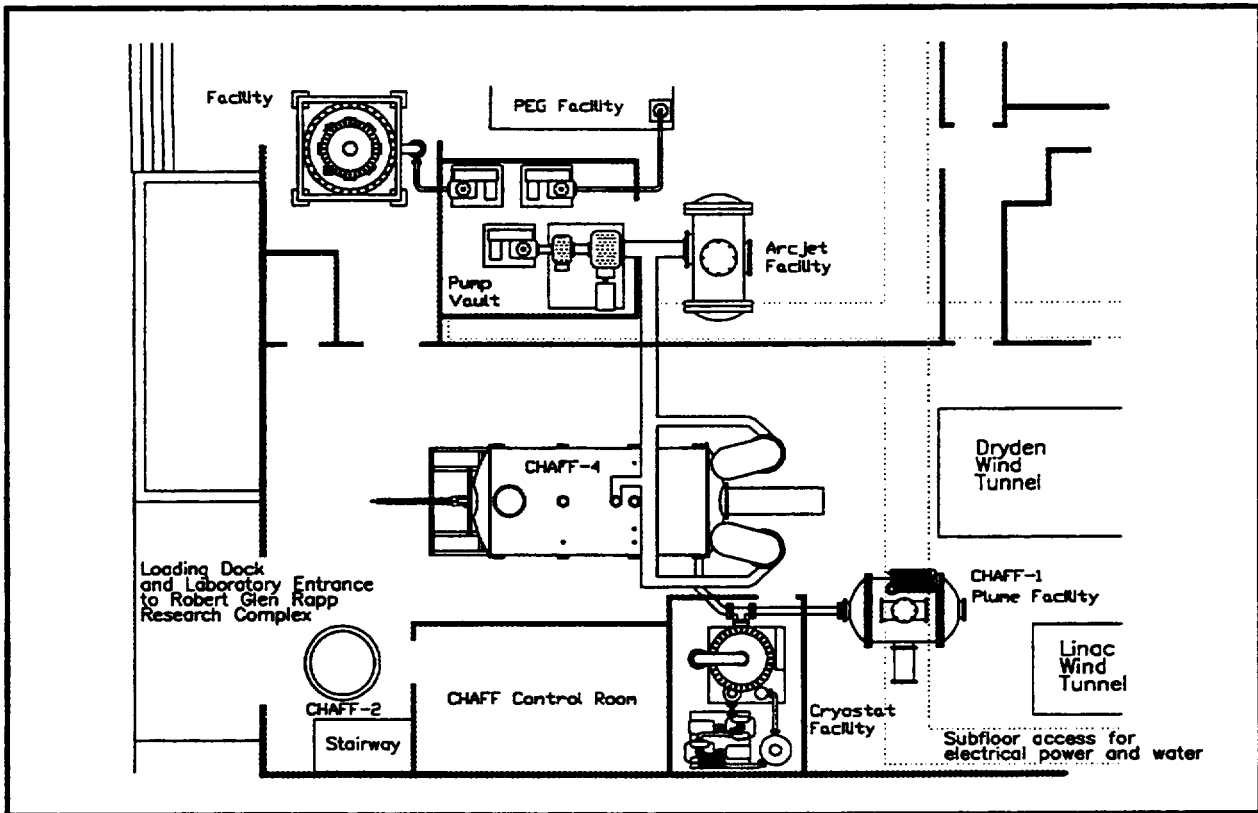


Figure 1: Layout of the David P. Weaver Collaborative High Altitude Flow Facility at USC.

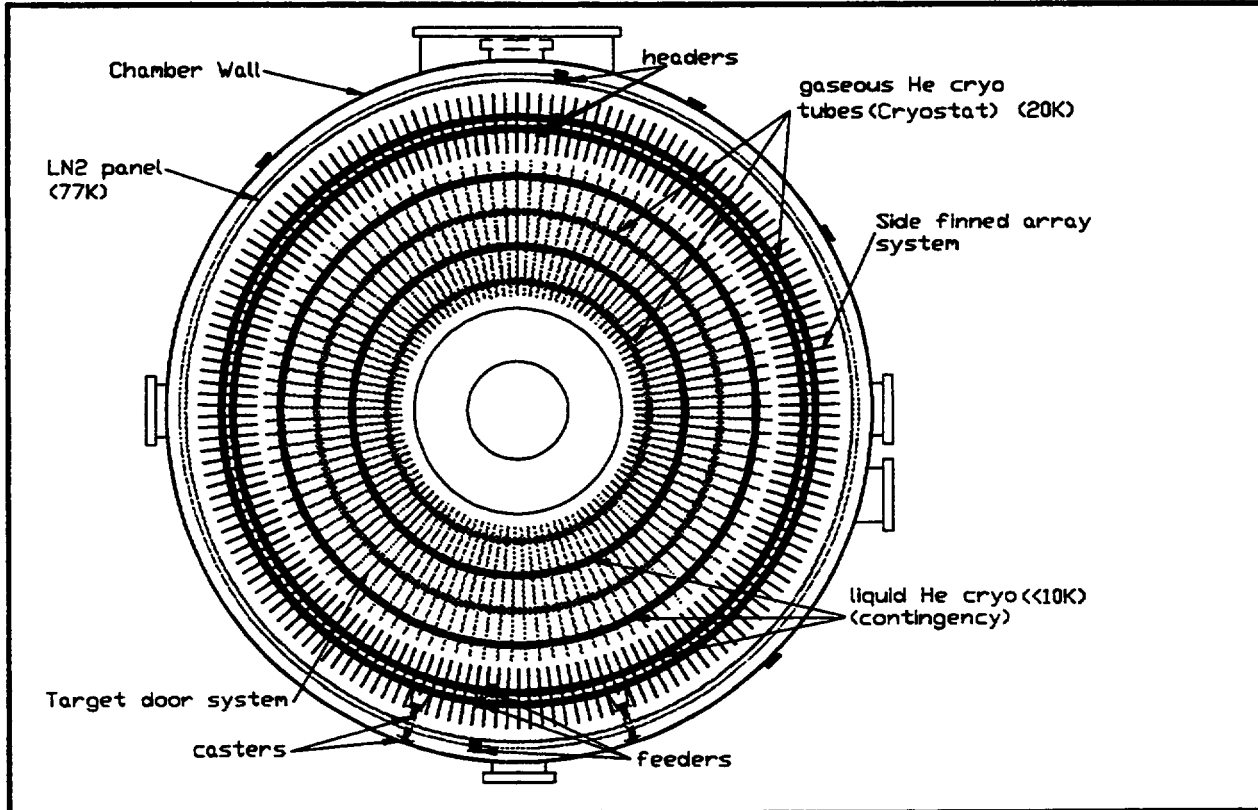


Figure 2: Front view of CHAFF-4 cryogenic array system.

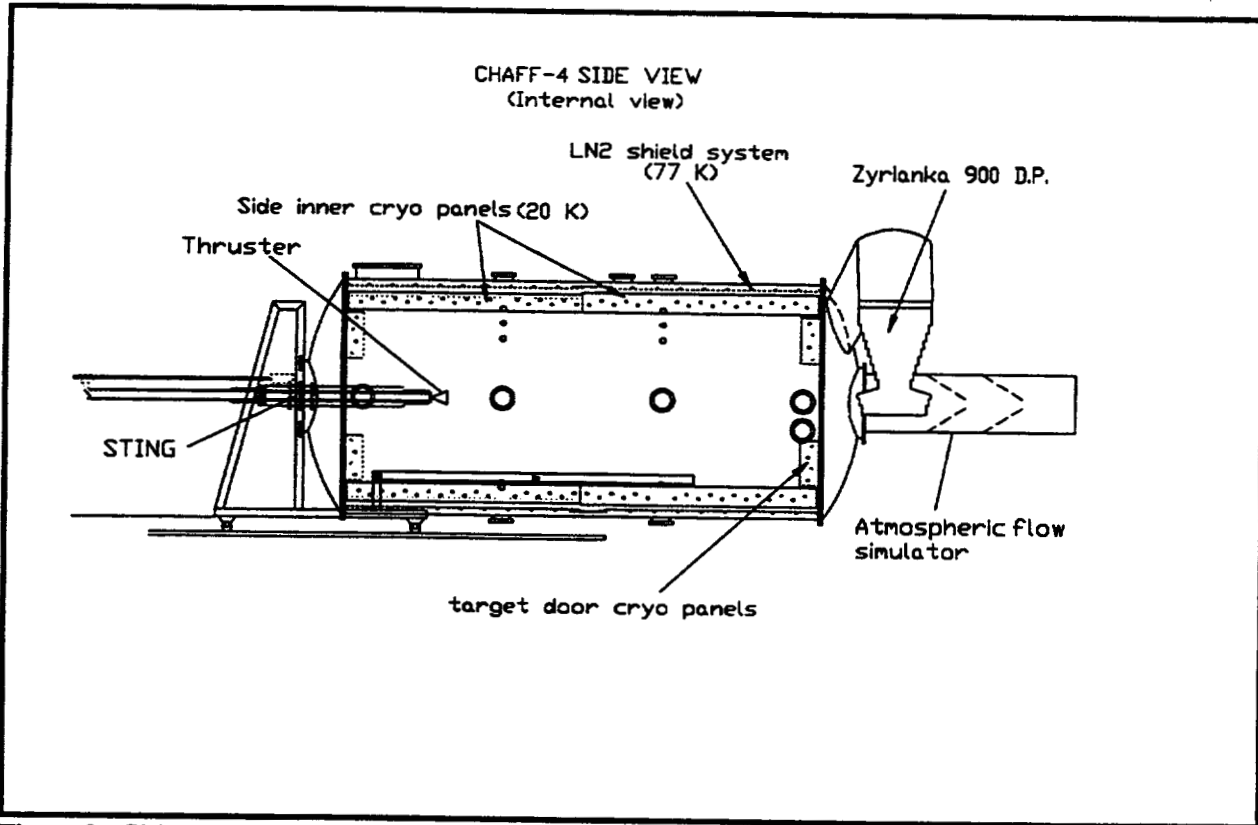


Figure 3: Side view of CHAFF-4 cryogenic system, STING apparatus and atmospheric flow simulator.

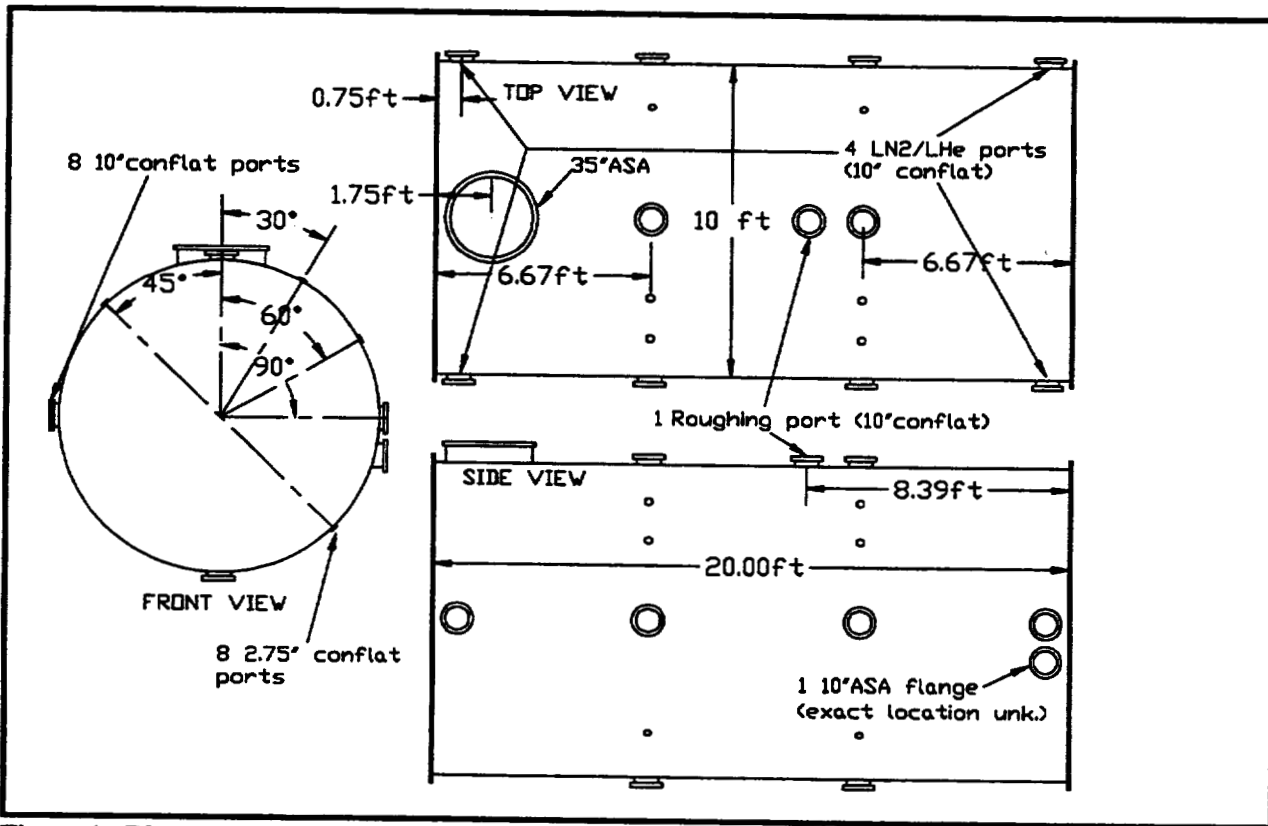


Figure 4: Blow up view of inner cryogenic shield geometry under ion bombardment.

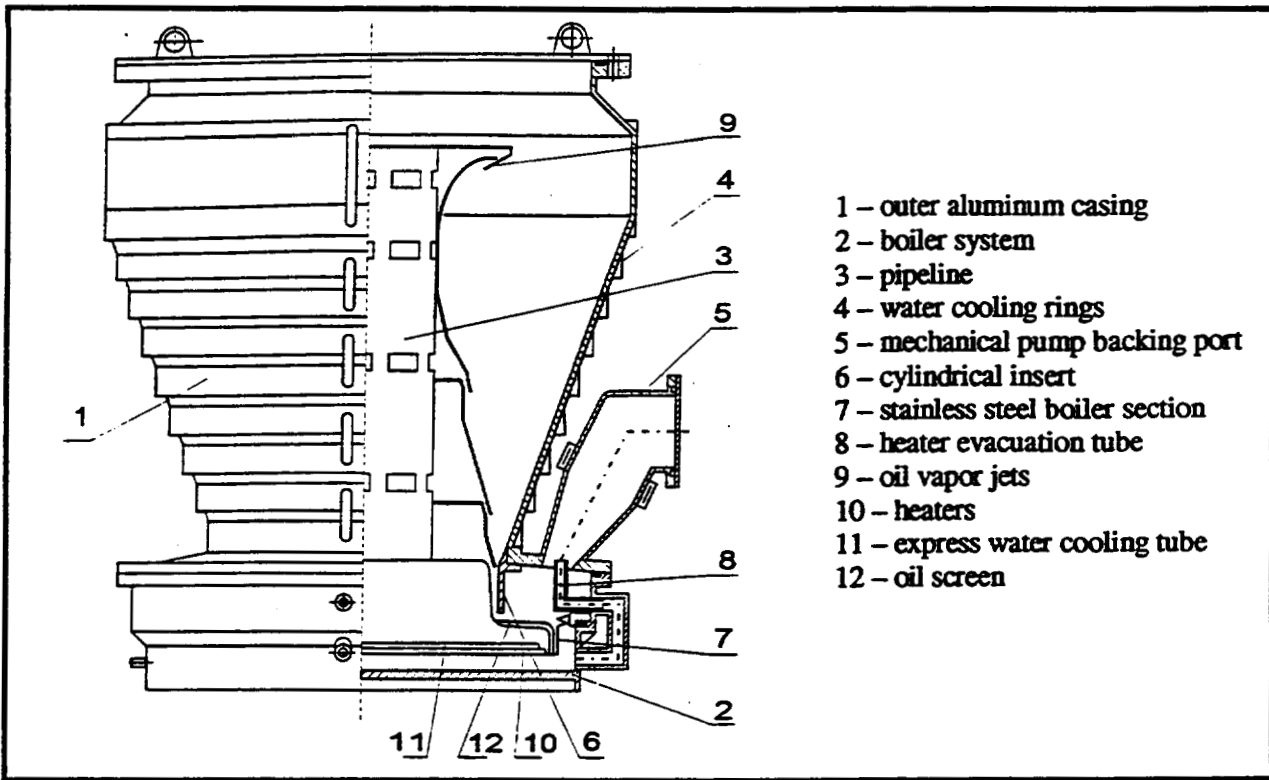


Figure 5: Zyrianka 900 diffusion pump schematic.

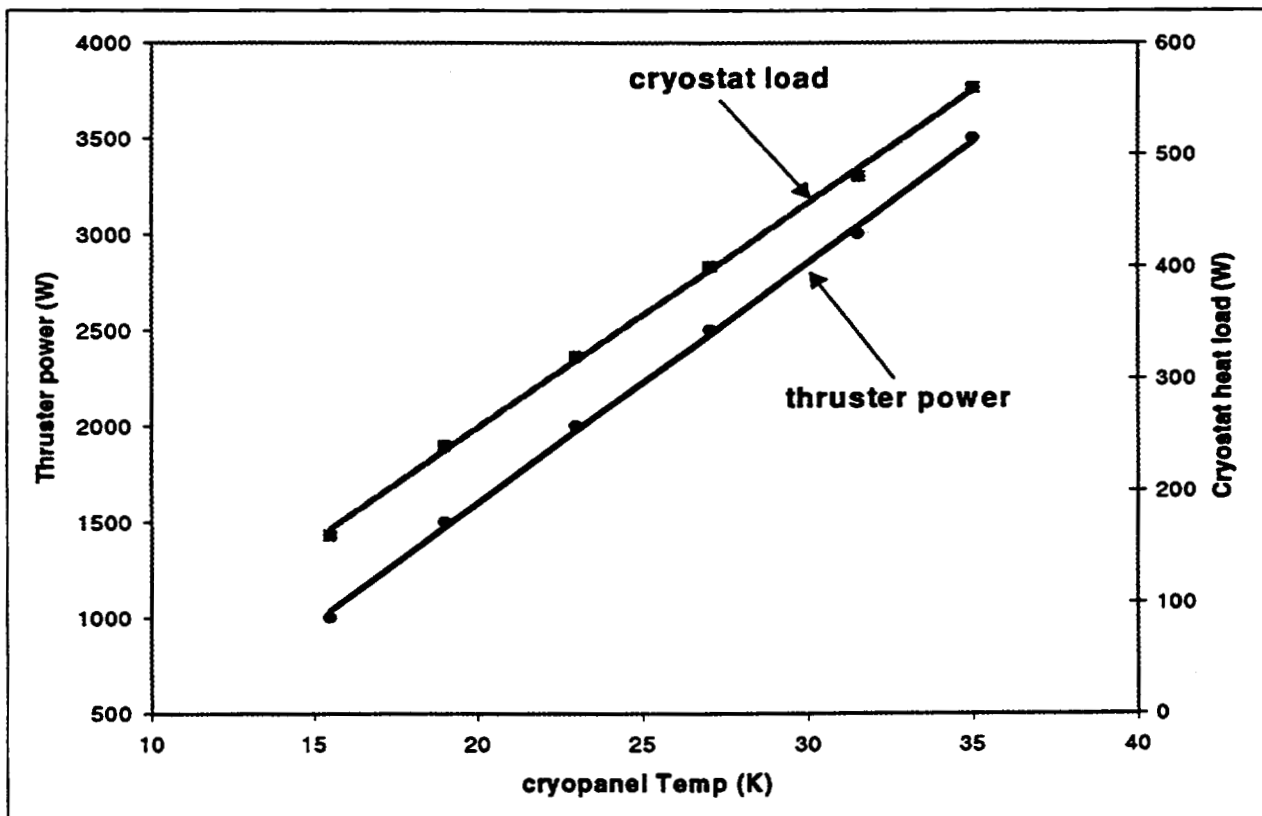


Figure 6: Heat load characteristics of CHAFF-4's cryostat vs inner shield array temperature.

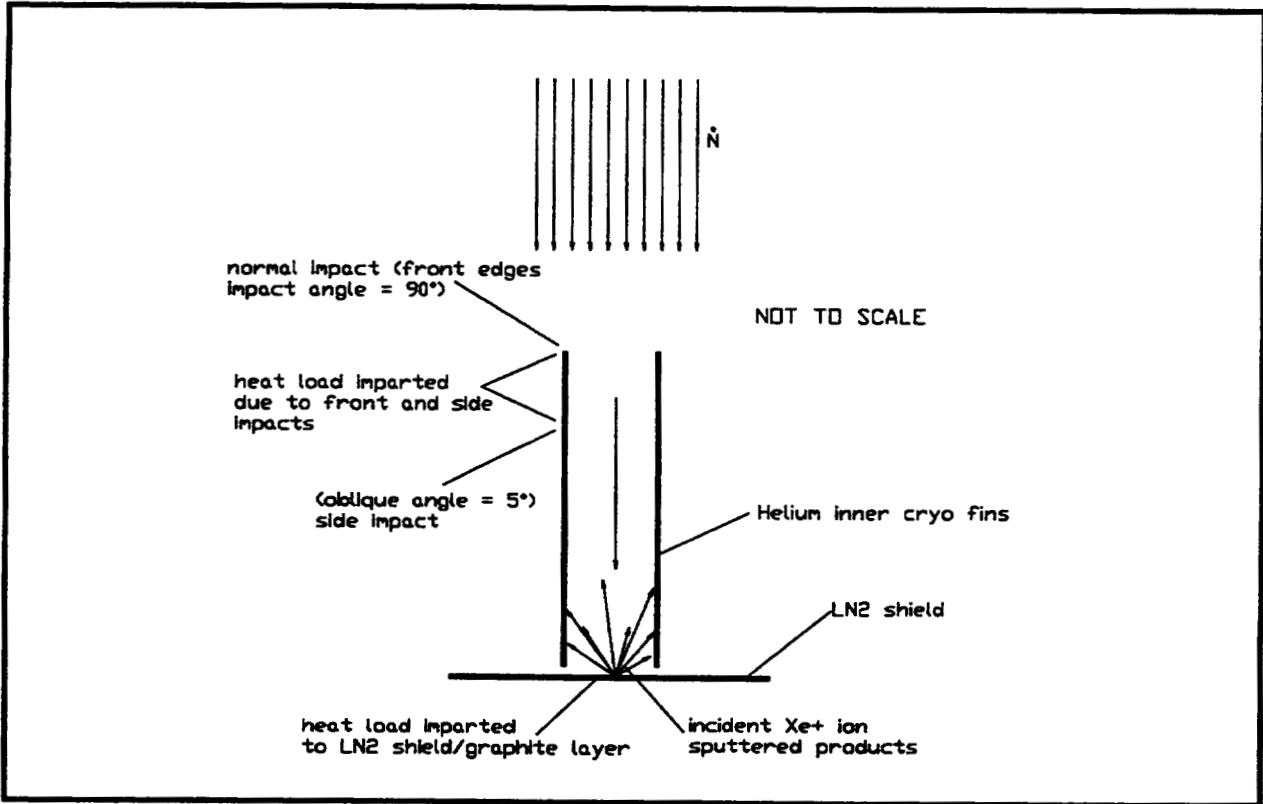


Figure 7: Blow up view of inner cryogenic shield geometry under ion bombardment.

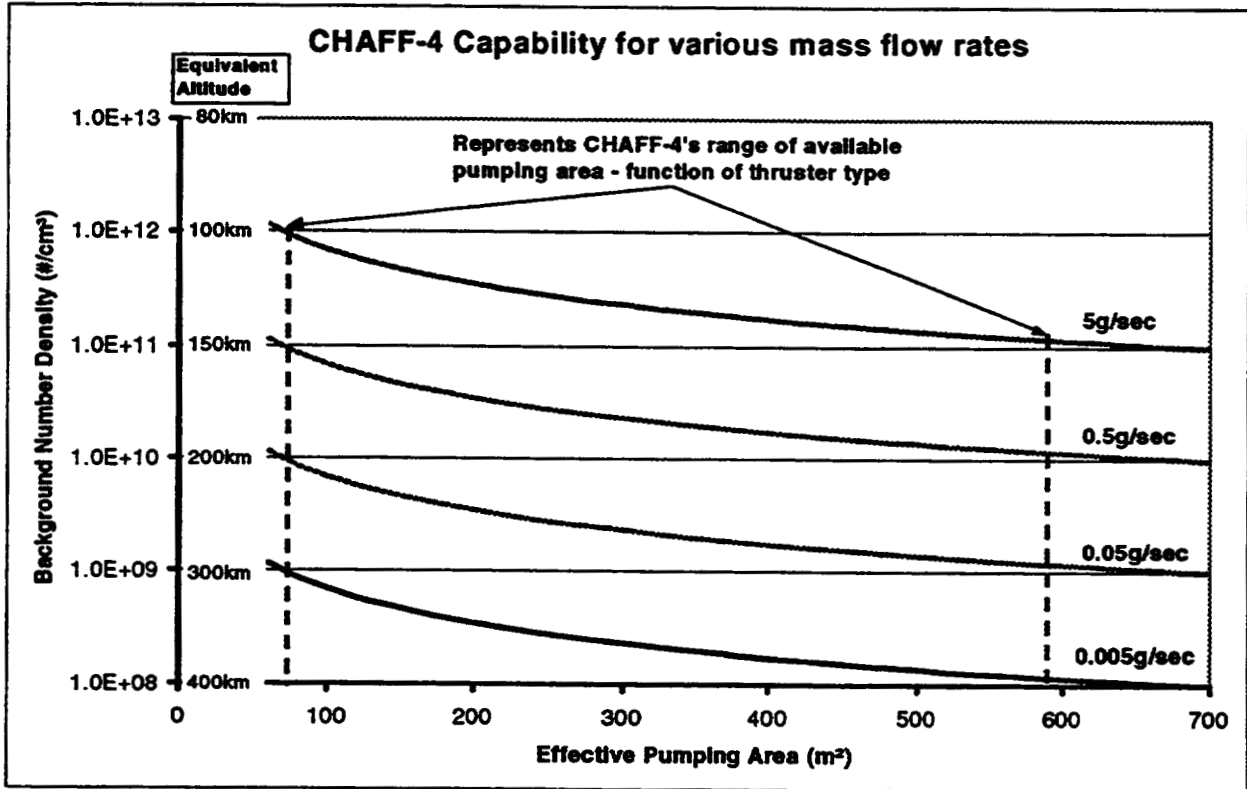


Figure 8: Background density and equivalent altitude capability versus effective pumping area.

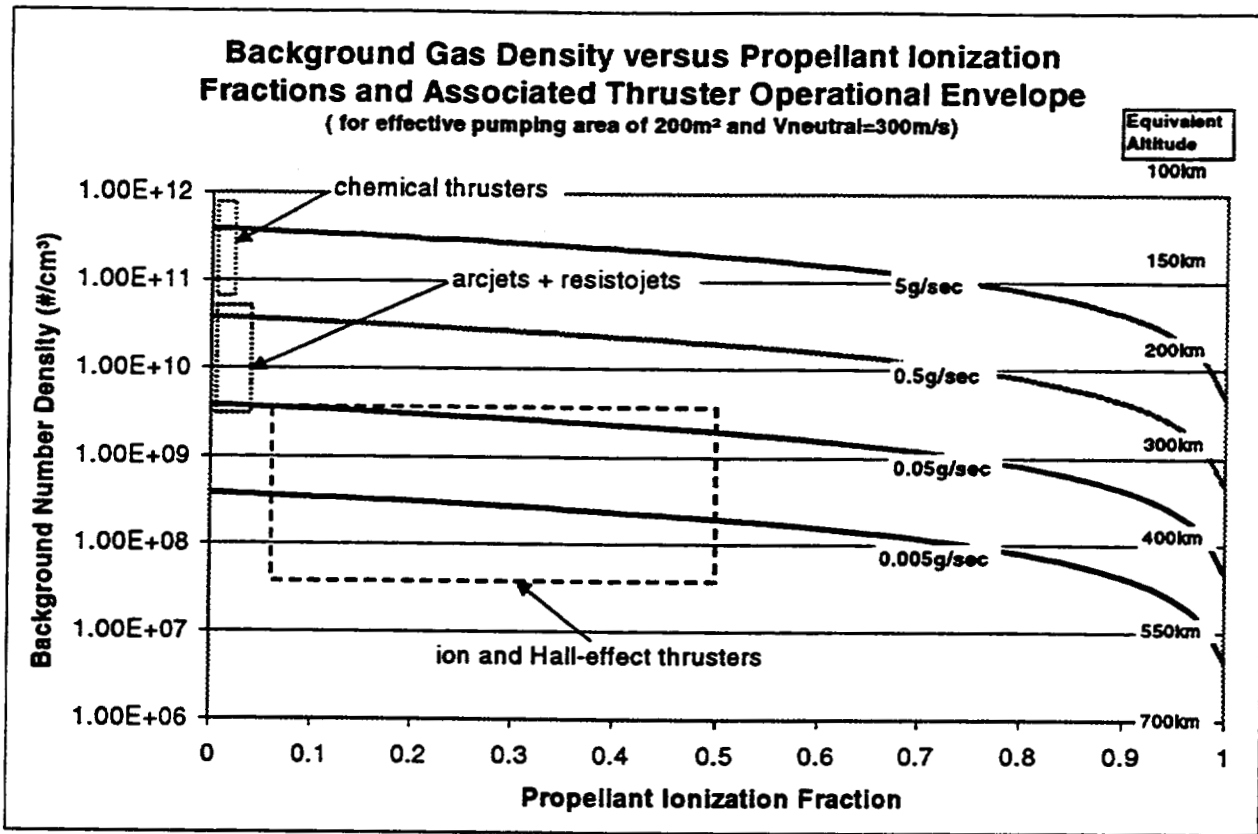


Figure 9: Background density and equivalent altitude capability versus propellant ionization fraction.

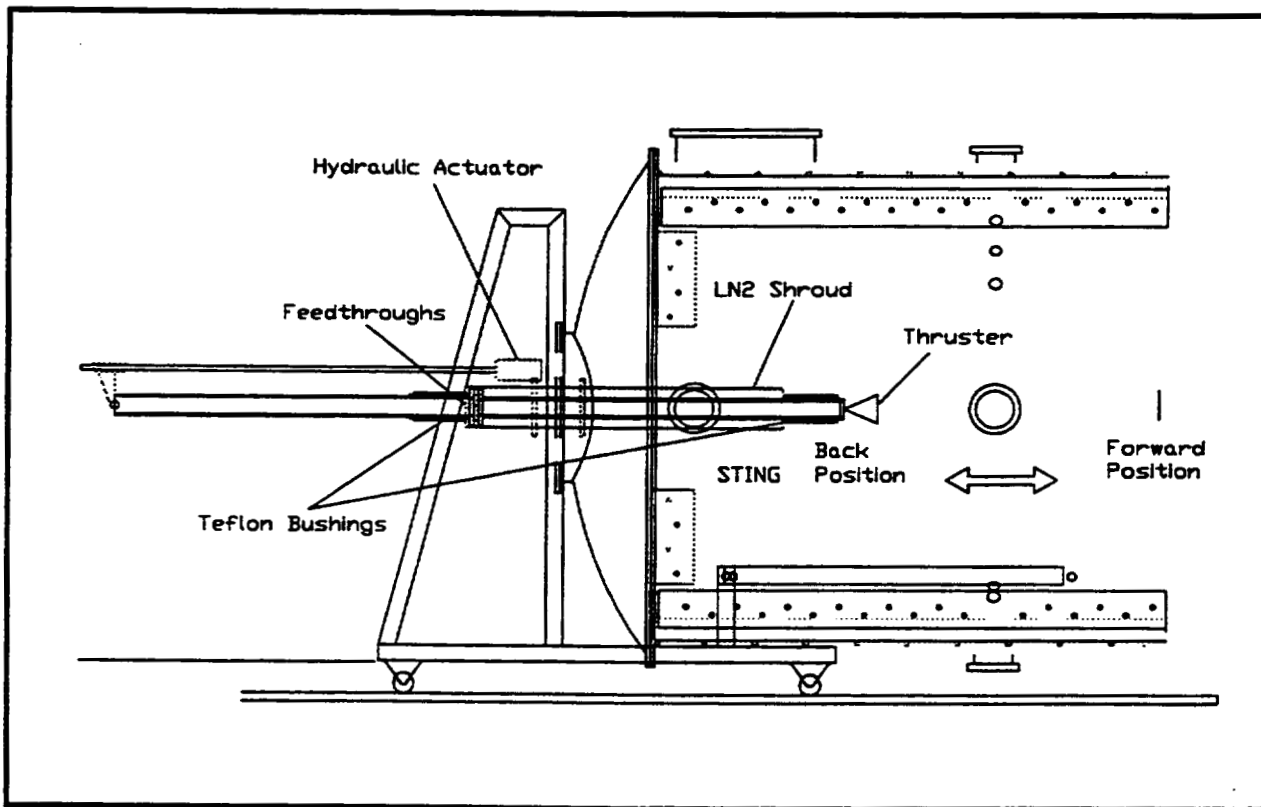


Figure 10: CHAFF-4's STING apparatus.



## PORTABLE MICROVIBRATION TEST FACILITY FOR SPACECRAFTS

Gabriel Martín  
C.A.S.A. Space Division  
Av. Aragón 404. E-28022 Madrid, Spain  
e-mail: gabriel@casa-de.es

### ABSTRACT

A new microvibration test facility is described. This test facility has been developed in C.A.S.A. Space Division in Madrid (Spain) and is used for microvibration tests of specimens as large as 2x2x4.5 m (6.5x6.5x14.7 ft). The facility is portable and can be used in any place with a minimum environmental conditions, needing two weeks of installation time and only mains and air-pressure supply ( 6 bar or 87 psi) for the facility to run.

One acoustic cabin is used for acoustic noise screening while an air-mounts system filters the groundfloor noise, acting as off-loading system at the same time. Specimens of 1500 kg (3300 lb) weight have been tested with good results, not being 1500 kg the weight of the heaviest specimen that can be tested. We have measured accelerometer background noise (including all the measurement chain) of  $10^{-6} \text{ ms}^{-2}$  ( $10^{-7} \text{ g}'\text{s}$ ) during test inside a standard clean room with large specimens and force sensors background noise during test of  $10^5 \text{ N}$ .

The paper describes in detail the facility, the type of measurements, excitation capabilities, previous measurements to qualify the site where the facility is going to be installed, type of inputs, suspension system features and the instrumentation.

### INTRODUCTION

Microvibrations can be of concern for optical components where jitter can disturb the line of sight stability or for experiments requiring zero gravity conditions. The platform vibrations where these equipments are mounted must be kept to a very low level. This has led to a number of investigations into the size of disturbing source vibrations. These may emanate from such sources as momentum and reaction wheels, solar array drives, attitude pointing mechanisms and mirrors. The mentioned microvibrations that are not under AOCs (attitude control system) and are amplified by structural resonance affect the sensitive payloads.

The degree of influence depends on the in-orbit structural behavior of the spacecraft structure. Therefore the structural transmissibility characterization is one of the main tasks when dealing with microvibration. The characterization of the transfer functions of a structure is a well known field and the data analysis techniques are already developed and well established. Nevertheless, when reference is made to microvibration levels then a wide spectrum of problems is added to the classical structural dynamic testing. Firstly, the input force levels are reduced to those expected at the on board equipment interfaces. Generating such low levels is something delicate with the available methods. Secondly, if the transfer functions are as low as expected by the system design engineers, the response levels will lie within the  $\mu\text{g}$  to  $\text{mg}$  range. Current instrumentation has noise levels not far away from these numbers. In addition, no influence of external noise sources is desired when performing the test. This imposes the strong requirement of isolating the structure from any electromagnetic, acoustic and ground borne input which will make the response measurement useless if signal-to-noise ratio is not kept above certain limits.

The procedures (both methodology and hardware/software support) developed at CASA for the performance of microvibration tests at spacecraft level are presented in this article. These procedures are still usable at any test location

provided that a minimum set of environmental conditions is satisfied.

## SYMBOLS AND ABBREVIATIONS

- AOCS - Attitude Orbital Control System
- CASA - Construcciones Aeronáuticas Sociedad Anónima
- SNR - Signal to Noise Ratio
- SPL - Sound Pressure Level
- EM - ElectroMagnetic

## MICROGRAVITY REQUIREMENTS

A review of various publications on microgravity payloads identified the need to characterize the structural dynamic behavior of the satellite with forcing functions input at the disturbing source locations. The forcing functions are of the following nature:

- band: [4 - 1000] Hz
- levels: [0.2 - 5] N

The transfer function values of interest for these type of structures are those ones above  $10^{-3} \text{ ms}^{-2}/\text{N}$  which leads to measure accurately acceleration levels of  $2 \cdot 10^{-4} \text{ ms}^{-2}$  ( $\approx 20 \mu\text{g}$ ). A rule of thumb for a good measurement is that the SNR is bigger than 20 dB. This in turn means that the measurement background noise should be 1/10 of the minimum value to be measured accurately.

## SITE PREPARATION

The place to be used for test needs an air-pressure supply of 6 bar (87 psi) capacity and enough room to receive the acoustic cabin which measures 4.8x4.8x6 m height. A standard mains plug is also needed for lighting, instrumentation and computer connection.

A previous background noise measurement is advisory to check the test location background noise characteristics. It is enough to record the air borne SPL with a microphone and the floor structural input with an accelerometer bonded to the test floor. As a first approach, if the results of these measurements at the hours when the test runs are to be performed are below 50 dBA  $10^{-3} \text{ ms}^{-2}$ , it is suitable to perform the test. Should higher values were to be detected a study of the curves should be done to assess the validity of the test location. In order to minimize the electromagnetic noise during test, the place should not be near to important electromagnetic field sources.

These tests can be performed in special environmental clean room conditions. A crane is needed for handling and acoustic cabin assembly.

## MICROGRAVITY TEST FACILITY

The facility is composed of:

- Suspension system.
- Acoustic cabin.
- Data acquisition and signal processing system.
- Excitation system.
- Measurement sensors.

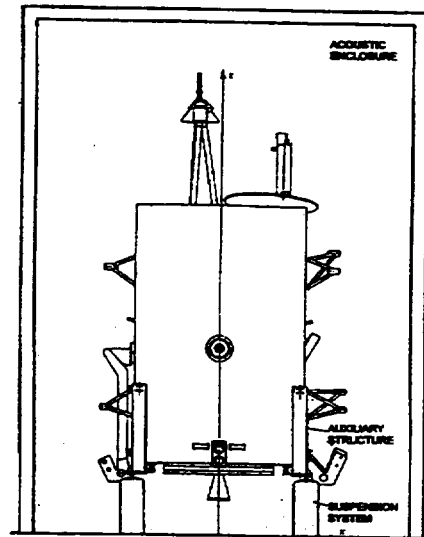


Fig. 1 Test set up

### Suspension System

The structure is mounted on top of a system of pneumatic isolators of the type used for high stability optical tables. A typical figure under which the rigid body modes of a setup for a 1500 kg (3300 lb) structure lay is 2.9 Hz. These devices filter the background floor vibration noise reducing thus the spurious noise input to the specimen during test.

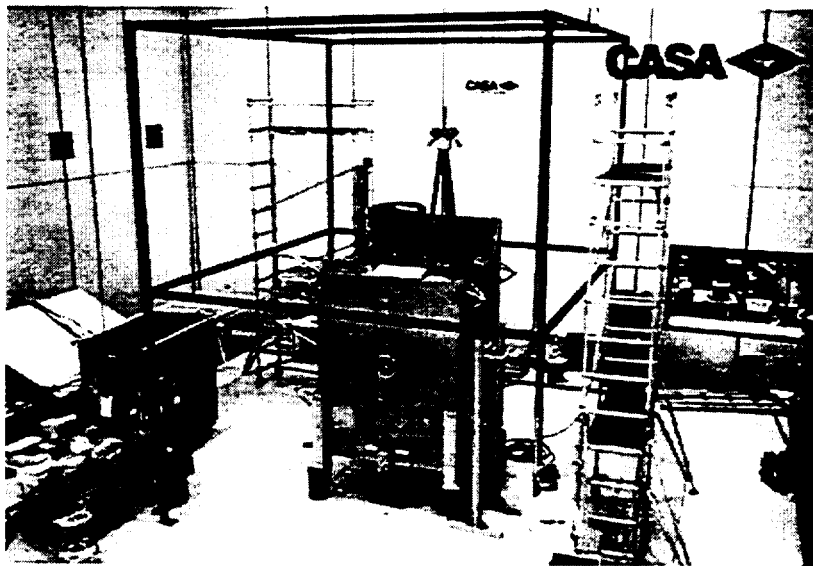


Fig. 2 Test setup already prepared with the suspension system, ready to be covered with the acoustic cabin

### Acoustic Cabin

The test setup (structure plus suspension system) is enclosed by an acoustic chamber made of steel plate-rockwool panels. The objective of the cabin is that of reducing the acoustic noise environment affecting the structure to

an acceptable level. One extra feature of the acoustic enclosure is that as it is made of steel plates it also acts as an EM filter when grounded to earth. The data acquisition system, signal conditioners and computers are located outside this area to avoid as much as possible interferences with true test signals.

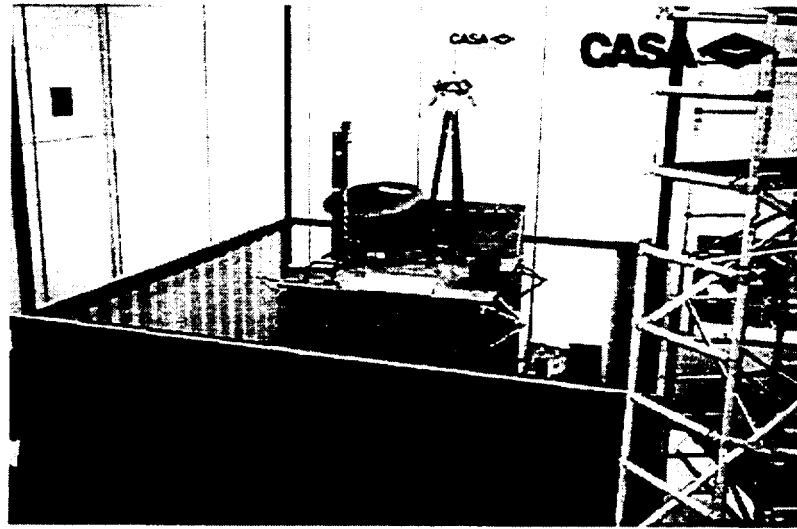


Fig 3. The acoustic cabin being mounted around the test setup

### Instrumentation and Data Acquisition

High sensitivity piezoelectric accelerometers are used for the test while standard piezoelectric force cells were found to be adequate for the levels to be measured in the tests. Several averages of the acquired data are necessary when running both random and sine excitation tests to reduce random noise contamination of the signals. All system control parameters are optimized in terms of signal noise reduction, measurement accuracy and overall test time (number of acquisition averages, cycles per step sine,...). Background noise levels of the accelerometers attached to the structure are  $10^{-6} \text{ ms}^{-2}$  ( $10^{-7} \mu\text{g}$ ). While values of  $10^{-5} \text{ N}$  of force cells background noise are obtained.

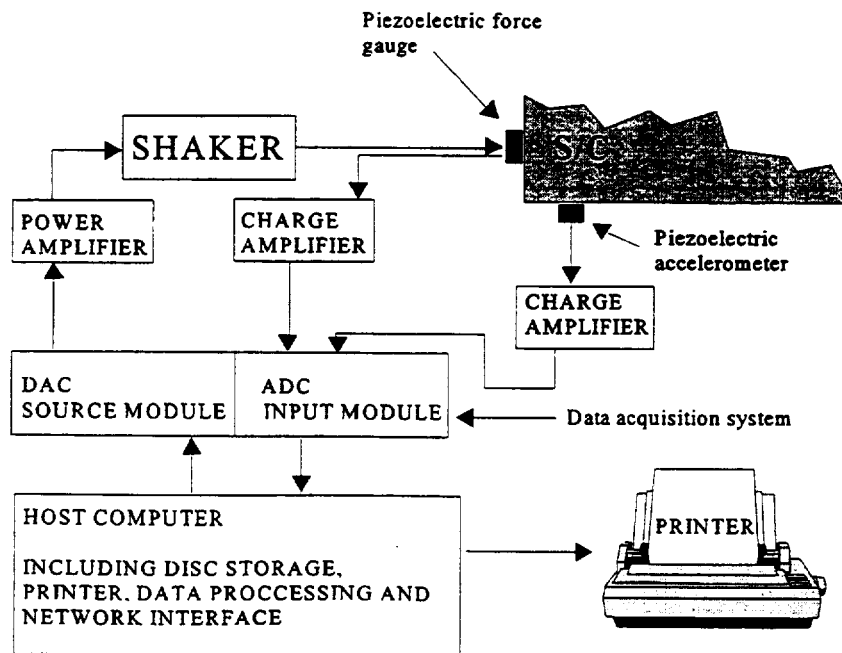


Fig. 4 Instrumentation

## Excitation Capabilities

The input force is generated by means of electrodynamic minishakers of the type used for modal testing, suspended from bungees to decouple them from external perturbations. The support system used to support the minishaker is configurable in order to reach any excitation location.

Two type of inputs have been used so far: sine and random. Examples of inputs and acquisition conditions used for microvibration tests are:

For random excitation:

- Force levels: 0.5 Nrms, 1.3 Nrms, 2.6 Nrms, 5.3 Nrms.
- Bandwidth: [3 - 1000] Hz.
- Frequency resolution: 0.25 Hz.
- 64 averages.

For sine sweep excitation:

- Force levels: 0.2 Nrms, 1.0 Nrms, 4.0 Nrms, 8.0 Nrms.
- Bandwidth: [4 - 200] Hz.
- Frequency resolution: 0.125 Hz.
- 16 cycles per acquisition



Fig 5. Force input at a momentum wheel dummy

## Test Performance

The facility is operated following the sequence:

- Noise characterization of the test site.
- Suspension system placement.
- Structure instrumentation.
- Structure location onto the suspension system.
- Suspension system characterization and tuning.
- Acoustic cabin assembly around the setup.
- Preparation runs performance (actual test background noise characterization)
- Microvibration runs. Data acquisition and processing.
- Acoustic cabin dismantling.
- Structure removal.
- Suspension system removal.

Time consuming operations include the acoustic cabin assembly and dismantling. Each mentioned operation takes 5 working days. The overall test duration is strongly dependant on the number of test runs to perform (one run can take up to one hour in the worst case) and on the number of different excitation locations. As an example, for the ARTEMIS spacecraft microvibration test campaign with 41 runs in 17 different configurations (different minishaker locations) the test duration was 6 weeks.

## TYPE OF MEASUREMENTS

The minimum test data supplied are the acceleration and force records together with their respective SNR to check the data quality. It is also normal practice to supply the corresponding transfer and coherence functions.

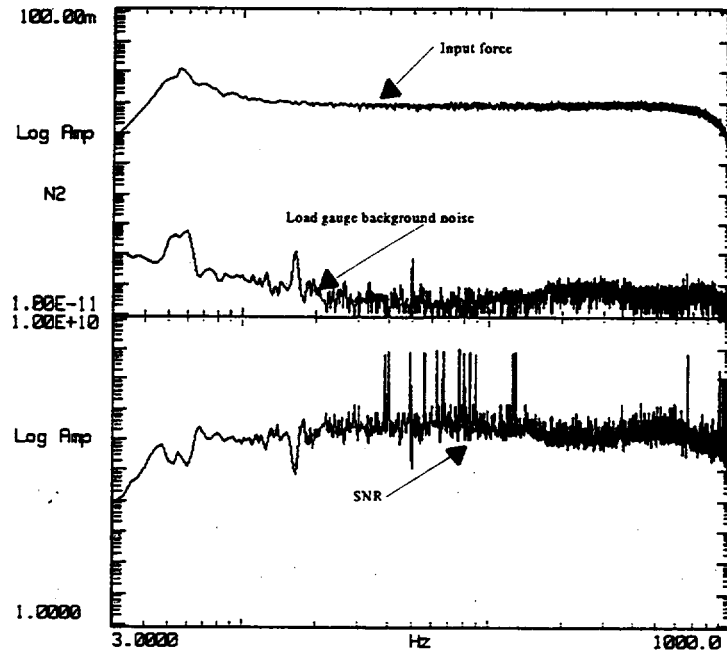


Fig 6. Input force for a random input spectrum 0.5 Nrms, 3-1000 Hz

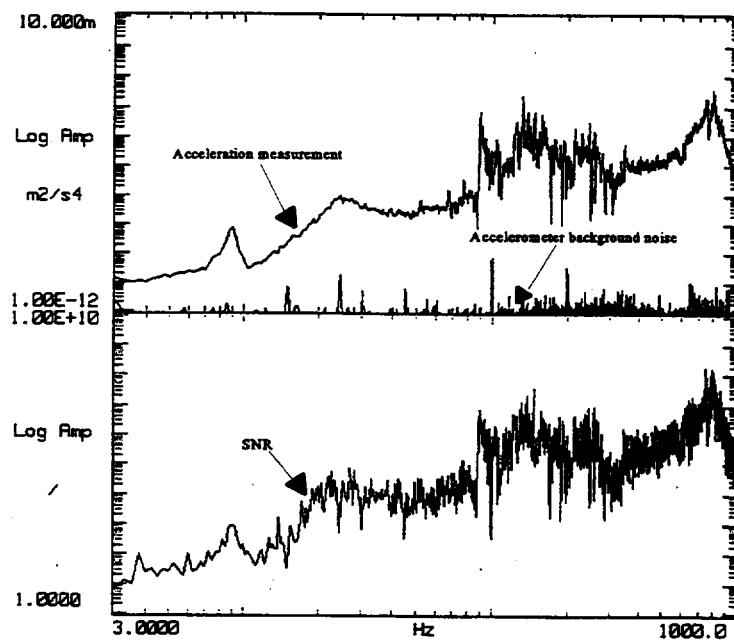


Fig. 7 Typical acceleration response for the above force input

Further processing of these data is also performed, if needed or requested, to obtain resonances damping or any other modal parameter. Standard and advanced signal processing and modal analysis tools are available.

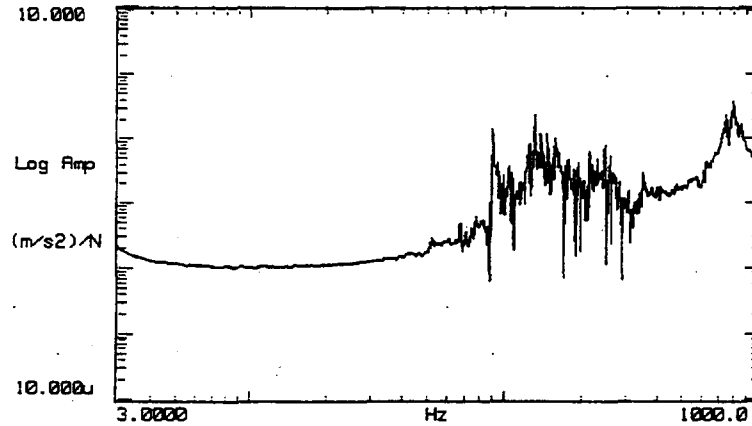


Fig. 8 Typical transfer function from an excitation point at a noisy equipment to the response at a payload sensitive point

## FACILITY VALIDATION

The test facility has been already used for the ARTEMIS structural model microvibration test campaign. The Advanced Relay and Technology Mission (ARTEMIS) is a telecommunication satellite developed for ESA by an industrial team lead by Alenia Aerospazio. Its structure (developed by CASA) supports on the earth facing panel a laser communication experiment (SILEX). The pointing requirement of such a device is very exigent and the characterization of the microvibration transmission paths from the noise sources to the SILEX experiment was the objective of the test.

## CONCLUSIONS

In the near past CASA Space Division has developed a microvibration test facility for spacecrafts. This facility can be transported, assembled and operated in any place where the spacecraft is being submitted to the integration and test campaign. It is shown in the paper how the facility is set up and the type and quality of the measurements and test results obtained with it.

## REFERENCES

- [1] JM Bétermier, F. Mercier, An overview of CNES's micro-dynamic research activities - An overview, IAF-93-I.2.221, Oct 1993
- [2] HR Stark, C Stavrinidis, ESA microgravity and microdynamic activities - An overview, IAF-93-I.2.218, Oct 1993
- [3] P. Collins, Important factors in microvibration testing - ESA conference on spacecraft structures materials &

mechanical testing, March 1996 ESA SP 386

- [4] John O. Lassiter, Microgravity acceleration measurements - Sound and vibration. February 1996
- [5] E.M. Marchante, L. Muñoz, Artemis satellite microvibrations testing and analysis activities - IAF 48<sup>th</sup> international astronautical congress, October 1997

## THE US AIR FORCE RESEARCH LABORATORY'S NEWLY UPGRADED SCEPTRE FACILITY

Clifford A. Cerbus  
University of Dayton Research Institute

### ABSTRACT

The US Air Force Research Laboratory Materials & Manufacturing Directorate has maintained some form of space simulation facility designed to expose thermal control materials to a simulated space environment for over 35 years. During that time the University of Dayton Research Institute (UDRI) has participated in these research efforts and is currently responsible for the operation of the facility which is known as the SCEPTRE (Space Combined Effects Primary Research and Test Equipment) Facility. In its previous configuration the SCEPTRE Facility simultaneously exposed thermal control materials to a combined vacuum, UV, and electron environment while monitoring the materials solar absorptance *in vacuo*. Over the years the facility's limitations had become increasingly unacceptable and a new configuration has been designed and assembled to overcome many of these shortcomings. The new system consists of a larger vacuum chamber with a two stage specimen load-lock system for both individual and group specimen introduction to the main chamber. The new design also incorporates the addition of a 50 KeV proton gun, a new solar simulator, and increased specimen throughput.

This paper will present a brief history of the facility along with its previous capabilities and a complete description of the upgraded design and its enhanced capabilities. Currently, construction of the new system has been completed and some initial testing has been completed to verify its performance.

### INTRODUCTION

The US Air Force Research Laboratory Materials & Manufacturing Directorate has a history of more than 35 years of continuous space materials activities and throughout that time period has maintained some form of space simulation facility. The University of Dayton Research Institute has assisted the Materials & Manufacturing Directorate with these efforts throughout most of this time period as well.

In the late 1950s the first space simulation chamber was developed which consisted of ultraviolet (UV) and vacuum exposure only. It allowed for only pretest and posttest analysis of the materials. This chamber verified the need for *in vacuo* reflectance measurements due to the "bleaching" of organic coatings after exposure to the atmosphere and was around in one form or another for about 10 years. The second generation facility, designed and built in 1968, incorporated an integrating sphere inside the vacuum chamber to monitor the material's solar absorptance *in vacuo* periodically throughout the duration of a test. It was designed to expose 24 specimens at a time, with a ring of light generated by shining a solar simulator onto a conical style mirror, but eventually it was discovered that the solar simulator was not able to provide accelerated exposure in this configuration. In 1975, a third generation design incorporated a CO<sub>2</sub> laser and was used to measure the material's change in solar absorptance due to laser radiation. This effort was unfruitful because the energy density required to damage the material was such that the laser was not capable of damaging a large enough area to be detected by the spectrophotometer. Electron radiation and accelerated UV exposure was added to the fourth generation facility in 1984. This design made use of the previous sample handling mechanism but restricted the exposure area to 5 specimens at a time. It was around this time that the facility was given the SCEPTRE moniker.

These space simulation efforts over the past 35+ years, have supported the US AFRL Materials & Manufacturing Directorate in their in-house and contractual thermal control coating material formulation and development programs. The SCEPTRE facility and its predecessors have provided the necessary testing during both the material development and space flight experiments used to ultimately quantify and validate a material's performance. Some of the space flight experiments that they participated in include: ML-101, Skylab, SCATHA, and LDEF. The Directorate's efforts have greatly aided the development of thermal control coating materials in use today.

Throughout the facility's more recent past, its age and hardware limitations became increasingly unacceptable. There were several major vacuum components being used that were still leftover from the 1968 design. The most significant of which was the sample wheel and its motion mechanism. These items greatly limited the facility's throughput (5 specimens per test) and were unreliable. Thus, in 1994 the USAF decided to upgrade the facility by purchasing a newly designed vacuum chamber and sample handling mechanism. Initially, numerous vacuum equipment vendors were contacted to aid in the design of the new facility and were asked to provide quotes on its manufacture. Of the many vendors who were contacted, only two chose to provide preliminary designs. Eventually, the Kurt J. Lesker Company, was awarded a contract to manufacture the new facility. After many iterations of design changes and approvals, and extreme delays in procurement, the new system was delivered to the USAF in 1997.

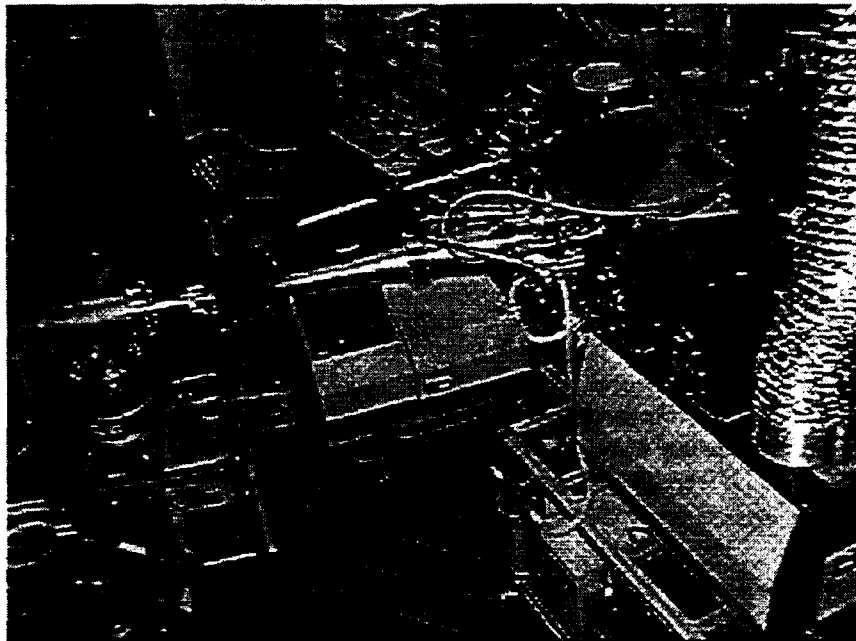


Figure 1. The US AFRL/ML SCEPTRE Facility

## SCEPTRE DESCRIPTION

The US AFRL/MLBT's Space Combined Effects Primary Test Research Equipment (SCEPTRE) Facility is the only Air Force owned facility designed specifically for testing and qualification of spacecraft thermal control coating materials. Testing at the facility is performed in accordance with the guidelines established by the American Society for Testing and Materials (ASTM) *E 512-94 Standard Practice for Combined, Simulated Space Environment Testing of Thermal Control Materials with Electromagnetic and Particulate Radiation* (ref. 1). The system has the capability of providing synergistic UV and electron radiation environments similar to those experienced by satellites orbiting in mid-to-high earth orbits and is shown in figure 1. In addition, the system has the ability to perform *in situ* measurements of sample temperature and *in vacuo* reflectance as a

function of wavelength. The vacuum level is maintainable from approximately  $6.7 \times 10^{-6}$  to  $6.7 \times 10^{-5}$  Pa ( $5 \times 10^{-8}$  to  $5 \times 10^{-7}$  Torr), the sample temperatures can range from  $10^{\circ}\text{C}$  ( $50^{\circ}\text{F}$ ) to  $80^{\circ}\text{C}$  ( $176^{\circ}\text{F}$ ), the sun level is approximately 2.5 equivalent ultraviolet suns (EUVS) (250-400 nm), and the electron flux is adjustable to a maximum of  $10^{12}$  e<sup>-</sup>/cm<sup>2</sup>/sec at energies adjustable to a maximum of 20 KeV, for each of the two electron guns. In the near future the facility will also be able to provide proton radiation with the flux adjustable to a maximum of  $10^{10}$  p<sup>+</sup>/cm<sup>2</sup>/sec at energies adjustable to a maximum of 50 KeV.

## Vacuum System

The vacuum system is composed of three separate chambers: the main vacuum vessel, the storage/transfer load-lock chamber, and an individual load-lock chamber. The main vacuum vessel is 76.2 cm (30 in) in diameter and 45.72 cm (18 in) in height. Attached to the main vacuum vessel is the storage/transfer load-lock chamber. It is comprised of a mixed six way cross. The primary leg of this secondary chamber has flange sizes of 25.4 cm (10 in) in diameter. The storage/transfer load-lock chamber has its own pumping system and is designed to store the test specimens in a vacuum environment while the main vacuum vessel is exposed to ambient conditions. Thus, the specimens can be maintained under vacuum while repairs are being made in the main vacuum vessel. The individual load-lock chamber allows for individual specimen introduction and removal without compromising the rest of the specimens by exposing them to atmosphere. The individual load-lock chamber is comprised of a five way cross with all legs of the cross having 15.24 cm (6 in) diameter flanges.

The main pumping system for the vacuum chamber is a CTI-CRYOGENICS-Helix Technology Corporation's *On-Board*<sup>®</sup> 8 cryopump. It has a 4000 liter/sec pumping speed for water vapor and is a new addition to the facility. Additionally, the chamber is also pumped by a Welch Vacuum Technology model 3106S turbomolecular pump which is the pumping system for the storage/transfer load-lock chamber. The 3106S turbomolecular pump is backed by a Welch Vacuum Technology model 1397 rotary pump. The chamber is monitored via 3 different ion gages: a Granville-Phillips Series 360 *STABIL-ION*<sup>®</sup>, a Granville-Phillips 271 Series, and a Fredricks-Televac model 3C5-2A2. The chamber has the capability of exposing eighteen, 2.38 cm (15/16 in) diameter, specimens to synergistic UV, electron, and proton radiation. Figure 2. shows the facility's sample platen, containing eighteen white thermal control coating specimens. The specimens are cooled via a "cooling dock" (located on the right side of the sample platen in figure 2) which the sample platen seats against when the specimens are positioned in the exposure location. This cooling dock consists of a flow through chamber which has chilled ethylene glycol/water circulating through it.

## Solar Simulator

The solar simulator consists of a water filtered 2500 Watt xenon arc lamp mounted in a Spectral Energy Corporation solar simulator. This new addition replaces the 33 year old, UDRI modified, Spectrolab X-25 solar simulator. The xenon arc lamp is water filtered and is capable of generating 3 EUVS with a reasonably uniform (variation of as much as 30%) intensity distribution across the beam's profile. The output of the solar simulator is measured with an EG&G model 580 spectroradiometer that is calibrated using an EG&G 1000 Watt quartz-tungsten-halogen FEL style lamp (250-1100 nm) traceable to the National Institute of Standards and Technology (NIST) data.

## Electron Guns

The SCEPTRE Facility utilizes two Kimball Physics Inc. EFG-11 electron guns. These guns are designed to provide a flood of electrons with energies ranging up to 20 KeV. Output is monitored by a Faraday cup situated 11.43 cm (4.5 in) below the center of the sample platen. A Keithley 617 programmable electrometer is used to measure the electron current generated by the Faraday cup. The electron beam is aligned using a phosphor screen and is assumed to be relatively uniform across all the specimens.

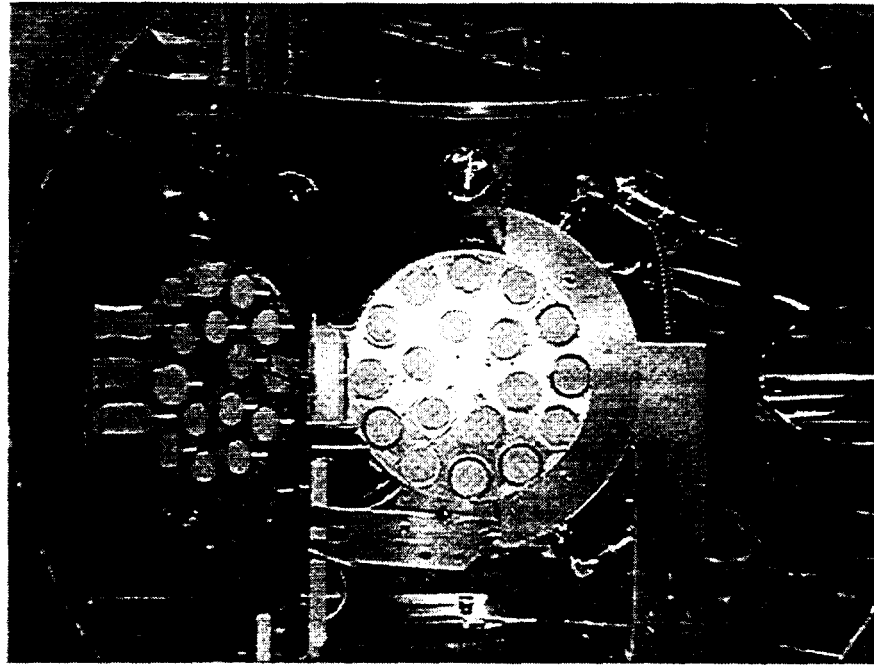


Figure 2. Sample Platen, Cooling Dock, and Faraday Cup

### **Proton Gun**

In order to provide a more complete simulation of the space environment, in 1990 it was decided to procure a proton gun. The gun purchased was built by the Physicon Corporation (Boston, MA) and is composed of a duoplasmatron ion source, an Einzel lens,  $E \times B$  mass filter, and a quadrupole and is designed to produce a flood of protons at the target. It has the capability of accelerating protons with energies up to 50 KeV. The gun was initially designed to be incorporated onto the old vacuum chamber, it was never installed on that system due to the continued anticipation of the procurement of the new system. Since the new system was designed with the installation of the proton gun as a prime consideration, the incorporation of the gun onto the new system was tremendously simplified compared to its installation on the old system.

### **Spectrophotometer**

The spectrophotometer used to monitor the specimens' solar absorptance is a Perkin-Elmer Lambda 9 UV-Vis-NIR double beam spectrophotometer that is fiber-optically coupled to a Labsphere Inc. integrating sphere located inside the vacuum chamber. The spectrophotometer is designed to provide *in vacuo* NIST traceable reflectance measurements periodically throughout the duration of a test.

### **Data Acquisition**

The data acquisition is performed by a Digital Equipment Corp. (DEC) VAXstation III/GPX, in conjunction with hardware from a variety of other vendors, and utilizes IEEE-488, RS-232, analog-to-digital, and digital-to-analog interfaces. The system periodically records and displays the electron flux, vacuum level, backface temperatures of 2 of the 18 exposed specimens (on opposite sides of the specimen platen to provide information on the temperature extremes of the specimens) throughout the duration of a test. It also used to acquire, analyze, and display data from the spectrophotometer and spectroradiometer.

## TESTING PROCEDURES

Testing in the SCEPTRE facility is intended to compare the relative performance of materials in a simulated, accelerated space environment. Each of the specimens receive approximately 2.5 EUVS, with electron exposure designed to provide accelerated low energy electron radiation compared to that experienced in geosynchronous orbits. By convention, the duration of the tests performed in the facility are usually intended to last for 1000 hours of exposure. This provides for about 2500 Equivalent Sun Hours (ESH) and approximately one year of actual geosynchronous orbit time (ref. 2).

Geosynchronous orbits contain both trapped and solar wind electrons that must be simulated. The facility's two electron guns are typically operated at energy levels of 1 KeV and 10 KeV. The AE8-MAX trapped electron model (ref. 3) and data originating from the SCATHA space flight experiment (ref. 4) were used in establishing values of  $3 \times 10^9 \text{ e}^-/\text{cm}^2/\text{sec}$  for the 10 KeV electrons and  $6 \times 10^9 \text{ e}^-/\text{cm}^2/\text{sec}$  for the 1 KeV electrons. At 1000 hours of exposure this generates a total fluence of  $3.24 \times 10^{16} \text{ e}^-/\text{cm}^2$ . Reference 4 indicates that the fluence of solar plasma electrons within the energy range of 0-10 KeV, in a 1000 hour period, would be  $5.8 \times 10^{15} \text{ e}^-/\text{cm}^2$ . Thus, the exposure rates used in the SCEPTRE facility provide a 5.5 acceleration factor for electron exposure.

Comparison of results between actual spaceflight experiments and the testing practices outlined above in the old facility have validated the appropriateness of these parameter choices. Figure 3. shows this comparison for testing performed in the old system in 1993 on Illinois Institute of Technology Research Institute's YB-71 (zinc orthotitanate in a potassium silicate binder) coating to data generated by Ahern and Karperos, Aerojet ElectroSystems Company (ref. 2). This graph shows that the ground-based simulation of the geosynchronous orbit performed in the SCEPTRE facility, did recreate both the rate and extent of damage experienced by the material on orbit. The major difference between the spaceflight data and the data generated at the SCEPTRE facility lies in the discrepancy between the beginning of life solar absorptance values. This discrepancy is unexplainable, but could be due to the more than 10 year difference between the manufacturing of the materials or perhaps due to instrumentation differences.

## INITIAL SCEPTRE PERFORMANCE EVALUATION

Performance of the inaugural test of the facility was not smooth. Several issues were noted that required attention to allow the facility to operate at the desired performance level. The most significant problems were with the power supply used on the new solar simulator and the excessive temperatures that the specimens experienced. The problems with the power supply have been solved, while efforts to resolve the excessive specimen temperature are still underway and are outlined below.

When designing the sample holding and cooling mechanisms for the new system, several assumptions were made which led to under estimating the thermal environment of the specimens. The old system used a poorly filtered solar simulator which had excess infrared energy, the new solar simulator has a water filter which would eliminate most of the excess energy. Additionally, the previous system had very minimal contact between its cooling plate and sample wheel. The new system provides much more direct contact between the cooling dock and the specimen platen. Thus, it was assumed that the specimens would actually be cooler in the new system. This did not prove to be true. The specimen temperatures in the old system were as warm as 80 °C (176 °F), while in the new system they rose to an unacceptable 140 °C (284 °F). An effort was made to reduce the specimen temperatures by covering the aluminum sample platen with a material that had a high thermal emittance. Thus, after this test was completed silverized FEP Teflon<sup>®</sup>, manufactured by E. I. du Pont de Nemours and Company, with an acrylic adhesive backing was applied to the sample platen and a second test was performed. The silverized FEP Teflon<sup>®</sup> significantly lowered the specimens' temperatures to about 80 °C (176 °F). New designs have been completed which will further reduce the specimen temperatures by: (i.)improving

intimate contact between sample holders and the platen, (ii.) increasing the size of the cooling dock, and (iii.) replacing construction materials with ones which have higher thermal conductivity. The drawings have been completed and the machining and manufacture of the modifications will begin next fiscal year.

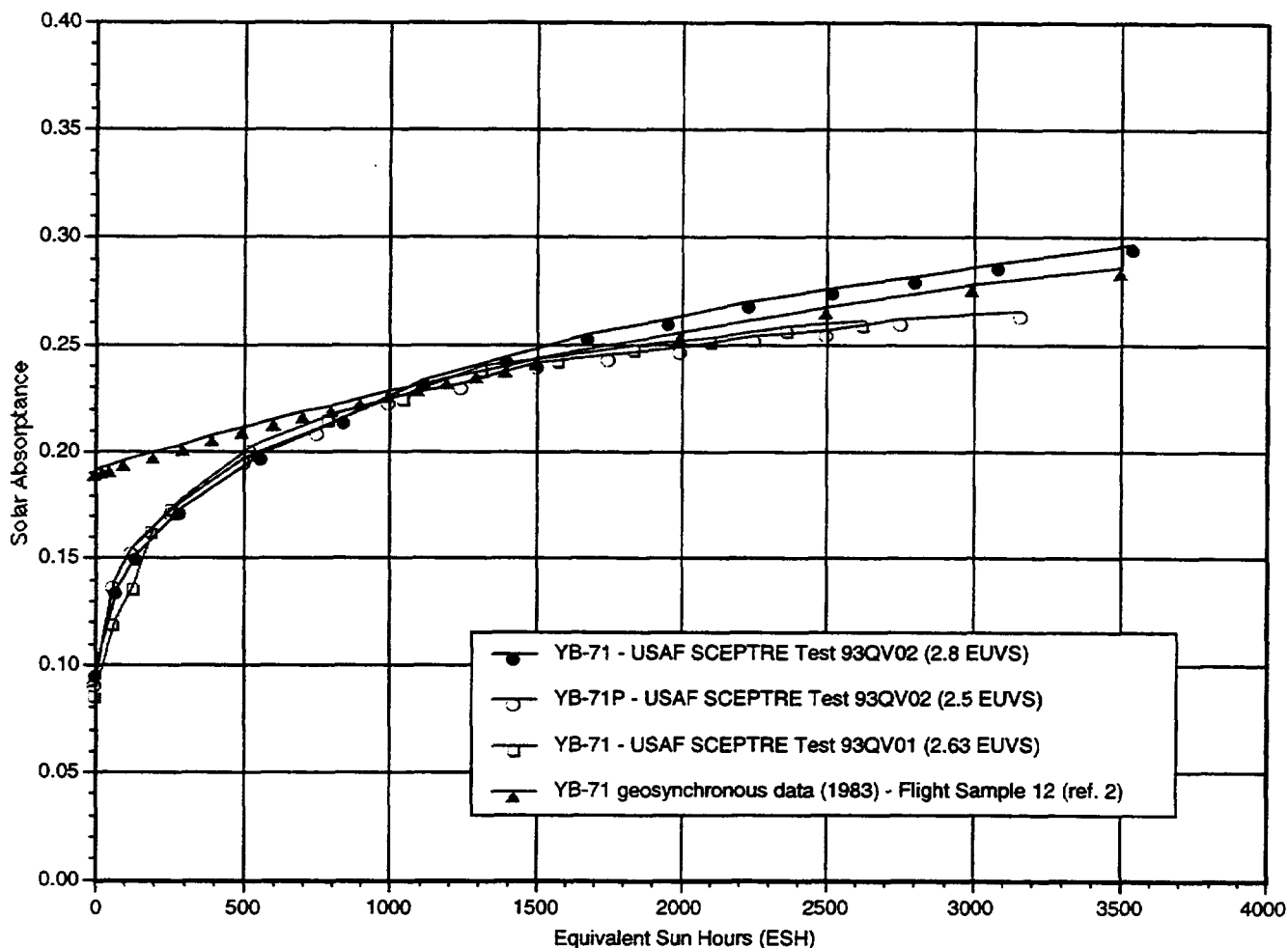


Figure 3. Comparison Between Spaceflight Data & Previous SCEPTRE Facility for IITRI YB-71

## CONCLUSION AND FUTURE

The new facility has already demonstrated its dramatic increase in specimen throughput and capabilities. With the incorporation of the specimen cooling modifications the system will be at peak performance. Future tasks will include replacing the software and hardware for the facility's data acquisition system and bringing the proton gun online to incorporate it into the simulation of the space environment. Additionally, future research efforts are being considered which would utilize the positive ion accelerating capabilities of the proton gun as a source for low energy ion scattering spectroscopy (LEISS) and secondary ion mass spectroscopy (SIMS) techniques. These techniques would provide additional characterization of materials *in vacuo* as they are exposed to a simulated space environment.

Finally, the USAF is seeking customers (both external and internal to the US government) who would be interested in using this facility. Interested parties should contact either Mr. Clifford A. Cerbus, UDRI, (937)255-7379, or Dr. Jeffrey H. Sanders, USAF, (937)255-9098, to explore the possibilities for testing.

## REFERENCES

1. American Society for Testing and Materials, "E 512-94 Standard Practice for Combined, Simulated Space Environment Testing of Thermal Control Materials with Electromagnetic and Particulate Radiation," 1997 *Annual Book of ASTM Standards, Vol. 15.03*, pp. 471-480.
2. Ahern, J. E., and Karperos, K., "Calorimetric Measurements of Thermal Control Surfaces on Operational Satellites," AIAA Paper No. 83-0075, 1983.
3. Vette, J. I., *The AE-8 Trapped Electron Model Environment*, National Space Science Data Center, NSSDC/WDC-A-R&S 91-24, Greenbelt, MD, 1991.
4. Judeikis, H. S., *Space Radiation Effects of Teflon and Nomex Fibers*, The Aerospace Corporation, ATM-89(4945-01)-7, 1988.



# REFURBISHMENT AND AUTOMATION OF THERMAL VACUUM FACILITIES AT NASA/GSFC

Jamie Dunn, Carlos Gomez, and John Donohue  
Goddard Space Flight Center  
Greenbelt, MD 20771

Chris Johnson, John Palmer, and Janet Sushon  
ManTech Systems Engineering Corporation  
Seabrook, MD 20706

## ABSTRACT

The thermal vacuum facilities located at the Goddard Space Flight Center (GSFC) have supported both manned and unmanned space flight since the 1960s. Of the eleven facilities, currently ten of the systems are scheduled for refurbishment or replacement as part of a five-year implementation.

*Expected return on investment includes the reduction in test schedules, improvements in safety of facility operations, and reduction in the personnel support required for a test. Additionally, GSFC will become a global resource renowned for expertise in thermal engineering, mechanical engineering, and for the automation of thermal vacuum facilities and tests.*

Automation of the thermal vacuum facilities includes the utilization of Programmable Logic Controllers (PLCs), the use of Supervisory Control and Data Acquisition (SCADA) systems, and the development of a centralized Test Data Management System. These components allow the computer control and automation of mechanical components such as valves and pumps. The project of refurbishment and automation began in 1996 and has resulted in complete computer control of one facility (Facility 281), and the integration of electronically controlled devices and PLCs in multiple others.

## INTRODUCTION

The thermal vacuum lab at Goddard Space Flight Center consists of nine (9) thermal vacuum chambers in Building 7 and one (1) thermal vacuum chamber in Building 10. The chambers in Building 7 range in size from 2'x2' to 12'x15' and are situated in an area covering approximately 7,000ft<sup>2</sup>. Command and control for these facilities is performed by an operations crew, numbering two to four, at various locations within this area, and on two different floor levels. Facility 290 in Building 10 is a 27'x40' vertical chamber that is controlled by a separate operations crew that is also positioned on two different floor levels.

Each chamber averages approximately 3,000 to 4,000 operational hours per year. This volume of work, coupled with the dispersion of the control systems, results in a large operational workload for the facility operators. One main objective of this project is to provide the operations personnel with the technology to more easily manage the amount of work that exists at any given time. In addition, it is also desired to provide real-time access of current as well as archived test data to experimenters in multiple locations. This paper is an update of the progress made to date, with the focus on the new data acquisition system and its expanded role in the overall system.

## PROJECT GOALS

There are five main objectives that this program is intended to address:

### *1. Centralized command and control capability.*

By positioning the facility controls in a centralized location, the capacity of the operations staff is effectively maximized without increased risk. This implies replacement of most manual controls with computer based operation.

### 2. Greater testing flexibility

The ability to alter data presentation to the operator or customer is highly valued, but very laborious if not built in from the beginning. Custom screen development without the need of a programmer was a top requirement for the new system.

### 3. Improved data accessibility

The current thermal vacuum data system stores data in a binary format on a proprietary Hewlett Packard network. HP no longer supports this network, and data retrieval from the archival media is quite tedious. The new system seeks to make test data readily available to anyone with a network connection.

### 4. Increased payload and personnel safety

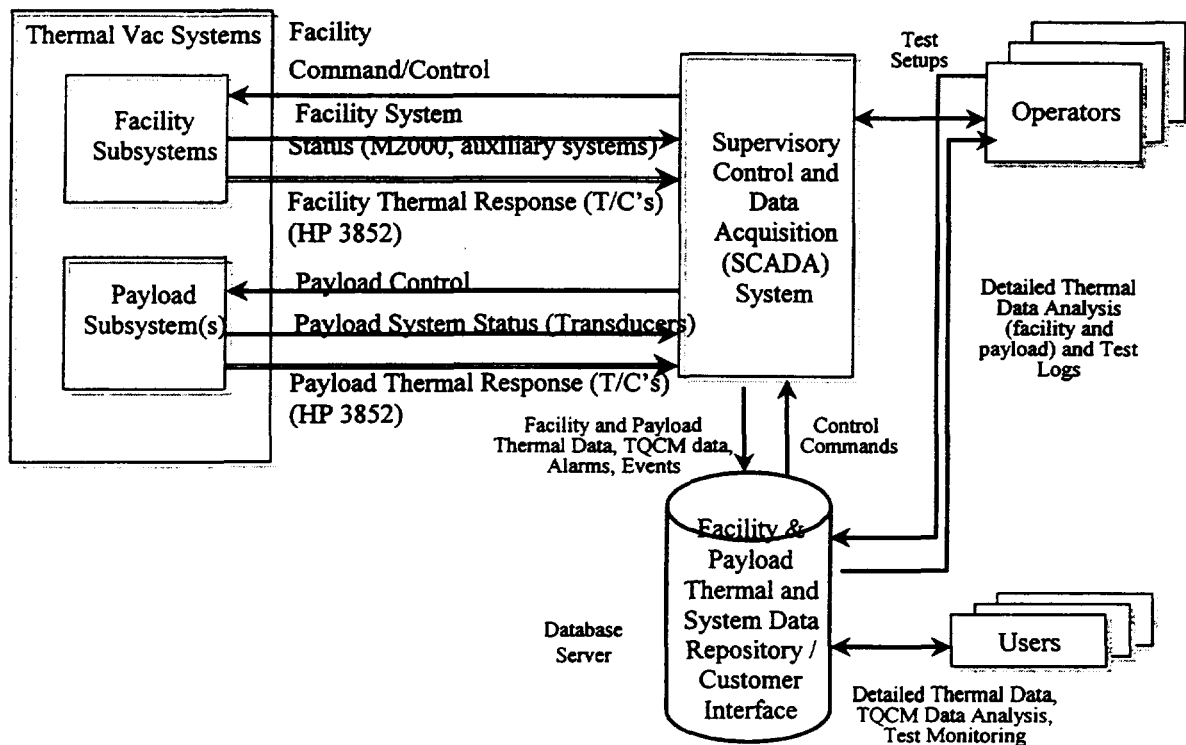
By providing the facility operators with real-time access to all critical chamber and payload parameters, payload safety is inherently increased. In addition, by making the information available to the operators at a single site, personnel safety is improved as well.

### 5. Overall reduced testing costs and improved performance

The net result of these cumulative efforts will be a more efficient and effective laboratory operating at a higher performance level.

## DESIGN PHILOSOPHY

A new approach was taken in the design for the laboratory. Once entirely separate entities, the facility command and control now interfaces with the payload data acquisition system. Command and control is still exclusively handled by the Programmable Logic Controllers (PLCs) and associated SCADA software, however, for some tasks the PLC actually receives inputs from the data system side of the project. A top-level functional diagram is shown below:



## **DATA SYSTEM**

For the purpose of this discussion, the new data system can be divided into three main subsystems; the Oracle Database Engine, External Interfaces, and the PowerBuilder Interface.

### ***Oracle Database Engine***

The core of the new data acquisition system is the Oracle Database Engine. The Oracle Database Engine was selected for its inherent flexibility and power. Oracle easily handles our data storage requirements and provides a powerful scripting tool. The database table structure includes support for alarms, custom client display definitions, data acquisition commands, security, test data storage/retrieval, and chamber automation. Database tables are normalized by the use of primary and foreign keys. A timestamp, tagname and test number uniquely identifies test data. Data acquisition, alarming, calculations and chamber automation are accomplished through the use of Oracle stored procedures and triggers. Stored procedures and triggers provide consistent application of business rules and a single point of maintenance. The use of Oracle transforms the data system into a Test Data Management System rather than just a mere data acquisition system.

### ***External Interfaces***

**SCADA to HP3852A:** Facility and payload thermal data is acquired by HP3852A-Data Acquisition units located throughout buildings 7 and 10. The HP3852A's are remotely interfaced to SCADA by the HP2050A LAN to IEEE-488 Gateway. The HP2050A allows remote operation of IEEE-488 instruments. A custom C language SCADA program was developed using the HP Standard Instrument Control Library (SICL). The C program reads and forwards HP3852A scan commands from Oracle. Scanned data is read back from the instruments and inserted into Oracle tables.

**SCADA to M2000:** Chamber contamination data is acquired by three QCM Research model M2000 data acquisition systems. The M2000 is directly connected to SCADA by a built in RS-232 interface. A custom SCADA driver controls M2000 operation and data collection. The driver functions by mapping SCADA real time database elements or tags to M2000 commands. The driver supports all M2000 modes of operation including calibration, operation and setup. Local control of the M2000 is performed through a SCADA software interface. Remote control of the M2000 is performed by an Oracle automation interface. The Oracle automation interface supports TQCM temperature control and criteria calculations. This functionality permits the unattended operation of facility bakeouts.

**SCADA to ORACLE:** The SCADA to ORACLE interface is the mechanism used for logging data collected by PLC's, HP3852A's, M2000's and future auxiliary systems. A custom C language SCADA program processes the data. The program was developed using the ORACLE Objects C Library. The Oracle library provides the hooks to write embedded SQL with C. This interface is faster, more flexible and lower cost than the Factory Link native Oracle interface.

### ***PowerBuilder Interface***

The Human Machine Interface is the "front-end" system that provides access to all measured test data. The use of PowerBuilder for the human machine interface allows for a Windows based client/server application that connects to the Oracle Database Engine. PowerBuilder applications are developed using PowerScript, an object oriented programming language that lets the developer dynamically control objects throughout the application. Techniques such as encapsulation, polymorphism and inheritance, which object oriented programming provides, allow for efficient, powerful and reusable code. The interface is run from an executable file residing on each computer or client. By running the application from each client, the server can be used exclusively for writing and retrieving data.

The interface is designed so that each chamber may be monitored from any computer at any time. Each computer independently retrieves data from the database tables. This allows for unique custom display editing of the same test for every computer. By reading data points for database tables instead of directly from the A/D boards, the user can look at data at any point in time, either as it is acquired or from hours or days past. The Oracle database is broken up into a series of tables based on each facility. This was done for two reasons. By limiting tables to hold data specific to a facility the size of the tables may be smaller and

easier to maintain, and it allows for a faster retrieval of data. Due to the large volumes of data that are involved in thermal vacuum testing, the speed of data retrieval is very important.

The presentation of data within the application can be customized both before and during the test without interrupting incoming data or other computer displays. Options available to the operator include activating or deactivating measuring devices or tags, setting alarms for any tag, configuring and monitoring multiple TQCM devices, creating and editing averages and gradients dynamically, access to tag libraries and printouts of all relevant data and test information. Data can also be saved and exported to a variety of file types including Plain Text, Microsoft Excel and Data Interchange format.

Data can be visualized in two formats: tabular and graphical. Both formats can present current test data as well as historical data from current or previous tests. By allowing the operator to customize each screen through simple screen editors, relevant data can be grouped together in any fashion so that tests can be monitored safely. The tabular data format displays measured test data on tab pages in columns. Each tab page can display up to 160 tags and up to 30 tab pages can be defined for each chamber. Data displayed in graphical or plot form is useful for monitoring trends during a test. Up to eight tags can be displayed on each plot and 30 plots can be defined for each chamber.

### **CONCLUSION**

Implementation of the new control and data acquisition system at Goddard is leading to improved lab efficiency and flexibility. Experimenters now have the ability to view real-time as well as historical data in a variety of ways, all user customizable. In addition, facility operators now have improved access to all chamber data from any and all locations throughout the laboratory.

# SIMULATED SPACE DEBRIS IMPACT EXPERIMENTS ON TOUGHENED LAMINATED THIN SOLAR CELL COVER GLASS

Robert Roybal, Pawel Tlomak, and Charles Stein  
Air Force Research Laboratory, Space Vehicles Directorate, VSSE

P. H. Stokes  
Space Debris Group, Space Department, Defense Research Agency

## ABSTRACT

Increasing demands on the design criteria of space craft components have driven efforts to develop advanced space debris ground simulation techniques suitable to be incorporated into a space environmental effects chamber. A laser driven flyer method suitable in such a chamber was used to conduct an initial investigation of space debris impact on a new toughened solar cell coverglass material. Damage characteristics, including mechanical damage and contamination generated by impact with a 3 mm diameter, 3 micron thick aluminum particle accelerated to 4.5 km/s, were looked at. Scanning electron microscopy, optical microscopy, and spectrophotometry were used to measure the mechanical damage and the loss of solar transmission. Because of the limited number of impact tests made in this initial study a quantitative analysis was not possible. However, much insight was obtained from the observed damage.

## INTRODUCTION

Spacecraft placed in low-Earth orbit (LEO) are exposed to a large flux of hypervelocity impacts with small particles of natural space micrometeorites and man generated debris (ref. 1, 2, 3 and 4). At risk are the proposed satellite constellation systems. These satellite constellations, predominantly used for communication systems, will be placed in low Earth, nearly polar, orbits. Because of the overall cost associated with the number of satellites required and the environmental issues involved with the orbital location of the satellites, design criteria must include the use of advanced spacecraft materials that reduce launch cost and still maintain high survivability merits (ref. 5). The implementation of innovative large area solar panels to reduce the cost and complexity of solar arrays requires the generation of an advanced coverglass capable of providing high operational solar transmission along with the necessary strength for fabrication, launch survival, and debris impact resistance.

The solar coverglass designed by Pilkington Space Technology (PST) is an effort to increase the cost efficiency of producing large volumes of spacecraft components (ref. 6). The active cell area is increased substantially, up to 0.1m<sup>2</sup> in area, reducing the number of components and allowing for the mass production of arrays. The traditional method for producing solar panels requires placement of a large number of interconnected small area cells onto delicate light weight substrates. This traditional method is labor intensive and requires highly skilled fabrication techniques.

A large area cell array relies primarily on the toughness of the coverglass. During fabrication the solar cell array and satellite must withstand the rigors of ground handling. Launch and deployment stresses must also be considered in the design strength of the solar cell arrays. A proprietary PST process is used by Pilkington to produce a strengthened coverglass by toughening both sides of a single large area glass. An active material such as a cadmium telluride thin-film, may be deposited onto the coverglass sheet which acts as a substrate. To achieve a suitably toughened laminate assembly, a second toughened coverglass is laminated to the first coverglass sheet with a resin layer between them.

A cross section of a typical coverglass laminate is shown in Figure 1. Silicon cells may also be fabricated by adhering two toughened cover glass sheets to a matrix of several large area silicon cells.

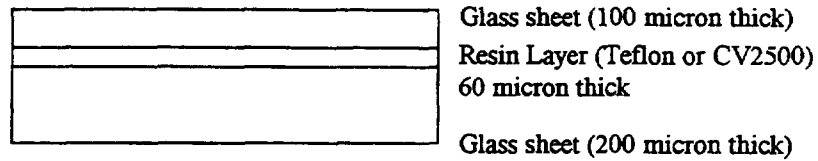


Figure 1. Cross section of a toughened solar cell coverglass.

## EXPERIMENTAL

The technique used to accelerate the particles is a laser driven flyer method as described in (ref. 7). A laser is used to vaporize the interface of a metal foil diffusively bonded to a glass substrate. A neodymium-glass, pulsed laser with energies ranging from 2 -5 joules with a 18 nanoseconds pulse was used in this work. The vapor reaches high pressures in the giga Pascal range and then cuts out and accelerates a metal disk the diameter of the periphery of the laser beam. Typical dimensions of flyers accelerated with this technique range from diameters of 500 microns to 3 mm with thickness of 3 to 25 microns. Velocities from 4.5 to 7.5 km/s have been achieved by the authors. Higher velocities are reported by others (ref. 8). This method is suitable for accelerating small, flat particles to hypervelocity impacts with targets in a space environmental effects chamber.

Impact testing on the Pilkington coverglass has been completed using flat aluminum flyers 3 mm in diameter and 3 microns thick. Work using this size particle was performed at Los Alamos National Labs. Further tests using smaller diameter particles are in progress at the Air Force Research Laboratory, Phillips site. The coverglass targets in the present work consist of two thin glass sheets laminated with a thin layer of Teflon or CV2500 resin. The glass varied in thicknesses, such that, laminates were fabricated with a combination of 100 and 200 micron thick glass, as well as with two layers of 300 micron thick glass. Target sample areas of solar coverglass were 40 mm by 40 mm. The samples were placed in a small vacuum chamber during testing. In order to minimize the effect of air cushioning the flyer impact. A diagram of the experimental setup is shown in Figure 2.

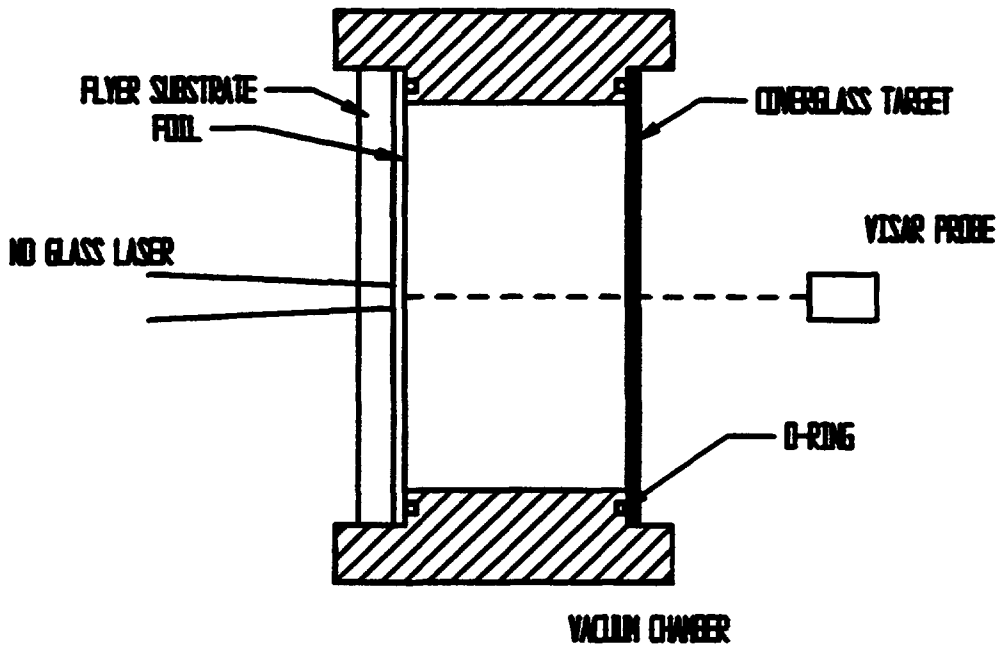


Figure 2. Schematic of cross-section of experimental setup.

The coverglass target was held in place with the same o-ring used to maintain vacuum. This mounting method avoids stresses introduced by a rigid fixed mount. The flyer traveled a distance of approximately 12 mm before impacting the target.

Velocity measurements of the flyer were made using a velocity interferometer system for any reflector (VISAR) manufactured by Valyn international (ref. 9). This technique uses an interferometer to measure a small Doppler shift in light frequency given to a beam of a "green light" from a diode laser as it is reflected from the moving flyer surface. The Doppler shift produces a number of light fringes in the interferometer proportional to the flyer velocity. Data reduction consists of counting the number of recorded light fringes produced in a given time and multiplying by a velocity-per-fringe constant of the interferometer to obtain a velocity. Since the solar cell coverglass target is transparent, velocity measurements of the flyer may be made through the target.

Only one impact was made per target. This was done to assess the amount of redeposited contamination attributed to ejecta from a single impact. The geometry and orientation of the flyer upon impact was determined by inspecting the shape of the impact crater. If a flyer impacted at an angle other than normal to the target, the crater produced would be non-symmetrical. The crater size should closely match the laser spot size if the flyer remained intact. Previous work employed a streak camera to characterize the flyers in flight (ref. 10). From this earlier work it was observed that the flyers remained intact and flew parallel to the target for the flight distance used in that experiment. Therefore we assumed another diagnostic for the monitoring integrity and orientation of the flyer is the intensity of the VISAR return signal. If the flyer maintains its' integrity and orientation the return signal is remains continuous.

## RESULTS

The damage observed in these experiments included: front surface cratering, front and rear surface radial and concentric cracks, rear surface uplift and spall; and contamination in the form of vaporized material ejected from the crater, some of which redeposited on the front surface. The mechanical damage to the targets was characterized using optical and scanning electron microscopy. In order to avoid charging by the electron beam scanning electron imaging required that the sample be electrically conductive. Because the coverglass is made of nonconductive materials, we coated the surface of the sample with a thin layer of gold and palladium which was sputtered onto the target surface. Figure 3 shows a typical optical micrograph image of an impacted coverglass target in which the mechanical damage resulted from an impact at 4 km/s. Radial cracks extend from the impact crater to the edge of the 4 cm sample. The dashed circle in the image represents the size and impact location of the 3 mm flyer. Figure 4 is a typical SEM image of the rear surface of an impacted target and shows that some glass material has been removed from the rear surface. The predominant damage observed on the rear surfaces of targets was cracking and uplifting of the glass, however the glass remains attached to the laminate, similar to common safety glass. This effect is shown in the optical micrograph of Figure 5.

Images of the cross section of coverglass targets were made and are shown in Figures 6 and 7. Figure 6 represents an area away from the impact site. The laminate is intact but was slightly damaged from the cross-sectioning process. The layers of glass laminated to a 60 micron thick Teflon resin layer are clearly visible. Figure 7 shows a typical image of the cross-section of an impacted cover glass laminate sample. The impacted side, as well as the surrounding areas, suffered extensive damage to all layers of the glass laminate. The damage included extensive cracking of the glass layers and permanent deformation primarily within the impact area. Upon impact, the aluminum particle formed a crater concave towards the impact direction. As a result, the glass on the impact side was extensively cracked but still remained attached to the deformed laminate. On the other hand, much of the cracked glass on the rear side of the impacted cover glass was uplifted and spalled off.

Contamination from the vapor blown out of the impact crater may actually be the most serious consequence of damage to the cover glass, when considering the overall efficiency of the solar cell. An interesting phenomena is seen when examining the deposition of ejecta from the impact crater onto the target surface. The ejected material forms bands of different material densities radiating out from the crater. Figure 8 is a schematic diagram of the impacted sample shown in Figure 3. Area (A) represents the size of particle impacting the surface. Region (B) is the crater area in which material has been removed from the target. While molten aluminum is found in Area (C). Aluminum is also found on the entire

sample in the form of trace deposited vapor. Area (D) remained relatively free of re-deposition. While at a distance of over 1 cm from the impact site, area (E), the surface is heavily coated with the vapor removed from the crater.

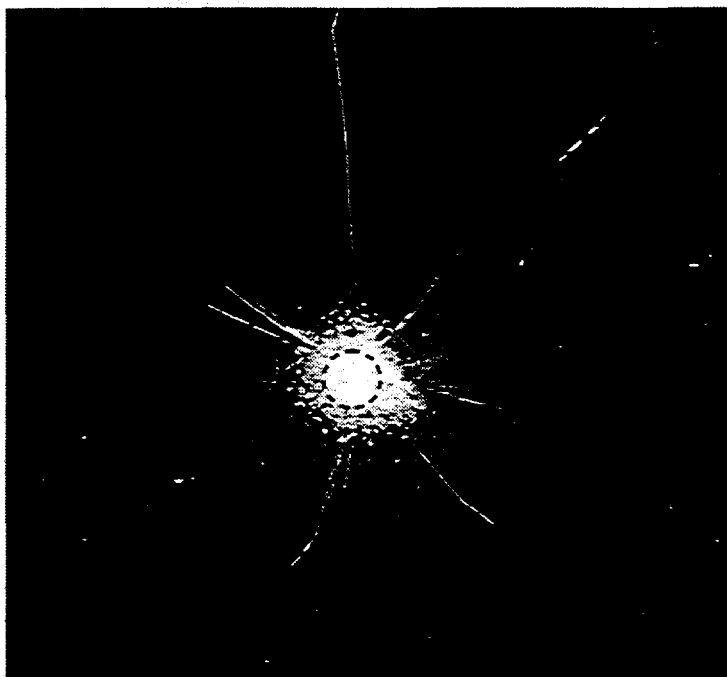


Figure 3. 4X Optical image of a coverglass laminate.

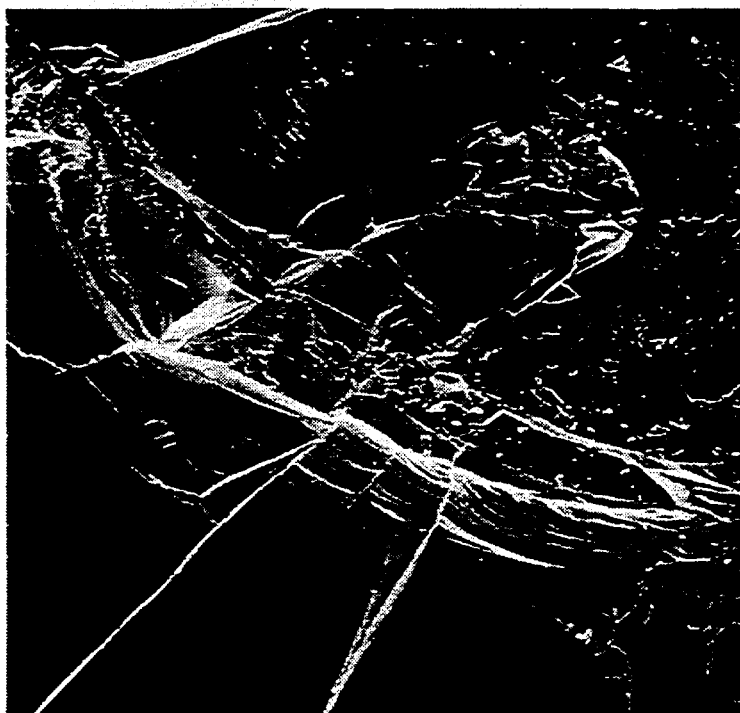


Figure 4. 40 X Typical SEM image of rear surface of a coverglass laminate.



Figure 5. 10X Optical image of a rear surface of a coverglass laminate.



Figure 6. Optical image of a cross section of a non-impacted laminate.

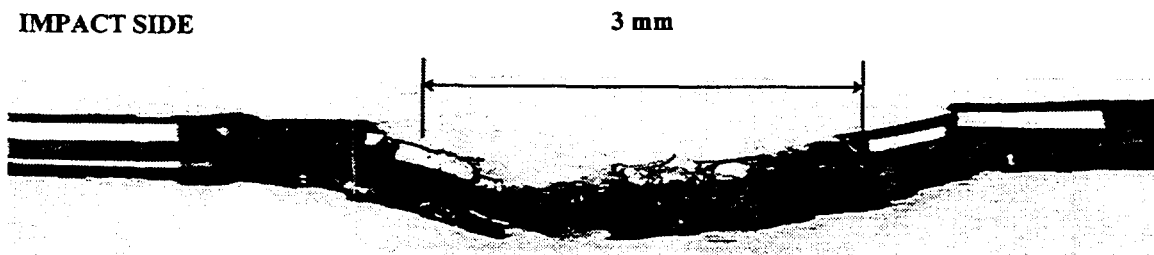


Figure 7. Optical image of a cross section of an impact site on a coverglass laminate.

An elemental analysis of the coverglass surface was completed using a PGT energy dispersive system attached to our scanning electron microscope, and produced the qualitative elemental analysis shown in Figures 9, 10 and 11.

Figure 9 shows a baseline spectra consisting predominantly of silicon and potassium for coverglass sample that has not been impacted. Figure 10 is an energy dispersive spectra of the impact crater, area (A). In the crater area much of the glass is removed revealing the resin layer below resulting in the presence of fluorine and carbon. An energy dispersive spectra in Figure 11 was collected for area (E) on the coverglass.

The above spectra show that a deposition of fluorine, carbon, and aluminum is now present in regions of the once clean surface. The fluorine and carbon are generated from the vaporization and ejecta of the Teflon resin layer of the laminate. The probable source of aluminum comes from vaporization of the aluminum flyer.

Light transmission measurements were over the wavelengths from 300 nanometers to 1500 nanometers made using a Cray 5 eV Spectrophotometer through impacted targets and control samples. This wave length range covers the useful solar spectra for solar cells. Figure 12 compares transmission spectra of an undamaged control sample to transmission spectra measured in area (E) 1.6 cm from the crater of an impacted sample. These spectra show that a maximum transmittance of 90 percent exists at the wavelengths of interest in a control sample. While degradation in the original sample transmittance of approximately 10 percent was measured across area (E) of the impacted sample.

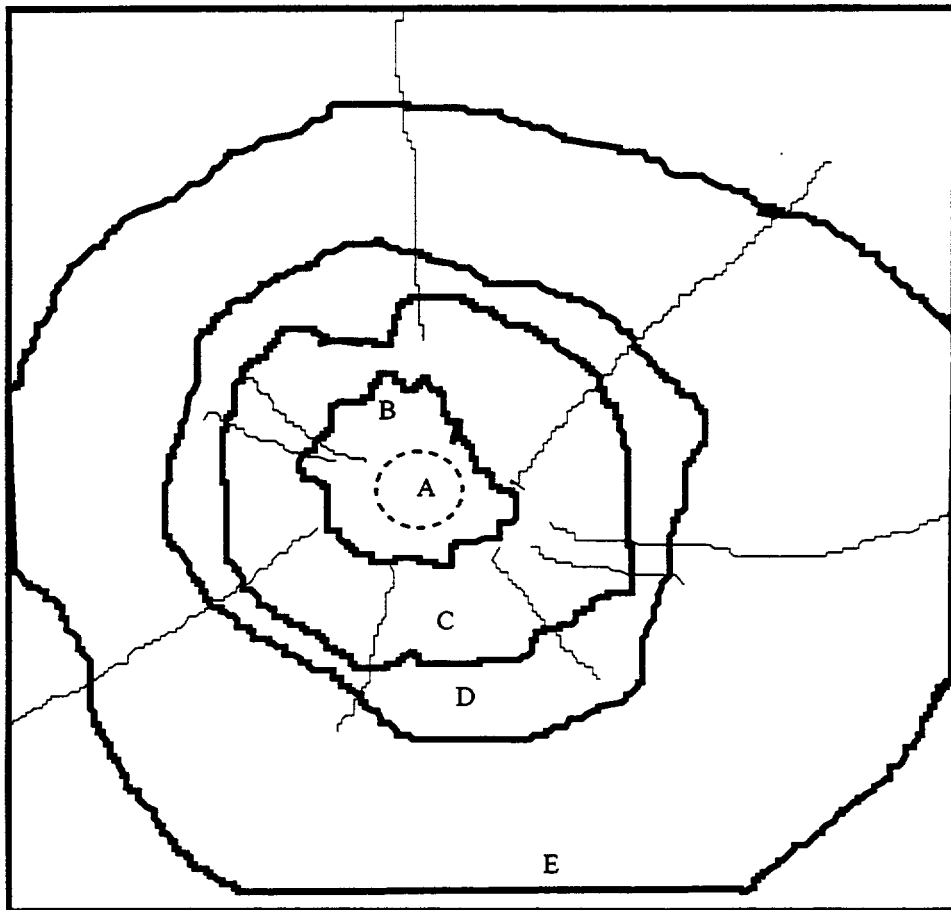


Figure 8. Schematic of an impact area showing outlines of re-deposition regions.

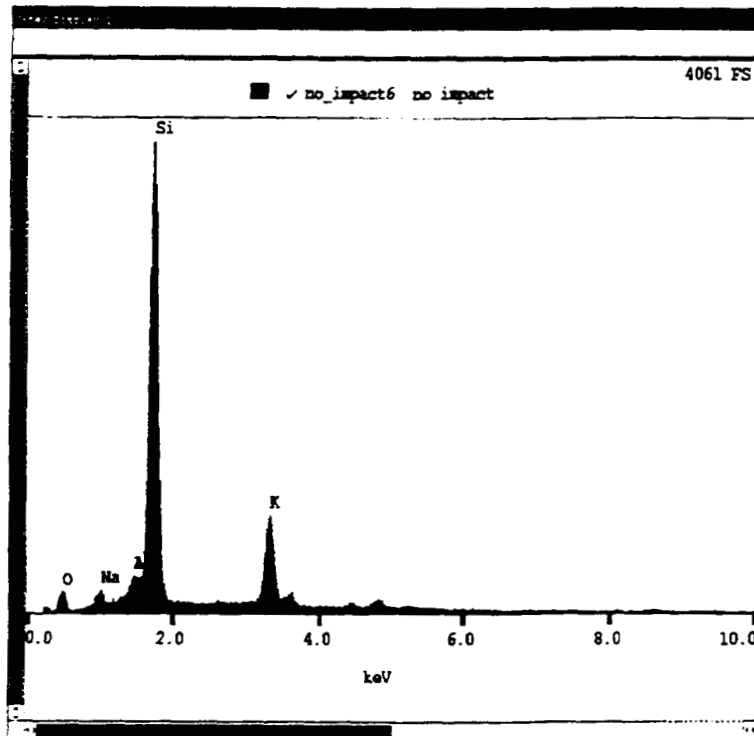


Figure 9. Energy dispersive spectrum of a non impacted coverglass.

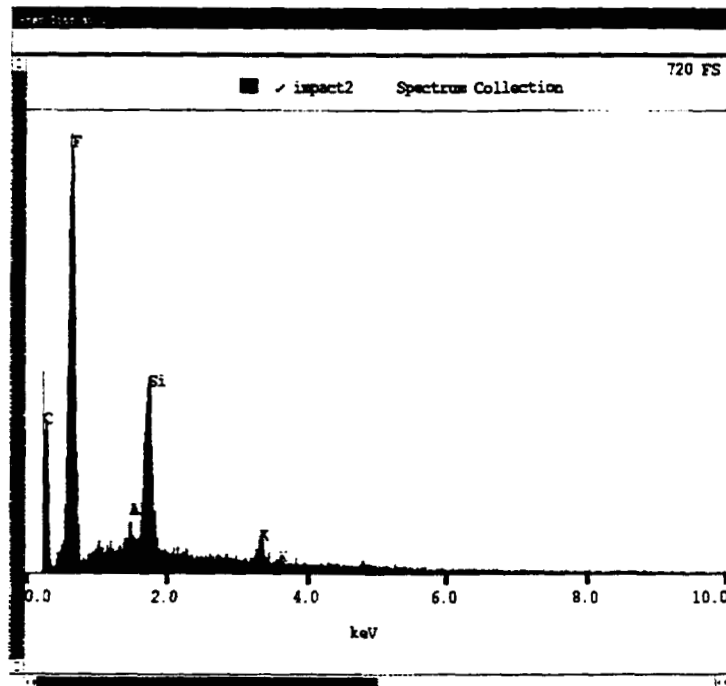


Figure 10. Energy dispersive spectrum of the crater area (A) on an impacted coverglass.

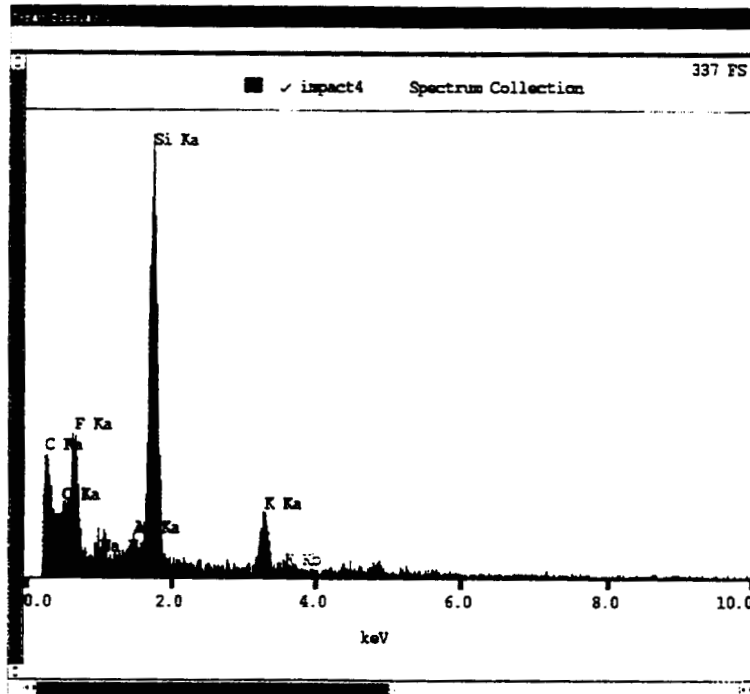


Figure 11. Energy Dispersive spectrum of area (E) on an impacted coverglass.

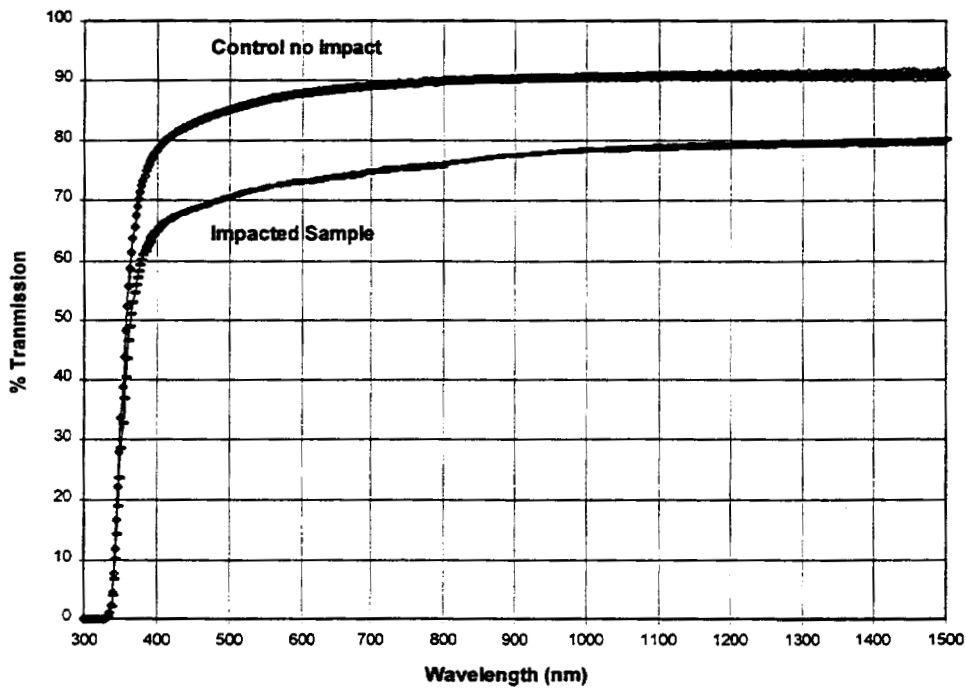


Figure 12. Transmission spectra of UV light through a coverglass target, pre and post impact.

## DISCUSSION AND CONCLUSIONS

The results of our investigations revealed a very complex morphology at the damage site of the cover glass samples exposed to hypervelocity impacts by aluminum debris particles at velocities ranging between 2.5 km/s and 5.0 km/s. The range of velocities and energy used in these experiments are relatively small and were limited by the configuration of the laser used in this set of tests. As such, the data reported in this paper are not sufficient to establish a quantitative relationship between the debris' velocity, its kinetic energy and the size and geometry of the post impact damage sites. Nevertheless, the results of our semi-quantitative analyses clearly indicates that there is a typical damage pattern consisting of both mechanical damage and contamination. Formation of the impact crater is accompanied by the presence of molten aluminum and post impact deposition of contamination on the surface of the damaged cover glass sample. The ejecta consists not only of the cover glass laminate material removed from the crater, but some fragments of the aluminum debris particle as well. Degradation of the solar cell efficiency due to loss of solar transmittance may be more critical to the solar cell performance than the actual mechanical damage from impact. Over 90 percent of the total sample area experienced at least a 10 percent loss in initial solar transmission. Results of our work presented in this paper are a part of our consistent and comprehensive effort to investigate the response of nonhomogeneous and composite materials to a very harsh space environment, including hypervelocity space debris impact damage.

## REFERENCES

1. Schneider, E., "Micrometeorite impact on solar panels", Proceedings of the 5<sup>th</sup> European Symposium: 'Photovoltaic Generators in Space', Scheveningen, The Netherlands, 30 September, 1986.
2. Rose, F. M., "Hypervelocity impact on solar cells", NASA Technical Report, NASA-CR-192444, Jan. 1993.
3. Dursch, H., "Results from testing and analysis of solar cells flown on LDEF", Proceedings of the LDEF Materials Workshop, NASA Langley, Part 2, pp. 649-660, September 1992.
4. Herbert, M. K., Kay, L., and McDonnell, J. A. M., "Decoding the Evolution of Rear Impact Morphologies on The Hubble Space Telescope Array", Proceedings of the 7<sup>th</sup> International Symposium on 'Materials in Space Environment, Toulouse France, June 1997.
5. Crowther, R., Marsh, V., Stokes, H., Walker, R., "Interaction Between Space Systems And The Orbital Environment", SPIE Conference, Denver, August 1996.
6. Kitchen, C. A., Dollery, A. A., Bogus, K. K., "Teflon bonding of solar assemblies using Pilkington CMZ and CMG coverglass- Now a production process." AIAA paper 94-3969, pp. 257-262, 1994.
7. Roybal, R., Shively, J., Stein, C., Miglionico, C., "Laboratory Simulation of Hypervelocity Debris", Proceedings of the 19<sup>th</sup> Space Simulation Conference, a NASA Conference Publication 3341, Baltimore, MD, October 28 - 31, 1996.
8. Paisley, D. L., et. al., in Ultra- and High-Speed Photography, Videography, Photonics, and Velocimetry, Proc. SPIE Vol. 1346 ,pp. 172-178, 1990.
9. Barker, L. M. and Hollenbach, R. E., "Laser interferometer for measuring high velocities of any reflecting surface", J. Appl. Phys. 43, pp. 4669-4675, 1972.
10. Roybal, R. and Tlomak, P., "Hypervelocity Space Debris Testing", Proceedings of the AIAA Defense and Space Programs Conference, Huntsville, AL, September 23-25, 1997.



# SMALL-SCALE DIGITAL PHOTOGRAMMETRY IN A CRYOGENIC VACUUM ENVIRONMENT

Richard E. Pazar  
Goddard Space Flight Center  
ManTech Systems Engineering Corporation

## **ABSTRACT**

A thermal vacuum test fixture was designed, built, tested and operated to position and protect a digital photogrammetry camera in a thermal vacuum chamber. The purpose of the work was to determine the mechanical deformations of the MAP (Microwave Anisotropy Probe) spacecraft as it was cooled from ambient temperature (293° Kelvin) to approximately 20° Kelvin. This paper describes the reasoning and methodology that were used to create the machine.

## **INTRODUCTION**

### MAP SPACECRAFT

The MAP spacecraft is designed to measure the temperature fluctuations of the cosmic microwave background. It has a very high resolution and a small field of view. It will use passively cooled differential microwave radiometers and dual Gregorian primary reflectors. MAP will be launched in the Fall of 2000. It will use a Delta-II launch vehicle, and have a halo orbit about the L2 LaGrange point. Further technical details of the spacecraft may be found at the MAP website, <http://map.gsfc.nasa.gov/Default.html>.

### PHOTOGRAMMETRY

Photogrammetry is the science of determining the size, shape and location of objects by photography. In simplest terms, photogrammetry relies on triangulation to determine the distances between points. The triangulation may be achieved with three images, two images and a common point, or within one image, a known scale, and several points. It has been used for aerial mapping since Civil War times, using daguerreotypes taken from balloons. Until recently it was an entirely optical process and was used mainly for aerial mapping and intelligence work.

Recent developments in digital photography have made photogrammetry a practical method for documenting objects of virtually any size. It was the method of choice for recording the deflections of the MAP reflectors. Photogrammetry introduces virtually no mechanical stresses on any object, and the heat load of the necessary photographic flashes was found to be negligible.

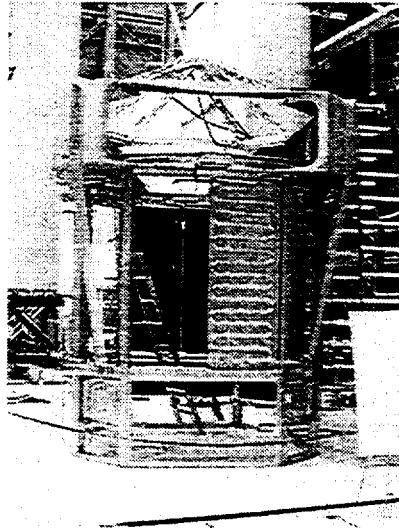
NASA worked closely with Geodetic Services Incorporated (GSI) of Melbourne, Florida, to determine the photogrammetric methodology needed to record the reflector deflections. It was decided that this was best done by rotating the camera about the spacecraft near the top of the reflectors, the camera pointing in and down at 45°. GSI is also the manufacturer of the photogrammetry camera and software used in the test.

## **DESIGN OF THE ROTATION FIXTURE**

The final definition of camera positions was made in late December 1997. Twenty-eight positions about a 10.5 Ft. diameter circle were required, the camera pointing toward the center and down at a 45° angle. The twenty-eight positions comprised approximately 350° of arc. It was also necessary to be able to rotate the camera 90° about its optical center. The photogrammetry camera needed to be protected from the extreme cold and vacuum. The fixture needed to be complete and ready to use by May 1998.

A number of decisions were made and conditions established at this point concerning the mechanical design of the fixture. They were:

The photogrammetry fixture would be built into the existing eight-sided crowned thermal vacuum fixture originally built for the Mid-Space Experiment (MSX) spacecraft.



Thermal Vacuum fixture during build-up. Note cryogenic panels. In this test helium was circulated through them.

It is a close fit for Delta payloads and supports either heater or cryogenic panels quite close to the spacecraft. The cryogenic panels would be cooled by helium.

No lubricant could be used. The cleanliness requirements of the spacecraft would not tolerate the few lubricants compatible with the conditions of vacuum and temperature.

A separate stepper motor would be used to drive each mechanical motion.

A canister would be used to isolate and protect the camera from the cryogenic vacuum environment. It would be maintained at 293° Kelvin and one atmosphere or very slightly higher pressure. Rotation about the camera's center would be done by rotating the canister and the camera.

A two-piece quartz window, supplied by GSI, would be used in the canister.

Wherever possible, materials and fits would be chosen so that running clearances would open, rather than tighten, with thermal contraction. Springs would be used to maintain constant pressures where necessary.

Materials used would be aluminum, 300 series stainless steel, and brass. Carbon steel, cast iron and other ferrous alloys could not be used because of temperature or outgassing criteria.

Wherever possible, items proved out by analysis to be workable would be used throughout the fixture.

The machine could not be designed for a long wear or fatigue life, given the complete lack of lubrication.

The fixture consists of four subassemblies. They are:

Camera and canister, and associated mounting parts

Great Wheel

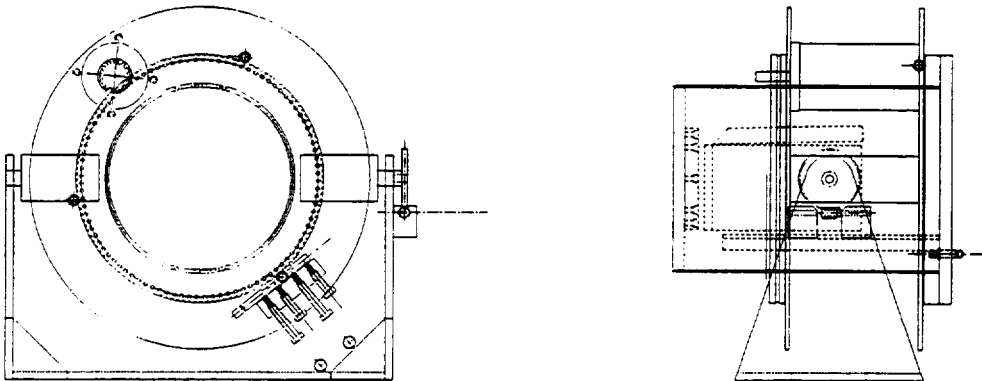
Great Wheel Drive

C-Frames and Great Wheel support

Illustrations of the various parts follow.

The camera and canister mount on a pair of round plates. Stainless steel ball bearings are mounted on the plates and the canister rotates on the bearings. There are twelve bearings which locate the

Camera, canister and Rotator, showing peg gearing and stepper motor

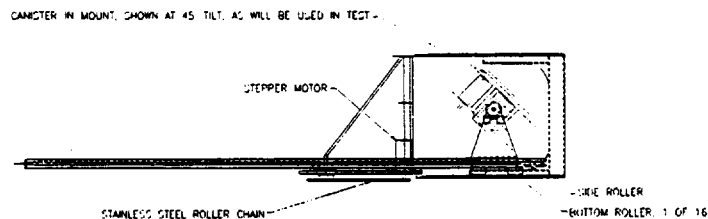
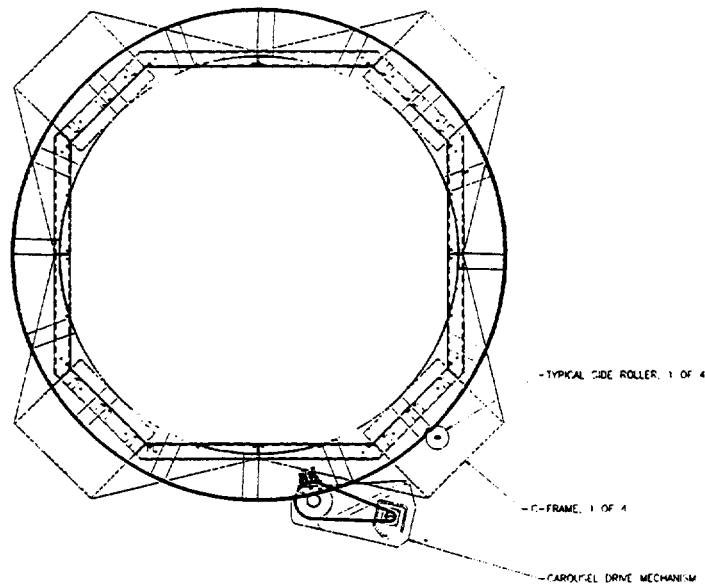


canister axially and radially. Two of the bearings are mounted on spring-loaded arms. This was done to provide compensation for thermal contraction. The bearings are tiny and do not have preload. The stepper motor for

canister rotation also mounts onto these round plates. The round plates are mounted on trunnions. The trunnion journals are mounted in a fork-type frame. This has a worm and worm gear, manually operated, to adjust tilt angle.

Gearing for the canister rotator is a throwback to 18<sup>th</sup> century mill practice. The canister has gear teeth, which are simply stainless steel pegs, threaded into the end flange. These engage with a pinion gear mounted on the stepper motor. The pinion gear teeth are unusually long, and the fit is loose. This was done to ensure that gear tooth mesh would be maintained at the extremes of thermal contraction. This worked well.

The Great Wheel is an aluminum weldment, hollow in the center. It consists of two thin rings, each made of four segments welded together, and connected by sixteen ribs. The wheel was deliberately made very light, for ease of handling as well as minimizing the radiative area. It is self-suspending, in that it will deflect to contact the support rollers when the section of the wheel supporting the canister assembly passes over them. This was necessary because of the enormous variation in weight over the diameter of the wheel. Approximately 20° of arc of the wheel are significantly loaded. The other 340° has virtually no load.

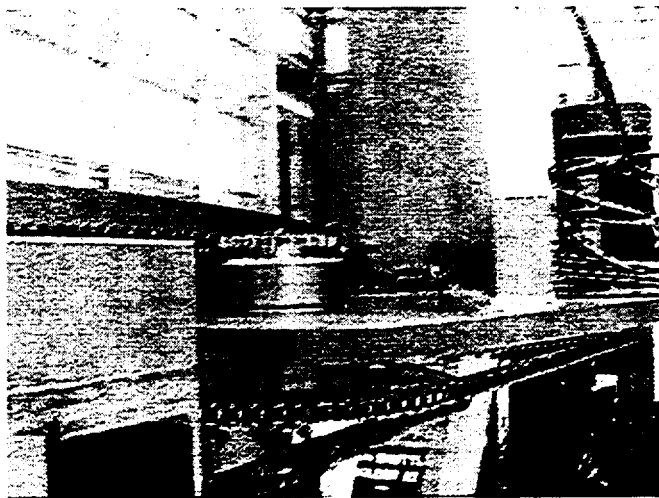


Plan and Elevation views, showing Great Wheel, C-frames and canister



Primary drive and helium plumbing

Eight hundred and twenty links of #40 stainless steel roller chain were wrapped around the Great Wheel weldment, turning it into an enormous gear. One end was fixed firmly to the wheel, the other end led through to the annulus between the rings and was spring loaded. The springs were stretched approximately two inches. This was done because the aluminum wheel contracts more than the stainless steel chain, and a



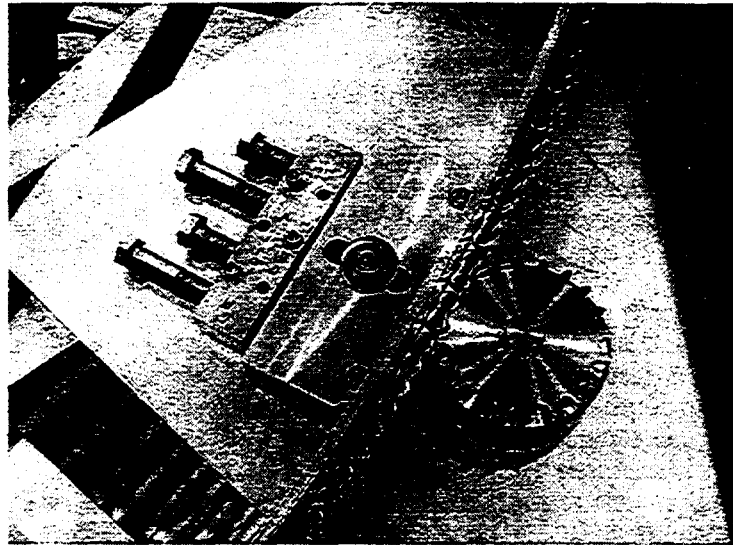
Final drive sprocket, Great Wheel, primary drive and drive plate. Stepper motor is in background.

means had to be found to keep the chain wrapped tightly at all temperatures. This worked well, but did introduce a temperature dependent gear ratio. This was compensated for in the stepper motor control software.

The Great Wheel drive consists of a hinged plate, a stepper motor, a primary chain drive, a final drive sprocket, and a spring-loaded traveling shoe. The shoe holds the Great Wheel and final drive sprocket in contact. The final drive sprocket drives the #40 chain wrapped around the Great Wheel. The stepper motor is mounted on a spring-loaded floating plate, so that chain tension is always maintained regardless of thermal excursions. This constant tension allowed a horizontal chain orientation (which is normally very bad with chain drive due to droop).

The primary drive output side sprocket and final drive sprockets are mounted on a common shaft, and use grooves machined into the hinged plate and the sprockets themselves as ball races, creating a crude pair of ball bearings. Preload was determined empirically and was maintained with Belleville washer springs.

Manufactured anti-friction bearings were not used here for several reasons. The first reason is that the thermal contraction of the various pieces would cause any conventional ball bearing to lose its preload and become loose. Other reasons were the long lead times and difficulty in obtaining larger stainless steel bearings. Stainless steel tapered roller bearings would have been ideal, but, unfortunately could not be gotten in time. The ball races had become rough after approximately ten hours of running but did not impair the operation of the fixture.



Final drive sprocket, Great Wheel chain, and traveling shoe.

The same stepper motor and controller were used for both the Great Wheel and Canister drives. The motors, indexers, and applicable software were made by Parker Compumotor. The motor was the largest of a family of Parker motors that we have used

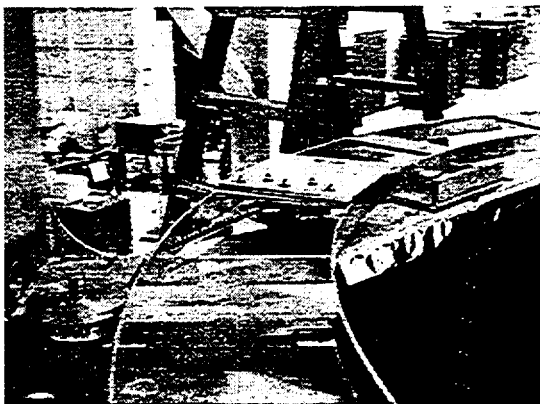
in vacuum in the past with good success. The motor chosen was grossly oversized for both applications. This was done deliberately. Motor sizing for vacuum applications is problematical due to the lack of convective cooling. The additional mass of copper in the oversized motors gives a longer duty cycle before critical temperature is reached. The additional torque was felt to be beneficial in the event of machine parts seizure due to cold. Stepper motors are easily controllable and work well in vacuum, while commutator motors are very unreliable in vacuum.

Heaters were applied to the motors, and the motors were made vacuum ready by disassembly, cleaning out of ordinary lubricants, and replacement with Braycoat 601, which is vacuum compatible. Vent holes were added to the motor end bells and the bearing shields. The heaters were added to maintain a safe temperature so that the aluminum motor end bells would not thermally contract over the bearings, seizing the motor, and also to keep the lubricant within its operating temperature range. The heaters were found to be unnecessary, the quiescent current flow being adequate to keep the motors at a safe temperature. Had the indexers failed, the heaters would have been used to keep the motors at a safe temperature. The motors operated correctly in vacuum.

C-frames, so named for their shape, and Great Wheel supports are aluminum weldments into which all the machinery is mounted. There are four C-frames,, and four auxiliary support roller assemblies. Each has a pair of two-inch diameter brass rollers, so that each ring is supported at eight equidistant points. There are four large side rollers, two of them spring loaded to adjust for thermal contraction of the Great Wheel. The Great Wheel drive is supported by the north side C-frame. Additional rollers and scuff blocks were added during testing.

All of the C-frames and auxiliary support roller assemblies are supported by the MSX fixture structure and are triangulated for rigidity during crane lifts and operation.

Great care was used in the choice of materials and surface finishes. At no point in the



These views show the construction of the Great Wheel, side and support rollers and tensioner for the Great Wheel chain.

fixture are similar metals rubbing or rolling on each other. Where more than two moving parts are in conjunction, they are all different materials. Surface finishes were chosen so that they are all different at the surfaces of contact; i.e. a brass roller would have a 32 RMS finish on it's bore, while it's stainless steel axle has a 16 RMS finish. In the brass roller/stainless axle, the bore of the roller was sized so that at the maximum  $\Delta T$ , there would still be approximately .001" to .003" clearance. These parts were loose fits at room temperature.

#### **FABRICATION, ASSEMBLY AND TRIAL OF FIXTURE**

The fabrication of most parts was by an outside vendor. Because of a very short lead time, parts were farmed out to six different welding and machine shops. Quality varied between parts from different sources, and some time was lost in reworking and/or returning various out-of-tolerance parts. The fixture was in operating condition by June 1998.

The motion of the Great Wheel and the canister is controlled by the stepper motors. The stepper motors are driven by indexers which in turn are controlled by software on an ordinary PC.

The fixture was assembled and tested outside of the thermal vacuum chamber. A period of adjustment followed in which the optimum operating speed of the fixture was found, and the ends of travel established.

Limit switches had to be fabricated. An off the shelf limit switch guaranteed to work in vacuum at the temperatures required could not be found.

A small guide roller and two Teflon guide blocks were added to the fixture to control the location of the Great Wheel. It was found that the Great Wheel would distort when started and could fall off its support rollers; decreasing the rate of acceleration and adding counterweights helped to minimize this problem as well.

The fixture underwent mechanical tryout and break-in at the same time the software was being debugged and tested. It was clear that good communication between the electrical engineer, the mechanical engineer, and the technicians was essential.

The fixture was loaded into the thermal vacuum chamber in June 1998. It was operated first at ambient temperature and pressure, then at ambient temperature and ultimate vacuum, again at 223° Kelvin, and finally at extreme cold soak, wherein some parts of the fixture were at 20° Kelvin and other parts were up to 50° Kelvin. The operation was viewed with a conventional video camera mounted some feet away from the fixture. The fixture operated correctly in all trials.

The only intractable problem in the mechanical design of the fixture was loud squealing and shrieking. We inserted Teflon washers and took other measures to prevent the noise without success. We found, however, that the fixture is very quiet when operated in vacuum.

As of this writing circumstances involving the MAP spacecraft have delayed the photogrammetry test until November 1998. No problems with the fixture are anticipated.

## HYPERVELOCITY METEORITE IMPACT SIMULATION

Shmuel Ben-Shmuel and Selma Goldstein  
The Aerospace Corporation

### ABSTRACT

A model has been created for the numerical simulation of a penetrator particle impacting a plate at very high velocities. The analysis was conducted with the finite element hydrocode, LS-DYNA3D. The model attempts to predict the consequences of a meteorite particle hitting a spacecraft in orbit. Results show that the breakup mechanism of the penetrating particle is highly dependent on the magnitude of the impact velocity relative to the elastic wave velocity (speed of sound) of the penetrator's material. The analysis concentrates on understanding the physics of hypervelocity impact and the importance of parameters such as relative particle and plate sizes, impact velocity, particle shape, and impact angle. Modeling of material properties in the high strain rate plastic regime needs to be augmented and verified with pertinent experimental data. Additional codes may be required for analysis capabilities absent in LS-DYNA3D such as thermal modeling and tracking of the debris cloud generated by the breakup of particle and plate.

### INTRODUCTION

There is a very large number of natural and man-made debris in low earth orbit where many spacecraft are located. The debris clutter is getting worse with the increasing number of new spacecraft launches and with the appearance of occasional meteoroid sources such as the Leonid meteoroid showers coming in November 1998 and November 1999. Larger pieces of debris can be tracked by radar and avoided, and the very small pieces will not cause major damage to a satellite. Intermediate size debris, however, can cause substantial damage up to and including the loss of manned spacecraft. There is growing awareness for the need to incorporate shielding of critical elements in spacecraft design (ref. 1). These concerns have resulted in experimental and numerical work on several spacecraft shielding concepts and the International Space Station, to give one example, has been designed from the start with the debris problem in mind (ref. 2).

Typical spacecraft shields such as the Whipple, Figure 1(a), incorporate a bumper shield, several layers of Nextel and Kevlar, and the back wall. Particles impacting the bumper shield break up into a cloud of fragments, Figure 1(b), which are further slowed down and broken up again during passage through the Nextel/Kevlar barriers. The back wall is not breached if the fragments reaching it do not possess sufficient kinetic energy. The work presented here concentrates on the initial, bumper shield penetration, Figure 1(b), and the subsequent penetrator-plate breakup process. The emphasis of the calculations is on the penetrator's dynamic behavior and the extent of its fragmentation.

Experimental techniques are used extensively in the study of high velocity impacts and on the effectiveness of various shielding concepts for the protection of vital satellites and components. Experimental methods have limitations mainly due to the relatively low velocities that can be achieved. Space debris can reach velocities of 70 km/sec or more while current earth-bound experiments rarely exceed 11 km/sec. Numerical methods have provided experimentally validated calculations in the low end of the impact velocity regime (ref. 1) and can be used to obtain simulations for velocities beyond the range of experimental techniques.

### High Velocity Impact Physics

The governing equations of high velocity impact dynamics are conservation of mass, conservation of momentum, and conservation of energy with inertia effects playing a dominant role (ref. 3). Stress wave propagation in the colliding bodies determines their breakup. Finally, high velocity impact events are transient phenomena; steady state conditions may not exist at all or may be attained long after the penetrating particle and its fragments have reached the final barrier.

The colliding, sliding, and eroding surfaces of penetrator and plate generate shock waves that propagate in both bodies as stress waves. The pattern and extent of the impacting bodies breakup depends on the impact kinetic energy, the shape of the stress waves, their velocity, and the extent of their advance.

The initial stress wave generated by the impact shock wave propagates into unstressed material at the elastic wave velocity (speed of sound) which can be shown to be

$$c = \sqrt{S/\rho} \quad (1)$$

where  $c$  is the elastic wave velocity,  $\rho$  is the material's density, and  $S$  is the slope of the material's stress-strain curve in the elastic regime (ref. 3). The elastic wave velocity in aluminum Al-7075, the material used in the calculations, is 5.2 km/sec. Similarly, plastic stress waves are formed once the material strains are in the plastic regime. Plastic stress waves travel at the plastic wave velocity which is also defined by Equation (1) except that  $S$  is now the slope of the material's stress-strain curve in the plastic regime. Typical plastic wave velocities are lower than their elastic counterparts due to the smaller slope of the stress-strain curve in the plastic regime.

The impact event depends heavily on the relative magnitude of the impact velocity and the elastic wave velocity. At subsonic impact velocities the stress waves will propagate deep into the colliding bodies while they are still in contact. At supersonic impact velocities the stress waves will form on the colliding surfaces and will complete their propagation into the bodies after contact has ended. The breakup process will take place over largely similar times regardless of the impact velocity as the stress waves travel at the material's elastic wave velocity.

## LS-DYNA3D MODEL

### LS-DYNA3D General Overview

LS-DYNA3D, a vectorized explicit three-dimensional finite element hydrocode, has been used to construct detailed computational models for the study of the dynamic behavior of bodies undergoing high velocity impacts. The program solves the time-dependent momentum equations in Lagrangian formulation subject to position and velocity initial conditions, and to traction (force) and displacement boundary conditions (ref.4). Contact discontinuities on internal boundaries are handled by satisfying stress boundary conditions at these interfaces. The code is capable of simulating stress wave propagation in inelastic solids and the resulting high strain rates and large deformations. A contact-impact algorithm permits gaps and sliding along material interfaces and friction can be modeled into the simulation. The code is therefore suited for the analysis of inertial high velocity impact and penetration problems. Inputs for the code are geometry, material properties, and contact surface specifications. The outputs from the code for the modeled system include time histories of the positions, displacements, velocities, accelerations, pressures, densities, energies, stresses, and strains for nodes and elements of all materials. These variables completely define the analyzed system for any point in the calculated time interval.

The energy equation in LS-DYNA3D does not include heat transfer terms and can not simulate thermal effects. This is of no concern in high velocity impacts where the time scales are in the microsecond range. Heat transfer effects require longer times and can be neglected in high velocity simulations.

LS-DYNA3D discards an element from the model after it fails under stress and is therefore unable to keep track of the debris cloud that is generated from the breakup ejecta of penetrator and plate. The scope of this work is therefore limited to the initial penetration of the bumper shield, Figure 1(b). Emphasis has been put on the penetrating particle's breakup behavior as it is of interest for the design of the intermediate shield layers and the terminal wall. Other hydrocodes such as CTH keep failed elements in the calculation, allowing the simulation of subsequent impacts of penetrator and bumper shield fragments with the intermediate layers and the last wall.

## Units

LS-DYNA3D does not have a preferred system of units and leaves its choice to the user. It is common to choose a system that is consistent with the problem's characteristic lengths, masses, and times. The system used in this work is gm, cm and microsecond ( $\mu\text{sec}$ ). LS-DYNA3D results are given in the following units -

Velocity -  $\text{cm}/\mu\text{sec} = 10^1 \text{ km/sec}$

Acceleration -  $\text{cm}/(\mu\text{sec})^2 = 10^{10} \text{ m}/(\text{sec})^2 = \sim 10^9 \text{ g}$

Pressure, stress - Megabars (Mbars) =  $10^6$  atmospheres

Energy -  $10^7 \text{ N-cm} = 10^5 \text{ Joule}$

## Finite Element Model

The model includes only two parts, a penetrator and a plate. Most configurations were reduced to a quarter model due to symmetries, except for the oblique angle case which required a half model. The calculations were performed on a Sparcstation 10 machine which imposed practical limitations on the grid size:  $\sim 8500$  nodes and  $\sim 6600$  elements for half the configurations, Figure 2, going up to  $\sim 19,300$  nodes and  $\sim 16,600$  elements for the thick plate case, Figure 3. The plate's grid was clustered around the penetration point to compensate for the relative grid coarseness, resulting in a fine mesh of the impact region. The clustering causes the plate calculations to be somewhat grid dependent.

Both penetrator and plate materials were assumed to be aluminum (Al-7075) whose elastic wave velocity is 5.2 km/sec. LS-DYNA3D lets the user choose the material types and the surface contact interfaces according to the problem at hand. The aluminum's material model was set up as an isotropic-elastic-plastic-hydrodynamic type with an equation of state given in (ref. 4). The equation of state is designed for the hypervelocity regime which is typified by high frequency, high magnitude pressures and accelerations. The material fails when it reaches a user selected strain level. The maximum stresses that the material can withstand are therefore determined only by the failure strain and the stress-strain curve, and are independent of the impact velocity. The interface between penetrator and plate was set up as surface to surface eroding contact (ref. 4). The material type and the interface are appropriate for the current problem which is characterized by colliding, sliding, and eroding surfaces. The colliding materials are in the plastic regime immediately after impact initiation, are subject to high strain rates, and behave like fluids.

## Configurations

| Configuration               | 1                     | 2                     | 3                     | 4                     | 5                                   | 6                     |
|-----------------------------|-----------------------|-----------------------|-----------------------|-----------------------|-------------------------------------|-----------------------|
| Penetrator (cm)             | Sphere,<br>1 diameter | Sphere,<br>1 diameter | Sphere,<br>1 diameter | Sphere,<br>1 diameter | Cylinder,<br>1 diameter, 1.5 length | Sphere,<br>1 diameter |
| Plate (cm)                  | 10X10, 0.03<br>thick  | 10X10, 0.03<br>thick  | 10X10, 0.03<br>thick  | 10X10, 0.03<br>thick  | 10X10, 0.03 thick                   | 10X10, 1<br>thick     |
| Impact Velocity<br>(km/sec) | 5                     | 25                    | 50                    | $V_{\text{normal}}=5$ | 5                                   | 5                     |
| Impact Angle<br>(degrees)   | 90                    | 90                    | 90                    | 45                    | 90                                  | 90                    |

Table 1 - Simulation Configurations

Table 1 summarizes the features of the six cases that were run. The penetrators in all cases were particles of a size that can not be tracked on radar but is sufficiently large to cause major damage to spacecraft. Configuration 1, a 1 cm diameter aluminum sphere penetrating a 0.03 cm thick aluminum plate at a right angle and at 5 km/sec was set up as the baseline case. Variations on the baseline case include a cylinder (1 cm diameter, 1.5 cm long) penetrating at a normal incidence along its axis, a 1 cm diameter sphere penetrating at 45 degrees, and a 1 cm diameter sphere penetrating a 1 cm thick plate at a right angle. The baseline configuration was also run for penetration velocities of 25

and 50 km/sec. The normal velocity component in the oblique impact case has been kept at 5 km/sec; the sphere's kinetic energy, which is based on the total velocity, is therefore twice the kinetic energy of the baseline sphere.

The plate was dropped out of the calculation at the end of the penetration stage since the emphasis of this work is on the penetrator's dynamic behavior. The only exception is the thick plate case where the sphere breaks up completely during penetration and the plate continues to erode long after that.

## RESULTS

Results for all six configurations are summarized in Table 2. Detailed discussion of the calculations follows.

### Sphere - Thin Plate 90° Impact at $V = 5$ km/sec

An aluminum sphere of 1cm diameter (0.367 gm) penetrates an aluminum plate of 5X5 cm, 0.03 cm thick (2.103 gm), at a right angle and with an impact velocity of 5 km/sec. The sphere is in contact with the plate for about 1  $\mu$ sec and passes through it in 2  $\mu$ sec. The stress wave front is moving at the aluminum's elastic wave velocity, 5.2 km/sec, and propagates into the sphere slightly faster than the sphere is moving through the plate, Figures 4 and 5. The stress wave propagates into the plate's plane in concentric circles; the numerical results, Figure 6, deviate from circular symmetry due to the clustering of the grid's elements along the plate's axes, Figures 2(b) and 3(b). The sphere starts breaking up immediately upon coming in contact with the plate, Figure 4(a) and completes the process in 17  $\mu$ sec, long after it has passed through the plate, Figure 5(d). The sphere's velocity is slightly reduced to 4.915 km/sec at the end of its breakup, Figure 7(a). The impact subjects the sphere to very high frequency accelerations that can reach 39 million g, Figure 7(b). The plate's velocity change during impact is negligible and its peak acceleration, 0.7 million g, is much lower than that of the sphere due to its larger mass, Figure 8.

The sphere's kinetic energy is decreased by the impact from 4,570 to 2,080 Joules, Figure 9(a), a 54.5% reduction. 3.4% of that comes from the velocity drop and 51% is caused by mass loss. The penetrating sphere, therefore, loses over half its mass to fragmentation. Note that the kinetic energy values given for all cases are for a quarter model, with the exception of the oblique impact configuration where it is given for a half model.

The impact creates a pressure spike of 0.6 Mbars magnitude in both sphere and plate shortly after contact initiation, Figure 10. The pressure drops to almost zero as the stress wave reaches the sphere's top surface at  $\sim 1.7$   $\mu$ sec, Figure 10(a). The pressure then increases as the stress wave is reflected back into the sphere. The oscillation is repeated with decreasing pressure magnitudes at  $\sim 3.2$   $\mu$ sec and at  $\sim 4.2$   $\mu$ sec. The plate pressures exhibit high frequency oscillations and decrease rapidly by  $\sim 1$   $\mu$ sec when contact with the penetrator ends, Figure 10(b).

### Sphere - Thin Plate 90° Impact at $V = 25$ km/sec

This configuration is identical to the baseline case except for the impact velocity. The penetrating sphere moves through the plate in 0.4  $\mu$ sec at a supersonic velocity. A stress wave front forms on the sphere along the contact surface and propagates inwards radially, Figure 11(a). The penetrator's erosion is confined to the lower surface even after 10  $\mu$ sec, Figure 11(b). The sphere is subject to accelerations of up to 54 million g, but the velocity is only slightly reduced to 24.974 km/sec. The plate's velocity and acceleration are similar to those of the baseline case.

The sphere's kinetic energy is reduced from 114,170 to 99,020 Joules, a loss of 13.3%. The velocity decrease contributes 0.2% of the energy loss and the balance, 13.1%, is the result of penetrator mass losses. The erosion in this case is less than in the baseline configuration and the sphere stays largely intact, Figure 11(b). The maximum pressures, reached at  $< 0.1$   $\mu$ sec after impact, are 0.6 Mbars in the sphere and 0.8 Mbars in the plate.

### Sphere - Thin Plate 90° Impact at $V = 50$ km/sec

The sphere in this case passes through the plate in 0.2  $\mu$ sec and the impact velocity is hypersonic. The stress wave front is a narrow layer along the penetrating sphere's contact surface, Figure 12(a). The sphere fragments almost

completely in  $\sim 15 \mu\text{sec}$ , Figure 12(b). The sphere's acceleration attains 536 million g and the plate is subject to 46 million g. The sphere's velocity is slightly reduced to 49.905 km/sec. The penetrator's kinetic energy decreases from 456,690 to 66,560 Joules, a loss of 85.4%. The velocity reduction accounts for 0.4% of the energy loss; the mass loss in the sphere's fragmentation is therefore 85%. The peak pressures, which occur in  $< 0.1 \mu\text{sec}$  from impact, are very high - 4.8 Mbars in the sphere and 4.1 Mbars in the plate.

#### Sphere - Thin Plate 45° Impact at $V_{\text{normal}} = 5 \text{ km/sec}$

The sphere passes through the plate in 2.0  $\mu\text{sec}$ , Figure 13(a), carving an oval shaped perforation in the plate, Figure 13(b). The penetrating sphere erodes on the surface normal to its velocity. Penetrator and plate peak pressures and accelerations and the sphere's velocities are similar to the baseline case.

The total impact velocity is  $V = \sqrt{2} V_{\text{normal}}$  doubling the kinetic energy. The penetrator's kinetic energy decreases from 18,268 to 10,449 Joules, a 42.8% loss - 2.4% from velocity drop and 40.4% from mass loss.

#### Cylinder - Thin Plate 90° Impact at $V = 5 \text{ km/sec}$

The cylinder passes through the plate in 3.0  $\mu\text{sec}$ . The erosion occurs only on the contact surface, Figure 14(a). The cylinder's breakup continues for  $\sim 15.0 \mu\text{sec}$  with a widening of the eroding surface, Figure 14(b). Both penetrator and plate peak accelerations are higher than in the baseline case, 95 million g and 26 million g, respectively. The peak pressures are 0.5 Mbars for the cylinder and 1.0 Mbars for the plate. The cylinder's velocity reduction is similar to the baseline case. The cylinder's kinetic energy drops from 10,306 to 7,965 Joules, a loss of 22.7% - 1.1% from velocity decrease and 21.6% from mass loss.

#### Sphere - Thick Plate 90° Impact at $V = 5 \text{ km/sec}$

The penetrating sphere breaks up completely in this case, Figures 15 and 16. The plate craters at the initial penetration stage, continues to fragment, and undergoes spalling, a separation of an exit surface section surrounding the penetration crater, Figure 16. Penetrator and plate maximum pressures are similar to the baseline case. The sphere's peak acceleration is the highest of all cases - 5,180 million g, but the plate's acceleration is similar to that of the baseline configuration. The sphere's kinetic energy is completely spent during impact.

### SUMMARY

| Configuration                                   | 1     | 2      | 3      | 4                         | 5     | 6     |
|---|-------|--------|--------|---------------------------|-------|-------|
| Initial Penetrator Velocity (km/sec)            | 5     | 25     | 50     | $V_{\text{normal}}=5$     | 5     | 5     |
| Terminal Penetrator Velocity (km/sec)           | 4.915 | 24.974 | 49.905 | $V_{\text{normal}}=4.940$ | 4.974 | 0     |
| Penetrator Peak Acceleration (Mg)               | 39    | 54     | 536    | 37                        | 95    | 5,180 |
| Plate Peak Acceleration (Mg)                    | 0.7   | 1.1    | 46     | 0.7                       | 26    | 0.6   |
| Penetrator Peak Pressure (Mbars)                | 0.6   | 0.6    | 4.8    | 0.7                       | 0.5   | 0.6   |
| Plate Peak Pressure (Mbars)                     | 0.6   | 0.8    | 4.1    | 0.9                       | 1.0   | 0.6   |
| Total Kinetic Energy Loss (%)                   | 54.5  | 13.3   | 85.4   | 42.8                      | 22.7  | 100   |
| Kinetic Energy Loss from Velocity Reduction (%) | 3.4   | 0.2    | 0.4    | 2.4                       | 1.1   | N/A   |
| Penetrator Mass Loss (%)                        | 51    | 13.1   | 85.0   | 40.4                      | 21.6  | 100   |

Table 2 - Simulation Results

#### Thin Plate Configurations

- The penetrators in all cases passed through the plate creating a small, clean hole with negligible kinetic energy losses - from 0.2 % to 3.4 %.

- Most of the kinetic energy loss is spent in the breakup of the penetrator. Mass loss varied from a low of 13.1 % to a high of 85 %.
- The plate received very little energy and momentum from the penetrator due to the very short contact times. Plate breakup is largely confined to a perforation large enough for the passage of the penetrator.
- Test data show penetrator fragmentation similar to that of the baseline case (ref. 5). Numerical simulations have been able to duplicate penetrators fragmenting into debris clouds for similar impact velocities (ref. 6 and 7).

### **Thick Plate Configuration**

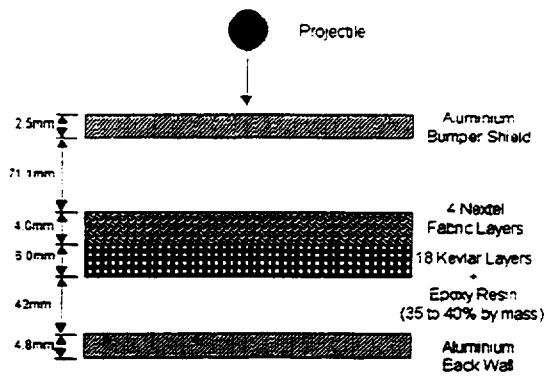
- The penetrator broke up completely, transferring all its kinetic energy and momentum to the plate. The plate's breakup continued long after the penetrator had disintegrated, eventually creating a hole through the entire plate thickness.
- The calculations show a section detaching from the exit wall (spalling), Figure 16, a phenomenon that's been confirmed analytically (ref. 3) and has been observed numerous times in cases such as that of an armor piercing shell penetrating an armor plate.

### **Conclusions**

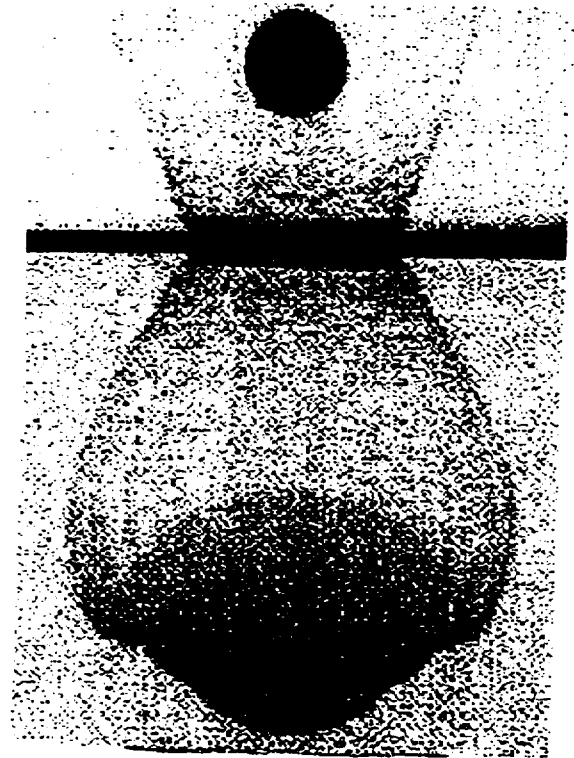
- The penetrator's velocity is largely unchanged after impact in all thin plate cases, leaving mass loss as the only way to reduce kinetic energy. Low fragmentation is therefore undesirable since it may leave the penetrator with enough kinetic energy to breach the terminal wall.
- High velocity impacts may be relatively benign. A penetrator will perforate an entrance hole and an exit hole in a satellite but will not cause major damage unless it hits a critical component.
- Stress wave patterns are dependent on the relative magnitude of the impact velocity to the elastic wave velocity in the materials. Stress waves will form in a layer on penetrator and plate contact surfaces during supersonic impact. The stress waves provide the fragmentation mechanism as they propagate into the materials at the elastic wave velocity, reflecting from the boundaries, Figures 4(b), 11(a), 11(b), and 14(b).
- The simulation results are applicable to the design of spacecraft shields. Features such as the number of Nextel and Kevlar layers, their arrangement, and the various spacings between barriers must take into account the range of penetrator particle sizes, the extent of their fragmentation, and the impact velocities to which the shield will be exposed.

### **REFERENCES**

1. *Proceedings of the Hypervelocity Shielding Workshop*. Sponsored by NASA Johnson Space Center and the Institute for Advanced Technology at the University of Texas at Austin, Galveston, Texas, March 8-11, 1998.
2. Christiansen, E.L., "Design Practices for Spacecraft Meteoroid/Debris (M/D) Protection", Hypervelocity Shielding Workshop, Galveston, Texas, March 8-11, 1998.
3. *High Velocity Impact Dynamics*. Edited by Jonas A Zukas, John Wiley & Sons, Inc., 1990.
4. *LS-DYNA3D Theoretical Manual*. Hallquist, J.O., Livermore Software Technology Corporation, LSTC Report 1018, Revision 3, April 1994.
5. Piekutowski, A.J., "Hypervelocity Impact of Nonspherical Projectiles: Observations and Lessons Learned from Impact Tests", Hypervelocity Shielding Workshop, Galveston, Texas, March 8-11, 1998.
6. Hayhurst, C.J., "Numerical Simulation of Hypervelocity Impacts", Hypervelocity Shielding Workshop, Galveston, Texas, March 8-11, 1998.
7. Fahrenthold, E., "Numerical Simulation of Impact on Hypervelocity Shielding", Hypervelocity Shielding Workshop, Galveston, Texas, March 8-11, 1998.



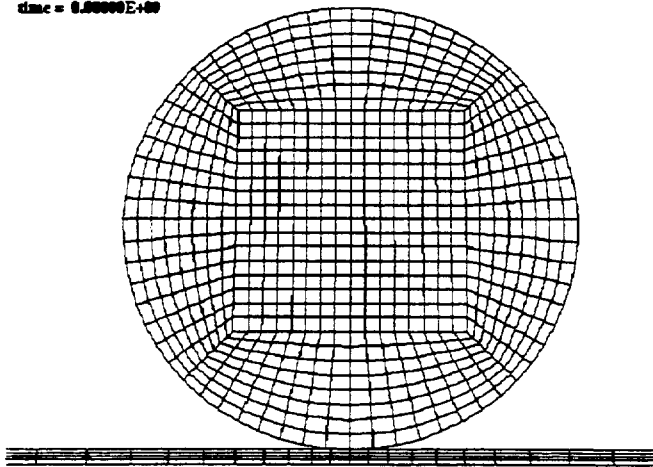
(a) Whipple shield



(b) X-ray of a debris cloud

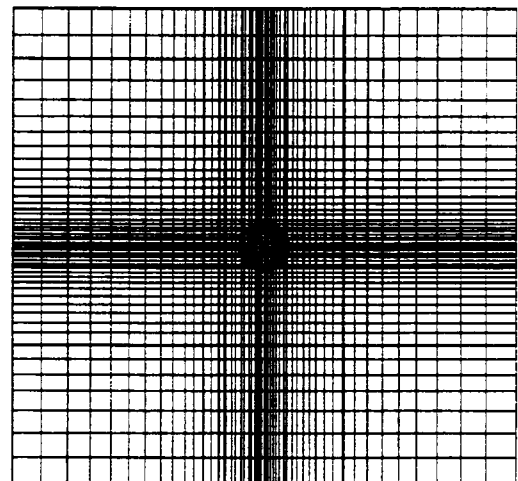
Figure 1 - Whipple shield and debris cloud

Hypervelocity Impact Model  
time = 8.80000E+00



(a) Side View

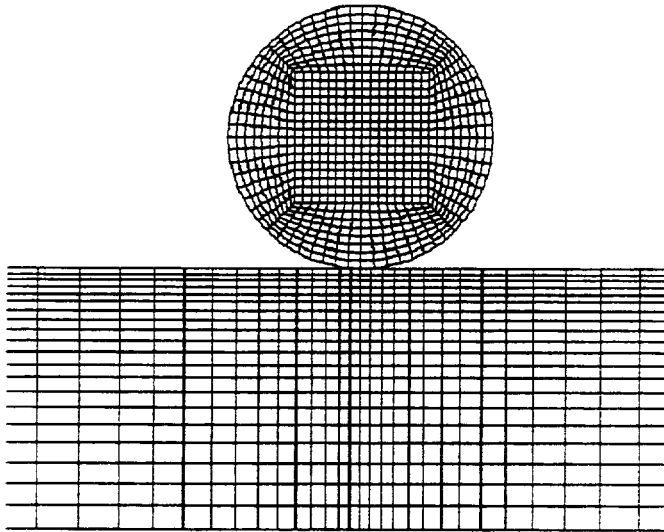
Hypervelocity Impact Model  
time = 8.80000E+00



(b) Top View

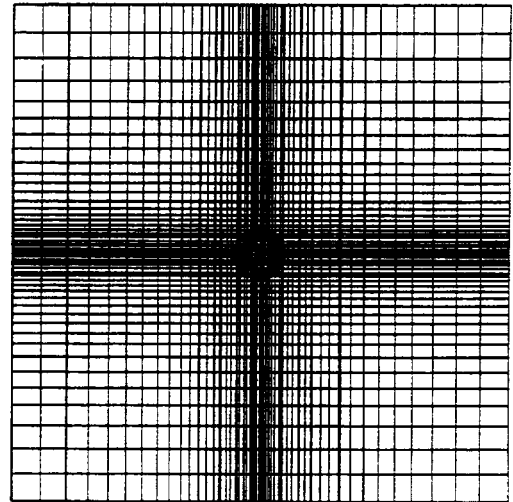
Figure 2 - Sphere - Thin Plate Grid

Hypervelocity Impact Model  
time = 0.00000E+00



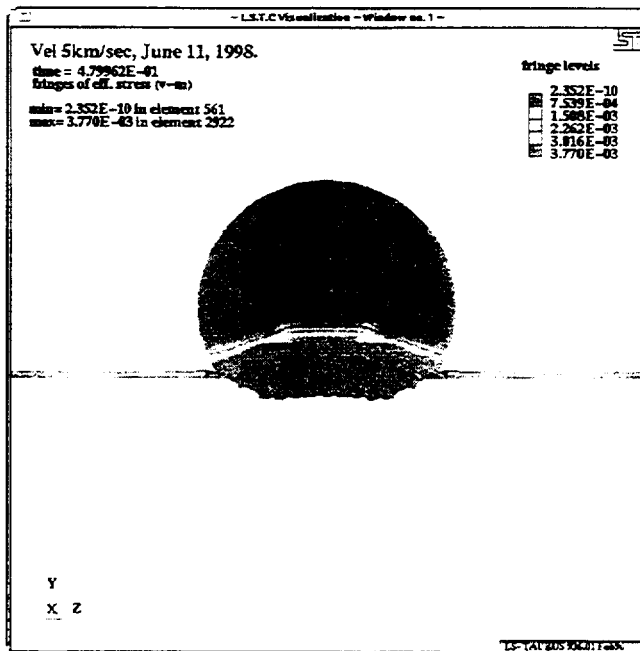
(a) Side View

Hypervelocity Impact Model  
time = 0.00000E+00

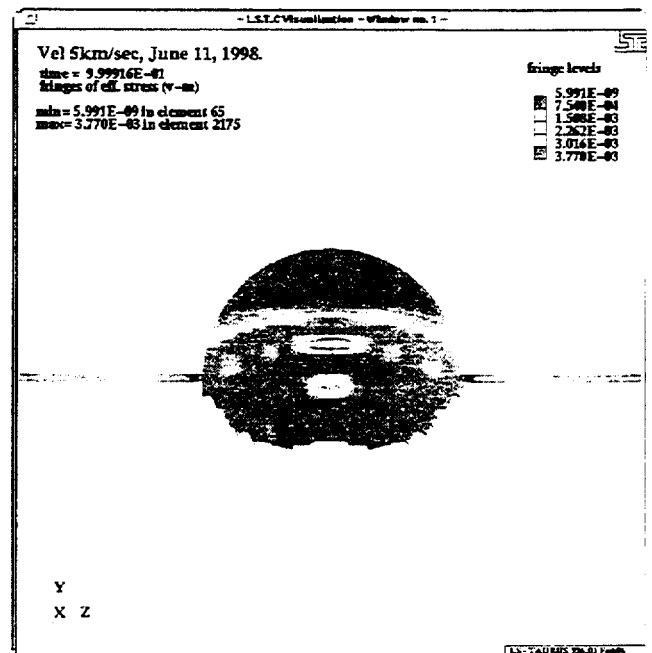


(b) Top View

Figure 3 - Sphere - Thick Plate Grid

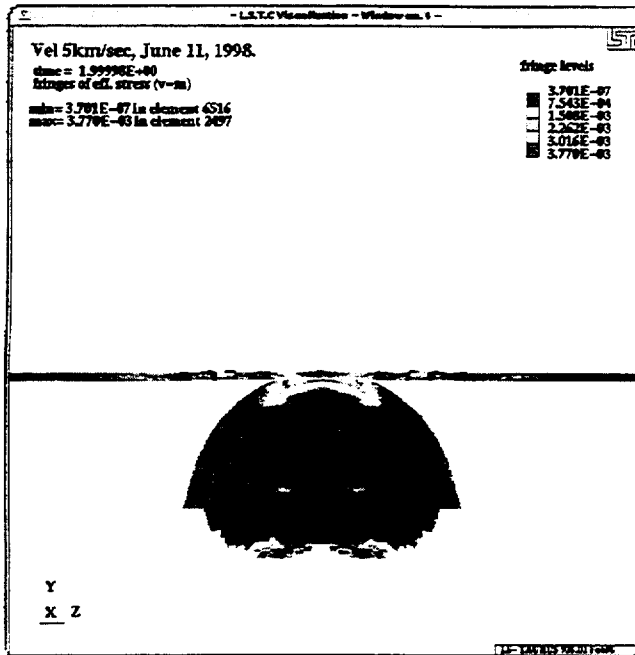


(a)  $t=0.48 \mu\text{s}$  after impact

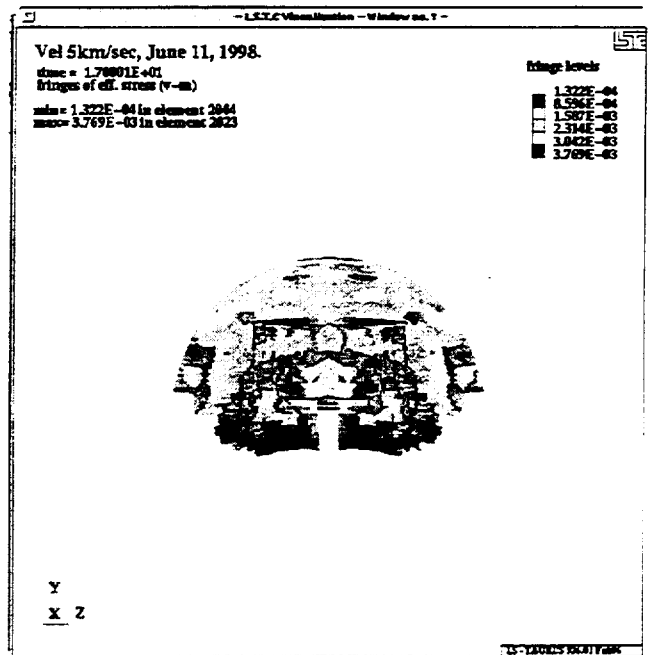


(b)  $t=1.0 \mu\text{s}$  after impact

Figure 4 - Sphere and plate effective stresses,  $V_{\text{impact}}=5 \text{ km/sec}$ , right angle impact, side view

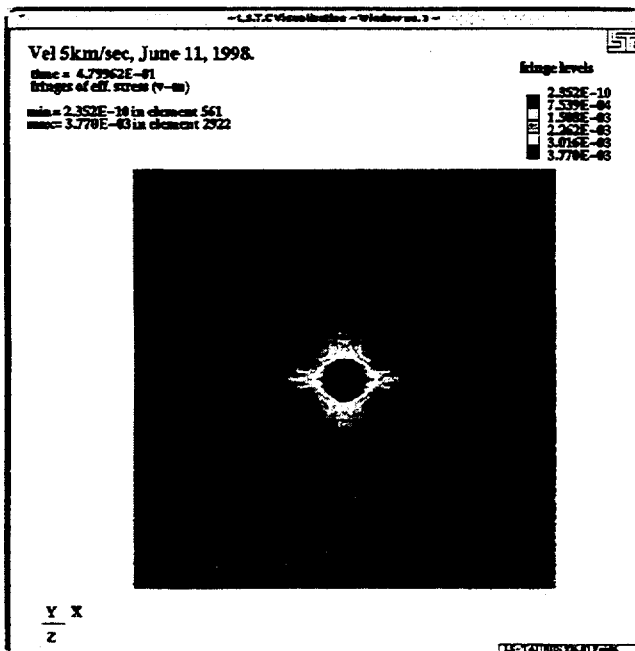


(c)  $t=2.0 \mu\text{sec}$  after impact

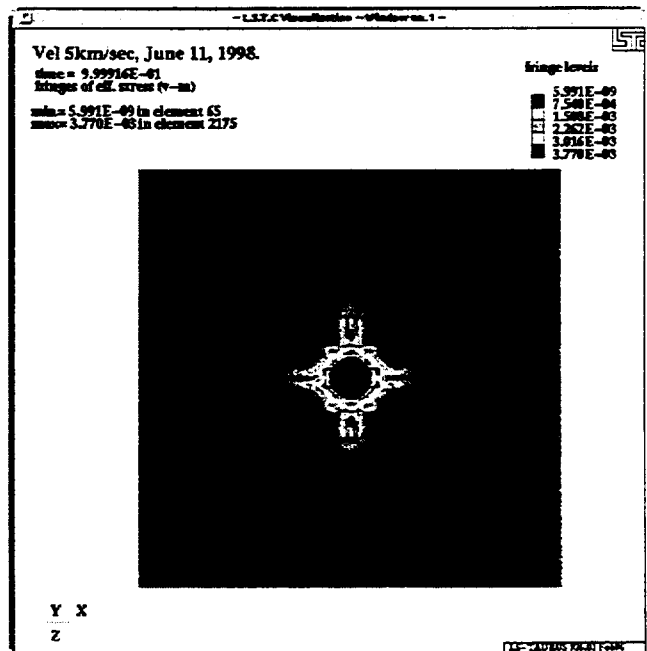


(d)  $t=17.0 \mu\text{sec}$  after impact

Figure 5 - Sphere and plate effective stresses,  $V_{\text{impact}}=5 \text{ km/sec}$ , right angle impact, side view

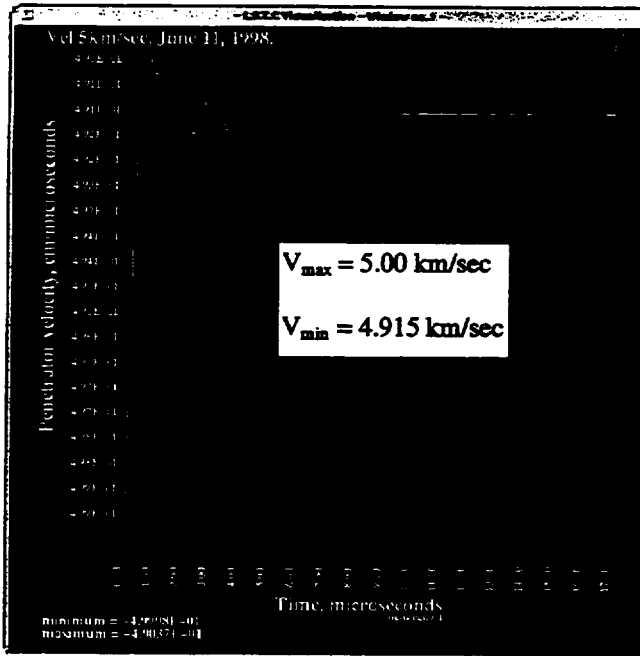


(a)  $t=0.48 \mu\text{sec}$  after impact

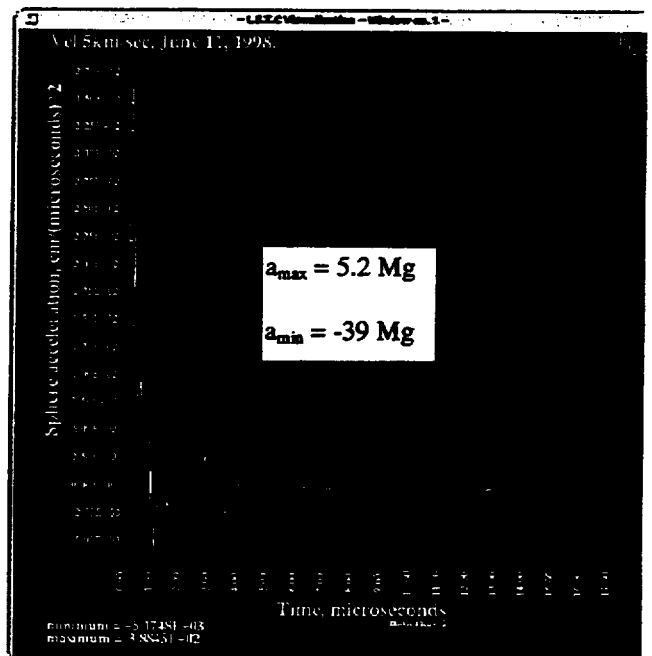


(b)  $t=1.0 \mu\text{sec}$  after impact

Figure 6 - Sphere and plate effective stresses,  $V_{\text{impact}}=5 \text{ km/sec}$ , right angle impact, top view

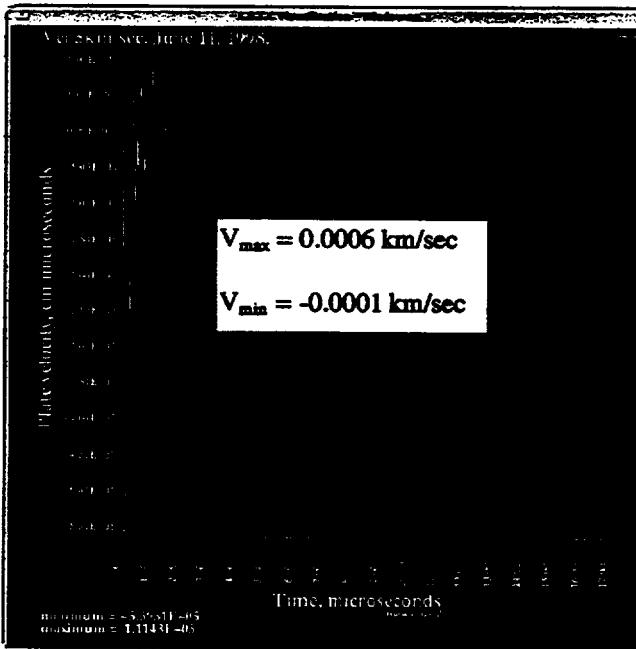


(a) Velocity

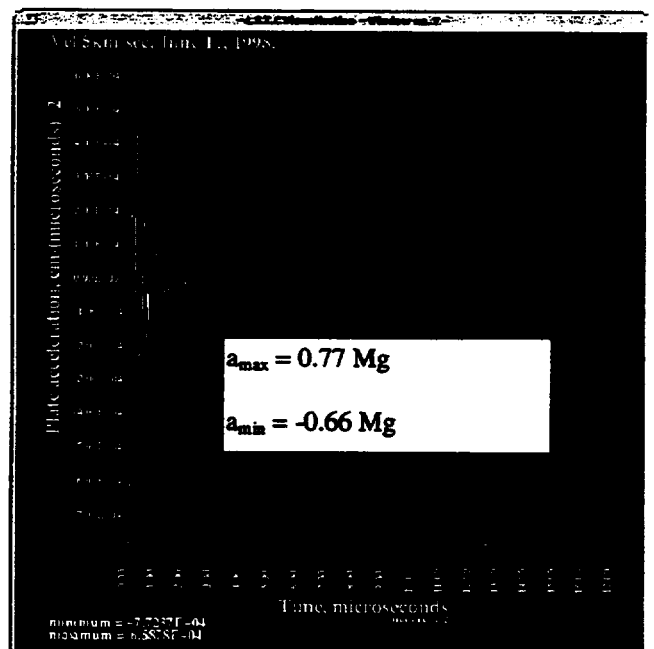


(b) Acceleration

Figure 7 - Sphere velocity and acceleration time histories,  $V_{impact}=5 \text{ km/sec}$

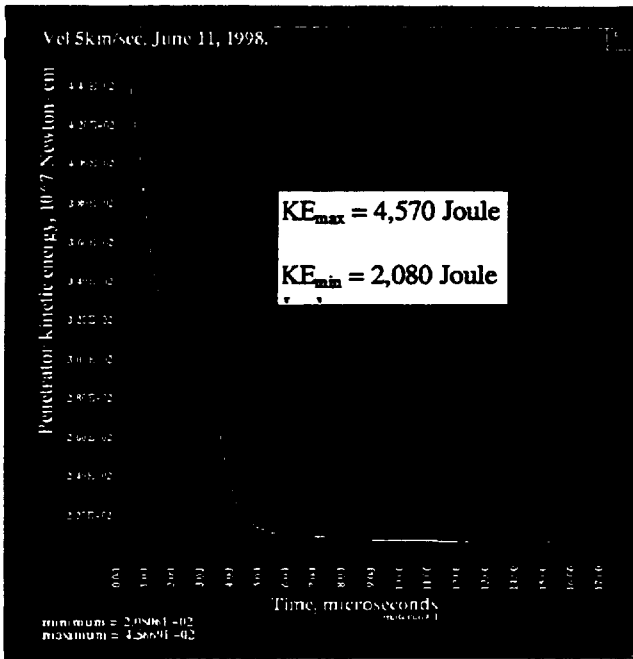


(a) Velocity

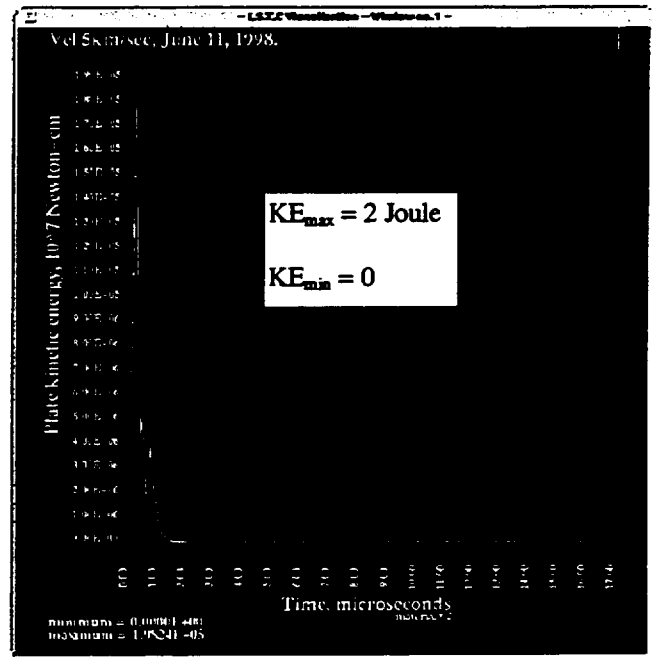


(b) Acceleration

Figure 8 - Plate velocity and acceleration time histories,  $V_{impact}=5 \text{ km/sec}$

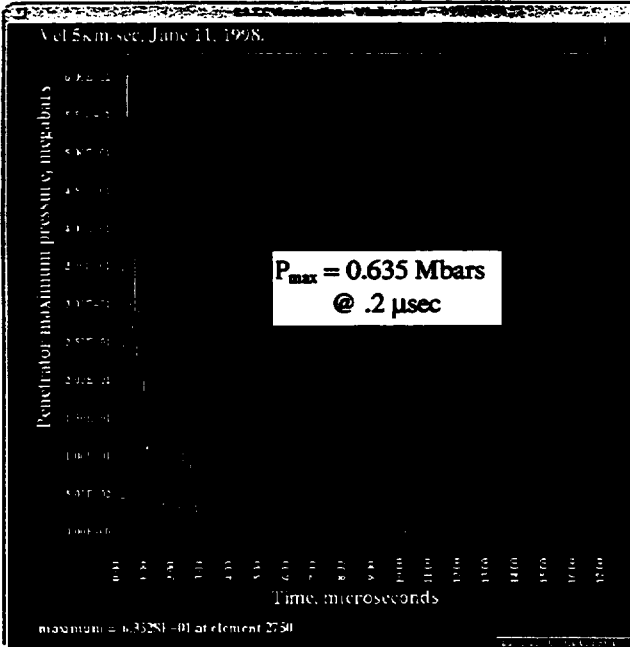


(a) Sphere

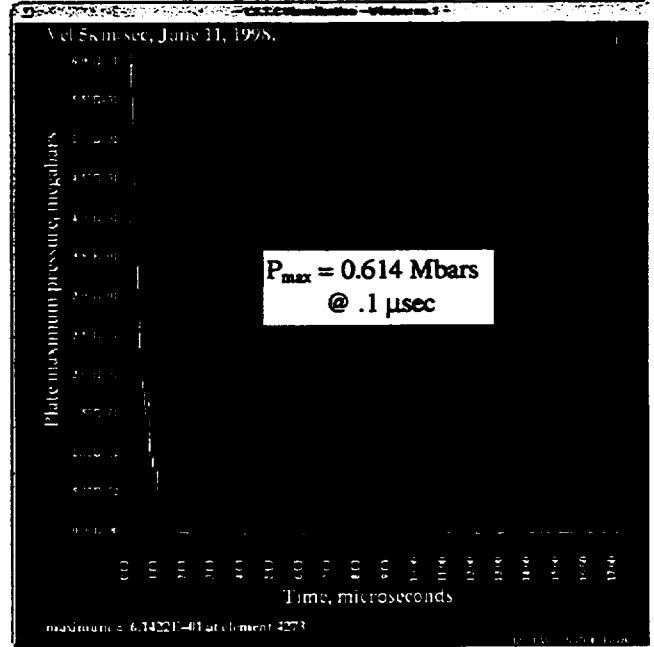


(b) Plate

Figure 9 - Sphere and plate kinetic energy time histories,  $V_{impact}=5$  km/sec

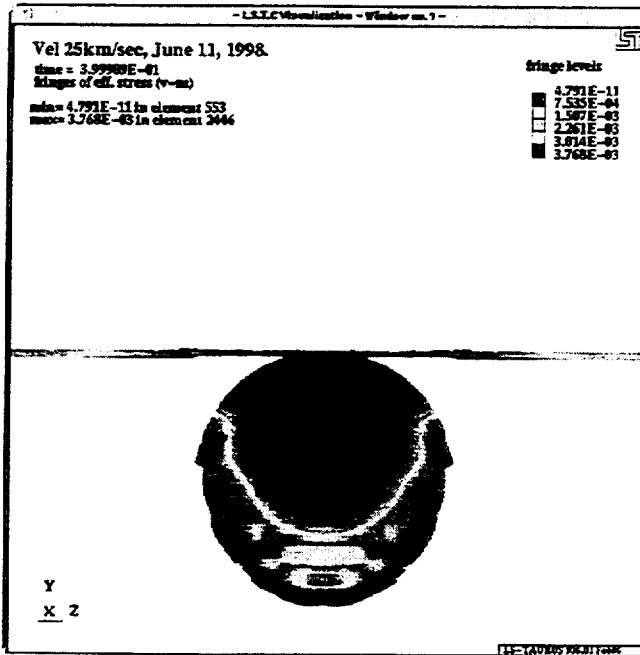


(a) Sphere

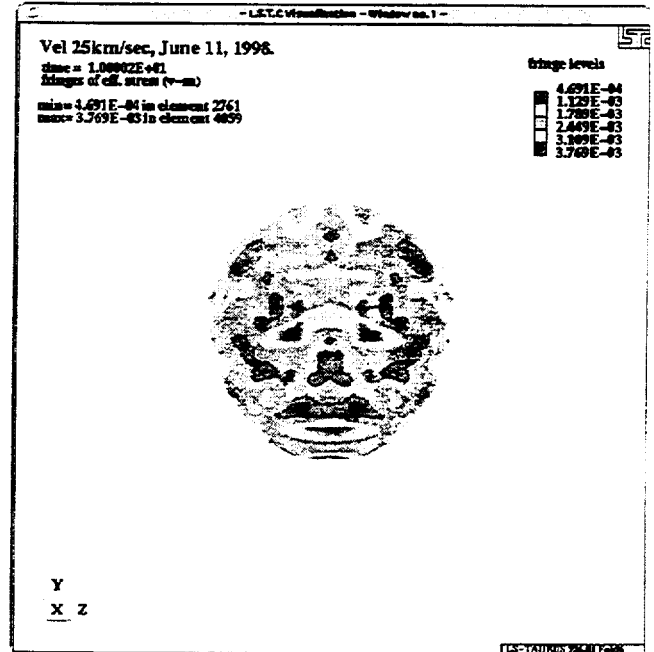


(b) Plate

Figure 10 - Sphere and plate maximum pressures time histories,  $V_{impact}=5$  km/sec

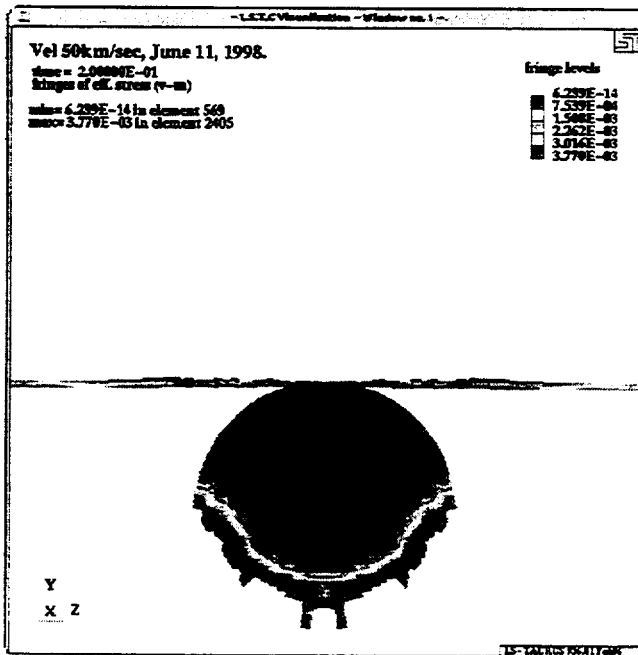


(a)  $t=0.4 \mu\text{sec}$  after impact

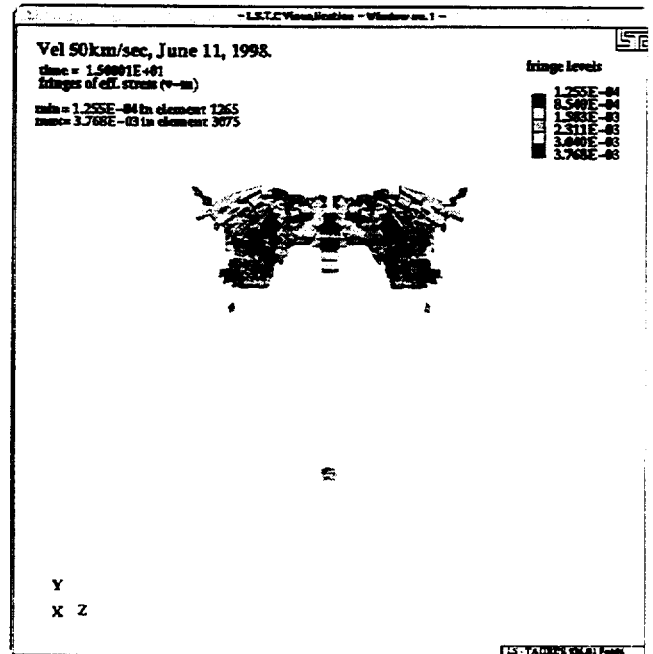


(b)  $t=10.0 \mu\text{sec}$  after impact

Figure 11 - Sphere and plate effective stresses,  $V_{\text{impact}}=25 \text{ km/sec}$ , right angle impact, side view

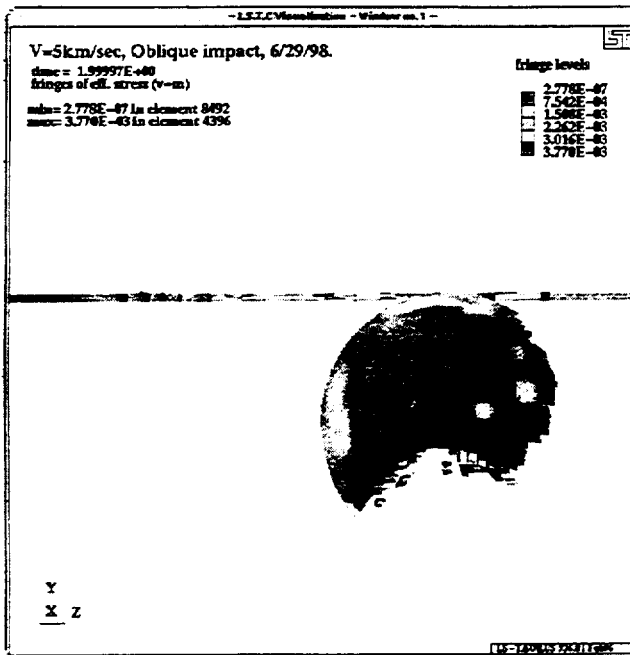


(a)  $t=0.2 \mu\text{sec}$  after impact

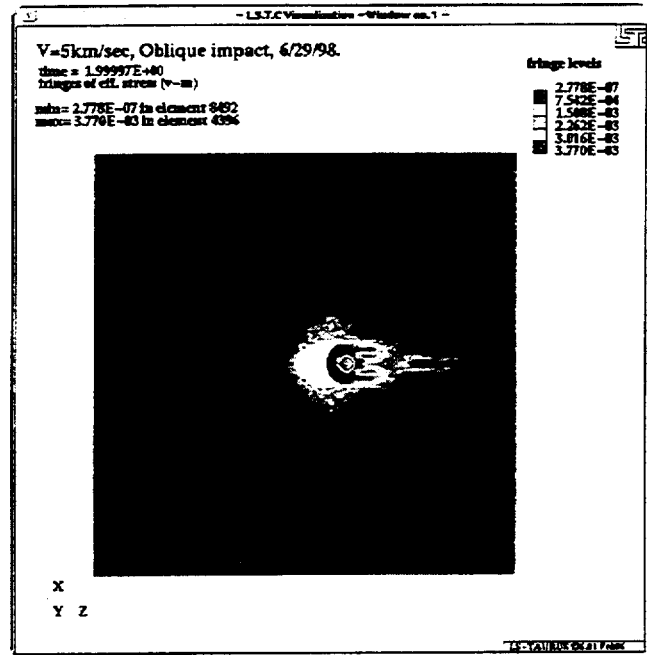


(b)  $t=15.0 \mu\text{sec}$  after impact

Figure 12 - Sphere and plate effective stresses,  $V_{\text{impact}}=50 \text{ km/sec}$ , right angle impact, side view

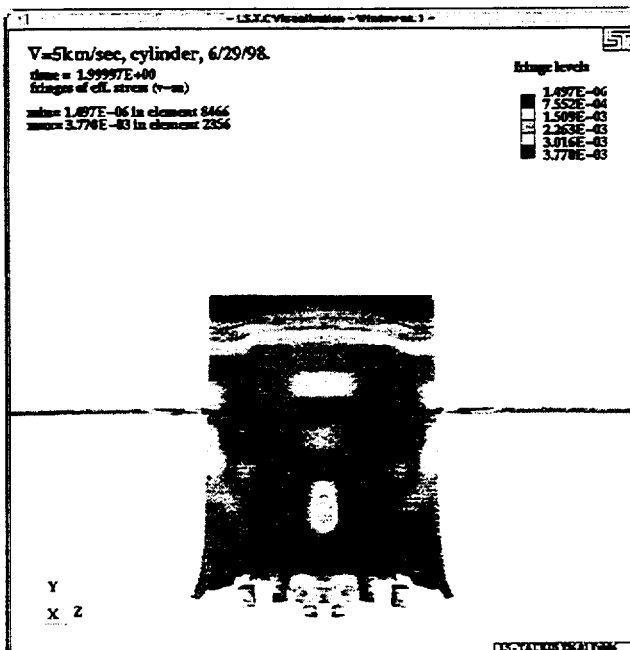


(a) Side view

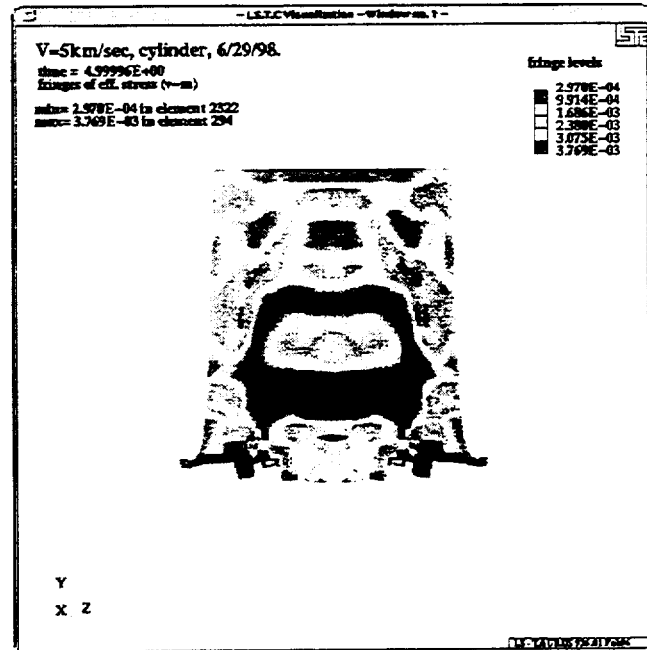


(b) Top view

Figure 13 - Sphere and plate effective stresses,  $V_{\text{impact}}=5$  km/sec, 45 degrees oblique impact,  $t=2.0 \mu\text{sec}$  after impact

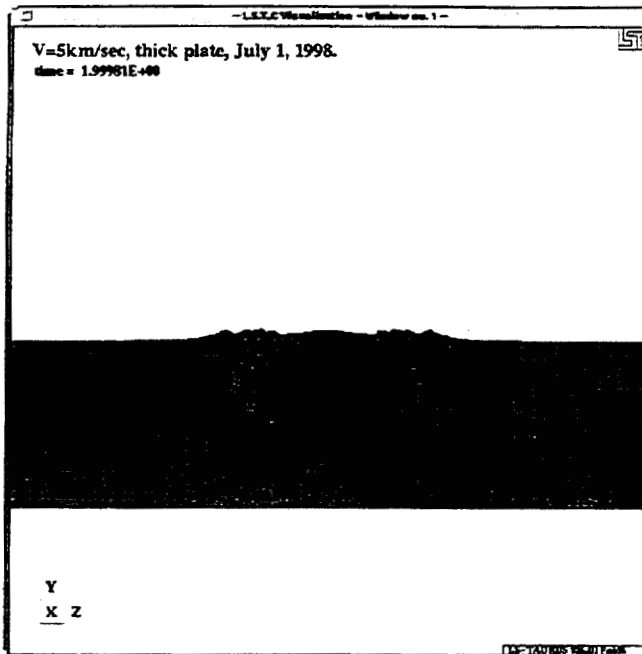


(a)  $t=2.0 \mu\text{sec}$  after impact

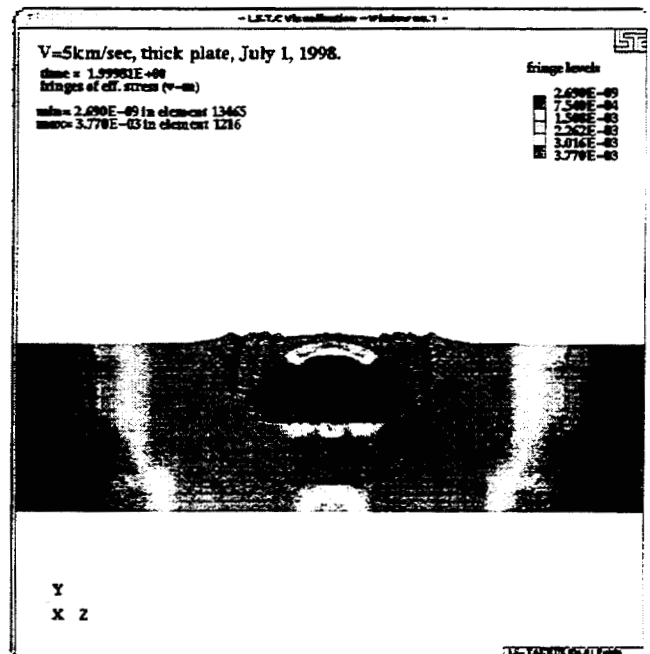


(b)  $t=5.0 \mu\text{sec}$  after impact

Figure 14 - Cylinder and plate effective stresses,  $V_{\text{impact}}=5$  km/sec, right angle impact, side view

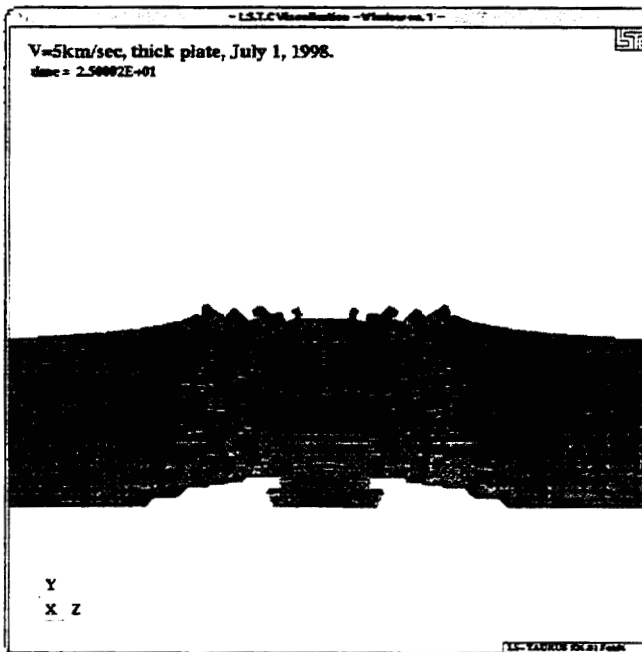


(a) Sphere and thick plate model components

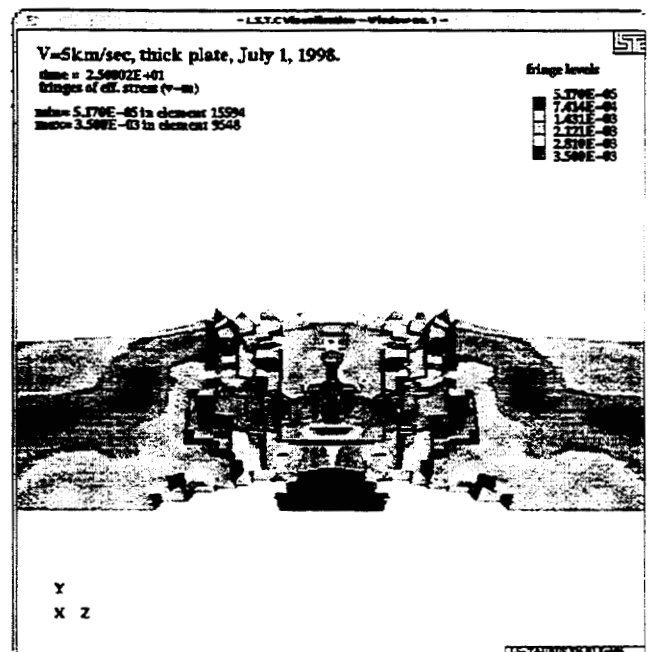


(b) Sphere and thick plate effective stresses

Figure 15 - Sphere and thick plate,  $V_{\text{impact}}=5$  km/sec, right angle impact,  $t=2.0 \mu\text{sec}$ , side view



(a) Sphere and thick plate model components



(b) Sphere and thick plate effective stresses

Figure 16 - Sphere and thick plate,  $V_{\text{impact}}=5$  km/sec, right angle impact,  $t=25.0 \mu\text{sec}$ , side view

## THE MISTRAL ANTENNA MEASUREMENT COMPACT RANGE AT INTESPACE

Jean-Louis MARCÉ, Pascal MEISSE and Rémi BERGÉ  
INTESPACE, Toulouse, France

### ABSTRACT

Leader in the field of space environment simulation (vibrations, thermal vacuum, acoustics, EMC), INTESPACE company has built a new compact range for antenna measurement called MISTRAL with a view to providing an overall satellite test service. The purpose of this new full-scale test facility is to determine the radioelectric characteristics of integrated satellite antennas covering :

- classic antenna tests such as radiation pattern and gain measurement,
- payload specific end-to-end tests such as EIRP, SFD, G/T, Gain/Frequency, etc.

The aim of this paper is :

- first, to present the main and extra features of the MISTRAL compact range and the results of the intensive quiet zone probing.
- second, to present the results of antenna and payload measurements confirming the high quality of this test facility.

### INTRODUCTION

Inaugurated the 24th of April, 1997, the MISTRAL Compact Range has just completed the satellite test means package of INTESPACE in Toulouse (figure 1).

That test facility was dimensioned to test class ariane 4 or dual-launch Ariane 5 satellites. The dimensions of the anechoic chamber, i.e. the core of the compact range are 30 x 20 x 15.5 m (W x L x H). To guarantee the privacy of test results and prevent external electromagnetic disturbance, the whole compact range (anechoic chamber + feed room + control room) is fully screened and responds to the requirements of French military standard GAM-T20. This Faraday cage is equipped with a large satellite entrance door of 6 x 11 m (W x H). The facility is also mechanically insulated from the outside world vibrations thanks to an anti-seismic slab and very clean (cleanness class 100000).

The illuminator system selected for MISTRAL is the DASA dual reflector system (Compensated Compact Range). The operational frequency range extends from 1.47 GHz to 40 GHz but the actual surface accuracy of the reflectors (< 12  $\mu$ m RMS) makes it possible further extension to 200 GHz over the next few years.

The Focused Quiet Zone dimensions are 5.5 x 5 x 6 m (WxHxD). Two 4-axes feed positioners (pol/lin/az/lin) shown in figure 3, can be used at the same time in two different quiet zones (at least one of the illuminator feeds is slightly moved out of the focal point, creating a so-called Scanned Quiet Zone). That capability is especially interesting for End-to-End test configuration set-up. Moreover, it extends the satellite test volume to 8.8 x 5 x 6 m (Focused + Scanned Quiet Zones) (figure 2)

The specimen positioner assembly provides positioning along 5 axes (from bottom to top) :

- transverse translation (linear axis from -7 to +3 m),
- longitudinal translation (linear axis from -2 to +2 m),
- lower azimuth axis ( $\pm 200^\circ$ ),
- elevation axis (+45 to -90.5 $^\circ$ ),
- upper azimuth axis in continuous rotation.

The overall alignment accuracy of the radioelectric axis of the antenna undergoing the test with respect to the RF axis of the Compact Range is within 0.014 $^\circ$ .

The specimen positioner load capacity is 6 tons. It is presented in figure 4

The measurement sequence comprising acquisition, processing, error correction, graphic result plotting, and command/control of equipment used in the measurement operation (specimen positioner, feed positioner, synthesizer, microwave receiver, etc.) is fully controlled by the system SA2095 (Scientific Atlanta). More specifically, multiple frequency measurement acquisition and equipment command/control is fully automatic.

Moreover, at low frequencies (below 6 GHz), measurement accuracy can be improved by using the so-called AAPC (Advanced Antenna Pattern Correction) error correction program.

(1) 18 avenue Edouard Belin - 31029 Toulouse Cedex 4 - France - Tél : 33 (0) 5 61 28 11 11 - Fax : 33 (0) 5 61 28 11 12  
(2) 31 avenue des Cosmonautes - 31402 Toulouse Cedex - France - Tél : 33 (0) 5 612 19 62 19 - Fax : 33 (0) 5 62 19 55 10  
(\*) 18 avenue Edouard Belin - 31401 Toulouse Cedex 4 - France - Tél : 33 (0) 5 61 27 31 31 - Fax : 33 (0) 5 61 27 31 79

## MISTRAL SYSTEM OPTIMIZATION

The MISTRAL Compact Range has benefit from several innovations throughout the study and development phases. The main system improvements are presented below, sorted by main assemblies :

### Illuminator System

The DASA standard dual reflector system was initially designed to fit a smaller anechoic chamber (24.8 x 17.5 x 10.8) with an RF axis at 5.5 m height. To take into account the growth of satellite dimensions (ARIANE 5 payload fairing internal diameter = 4,57 m, i.e. +25% wrt ARIANE 4), the illuminator system has been rotated of 3.3° and the RF axis rised up to 6.20 m for MISTRAL. That modification increased considerably the operational capability of measuring large satellites in MISTRAL and was only possible because of the relevant huge volume of the anechoic chamber. As the chamber walls are more distant from the measurement volume of the satellite, it also induces less extraneous field caused by reflections. The large piramidal absorbers on the back wall are also more efficient at small angle of incidence of the range field.

Special attention has been payed for the study and improvement of the scanned quiet zones performances. Several tools, based on optical geometry, have been developed to optimize the quality of the scanned quiet zones in the user desired areas. Moreover, the accuracy of the MISTRAL scanner makes it possible to define a new practical method and operational procedure to optimize the position of the scanned feed and determine the scanned RF axis orientation with almost the same accuracy as for the Focused quiet zone.

### Specimen Positioner

The MISTRAL specimen positioner has been provided by Scientific Atlanta. The upper stack (Az/EI/Az) is derived from the SA models 53450B and 51450B. To fulfill the INTESPACE requirement of 0.01° of positioning accuracy, several improvements have been implemented with. mainly, the addition of a counterweight system in order to balance the satellite assembly on the elevation axis and a new mechanical arrangement of the elevation axis encoder. This encoder has been mounted independently to the lower axis turntable so that the bending of the upper structure due to specimen heavy load can be detected and measured.

The lower assemblies (translation axes) are a completely new SA design for MISTRAL and have proven very good accuracy performance during on-site acceptance.

In order to extend the preparation area for the satellite, the lower linear axis has been both embedded in the chamber floor and extended of 4 meters towards the left wall (looking towards reflectors) creating a parking area for the positioner (initially, the transverse translation range was from -3 to +3 m).

### Absorbers

The quality of the absorber layout has a direct impact on the range performance. A careful study was performed for MISTRAL with the know-how of experts to reduce extraneous field caused by reflection or diffraction.

One interesting innovation was to create a slanted wall of absorbers hiding the feed room alcove and the scanning linear axis overhang in such a way that only the end of the illuminator feeds are visible from inside the anechoic chamber.

A horizontal slot of one-absorber-panel height was made to enable horizontal displacement of feed positioner arms for scanned quiet zone configuration. The slot is filled with absorbers blocs after having positioned the feeds so that the feed room is completely insulated from the chamber and can easily be accessed for operations. To suppress direct leakage from the illuminator feed, the user can either use a baffle (cylinder covered by absorbers) or a Time Gating hardware.

The feed room wall was covered with high-power absorbers (1.5 W/cm<sup>2</sup>) to withstand full power RF of the satellite during End-to-end tests (e.g. EIRP payload test).

The MISTRAL absorbers have been manufactured and installed by Emerson & Cuming.

### Polar Scanner

A specific large Plane Wave Scanner of so far unprecedented accuracy was designed and manufactured by ORBIT for MISTRAL and intensely used for the acceptance tests.

That plane-polar type scanner can automatically evaluated a full circular plane of 5.5 m diameter. The accuracy of the precision linear axis and the polar axis is such that the mechanical overall planarity is better than ±80 μm peak to peak (i.e. ±3.8° at 40 GHz). Special attention was given to the design of the RF cable track in order not to

spoil the mechanical performance by phase variation due to cable movements.

The performance of the MISTRAL scanner is so good that it was possible to verify the actual boresight of the plane wave in both focused and scanned quiet zones by comparison of optical and RF alignment during the system acceptance (the scanner was equipped with an optical mirror cube for this purpose). An other new application for this scanner is the optimization of the scanned quiet zone performance in user defined areas.

## MISTRAL QUIET ZONE PROBING

### Probing Program

A very careful and complete probing of the quiet zones from 1.47 to 40 GHz have been performed for MISTRAL system acceptance.

The following parameters have been measured by using the polar scanner mounted on the specimen positioner :

- amplitude taper,
- amplitude ripple,
- phase taper,
- phase ripple,
- linear cross-polarisation.

Three quiet zones have been fully evaluated :

- the Focused Quiet Zone (FQZ) when the feed is at the focal point,
- the extreme Left Quiet Zone (LQZ) corresponding to the worst case translation of the feed to the left (+2.8 m equivalent to a rotation of +9° of the RF axis),
- the extreme Right Quiet Zone (RQZ) corresponding to the worst case translation of the feed to the right (-0.95 m equivalent to a rotation of -3° of the RF axis).

These quiet zones are presented in figure 6.

Four planes were measured in depth for the FQZ, two for the LQZ and two for the RQZ.

For a given plane, 16 cuts with an angular spacing of 11.25° were measured by the polar scanner automatically controlled by the 2095 system (figure 7). The spatial probing was linked to the frequency (< 0.4 wavelength - e.g.: 1834 points at 40 GHz to cover the 5.5 m of the precision linear axis of the scanner). The four combinations of primary source and probe vertical and horizontal polarisations were measured in amplitude and phase (EHH, EHV, EVH, EVV).

At last, for each of the 8 frequency bands covering 1.47 to 40 GHz (each band corresponding to one primary source),

measurements at three frequencies (low, medium and high) were performed (table 1).

The Quiet Zones Probing had consequently lasted 6 weeks of continuous measurements (work in three shifts). The collected data have been completely processed, from raw measurements to statistical results. After this exceptional acceptance campaign, INTESPACE has now available a unique database for its future customers.

### Results Of MISTRAL Quiet Zone Probing

Compact range performance is reported in tables 2, 3 and 4. This performance is obtained with 13 to 16 dBi gain probes (large beamwidth)

### Illustration Example

As an illustration, the curves for the parameters presented in paragraph «probing program ». are shown in figures 8a to 8f for frequencies 2.35 GHz and 27 GHz, at the center of the focused quiet zone.

## ANTENNA AND PAYLOAD MEASUREMENTS

### Validation Program For Antenna Measurements

To validate the ability of the Mistral compact range to perform antenna measurements with the required accuracy, the antenna measurement results were compared with the CNES compact range, BCMA (Base Compact de Mesures d'Antennes - CNES Antenna Measurement Compact Range). Five antennas were measured and their main characteristics are displayed in table 5.

The parameters measured are:

- copolarization pattern
- cross-polarization pattern
- main cuts (azimuth and elevation)
- gain

### Comparison Between MISTRAL And BCMA Measurements

The curves in figure 9a, 9b and 9c show the comparison for antenna n° 4.

The curves show excellent similarity between the two results. Thus, for all antennas tested, the results achieved with MISTRAL and those obtained with BCMA agree to an excellent extent from the standpoint of copolarization, cross-polarization and gain. The accuracy of the measurements specified was checked.

## Comparison Between FQZ And SQZ Antenna Measurement

To confirm the capacity of MISTRAL to perform antenna measurements in scanned quiet zones, the antenna results obtained in the main focused quiet zone have been compared to those obtained in Left and Right quiet zones. Thus, the same main cuts were measured independently for each antenna in the three tested quiet zones of MISTRAL.

The curves have shown excellent similarity between the three results for all of the antennas. As an illustration, azimuth and elevation main cuts for cross-polarization of antenna 1 (TUD) obtained first in Focused quiet zone and then in Left quiet zone are compared on figures 10a and 10b.

## Validation Program For Payload Measurements

to validate the ability of the MISTRAL compact range to perform payload measurements, a mini-payload, representative of a satellite channel, has been designed. This mini-payload is composed of two antennas, one only in RX mode and the other one in RX/TX mode (figure 11). It operates in Ku-band, between 14 and 14.5 GHz for uplink frequency and between 12.5 and 12.75 GHz.

For the payload measurements, the following tests have been performed :

- EIRP measurements
- SFD measurements
- G/T measurements
- Gain / Frequency measurements.

For EIRP, SFD and Gain / Frequency measurements, two configurations have been tested :

- use of the RX/TX antenna for uplink and downlink signals,
- use of the TX antenna for uplink signal separated from the TX antenna for downlink signal.

G/T measurement have been only performed in the RX/TX antenna configuration.

Moreover, for EIRP, SFD and G/T measurements, two methods have been compared :

- substitution method, by using a reference antenna (a Standard Gain Horn - SGH). This method requires two measurements (one SGH measurement and one Antenna Under Test - AUT - measurement),
- absolute method, by using the equivalent free-space length of the compact range. This method requires only one measurement and needs the calculation of the free-space losses of the compact range.

## Results Of Payload Measurements

For the two configurations and the two methods, the results of payload measurements are as follows :

- for EIRP measurements, the difference with respect to the expected value (approximately + 52 dBW) doesn't exceed  $\pm 1.5$  dB in the frequency band,
- for SFD measurements, the difference with respect to the expected value (approximately - 89 dBW/m<sup>2</sup>) doesn't exceed  $\pm 1.5$  dB in the frequency band,
- for G/T measurements (only one configuration), the difference with respect to the expected value (approximately 15 dB/°K) doesn't exceed  $\pm 1.5$  dB in the frequency band.

Considering the length of cabling used for the different measurements (about 40 m) and the average accuracy of feed gains for absolute method, these results are very satisfactory.

## SUMMARY

To be able to provide an overall space environment simulation package, INTESPACE has built a compact range to perform RF tests on integrated satellites. The dimensions of this facility, the precision of the component instrumentation and the quality of construction make the Mistral compact base an exceptional simulation tool whose validation results in terms of performance, quiet zones, antenna and payload measurements, are extremely satisfactory.

|        | Low  | Medium | High |
|--------|------|--------|------|
| Feed 1 | 1.5  | 2.0    | 2.4  |
| Feed 2 | 2.4  | 3.0    | 3.6  |
| Feed 3 | 3.6  | 4.5    | 5.4  |
| Feed 4 | 5.4  | 6.7    | 8.0  |
| Feed 5 | 8.0  | 10.0   | 12.0 |
| Feed 6 | 12.0 | 15.0   | 18.0 |
| Feed 7 | 18.0 | 22.5   | 27.0 |
| Feed 8 | 27.0 | 33.5   | 40.0 |

Table n° 1 : Probing frequencies (in GHz)

|                           | 1,47 to 3 GHz | 3 to 18 GHz | 18 to 40 GHz |
|---------------------------|---------------|-------------|--------------|
| Amplitude taper           | < 1,3 dB      | < 1 dB      | < 1 dB       |
| Phase taper               | < 5°          | < 5°        | < 5°         |
| Amplitude ripple          | ± 0,7 dB      | ± 0,5 dB    | ± 0,3 dB     |
| Phase ripple              | ± 8°          | ± 6°        | ± 10°        |
| Linear cross-polarization | < - 36 dB     | < - 40 dB   | < - 40 dB    |

Table 2 : Focused quiet zone performance

|                           | 1,47 to 3 GHz | 3 to 18 GHz | 18 to 40 GHz |
|---------------------------|---------------|-------------|--------------|
| Amplitude taper           | < 1,3 dB      | < 1 dB      | < 1 dB       |
| Phase taper               | < 12°         | < 12°       | < 12°        |
| Amplitude ripple          | ± 1,2 dB      | ± 0,7 dB    | ± 0,5 dB     |
| Phase ripple              | ± 10°         | ± 10°       | ± 8°         |
| Linear cross-polarization | < - 36 dB     | < - 40 dB   | < - 40 dB    |

Table 3 : Left quiet zone performance

|                           | 1,47 to 3 GHz | 3 to 18 GHz | 18 to 40 GHz |
|---------------------------|---------------|-------------|--------------|
| Amplitude taper           | < 1,3 dB      | < 1 dB      | < 1 dB       |
| Phase taper               | < 15°         | < 12°       | < 12°        |
| Amplitude ripple          | ± 1,5 dB      | ± 0,7 dB    | ± 0,5 dB     |
| Phase ripple              | ± 12°         | ± 10°       | ± 8°         |
| Linear cross-polarization | < - 33 dB     | < - 40 dB   | < - 40 dB    |

Table 4 : Right quiet zone performance

| Antenna | Reflector size (in m) | polarization  | frequency (in GHz) | type           |
|---------|-----------------------|---------------|--------------------|----------------|
| n° 1    | 0,4 x 0,8             | single linear | 12                 | Shaped beam    |
| n° 2    | 2,4 (diameter)        | dual linear   | 1,5 to 2,4         | Parabolic dish |
| n° 3    | 2,4 (diameter)        | dual linear   | 2,4 to 3           | Parabolic dish |
| n° 4    | 0,4 x 0,8             | dual circular | 3,7 to 4,1         | ELCA           |
| n° 5    | 0,4 x 0,8             | dual circular | 5,8 to 6,3         | ELCA           |

Table 5 : Characteristics of antennas used for measurements

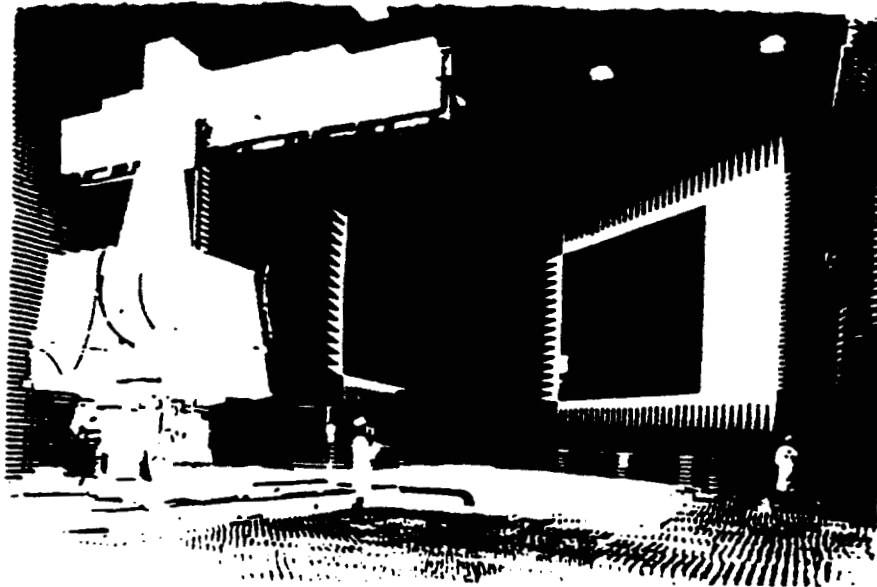


Figure 1 : View of the anechoic chamber of the MISTRAL compact range

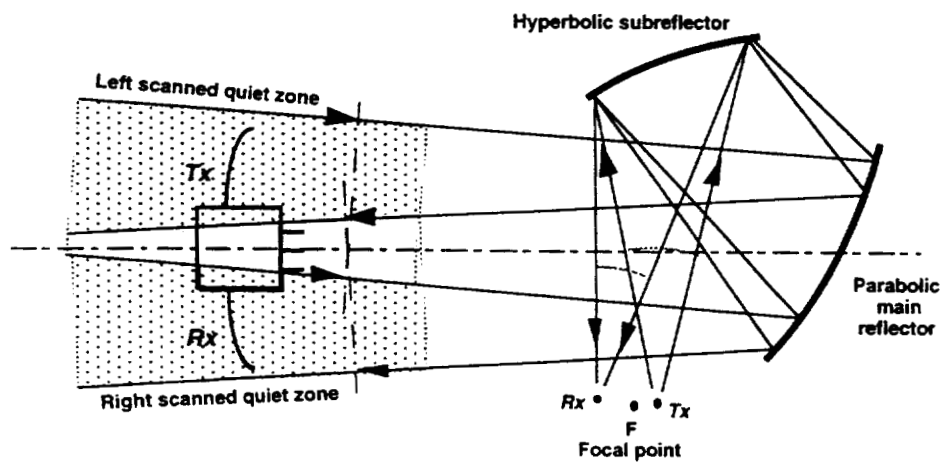


Figure 2 : Exemple of End-to-End test configuration

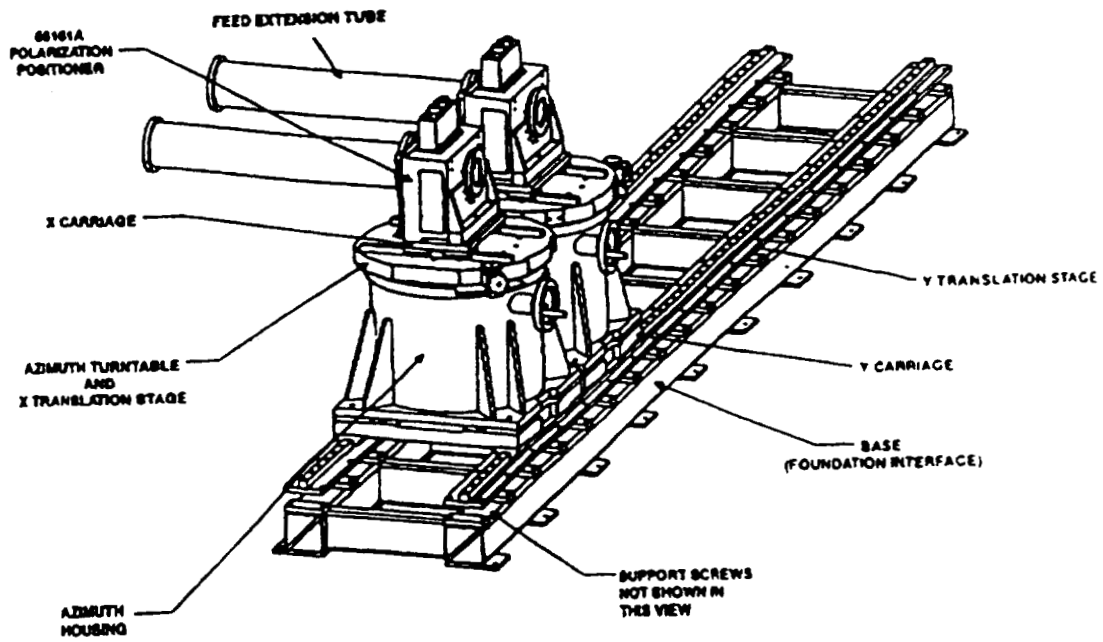


Figure 3 : View of the feed positioner

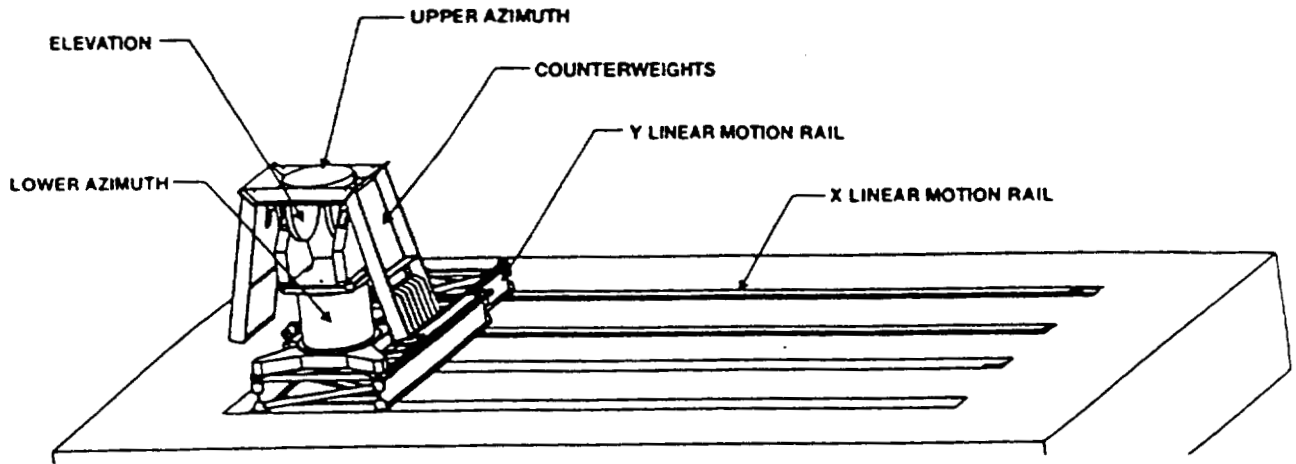


Figure 4 : View of the specimen positioner

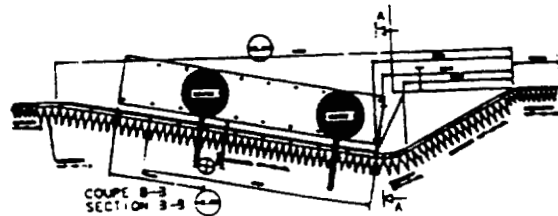


Figure 5 : Top view of the feed room slanted wall

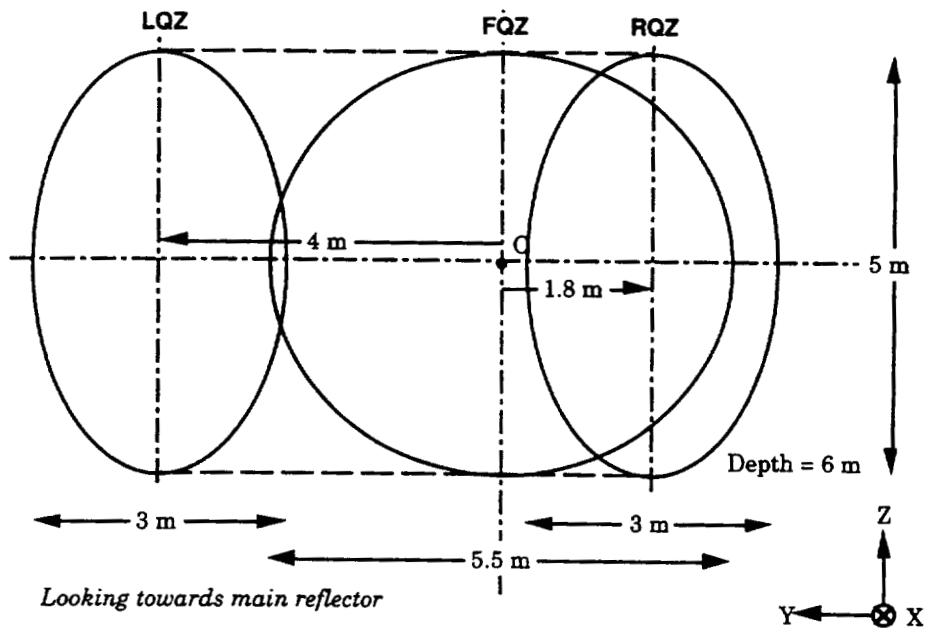


Figure 6 : Sizes and positions of the probed quiet zones

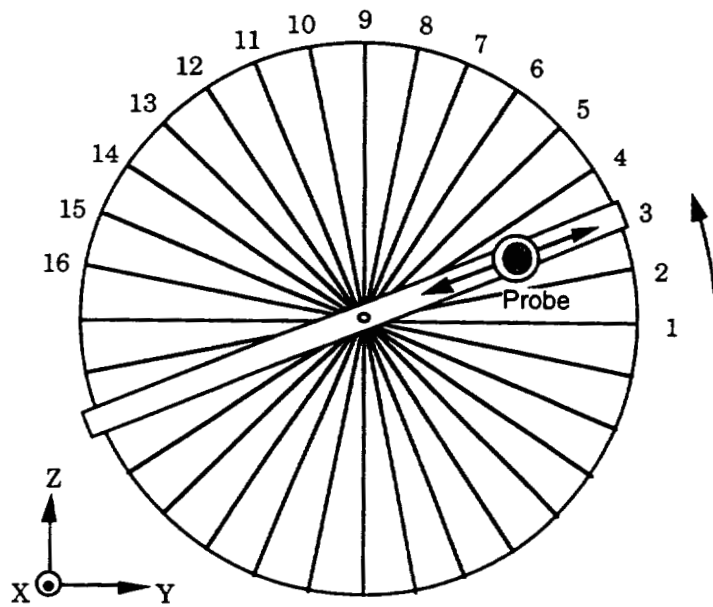


Figure 7 : Plane Wave probing angular spacing

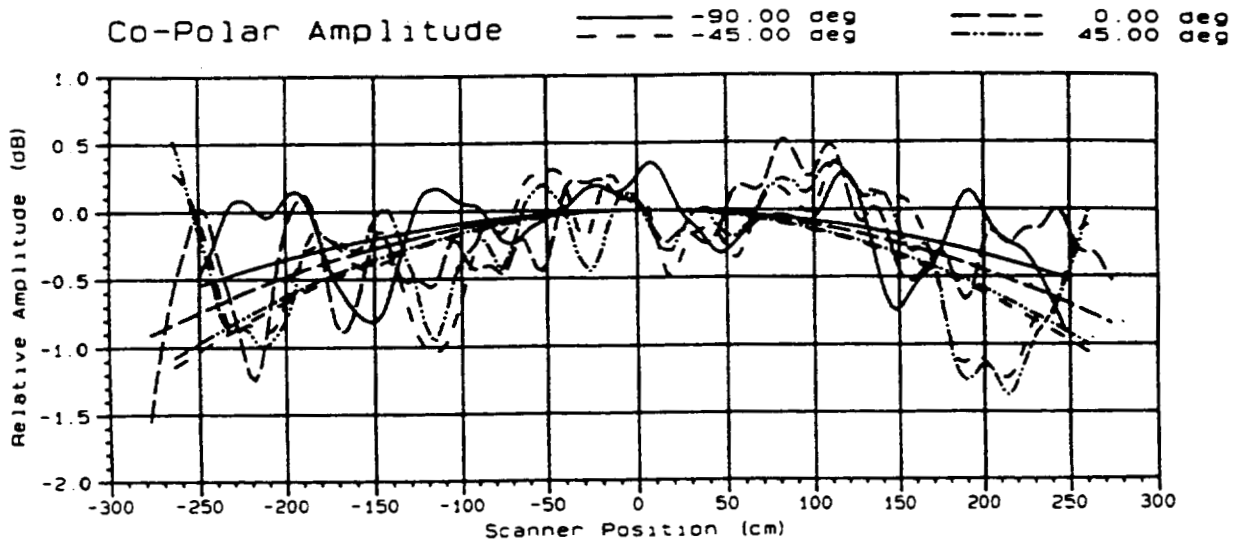


Figure n° 8a : Amplitude taper and ripple at 2,35 GHz

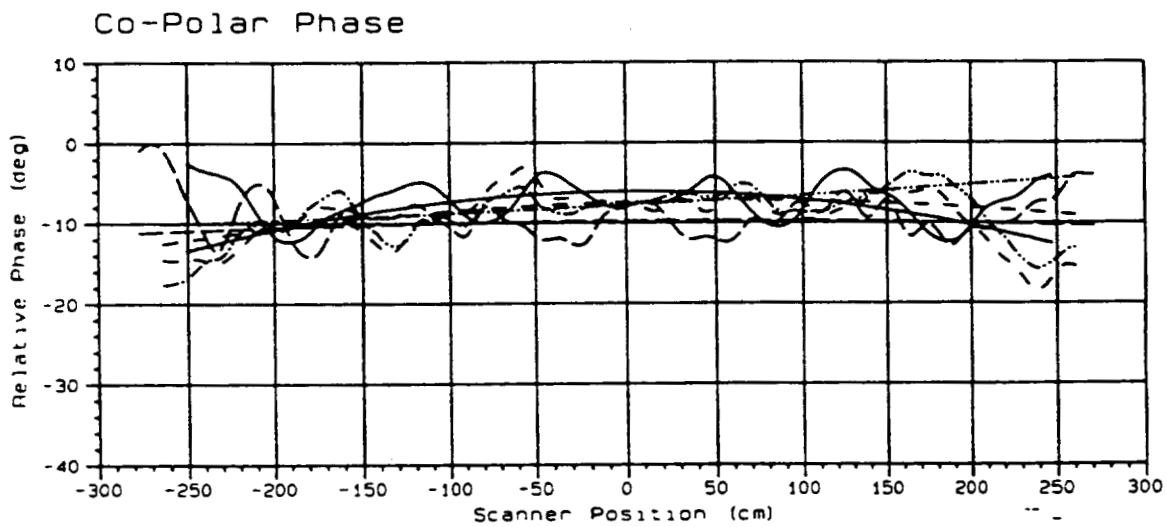


Figure n° 8b : Phase taper and ripple at 2,35 GHz

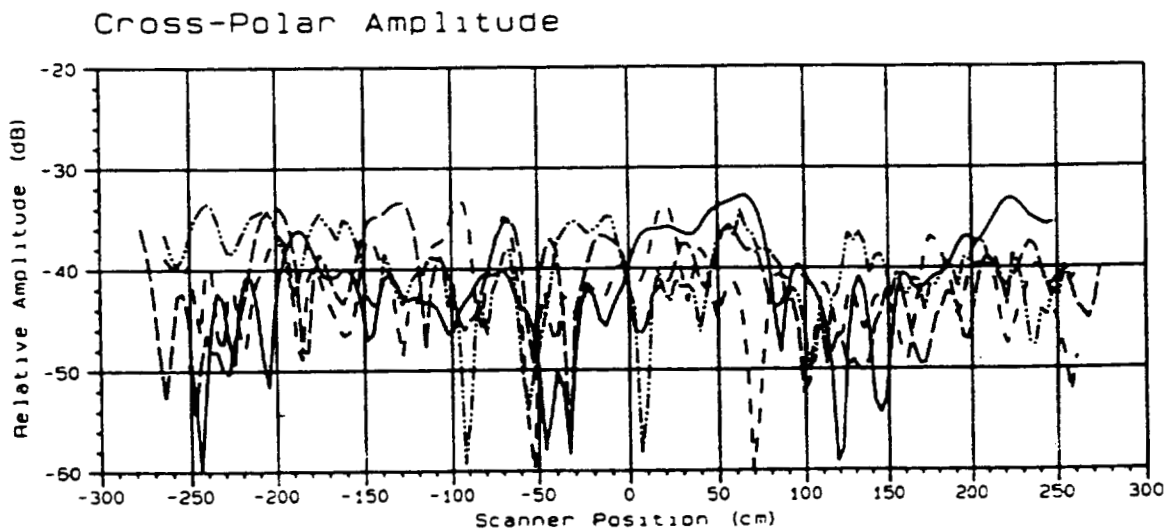


Figure n° 8c : Cross-polarization at 2.35 GHz

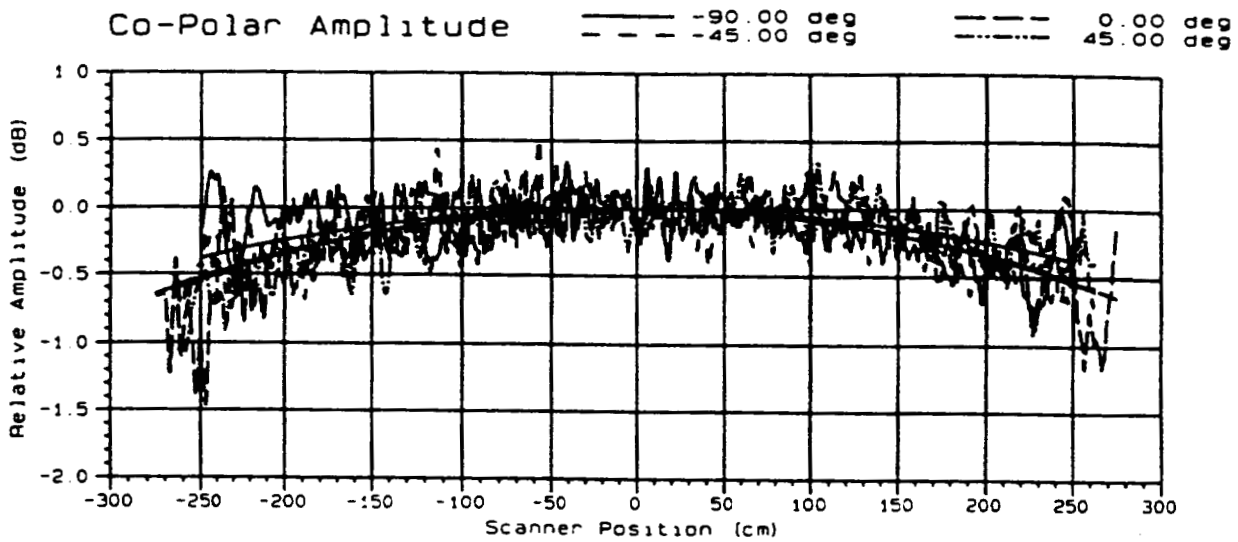


Figure n° 8d : Amplitude taper and ripple at 27 GHz

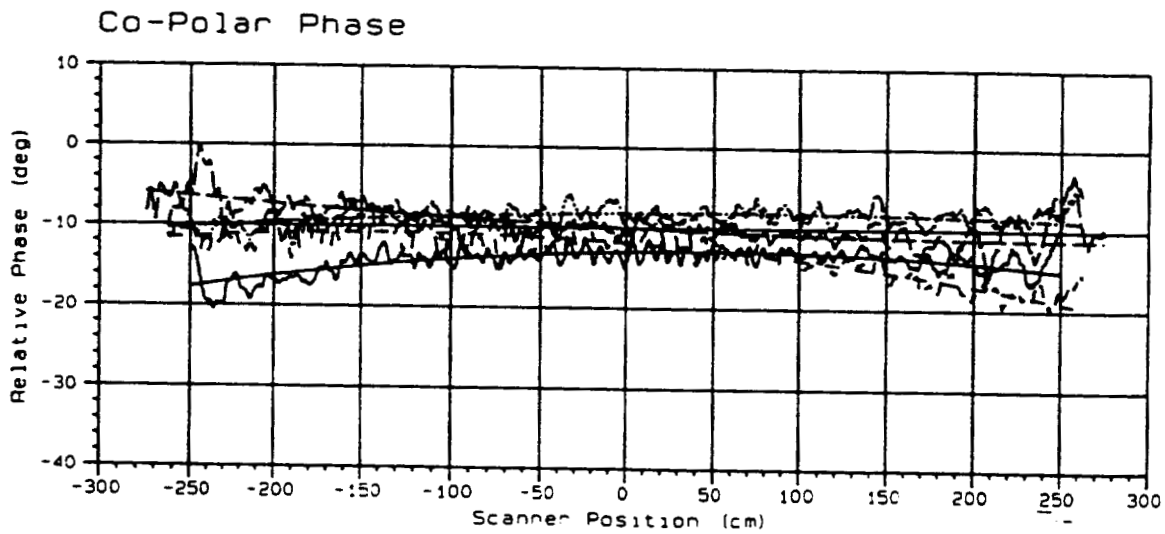


Figure n° 8e : Phase taper and ripple at 27 GHz

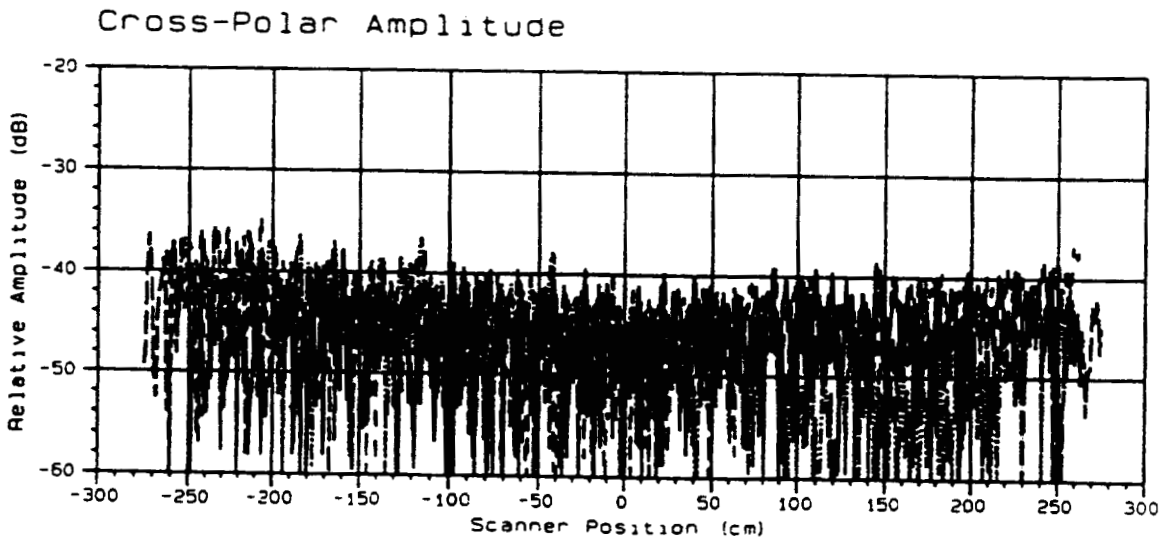
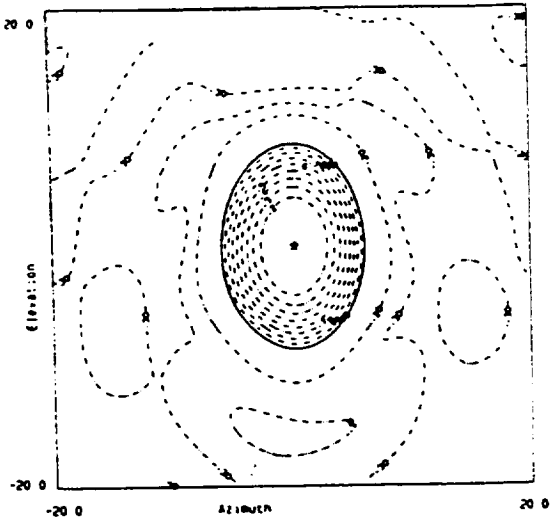


Figure n° 8f : Cross-polarization at 27 GHz

Mistral Reference Antenna Measurement  
Antenna 4 (ACL4) Circular  
Co-Polar



CNES Reference Antenna Measurement  
Antenna 4 (ACL4) Circular  
Co-Polar

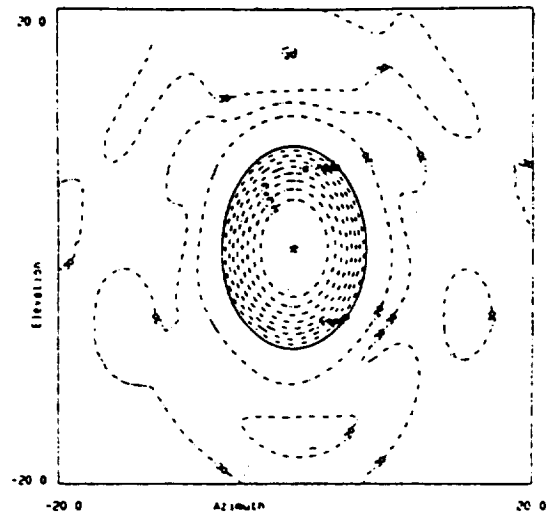


Figure n° 9a : Comparison of rasterscans for copolarization

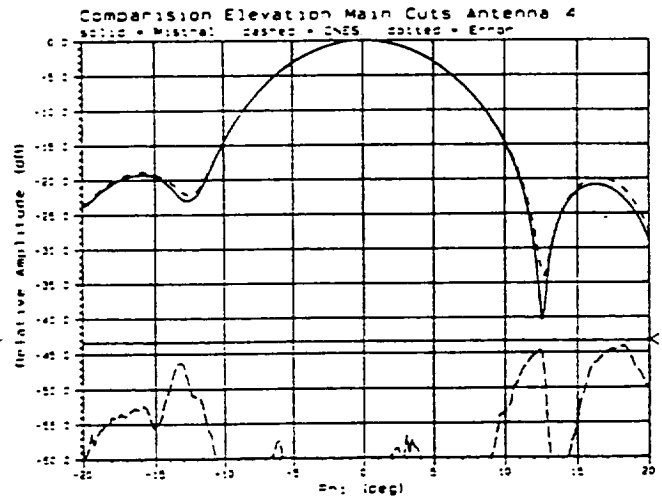
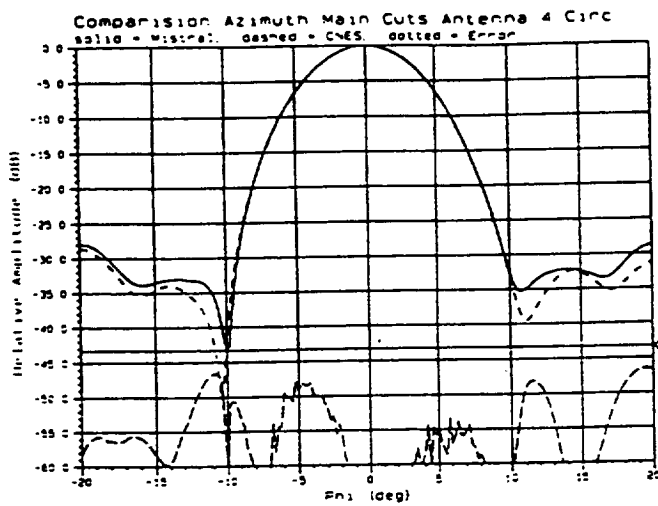


Figure n° 9b : Comparison of azimuth and elevation cuts for copolarisation

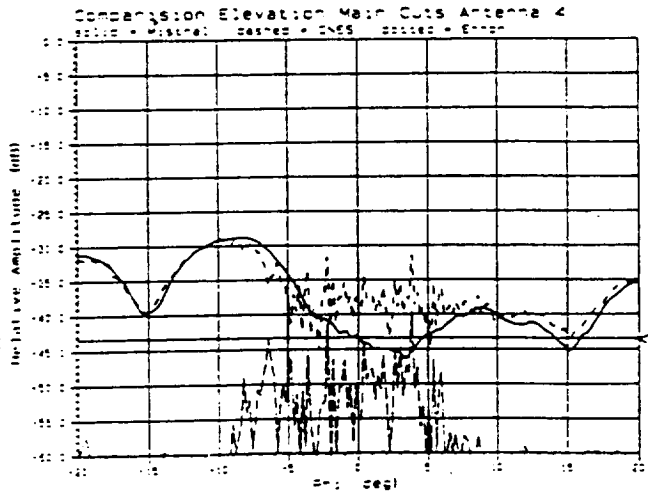
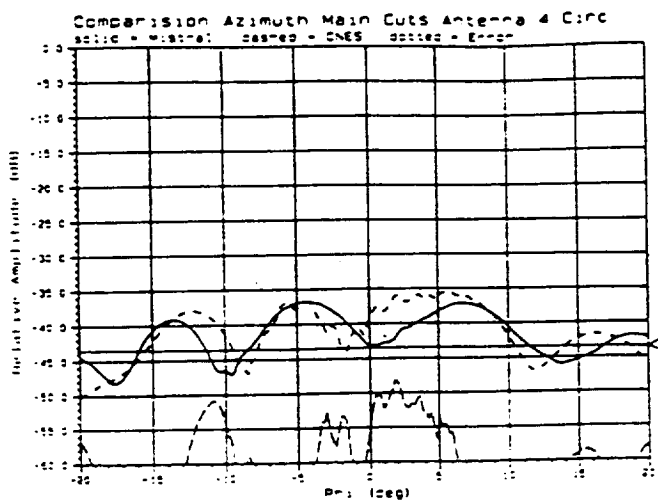


Figure n° 9c : Comparison of azimuth and elevation cuts for cross-polarization

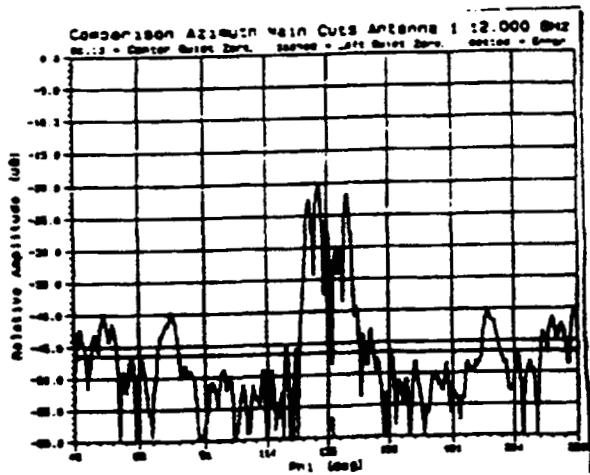


Figure 10a : Comparison between LQZ and FQZ for azimuth main cut of antenna 1 in cross-polarization

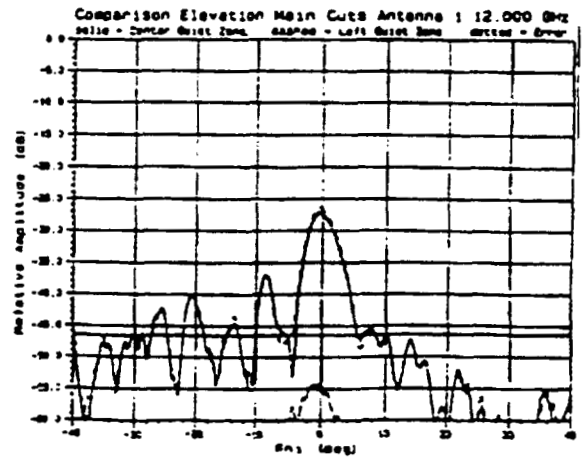


Figure 10b : Comparison between LQZ and FQZ for elevation main cut of antenna 1 in cross-polarization

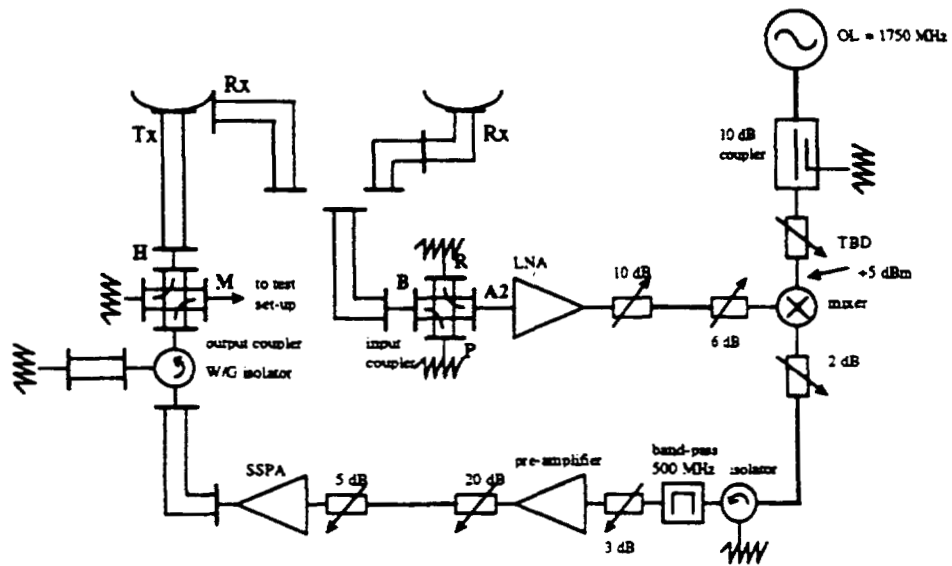


Figure 11 : Mini payload schematic

# REPORT DOCUMENTATION PAGE

*Form Approved*  
OMB No. 0704-0188

Public reporting burden for this collection of information is estimated to average 1 hour per response, including the time for reviewing instructions, searching existing data sources, gathering and maintaining the data needed, and completing and reviewing the collection of information. Send comments regarding this burden estimate or any other aspect of this collection of information, including suggestions for reducing this burden, to Washington Headquarters Services, Directorate for Information Operations and Reports, 1215 Jefferson Davis Highway, Suite 1204, Arlington, VA 22202-4302, and to the Office of Management and Budget, Paperwork Reduction Project (0704-0188), Washington, DC 20503.

|  |   |  |   |  |
|--|---|--|---|--|
| <b>1. AGENCY USE ONLY (Leave blank)</b>  |   | <b>2. REPORT DATE</b><br>February 1999                         | <b>3. REPORT TYPE AND DATES COVERED</b><br>Conference Publication             |  |
| <b>4. TITLE AND SUBTITLE</b><br>Twentieth Space Simulation Conference<br>The Changing Testing Paradigm   |   |  | <b>5. FUNDING NUMBERS</b><br><br>Code 540                                     |  |
| <b>6. AUTHOR(S)</b><br><br>Compiled by Joseph L Stecher III  |   |  |   |  |
| <b>7. PERFORMING ORGANIZATION NAME(S) AND ADDRESS (ES)</b><br><br>Goddard Space Flight Center<br>Greenbelt, Maryland 20771   |   |  | <b>8. PERFORMING ORGANIZATION REPORT NUMBER</b><br><br>98A01761               |  |
| <b>9. SPONSORING / MONITORING AGENCY NAME(S) AND ADDRESS (ES)</b><br><br>National Aeronautics and Space Administration<br>Washington, DC 20546-0001  |   |  | <b>10. SPONSORING / MONITORING AGENCY REPORT NUMBER</b><br><br>CP-1999-208598 |  |
| <b>11. SUPPLEMENTARY NOTES</b><br><br>Co-sponsors: Institute of Environmental Sciences and Technology, American Institute for Aeronautics and Astronautics, American Society for Testing and Materials, and Canadian Space Agency  |   |  |   |  |
| <b>12a. DISTRIBUTION / AVAILABILITY STATEMENT</b><br>Unclassified-Unlimited<br>Subject Category: 18<br>Report available from the NASA Center for AeroSpace Information,<br>7121 Standard Drive, Hanover, MD 21076-1320. (301) 621-0390.  |   |  | <b>12b. DISTRIBUTION CODE</b>   |  |
| <b>13. ABSTRACT (Maximum 200 words)</b><br><br>The Institute of Environmental Sciences and Technology's Twentieth Space Simulation Conference, "The Changing Testing Paradigm" provided participants with a forum to acquire and exchange information on the state-of-the-art in space simulation, test technology, atomic oxygen, program/system testing, dynamics testing, contamination, and materials. The papers presented at this conference and the resulting discussions carried out the conference theme "The Changing Testing Paradigm." |   |  |   |  |
| <b>14. SUBJECT TERMS</b><br>Space Simulation, Thermal Simulation, Contamination Control, Dynamic Testing,<br>Spacecraft Materials, New Approaches and Facilities   |   |  | <b>15. NUMBER OF PAGES</b><br>366   |  |
|  |   |  | <b>16. PRICE CODE</b>   |  |
| <b>17. SECURITY CLASSIFICATION OF REPORT</b><br>Unclassified   | <b>18. SECURITY CLASSIFICATION OF THIS PAGE</b><br>Unclassified | <b>19. SECURITY CLASSIFICATION OF ABSTRACT</b><br>Unclassified | <b>20. LIMITATION OF ABSTRACT</b><br>UL                                       |  |